



Delft University of Technology

BiGlobal Stability of Shear Flows Spanwise & Streamwise Analyses

Groot, Koen

DOI

[10.4233/uuid:60ef07b2-00db-418b-9495-5a9baf6105df](https://doi.org/10.4233/uuid:60ef07b2-00db-418b-9495-5a9baf6105df)

Publication date

2018

Document Version

Final published version

Citation (APA)

Groot, K. (2018). *BiGlobal Stability of Shear Flows: Spanwise & Streamwise Analyses*. [Dissertation (TU Delft), Delft University of Technology]. <https://doi.org/10.4233/uuid:60ef07b2-00db-418b-9495-5a9baf6105df>

Important note

To cite this publication, please use the final published version (if applicable).

Please check the document version above.

Copyright

Other than for strictly personal use, it is not permitted to download, forward or distribute the text or part of it, without the consent of the author(s) and/or copyright holder(s), unless the work is under an open content license such as Creative Commons.

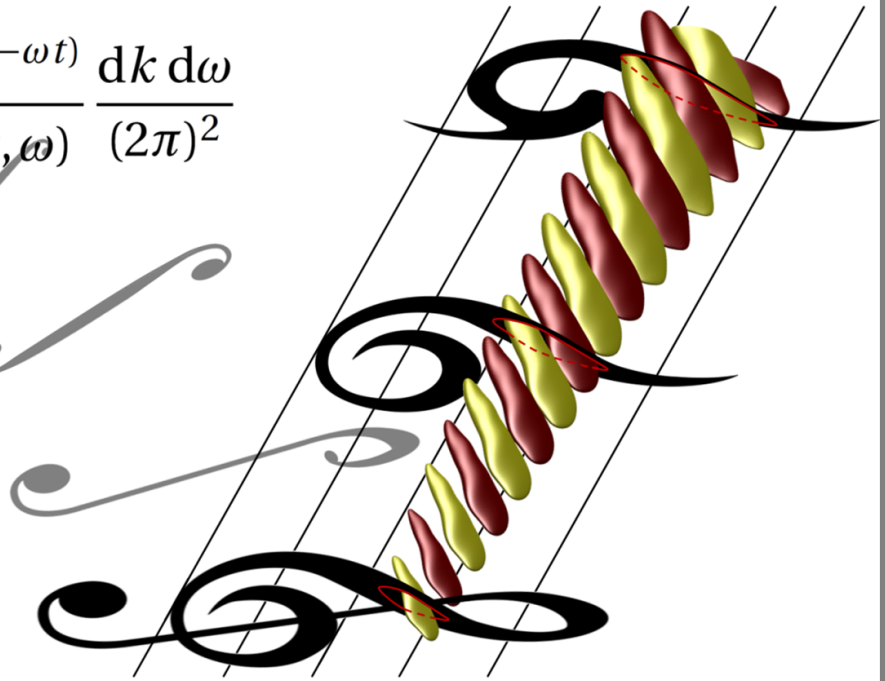
Takedown policy

Please contact us and provide details if you believe this document breaches copyrights.
We will remove access to the work immediately and investigate your claim.

BiGlobal Stability of Shear Flows

Spanwise & Streamwise Analyses

$$\iint \frac{e^{i(ky - \omega t)}}{\tilde{\mathcal{D}}(k, \omega)} \frac{dk d\omega}{(2\pi)^2}$$



Koen Jasper Groot

BiGLOBAL STABILITY OF SHEAR FLOWS

SPANWISE & STREAMWISE ANALYSES

BiGLOBAL STABILITY OF SHEAR FLOWS

SPANWISE & STREAMWISE ANALYSES

Proefschrift

ter verkrijging van de graad van doctor
aan de Technische Universiteit Delft,
op gezag van de Rector Magnificus prof. dr. ir. T.H.J.J. van der Hagen,
voorzitter van het College voor Promoties,
in het openbaar te verdedigen op
vrijdag 7 december 2018 om 15:00 uur

door

Koen Jasper GROOT

Ingenieur in de Lucht- en Ruimtevaart,
Technische Universiteit Delft, Nederland,
geboren te Hoorn, Nederland.

Dit proefschrift is goedgekeurd door de promotor en copromotoren.

Samenstelling promotiecommissie:

Rector Magnificus,	voorzitter
Dr.ir. B.W. van Oudheusden,	Technische Universiteit Delft, promotor
Dr.ir. M. Kotsonis,	Technische Universiteit Delft, copromotor
Dr.ir. H.M. Schuttelaars,	Technische Universiteit Delft, copromotor

Onafhankelijke leden:

Prof.dr. H.L. Reed,	Texas A&M University, Verenigde Staten
Prof.dr. D. Henningson,	Kungliga Tekniska Högskolan, Zweden
Prof.dr.habil. S. Hickel,	Technische Universiteit Delft
Dr. L. Lesshaft,	Laboratoire d'Hydrodynamique de École polytechnique, Frankrijk
Prof.dr.ing. F. Scarano,	Technische Universiteit Delft, reservelid

Dr. F. Pinna aan het Von Kármán Institute for Fluid Dynamics heeft in belangrijke mate aan de totstandkoming van het proefschrift bijgedragen.



<i>Keywords:</i>	Flow instability, measured base flows, Micro-ramp, Swept-wing boundary layer, Crossflow instability, Streamwise BiGlobal problem
<i>Printed by:</i>	Rijnja Repro Delft
<i>Front:</i>	Author's cartoon of how complex integration theory and the instability of flows, specifically the secondary instability of crossflow vortices, together make an art form. Detail: the integral grasps for an understanding of the complex frequency (ω -)spectrum
<i>Back:</i>	The maroon fields represent how a advection transfers a chunk of energy (left field) through an inflow boundary (on) to the eigenfunction in the interior (right field). The eigenfunction must decay in the streamwise direction for the total energy to be conserved. See figure 8.18 for an elaboration of the outflow case

Copyright © 2018 by K.J. Groot

ISBN 978-94-6366-115-7

An electronic version of this dissertation is available at
<http://repository.tudelft.nl/>.

CONTENTS

Summary	xi
Samenvatting	xv
1 Introduction	1
1.1 Transition mechanisms	2
1.2 Transition prediction based on stability analysis	4
1.3 Higher-dimensional flows: BiGlobal stability	6
1.4 Thesis scope: advances in BiGlobal stability	8
1.4.1 Applicability of BiGlobal analysis on experimentally measured base flows	8
1.4.2 Numerical issues in streamwise BiGlobal analyses	10
1.5 Model problems	13
1.5.1 Measured base flows: analytical profiles	14
1.5.2 Measured base flows: micro-ramp wake	14
1.5.3 Measured base flows: crossflow vortices	16
1.5.4 Streamwise BiGlobal problem: non-parallel boundary layer	18
1.6 Thesis Objectives and Outline	20
References	21
2 Stability Theory	29
2.1 Navier-Stokes equations	29
2.2 Perturbations equations	30
2.3 Stability equations	31
2.3.1 Dimensionality reduction: Fourier transformation	32
2.3.2 Atoms of dynamics: discrete eigensolutions	32
2.3.3 Specific expansion ansatzes	34
2.3.4 LST: non-parallel Orr-Sommerfeld equation	36
2.3.5 Parallel flow assumption	37
2.4 Basic solution features	38
2.4.1 The amplitude factor \tilde{q}	39
2.4.2 The factor $e^{i(\Theta-\omega t)}$ for individual modes: Phase speed	39
2.4.3 The factor $e^{i(\Theta-\omega t)}$ for an ensemble of modes: Group speed	39
2.4.4 Amplification in space	42
2.4.5 The Gaster-transformation	43
2.4.6 Negative wavenumbers and frequencies	44
2.5 Assessing the underlying physical mechanisms	45
2.5.1 Reynolds-Orr equation	46
2.5.2 Transport equations for the eigenfunctions	49

2.6	Boundary conditions	51
2.7	Extension to compressible flow	53
	References	56
3	Numerical Methodology	59
3.1	Discretisation	59
3.1.1	Chebyshev polynomials	59
3.1.2	Characteristic Lagrange polynomials	61
3.1.3	Spectral derivatives	65
3.1.4	Mappings	68
3.1.5	Amplitude-Coefficient Matrices (ACM's)	71
3.1.6	Quadratic eigenvalue problems	73
3.1.7	Boundary conditions	74
3.1.8	Boundary condition implementation	79
3.2	Eigensolvers	80
3.2.1	QZ algorithm	81
3.2.2	Arnoldi algorithm	82
	References	83
4	Measured Base Flows: Generic Shear Profiles	85
4.1	Introductory remarks	85
4.2	Stability problem formulation	87
4.2.1	Extracting the underlying mechanisms	89
4.3	Discretization specifics & verification	90
4.3.1	Convergence and verification with literature	91
4.4	Spectrum and eigenfunctions	92
4.5	Exposing the physical mechanism of the eigenmode	95
4.5.1	Decomposition of the eigenvalue	95
4.5.2	Decomposition of the eigenfunctions	97
4.5.3	Decomposition of $\tilde{u}^*\tilde{v}$	98
4.6	Physical parametric effects	100
4.6.1	Effect of the inflection point location	100
4.6.2	Effect of the Reynolds number	102
4.6.3	Role of a non-zero spanwise wavenumber	103
4.6.4	Effect of wall proximity	105
4.7	Effects associated to using a measured base flow	106
4.7.1	Spatial resolution	106
4.7.2	Spatial smoothing	109
4.7.3	Residual perturbations	115
4.8	Conclusion	117
	References	118
5	Measured Base Flows: Micro-Ramp Wake	121
5.1	Introductory remarks	121
5.2	Base flow description	124
5.3	Results	126
5.3.1	Baseline case	126

5.4	Varicose mode: spectral behaviour	129
5.5	Varicose mode: streamwise development	132
5.6	Conclusion	135
	References	135
6	Measured Base Flows: Crossflow Vortices	139
6.1	Introductory remarks	140
6.1.1	Present study	142
6.2	Experimental base flow	144
6.2.1	Tomographic PIV	145
6.2.2	Pre-processing for stability analysis	146
6.2.3	Distorted base flow and shear fields	148
6.3	Spanwise BiGlobal stability analysis.	151
6.3.1	Formulation	151
6.3.2	Reynolds-Orr equation	153
6.3.3	Discretization specifics	154
6.3.4	Shift-invert strategy	155
6.4	Results	157
6.4.1	Base spectrum	157
6.4.2	Effect of ensemble size	162
6.4.3	Divergence of the in-plane flow	166
6.4.4	Effect of wall-normal extrapolation	167
6.4.5	Applicability of the Gaster-transformation	167
6.4.6	Comparison with experiments	170
6.4.7	Effect of primary vortex strength	175
6.4.8	Effect of periodic boundary conditions	180
6.4.9	Reynolds number dependence	181
6.5	Conclusion	185
	References	187
7	Local approach: Briggs's Criterion for Absolute Instability	193
7.1	The Fourier inversion integrals	194
7.1.1	Green's function formulation	194
7.1.2	The dispersion relation	196
7.1.3	Absolute stability: zero group speed	197
7.1.4	Integration order	199
7.2	The k -integral	199
7.3	The ω -integral	205
7.4	The case $\bar{V}_e \neq 0$	208
7.4.1	The role of the Ω -branch	209
7.4.2	Manipulating the branches and contours for $\bar{V} \neq 0$	210
7.4.3	The problematic spatial character and boundary conditions	213
7.4.4	Inconclusiveness of unstable parabolic branches	216
7.5	Non-holomorphic regions in the ω -integrand	218
7.5.1	The case $\bar{V}_e = 0$	220
7.5.2	The case $\bar{V}_e \neq 0$	223

7.6 Conclusion	227
References	228
8 Global approach: Absolute Stability from Global Spectra	231
8.1 Introductory remarks	231
8.1.1 Present study	232
8.2 Model problem	233
8.3 Algebraic spectrum analysis	235
8.3.1 Separated boundary conditions	236
8.3.2 Periodic boundary conditions	237
8.3.3 Absolute and essential spectrum limits	239
8.3.4 Solution method: weighted formulation (symmetrization)	240
8.4 Computational spectrum analysis for large L	242
8.4.1 Constant coefficient problem	242
8.4.2 Blasius boundary layer problem	246
8.4.3 Enforced periodicity and vanishing inhomogeneity	250
8.5 Wave packet evolution	254
8.6 Discussion of physical interpretations	260
8.6.1 The spatial growth rate: a physical imperative	260
8.6.2 Physical interpretation of symmetrization	264
8.7 Conclusion	266
References	268
9 Conclusion	271
9.1 Measured base flows	271
9.1.1 Analytical generic shear profiles	271
9.1.2 Micro-ramp wake	272
9.1.3 Crossflow vortices	273
9.2 The streamwise BiGlobal problem	274
A Complex Integration Theory	277
A.1 Decomposing complex integrals	279
A.1.1 Cauchy-Goursat theorem	279
A.1.2 Deforming integration contours	282
A.1.3 Closing the integration contour	283
A.1.4 Jordan's lemma	286
A.1.5 The temporal ansatz & causality	288
A.2 Evaluation for simple poles	289
A.2.1 Residue at the pole	289
A.2.2 Possible placements of the contour	291
A.2.3 Discrete mode ansatz and δ -functions	293
A.3 Singularities: poles moving onto the contour	294
A.3.1 Single pole	295
A.3.2 Double pole	297
A.3.3 Single poles from opposite sides	297
A.3.4 Analytical continuation and contour pinching	298
References	298

B Model problem in chapter 8	301
References	302
Acknowledgements	305
Curriculum Vitæ	311
List of Publications	313

SUMMARY

Laminar-turbulent transition dictates an increase in skin friction. The resulting turbulent skin friction contributes to approximately 40% of the total drag of commercial aircraft. Reducing the turbulent flow region by postponing transition can therefore significantly reduce the carbon footprint and costs of flying. Transition prediction is required in order to do so, which depends on a detailed understanding of the transition process.

The first ingredient for transition prediction is determining the disturbance amplification for a given flow. Tools used in industry adopt simplifying assumptions, restricting the incorporated perturbation dynamics. For that reason the transition process is understood only up to locations in the flow where the essential dynamics is more complicated. The BiGlobal stability method provides the next step, as it incorporates all dynamics of infinitesimal perturbations to two-dimensional laminar flows, i.e. flows that support shear components contained in a plane. This is the point where it supersedes the commonly used, lower fidelity methods, that account for a second dimension to a partial extent only or not at all.

The second ingredient for transition prediction is the amplitude threshold at which transition occurs, which is usually measured experimentally. Advances in measurement techniques, specifically tomographic Particle Image Velocimetry (tomo-PIV), allow capturing all flow components in a three-dimensional volume with high resolution. Necessarily having to measure the transition location prompts the question whether the perturbation amplification can be determined by performing stability analysis on the measured base flow. This is the first main objective of this thesis: establishing the applicability of stability theory to measured base flows. Three model problems are considered in its regard.

The first problem considers one-dimensional analytical profiles of a free shear layer; allowing studying the approach within a well controlled analytical and computational setting first. The effects of limited spatial resolution, spatial smoothing and using a finite number of instantaneous fields (snapshots) to construct a mean flow are assessed. The spatial smoothing inherent to the PIV post-processing procedure is found to have the most significant impact, because it directly reduces the shear magnitude. However, the processes underlying the instability modes are found to be robust. Therefore, if the results can be validated with the instantaneous experimental data, the stability solutions deliver insight into the perturbation dynamics. An outlook is the generalisation to two-dimensional analytical flows. It is suggested that the generality of such an approach can outweigh the stipulation that the base flow should satisfy the Navier-Stokes equations.

The second problem considers the wake of a micro-ramp vortex generator, the first case using experimental measurement data. A challenge is the significant perturbation amplitude close to the ramp. The BiGlobal stability method successfully resolves the two inherent modes (the varicose and sinuous modes) supported by the wake. The most unstable wavelength and hairpin structure of the dominant varicose mode matches with

the experimental data. Limited amplification factors are retrieved, which is expected, because the wake does not transition to turbulence in the considered region. The results are converged with the number of snapshots. Furthermore, it is found that the two-dimensional stability characteristics closely match one-dimensional analyses applied to the centerline profile, modelling the spanwise extent of the shear layer by imposing a spanwise wavelength. An outlook is to compare the results to the analysis of a direct numerical simulation (DNS) to validate the approach. Successfully comparing the computational and experimental data on the level of the stability results is unprecedented.

The third problem considers crossflow vortices in a swept-wing boundary layer, also in conjunction to experimental measurements. A challenge in this case is the base flow's complicated topology, housing three different modes. Technical difficulties involve a low frequency spanwise shake of the crossflow vortices and the strong shear close to the wall. Nevertheless, the BiGlobal stability method successfully retrieves all pertinent instability modes, labelled type I, II and III. Mode III is discarded for further analysis in anticipation of the effect of the base flow uncertainty close to the wall. The type I eigenmode's spatial structure matches that of a representative POD mode, when selecting the same streamwise wavelength. The eigenmode's spatial growth is smaller than that of the POD mode couple, but it matches with hot-wire measurements. Establishing the convergence with the number of snapshots is challenging due to the spanwise shake. The growth rates fluctuate, but the uncertainty decays as the number of snapshots is increased. The Reynolds-Orr terms, which represent the eigenmode's signature through terms in the governing equations, are found to be robust. The structural impact of the in-plane advection terms is identified, which provides an explanation for the relative uncertainty of the type II over the type I mode. A weaker crossflow vortex is analysed, so to assess the vortex strength effect. The spanwise shear is found to be the main translator of the crossflow vortex strength for both modes, while the wall-normal shear produces the type II mode most significantly. This is corroborated by the snapshot convergence study. An outlook is analysing cases where computational approaches are very challenging, for example, such as merging crossflow vortices.

In the previous model problems, the stability domains are chosen such that they do not contain the predominant (streamwise) velocity component. The aforementioned situations in which the lower fidelity stability methods are inapplicable involve the perturbation dynamics over two-dimensional geometries oriented in the streamwise direction. If the BiGlobal domain is aligned with the streamwise direction, however, numerical solutions are subject to convergence problems, e.g. the results are sensitive to the streamwise domain length and truncation boundary conditions. No ideal truncation boundary conditions exist, so the literature views this problem as one of the boundary conditions. For this reason, next to leaving many theoretical questions unanswered, the BiGlobal stability method has never prospered over the traditional, lower fidelity tools used in industry. Finding the cause and solving these problems is the second main objective of this thesis.

The model problem considered for this objective is a one-dimensional non-parallel boundary layer flow. The non-parallel advection represents the new term in the BiGlobal equations and the single spatial dimension allows coping with the very low convergence rates numerically. It is found that the solutions of interest grow exponentially in space

due to the combination of advection and flow inhomogeneity, both in the streamwise direction. This growth is found to be the cause for the numerical issues, which are annihilated by using a weighted problem formulation. In doing so, the spectrum converges to the so-called *absolute spectrum* as the domain length tends to infinity. This spectrum provides stability properties of the least stable wave packet. If it is unstable, the problem supports a globally absolutely unstable perturbation in the considered reference frame. For this (class of) problem(s), it is mathematically proven that the spectrum converges to this limit if so-called *separated boundary conditions* are deployed, which resolves the issue of the unknown truncation boundary conditions. So, what appeared to be a problem of the boundary conditions was instead induced by advection; the system's internal dynamics. If the weighted formulation is not used, the spectrum diverges toward a different limit (the so-called *essential spectrum*) for too large domain lengths, due to finite precision arithmetic. Once this occurs, the spectrum is sensitive to machine errors and the absolute stability information can then no longer be extracted from the spectrum. An outlook is the extension to two-dimensional flow cases. A first endeavour should demonstrate the global absolute stability of the Blasius boundary layer. Long term unanswered questions can then be approached, such as whether laminar separation bubbles or the flow around steps support global absolute instability mechanisms.

SAMENVATTING

Laminaire-turbulente transitie dicteert in een toename in huid wrijving. De resulterende turbulente wrijving draagt ongeveer 40% bij aan de totale weerstand van een commercieel vliegtuig. Het verminderen van de turbulente regio door transitie uit te stellen kan daarom significant de ecologische voetafdruk en de kosten om te vliegen verminderen. Transitie voorspelling is hiervoor nodig, welke afhangt van een gedetailleerd begrip van het transitie proces.

Het eerste ingrediënt nodig voor transitie voorspelling is het bepalen van de verstoringssamplificatie voor een gegeven stroming. Het door de industrie gebruikte gereedschap hiervoor ontleent versimpelende aannames, die de belichaamde verstoringsdynamica beperken. Om die reden is het transitie proces alleen begrepen tot aan plaatsen in de stroming waar de essentiële dynamica gecompliceerder is. De BiGlobale stabiliteitsmethode biedt de volgende stap, omdat het alle mogelijke dynamica van infinitesimale verstoringen op tweedimensionale laminaire stromingen, d.w.z. stromingen die scheringscomponenten ondersteunen in een vlak, aankan. Dit is het punt waar het voorbijstreeft aan de veelal gebruikte methoden met lagere getrouwheid, welke alleen gedeeltelijk of helemaal niet rekening houden met een tweede dimensie.

Het tweede ingredient voor transitie voorspelling is de amplitude drempel waarop transitie plaatsvindt; deze wordt voornamelijk experimenteel gemeten. Voortgangen in de meettechnieken, specifiek tomografische Particle Image Velocimetrie (PIV), staan toe alle snelheidscomponenten in een driedimensionaal volume te vangen met een hoge resolutie. Als de transitie locatie al gemeten wordt, roept dat de vraag op of de verstoringssamplificatie kan worden bepaald door stabiliteitsanalyse toe te passen op een gemeten achtergrondstroming. Dit is het eerste hoofddoel van deze thesis: het bepalen van de toepasbaarheid van stabiliteitstheorie op gemeten achtergrondstromingen. Drie model problemen worden beschouwd in deze trant.

Het eerste probleem beschouwt eendimensionale profielen van een vrije afschuiflaag; welke toestaat de aanpak eerst te bestuderen binnen een goed gecontroleerde analytische en numerieke omgeving. De effecten van een gelimiteerde ruimtelijke resolutie, ruimtelijke afvlakking en het gebruik van een eindig aantal onmiddellijke velden (snapshots) om een gemiddelde stroming te construeren zijn getoetst. De ruimtelijke afvlakking inherent aan de nabewerkingsprocedure van PIV vertoont de meest significante impact, omdat dit effect de schering magnitude direct vermindert. Desondanks, zijn de processen achter de stabiliteitsmodellen robuust te zijn. Als derhalve de resultaten kunnen worden gevalideerd met de instantane experimentele data, leveren de stabiliteitsoplossingen een inzicht in de verstoringsdynamica. Een uitzicht is de analyse te generaliseren naar tweedimensionale analytische stromingen. Het is voorgesteld dat de algemeenheid van een dergelijke aanpak zwaarder kan wegen dan de eis dat de achtergrondstroming voldoet aan de Navier-Stokes vergelijkingen.

Het tweede probleem beschouwt het zog van een micro-helling (micro-ramp) vortex

generator, het eerste geval waarin experimentele data gebruikt wordt. Een uitdaging is de significante verstoringssamplitude dicht bij de helling. De BiGlobale stabiliteitsmethode representeert de twee inherente modes (de symmetrische en antisymmetrische modes) ondersteund door het zog met succes. De meest instabiele golflengte en haarspeld structuren van de dominante symmetrische mode kloppen met de experimentele data. Een gelimiteerde amplificatie factor is verkregen, welke te verwachten is, omdat het zog geen transitie naar turbulentie vertoond in deze regio. De resultaten zijn geconvergeerd met het aantal snapshots. Het is verder bepaald dat de tweedimensionale stabiliteitskarakteristieken nauw aansluiten met eendimensionale analyses toegepast op het middellijn profiel, terwijl de spanwijze grootte van de afschuiflaag gemodelleerd wordt door het opleggen van een spanwijze golflengte. Een uitzicht is de resultaten te vergelijken met de analyse van een directe numerieke simulatie (DNS) om de aanpak te valideren. Het succesvol vergelijken van de berekende en gemeten data op het niveau van de stabiliteitsresultaten zijn ongeëvenaard.

Het derde probleem beschouwt kruisstromingswervelingen (crossflow vortices) in een grenslaag op een vleugel met pijlstelling, ook in conjunctie met experimentele metingen. Een uitdaging in dit geval is de complexe topologie van de achtergrondstroming, die onderdak biedt aan drie verschillende modes. Technische moeilijkheden betreffen een laagfrequente spanwijze schudden van de kruisstromingswervelingen en de sterke schering dicht bij de wand. Desalniettemin is de BiGlobale stabiliteitsmethode succesvol in het representeren van alle drie pertinente instabiliteitsmodes, bestempeld als type I, II en III. Mode III is weggelaten in verdere analyses in verwachting van een invloed van de onzekerheid van de achtergrondstroming dichtbij de wand. De ruimtelijke structuur van de type I eigenmode klopt met die van een representatieve POD mode, als dezelfde stroomwijze golflengte geselecteerd wordt. De ruimtelijke groei van de eigenmode is kleiner dan dat van het POD mode paar, maar komt overeen met hot-wire metingen. Het vaststellen van de convergentie met het aantal snapshots is uitdagend door het spanwijze schudden. De groeiratio's fluctueren, maar de onzekerheid neemt af als het aantal snapshots vergroot wordt. De Reynolds-Orr termen, welke de signatuur van een eigenmode zijn door de termen van de beschrijvende vergelijkingen, zijn bevonden robuust te zijn. De structurele impact van de advectieve termen in het vlak is geïdentificeerd, welke de relatieve onzekerheid van de type II over de type I mode uitlegt. Een zwakkere kruisstromingswerveling is geanalyseerd, om het effect van de wervelsterkte te doorgroonden. De spanwijze schering is bevonden de hoofdvertaler te zijn van de kruiswervelsterkte voor beide modes, terwijl de wandloodrechte schering de type II mode het meest significant produceert. Dit is bekrachtigd door de snapshot convergentie studie. Een uitzicht is de analyse van gevallen waarin rekenaanpakken heel uitdagend zijn, zoals in het geval van samensmelende kruisstromingswervels.

In de vorige model problemen zijn de stabiliteitsdomeinen zo gekozen dat ze niet het dominante stroomwijze snelheidscomponent betreffen. De voorgenomen situaties in welke de stabiliteitsmethodes met lagere getrouwheid niet toepasbaar zijn omvatten verstoringsdynamica over tweedimensionale geometrieën georiënteerd in de stroomwijze richting. Als het BiGlobale domein echter uitgelijnd is met de stroomwijze richting, zijn de numerieke oplossingen onderhevig aan convergentieproblemen, de resultaten zijn bijvoorbeeld gevoelig voor de stroomwijze lengte van het domein en de inkortings-

randvoorwaarden. De ideale inkortingsrandvoorwaarden bestaan niet, dus de literatuur ziet dit als een probleem van de randvoorwaarden. Om deze reden, naast het onbeantwoord laten van vele theoretische vraagstukken, heeft de BiGlobal stabiliteitsmethode nooit zegegevierd over de traditionele methoden met lagere getrouwheid gebruikt in de industrie. Het vinden van de oorzaak en oplossing van deze problemen is het tweede hoofddoel van deze thesis.

Het model probleem beschouwd voor dit doel is een eendimensionaal niet-parallel grenslaag profiel. De niet-parallelle advectie representeert de nieuwe term in de BiGlobale vergelijkingen en de enkelzijdige ruimtelijke dimensie staat toe de lage convergentiesnelheid numeriek het hoofd te bieden. Het is bepaald dat de oplossingen die van belang zijn exponentieel groeien in de ruimte door een combinatie van advectie en stromingsinhomogeniteit, beide in de stroomwijze richting. Het is aangetoond dat deze groei de oorzaak is van de numerieke kwesties, welke vernietigd kunnen worden door een gewogen probleem formulering te gebruiken. Door dat te doen convergeert het spectrum naar het zogenaamde absolute spectrum als de domeinlengte naar oneindig gaat. Dit spectrum levert de stabiliteitskarakteristieken van het minst stabiele golfpakket. Als deze instabiel is, dan is een globale absoluut instabiele verstoring in het beschouwde referentie kader ondersteund. Voor deze (klasse van) problemen is het wiskundig bewezen dat het spectrum convergeert naar dit limiet als zogenaamde gescheiden randvoorwaarden worden ingezet, welke het probleem van de onbekende afkortingsrandvoorwaarden oplost. Dus, wat een probleem van de randvoorwaarden leek te zijn, was in de plaats daarvan geïnduceerd door advectie; de interne dynamica van het systeem. Als de gewogen methode niet gebruikt wordt, dan convergeert het spectrum naar een ander limiet (het zogenaamde essentiële spectrum) voor te grote domein lengtes, door het rekenen met een eindige precisie. Zodra dit gebeurt, wordt het spectrum gevoelig voor machinefouten en de absolute stabiliteitsinformatie kan dan niet langer uit het spectrum afgelezen worden. Een uitzicht is om de methode uit te breiden naar tweedimensionale stromingsgevallen. Een eerste inspanning moet de absolute stabiliteit van de Blasius grenslaag aantonen. Lange termijn onbeantwoorde vragen kunnen pas daarna worden aangepakt, zoals of laminaire loslatingsblazen of de stroming rondom treden (steps) globale absolute instabiliteitsmechanismen vertonen.

1

INTRODUCTION

As a consequence of the second law of thermodynamics, nature has a tendency to promote disorder. An example of this in the realm of fluid dynamics is laminar-turbulent transition. An every day example that serves as a good illustration of this phenomenon is the water flow out of a faucet. If opened slightly, the flow establishes itself in a neat and orderly way. It is usually transparent and steady. This flow regime is referred to as laminar. If opened further, the flow turns turbulent, often displaying chaotic structures that render the stream opaque. The air flow over the surfaces of air- and spacecraft wings and bodies undergoes a similar change as the flow develops along the streamwise direction. This is important, because a turbulent flow yields a higher skin friction and heat transfer, see figure 1.1.

In the case of commercial aircraft, the increase in skin friction due to turbulent flow is important, because it contributes significantly to the total drag of the aircraft [4, 5]. This, in turn, requires burning a larger amount of fuel, which yields extra service costs and

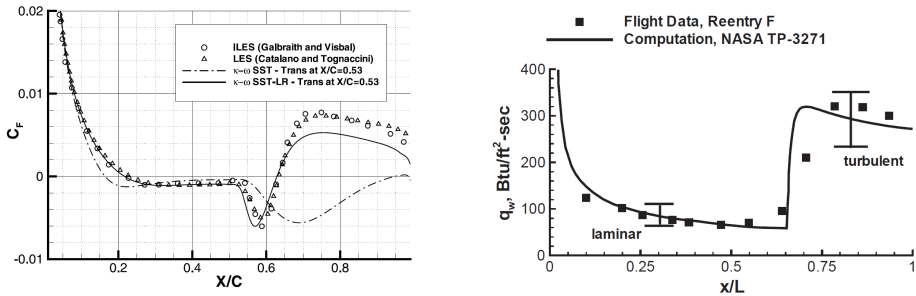


Figure 1.1: (left) Skin friction coefficient along an airfoil at incompressible conditions with a chord Reynolds number of 6.0×10^4 , from Catalano & Tognaccini [1] (scope in paper: illustrate performance of the $\kappa-\omega$ SST-LR RANS model as compared to LES simulations over the conventional SST model). (right) Heat transfer rate on the surface of a spherically blunted cone at $M = 19.97$, at the altitude 80 000 ft and an angle of attack of -0.15° , from Hamilton *et al.* [2] (scope in paper: comparison RANS and flight data, see Zoby & Rumsey [3]).

CO_2 emission. The aviation industry contributes significantly to the total CO_2 emissions on a global scale. To achieve the environmental goals set by the International Civil Aviation Organization (ICAO) in 2050, the performance of the next generation of aircraft has to be significantly enhanced. In particular, the CO_2 emission problem can be attacked by reducing the fuel consumption of modern business jets and long haul transports. Together with roughness induced pressure drag, skin friction contributes to over 50% of the total drag budget, of which 80% is manifested by turbulent flow [4, 5]. Postponing laminar-turbulent transition of the flow, therefore, promises to yield a significant overall drag reduction, which, in turn, aids in reducing the carbon footprint and costs of flying.

In the case of spacecraft, the increase in heat transfer is imperative. Re-entry vehicles returning to earth encounter the atmosphere with very high speeds, up to Mach 32. These speeds cause the air to densely compress onto the surface of the spacecraft giving rise to very high heat loads. To ensure the safe progression of the re-entry, these vehicles are equipped with heat shields. A thicker heat shield imposes a reduction of the payload weight. So, it is crucial to carefully optimize the design of the heat shields. The conditions for which the heat transfer undergoes a steep increase due to laminar-turbulent transition have an important role in this.

These considerations illustrate the importance of providing accurate information on the transition region. A particular knowledge must be accumulated for specific flow situations, so new theories describing the transition process can be derived and carefully validated. To understand these theories, taking a deeper look into the underlying mechanisms is required.

1.1. TRANSITION MECHANISMS

The first experimental analysis of the laminar to turbulent transition phenomenon was performed by Reynolds [6] in 1883. Reynolds was the first to properly distinguish the laminar and turbulent flow regimes and to determine the relevant conditions for which the transition to turbulence occurred. His experiments involved injecting ink into a water flow through a pipe. Reynolds identified that, when a specific dimensionless parameter exceeds a threshold, disturbances on the jet flow suddenly grow and break down to turbulence. We now refer to this dimensionless parameter, establishing the characteristic ratio of inertial to viscous forces, as the Reynolds number:

$$Re = \frac{\rho UL}{\mu}, \quad (1.1)$$

where ρ , μ , U and L denote the fluid density, molecular viscosity and a characteristic speed and length scale of the flow, respectively, see Jackson & Launder [7]. Given the fact that the breakdown to turbulence emerges suddenly, Reynolds deduced that this parameter must control whether the flow is stable or unstable to perturbations.

A similar scenario is observed in boundary layers over airfoils. The simplest case is the flow over an unswept flat plate at subsonic speeds, immersed in a low disturbance environment. That is, the incoming disturbances in the flow have a very small (infinitesimal) amplitude. Although this particular scenario is not considered in the remainder of the model problems studied in this thesis, it is a good example for illustrating the pre-

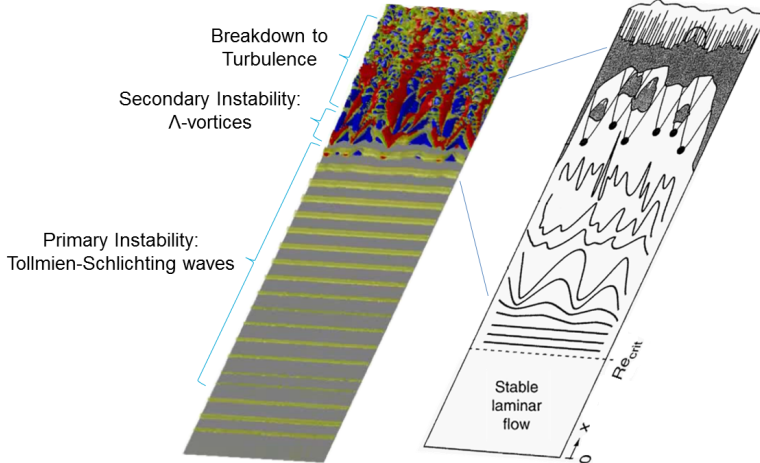


Figure 1.2: Tollmien-Schlichting wave transition illustrated by Schlichting's [8] illustration (right) and Large-Eddy Simulations (LES) by Schlatter *et al.* [9] (left) (digital copy: 2 clicks to activate video). The frequency of the TS wave is directly forced, while the Λ -vortices are triggered with small-scale noise. The noise used to trigger the (aligned) K-type vortices (shown here) is random in the spanwise direction, but constant in time. The (staggered) H-type vortices are triggered with noise that is random in both the spanwise direction and time.

sumed path to turbulence. This path is illustrated in the figure 1.2, combining the work of Schlichting *et al.* [8] and Schlatter *et al.* [9].

Close to the leading edge, the boundary layer flow is stable. In this region, all small perturbations are damped. Beyond a specific streamwise location, corresponding to the critical Reynolds number, Re_{crit} , perturbations start growing. A particular wavelength is amplified most, so the resulting flow structure appears in the form of a wave. Perturbations with this form are referred to as Tollmien-Schlichting (TS) waves. They manifest themselves as two-dimensional spanwise vortices, which grow in amplitude as they are convected downstream by the flow.

As they attain a significant amplitude, they cause a new type of vortices to emerge, denoted in figure 1.2 as Λ -vortices. In the shown case, these vortices are aligned with the phase of the TS waves and are denoted as K-type waves, after Klebanoff [10]. If they appear in a staggered (subharmonic) pattern, they are referred to as H-type (after Herbert [11]) or C-type (after Craik [12]) waves. In either case, the Λ -vortices undergo an explosive growth that ultimately results in the breakdown to turbulence. Note that the TS waves grow over a much longer spatial region than the Λ -vortices do in figure 1.2. This indicates that the TS waves undergo a much slower growth than the Λ -vortices.

This path to turbulence is the common one for low speed, low disturbance and low surface roughness cases. The particular example illustrates a two-dimensional boundary layer, but the same path applies for three-dimensional boundary layers as encountered on swept wings. Although the specific emergent flow patterns change from case to case, a (primary) instability develops, grows in amplitude and causes a subsequent (secondary) instability, after attaining a sufficiently large amplitude. Throughout this thesis, this is the main conceptual path of consideration. For more details and alterna-

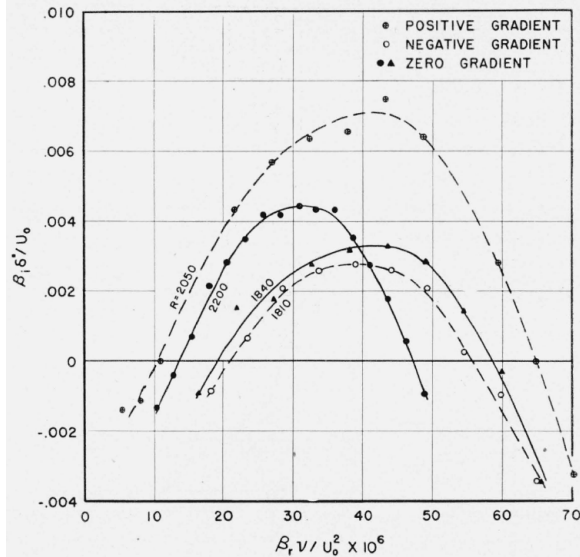


Figure 1.3: Comparison of computed and measured amplification rates versus the frequency of TS waves by Schubauer and Skramstad [19].

tive processes encountered for increasing disturbance levels, such as transient growth and by-pass transition, see Reshotko [13]. These matters are immaterial for the focus of this thesis, which justifies discarding their examination.

1.2. TRANSITION PREDICTION BASED ON STABILITY ANALYSIS

The conceptual establishment of the path to turbulence dates back to Reynolds's observations. It took many years, however, for this concept to be rigorously validated for boundary layers, i.e. to link the mathematical description of the perturbations through stability theory with experimental measurements. The Orr-Sommerfeld equation, that provides a mathematical description of the behaviour of the perturbations, was derived by Orr and Sommerfeld in 1907-1908 [14, 15], quickly following the work of Prandtl on his physically and mathematically revolutionary boundary layer theory at the start of the 20th century. Its unstable solutions, derived by his students Tollmien [16, 17] and Schlichting [18] in 1929-1933, however, were not corroborated by experiments for a long time. During the second world war, Schubauer and Skramstad [19] were the first to perform experiments in a specialized windtunnel with a sufficiently low turbulence environment for the TS waves to be observable, the results of which they published in 1948. The remarkable agreement of computed and measured amplification rates found by Schubauer and Skramstad [19] is shown in figure 1.3. The flat plate they used can nowadays still be found in the lab of Texas A&M University. Specifically, they showed that the growth rates obtained in the experiments match with stability theory. This opened the way to predict transition by using stability theory.

Their small initial amplitude allows perceiving these waves as infinitesimal pertur-

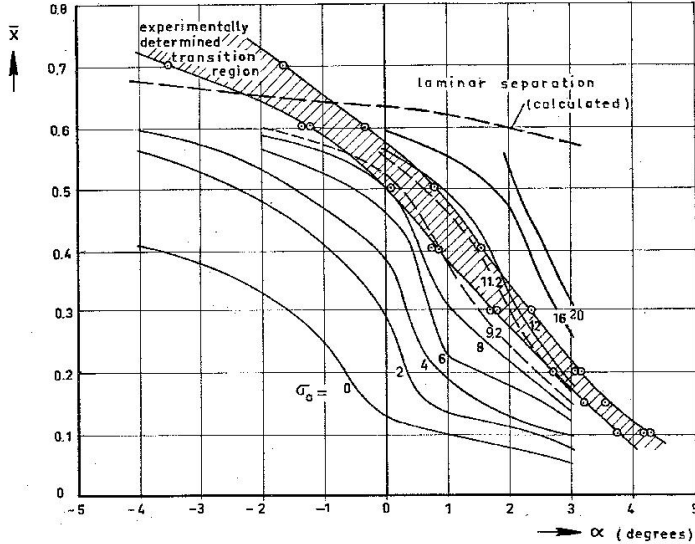


Figure 1.4: Measured transition locations and constant N -factor (then σ_0) locations versus angle of attack of the EC 1440 airfoil section by Van Ingen [20, 21]: transition occurs for $N = 8 - 13$.

bations to the boundary layer base flow. This assumption justifies the use of linear stability methods. The classical stability method describes perturbations as eigenmodes of a wall-normal boundary layer profile at a given location in the flow. The method determines the amplification of the perturbations as they develop in space.

The shear of the flow is the most important driver of the instability. The boundary layers of consideration display the largest shear component in the wall-normal direction and develop slowly in the streamwise direction, which justifies principally accounting for the wall-normal boundary layer shape. Local changes in the profile in the streamwise and spanwise directions are assumed to be negligible, essentially casting the problem for the perturbations into a one dimensional form. The collection (e.g. incompressible and compressible versions) of these one dimensional problems will be further referred to as the LST (Linear Stability Theory) problem.¹ In figure 1.5, the LST approach is visualised as a line, representing the base flow information it accounts for. For more details, see the elaboration that follows in this thesis or Schlichting *et al.* [8], Mack [22], Reed *et al.* [23], Schmid and Henningson [24], Drazin and Reid [25] or Craik [26]. The appearance of subsequent instabilities and the breakdown to turbulence are non-linear mechanisms and therefore are not accounted for in linear stability approaches.

In transition prediction applications, the gap consistent of non-linear mechanisms is bridged by deploying the semi-emperical e^N -method, established independently by Van Ingen [20, 21] and Smith and Gamberoni [27] in 1956. Based on experimental measurements, this method provides the *linear* amplification threshold at which transition

¹Technically speaking, this is a misnomer. All introduced methods in this chapter (the whole thesis, in fact) can be factored under linear stability theory.

is observed, given a particular flow environment. The underlying assumption is that the non-linear mechanisms set in at an explosive rate, causing the breakdown to turbulence to occur in a relatively small spatial region as opposed to the development of the primary instability, as seen in figure 1.2. This condones the extrapolation of the linear amplification. The correlation between the N -factor and the measured transition location as found by Van Ingen [20, 21] is illustrated in figure 1.4. Despite its simplicity and age, the e^N -method remains, up to this day, the prevalent tool for transition prediction and therefore forms the base of transition prediction codes used throughout industry [28–31].

Advanced stability methods improve the incorporated physics, yielding a better understanding of (parts of) the gap separating the linear perturbation dynamics from the fully turbulent flow. An example of this is non-linearity. This thesis, however, remains loyal to describing disturbances as linear (infinitesimally small) perturbations. Instead, this thesis focusses on extending the applicability of the analysis tools to base flows that have a higher spatial dimensionality.

1.3. HIGHER-DIMENSIONAL FLOWS: BiGLOBAL STABILITY

Nowadays, industry tends toward more extended regions of laminar flow on their aerodynamic surfaces by implementing the concepts of Natural Laminar Flow (NLF, tuning the airfoil shape [32]) and Hybrid Laminar Flow Control (HLFC, e.g. introducing suction [33]). The e^N -method is deployed for transition prediction in both cases. The tendency is therefore to postpone transition on the wings of next generation aircraft up to regions where the flow is more complicated than the LST can handle.

Attacking these more complicated flow configurations is the next frontier to postponing laminar-turbulent transition. Typical examples involve the wakes of roughness elements [34–37], the secondary crossflow instability in swept-wing boundary layers [38–42], step excrescences [43, 44] and Laminar Separation Bubbles (LSB, [45]).

As opposed to the natural transition scenario on smooth airfoils, the dynamics of perturbations to these flows are in general far from completely understood. Moreover, the traditional linear stability approach is inapplicable, because the aforementioned flows either do not develop gradually in the streamwise direction or display strong dimensionality in the spanwise direction. All examples quoted above have a significant shear component in two spatial directions, so the essential details of the flow can no longer be reasonably captured in a one-dimensional description characterised by a single velocity profile. For that reason, more general methods have to be considered to, first, analyse and, subsequently, predict the perturbation development in these flows.

A direct generalization of the traditional linear stability approach is to regard perturbations generated by two-dimensional shear layers and assuming the flow to be invariant in a third direction. The latter direction should thus be aligned with the direction in which the laminar background flow varies the least. Special examples involve the alignment of this third direction with the streamwise or spanwise direction. The corresponding systems of equations are referred to as the BiLocal and BiGlobal stability equations [46, 47], respectively. The indications local and global refer to the coverage of the streamwise direction, see figure 1.5. The BiLocal approach considers one streamwise point, while the BiGlobal approach covers a whole streamwise range. The slowly developing

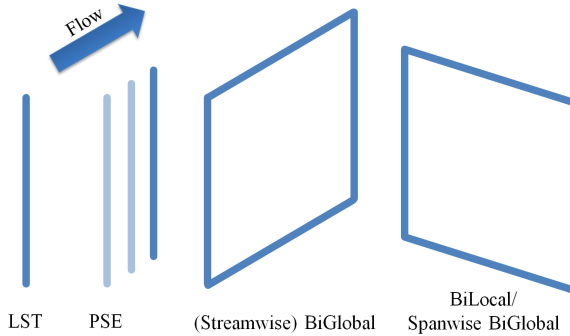


Figure 1.5: Dimensionality incorporated by the LST, PSE and BiGlobal stability methods.

wakes of roughness elements are usually analysed using the BiLocal approach [48], while LSBs are typical cases where the BiGlobal approach is deployed [45]. In the remainder, the BiLocal and BiGlobal analysis types will be collectively referred to as BiGlobal analysis. If needed, the orientation of the plane will be indicated.

Together with boundary conditions, these equations constitute an eigenvalue problem, that in turn forms the dispersion relation for the perturbations. The classical linear stability approach revolves around solutions of the Orr-Sommerfeld equation (or compressible equivalents), which is a one dimensional, ordinary differential equation or a system thereof. In conclusion, with respect to the original one dimensional eigenvalue problem, the more general BiGlobal problems are thus just the two dimensional extension of the LST problem. This is not the only possible generalization of the LST framework. Another important method exists, of which the governing equations are referred to as the Parabolized Stability Equations (PSE). As opposed to LST, this method incorporates the effect of *small* derivatives of the flow in the streamwise direction. Instead of an eigenvalue problem, an initial value problem is set up in space and the perturbation amplification is solved by marching the solution in the streamwise direction. In figure 1.5, this is indicated as the sequence of lines in the streamwise direction. For more details, see Bertolotti [49], Bertolotti *et al.* [50], Li and Malik [51], Herbert [52] and Chang [53].

Whenever the streamwise derivatives become large, however, the LST and PSE approaches break down. In this case, the BiGlobal problem should be adopted, since this approach is capable of analysing any two-dimensional flow. No *a-priori* restrictions apply for the in-plane flow. The incorporated dimensionality of LST, PSE and BiGlobal stability methods is summarised in figure 1.6. In particular, the BiGlobal stability method can be applied to flows over discontinuous geometries.

Next to the incorporation of new effects of the base flow, different kinds of perturbation dynamics are incorporated. In LST, only local information of the base flow is incorporated; no streamwise history effects can be accounted for. PSE incorporates small streamwise derivatives, so the effect of small streamwise curvature of airfoils and downstream travelling history effects can be accounted for. The BiGlobal stability method incorporates all possible effects contained in a given plane simultaneously. Perturbations are allowed to travel upstream and establish global mechanisms such as feedback loops (resonances).

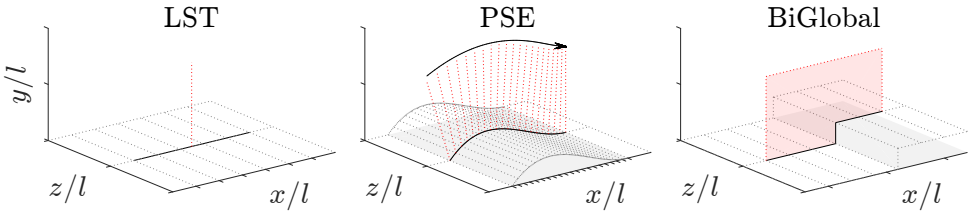


Figure 1.6: Dimensionality incorporated by the LST, PSE and BiGlobal stability methods; expressed in the kind of surface geometries can be considered.

1.4. THESIS SCOPE: ADVANCES IN BiGLOBAL STABILITY

The importance of stability analyses for the design of laminar wings is established. Moreover, it is demonstrated that the state of the art methods capture a subset of all perturbation dynamics. The BiGlobal stability method significantly expands the horizon of incorporated physics.

The general applicability of the BiGlobal method is impeded on several important fronts, however. The first problem involves the strict requirements on the base flow of interest that apply to stability methods in general. Experimental measurements of the transition location are required by standard for the execution of the e^N -method. It is logical, therefore, to inquire whether performing stability analysis on experimentally measured base flows can be successful. The second problem concerns the deployment of the method in cases involving a plane oriented in the streamwise direction. While this is the prevalent case in all aerospace applications of interest, obtaining numerically converged data is problematic in this particular situation. These are the central aspects investigated in this thesis. The generative details for each aspect are further outlined in this section.

1.4.1. APPLICABILITY OF BiGLOBAL ANALYSIS ON EXPERIMENTALLY MEASURED BASE FLOWS

As mentioned before, the principal driver of perturbation growth is the flow's shear, the gradient of the flow field. To achieve reliable stability data, therefore, flow derivatives have to be accurately represented. It is in this regard commonly suggested that the base flow should satisfy the Navier-Stokes equations to extreme accuracy, see Theofilis [46]. The shear layers principally contributing to the production of perturbation energy need to be resolved, see Arnal [54], and that the stability results must be converged as the resolution of the basic state is increased, see Reed *et al.* [23]. Of course, this applies to computational results.

In many cases, however, experimental measurement data is available only or numerical data is difficult to obtain for complex geometries at high Reynolds numbers. Considering measured base flows allows taking into account features that are specifically associated to the experiments that are possibly hard to model computationally. Examples are effects associated to symmetry imperfections, an unaccounted ambient pressure difference, the use of different leading edge shapes or even tunnel confinements, just to name a few. Other examples of base flows can be imagined that are very challenging to com-

pute, while being relatively easy and cheap to measure.

Experimental measurements are required to determine the transition location in the application of the e^N -method, so a natural question is whether the stability analysis can be applied to a measured base flow to determine the linear perturbation amplification. The experimental measurement techniques have undergone major improvements over the years. State of the art tomographic Particle Image Velocimetry (tomo-PIV) measurements yield the complete three dimensional velocity field, given in a volume in space at a resolution yielding graphical representations comparable to computations. Modern measurement techniques can therefore provide a complete description of the base flow, which is required for the BiGlobal stability analysis.

Investigating the applicability of the BiGlobal stability framework to measured base flows is deemed very fruitful for that reason, allowing direct comparison with the instantaneous experimental data. In turn, the stability approach provides a deeper understanding of the underlying physical mechanisms giving rise to the measured flow dynamics and one hence extends the measurability. Consecutively, this allows improving the experimental set-up using this knowledge to one's advantage.

Moreover, in their review, Gómez *et al.* [55] state regarding experimental validation:

“... what is largely missing from reported analyses of global flow instability is a culture of using experimental reality both as a sanity check of theory and as guidance for its further development.”

In this thesis, this statement is taken to the extreme, by applying the BiGlobal stability theory directly to experimental data.

This methodology also provides a deeper means of validating computational with experimental results. Matching stability data based on an experimentally measured and numerically computed base flow is unprecedented. Bringing the experimental and computational results closer together, given the insights based on the stability results, can provide a better understanding on both the computational and experimental sides.

Despite the aforementioned merits, there are two main disadvantages of the proposed approach. First of all, linear stability methods require the specification of a laminar base flow that satisfies the governing physical laws. Experimental measurements have access to the mean flow, which, in cases of significant perturbation amplitudes, may not satisfactorily approximate the laminar flow. The literature shows, however, that this does not impede the success of the stability approach in predicting the behaviour of the perturbation field. This even applies in the case of turbulent flows, see Jordan and Colonius [56] for example, just to mention an extreme case where Reynolds stresses are significantly more dominant than in the presently considered cases, that are observed to be laminar. The assumption that the mean and base flow are equal is cast into what is here referred to as the “mean = base flow” hypothesis. Other challenges are found in features related to the post-processing and inherent limitations of the PIV measurement technique, e.g. the resolution of the measurement is restricted.

These two aspects are first studied within the confinements of a highly simplified, but representative, model problem. Thereafter they are considered separately within the context of two application cases, linked to different experimental campaigns. The results of these experiments are published independently, see Ye, Schrijer, and Scarano

[57] and Serpieri and Kotsonis [58]. The configurations are the wake of a micro-ramp vortex generator and the crossflow vortices encountered in the boundary layer flow on swept wings. Both cases are to be analysed with the spanwise BiGlobal approach; they present shear layers that are dominant in the wall-normal and spanwise directions.

The aforementioned cases are further detailed in §1.5. The next subsection introduces the second, independent investigation aspect.

1.4.2. NUMERICAL ISSUES IN STREAMWISE BiGLOBAL ANALYSES

Shear is one of the most important features in the base flow in the context of perturbations, because it produces perturbation energy. Shear, however, is not the only important flow feature for the analysis. A, maybe surprising but important, newcomer in the BiGlobal approach is the in-plane base flow advection. That is, the effect of the flow itself, as opposed to that of its derivatives. In the LST and PSE approaches, the only ‘in-domain’ advection is that due to the wall-normal, or the so-called non-parallel, velocity, which is prohibited and restricted to be small in size within the constraints of these methods, respectively.

General advection yields new solution characteristics, equally in both the spanwise and streamwise BiGlobal approaches, of which the implications have not been thoroughly scrutinized before. In particular, an identity trilemma can be posed: the perturbations can be classified as convectively, absolutely or globally unstable.

INFINITE VERSUS FINITE SHEAR LAYERS: AN IDENTITY TRILEMMA

Cases that are analysed using the spanwise BiGlobal approach typically feature shear layers that are isolated in the spatial plane of consideration. The perturbations are generated in and often remain confined to this isolated region. This will be reflected by the micro-ramp and crossflow vortex applications. The in-plane advection, as shown for these cases in figure 1.7, takes the role of redistributing perturbation energy over different segments of the shear layer; the red regions in the figures.

The confinement of the eigenfunctions to a localized region within the plane of consideration poses an important implication for the applied numerical approach. In approximating the eigenfunctions numerically, it is required to truncate the domain in the farfield. At the introduced boundaries, boundary conditions must be imposed that are generally unknown from a physical perspective. In the case of eigenfunctions that ap-

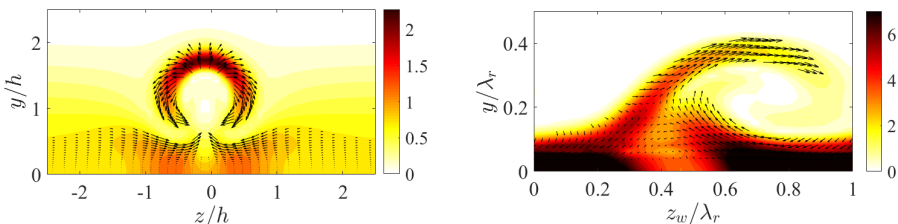


Figure 1.7: In-plane flow and shear for the micro-ramp (top left), crossflow vortex (top right), presenting spanwise cases. The in-plane flow is indicated in the regions of relatively strong shear.

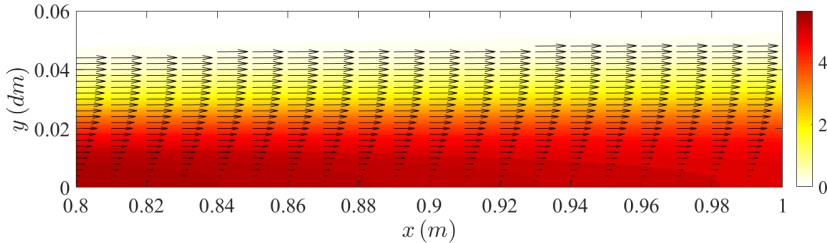


Figure 1.8: In-plane flow and shear for a boundary layer, presenting a streamwise case. The in-plane flow is indicated in the regions of relatively strong shear.

pear in a spatially isolated shear layer, the truncation boundaries can be positioned far away from this shear layer. The small magnitude of the perturbations near the boundaries in that case implies the truncation boundary conditions have a negligible impact.

This is no longer the case when boundary layers are considered with the streamwise BiGlobal approach. As illustrated in figure 1.8, the shear layer then connects the in- and outflow boundaries. From experiments, boundary layers are known to be convectively unstable. This implies a pulse disturbance only propagates downstream. While the shear produces perturbation energy, advection carries perturbations downstream. In general, however, this behaviour cannot be *a-priori* inferred. In fact, whether perturbations are supported that solely amplify as they are advected downstream (*a convective instability*), whether they can also grow upstream (*absolute instability*) or whether they are associated to an isolated (self-excitation) region in the domain (*global instability*) has become a part of the stability problem [59–61], figure 1.9 summarises these mechanisms.

THE BiGLOBAL SPECTRUM: CONTINUUM VERSUS DISCRETE MODES

The pertinent identity of the instability mechanism in question is encoded in the infamous BiGlobal eigenvalue spectrum. This spectrum forms, together with the eigenfunctions, the solution to a given BiGlobal eigenvalue problem.

A typical spectrum for the LST analysis of the Blasius boundary layer is shown in figure 1.10. In that problem, the Tollmien-Schlichting solution appears as an unstable

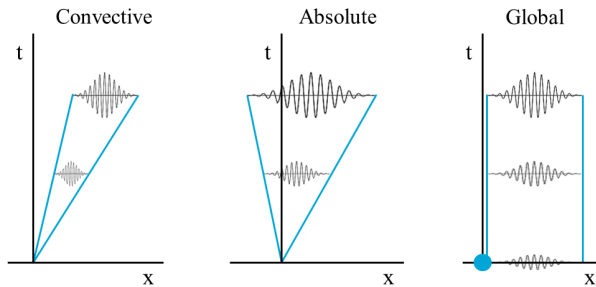


Figure 1.9: Evolution of the support of a convective, absolute and global instability mechanism in time. Whereas convective and absolute mechanisms are free to propagate in space, a global mechanism has a well-defined, fixed and finite spatial support (a self-excitation region).

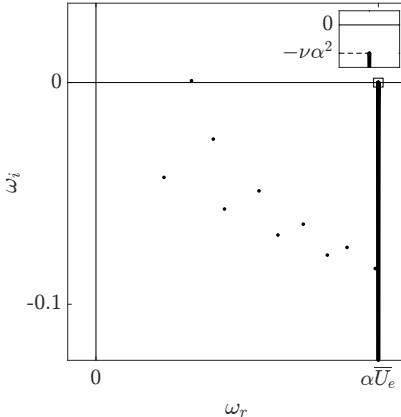


Figure 1.10: Typical temporal spectrum corresponding to the Blasius boundary layer [24, 62].

discrete eigenvalue in the spectrum. Next to a finite number of discrete modes, a continuous branch appears. The latter is required to represent perturbations of arbitrary shapes [63], but it never becomes unstable for this LST problem.

In BiGlobal spectra, the overwhelming majority of solutions appears as continuum modes. Interpreting these branches is the main difficulty when practising BiGlobal stability analysis, because no clear guideline exists in the literature. In short, isolated eigenfunctions or global mechanisms appear as discrete modes in the spectrum, while continuum solutions can represent absolute and/or convective instabilities. The distinction of discrete and continuum modes deserves a careful explanation.

Discrete modes have the inherent characteristic that they ‘latch’ onto a finite length scale of the base flow, which can be thought of as the length or width of a shear layer. Correspondingly, these discrete modes have a finite largest wavelength equal to this length scale. The solutions of interest for the micro-ramp and crossflow vortex cases are good examples of this. The corresponding eigenfunctions are contained in an isolated region in the interior of the spanwise plane. In case of the streamwise BiGlobal analysis of boundary layers, no largest length scale exists in the streamwise direction. In theory, the largest wavelength is infinite.

In the numerical approach, this means that the largest wavelength is associated to the truncated domain size. The corresponding solutions reach from the in- to the outflow boundary. Truncating the domain at a finite length is the specific reason for numerical approximations of solutions to an eigenvalue problem to be discrete. In the limit of an infinitely long domain, the solutions in the shear layer are allowed to have all real-valued streamwise wavelengths, because all wavelengths ‘fit’ in the domain. In this limit, the eigenvalues corresponding to these solutions form a continuous branch in the spectrum. Also, this illustrates that, per definition, these solutions are intimately tied to the domain truncation boundaries. That is, the spatial flow structure of the solutions are dominant near the boundary of the domain. This yields a problem, because the unknown truncation boundary conditions have an influence in that case. Moreover,

typically the spatial structure of the perturbations grow towards these boundaries.

CONTINUUM CONVERGENCE CONTROVERSY

Retrieving solutions whose spatial structure grows towards the truncation boundaries in a computationally converged form is problematic. In particular, these results strongly depend on the in-/outflow boundary conditions and the length of the considered domain. This is especially true for flow cases that support globally stable, but convectively unstable mechanisms. Despite initial efforts [64–67], convergence issues of the eigenvalue spectrum have been left unsolved over the last 13 years. *Ad-hoc* solutions have been proposed in terms of boundary conditions, but none have delivered robust results. This is a fundamental problem of the approach. To make matters worse, Theofilis [46] claims that: ‘the discretized approximation of the continuous spectrum will always be under-resolved’.

Figure 1.11 illustrates the typical movement of the modes in the spectrum, i.e. towards the unstable half-plane, as the streamwise domain length is increased. It is for this reason, that the global stability analysis community nowadays revolves around a hunt for discrete modes. These global modes do not suffer from the convergence obstacle, because the spatial structure decays exponentially towards the truncation boundaries [68, 69]. The continuous spectrum is usually completely avoided.

The continuous spectrum is required to represent the prevalent convective perturbations encountered in aerospace applications. So, the continuous spectrum convergence problem inhibits the deployment of the BiGlobal method for this very broad application range. Even in the cases where LST and PSE can readily provide highly accurate solutions, the technically ‘superior’ BiGlobal method has not been deployed successfully on the same ‘inferior’ applications. Replacing LST or PSE in their domain of applicability (i.e. mildly parallel, streamwise homogeneous flows) by the BiGlobal approach is unnecessarily expensive, given the extra theoretical and numerical difficulties that have to be faced. These can only be justified when BiGlobal stability analysis is used for more complex, two-dimensional and streamwise inhomogeneous cases. However, the behaviour of the spectrum provided by this method is insubstantially understood, even for the simple flow cases like that over a flat plate, see Ehrenstein and Gallaire [64], Alizard and Robinet [65], Åkervik *et al.* [66], Rodríguez [67], Rodríguez *et al.* [70]. Understanding the BiGlobal spectrum in simplified cases is essential before more complex flows can be studied rigorously.

This thesis attacks this problem with a mathematically rigorous procedure for a model problem that solves the convergence issues at its unexpected core: streamwise advection. Presenting an omni-present entity in aerospace applications, the streamwise advection causes the continuum eigenmodes to display an exponential growth towards the in-/outflow boundaries. Surprisingly, this growth is unrelated to the amplification induced by the flow’s shear. As will be shown in this thesis, this causes the numerical solutions’ sensitivity to the boundary conditions and domain length.

1.5. MODEL PROBLEMS

To approach the aspects presented in the previous section, model problems are set up that are each individually treated in a chapter of the thesis. Three model problems are

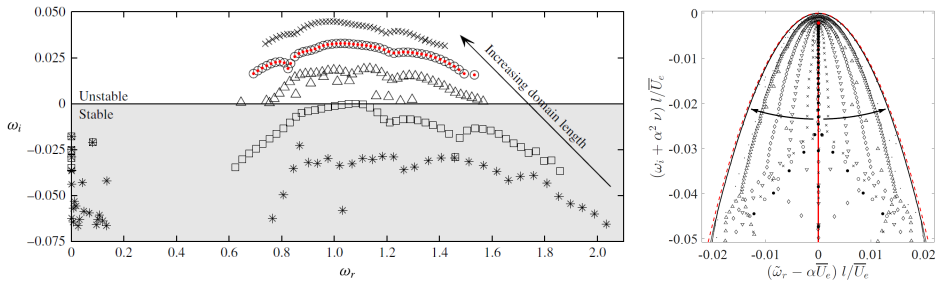


Figure 1.11: Movement of the spectrum as the streamwise domain length is increased, corresponding to (left) the TriGlobal analysis of Brynjell-Rahkola *et al.* [71] and (right) the analysis presented in chapter 8. Arrows indicate the movement direction as the streamwise domain length is increased.

considered with respect to performing the stability analysis of using *measured base flows*, see §§1.5.1 to 1.5.3. A single model problem is considered in regard to the streamwise BiGlobal problem, see §1.5.4. An overview of the problem statement is given and the underlying reasoning and objectives are discussed. A common factor to all cases is that the considered flows are incompressible.

1.5.1. MEASURED BASE FLOWS: ANALYTICAL PROFILES

Before considering experimental data, the expected effects that come into play when considering measured base flows are quantified computationally. The methodological effects associated to PIV measurements that are important within the context of stability analysis are: the limited spatial resolution, spatial smoothing and the presence of physical perturbations in the instantaneous flow.

The experimental studies involve shear layers that are positioned relatively far from the wall. The simplest, well-known model of such shear layers is the hyperbolic tangent profile. See figure 1.12 for a concise statement of the stability problem formulation. On the left and right hand side, the mathematical ansatz is described and a representative velocity profile is shown, respectively. Further explanations of the ansatzes will be given in chapter 2. Here, the ansatzes are presented to complete the overall picture, allowing to distinguish the analysis type considered in the different chapters.

In this case, a one-dimensional stability analysis is performed to extract behavioural characteristics of the stability results as a function of the resolution of the base flow and the residual perturbations in the mean flow. This is done by first determining reference solutions and studying their behaviour in detail, using analytical profile representations. Given this data and knowledge, the influence of the aforementioned methodological effects can be directly identified. Furthermore, it allows identifying general physical solution characteristics.

1.5.2. MEASURED BASE FLOWS: MICRO-RAMP WAKE

The next model problem involves a case for which experimental data is available: the wake of a micro-ramp. Micro-ramps are sub-boundary layer or micro vortex generators that are applied to suppress Shock-Wave/Boundary-Layer Interaction (SWBLI), encoun-

$$q = \bar{Q}(y) + q'(x, y, z, t)$$

$$q' = \tilde{q}(y) e^{i(\alpha x + \beta z - \omega t)} + c.c.$$

$$\bar{Q} = [\bar{U} \bar{V} \bar{W} \bar{P}]^T = \left[\tanh\left(\frac{2y}{\delta_v}\right) \ 0 \ 0 \ c^{st} \right]^T$$

$$q' = [u' v' w' p']^T$$

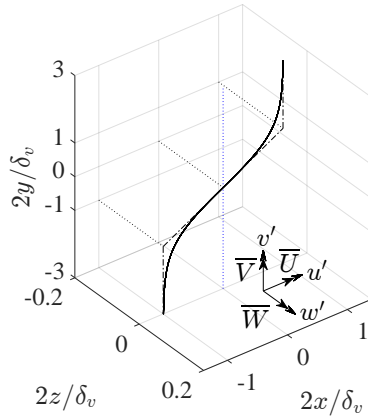


Figure 1.12: Situation sketch for chapter 4, generic LST analysis (see §2.3) of generalized hyperbolic tangent \bar{U} -profiles, $\bar{V} = \bar{W} \equiv 0$. Characteristic length scale: vorticity thickness divided by 2, $\delta_v/2$.

tered in supersonic internal flows like supersonic inlet cones. These geometries were introduced for SWBLIs by Anderson *et al.* [72], who pointed out their superior performance with respect to boundary bleed basing the conclusions on Reynolds averaged Navier-Stokes flow simulations. Babinsky *et al.* These devices are structurally very robust and therefore attractive for manufacturers in a practical sense [73].

Their working principle is to reduce the extent of flow separation in the SWBLI by generating two steady counter-rotating vortices that yield an upwash in the symmetry plane [75, 76], see figure 1.13. An instantaneous flow aspect is a train of hairpin vortices that develops in the arc-shaped shear layer surrounding the ramp's wake [77]. Figure 1.14 shows an instantaneous tomographic Particle Image Velocimetry (tomo-PIV) measurement of the micro-ramp wake, performed by Ye *et al.* [78], clearly showing these hairpins. Their definite streamwise wavelength and positioning around the region of

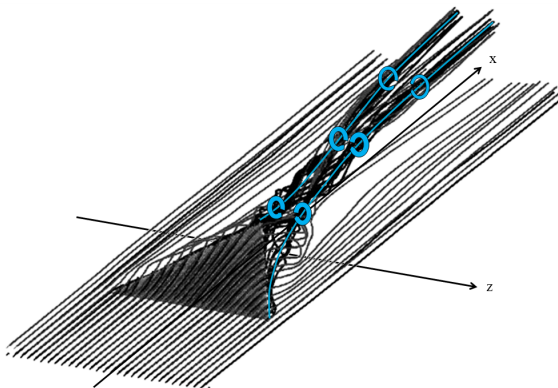


Figure 1.13: Streamlines and representation of the streamwise vortices in the wake of a micro-ramp roughness element, adapted from Ghosh *et al.* [74].

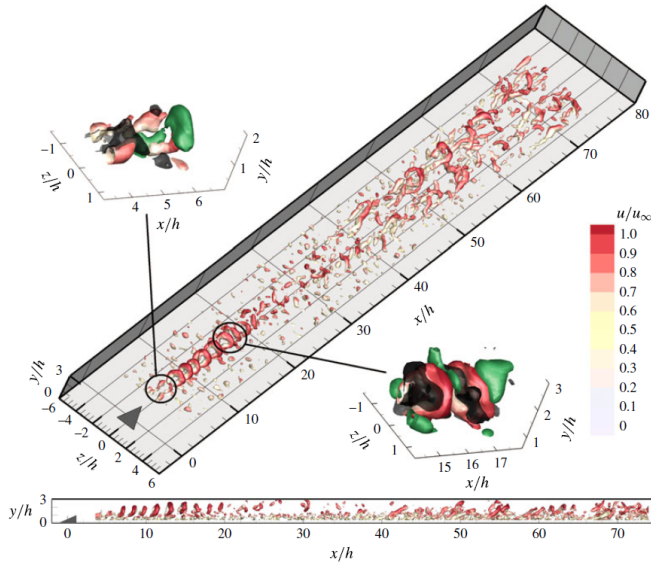


Figure 1.14: Instantaneous flow (isosurfaces of λ_2 and ejection (black) and sweep (green) events over the micro-ramp roughness element measured by Ye *et al.* [78].

the base flow's maximum shear supports their interpretation as Kelvin-Helmholtz (KH) modes. However, the waves attain significant amplitudes in a close vicinity of the micro-ramp, so it is not *a-priori* clear whether the a linear mechanism is the driving mechanism. It should be emphasized that the experiment is performed in an incompressible flow environment despite the possible application for the suppression of SWBLI-induced separation.

From the physical perspective, the generation of the hairpin vortices is studied. The wake evolves slowly in the streamwise direction, justifying neglecting the streamwise derivatives of the flow. Given that the wake is two-dimensional, in the spanwise and wall-normal directions, the appropriate approach to this problem therefore is the spanwise BiGlobal problem. An outline of the stability problem is given in figure 1.15.

This thesis will be concerned with several questions regarding this flow case, focusing on the perturbations in the near-wake region of the micro-ramp in incompressible flow conditions, as a continuation of the work of Ye [79]. From the perspective of applying stability theory to measured base flows as a methodology, it will be tested whether stability results can reproduce the instantaneous flow field and yield the same instability modes as expected from the literature. The significant amplitude of perturbations close to the ramp is expected to pose a challenge.

1.5.3. MEASURED BASE FLOWS: CROSSFLOW VORTICES

After having handled the micro-ramp case, an entirely different model problem is considered. Swept-wing crossflow-dominated boundary layers subject to low freestream-turbulence are well-known to develop stationary streamwise-oriented crossflow vortices

$$\begin{aligned} q &= \bar{Q}(z, y) + q'(x, y, z, t) \\ q' &= \tilde{q}(z, y) e^{i(\alpha x - \omega t)} + c.c. \end{aligned}$$

$$\begin{aligned} \bar{Q} &= [\bar{U} \bar{V} \bar{W} \bar{P}]^T \\ q' &= [u' v' w' p']^T \end{aligned}$$

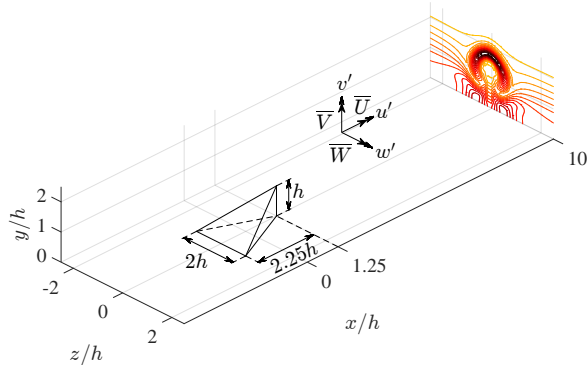


Figure 1.15: Situation sketch for chapter 5, spanwise BiGlobal analysis (see §2.3) of a measured micro-ramp wake. Isocontours of the in-plane shear in the \bar{U}_w component are shown and the dimensions of the micro-ramp are indicated. Characteristics length scale: micro-ramp height, $h = 2$ (mm). Freestream Reynolds number: $\bar{U}_\infty h/\nu = 700.30$, roughness Reynolds number: $\bar{U}(y = h, z = -\infty)h/\nu = 468.13$.

as a primary instability. A visualisation of these vortices is provided in figure 1.16 (left).

Despite the small amplitude of the primary vortices, they result in a mean flow distortion giving rise to high-frequency secondary instabilities, which ultimately breakdown to turbulence, see Bonfigli and Kloker [48], Reed, Saric, and Arnal [23], Saric, Reed, and White [80] and White and Saric [41]. The main effect of the primary stationary crossflow vortices on the laminar flow is to redistribute momentum across the boundary layer by advection about their vortical axis. The resulting instantaneous and mean flow present elevated shear stress components in two spatial directions.

Detailed information on the secondary instabilities, specifically their amplification and spatial topology, is instrumental in understanding, and ultimately predicting, where laminar-turbulent transition will occur in this case. Malik, Li, and Chang [38] identified 3 classes of instabilities in the distorted base flow. The type I mode is generated by the spanwise shear layer in the upwash region of the primary vortex and is usually dominant.

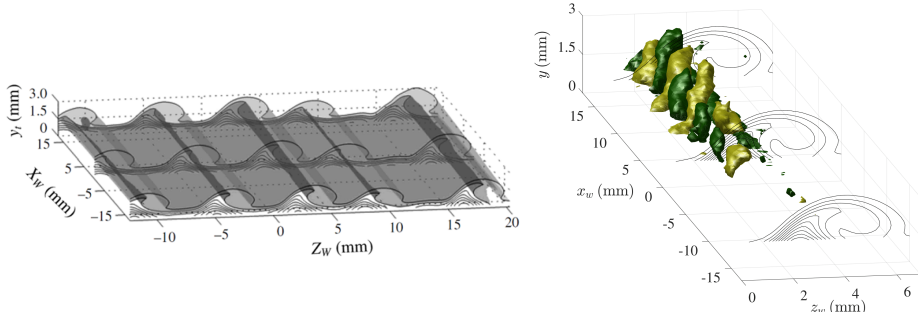


Figure 1.16: Measurement data by Serpieri & Kotsonis [58]. (left) Isosurfaces of the streamwise velocity of the distorted swept-wing boundary layer. (right) POD mode (isosurfaces of x_w -velocity perturbation, Φ_{10}) representative of the type I instability on the crossflow vortices and contour levels of the x_w -velocity of the base flow.

$$q = \bar{Q}(z_w, y) + q'(x_w, y, z_w, t)$$

$$q' = \tilde{q}(z_w, y) e^{i(\alpha x_w - \omega t)} + c.c.$$

$$\bar{Q} = [\bar{U}_w \bar{V} \bar{W}_w \bar{P}]^T$$

$$q' = [u'_w v' w'_w p']^T$$

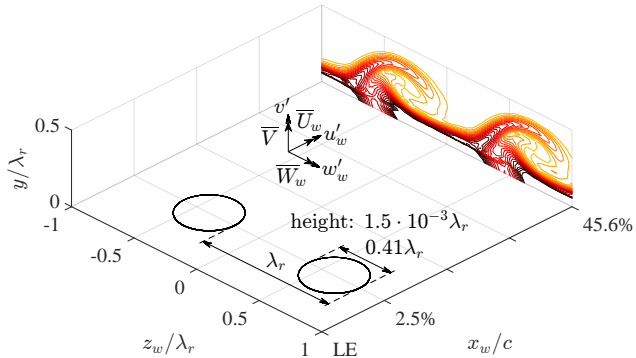


Figure 1.17: Situation sketch for chapter 6, spanwise BiGlobal analysis (see §2.3) of measured crossflow vortices in the swept-wing boundary layer on the 66018M3J airfoil. Isocontours of the in-plane shear in the \bar{U}_w component are shown and the dimensions of the Discrete Roughness Elements (DREs) are indicated schematically; their relative spanwise position to the shear layers is guessed. The streamwise coordinate is not to scale. Characteristic length scale: crossflow vortex wavelength: $\lambda_r = 9 \cos 40^\circ$ (mm), chord: $c = 1.27$ (m). Edge Reynolds number: $\bar{U}_0 \lambda_r / v = 13208$.

Its spatial structure is illustrated in figure 1.16 (right).

A handle to the stability features of secondary perturbations can be obtained by applying spanwise BiGlobal stability analysis on the distorted base flow. An overview of the stability problem is shown in figure 1.17.

In this thesis, this case will be regarded from the point of view of applying the stability approach using the measured mean flow data of [58] as the base flow. Similarly as for the micro-ramp wake case, it will be tested whether the secondary stability results can reproduce the instantaneous flow field. A challenge in this model problem as opposed to the previous cases is the complicated topology of the base flow, which houses three different instability types. From the physical point of view, an emphasis will be put on the effect of the in-plane flow velocity components. Bonfigli and Kloker [48] found that accurately representing the small in-plane (wall-normal and crossflow) velocity components is crucial in this regard; reporting significant growth rate reductions. Kloker and coworkers exploited this by controlling the developed crossflow vortices with suction and plasma actuators [87–91]. However, only a conceptual account of how these components affect the secondary stability modes is given by Bonfigli and Kloker [48].

From the methodological point of view, technical difficulties involve a low frequency spanwise shake of the crossflow vortices and detrimental effects due to the strong shear close to the wall. The effect of the number of instantaneous snapshots (i.e. the *ensemble size*) used to build the mean flow will be considered in detail, so to assess the effect of the most energetic POD mode presented by Serpieri and Kotsonis [58], which reflects the spanwise shake.

1.5.4. STREAMWISE BiGLOBAL PROBLEM: NON-PARALLEL BOUNDARY LAYER

The previous test cases all concerned investigating measured base flows. In contrast, the last case is entirely dedicated to the convergence problems of the streamwise BiGlobal spectrum as alluded to in §1.4.2 and is very different in nature.

$$\begin{aligned} q &= \bar{Q}(y) + q'(x, y, t) \\ q' &= \tilde{q}(y) e^{i(\alpha x - \omega t)} + c.c. \end{aligned}$$

$$\begin{aligned} \bar{Q} &= [\bar{U} \bar{V} \bar{W} \bar{P}]^T = [\bar{U} \bar{V} 0 \bar{P}]^T \\ q' &= [u' v' w' p']^T = [0 0 w' 0]^T \end{aligned}$$

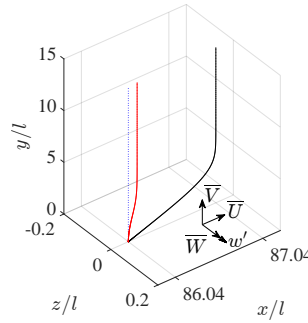


Figure 1.18: Situation sketch for chapter 8, LST analysis with the Squire equation for \tilde{w} only (see §8.2) of a uniform flow and Blasius profile. Characteristic length scale: local Blasius length, l .

The challenge in tackling the convergence problems encountered in the streamwise BiGlobal stability analysis is one of its definition. This method is hierarchically the first that incorporates large advection terms. The problem cannot be cast into a known stability problem without rejecting the accompanying assumptions. To understand this theoretical problem down to its very core, the model problem was reduced to the outer minimum of the minimum, removing all possible physical complications from the set-up of the problem. An overview of the problem set-up is given in figure 1.18.

In particular, a one-dimensional non-parallel problem is considered, including the necessary advection term that violates the parallel flow assumption. As displayed, the perturbation field is reduced to just the spanwise component w' as a function of x , y and t , not of z , governed by the non-parallel Squire equation. The base flow, on the other hand, is reduced to one-dimensional (y -)profiles; having a streamwise and wall-normal velocity component only. Considering a one-dimensional problem renders the available computational power to be virtually unlimited. This is required, because the spectrum converges extremely slowly (algebraically) with the domain length when the numerical issues set in.

The latter is the first, seemingly conceptually strange aspect of this case's set-up. The streamwise BiGlobal problem, which seems to be inherently two-dimensional, is reduced to a one-dimensional problem. It turns out the problems arising in the streamwise BiGlobal problem are just one-dimensional in nature. Moreover, the restriction to a one-dimensional problem allows deploying serious numerical power.

The second strange aspect is identified as follows. The 'dangerous' advection component in the *streamwise* BiGlobal analysis is, expectedly, the streamwise velocity component: \bar{U} . However, for several important reasons the model problem corresponding to this test case considers a transposed situation, where \bar{V} provides the malicious advection. Examples of the underlying reasons are that the wall-normal problem possesses a physical (no-slip) boundary condition, reducing the conceptual complexity, and that \bar{V} is usually small, which somewhat tames the issues at hand.

Most importantly, this test case belongs to the class of problems for which the theorems of Sandstede and Scheel [68] are applicable. Their theorems describe the limits of the eigenvalue spectrum for these classes of problems, in general. This formed the basis

for understanding why the spectrum behaves the way it does (from a physical perspective), why that resulted in numerical problems and how that could be solved, for this model problem at least. For a detailed account of all reasons underlying the choice of this model problem, see appendix B.

1.6. THESIS OBJECTIVES AND OUTLINE

The mathematical theory of the BiGlobal stability problem will be elaborated upon in chapter 2. Subsequently, the numerical set-up used to solve the obtained system of equations is presented in 3. Hereafter, this thesis addresses the two main topics.

The first main topic focuses on establishing the applicability of the BiGlobal stability method for experimentally measured base flows. Three dimensional flow descriptions are accessed through the use of tomographic particle image velocimetry (tomo-PIV), forming a complete representation required for the spanwise BiGlobal stability analysis. An approach that maximally strengthens the relationship between stability methods and experiments in general is applying the stability methods to the experimental measurement data itself.

The following objective is formulated in this specific regard:

- establish the applicability of BiGlobal stability theory to measured base flows

This is accomplished by testing a number of critical aspects:

1. literature describes the expected instability mechanisms for every model problem, these have to be recovered and, when possible, compared against the instantaneous measurement data
2. the effect due to the spatial resolution on the derivatives of the base flow and the limited domain size has to be determined
3. the convergence of the results with respect to the number of instantaneous snapshots used to determine the mean flow has to be established

It is assumed throughout that the considered mean flow is a good approximation of the base flow. This is referred to as the “mean = base flow”-hypothesis.

In chapter 4, the aforementioned features are first considered in high detail by considering analytical profiles representative of the application cases that are considered later. They are separately addressed within the context of the micro-ramp and crossflow vortex cases in chapters 5 and 6, respectively.

The second main topic of this thesis involves the streamwise BiGlobal stability analysis of developing boundary layers. Although the physics of perturbations living in laminar boundary layers is well-established and understood, the interpretation from the point of view of the BiGlobal stability framework is not. This is mostly due to the fact that numerical results are very sensitive to numerical parameters, like the domain size, truncation boundary conditions, etc. This is here referred to as the streamwise BiGlobal stability problem. This leads to the final objective:

- identify the cause of and a solution for the streamwise BiGlobal problem

Before the main problem can be tackled, a technique to analyse the behaviour of continuous spectrum solutions is elaborated upon in chapter 7, leading to Briggs's criteria for an absolute instability. By considering an advection-diffusion model, the implications of a “dangerous” advection on the continuous spectrum are identified. The used elements of complex integration theory are derived in appendix A; essentially covering the application of the theory to a spectrum consistent of discrete eigenvalues only. While the problem is treated analytically in chapter 7, the equivalent problem is considered from a numerical perspective in chapter 8. That chapter is devoted to attacking the numerical aspect of the streamwise BiGlobal stability problem within the confinements of the one-dimensional model problem.

To be gradually introduced to all required mathematics that lead up to chapter 8, it is suggested to read appendix A, chapter 7 and 8 in that order. An effort is made to introduce and gradually build upon complex integration theory starting from an elementary knowledge of calculus and differential equations taught to engineers.

REFERENCES

- [1] P. Catalano and R. Tognaccini, *RANS analysis of the low-Reynolds number flow around the SD7003 airfoil*, Aerospace Science and Technology **15**, 615 (2011).
- [2] I. Hamilton, D. Millman, and R. Greedyke, *Finite-Difference Solution for Laminar or Turbulent Boundary Layer Flow Over Axisymmetric Bodies With Ideal Gas, CF4, or Equilibrium Air Chemistry*, Tech. Rep. (NASA Langley, 2003).
- [3] E. V. Zoby and C. B. Rumsey, *Analysis of free-flight laminar, transitional, and turbulent heat-transfer results at free-stream Mach numbers near 20 (Reentry F)*, Tech. Rep. NASA-TM-X-2335, L-7803 (NASA Langley Research Center, 1971).
- [4] T. Washburn, *Airframe drag/weight reduction technologies*, Green Aviation Summit-Fuel Burn Reduction, NASA Ames Research Centre (2010).
- [5] J. N. Hefner and D. M. Bushnell, *An overview of concepts for aircraft drag reductions*, in AGARD Spec. Course on Concepts for Drag Reduction 30 p (1977).
- [6] O. Reynolds, *An experimental investigation of the circumstances which determine whether the motion of water shall be direct or sinuous, and of the law of resistance in parallel channels*, Philosophical Transactions of the Royal Society of London **174**, 935 (1883).
- [7] D. Jackson and B. Launder, *Osborne Reynolds and the publication of his papers on turbulent flow*, Annual Review of Fluid Mechanics **39**, 19 (2007).
- [8] H. Schlichting, E. Krause, H. Oertel, K. Gersten, and C. Mayes, *Boundary-Layer Theory* (Springer, 2003).
- [9] P. Schlatter, E. Deusebio, R. de Lange, and L. Brandt, *Numerical study of the stabilisation of boundary-layer disturbances by finite amplitude streaks*, International Journal of Flow Control **2**, 259 (2010).

- 1**
- [10] P. S. Klebanoff, K. D. Tidstrom, and L. M. Sargent, *The three-dimensional nature of boundary-layer instability*, Journal of Fluid Mechanics **12**, 1–34 (1962).
 - [11] T. Herbert, *Secondary instability of plane channel flow to subharmonic three dimensional disturbances*, The Physics of Fluids **26**, 871 (1983).
 - [12] A. D. D. Craik, *Non-linear resonant instability in boundary layers*, Journal of Fluid Mechanics **50**, 393–413 (1971).
 - [13] E. Reshotko, *Paths to transition in wall layers*, in *Advances in laminar-turbulent transition modeling* (Von Kármán Institute for Fluid Dynamics, 2008).
 - [14] W. M. Orr, *The stability or instability of the steady motions of a liquid*, Proceedings of the Royal Irish Academy. A. **27**, 9 (1907).
 - [15] A. Sommerfeld, *Ein Beitrag zur hydrodynamische Erklärung der turbulenten Flüssigkeitsbewegungen*, Proceedings of the 4th International Congress of Mathematicians. III. Rome , 116–124 (1907).
 - [16] W. Tollmien, *Über die Entstehung der Turbulenz. 1.* in *Nachrichten von der Gesellschaft der Wissenschaften zu Göttingen. Mathematisch-Physikalische Klasse* (Göttingen, 1929) pp. 21–44, translation in NACA TM No. 609 (1931).
 - [17] W. Tollmien, *Grenzschichttheorie*, Handbuch Experimentalphysik **4**, 241 (1931).
 - [18] H. Schlichting, *Zur Entstehung der Turbulenz bei der plattenströmung*, Nachrichten von der Gesellschaft der Wissenschaften zu Göttingen, Mathematisch-Physikalische Klasse , 181 (1933).
 - [19] G. B. Schubauer and H. K. Skramstad, *Laminar-boundary-layer oscillations and transition on a flat plate*, Tech. Rep. (National Aeronautics and Space Administration Washington DC, 1948).
 - [20] J. L. Van Ingen, *A suggested semi-empirical method for the calculation of the boundary layer transition region*, VTH-74 (Delft University of Technology, The Netherlands, 1956).
 - [21] J. L. Van Ingen, *The e^N -method for transition prediction. Historical review of work at TU Delft*, in *38th Fluid Dynamics Conference & Exhibit*, 2008-3830 (AIAA, Seattle, Washington, 2008).
 - [22] L. Mack, *Boundary layer stability theory*, in *AGARD, Special Course of Stability and Transition of Laminar Flows* (North Atlantic Treaty Organization, 1984).
 - [23] H. L. Reed, W. S. Saric, and D. Arnal, *Linear stability theory applied to boundary layers*, Annual Review of Fluid Mechanics **28**, 389 (1996).
 - [24] P. J. Schmid and D. S. Henningson, *Stability and Transition in Shear Flows* (Springer Verlag, 2001).

- [25] P. G. Drazin and W. H. Reid, *Hydrodynamic Stability* (Cambridge University Press, 2004).
- [26] A. D. D. Craik, *Wave interactions and fluid flows* (Cambridge University Press, 1988).
- [27] A. Smith and N. Gamberoni, *Transition, pressure gradient and stability theory*, in *Aircraft Co., Report No. ES 26 388, El Segundo, CA* (1956).
- [28] G. Schrauf, *Transition prediction using different linear stability analysis strategies*, AIAA Paper, 1848-1994 (1994).
- [29] J. Crouch and L. Ng, *Variable N-factor method for transition prediction in three-dimensional boundary layers*, AIAA journal **38**, 211 (2000).
- [30] G. Schrauf, *Industrial view on transition prediction*, in *Recent Results in Laminar-Turbulent Transition* (Springer, 2004) pp. 111–122.
- [31] J. Crouch, *Modeling transition physics for laminar flow control*, AIAA Paper, 3832-2008 (2008).
- [32] Honda, *Honda-developed Natural Laminar Flow (NLF) wings and nose*, <http://world.honda.com/HondaJet/innovation/02/> (2017), online; accessed 31-August-2017.
- [33] FlightGlobal, M. Kingsley-Jones, *Farnborough: Aero secrets of Boeing's new dreamliner*, <https://www.flightglobal.com/news/articles/farnborough-aero-secrets-of-boeings-new-dreamliner-401784/> (2014), online; accessed 31-August-2017.
- [34] N. De Tullio, P. Paredes, N. D. Sandham, and V. Theofilis, *Laminar-turbulent transition induced by a discrete roughness element in a supersonic boundary layer*, Journal of Fluid Mechanics **735**, 613–646 (2013).
- [35] J.-C. Loiseau, J.-C. Robinet, S. Cherubini, and E. Leriche, *Investigation of the roughness-induced transition: global stability analyses and direct numerical simulations*, Journal of Fluid Mechanics **760**, 175–211 (2014).
- [36] V. Citro, F. Giannetti, P. Luchini, and F. Auteri, *Global stability and sensitivity analysis of boundary-layer flows past a hemispherical roughness element*, Physics of Fluids **27**, 084110 (2015).
- [37] H. B. E. Kurz and M. J. Kloker, *Mechanisms of flow tripping by discrete roughness elements in a swept-wing boundary layer*, Journal of Fluid Mechanics **796**, 158 (2016).
- [38] M. R. Malik, F. Li, and C.-L. Chang, *Nonlinear crossflow disturbances and secondary instabilities in swept-wing boundary layers*, in *IUTAM Symposium on Nonlinear Instability and Transition in Three-Dimensional Boundary Layers: Proceedings of the IUTAM Symposium held in Manchester, U.K., 17–20 July 1995* (Springer Netherlands, Dordrecht, 1996) pp. 257–266.

- [39] W. Koch, F. P. Bertolotti, A. Stolte, and S. Hein, *Nonlinear equilibrium solutions in a three-dimensional boundary layer and their secondary instability*, Journal of fluid mechanics **406**, 131 (2000).
- [40] P. Wassermann and M. Kloker, *Mechanisms and passive control of crossflow-vortex-induced transition in a three-dimensional boundary layer*, Journal of Fluid Mechanics **456**, 49 (2002).
- [41] E. B. White and W. S. Saric, *Secondary instability of crossflow vortices*, Journal of Fluid Mechanics **525**, 275 (2005).
- [42] J. Serpieri and M. Kotsonis, *Spatio-temporal characteristics of secondary instabilities in swept wing boundary layers*, AIAA Paper (2016).
- [43] B. J. Holmes, C. J. Obara, G. L. Martin, and C. S. Domack, *Manufacturing tolerances for natural laminar flow airframe surfaces*, Tech. Rep. (SAE Technical Paper, 1985).
- [44] M. W. Tufts, H. L. Reed, B. K. Crawford, G. T. Duncan Jr, and W. S. Saric, *Computational investigation of step excrescence sensitivity in a swept-wing boundary layer*, Journal of Aircraft (2016).
- [45] D. Rodríguez, E. M. Gennaro, and M. P. Juniper, *The two classes of primary modal instability in laminar separation bubbles*, Journal of Fluid Mechanics **734** (2013).
- [46] V. Theofilis, *Advances in global linear instability analysis of nonparallel and three-dimensional flows*, Progress in Aerospace Sciences **39**, 249 (2003).
- [47] V. Theofilis, *Global linear instability*, Annual Review of Fluid Mechanics **43**, 319 (2011).
- [48] G. Bonfigli and M. Kloker, *Secondary instability of crossflow vortices: validation of the stability theory by direct numerical simulation*, Journal of Fluid Mechanics **583**, 229 (2007).
- [49] F. Bertolotti, *Linear and nonlinear stability of boundary layers with streamwise varying properties*, Ph.D. thesis, Ohio State University, Columbus (1991).
- [50] F. P. Bertolotti, T. Herbert, and P. R. Spalart, *Linear and nonlinear stability of the blasius boundary layer*, Journal of Fluid Mechanics **242**, 441 (1992).
- [51] F. Li and M. R. Malik, *Mathematical nature of parabolized stability equations*, in *Laminar-Turbulent Transition*, IUTAM Symposia (Springer, 1995) pp. 205–212.
- [52] T. Herbert, *Parabolized stability equations*, Annual Review of Fluid Mechanics **29**, 245 (1997).
- [53] C.-L. Chang, *The Langley stability and transition code (LASTRAC): LST, linear & nonlinear PSE for 2-D, axisymmetric and inite swept wing boundary layers*, in *41st Aerospace Sciences Meeting & Exhibit*, 2003-0974 (AIAA, Reno, Nevada, 2003).

- [54] D. Arnal, *Boundary layer transition: Predictions based on linear theory*, in *Special course on Progress in Transition Modelling*, R-793 (AGARD, 1994).
- [55] F. Gómez, S. L. Clainche, P. Paredes, M. Hermanns, and V. Theofilis, *Four decades of studying global linear instability: Progress and challenges*, AIAA Journal **50**, 2731 (2012).
- [56] P. Jordan and T. Colonius, *Wave packets and turbulent jet noise*, Annual review of fluid mechanics **45**, 173 (2013).
- [57] Q. Ye, F. F. J. Schrijer, and F. Scarano, *On Reynolds number dependence of micro-ramp-induced transition*, Journal of Fluid Mechanics **837**, 597 (2018).
- [58] J. Serpieri and M. Kotsonis, *Three-dimensional organisation of primary and secondary crossflow instability*, J. Fluid Mech. **799**, 200 (2016).
- [59] P. Huerre and P. A. Monkewitz, *Absolute and convective instabilities in open shear layers*, Journal of Fluid Mechanics **159**, 151 (1985).
- [60] P. Huerre and P. A. Monkewitz, *Local and global instabilities in spatially developing flows*, Annual Review of Fluid Mechanics **22**, 473 (1990).
- [61] J.-M. Chomaz, *Global instabilities in spatially developing flows: non-normality and nonlinearity*, Annu. Rev. Fluid Mech. **37**, 357 (2005).
- [62] L. Mack, *A numerical study of the temporal eigenvalue spectrum of the Blasius boundary layer*, Journal of Fluid Mechanics **73**, 497 (1976).
- [63] C. E. Grosch and H. Salwen, *The continuous spectrum of the Orr-Sommerfeld equation. part 1. the spectrum and the eigenfunctions*, J. Fluid Mech. **87**, 33 (1978).
- [64] U. Ehrenstein and F. Gallaire, *On two-dimensional temporal modes in spatially evolving open flows: the flat-plate boundary layer*, Journal of Fluid Mechanics **536**, 209 (2005).
- [65] F. Alizard and J. C. Robinet, *Spatially convective global modes in a boundary layer*, Physics of Fluids **19**, 114-105 (2007).
- [66] E. Åkervik, U. Ehrenstein, F. Gallaire, and D. S. Henningson, *Global two-dimensional stability measures of the flat plate boundary-layer flow*, European Journal of Mechanics B/Fluids **27**, 501 (2008).
- [67] D. A. Rodríguez, *Global Instability of Laminar Separation Bubbles*, Ph.D. thesis, Universidad Politécnica de Madrid (2010).
- [68] B. Sandstede and A. Scheel, *Absolute and convective instabilities of waves on unbounded and large bounded domains*, Physica D: Nonlinear Phenomena **145**, 233 (2000).
- [69] T. Kapitula and K. Promislow, *Spectral and dynamical stability of nonlinear waves* (Springer, 2013).

- [70] D. A. Rodríguez, A. Tumin, and V. Theofilis, *Towards the foundation of a global modes concept*, 6th AIAA Theoretical Fluid Mechanics Confer , 1 (2011).
- [71] M. Brynjell-Rahkola, N. Shahriari, P. Schlatter, A. Hanifi, and D. S. Henningson, *Stability and sensitivity of a cross-flow-dominated Falkner–Skan–Cooke boundary layer with discrete surface roughness*, Journal of Fluid Mechanics **826**, 830 (2017).
- [72] B. H. Anderson, J. Tinapple, and L. Surber, *Optimal control of shock wave turbulent boundary layer interactions using micro-array actuation*, AIAA Paper, 3197-2006 , 1 (2006).
- [73] H. Babinsky, Y. Li, and C. W. Pitt Ford, *Microramp control of supersonic oblique shock-wave/boundary-layer interactions*, AIAA Journal **47**, 668 (2009).
- [74] S. Ghosh, J.-I. Choi, and J. R. Edwards, *RANS and hybrid LES/RANS simulations of the effects of micro vortex generators using immersed boundary methods*, AIAA Paper, 3728-2008 (2008).
- [75] R. H. M. Giepmans, F. F. J. Schrijer, and B. W. van Oudheusden, *Flow control of an oblique shock wave reflection with micro-ramp vortex generators: Effects of location and size*, Physics of Fluids **26**, 066101 (2014).
- [76] M. R. Saad, H. Zare-Behtash, A. Che-Idris, and K. Kontis, *Micro-ramps for hypersonic flow control*, Micromachines **3**, 364 (2012).
- [77] Z. Sun, F. F. J. Schrijer, F. Scarano, and B. W. van Oudheusden, *The three-dimensional flow organization past a micro-ramp in a supersonic boundary layer*, Physics of Fluids **24**, 1 (2012).
- [78] Q. Ye, F. F. J. Schrijer, and F. Scarano, *Boundary layer transition mechanisms behind a micro-ramp*, Journal of Fluid Mechanics **793**, 132 (2016).
- [79] Q. Ye, *Mechanisms of Boundary layer Transition Induced by Isolated Roughness*, Ph.D. thesis, Delft University of Technology, Delft, The Netherlands (2017).
- [80] W. S. Saric, H. L. Reed, and E. B. White, *Stability and transition of three-dimensional boundary layers*, Annual Review of Fluid Mechanics **35**, 413 (2003).
- [81] M. R. Malik, F. Li, and C.-L. Chang, *Crossflow disturbances in three-dimensional boundary layers: nonlinear development, wave interaction and secondary instability*, Journal of Fluid Mechanics **268**, 1 (1994).
- [82] M. R. Malik, F. Li, M. M. Choudhari, and C.-L. Chang, *Secondary instability of cross-flow vortices and swept-wing boundary-layer transition*, Journal of Fluid Mechanics **399**, 85 (1999).
- [83] Y. Kohama, W. Saric, and J. Hoos, *A high frequency, secondary instability of crossflow vortices that leads to transition*, in *Proc. R. Aeronaut. Soc. Conf. on Boundary-Layer Transition and Control*, Cambridge, UK (1991).

- [84] M. Kawakami, Y. Kohama, and M. Okutsu, *Stability characteristics of stationary crossflow vortices in three-dimensional boundary layer*, in *37th Aerospace Sciences Meeting & Exhibit, Reno* (AIAA, 1998).
- [85] H. Bippes and T. Lerche, *Transition prediction in three-dimensional boundary-layer flows unstable to crossflow instability*, AIAA Paper, 1906-1997 (1997).
- [86] H. Bippes, *Basic experiments on transition in three-dimensional boundary layers dominated by crossflow instability*, Progress in aerospace sciences **35**, 363 (1999).
- [87] M. Kloker, *Advanced laminar flow control on a swept wing-useful crossflow vortices and suction*, in *38th Fluid dynamics conference and exhibit* (2008) p. 3835.
- [88] R. Messing and M. J. Kloker, *Investigation of suction for laminar flow control of three-dimensional boundary layers*, Journal of Fluid Mechanics **658**, 117 (2010).
- [89] T. Friederich and M. J. Kloker, *Control of the secondary cross-flow instability using localized suction*, Journal of Fluid Mechanics **706**, 470 (2012).
- [90] P. C. Dörr and M. J. Kloker, *Stabilisation of a three-dimensional boundary layer by base-flow manipulation using plasma actuators*, Journal of Physics D: Applied Physics **48**, 285205 (2015).
- [91] P. C. Dörr and M. J. Kloker, *Transition control in a three-dimensional boundary layer by direct attenuation of nonlinear crossflow vortices using plasma actuators*, International Journal of Heat and Fluid Flow **61**, 449 (2016).

2

STABILITY THEORY

This chapter introduces the elements of stability theory. The governing equations are derived by considering the Navier-Stokes equations for instantaneous flow in §2.1, the non-linear perturbation equations in §2.2 and the stability equations in §2.3. In the first part of the thesis (chap. 2, 4, 5 and 6), the attention is restricted to discrete mode mechanisms. This assumption is elaborated upon in §2.3.2, which leads to the commonly considered ansatzes in §2.3.3. In §2.4, it is explained exactly ‘what’ a solution describes and, in §2.5, it is shown how the governing equations can be used to assess ‘why’ a certain solution is a solution. This is done separately for both the eigenvalue (§2.5.1) and -functions (§2.5.2). The boundary conditions are discussed in §2.6.

The application cases treated in this thesis all concern very low Mach numbers ($M \leq 0.1$), qualifying the flows as incompressible [1]. Therefore *the treatment is restricted to incompressible flows throughout*. All discussed theory can be easily extended to the compressible regime. So, to be complete, this extension is discussed in §2.7.

2.1. NAVIER-STOKES EQUATIONS

Incompressible flows are governed by the Navier-Stokes equations:

$$\frac{\partial u}{\partial t} + u \frac{\partial u}{\partial x} + v \frac{\partial u}{\partial y} + w \frac{\partial u}{\partial z} = -\frac{1}{\rho} \frac{\partial p}{\partial x} + \nu \left(\frac{\partial^2 u}{\partial x^2} + \frac{\partial^2 u}{\partial y^2} + \frac{\partial^2 u}{\partial z^2} \right), \quad (2.1a)$$

$$\frac{\partial v}{\partial t} + u \frac{\partial v}{\partial x} + v \frac{\partial v}{\partial y} + w \frac{\partial v}{\partial z} = -\frac{1}{\rho} \frac{\partial p}{\partial y} + \nu \left(\frac{\partial^2 v}{\partial x^2} + \frac{\partial^2 v}{\partial y^2} + \frac{\partial^2 v}{\partial z^2} \right), \quad (2.1b)$$

$$\frac{\partial w}{\partial t} + u \frac{\partial w}{\partial x} + v \frac{\partial w}{\partial y} + w \frac{\partial w}{\partial z} = -\frac{1}{\rho} \frac{\partial p}{\partial z} + \nu \left(\frac{\partial^2 w}{\partial x^2} + \frac{\partial^2 w}{\partial y^2} + \frac{\partial^2 w}{\partial z^2} \right), \quad (2.1c)$$

$$\frac{\partial u}{\partial x} + \frac{\partial v}{\partial y} + \frac{\partial w}{\partial z} = 0, \quad (2.1d)$$

i.e. including the continuity equation. Commonly considered geometries include a solid surface that bounds the wall-normal coordinate. Here, u , v and w are the velocity components in the x - (streamwise), y - (wall-normal) and z - (spanwise) directions, t is time,

p is the static pressure, ρ is the density and ν is the kinematic viscosity. The velocity component and pressure variables in system (2.1) are instantaneous quantities, meaning their dependence on the independent variables can be expressed as:

$$q = q(x, y, z, t), \quad (2.2)$$

2

while ρ and ν are constants. In what follows, the combination of the momentum and continuity equations are together referred to as the Navier-Stokes equations and a short-hand notation is introduced: $\mathcal{N}(q) = 0$.

2.2. PERTURBATIONS EQUATIONS

When considering flow perturbations, a reference flow has to be defined. First of all, this reference flow is assumed to be steady; independent of time. Requiring a reference *flow*, has an implicit meaning: the reference must itself satisfy the governing equations, i.e. the steady form of system (2.1). In the context of flows, one refers to these solutions as the base flow or laminar flow. Base flow variables are denoted by:

$$\bar{Q} = \bar{Q}(\mathbf{x}), \quad (2.3)$$

where \mathbf{x} denotes a vector spanning the combination of spatial dimensions of the base flow. The variable \bar{Q} is also used to denote the entire base flow entity as a whole. The fact that \bar{Q} satisfies the steady Navier-Stokes equations is denoted by: $\mathcal{N}(\bar{Q}) = 0$.

Describing the instantaneous flow as a perturbation of the base flow \bar{Q} leads to:

$$q(x, y, z, t) = \bar{Q}(\mathbf{x}) + q'(x, y, z, t), \quad (2.4)$$

where q' denotes the perturbation.

The governing equations are derived by applying the perturbation expansion to the Navier-Stokes equations; evaluating $\mathcal{N}(\bar{Q} + q')$ yields:

$$\begin{aligned} \frac{\partial u'}{\partial t} + \bar{U} \frac{\partial u'}{\partial x} + u' \frac{\partial \bar{U}}{\partial x} + u' \frac{\partial u'}{\partial x} + \bar{V} \frac{\partial u'}{\partial y} + v' \frac{\partial \bar{U}}{\partial y} + v' \frac{\partial u'}{\partial y} + \bar{W} \frac{\partial u'}{\partial z} + w' \frac{\partial \bar{U}}{\partial z} + w' \frac{\partial u'}{\partial z} \\ = -\frac{1}{\bar{\rho}} \frac{\partial p'}{\partial x} + \bar{\nu} \left(\frac{\partial^2 u'}{\partial x^2} + \frac{\partial^2 u'}{\partial y^2} + \frac{\partial^2 u'}{\partial z^2} \right), \end{aligned} \quad (2.5a)$$

$$\begin{aligned} \frac{\partial v'}{\partial t} + \bar{U} \frac{\partial v'}{\partial x} + u' \frac{\partial \bar{V}}{\partial x} + u' \frac{\partial v'}{\partial x} + \bar{V} \frac{\partial v'}{\partial y} + v' \frac{\partial \bar{V}}{\partial y} + v' \frac{\partial v'}{\partial y} + \bar{W} \frac{\partial v'}{\partial z} + w' \frac{\partial \bar{V}}{\partial z} + w' \frac{\partial v'}{\partial z} \\ = -\frac{1}{\bar{\rho}} \frac{\partial p'}{\partial y} + \bar{\nu} \left(\frac{\partial^2 v'}{\partial x^2} + \frac{\partial^2 v'}{\partial y^2} + \frac{\partial^2 v'}{\partial z^2} \right), \end{aligned} \quad (2.5b)$$

$$\begin{aligned} \frac{\partial w'}{\partial t} + \bar{U} \frac{\partial w'}{\partial x} + u' \frac{\partial \bar{W}}{\partial x} + u' \frac{\partial w'}{\partial x} + \bar{V} \frac{\partial w'}{\partial y} + v' \frac{\partial \bar{W}}{\partial y} + v' \frac{\partial w'}{\partial y} + \bar{W} \frac{\partial w'}{\partial z} + w' \frac{\partial \bar{W}}{\partial z} + w' \frac{\partial w'}{\partial z} \\ = -\frac{1}{\bar{\rho}} \frac{\partial p'}{\partial z} + \bar{\nu} \left(\frac{\partial^2 w'}{\partial x^2} + \frac{\partial^2 w'}{\partial y^2} + \frac{\partial^2 w'}{\partial z^2} \right), \end{aligned} \quad (2.5c)$$

$$\frac{\partial u'}{\partial x} + \frac{\partial v'}{\partial y} + \frac{\partial w'}{\partial z} = 0. \quad (2.5d)$$

System (2.5) governs all possible three-dimensional incompressible non-linear perturbation dynamics [2–5].

Note that no terms appear that solely consist of base flow variables, all terms are linear or quadratic in the perturbation terms. When evaluating $\mathcal{N}(\bar{Q} + q')$, these terms together form the equation $\mathcal{N}(\bar{Q}) = 0$ and thus cancel.

The base flow variables do make an appearance as the coefficients to linear perturbation terms. These terms are always the result of the non-linear convection terms in the instantaneous equation. They appear in two ways, as advection terms with the form $\bar{Q} \partial q' / \partial x$, or as reaction terms in the form $q' \partial \bar{Q} / \partial x$. In a sense, the latter terms are new. As will be illustrated in the body of this thesis, they are very important, because they are directly responsible for linear perturbation amplification, see Mack [6]. The factor $\partial \bar{Q} / \partial x$ represents the *base flow shear* in general, which illustrates the importance of this quantity and explains why attention is focussed on regions in the flow that support a strong shear.

The attention is restricted to infinitesimally small perturbations, which means that the quadratic terms are negligibly small with respect to the linear terms. Simplifying system (2.5) accordingly yields:

$$\begin{aligned} \frac{\partial u'}{\partial t} + \bar{U} \frac{\partial u'}{\partial x} + u' \frac{\partial \bar{U}}{\partial x} + \bar{V} \frac{\partial u'}{\partial y} + v' \frac{\partial \bar{U}}{\partial y} + \bar{W} \frac{\partial u'}{\partial z} + w' \frac{\partial \bar{U}}{\partial z} \\ = -\frac{1}{\bar{\rho}} \frac{\partial p'}{\partial x} + \bar{v} \left(\frac{\partial^2 u'}{\partial x^2} + \frac{\partial^2 u'}{\partial y^2} + \frac{\partial^2 u'}{\partial z^2} \right), \end{aligned} \quad (2.6a)$$

$$\begin{aligned} \frac{\partial v'}{\partial t} + \bar{U} \frac{\partial v'}{\partial x} + u' \frac{\partial \bar{V}}{\partial x} + \bar{V} \frac{\partial v'}{\partial y} + v' \frac{\partial \bar{V}}{\partial y} + \bar{W} \frac{\partial v'}{\partial z} + w' \frac{\partial \bar{V}}{\partial z} \\ = -\frac{1}{\bar{\rho}} \frac{\partial p'}{\partial y} + \bar{v} \left(\frac{\partial^2 v'}{\partial x^2} + \frac{\partial^2 v'}{\partial y^2} + \frac{\partial^2 v'}{\partial z^2} \right), \end{aligned} \quad (2.6b)$$

$$\begin{aligned} \frac{\partial w'}{\partial t} + \bar{U} \frac{\partial w'}{\partial x} + u' \frac{\partial \bar{W}}{\partial x} + \bar{V} \frac{\partial w'}{\partial y} + v' \frac{\partial \bar{W}}{\partial y} + \bar{W} \frac{\partial w'}{\partial z} + w' \frac{\partial \bar{W}}{\partial z} \\ = -\frac{1}{\bar{\rho}} \frac{\partial p'}{\partial z} + \bar{v} \left(\frac{\partial^2 w'}{\partial x^2} + \frac{\partial^2 w'}{\partial y^2} + \frac{\partial^2 w'}{\partial z^2} \right), \end{aligned} \quad (2.6c)$$

$$\frac{\partial u'}{\partial x} + \frac{\partial v'}{\partial y} + \frac{\partial w'}{\partial z} = 0. \quad (2.6d)$$

This system of partial differential equations is referred to as the Linearized Navier-Stokes (LNS) equations.

The infinitesimal proximity of q to \bar{Q} means that the quantity q' is infinitesimal with respect to \bar{Q} everywhere, i.e. at all points in space and time. That is, if $\bar{Q} = O(1)$, then $q' = O(\epsilon)$, where $\epsilon \ll 1$. Note that q' is considered to be dependent on all spatial dimensions and time.

2.3. STABILITY EQUATIONS

Turbulent flows are inherently three-dimensional and unsteady. Models of such flows, that are required to resolve all important physical mechanisms, therefore must be three-dimensional and unsteady as well. When studying perturbations within the context of

stability theory, a similar argument applies. For this reason, it is stipulated that the perturbation q' should, most generally, depend on all spatial dimensions and time. The same, however, does not necessarily apply for the laminar base flow. In fact, many of the more complicated flow configuration examples named in the introduction, for which there is an interest in the perspective of laminar-turbulent transition, the base flows are essentially two-dimensional in space.

2.3.1. DIMENSIONALITY REDUCTION: FOURIER TRANSFORMATION

Inserting base flows dependent on less than 3 spatial dimensions into system (2.6), renders the system to have constant coefficients with respect to the direction of invariance. This is good news, because the general solution to linear differential equations with constant coefficients can be decomposed into a sum of exponential functions; the problem can be Fourier transformed in the directions of invariance (without introducing convolution terms). In light of the upcoming discussion, it is important to illustrate this transformation in detail.

Specifically, one defines \mathbf{x}^\perp to be the vector of spatial dimensions orthogonal to the spatial dimensions on which \bar{Q} depends, i.e. $\mathbf{x}^\perp \perp \mathbf{x}$. It is important to emphasize this convention, as introduced before, \mathbf{x} does not just denote a position vector, it specifically denotes the spatial dimensions of \bar{Q} . The perturbation solutions can be Fourier transformed as follows:

$$q'(\mathbf{x}, \mathbf{x}^\perp, t) = \int_{-\infty}^{\infty} \int_{\mathbb{R}^d} \cdots \int_{\mathbb{R}^d} \tilde{q}(\mathbf{x}; \mathbf{k}, \omega) e^{i(\mathbf{k} \cdot \mathbf{x}^\perp - \omega t)} d\mathbf{k} d\omega, \quad (2.7)$$

where \tilde{q} represents the combination of the perturbation amplitude distribution in \mathbf{x} and the Fourier transform of the perturbations in \mathbf{x}^\perp , \mathbf{k} is the wavenumber vector in \mathbf{x}^\perp , ω is the angular frequency and $\int \cdots \int_{\mathbb{R}^d}$ denotes the iterated integrals over the real line over all components of \mathbf{k} .

Expression (2.7) is just the Fourier transform of the solution q' in \mathbf{x}^\perp and t , no extra information is added. First of all, it is required that the solution satisfies the governing equations. This is done by substituting the Fourier ansatz into system (2.6). The equations that result are generally referred to as the stability equations. The resulting problem is a partial-differential-eigenvalue problem for the combination $\{\tilde{q}; \mathbf{k}, \omega\}$. Instead of a full differential problem in time and three-dimensional space, the stability problem governs general functions \tilde{q} in \mathbf{x} , while the residual dimensionality is condensed in $\{\mathbf{k}, \omega\}$.

2.3.2. ATOMS OF DYNAMICS: DISCRETE EIGEN SOLUTIONS

It is customary to moreover require that the solution is an *eigensolution*; a discrete mode of the system. A simplified illustration of enforcing this constraint is given here. A thorough elaboration is given in appendix A. To illustrate how this is enforced onto equation (2.7), one of the spectral variables, i.e. ω or a component of \mathbf{k} , has to be chosen, depending on the solution character of interest. Here, the temporal problem is considered as an example. In this case, one considers the problem to be an initial value problem in time. A solution shape is assumed at a point in time and its evolution in time is the unknown. The derivation for the equivalent spatial problem is directly analogous. In that case, a solution is assumed to be given at a point in space and the approach yields its evolution in space, so it is an initial value problem in space.

In the set-up of the temporal problem, the unknown is the temporal dynamics, which are completely contained in ω . This means that the problem is to be solved for ω . The prescription of the solution shape in \mathbf{x}^\perp is completely contained in the specification of the components of $\mathbf{k} = \mathbf{k}_c$, where the subscript c implies the free ‘choice’ of this prescription. The spatial problem, instead, would be solved for (one of the components of) \mathbf{k} , while prescribing (the other components and) $\omega = \omega_c$. The chosen parameters are usually taken to be real. The corresponding unknown variable is generally complex-valued.

An inherent property of a discrete temporal solution is that it is completely monochromatic in Fourier space. This statement is captured in assuming the following form of \tilde{q} :

$$\tilde{q}(\mathbf{x}; \mathbf{k}, \omega) = \sum_j a_j \tilde{q}_j(\mathbf{x}) \delta(\mathbf{k} - \mathbf{k}_c) \tilde{\delta}(\omega - \Omega_j(\mathbf{k})), \quad (2.8)$$

where $\tilde{\delta}$ is a delta function behaving similarly as the Dirac delta function, δ ; its precise characteristics are further elaborated upon in appendix A. Furthermore, $\Omega_j(\mathbf{k})$, a_j and \tilde{q}_j are the dispersion relation, amplitude and amplitude shape function for the discrete mode with index j , respectively. The entities Ω_j , a_j and \tilde{q}_j all depend on \mathbf{k} , but the dependency is here not written explicitly for a_j and \tilde{q}_j . The equation $\omega = \Omega_j(\mathbf{k})$ denotes that ω is the solution of the governing partial differential equations, given \mathbf{k} . The assumed discrete nature of the modes allows evaluating (2.7) for each mode j separately.¹

$$\begin{aligned} q'(\mathbf{x}, \mathbf{x}^\perp, t) &= \int_{-\infty}^{\infty} \int \cdots \int_{\mathbb{R}^d} \sum_j a_j \tilde{q}_j(\mathbf{x}) \delta(\mathbf{k} - \mathbf{k}_c) \tilde{\delta}(\omega - \Omega_j(\mathbf{k})) e^{i(\mathbf{k} \cdot \mathbf{x}^\perp - \omega t)} d\mathbf{k} d\omega \\ &= \sum_j a_j \int_{-\infty}^{\infty} \int \cdots \int_{\mathbb{R}^d} \tilde{q}_j(\mathbf{x}) \delta(\mathbf{k} - \mathbf{k}_c) \tilde{\delta}(\omega - \Omega_j(\mathbf{k})) e^{i(\mathbf{k} \cdot \mathbf{x}^\perp - \omega t)} d\mathbf{k} d\omega \\ &= \sum_j a_j \int_{-\infty}^{\infty} \tilde{q}_j(\mathbf{x}) \tilde{\delta}(\omega - \Omega_j(\mathbf{k}_c)) e^{i(\mathbf{k}_c \cdot \mathbf{x}^\perp - \omega t)} d\omega + c.c. \\ &= \sum_j a_j \underbrace{\tilde{q}_j(\mathbf{x}) e^{i(\mathbf{k}_c \cdot \mathbf{x}^\perp - \Omega_j(\mathbf{k}_c) t)}}_{q'_j(\mathbf{x}, \mathbf{x}^\perp, t)} + c.c. \end{aligned} \quad (2.9)$$

Here, *c.c.* denotes the complex conjugate. The entities q'_j live entirely in physical space, as opposed to in Fourier space, and each is a solution of system (2.6). Furthermore, each q'_j has its own (or: ‘eigen’) behaviour, meaning the dynamics of q'_j is independent of the other q'_l with $l \neq j$. For that reason, only the few q'_j solutions that are of interest can be considered.

When the methodology is introduced in the literature, usually the treatment jumps directly to considering the *individual* discrete modes *a priori*, without referring to the underlying complex analysis associated to the Fourier transform. As a consequence, one usually encounters the following ansatz form in the literature:

$$q'(\mathbf{x}, \mathbf{x}^\perp, t) = \tilde{q}(\mathbf{x}) e^{i(\mathbf{k} \cdot \mathbf{x}^\perp - \omega t)} + c.c. \quad (2.10)$$

The sum and the amplitudes a_j are accordingly dropped.

¹Cases may occur where two solutions Ω_j and Ω_l intersect, i.e. $\Omega_j = \Omega_l$, while $j \neq l$. This situation is not encountered here specifically and therefore ignored.

An alternative form is written as:

$$q'(\mathbf{x}, \mathbf{x}^\perp, t) = \tilde{q}(\mathbf{x}) e^{i(\Theta(\mathbf{x}^\perp) - \omega t)} + c.c., \quad (2.11)$$

where Θ is the complex phase in \mathbf{x}^\perp . The phase Θ is a linear function of \mathbf{x}^\perp , such that the corresponding wavenumber vector $\mathbf{k} = \partial\Theta/\partial\mathbf{x}^\perp$ is constant. Here, $\partial/\partial\mathbf{x}^\perp$ denotes the gradient with respect to the directions contained in \mathbf{x}^\perp .

Conventionally, one defines:

$$\alpha = \frac{\partial\Theta}{\partial x}, \quad \text{and:} \quad \beta = \frac{\partial\Theta}{\partial z}, \quad (2.12)$$

such that, for example, $\mathbf{k} = [\alpha \ \beta]^T$, if $\mathbf{x}^\perp = [x \ z]^T$. These are the definitions of the streamwise, α , and spanwise, β , wavenumbers, respectively, corresponding to the streamwise and spanwise labels associated to x and z .

By expanding the exponents of the exponential function, it can be deduced that:

$$\omega_i > 0, \quad \alpha_i < 0 \quad \text{and} \quad \beta_i < 0 \quad (2.13)$$

all respectively correspond to exponential growth of the solutions in the positive t -, x - and z -directions. All stability characteristics inferred from the eigenvalues apply asymptotically in time, i.e. as $t \rightarrow \infty$ [5, 7].

The eigensolutions can be viewed as the building blocks of perturbations; the eigensolutions form an eigenfunction expansion basis. Equation (2.11) refers to a single eigensolution, but an infinitude of solutions $\{\tilde{q}; \mathbf{k}, \omega\}$ (harmonics) is expected in every dimension of the domain spanned by \mathbf{x} . This is required for the eigenfunction basis to be complete. For an important related elaboration in the context of flow stability theory, see Grosch and Salwen [8], Salwen and Grosch [9].

However, usually only very few eigensolutions become unstable. This yields the main advantage of considering stability approaches. Due to the exponential decay of the stable modes, those can usually be discarded. So, instead of considering the full dynamics of the system (i.e. considering all modes), the problem is reduced to solving for individual modes (the building blocks or dynamical atoms) that most prominently rule the dynamics of the system. This is where the Fourier ansatz pays off in reducing the dimensionality of the problem.

2.3.3. SPECIFIC EXPANSION ANSATZES

As elaborated on in the introduction, the different stability methods directly correspond to the base flow dimensionality incorporated in the stability approach. In summary, the methods relevant for the current purposes are defined in terms of the following ansatzes for the perturbations:

$$\begin{aligned} \text{LST: } q' &= \tilde{q}(y) e^{i(\alpha x + \beta z - \omega t)} &+ c.c., \\ \text{PSE: } q' &= \tilde{q}(\varepsilon x, y) e^{i(\int^x \alpha(\varepsilon \hat{x}) d\hat{x} + \beta z - \omega t)} &+ c.c., \\ \text{Streamwise BiGlobal: } q' &= \tilde{q}(x, y) e^{i(\beta z - \omega t)} &+ c.c., \\ \text{Spanwise BiGlobal: } q' &= \tilde{q}(z, y) e^{i(\alpha x - \omega t)} &+ c.c., \end{aligned} \quad (2.14)$$

This explicitly denotes the one-dimensionality of the LST approach and the streamwise (BiGlobal) and spanwise (BiLocal) orientations of the planes of consideration for the most recurring variants of the BiGlobal approaches mentioned in the introduction.

It should be emphasized that the dimensionality of \tilde{q} in all different stability approaches (including PSE) directly corresponds to the incorporated dimensionality of the base flow \bar{Q} .

To give the link to the classical theory, the famous Orr-Sommerfeld (and Squire) equation are derived by substituting the LST ansatz into system (2.6) and eliminating the pressure and streamwise and spanwise velocity amplitudes. Effectively, the wall-normal-velocity/wall-normal-vorticity formulation is derived, where the Orr-Sommerfeld equation and Squire equations govern the wall-normal velocity component and the wall-normal vorticity component, respectively.

The spanwise BiGlobal stability problem is considered to exemplify the resulting system of equations. In that case, it is assumed that $\partial \bar{Q} / \partial x = 0$, because $\mathbf{x}^\perp = [x]$ and $\mathbf{x} = [y, z]$. Incorporating this assumption and substituting the spanwise BiGlobal ansatz into system (2.6) results in the following system of equations:

$$-\mathrm{i}\omega \tilde{u} + \mathrm{i}\alpha \bar{U} \tilde{u} + \bar{V} \frac{\partial \tilde{u}}{\partial y} + \bar{W} \frac{\partial \tilde{u}}{\partial z} + \tilde{v} \frac{\partial \bar{U}}{\partial y} + \tilde{w} \frac{\partial \bar{U}}{\partial z} = -\mathrm{i}\alpha \tilde{p} + \frac{1}{Re} \left(-\alpha^2 + \frac{\partial^2}{\partial y^2} + \frac{\partial^2}{\partial z^2} \right) \tilde{u}; \quad (2.15a)$$

$$-\mathrm{i}\omega \tilde{v} + \mathrm{i}\alpha \bar{U} \tilde{v} + \bar{V} \frac{\partial \tilde{v}}{\partial y} + \bar{W} \frac{\partial \tilde{v}}{\partial z} + \tilde{v} \frac{\partial \bar{V}}{\partial y} + \tilde{w} \frac{\partial \bar{V}}{\partial z} = -\frac{\partial \tilde{p}}{\partial y} + \frac{1}{Re} \left(-\alpha^2 + \frac{\partial^2}{\partial y^2} + \frac{\partial^2}{\partial z^2} \right) \tilde{v}; \quad (2.15b)$$

$$-\mathrm{i}\omega \tilde{w} + \mathrm{i}\alpha \bar{U} \tilde{w} + \bar{V} \frac{\partial \tilde{w}}{\partial y} + \bar{W} \frac{\partial \tilde{w}}{\partial z} + \tilde{v} \frac{\partial \bar{W}}{\partial y} + \tilde{w} \frac{\partial \bar{W}}{\partial z} = -\frac{\partial \tilde{p}}{\partial z} + \frac{1}{Re} \left(-\alpha^2 + \frac{\partial^2}{\partial y^2} + \frac{\partial^2}{\partial z^2} \right) \tilde{w}; \quad (2.15c)$$

$$\mathrm{i}\alpha \tilde{u} + \frac{\partial \tilde{v}}{\partial y} + \frac{\partial \tilde{w}}{\partial z} = 0. \quad (2.15d)$$

This equation is presented in non-dimensional form,² introducing a particular length, velocity, density and first viscosity coefficient scale, which are respectively denoted by \bar{U}_s , l_s , $\bar{\rho}_s$ and $\bar{\mu}_s$ in this chapter. The subscript s just denotes scale in this chapter. Appropriate length scales are introduced for every application test case. The pressure scale consistently corresponds to (twice the) dynamic pressure associated to these scales: $\bar{\rho}_s \bar{U}_s^2$. The corresponding Reynolds number is defined as:³

$$Re = \frac{\bar{\rho}_s \bar{U}_s l_s}{\bar{\mu}_s}. \quad (2.16)$$

System (2.15) has a particular form in the perspective of the temporal stability framework, in which ω is the unknown, and spatial stability framework, in which α is the unknown. In particular, one defines $\Xi = [\tilde{u}, \tilde{v}, \tilde{w}, \tilde{p}]^T$, such that the two problems can be

²In this chapter, the convention is used to write the stability equations, governing the \tilde{q} -variables, in a non-dimensional form, while the perturbations equations, governing the q' -variables, in dimensional form.

³For the currently presumed incompressible flow circumstance, \bar{v} is constant and equal to $\bar{\mu}_s / \bar{\rho}_s$, which, in turn, is absorbed into the Reynolds number.

written as follows:

$$\text{temporal problem: } \mathbf{A}_\omega \Xi = \omega \mathbf{B}_\omega \Xi \quad (2.17)$$

$$\text{spatial problem: } \mathbf{A}_\alpha \Xi = \alpha \mathbf{B}_\alpha \Xi + \alpha^2 \mathbf{C}_\alpha \Xi, \quad (2.18)$$

2

where \mathbf{A}_ω , \mathbf{B}_ω , \mathbf{A}_α and \mathbf{C}_α represent the coefficient matrices multiplying ω^0 , ω^1 , α^0 , α^1 and α^2 , respectively. Per convention, Ξ is referred to as the *eigenvector* of the system, while the variables \tilde{q} are referred to as *eigenfunctions*.

Even though the PSE method will not be considered in this thesis, it is important to illustrate the difference in the approach compared to the LST approach. In the PSE method, a small dependency in the streamwise direction is retained, which corresponds to the following ansatz:

$$\text{PSE: } q' = \tilde{q}(\varepsilon x, y) e^{i(\int^x \alpha(\varepsilon \hat{x}) d\hat{x} + \beta z - \omega t)} + c.c., \quad (2.19)$$

where \hat{x} denotes the integration variable equivalent of x and the currently introduced $\varepsilon \ll 1$ encodes the slowly developing character of the base flow in the streamwise direction: $\partial/\partial x = \varepsilon \partial/\partial y$. It is independent of the ε mentioned in relation to the size of $q' = O(\varepsilon)$ with respect to $\bar{Q} = O(1)$.

2.3.4. LST: NON-PARALLEL ORR-SOMMERFELD EQUATION

The LST framework will be used for reference in multiple occasions in this thesis. A proper derivation of the Orr-Sommerfeld equation (and its non-parallel equivalent) are in place. The starting point is the full system that results when applying the LST ansatz to system 2.6. In this case, it is assumed that $\mathbf{x}^\perp = [x, z]$ and $\mathbf{x} = [y]$, such that $\partial \bar{Q}/\partial x = \partial \bar{Q}/\partial z = 0$, which yields:

$$-i\omega \tilde{u} + i\alpha \bar{U} \tilde{u} + \bar{V} \frac{d\tilde{u}}{dy} + \tilde{v} \frac{d\bar{U}}{dy} + i\beta \bar{W} \tilde{u} = -i\alpha \tilde{p} + \frac{1}{Re} \left(\frac{d^2}{dy^2} - \alpha^2 - \beta^2 \right) \tilde{u}, \quad (2.20a)$$

$$-i\omega \tilde{v} + i\alpha \bar{U} \tilde{v} + \bar{V} \frac{d\tilde{v}}{dy} + \tilde{v} \frac{d\bar{V}}{dy} + i\beta \bar{W} \tilde{v} = -\frac{d\tilde{p}}{dy} + \frac{1}{Re} \left(\frac{d^2}{dy^2} - \alpha^2 - \beta^2 \right) \tilde{v}, \quad (2.20b)$$

$$-i\omega \tilde{w} + i\alpha \bar{U} \tilde{w} + \bar{V} \frac{d\tilde{w}}{dy} + \tilde{v} \frac{d\bar{W}}{dy} + i\beta \bar{W} \tilde{w} = -i\beta \tilde{p} + \frac{1}{Re} \left(\frac{d^2}{dy^2} - \alpha^2 - \beta^2 \right) \tilde{w}, \quad (2.20c)$$

$$i\alpha \tilde{u} + \frac{d\tilde{v}}{dy} + i\beta \tilde{w} = 0. \quad (2.20d)$$

Note that the *parts* of the operators in equations (2.20a) and (2.20c) that solely operate on \tilde{u} and \tilde{w} , respectively; given by:

$$\tilde{\mathcal{D}}_{\bar{V}} = -i\omega + i\alpha \bar{U} + \bar{V} \frac{d}{dy} + i\beta \bar{W} - \frac{1}{Re} \left(\frac{d^2}{dy^2} - \alpha^2 - \beta^2 \right), \quad (2.21)$$

are identical. By combining equations $i\alpha(2.20a) + i\beta(2.20c)$, the sum $i\alpha \tilde{u} + i\beta \tilde{w}$ can be isolated and replaced by $-d\tilde{v}/dy$, by using the continuity equation (2.20d):

$$-\tilde{\mathcal{D}}_{\bar{V}} \frac{d\tilde{v}}{dy} + i\alpha \frac{d\bar{U}}{dy} \tilde{v} + i\beta \frac{d\bar{W}}{dy} \tilde{v} = (\alpha^2 + \beta^2) \tilde{p}. \quad (2.22)$$

This has completely eliminated \tilde{u} and \tilde{w} . Differentiating equation (2.22) with respect to y yields:

$$\begin{aligned} & -i\omega \left(-\frac{d^2 \tilde{v}}{dy^2} \right) + i\alpha \cancel{\frac{d\bar{U}}{dy} \left(-\frac{d\tilde{v}}{dy} \right)} + i\alpha \bar{U} \left(-\frac{d^2 \tilde{v}}{dy^2} \right) + \frac{d\bar{V}}{dy} \left(-\frac{d^2 \tilde{v}}{dy^2} \right) + \bar{V} \left(-\frac{d^3 \tilde{v}}{dy^3} \right) \\ & + i\beta \cancel{\frac{d\bar{W}}{dy} \left(-\frac{d\tilde{v}}{dy} \right)} + i\beta \bar{W} \left(-\frac{d^2 \tilde{v}}{dy^2} \right) - \frac{1}{Re} \left(\frac{d^2}{dy^2} - \alpha^2 - \beta^2 \right) \left(-\frac{d^2 \tilde{v}}{dy^2} \right) \\ & + i\alpha \frac{d^2 \bar{U}}{dy^2} \tilde{v} + i\alpha \cancel{\frac{d\bar{U}}{dy} \frac{d\tilde{v}}{dy}} + i\beta \frac{d^2 \bar{W}}{dy^2} \tilde{v} + i\beta \cancel{\frac{d\bar{W}}{dy} \frac{d\tilde{v}}{dy}} = (\alpha^2 + \beta^2) \frac{d\tilde{p}}{dy}, \end{aligned} \quad (2.23)$$

where the terms with the same slope strike-through lines cancel. After rearranging, gives:

$$\begin{aligned} & \left[-i\omega + i\alpha \bar{U} + \frac{d\bar{V}}{dy} + \bar{V} \frac{d}{dy} + i\beta \bar{W} - \frac{1}{Re} \left(\frac{d^2}{dy^2} - \alpha^2 - \beta^2 \right) \right] \left(-\frac{d^2 \tilde{v}}{dy^2} \right) \\ & + i\alpha \frac{d^2 \bar{U}}{dy^2} \tilde{v} + i\beta \frac{d^2 \bar{W}}{dy^2} \tilde{v} - (\alpha^2 + \beta^2) \frac{d\tilde{p}}{dy} = 0. \end{aligned} \quad (2.24)$$

The factor $d\tilde{p}/dy$ can be eliminated by using the y -momentum equation (2.20b). Note that the y -momentum equation, excluding the $d\tilde{p}/dy$ term, can be written in terms of the operator indicated with the square brackets in equation (2.24), including the Reynolds stress term $\tilde{v} d\bar{V}/dy$. Multiplying the y -momentum equation with $(\alpha^2 + \beta^2)$ gives an expression compatible with equation (2.24):

$$\left[-i\omega + i\alpha \bar{U} + \frac{d\bar{V}}{dy} + \bar{V} \frac{d}{dy} + i\beta \bar{W} - \frac{1}{Re} \left(\frac{d^2}{dy^2} - \alpha^2 - \beta^2 \right) \right] (\alpha^2 + \beta^2) \tilde{v} = -(\alpha^2 + \beta^2) \frac{d\tilde{p}}{dy}. \quad (2.25)$$

Substituting yields the non-parallel equivalent of the Orr-Sommerfeld equation; here expressed as the operator solely acting on \tilde{v} :

$$\begin{aligned} \tilde{\mathcal{D}} = & \left(-i\omega + i\alpha \bar{U} + \bar{V} \frac{d}{dy} + \frac{d\bar{V}}{dy} + i\beta \bar{W} \right) \left(\frac{d^2}{dy^2} - \alpha^2 - \beta^2 \right) \\ & - i\alpha \frac{d^2 \bar{U}}{dy^2} - i\beta \frac{d^2 \bar{W}}{dy^2} - \frac{1}{Re} \left(\frac{d^2}{dy^2} - \alpha^2 - \beta^2 \right)^2. \end{aligned} \quad (2.26)$$

To arrive at the proper Orr-Sommerfeld equation, the impact of the used ansatz on the base flow properties has to be incorporated.

2.3.5. PARALLEL FLOW ASSUMPTION

The use of the modal ansatzes (2.14) is based on which directions of the base flow are homogeneous. That is, which directions are contained in \mathbf{x}^\perp , as stated in equation (2.11). In many cases, however, the variation of a base flow is very small in a particular direction. For that reason, assuming the base flow to be homogeneous in such a direction is reasonable. However, there are other important, unexpected, implications associated to this. Next to these spatial homogeneity assumptions, it is inherently assumed in all

stability approaches that the base flow satisfies the Navier-Stokes equations, including the continuity equation.

Considering the LST framework ($\partial \bar{Q}/\partial x = \partial \bar{Q}/\partial z = 0$), the homogeneity assumption turns the continuity equation⁴ for the base flow into the following requirement:

$$\frac{\partial \bar{U}}{\partial x} + \frac{\partial \bar{V}}{\partial y} + \frac{\partial \bar{W}}{\partial z} = 0$$

$$\bar{V} = c^{\text{st}} \quad \text{in } y \quad \Rightarrow \quad \bar{V}|_{y=0} = 0 \quad \bar{V} = 0.$$

So, the inhomogeneity assumptions of LST are equivalent to assuming the wall-normal, non-parallel velocity of the base flow to be zero. A consistent LST analysis of a generic, non-parallel base flow only incorporates the physics represented by the “parallel part” of this base flow. Hence, the use of the ansatz corresponding to LST analysis amongst the ansatzes (2.14) is also referred to as the parallel flow assumption. For PSE analyses, the equivalent condition allows non-zero vertical flow momentum $\bar{\rho}\bar{V}$, but it is restricted to be small. Specifically, it has to be $O(1/Re)$.

Incorporating the parallel flow assumption in equation (2.26) yields the (proper) Orr-Sommerfeld operator, that again acts upon \tilde{v} :

$$\begin{aligned} \tilde{\mathcal{D}}_{\text{os}} = & \left(-i\omega + i\alpha \bar{U} + i\beta \bar{W} \right) \left(\frac{d^2}{dy^2} - \alpha^2 - \beta^2 \right) \\ & - i\alpha \frac{d^2 \bar{U}}{dy^2} - i\beta \frac{d^2 \bar{W}}{dy^2} - \frac{1}{Re} \left(\frac{d^2}{dy^2} - \alpha^2 - \beta^2 \right)^2. \end{aligned} \quad (2.27)$$

Sometimes this operator is presented in a form where it is divided by $i\alpha$.

For the BiGlobal stability framework, a similar, but less restrictive, argument applies. In that case, the equivalent condition is that the in-plane base flow (the momentum field) should be divergence free [10, 11]. It should be emphasized, once again, that *this renders the BiGlobal analysis to be the first hierarchical stability method, as opposed to LST and PSE, that allows O(1) base flow momentum in the direction of \mathbf{x}* , the spatial dimensions of \tilde{q} . The components of the corresponding velocity fields are referred to as the in-plane flow. For example, for $\mathbf{x} = [x, y]$, the in-plane flow is composed of the \bar{U} and \bar{V} components. As opposed to the case of LST, the divergence-free condition on the in-plane flow does not yield a (useful) simplification of system (2.15).

2.4. BASIC SOLUTION FEATURES

The Fourier ansatzes ‘complexify’ the problem. This introduces some basic solution features that deserve a brief elaboration.

The exponential part in equation (2.11) contains an imaginary part and so do the eigenfunctions in $\tilde{q}(\mathbf{x})$. This efficiently represents solutions having a travelling wave character. It is important to first consider the character of the factors \tilde{q} and $e^{i(\Theta-\omega t)}$. Recall that, per definition, \tilde{q} solely depends on \mathbf{x} , $\tilde{q} = \tilde{q}(\mathbf{x})$, while Θ depends solely on \mathbf{x}^\perp , $\Theta = \Theta(\mathbf{x}^\perp)$.

⁴This result can be easily extended to compressible flow, where the momentum field must be solenoidal.

2.4.1. THE AMPLITUDE FACTOR \tilde{q}

First of all, note that $e^{i(\Theta-\omega t)}$ is a factor of the eigenvector $\Xi = [\tilde{u}, \tilde{v}, \tilde{w}, \tilde{p}]^T$, i.e. it is a common factor to all eigenfunctions corresponding to the same Ξ . Due to the linearity of the eigenvalue problem, Ξ is defined up to a complex multiplicative constant. It is important to realise that the mutual complex proportionality of the eigenfunctions is fixed; e.g. \tilde{u} can generally not be scaled independently of \tilde{v} .

Note that each \tilde{q} can be divided into both the perturbation magnitude $|\tilde{q}|$ and phase $\arg(\tilde{q})$ in \mathbf{x} , by writing:

$$\tilde{q} = |\tilde{q}| e^{i\arg(\tilde{q})}, \quad (2.28)$$

where $\arg(\tilde{q})$ is unique to within an additive constant [12]. But, again, this non-uniqueness applies to the eigenvector Ξ as a whole; it is equal to the complex argument of the non-unique multiplicative constant of Ξ . For that reason, it is common for the different eigenfunctions corresponding to each Ξ .

Regions where $\arg(\tilde{q})$ increases linearly with \mathbf{x} implies the solution has a wavenumber (vector) $\partial \arg(\tilde{q}) / \partial \mathbf{x}$, which is always unique. Whenever $\partial \arg(\tilde{q}) / \partial \mathbf{x} = \mathbf{0}$, the solution locally behaves like a standing wave. Due to this qualitative interpretation and its uniqueness, $\partial \arg(\tilde{q}) / \partial \mathbf{x}$ is a proper characteristic of \tilde{q} , next to the modulus $|\tilde{q}|$. Note that, via the non-unique multiplicative constant, the real and imaginary parts of \tilde{q} can be arbitrarily phase shifted together to yield a pair of functions that are equally valid as the real and imaginary parts of the function \tilde{q} .

2.4.2. THE FACTOR $e^{i(\Theta-\omega t)}$ FOR INDIVIDUAL MODES: PHASE SPEED

The exponential part $e^{i(\Theta(\mathbf{x}^\perp)-\omega t)}$ describes the wave kinematics in the directions spanned by \mathbf{x}^\perp . It can be written in the following way:

$$e^{i(\mathbf{k} \cdot \mathbf{x}^\perp - \omega t)} = e^{i\mathbf{k} \cdot (\mathbf{x}^\perp - \mathbf{c}_{ph} t)}, \quad \text{where: } \mathbf{c}_{ph} = \frac{\mathbf{k}\omega}{\mathbf{k} \cdot \mathbf{k}} \quad (2.29)$$

such that $\mathbf{k} \cdot \mathbf{c}_{ph} = [\alpha \beta] \left[\frac{\alpha\omega}{\alpha^2 + \beta^2} \frac{\beta\omega}{\alpha^2 + \beta^2} \right]^T = \omega$ for the case where $\mathbf{x}^\perp = [x, z]$. In the previous relationship the variable $\mathbf{x}^\perp - \mathbf{c}_{ph} t$ represents a transformed coordinate. The quantity \mathbf{k} represents the wavenumber vector with respect to this coordinate. The new coordinate travels with the phase velocity, which is the real part⁵ of \mathbf{c}_{ph} with respect to \mathbf{x}^\perp . Note that \mathbf{c}_{ph} is oriented parallel to \mathbf{k} whenever $\omega_r \neq 0$. This implies that the wave's crests move with this velocity. This explains the kinematics of the majority of the 'discrete' mode solutions considered in this thesis.

2.4.3. THE FACTOR $e^{i(\Theta-\omega t)}$ FOR AN ENSEMBLE OF MODES: GROUP SPEED

It is important to consider the entity that results if multiple solutions are superposed, because it reveals the additional kinematics of continuum modes. The latter modes are discussed in detail in chapters 7 and 8 and appendix A. Here just a flavour is given, automatically leading to the introduction of the group speed.

⁵In this thesis, the Reynolds number will be indicated in italics, Re , while the operation of taking the real part is denoted by: $\text{Re}\{\cdot\}$. The curly braces indicate the distinction.

Assume $\mathbf{x}^\perp = [x]$ and take two (“discrete mode”) solutions with an equal amplitude, $\tilde{q}_{1,2}(\mathbf{x}) = 1$ for simplicity, while one has the wavenumber and frequency $(\alpha, \omega) = (\alpha_1, \omega_1)$ and the other (α_2, ω_2) . The sum of these solutions can be evaluated as follows:

$$\begin{aligned} e^{i(\alpha_1 x - \omega_2 t)} + e^{i(\alpha_2 x - \omega_2 t)} &= e^{i\left(\frac{\alpha_2 + \alpha_1}{2} x - \frac{\omega_2 + \omega_1}{2} t\right)} \left(e^{i\left(\frac{\alpha_2 - \alpha_1}{2} x - \frac{\omega_2 - \omega_1}{2} t\right)} + e^{-i\left(\frac{\alpha_2 - \alpha_1}{2} x - \frac{\omega_2 - \omega_1}{2} t\right)} \right) \\ &= e^{i\left(\frac{\alpha_2 + \alpha_1}{2} x - \frac{\omega_2 + \omega_1}{2} t\right)} \cos\left(\frac{\alpha_2 - \alpha_1}{2} x - \frac{\omega_2 - \omega_1}{2} t\right) \\ &= e^{i\frac{\alpha_2 + \alpha_1}{2}\left(x - \frac{\omega_2 + \omega_1}{\alpha_2 + \alpha_1} t\right)} \cos\left(\frac{\alpha_2 - \alpha_1}{2} \left(x - \frac{\omega_2 - \omega_1}{\alpha_2 - \alpha_1} t\right)\right). \end{aligned} \quad (2.30)$$

This illustrates that superposing two waves results in a new wave that has an adapted wave-like part (the familiar complex exponential factor), but it also has a real wave envelope (the cosine factor). Note that the envelope travels with the speed $(\omega_2 - \omega_1)/(\alpha_2 - \alpha_1)$ and has the wavenumber $(\alpha_2 - \alpha_1)/2$, while the wave part travels with the speed $(\omega_2 + \omega_1)/(\alpha_2 + \alpha_1)$ and has the wavenumber $(\alpha_2 + \alpha_1)/2$.

Taking $\alpha_2 = \alpha + 2d\alpha = \alpha_1 + 2d\alpha$ and $\omega_2 = \omega + 2d\omega = \omega_1 + 2d\omega$ models the situation where $\omega = \omega(\alpha)$ is a continuous function of α . The sum of the exponentials is linked to a particular form of the Fourier transform \tilde{g} , defined as:

$$\tilde{g}(\bar{\alpha}) = \delta(\bar{\alpha} - \alpha) + \delta(\bar{\alpha} - (\alpha + 2d\alpha)). \quad (2.31)$$

One can perform the following derivation:

$$q'(x, t) = \int_{-\infty}^{\infty} \tilde{g}(\bar{\alpha}) e^{i(\bar{\alpha}x - \omega(\bar{\alpha})t)} d\bar{\alpha} \quad (2.32)$$

$$= \int_{-\infty}^{\infty} \delta(\bar{\alpha} - \alpha) e^{i(\bar{\alpha}x - \omega(\bar{\alpha})t)} d\bar{\alpha} + \int_{-\infty}^{\infty} \delta(\bar{\alpha} - (\alpha + 2d\alpha)) e^{i(\bar{\alpha}x - \omega(\bar{\alpha})t)} d\bar{\alpha}$$

$$= e^{i(\alpha x - \omega(\alpha)t)} + e^{i((\alpha + 2d\alpha)x - \omega(\alpha + 2d\alpha)t)}$$

$$= e^{i(\alpha + 2d\alpha)\left(x - \frac{\omega + 2d\omega}{\alpha + 2d\alpha} t\right)} \cos\left(d\alpha \left(x - \frac{d\omega}{d\alpha} t\right)\right)$$

$$\approx e^{i\alpha(x - c_{ph}t)} \cos(d\alpha(x - c_g t)). \quad (2.33)$$

Equation (2.32) is a way of writing the general solution of the linear problem, where $\tilde{g}(\bar{\alpha})$ is the Fourier transform of the initial condition for q' in the x -direction, $q'(x, 0)$. This can be deduced by inserting $t = 0$, see Haberman [13, chapter 10] for more details.

The considered \tilde{g} corresponds to an initial condition built out of two sinusoids with wavenumbers α and $\alpha + 2d\alpha$ and equal amplitudes. The resulting solution consists of a wave-like part that, when neglecting the effect of the infinitesimals, has the wavelength α and travels at the speed $c_{ph} = \omega/\alpha$. The other factor represents an envelope that has an extent that tends to infinity: $2\pi/d\alpha$, while having a finite propagation speed: $d\omega/d\alpha$. The latter speed turns out to be important for various reasons discussed in what follows. It can be regarded as the speed with which the combination⁶ of the 2 waves travels. This is therefore referred to as the group speed, c_g .

⁶Haberman [13, chapter 14] notes that the energy associated to the waves travels with this speed.

The consideration of two infinitely close Dirac δ pulses generates a solution envelope structure that has an infinitely large periodicity length. This makes one question whether it is possible to construct a solution with a finite envelope extent or even a finite support. Expression (2.32) generalises building a solution corresponding to an initial condition with an arbitrary shape from a continuous function of $\tilde{\alpha}$. In fact, a direct use can be made of the uncertainty principle for functions and their Fourier transform. This states that the ‘width’ of a function and of its Fourier transform are linked. If the function is ‘broad’, its Fourier transform must be concentrated and vice versa [14]. The previous example represents an extreme case. The function \tilde{g} consisted of (a finite number of) Dirac δ functions and therefore classifies as infinitely concentrated in the α -space. The corresponding q' is a sum of sinusoids, which have an infinite support and therefore classify as infinitely broad.

The uncertainty principle can be properly illustrated with the Gaussian function. That is, for the initial condition take:

$$q'(x, 0) = g_\sigma(x) = e^{-\frac{x^2}{2\sigma^2}}, \quad (2.34)$$

where σ^2 encodes the width of $g_\sigma(x)$. The Fourier transform of $g_\sigma(x)$, $\tilde{g}_\sigma(\alpha)$, and the Gaussian integral, $\tilde{g}_\sigma(0)$, are written as follows:

$$\begin{aligned} \tilde{g}_\sigma(\alpha) &= \int_{-\infty}^{\infty} g_\sigma(x) e^{-i\alpha x} dx = \int_{-\infty}^{\infty} e^{-\frac{x^2}{2\sigma^2}} e^{-i\alpha x} dx; \\ \tilde{g}_\sigma(0) &= \int_{-\infty}^{\infty} g_\sigma(x) dx = \int_{-\infty}^{\infty} e^{-\frac{x^2}{2\sigma^2}} dx. \end{aligned} \quad (2.35)$$

The value $\tilde{g}_\sigma(0)$ is required to derive $\tilde{g}_\sigma(\alpha)$, so both quantities are derived together in what follows. The derivative of the Gaussian:

$$\frac{dg_\sigma}{dx} = -\frac{x}{\sigma^2} e^{-\frac{x^2}{2\sigma^2}}, \quad (2.36)$$

is used on essential points. The derivations are done as follows:

$$\begin{aligned} \tilde{g}_\sigma^2(0) &= \int_{-\infty}^{\infty} e^{-\frac{x^2}{2\sigma^2}} dx \int_{-\infty}^{\infty} e^{-\frac{y^2}{2\sigma^2}} dy & \frac{d\tilde{g}_\sigma}{d\alpha} &= \int_{-\infty}^{\infty} e^{-\frac{x^2}{2\sigma^2}} (-ixe^{-i\alpha x}) dx \\ &= \int_{-\infty}^{\infty} \int_{-\infty}^{\infty} e^{-\frac{x^2+y^2}{2\sigma^2}} dx dy & &= i\sigma^2 \int_{-\infty}^{\infty} \left(-\frac{x}{\sigma^2} e^{-\frac{x^2}{2\sigma^2}}\right) e^{-i\alpha x} dx \\ &= \int_0^{2\pi} d\theta \int_0^{\infty} e^{-\frac{r^2}{2\sigma^2}} r dr & &= i\sigma^2 \int_{-\infty}^{\infty} \frac{d}{dx} \left(e^{-\frac{x^2}{2\sigma^2}}\right) e^{-i\alpha x} dx \\ &= 2\pi \int_0^{\infty} e^{-\frac{r^2}{2\sigma^2}} r dr & &= i\sigma^2 \left[e^{-\frac{x^2}{2\sigma^2}} e^{-i\alpha x} \right]_{-\infty}^{\infty} \\ &= -2\pi\sigma^2 \int_0^{\infty} -\frac{r}{\sigma^2} e^{-\frac{r^2}{2\sigma^2}} dr & & \quad - \int_{-\infty}^{\infty} e^{-\frac{x^2}{2\sigma^2}} (-i\alpha e^{-i\alpha x}) dx \\ &= -2\pi\sigma^2 \int_0^{\infty} d\left(e^{-\frac{r^2}{2\sigma^2}}\right) & &= i\sigma^2 \left[0 + i\alpha \int_{-\infty}^{\infty} e^{-\frac{x^2}{2\sigma^2}} e^{-i\alpha x} dx \right] \\ &= -2\pi\sigma^2 [0 - 1] & &= -\sigma^2 \alpha \tilde{g}_\sigma \\ &= 2\pi\sigma^2 & \frac{d\tilde{g}_\sigma}{\tilde{g}_\sigma} &= -\sigma^2 \alpha d\alpha \end{aligned} \quad (2.37)$$

so $\tilde{g}_\sigma(0)$ evaluates to $\sigma\sqrt{2\pi}$. The differential equation (2.37) can be solved to give:

$$\begin{aligned}\ln \tilde{g}_\sigma &= -\frac{\sigma^2 \alpha^2}{2} + C \\ \tilde{g}_\sigma &= \tilde{g}_\sigma(0) e^{-\frac{\sigma^2 \alpha^2}{2}} \\ \tilde{g}_\sigma &= \sigma\sqrt{2\pi} e^{-\frac{\sigma^2 \alpha^2}{2}},\end{aligned}\quad (2.38)$$

2

completing the derivation. This is the classical result that the Fourier transform of a Gaussian is again a Gaussian.

It is crucial to notice that the width of \tilde{g}_σ depends on $1/\sigma^2$; so inversely to the width of g_σ . In the limit of $\sigma \rightarrow 0$, g_σ is extremely concentrated in the x -direction. In that case, $\tilde{g}_\sigma \rightarrow \sigma\sqrt{2\pi}$, i.e. it approaches infinitesimally small values, but, more importantly, it approaches the constant function in α . This hints at the link with the Dirac δ function. The Fourier transform of the Dirac δ at $x = x_0$ is:

$$\tilde{g}(\alpha) = \int_{-\infty}^{\infty} \delta(x - x_0) e^{-i\alpha x} dx = e^{-i\alpha x_0} \quad (2.39)$$

As mentioned before, the sinusoid $\tilde{g}(\alpha) = e^{-i\alpha x_0}$ has an infinite support. Moreover, if $x_0 = 0$, $\tilde{g}(\alpha) = 1$ for all α . So, in this sense, the Fourier transform of the Dirac δ is the constant function.

The uncertainty principle is a consequence of the Parseval-Plancherel theorem, see Yoshida [14], which states that the Fourier transform of a square-integrable function is itself square-integrable. The principle implies that an initial condition that has a finite support can only be represented by a continuous Fourier transform (continuum of modes); in a strict sense, such a function cannot be created with a finite sequence of Dirac δ pulses (discrete modes). Strictly speaking, a finite sequence of Dirac δ pulses can only represent functions that have an infinite support.

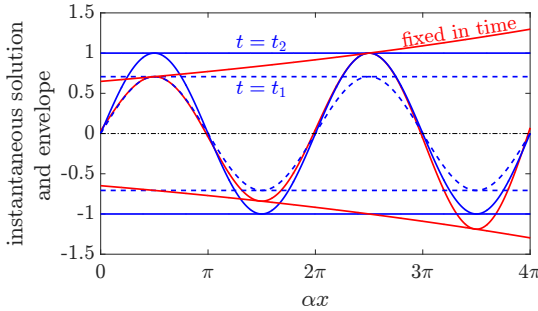
2.4.4. AMPLIFICATION IN SPACE

In the context of laminar-turbulent transition, the most important parameter is the perturbation amplitude gain in the streamwise direction. Given a particular (real) frequency, one is interested in the amplitudes that the perturbations attain. In this case, the LST and spanwise BiGlobal problems are evaluated in the spatial formulation at different streamwise stations. The eigenvalue in this problem formulation is α , of which $-\alpha_i$ denotes the spatial exponential growth rate in x .⁷ Integrating the growth rate yields the amplification of the perturbation energy:

$$N(x) = - \int_{x_0}^x \alpha_i(\hat{x}) d\hat{x}. \quad (2.40)$$

That is to say, if at $x = x_0$ the perturbation amplitude is 1, the amplitude equals $e^{N(x)}$ at other stations. This explains the name of the e^N -method. In terms of this method, x_0 denotes the first streamwise location where perturbations become unstable.

⁷In the remainder, real and imaginary parts are indicated with subscripts r and i , respectively, if not indicated otherwise.



2

Figure 2.1: Illustration of the equivalence of spatial and temporal growth for travelling waves. Spatial (red lines) and temporal (blue) solutions. Click twice for animation.

For the streamwise BiGlobal stability framework, the eigenfunction shapes $\tilde{q}(x, y)$ directly contain the size of the perturbations in the streamwise direction. One can directly evaluate:

$$N(x) = \ln\left(\frac{|\tilde{q}(x, y_m)|}{|\tilde{q}(x_0, y_m)|}\right), \quad (2.41)$$

where $\tilde{q}(x, y_m)$ can denote different representative quantities indicating the amplitude of the perturbations. For example, this can be a perturbation quantity (\tilde{u} , \tilde{v} , etc. or a combination) evaluated at a particular wall-normal location $y = y_m(x)$, but also a local integral quantity, like $\int_0^\infty |\tilde{u}(x, y)| dy$. Note that α is not a parameter of the streamwise BiGlobal problem. Consistently defining the spatial growth rate utilises:

$$-\alpha_i = \frac{dN}{dx}. \quad (2.42)$$

Given the definition of the nomenclature, the premise of the e^N -method can be illustrated in these terms. Given a particular disturbance environment, it was observed by Van Ingen [15, 16], Smith and Gamberoni [17] that transition occurs at approximately the same N -factor: $N = 9$,⁸ meaning the perturbations undergo a fixed linear amplification in space before transition occurs. Mack [18] proposed a correlation of the N -factor with different initial disturbance levels, based on the freestream turbulence intensity.

2.4.5. THE GASTER-TRANSFORMATION

Convective perturbations travel in a definite direction as they grow in amplitude. As shown, wavepackets travel with the group speed c_g . If $c_g \neq 0$, spatial and temporal growth are equivalent. By tracking the amplitude of individual wave crests, they seem to undergo the same amplitude increase in time and space, see figure 2.1 for an illustration/animation. So, a wave that displays spatial growth only, i.e. $(\alpha, \omega) \in \mathbb{C} \times \mathbb{R}$, can be transformed into a wave displaying temporal growth only, i.e. having $(\alpha, \omega) \in \mathbb{R} \times \mathbb{C}$. To distinguish the combination (α, ω) corresponding to the spatial and temporal solutions, one respectively writes: $(\alpha^S, \omega^S) \in \mathbb{C} \times \mathbb{R}$ and $(\alpha^T, \omega^T) \in \mathbb{R} \times \mathbb{C}$, i.e. $\alpha_i^T = \omega_i^S = 0$.

⁸Note: $e^{13} \approx 4.4 \times 10^5$, $e^9 \approx 8.1 \times 10^3$, $e^5 \approx 1.5 \times 10^2$, this N -factors recur throughout literature.

The Gaster-transformation [19] establishes an approximate relationship between these two combinations:

$$\alpha_r^S = \alpha_r^T, \quad \omega_r^S = \omega_r^T, \quad \frac{-\alpha_i^S}{\omega_i^T} = 1 / \frac{d\omega_r}{d\alpha_r} = \frac{1}{c_g}, \quad (2.43)$$

where the group speed c_g can be evaluated with the variables evaluated in either the spatial or temporal limits. These relations are accurate up to $O((\omega_i^T)^2)$, i.e. second order in ω_i^T , which is usually small.

When solving the problem numerically, the spatial problem is twice as large as the temporal problem with the same spatial resolution, due to the quadratic nature of the problem in α . This will be further detailed in §3.1.6. For this reason, using the Gaster-transformation on the cheaper temporal solutions is a very attractive option. Its applicability to instabilities with large growth rates should in general be carefully checked, however. Brevdo [20] notes that temporal growth rates, in general, cannot be transformed into spatial growth rates. Absolute instabilities, that display temporal growth for $c_g = 0$ per definition, are obvious examples of this.

2.4.6. NEGATIVE WAVENUMBERS AND FREQUENCIES

As neatly hidden in the integration limits in ansatz (2.7), negative (real) wavenumbers and frequencies are considered. Negative wavenumbers and frequencies are devoid of physical interpretation, so why include that part? All quantities in the integrand are complex. Integrating over the negative values in fact ensures that q' remains a real quantity. This can be shown as follows.

If q' is real, it equals its complex conjugate, $(q')^* = q'$. Determining an expression for the complex conjugate yields:

$$\begin{aligned} \left(\int_{-\infty}^{\infty} \int \cdots \int_{\mathbb{R}^d} \tilde{q}(\mathbf{x}; \mathbf{k}, \omega) e^{i(\mathbf{k} \cdot \mathbf{x}^\perp - \omega t)} d\mathbf{k} d\omega \right)^* &= \int_{-\infty}^{\infty} \int \cdots \int_{\mathbb{R}^d} \tilde{q}^*(\mathbf{x}; \mathbf{k}, \omega) e^{-i(\mathbf{k}^* \cdot \mathbf{x}^\perp - \omega^* t)} d\mathbf{k}^* d\omega^* \\ &= \int_{-\infty}^{\infty} \int \cdots \int_{\mathbb{R}^d} \tilde{q}^*(\mathbf{x}; \mathbf{k}, \omega) e^{i(-\mathbf{k}^* \cdot \mathbf{x}^\perp - (-\omega^*)t)} d\mathbf{k}^* d\omega^* \\ &= \int_{-\infty}^{\infty} \int \cdots \int_{\mathbb{R}^d} \tilde{q}^*(\mathbf{x}; -\mathbf{k}^*, -\omega^*) e^{i(\mathbf{k} \cdot \mathbf{x}^\perp - \omega t)} d\mathbf{k} d\omega \end{aligned} \quad (2.44)$$

In the final step, $-\mathbf{k}^*$ and $-\omega^*$ are exchanged for \mathbf{k} and ω . Note that this implies that the limits of integration switch sign (because they are real), but also the direction of integration does. The final expression must be equal to the right hand side of equation (2.7). Comparing yields:

$$\tilde{q}^*(\mathbf{x}; -\mathbf{k}^*, -\omega^*) = \tilde{q}(\mathbf{x}; \mathbf{k}, \omega), \quad \text{or: } \tilde{q}^*(\mathbf{x}; \mathbf{k}, \omega) = \tilde{q}(\mathbf{x}; -\mathbf{k}^*, -\omega^*). \quad (2.45)$$

That is, evaluating the complex conjugate of \tilde{q} is the same as evaluating the function for negative real parts of the wavenumber vector and frequency. Hence, by running over the positive and negative real parts of the wavenumber vector and the frequency, q' is ensured to be real.

Under special circumstances, an important basic rule for the spectrum can be derived from this relationship. Consider the temporal problem (analogous deductions apply for the spatial problem). If \mathbf{k} is purely imaginary or zero, the ω -spectrum must be symmetric about the imaginary axis, because $\tilde{q}^*(\mathbf{x}; i\mathbf{k}_i, \omega) = \tilde{q}(\mathbf{x}; i\mathbf{k}_i, -\omega^*)$ both encode the same solution. In addition, the functions \tilde{q}_1 and \tilde{q}_2 respectively corresponding to ω and $-\omega^*$ are complex conjugates and, if $\omega_r = 0$, the corresponding \tilde{q} is real.

2.5. ASSESSING THE UNDERLYING PHYSICAL MECHANISMS

The appearance of an unstable solution to the stability equations indicates that the base flow supports an instability. The eigenvalue contains the growth rate and the eigenfunction the shape of the corresponding perturbation; that sounds simple enough. However, the solution does not indicate the underlying physical mechanism, that renders the solution the way it is. It is important to show in what sense this poses a problem for working with eigenvalue problems in practice.

Typically, Computational Fluid Dynamics (CFD) considers problems of the initial value problem type. Take the calculation of a steady-state solution by using a time-marching approach, for example. In that case, an initial solution is guessed and the governing equations are evaluated with the effect of letting the solution adapt in time. This process is continued until the solution is sufficiently close to a steady-state. If approached appropriately, the transient solution dynamics during this process closely complies with the unsteady versions of the physical laws and therefore yields an immediate sanity check on whether the problem is set-up and solved correctly. Existential questions about the final steady state solution can be answered by backtracking its features to the guessed initial condition and its transient dynamics.

In the case of eigenvalue problems, no such approach is possible. When approaching the problem numerically, in particular, eigensolvers return a complete eigenvalue spectrum directly. There are typical characteristics that recur given certain features of the base flows, but, in general, the peculiarities of the spectrum's structure have to be carefully re-examined per case. Given that the spectrum can consist of a large cloud of (potentially spurious) modes, this can be a daunting task in itself.

Given representative solutions are found, their behaviour can be tested by cleverly varying the problem's parameters. However, the solution in itself does not reveal the underlying physical mechanisms that render it to behave the way it does. These physical mechanisms are encoded in the terms of the governing equations. Substituting the solution into the individual terms quantifies the role of each individual term for the solution of consideration and allows inferring the underlying physical mechanism.

This is an absolutely essential step in understanding the solutions of stability problems.

Explicit equations are derived in the following subsections, that decompose the solution into the contributions of the individual terms of the governing equations. Specifically, the Reynolds-Orr equation for the eigenvalue ω is derived and the general recipe to obtain the equation for the eigenfunctions is illustrated.

2.5.1. REYNOLDS-ORR EQUATION

The variable ω is a global property of the solution in the sense that it is constant over the domain on which the eigenfunctions are given, which for system (2.15) is a particular portion of the zy -plane. The same applies for the parameter α . Therefore, the integral of the system's terms over this domain is considered, because they describe the global contribution of the term to ω .⁹

Furthermore, ω appears linearly in system (2.15), as the coefficient of the velocity component eigenfunctions. It is desired to factor out the multiplication with the eigenfunctions, such that the resulting equation is independent of their absolute size. By multiplying the x -, y - and z -momentum equations with the complex conjugates \tilde{u}^* , \tilde{v}^* and \tilde{w}^* , respectively, the coefficients of ω are transformed into the form $-i|\tilde{q}|^2$, where $|\tilde{q}|^2 = \tilde{q}^* \tilde{q}$.¹⁰

The combination of these operations is illustrated for the x -momentum equation as follows:

$$\begin{aligned} & \iint \tilde{u}^* \left(-i\omega \tilde{u} + i\alpha \bar{U} \tilde{u} + \bar{V} \frac{\partial \tilde{u}}{\partial y} + \bar{W} \frac{\partial \tilde{u}}{\partial z} + \tilde{v} \frac{\partial \bar{U}}{\partial y} + \tilde{w} \frac{\partial \bar{U}}{\partial z} \right) dy dz \\ &= \iint \tilde{u}^* \left(-i\alpha \tilde{p} + \frac{1}{Re} \left(-\alpha^2 + \frac{\partial^2}{\partial y^2} + \frac{\partial^2}{\partial z^2} \right) \tilde{u} \right) dy dz. \end{aligned}$$

Manipulating this expression allows isolating ω :

$$\begin{aligned} -i\omega \iint |\tilde{u}|^2 dy dz &= -\iint \tilde{u}^* \left(i\alpha \bar{U} \tilde{u} + \bar{V} \frac{\partial \tilde{u}}{\partial y} + \bar{W} \frac{\partial \tilde{u}}{\partial z} + \tilde{v} \frac{\partial \bar{U}}{\partial y} + \tilde{w} \frac{\partial \bar{U}}{\partial z} \right) dy dz \\ &\quad + \iint \tilde{u}^* \left(-i\alpha \tilde{p} + \frac{1}{Re} \left(-\alpha^2 + \frac{\partial^2}{\partial y^2} + \frac{\partial^2}{\partial z^2} \right) \tilde{u} \right) dy dz. \end{aligned} \quad (2.46)$$

Further simplifying the expression, defining $\|\tilde{u}\|^2 = \iint |\tilde{u}|^2 dy dz$ and assuming $\|\tilde{u}\|^2 \neq 0$, yields:

$$\begin{aligned} \omega &= \iint \left(\alpha \bar{U} |\tilde{u}|^2 - i\bar{V} \tilde{u}^* \frac{\partial \tilde{u}}{\partial y} - i\bar{W} \tilde{u}^* \frac{\partial \tilde{u}}{\partial z} - i\tilde{u}^* \tilde{v} \frac{\partial \bar{U}}{\partial y} - i\tilde{u}^* \tilde{w} \frac{\partial \bar{U}}{\partial z} \right. \\ &\quad \left. + \alpha \tilde{u}^* \tilde{p} + \frac{i}{Re} \left(-\alpha^2 |\tilde{u}|^2 + \tilde{u}^* \frac{\partial^2 \tilde{u}}{\partial y^2} + \tilde{u}^* \frac{\partial^2 \tilde{u}}{\partial z^2} \right) \right) \frac{dy dz}{\|\tilde{u}\|^2}, \end{aligned} \quad (2.47)$$

where the integral can be evaluated per term.

It was assumed that $\|\tilde{u}\|^2 \neq 0$. This does not necessarily have to be the case, although this corresponds to very special conditions.¹¹ To avoid dividing by zero, the equivalent of

⁹The solutions corresponding to the spanwise BiGlobal stability equations considered in this thesis converge exponentially outside the domain where they are produced, so these integrals converge as the considered domain size is increased.

¹⁰Recall that the eigenfunctions contain a common, non-unique phase shift, elaborated on in relation to equation (2.28). Note that, by forming the product of the eigenfunctions with any of the complex conjugate eigenfunctions, such as $\tilde{u}^* \tilde{u}$, $\tilde{v}^* \tilde{v}$, $\tilde{w}^* \tilde{w}$, the non-unique phase shift common to all functions is removed. Name the random phase shift c , then: $\tilde{p}^* \tilde{q} = |\tilde{p}| e^{-i(\arg(\tilde{p})+c)} |\tilde{q}| e^{i(\arg(\tilde{q})+c)} = |\tilde{p}| |\tilde{q}| e^{i(\arg(\tilde{q})-\arg(\tilde{p}))}$, so the random part cancels.

¹¹In the case where $\alpha = 0$, for example, the x -momentum equation decouples from system (2.15), meaning the solution set is split into two parts, one part with $\tilde{u} = 0$ and the other with $\tilde{v} = \tilde{w} = 0$.

equation (2.46) is constructed for all velocity components. When summing the resulting expressions, one can divide by the combination $\iint (|\tilde{u}|^2 + |\tilde{v}|^2 + |\tilde{w}|^2) dy dz$. To condense the expressions, one defines $\tilde{\mathbf{q}} = [\tilde{u}, \tilde{v}, \tilde{w}]^T$ and $\|\tilde{\mathbf{q}}\|^2 = \iint \tilde{\mathbf{q}} \cdot \tilde{\mathbf{q}} dy dz$.¹²

The general equivalent of equation (2.47) can then be expressed as:

$$\omega = \iint \left[\alpha \bar{U} \tilde{\mathbf{q}}^* \cdot \tilde{\mathbf{q}} - i \bar{V} \tilde{\mathbf{q}}^* \cdot \frac{\partial \tilde{\mathbf{q}}}{\partial y} - i \bar{W} \tilde{\mathbf{q}}^* \cdot \frac{\partial \tilde{\mathbf{q}}}{\partial z} \right. \\ - i \tilde{u}^* \tilde{v} \frac{\partial \bar{U}}{\partial y} - i \tilde{u}^* \tilde{w} \frac{\partial \bar{U}}{\partial z} - i |\tilde{v}|^2 \frac{\partial \bar{V}}{\partial y} - i \tilde{v}^* \tilde{w} \frac{\partial \bar{V}}{\partial z} - i \tilde{w}^* \tilde{v} \frac{\partial \bar{W}}{\partial y} - i |\tilde{w}|^2 \frac{\partial \bar{W}}{\partial z} \\ + \alpha \tilde{u}^* \tilde{p} - i \tilde{v}^* \frac{\partial \tilde{p}}{\partial y} - i \tilde{w}^* \frac{\partial \tilde{p}}{\partial z} \\ \left. + \frac{i}{Re} \left(-\alpha^2 \tilde{\mathbf{q}}^* \cdot \tilde{\mathbf{q}} + \tilde{\mathbf{q}}^* \cdot \frac{\partial^2 \tilde{\mathbf{q}}}{\partial y^2} + \tilde{\mathbf{q}}^* \cdot \frac{\partial^2 \tilde{\mathbf{q}}}{\partial z^2} \right) \right] \frac{dy dz}{\|\tilde{\mathbf{q}}\|^2}. \quad (2.48)$$

Two further operations are usually performed to further reduce this equation.

First, the partial derivative terms of the pressure can be eliminated by using the continuity equation. Multiplying equation (2.15d) with \tilde{p}^* yields:

$$i \alpha \tilde{p}^* \tilde{u} + \tilde{p}^* \frac{\partial \tilde{v}}{\partial y} + \tilde{p}^* \frac{\partial \tilde{w}}{\partial z} = 0. \quad (2.49)$$

This is transformed into an expression for the partial derivatives of the pressure in equation (2.48). First multiply equation (2.49) by i , isolate the partial derivatives on the right hand side and then perform integration by parts:

$$-\alpha \iint \tilde{p}^* \tilde{u} dy dz = \iint \left(-i \tilde{p}^* \frac{\partial \tilde{v}}{\partial y} - i \tilde{p}^* \frac{\partial \tilde{w}}{\partial z} \right) dy dz \\ = -i \int [\tilde{p}^* \tilde{v}]_{y=y_1}^{y_2} dz - i \int [\tilde{p}^* \tilde{w}]_{z=z_1}^{z_2} dy + \iint \left(i \tilde{v} \frac{\partial \tilde{p}^*}{\partial y} + i \tilde{w} \frac{\partial \tilde{p}^*}{\partial z} \right) dy dz \quad (2.50)$$

where y_1 , y_2 , z_1 and z_2 are the locations of the boundaries of the considered domain. In the application cases considered in this thesis, the boundary conditions are either the no-slip ($\tilde{u} = \tilde{v} = \tilde{w} = 0$), discrete far-field ($\tilde{u} = \tilde{v} = \tilde{w} = \tilde{p} = 0$)¹³ or periodic conditions ($\tilde{u}|_{z=z_1}^{z_2} = 0$ for all variables), see §2.6 for more details. For each of these cases, the boundary terms evaluate to zero. Therefore these terms are dropped from consideration.

Taking the complex conjugate of equation (2.50) yields:

$$-\alpha^* \iint \tilde{u}^* \tilde{p} dy dz = \iint \left(-i \tilde{v}^* \frac{\partial \tilde{p}}{\partial y} - i \tilde{w}^* \frac{\partial \tilde{p}}{\partial z} \right) dy dz. \quad (2.51)$$

¹²Note that $\tilde{\mathbf{q}}$ generally refers to any eigenfunction in general, while $\tilde{\mathbf{q}}$ denotes the *velocity* amplitude vector specifically.

¹³The discrete modes of interest decay exponentially in the freestream and therefore all functions approach zero amplitude.

Second, the viscous terms are approached similarly:

$$\begin{aligned} \frac{i}{Re} \iint \left(\tilde{\mathbf{q}}^* \cdot \frac{\partial^2 \tilde{\mathbf{q}}}{\partial y^2} + \tilde{\mathbf{q}}^* \cdot \frac{\partial^2 \tilde{\mathbf{q}}}{\partial z^2} \right) dy dz &= \frac{i}{Re} \int \left[\tilde{\mathbf{q}}^* \cdot \frac{\partial \tilde{\mathbf{q}}}{\partial y} \right]_{y=y_1}^{y_2} dz + \frac{i}{Re} \int \left[\tilde{\mathbf{q}}^* \cdot \frac{\partial \tilde{\mathbf{q}}}{\partial z} \right]_{z=z_1}^{z_2} dy \\ &\quad - \frac{i}{Re} \iint \left(\frac{\partial \tilde{\mathbf{q}}^*}{\partial y} \cdot \frac{\partial \tilde{\mathbf{q}}}{\partial y} + \frac{\partial \tilde{\mathbf{q}}^*}{\partial z} \cdot \frac{\partial \tilde{\mathbf{q}}}{\partial z} \right) dy dz, \end{aligned} \quad (2.52)$$

2

where, again, the boundary terms vanish for the indicated boundary conditions. For periodic conditions, note that also the derivatives of the eigenfunctions on the different boundaries are equal to each other, causing their cancellation. Note that the remaining integral has an integrand that consists of the squared modulus of the partial derivatives of the amplitude velocity vector. This implies that these terms always yield a negative imaginary, thus stabilising, contribution to ω .

Combining equations (2.51) and (2.52) into equation (2.48) yields the Reynolds-Orr equation [5] with respect to system (2.15): ¹⁴

$$\omega = A + R + P - D. \quad (2.53)$$

From left to right, the right hand side terms represent advection A , Reynolds stress work R , pressure work P (zero when $\alpha_i = 0$) and viscous dissipation D , where:

$$\begin{aligned} A &= \iint \left(\alpha \bar{U} \tilde{\mathbf{q}}^* \cdot \tilde{\mathbf{q}} - i \bar{V} \tilde{\mathbf{q}}^* \cdot \frac{\partial \tilde{\mathbf{q}}}{\partial y} - i \bar{W} \tilde{\mathbf{q}}^* \cdot \frac{\partial \tilde{\mathbf{q}}}{\partial z} \right) \frac{dy dz}{\|\tilde{\mathbf{q}}\|^2}, \\ R &= -i \iint \left(\tilde{u}^* \tilde{v} \frac{\partial \bar{U}}{\partial y} + \tilde{u}^* \tilde{w} \frac{\partial \bar{U}}{\partial z} + |\tilde{v}|^2 \frac{\partial \bar{V}}{\partial y} + \tilde{v}^* \tilde{w} \frac{\partial \bar{V}}{\partial z} \right. \\ &\quad \left. + \tilde{w}^* \tilde{v} \frac{\partial \bar{W}}{\partial y} + |\tilde{w}|^2 \frac{\partial \bar{W}}{\partial z} \right) \frac{dy dz}{\|\tilde{\mathbf{q}}\|^2} \\ P &= (\alpha - \alpha^*) \iint \tilde{u}^* \tilde{p} \frac{dy dz}{\|\tilde{\mathbf{q}}\|^2} \\ D &= \frac{i}{Re} \left\{ \alpha^2 + \iint \left(\left| \frac{\partial \tilde{u}}{\partial y} \right|^2 + \left| \frac{\partial \tilde{u}}{\partial z} \right|^2 + \left| \frac{\partial \tilde{v}}{\partial y} \right|^2 + \left| \frac{\partial \tilde{v}}{\partial z} \right|^2 + \left| \frac{\partial \tilde{w}}{\partial y} \right|^2 + \left| \frac{\partial \tilde{w}}{\partial z} \right|^2 \right) \frac{dy dz}{\|\tilde{\mathbf{q}}\|^2} \right\}. \end{aligned}$$

Note the negative sign of D in equation (2.53). Furthermore, note the single appearance of the complex conjugate of α in P . This is important, because this prohibits the isolation of α in general; equation (2.53) cannot be expressed in a way where α appears on its own at the left hand side.

The various terms of equation (2.53) represent the complex contribution to ω associated to specific physical mechanisms pertinent to the base flow. Usually, the equation is used in the Lagrangian form that excludes the advection terms, see [5] and [21]. Here these terms do appear as the Eulerian form is considered instead.

¹⁴The short-hand recipe is to form the dot product of the system of equations (taking the complex conjugate of the continuity equation) with the variable vector $[\tilde{u}^* \tilde{v}^* \tilde{w}^* \tilde{p}]^T$ and establish the double integral (executing the proper function inner product). Integrating the continuity equation by parts allows eliminating the pressure derivatives.

By substituting the eigensolutions, each (sub)term on the right hand side of equation (2.53) can be evaluated. The advection terms generally have a large real part and thus dominate the real part of ω ; i.e. the ω_r -budget. The Reynolds stresses and viscous dissipation have a larger imaginary part and therefore determine the growth rate, i.e. the ω_i -budget, which is a measure of the production or destruction of the perturbation energy. All terms that do not involve the absolute magnitude of an amplitude function are generally complex. Thus the advection terms and Reynolds (shear) stresses do generally contribute respectively to the ω_i - and ω_r -budgets as well, albeit to a minor extent. Nevertheless, as will be shown in chapter 6, the advection terms can have a structural impact on the solution behaviour.

Much more information can be extracted from the underlying approach of equation (2.53) than just the decomposition of the eigenvalue ω into the integral contributions. If the dominant integral contributions are identified, the integrands of the individual terms can be investigated to identify the spatial region associated with the activity of the term.

A general criterion can be derived that indicates a local destabilizing contribution due to advection. The advection terms in the ω_i -budget can be written as:¹⁵

$$\begin{bmatrix} \bar{U} \\ \bar{V} \\ \bar{W} \end{bmatrix} \cdot \operatorname{Re} \left\{ - \begin{bmatrix} \tilde{\mathbf{q}}^* \cdot & -\alpha \tilde{\mathbf{q}} \\ \tilde{\mathbf{q}}^* \cdot & \partial \tilde{\mathbf{q}} / \partial y \\ \tilde{\mathbf{q}}^* \cdot & \partial \tilde{\mathbf{q}} / \partial z \end{bmatrix} \right\} = \begin{bmatrix} \bar{U} \\ \bar{V} \\ \bar{W} \end{bmatrix} \cdot \left(- \begin{bmatrix} -2\alpha_i \\ \partial / \partial y \\ \partial / \partial z \end{bmatrix} \frac{1}{2} \tilde{\mathbf{q}}^* \cdot \tilde{\mathbf{q}} \right), \quad (2.54)$$

which is (non-)zero whenever the perturbation amplitude gradient is (non-)orthogonal to the in-plane flow.

Whenever the base flow velocity vector $[\bar{U} \bar{V} \bar{W}]^T$ is aligned with the direction in which the perturbation decays, this results in a positive (destabilising) contribution to ω_i , i.e. a region of high perturbation energy is moved so as to replace a lower energy region. This scenario is illustrated in figure 2.2 (a). On the other hand, if the perturbation grows in the advection direction, that yields a negative (stabilizing) contribution to ω_i , which is the scenario illustrated in figure 2.2 (b). Generally, advection is destabilizing if it is effective in transferring energy to the exterior of the core of the shear layer.

2.5.2. TRANSPORT EQUATIONS FOR THE EIGENFUNCTIONS

Given an approach for decomposing the eigenvalue into the terms of the governing equation, the next step is to derive a similar transport equation for the eigenfunctions.

In the stability momentum equations, an example of a representative of the material derivative D/Dt is the combination $-i\omega + ia\bar{U}$.¹⁶ Accordingly, each momentum equation (2.15a) through (2.15c), can be transformed into a relation for $|\tilde{u}|^2$, $|\tilde{v}|^2$ and $|\tilde{w}|^2$ or the phase (the position of wave fronts) associated to \tilde{u} , \tilde{v} and \tilde{w} , etc.

For the x -momentum equation, for example, one derives:

¹⁵For an elaboration on the equality, see equation (2.57).

¹⁶Another viable representation is just the constant $-i\omega$.

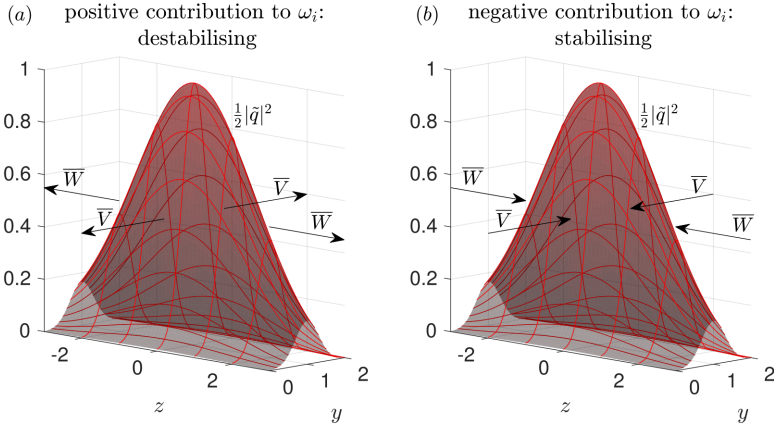


Figure 2.2: Illustration of the scenarios where the in-plane flow: $[\bar{V}, \bar{W}]^T$, points in the opposite (a) and the same (b) direction as the in-plane gradient of $\frac{1}{2}|\tilde{q}|^2$: $\frac{1}{2}[\partial|\tilde{q}|^2/\partial y, \partial|\tilde{q}|^2/\partial z]^T$.

$$\begin{aligned} & \overbrace{\tilde{u}^* \left(-i\omega + i\alpha \bar{U} \right) \tilde{u} + \bar{V} \tilde{u}^* \frac{\partial \tilde{u}}{\partial y} + \bar{W} \tilde{u}^* \frac{\partial \tilde{u}}{\partial z} + \tilde{u}^* \tilde{v} \frac{\partial \bar{U}}{\partial y} + \tilde{u}^* \tilde{w} \frac{\partial \bar{U}}{\partial z}}^{\tilde{u}^* \frac{D\tilde{u}}{Dt}} \\ &= -i\alpha \tilde{u}^* \tilde{p} + \frac{1}{Re} \left(-\alpha^2 |\tilde{u}|^2 + \tilde{u}^* \frac{\partial^2 \tilde{u}}{\partial y^2} + \tilde{u}^* \frac{\partial^2 \tilde{u}}{\partial z^2} \right), \end{aligned} \quad (2.55)$$

where, due to the algebraic nature of $-i\omega + i\alpha \bar{U}$, one can isolate an expression for $|\tilde{u}|^2$, assuming $\omega \neq \alpha \bar{U}$ at any point in the domain (which is always the case for unstable temporal ($\omega \in \mathbb{C}$, $\alpha \in \mathbb{R}$) or spatial ($\omega \in \mathbb{R}$, $\alpha \in \mathbb{C}$) solutions of interest):

$$\begin{aligned} |\tilde{u}|^2 = & \frac{1}{\omega - \alpha \bar{U}} \left(-i\bar{V} \tilde{u}^* \frac{\partial \tilde{u}}{\partial y} - i\bar{W} \tilde{u}^* \frac{\partial \tilde{u}}{\partial z} - i\tilde{u}^* \tilde{v} \frac{\partial \bar{U}}{\partial y} - i\tilde{u}^* \tilde{w} \frac{\partial \bar{U}}{\partial z} + \alpha \tilde{u}^* \tilde{p} \right. \\ & \left. + \frac{i}{Re} \left(-\alpha^2 |\tilde{u}|^2 - \left| \frac{\partial \tilde{u}}{\partial y} \right|^2 - \left| \frac{\partial \tilde{u}}{\partial z} \right|^2 + \frac{\partial}{\partial y} \left(\tilde{u}^* \frac{\partial \tilde{u}}{\partial y} \right) + \frac{\partial}{\partial z} \left(\tilde{u}^* \frac{\partial \tilde{u}}{\partial z} \right) \right) \right). \end{aligned} \quad (2.56)$$

Note that the real part of the right hand side sums to $|\tilde{u}|^2$, while the imaginary part must evaluate to zero. Due to $\omega - \alpha \bar{U} \in \mathbb{C}$, it is very hard to infer which terms contribute to $|\tilde{u}|^2$ from this expression in general. It is instead suggested to substitute a given solution into the individual terms weighted with the factor $1/(\omega - \alpha \bar{U})$ and to take the real part of the resulting expression. This yields the contribution to $|\tilde{u}|^2$ per term directly.

In this case, the pressure is not a dynamical variable, so no transport equation can be derived analogously to those for the velocity components. Instead, it is suggested to consider the pressure-Poisson equation (2.63), which will be introduced in §2.6. The analogue of the preceding analysis is significantly complicated due to the need of inverting the Helmholtz (transformed Laplace) operator $(-\alpha^2 + \partial^2/\partial y^2 + \partial^2/\partial z^2)$.

Note that the choice of $D/Dt = -i\omega + i\alpha \bar{U}$ was arbitrary. The preceding analysis can be properly generalized by deriving a transport equation for both the absolute magnitude and a complex phase of the eigenfunction. That is, deriving relations for $D|\tilde{q}|^2/Dt$

and $D \arg(\tilde{q})/Dt$, where D/Dt is a chosen representation of the material derivative. Using the following identities:

$$\begin{aligned} \operatorname{Re}\left\{\tilde{q}^* \frac{D \tilde{q}}{D t}\right\} &= \frac{1}{2}\left(\tilde{q}^* \frac{D \tilde{q}}{D t}+\left(\tilde{q}^* \frac{D \tilde{q}}{D t}\right)^*\right) \\ &= \frac{1}{2}\left(\tilde{q}^* \frac{D \tilde{q}}{D t}+\tilde{q} \frac{D \tilde{q}^*}{D t}\right) \\ &= \frac{1}{2} \frac{D \tilde{q}^* \tilde{q}}{D t} \\ &= \frac{D \frac{1}{2}|\tilde{q}|^2}{D t} ; \end{aligned} \quad (2.57)$$

$$\begin{aligned} \operatorname{Im}\left\{\tilde{q}^* \frac{D \tilde{q}}{D t}\right\} &= \frac{|\tilde{q}|^2}{2 i}\left(\frac{\tilde{q}^*}{\tilde{q}^* \tilde{q}} \frac{D \tilde{q}}{D t}-\frac{\tilde{q}}{\tilde{q} \tilde{q}^*} \frac{D \tilde{q}^*}{D t}\right) \\ &= \frac{|\tilde{q}|^2}{2 i}\left(\frac{D \ln \tilde{q}}{D t}-\frac{D \ln \tilde{q}^*}{D t}\right) \\ &= \frac{|\tilde{q}|^2}{2 i} \frac{D}{D t}\left[\ln \left(\frac{\tilde{q}^2}{|\tilde{q}|^2}\right)\right] \\ &=|\tilde{q}|^2 \frac{D \arg (\tilde{q})}{D t}, \end{aligned} \quad (2.58)$$

2

shows that both quantities are contained in the product $\tilde{q}^* D \tilde{q} / D t$. Note that:

$$\ln \tilde{q}-\ln \tilde{q}^{*}=\ln \frac{\tilde{q}}{\tilde{q}^{*}}=\ln \frac{\tilde{q} \tilde{q}}{\tilde{q}^{*} \tilde{q}}=\ln \frac{\tilde{q}^2}{|\tilde{q}|^2}=2 \ln e^{i \arg (\tilde{q})}=2 i \arg (\tilde{q}), \quad (2.59)$$

where care has to be taken with the non-uniqueness of $\ln e^{ix}=i(x+2\pi n)$, with $n \in \mathbb{Z}$.

A similar relationship can be derived for cross products of amplitude quantities, like $\tilde{p}^* \tilde{q}$. This quantity is generally complex-valued, so one can be interested in a transport equation for both the real and imaginary parts. The following manipulation can be used in their specific regard:

$$\begin{aligned} \frac{D \operatorname{Re}\left\{\tilde{p}^* \tilde{q}\right\}}{D t} &= \frac{D\left(\tilde{p}^* \tilde{q}+\tilde{q}^* \tilde{p}\right)}{2 D t}=\frac{1}{2}\left(\tilde{q} \frac{D \tilde{p}^*}{D t}+\tilde{p}^* \frac{D \tilde{q}}{D t}+\tilde{p} \frac{D \tilde{q}^*}{D t}+\tilde{q}^* \frac{D \tilde{p}}{D t}\right) \\ &= \frac{1}{2}\left(\tilde{p}^* \frac{D \tilde{q}}{D t}+\tilde{q}^* \frac{D \tilde{p}}{D t}+\left(\tilde{p}^* \frac{D \tilde{q}}{D t}+\tilde{q}^* \frac{D \tilde{p}}{D t}\right)^*\right) \\ &=\operatorname{Re}\left\{\tilde{p}^* \frac{D \tilde{q}}{D t}+\tilde{q}^* \frac{D \tilde{p}}{D t}\right\}, \end{aligned} \quad (2.60 a)$$

and similarly:

$$\frac{D \operatorname{Im}\left\{\tilde{p}^* \tilde{q}\right\}}{D t}=\operatorname{Im}\left\{\tilde{p}^* \frac{D \tilde{q}}{D t}-\tilde{q}^* \frac{D \tilde{p}}{D t}\right\} . \quad (2.60 b)$$

This is useful for tracing the origin of the (linear equivalent of the) Reynolds stress: $\tilde{u}^* \tilde{v}$.

2.6. BOUNDARY CONDITIONS

The stability problems are completed by specifying appropriate boundary conditions. Such conditions necessarily have to be homogeneous, i.e. expressible in the form $\mathbf{A} \Xi=\lambda \mathbf{B} \Xi$, where λ is the eigenvalue.

Suppose ξ is one of the coordinates of \mathbf{x} in equation (2.11). Typical examples of conditions are the Dirichlet: $\tilde{q}(\xi_1)=0$, Neumann: $\partial \tilde{q} / \partial \xi(\xi_1)=0$ and periodic boundary conditions: $\tilde{q}(\xi_1)=\tilde{q}(\xi_2)$ and $\partial \tilde{q} / \partial \xi(\xi_1)=\partial \tilde{q} / \partial \xi(\xi_2)$, where ξ_1 and ξ_2 denote two opposite boundaries. Note that the boundary conditions on the perturbation amplitude variables

\tilde{q} , just like the stability equations, arise from the boundary conditions on the instantaneous flow. So, just like substituting the perturbation expansion (2.4) and modal ansatz (2.11) into the Navier-Stokes equations, this is also done for the boundary conditions.

If a problem contains farfield boundaries, the required boundary condition depends on whether the modes of interest are discrete or continuous. In the discrete mode case, the eigenfunctions decay exponentially towards farfield boundaries [7, 22], this implies that Dirichlet conditions on all variables, including the pressure, are justified as the domain limits are placed far enough away. What boundary conditions to apply in the farfield for continuum modes is discussed in chapter 8.

On a solid wall, the instantaneous flow must satisfy the no-slip condition. This implies that Dirichlet conditions are applied on all velocity components, \tilde{u} , \tilde{v} and \tilde{w} . It is not directly clear from the underlying physics what condition must be imposed for the pressure in this case. Compatibility conditions have been derived as an *ad-hoc* solution in this regard.

Examples are conditions that ensure that the pressure satisfies the wall-normal momentum equation at the boundary, see the treatments of Gómez *et al.* [23] and Theofilis [24]. These conditions are derived by taking the momentum equations and evaluating them at the corresponding no-slip boundary. For matters of completeness, the derivation process is illustrated using equation (2.15b) considering an $y = c^{\text{st}}$ boundary to be a no-slip boundary:

$$-i\omega \tilde{v} + i\alpha \bar{U} \tilde{v} + \bar{V} \frac{\partial \tilde{v}}{\partial y} + \bar{W} \frac{\partial \tilde{v}}{\partial z} + \tilde{v} \frac{\partial \bar{V}}{\partial y} + \tilde{w} \frac{\partial \bar{V}}{\partial z} = -\frac{\partial \tilde{p}}{\partial y} + \frac{1}{Re} \left(-\alpha^2 + \frac{\partial^2}{\partial y^2} + \frac{\partial^2}{\partial z^2} \right) \tilde{v}.$$

First, all non-derivative perturbation velocity amplitudes are zeroed, because they vanish on the no-slip boundary:

$$\bar{V} \frac{\partial \tilde{v}}{\partial y} + \bar{W} \frac{\partial \tilde{v}}{\partial z} = -\frac{\partial \tilde{p}}{\partial y} + \frac{1}{Re} \left(\frac{\partial^2}{\partial y^2} + \frac{\partial^2}{\partial z^2} \right) \tilde{v}$$

In the z -direction, along the boundary, the velocity amplitudes remain identically zero, so all tangential (in this case z -) derivatives of these amplitudes vanish as well:

$$\bar{V} \frac{\partial \tilde{v}}{\partial y} = -\frac{\partial \tilde{p}}{\partial y} + \frac{1}{Re} \frac{\partial^2 \tilde{v}}{\partial y^2}$$

Lastly, zero base flow velocities are imposed at the solid boundary, which yields:

$$\frac{\partial \tilde{p}}{\partial y} = \frac{1}{Re} \frac{\partial^2 \tilde{v}}{\partial y^2} \quad (2.61)$$

Equation (2.61) forms a compatibility equation for the pressure at $y = c^{\text{st}}$.

Recently, Theofilis [25] indicated that, instead of the momentum compatibility equation, using the Poisson equation for the pressure as a boundary condition is preferred over the former compatibility condition. The Poisson equation is independent of the equations valid in the interior of the domain and hence avoids the appearance of spurious eigenmodes.

For the instantaneous flow, the Poisson equation for the pressure is derived by evaluating the divergence of the momentum equations (2.1a) to (2.1c) and cancelling the terms that together form the continuity equation (after exchanging order of differentiation). This yields:

$$\begin{aligned} -\frac{1}{\rho} \left(\frac{\partial^2}{\partial x^2} + \frac{\partial^2}{\partial y^2} + \frac{\partial^2}{\partial z^2} \right) p = & \left(\frac{\partial u}{\partial x} \right)^2 + 2 \frac{\partial v}{\partial x} \frac{\partial u}{\partial y} + 2 \frac{\partial w}{\partial x} \frac{\partial u}{\partial z} \\ & + \left(\frac{\partial v}{\partial y} \right)^2 + 2 \frac{\partial w}{\partial y} \frac{\partial v}{\partial z} \\ & + \left(\frac{\partial w}{\partial z} \right)^2 \end{aligned} \quad (2.62)$$

2

Evaluating the recipe leading to the spanwise BiGlobal stability problem ($\partial \bar{Q} / \partial x = 0$) for incompressible flow, the stability equation corresponding to the pressure-Poisson equation is:

$$\left(-\alpha^2 + \frac{\partial^2}{\partial y^2} + \frac{\partial^2}{\partial z^2} \right) \tilde{p} = -2 \left(i\alpha \frac{\partial \bar{U}}{\partial y} + \frac{\partial \bar{V}}{\partial y} \frac{\partial}{\partial y} + \frac{\partial \bar{W}}{\partial y} \frac{\partial}{\partial z} \right) \tilde{v} - 2 \left(i\alpha \frac{\partial \bar{U}}{\partial z} + \frac{\partial \bar{V}}{\partial z} \frac{\partial}{\partial y} + \frac{\partial \bar{W}}{\partial z} \frac{\partial}{\partial z} \right) \tilde{w}. \quad (2.63)$$

Again considering the evaluation at a solid boundary at $y = c^{\text{st}}$, the no-slip condition requires $\tilde{v} = 0$, although $\partial \tilde{v} / \partial y \neq 0$ and, similarly as before, the z -derivative of the base flow velocity components and \tilde{v} vanish. Equation (2.63) then becomes:

$$\left(-\alpha^2 + \frac{\partial^2}{\partial y^2} + \frac{\partial^2}{\partial z^2} \right) \tilde{p} = -2 \frac{\partial \bar{V}}{\partial y} \frac{\partial \tilde{v}}{\partial y}. \quad (2.64)$$

Note the first and second order y -derivative duality of equations (2.61) and (2.64). Through the continuity equation for the base flow, $\partial \bar{V} / \partial y$ is also zero at the wall. This indicates that the pressure should behave as prescribed by the Helmholtz equation formed by the left hand side terms.

2.7. EXTENSION TO COMPRESSIBLE FLOW

As mentioned before, the considered application cases involve essentially incompressible flows. Therefore the equations valid for incompressible flows are primarily considered throughout this thesis.

Stability approaches are not restricted to incompressible flows, however. The main difference in compressible flows is that large changes in density are encountered. Accordingly, changes in momentum, which drive instability mechanisms in general, cannot be identified with changes in the velocity only. Other transport properties, like viscosity and thermal conductivity, also become functions of temperature. To account for this appropriately, the thermodynamics associated to, for example, an ideal gas must be accounted for.

This is done by considering the compressible Navier-Stokes equations (meaning the collection of the momentum, enthalpy and continuity equations) from the start and de-

rive the stability equations accordingly. Using tensor notation, the compressible Navier-Stokes equations are written as:

$$\rho \frac{\partial u^i}{\partial t} + \rho u^j u_{,j}^i = -g^{ij} p_{,j} + \frac{1}{Re} \left(\lambda g^{ij} u_{,jk}^k + \lambda_{,j} g^{ij} u_{,k}^k + \mu g^{jk} u_{,jk}^i + \mu g^{ik} u_{,jk}^j + \mu_{,j} g^{jk} u_{,k}^i + \mu_{,j} g^{ik} u_{,k}^j + \mu g_{,j}^{jk} u_{,k}^i \right) \quad (2.65a)$$

$$\rho \frac{\partial T}{\partial t} + \rho u^j T_{,j} = Ec \left(\frac{\partial p}{\partial t} + u^j p_{,j} \right) + \frac{1}{Re Pr} \left(k g^{ij} T_{,i} \right)_{,j} + \frac{Ec}{Re} \Phi \quad (2.65b)$$

$$\frac{\partial \rho}{\partial t} + \rho_{,i} u^i + \rho u_{,i}^i = 0 \quad (2.65c)$$

where additional variables are considered, specifically T is the temperature, λ is the second viscosity coefficient and k (as a variable, not a tensor index) is the thermal conductivity. Furthermore, g represents the metric tensor, see [26]. Lastly, Φ represents the dissipation function:

$$\Phi = \lambda u_{,j}^j u_{,m}^m + 2\mu g_{ik} g^{jm} u_{,m}^k u_{,j}^i \quad (2.66)$$

The system is closed with the equation of state, letting R denote the specific gas constant:

$$p = \rho RT, \quad (2.67)$$

Sutherland's law for $\mu = \mu(T)$ and $k = k(T)$ and Stokes's hypothesis for $\lambda = -\frac{2}{3}\mu$ [1, 27]. The gas is assumed calorically perfect, rendering the specific heats constant.

System (2.65) and equation (2.66) are presented in non-dimensional form (while equation (2.67) is not), leading to the introduction of extra non-dimensional numbers. Specifically, these numbers are the Eckert, Prandtl and Mach number, which are defined as:

$$Ec = \frac{\bar{U}_s^2}{\bar{c}_{p,s} \bar{T}_s} \quad Pr = \frac{\bar{c}_{p,s} \bar{\mu}_s}{\bar{k}_s} \quad M = \frac{\bar{U}_s}{\bar{a}_s} \quad (2.68)$$

where the newly introduced scales are: \bar{k}_s and \bar{T}_s , corresponding to the variables introduced earlier. The scale $\bar{c}_{p,s}$ is the specific heat at constant pressure and $\bar{a}_s = \sqrt{\bar{\rho}_s R \bar{T}_s}$ denotes the reference speed of sound. The scale for λ is the previously introduced $\bar{\mu}_s$.

It is important to note that, next to u^i and p , also the variables T , ρ , μ , λ and k are perturbed in general. The corresponding effects must be accounted for in the stability equations. For this reason, next to using the perturbation expansion (2.4) on system (2.65), it must also be applied to the constitutive equations.

First of all, ρ is eliminated by inserting the equation of state into (2.65). This reduces the dependent variables to u^i , p and T and the remaining transport coefficients. The non-dimensional form of the equation of state for the base flow can be derived as follows

[28–30]:

$$\begin{aligned} p &= \rho RT \\ \bar{\rho}_s \bar{U}_s^2 p^{nd} &= \rho^{nd} \bar{\rho}_s R \bar{T}_s T^{nd} \\ \gamma \bar{U}_s^2 p^{nd} &= \rho^{nd} \underbrace{\gamma R \bar{T}_s T^{nd}}_{= \bar{a}_s^2} \end{aligned} \quad (2.69)$$

$$p = \frac{\rho T}{\gamma M^2} \quad \stackrel{\text{Base flow}}{\Rightarrow} \quad \bar{P} = \frac{\bar{\rho} \bar{T}}{\gamma M^2} \quad (2.70)$$

2

Equation (2.69) is obtained by making the equation of state dimensionless using (twice) the dynamic pressure, $\bar{\rho}_s \bar{U}_s^2$, as the scale for the pressure. Thereafter, $\bar{\rho}_s$ is swapped for the ratio of specific heats $\gamma = \bar{c}_{p,s}/(\bar{c}_{p,s} - R)$. Non-dimensional variables are temporarily indicated with the superscript *nd*, which is dropped in equation (2.70).

The corresponding perturbation equation is derived by substituting decomposition (2.4). Removing the non-linear terms and those satisfying equation (2.70) yields:

$$p' = \frac{\rho' \bar{T} + \bar{\rho} T'}{\gamma M^2} \quad (2.71)$$

Using equations (2.70) and (2.71), one can determine $\bar{\rho}$ and ρ' , given the base flow and perturbation solutions in terms of the pressure and temperature.

Furthermore, the variation and perturbation of the transport coefficients μ , λ and k have to be handled. The coefficients are conventionally assumed to be functions of temperature, when considering the compressible (calorically perfect) context. Although Sutherland's law is suggested as the representative constitutive law, many different models exist. For that reason it was decided to treat the variation of the transport coefficients as generally as possible.

The used constitutive law automatically holds for the coefficients corresponding to the base flow. When partially differentiating the coefficients in a spatial direction, the result is:

$$\frac{\partial \bar{\mu}}{\partial x} = \frac{d \bar{\mu}}{dT} \frac{\partial \bar{T}}{\partial x}. \quad (2.72)$$

Through specifying $d \bar{\mu} / d \bar{T}$, which follows from the assumed constitutive law, the variation of the transport coefficients can be accounted for in general.

Next to the variation of the base flow transport coefficients, they are also perturbed. This requires explicit relations to be established (e.g. explicit equations for μ' , λ' and k' in terms of temperature). A Taylor expansion of the coefficients is performed with respect to the temperature perturbations around the base flow variables. For the first viscosity coefficient, for example, this yields [28–30]:

$$\mu' + \bar{\mu}|_{\bar{T}} = \bar{\mu}|_{\bar{T}} + \frac{d \bar{\mu}}{dT} \Big|_{\bar{T}} (\bar{T} + T' - \bar{T}) + \underbrace{\frac{1}{2} \frac{d^2 \bar{\mu}}{dT^2} \Big|_{\bar{T}} T'^2}_{\mathcal{O}(\epsilon^2)} + \mathcal{O}(T'^3)$$

which, after cancelling the base flow terms and the higher order terms in ϵ , results in:

$$\mu' = \frac{d\bar{\mu}}{dT} \Big|_{\bar{T}} T' \quad (2.73)$$

2

The explicit indication of the evaluation at \bar{T} , $|_{\bar{T}}$, is generally dropped; note that $\bar{\mu} = \bar{\mu}|_{\bar{T}}$ definition.

Equivalent relations hold for λ and k . By using this formulation, \bar{T} -derivatives are introduced in the resulting stability equations (even of second order) through equations (2.72) and (2.73). This closes the system of equations, reducing the unknowns to the perturbation variables corresponding to u^i , p and T .

For a detailed account of the derivation of the compressible flow equivalents of the Parabolised and BiGlobal stability equations, see [28, 31–33] and [11, 24, 34], respectively.

The boundary conditions are treated equivalently in the case of compressible flow. For example, a compressible momentum equation can be used as the pressure compatibility condition and the Poisson equation can be extended to include the temperature dependency of the transport coefficients.

Furthermore, the usual condition used for the perturbation amplitude of the temperature is Dirichlet. This would be in conflict with an adiabatic wall condition for the instantaneous flow, which is a Neumann condition. Malik [35] explains that imposing a Dirichlet condition is reasonable when assuming high frequency perturbations are considered. These perturbations are expected not to be capable of instantaneously heating up the wall, due to the wall's thermal inertia.

REFERENCES

- [1] J. Anderson, *Fundamentals of Aerodynamics* (McGraw-Hill, 2006).
- [2] C. Canuto, M. Hussaini, A. Quarteroni, and T. Zang, *Spectral Methods - Fundamentals in Single Domains* (Springer Verlag, Berlin, 2006).
- [3] P. G. Drazin and W. H. Reid, *Hydrodynamic Stability* (Cambridge University Press, 2004).
- [4] H. Schlichting, E. Krause, H. Oertel, K. Gersten, and C. Mayes, *Boundary-Layer Theory* (Springer, 2003).
- [5] P. J. Schmid and D. S. Henningson, *Stability and Transition in Shear Flows* (Springer Verlag, 2001).
- [6] L. Mack, *Boundary layer stability theory*, in AGARD, *Special Course of Stability and Transition of Laminar Flows* (North Atlantic Treaty Organization, 1984).
- [7] T. Kapitula and K. Promislow, *Spectral and dynamical stability of nonlinear waves* (Springer, 2013).
- [8] C. E. Grosch and H. Salwen, *The continuous spectrum of the Orr-Sommerfeld equation. part 1. the spectrum and the eigenfunctions*, J. Fluid Mech. **87**, 33 (1978).

- [9] H. Salwen and C. E. Grosch, *The continuous spectrum of the Orr-Sommerfeld equation. part 2. eigenfunction expansions*, J. Fluid Mech. **104**, 445 (1981).
- [10] G. Bonfigli and M. Kloker, *Secondary instability of crossflow vortices: validation of the stability theory by direct numerical simulation*, Journal of Fluid Mechanics **583**, 229 (2007).
- [11] V. Theofilis, *Global linear instability*, Annual Review of Fluid Mechanics **43**, 319 (2011).
- [12] Y. K. Kwok, *Applied complex variables for scientists and engineers* (Cambridge University Press, 2010).
- [13] R. Haberman, *Applied Partial Differential Equations: With Fourier Series and Boundary Value Problems* (Pearson Education, Limited, 2012).
- [14] K. Yoshida, *Functional Analysis*, Classics in mathematics (World Publishing Company, 1980).
- [15] J. L. Van Ingen, *A suggested semi-empirical method for the calculation of the boundary layer transition region*, VTH-74 (Delft University of Technology, The Netherlands, 1956).
- [16] J. L. Van Ingen, *The e^N -method for transition prediction. Historical review of work at TU Delft*, in *38th Fluid Dynamics Conference & Exhibit*, 2008-3830 (AIAA, Seattle, Washington, 2008).
- [17] A. Smith and N. Gamberoni, *Transition, pressure gradient and stability theory*, in *Aircraft Co., Report No. ES 26 388, El Segundo, CA* (1956).
- [18] L. M. Mack, *Transition prediction and linear stability theory*, in *In AGARD Laminar-Turbulent Transition 22 p (SEE N78-14316 05-34)* (1977).
- [19] M. Gaster, *A note on the relation between temporally-increasing and spatially-increasing disturbances in hydrodynamic stability*, Journal of Fluid Mechanics **14**, 222 (1962).
- [20] L. Brevdo, *A note on the gaster transformation*, ZAMM-Journal of Applied Mathematics and Mechanics/Zeitschrift für Angewandte Mathematik und Mechanik **72**, 305 (1992).
- [21] M. R. Malik, F. Li, and C.-L. Chang, *Nonlinear crossflow disturbances and secondary instabilities in swept-wing boundary layers*, in *IUTAM Symposium on Nonlinear Instability and Transition in Three-Dimensional Boundary Layers: Proceedings of the IUTAM Symposium held in Manchester, U.K., 17–20 July 1995* (Springer Netherlands, Dordrecht, 1996) pp. 257–266.
- [22] B. Sandstede and A. Scheel, *Absolute and convective instabilities of waves on unbounded and large bounded domains*, Physica D: Nonlinear Phenomena **145**, 233 (2000).

- [23] F. Gómez, S. L. Clainche, P. Paredes, M. Hermanns, and V. Theofilis, *Four decades of studying global linear instability: Progress and challenges*, AIAA Journal **50**, 2731 (2012).
- [24] V. Theofilis, *Advances in global linear instability analysis of nonparallel and three-dimensional flows*, Progress in Aerospace Sciences **39**, 249 (2003).
- [25] V. Theofilis, *The linearized pressure Poisson equation for global instability analysis of incompressible flows*, Theoretical and Computational Fluid Dynamics , 1 (2017).
- [26] R. Aris, *Vectors, Tensors and the Basic Equations of Fluid Mechanics* (Dover Publications, Inc., 1990).
- [27] F. White, *Viscous Fluid Flow*, McGraw Hill Series in Mechanical Engineering (McGraw-Hill Professional Publishing, 1991).
- [28] F. Bertolotti, *Linear and nonlinear stability of boundary layers with streamwise varying properties*, Ph.D. thesis, Ohio State University, Columbus (1991).
- [29] H. Salinas, *Stabilité Linéaire et Faiblement Non Linéaire d'une Couche Limite Laminaire Compressible Tridimensionnelle par l'Approche PSE*, Ph.D. thesis, L'École Nationale Supérieure de l'Aéronautique et de l'Espace, Toulouse (1998).
- [30] V. Theofilis and T. Colonius, *Three-dimensional instabilities of compressible flow over open cavities: Direct solution of the BiGlobal eigenvalue problem*, in *34th AIAA Fluid Dynamics Conference & Exhibit* (American Institute of Aeronautics and Astronautics, Portland, Oregon, 2004).
- [31] T. Herbert, *Parabolized stability equations*, in *Special course on Progress in Transition Modelling*, R-793 (AGARD, 1994).
- [32] T. Herbert, *Parabolized stability equations*, Annual Review of Fluid Mechanics **29**, 245 (1997).
- [33] K. J. Groot, *Error Free Derivation of Parabolized Stability Equations*, VKI PR 2012-12 (Von Kármán Institute for Fluid Dynamics, Belgium, 2012).
- [34] K. J. Groot, *Derivation of and Simulations with BiGlobal Stability Equations*, M.Sc. thesis, Delft University of Technology, The Netherlands (2013).
- [35] M. R. Malik, *Numerical methods for hypersonic boundary layer stability*, Journal of Computational Physics **86**, 376 (1990).

3

NUMERICAL METHODOLOGY

This chapter describes the numerical approach deployed to solve the stability problems considered in this thesis. The presentation is divided into two main parts, that establish an extended presentation of the work presented by Groot [1]. The primary subject of §3.1 is the discretisation of the eigenvalue problem. The essentials of the used scheme are discussed and the implementation of the equations and boundary conditions are treated in detail. Lastly, §3.2 treats the used solvers. Next to the working principles, error estimates are provided.

3.1. DISCRETISATION

In this section, all necessary features regarding the discretisation and the implementation of the problem is presented using the Chebyshev spectral collocation method. In sections 3.1.1 through 3.1.4, the discretisation of the problem is handled. Thereafter, the structure of the problem and the principles of the thereupon based automatic equation implementation tool are elaborated on in sections 3.1.5. Section 3.1 is concluded with a treatment of the discretisation of the boundary conditions in section 3.1.7 and, concisely, the implementation thereof in section 3.1.8. The information is mainly collected from the work of Batterson [2], Canuto *et al.* [3, 4], Piot [5], Robitaille-Montané [6] and Trefethen [7].

3.1.1. CHEBYSHEV POLYNOMIALS

Before the discretisation method can be elaborated on, several basic steps have to be taken. First of all, the Chebyshev polynomials are concisely touched upon. Note that the Chebyshev spectral collocation method does *not directly* use the Chebyshev polynomials themselves to represent the to-be-approximated functions. They are used to derive a special form of the *characteristic Lagrange polynomials*, handled in the next section.

The Chebyshev polynomials are the solution to a specific Sturm-Liouville differential

equation [3]:

$$\frac{d}{d\xi} \left(\sqrt{1-\xi^2} \frac{dT_{N-1}}{d\xi} \right) + \frac{(N-1)^2}{\sqrt{1-\xi^2}} T_{N-1} = 0$$

or: $(1-\xi^2) \frac{d^2 T_{N-1}}{d\xi^2} - \xi \frac{dT_{N-1}}{d\xi} + (N-1)^2 T_{N-1} = 0.$ (3.1)

By making the change of variables $\xi = \cos\theta$, i.e. $d\xi = -\sin\theta d\theta$, in equation (3.1), the following will result:

3

$$\begin{aligned} (1-\cos^2\theta) \frac{d\theta}{d\xi} \frac{d}{d\theta} \left(\frac{d\theta}{d\xi} \frac{dT_{N-1}}{d\theta} \right) - \cos\theta \frac{d\theta}{d\xi} \frac{dT_{N-1}}{d\theta} + (N-1)^2 T_{N-1} &= 0 \\ -\frac{\sin^2\theta}{\sin\theta} \frac{d}{d\theta} \left(-\frac{1}{\sin\theta} \frac{dT_{N-1}}{d\theta} \right) + \frac{\cos\theta}{\sin\theta} \frac{dT_{N-1}}{d\theta} + (N-1)^2 T_{N-1} &= 0 \\ -\sin\theta \left(\frac{\cos\theta}{\sin^2\theta} \frac{dT_{N-1}}{d\theta} - \frac{1}{\sin\theta} \frac{d^2 T_{N-1}}{d\theta^2} \right) + \frac{\cos\theta}{\sin\theta} \frac{dT_{N-1}}{d\theta} + (N-1)^2 T_{N-1} &= 0 \\ -\underbrace{\frac{\cos\theta}{\sin\theta} \frac{dT_{N-1}}{d\theta}}_{\text{Cancels}} + \underbrace{\frac{d^2 T_{N-1}}{d\theta^2}}_{\text{Cancels}} + \underbrace{\frac{\cos\theta}{\sin\theta} \frac{dT_{N-1}}{d\theta}}_{\text{Cancels}} + (N-1)^2 T_{N-1} &= 0 \\ \frac{d^2 T_{N-1}}{d\theta^2} + (N-1)^2 T_{N-1} &= 0. \end{aligned} \quad (3.2)$$

The differential equation reduces to the simple oscillator equation (3.2) in θ . The fundamental solutions to the equation are called the Chebyshev polynomials of first and second kind:

$$T_{N-1} = \cos((N-1)\theta), \quad U_{N-1} = \sin((N-1)\theta), \quad (3.3)$$

which can be expressed as polynomials of order $N-1$. When using the inverse transformation $\theta = \arccos\xi$, it must be noted that it is not uniquely defined out of the interval $\xi \in [-1, 1]$. Therefore, the resulting polynomials are considered only within that interval:

$$T_{N-1}(\xi) = \cos((N-1)\arccos\xi), \quad U_{N-1}(\xi) = \sin((N-1)\arccos\xi), \quad \xi \in [-1, 1]. \quad (3.4)$$

Illustrations of these polynomials can be found throughout the literature [2, 8]. These are not reported here, because only the zeros of the Chebyshev polynomial of the second kind are used in the current development. These can be found through solving:

$$U_{N-1} = 0, \quad \xi \in [-1, 1]$$

$$\begin{aligned} \sin((N-1)\arccos\xi) &= 0, \\ (N-1)\arccos\xi_i &= (i-1)\pi, \quad i \in \mathbb{Z} \end{aligned} \quad (3.5)$$

$$\xi_i = \cos \frac{(i-1)\pi}{N-1}, \quad i = 1, 2, \dots, N. \quad (3.6)$$

The range of chosen i -values represents a unique set of ξ values in the ξ -domain. In equation (3.5), the factor $i-1$ was introduced to let i start at 1 in equation (3.6). The variable N turns out to be the number of collocation points. It is more practical to consider

the number of discretisation points instead of the polynomial order. For this reason, $N - 1$ was introduced in equation (3.1).

The points defined by equation (3.6) are generally referred to as Chebyshev Gauss-Lobatto (CGL) points, see page 86 of Canuto *et al.* [3].¹ It must be emphasized that these points are ordered from right to left. That is, $i = 1$ corresponds to $\xi = 1$ and $i = N$ to $\xi = -1$, meaning the position coordinate decreases as the index increases.

3.1.2. CHARACTERISTIC LAGRANGE POLYNOMIALS

The solution must satisfy a partial derivative eigenvalue problem. To do this, one must be able to represent its derivatives, at least at the points for which the solution is required. Before the derivatives of a function can be considered, one must choose a way to represent the function itself.

In this case, a nodal (Lagrange) basis is considered [3]. This implies that the solution is described at pre-defined locations by individual basis functions. The perfect example of a set of these functions is a combination of *discrete delta functions*. For a one-dimensional case, these can be represented as follows:

$$\psi_j(\xi_k) = \delta_{jk} \begin{cases} = 1 & \text{for } j = k \\ = 0 & \text{for } j \neq k \end{cases}. \quad (3.7)$$

Here, ψ_j are the discrete delta functions and ξ_k are the *collocation points*; the points for which the function is approximated. One can express these functions as polynomials in the following way:

$$\psi_j = \prod_{\substack{j \neq k \\ 1 \leq j, k \leq N}} \frac{\xi - \xi_k}{\xi_j - \xi_k}, \quad (3.8)$$

this illustrates the difference between the Dirac δ function and discrete equivalents; the latter are relatively smooth. These polynomials are called the *characteristic Lagrange polynomials* and are displayed in figure 3.1. The collocation points are highlighted with circles on the ξ -axis. The first function ψ_1 , which has value 1 at the first collocation point, appears at the far right.

A complete function can be represented by multiplying the basis functions with the function values (samples) at the collocation points and adding all resulting polynomials together. The formula is thus as follows:

$$f_N(\xi) = \sum_{j=1}^N f_j \psi_j(\xi), \quad \text{where } f_j = f_{\text{exact}}(\xi_j). \quad (3.9)$$

The distinction between f_{exact} , f_N and f must be emphasized. The discrete version of the exact function f_{exact} is denoted with the subscript N , showing that N collocation points are used. In the two-dimensional case, the number of points in both directions is subscribed. In this case, f is the coefficient vector whose j^{th} element is the weight of the j^{th} basis function ψ_j . In the two-dimensional case, f will be a matrix. The obtained approximation f_N of the function f_{exact} can be used to obtain certain properties, such as derivatives. This is based on the principle of *analytic substitution* [9].

¹Other names are used as well, a collection can be found on page 42 of Trefethen [7].

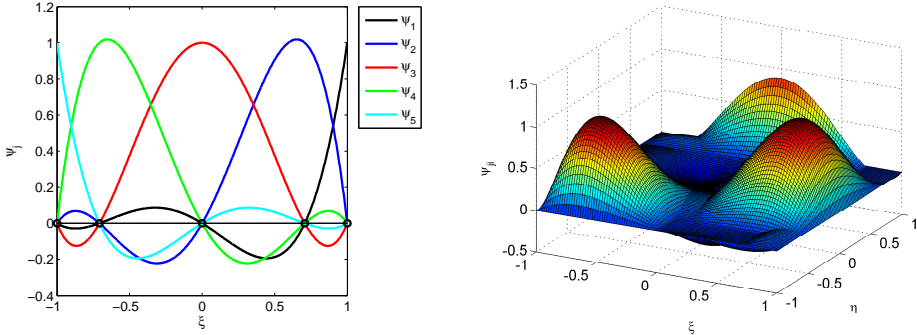


Figure 3.1: Illustration of all independent one-dimensional (left) characteristic Lagrange polynomials for $N = 5$ CGL collocation points, see equation (3.7) or (3.10) and the two-dimensional (right) characteristic Lagrange polynomials ψ_{32} , ψ_{13} and ψ_{44} , for $N_x \times N_y = 5 \times 5$ CGL collocation points, see equation (3.14).

When CGL collocation points, given by equation (3.6), are considered (as already done in figure 3.1) some special features can be used. For example, representation (3.7) can be written more compactly in terms of the Chebyshev polynomials:

$$\begin{aligned}\psi_j &= \lambda_j = \frac{(-1)^{j-1}}{\bar{c}_j(N-1)^2} \frac{1-\xi^2}{\xi-\xi_j} \frac{dT_{N-1}}{d\xi} \quad \text{where } \begin{cases} \bar{c}_j = 2 & \text{for } j = 1 \vee j = N \\ \bar{c}_j = 1 & \text{for } 2 \leq j \leq N-1 \end{cases} \\ &= \frac{(-1)^j}{\bar{c}_j(N-1)} \frac{\sqrt{1-\xi^2}}{\xi-\xi_j} U_{N-1}\end{aligned}\quad (3.10)$$

Here, equation (3.10) is acquired by using the derivative of T_{N-1} evaluated in the derivation of equation (3.5). See, for example, Batterson [2], Canuto *et al.* [3], Piot [5] and Robitaille-Montané [6].

The discrete delta function behaviour of ψ_j is demonstrated as follows. Take $\xi_k = \cos \frac{(k-1)\pi}{N-1}$ to be a generic location in the domain $[-1, 1]$, i.e. k may take any real value in $[1, N]$. It is relatively easy to see that, when k takes integer values and is unequal to j , $\psi_j(\xi_k) = 0$. In that case, $\xi_k - \xi_j$ is non-zero, while $U_{N-1}(\xi_k) = 0$ for $k = 2, \dots, N-1$, this holds per definition of the interior CGL-nodes, and $\sqrt{1-\xi^2} = 0$ for $k = 1, N$.

The limit $k \rightarrow j$ is more complicated. Using $U_{N-1}(\xi_k) = \sin(k-1)\pi$, equation (3.10) evaluates to:

$$\psi_j(\xi_k) = \frac{(-1)^j}{\bar{c}_j(N-1)} \frac{\sqrt{1-\cos^2 \frac{(k-1)\pi}{N-1}}}{\cos \frac{(k-1)\pi}{N-1} - \cos \frac{(j-1)\pi}{N-1}} \sin(k-1)\pi \quad (3.11)$$

$$= \frac{(-1)^{j-1}}{2\bar{c}_j(N-1)} \frac{\sin \frac{(k-1)\pi}{N-1} \sin(k-1)\pi}{\sin \frac{(k+j-2)\pi}{2(N-1)} \sin \frac{(k-j)\pi}{2(N-1)}} \quad (3.12)$$

where use is made of the trigonometric relation $\cos a - \cos b = -2 \sin \frac{a+b}{2} \sin \frac{a-b}{2}$. For $j \neq 1$ or N , letting $k \rightarrow j$ is problematic, because $\sin \frac{(k-j)\pi}{2(N-1)}$ in the denominator approaches 0, just like $\sin(k-1)\pi$ in the nominator. Note that the fraction of remaining sine functions

evaluates to unity, due to the assumption $j \neq 1, N$. The limit of the indefinite expression is determined using l'Hôpital's rule:

$$\begin{aligned}\lim_{k \rightarrow j} \psi_j(\xi_k) &= \lim_{k \rightarrow j} \frac{(-1)^{j-1}}{2\bar{c}_j(N-1)} \frac{\sin(k-1)\pi}{\sin \frac{(k-j)\pi}{2(N-1)}} \\ &= \lim_{k \rightarrow j} \frac{(-1)^{j-1}}{2\bar{c}_j(N-1)} \frac{\pi \cos(k-1)\pi}{\frac{\pi}{2(N-1)} \cos \frac{(k-j)\pi}{2(N-1)}} = \frac{(-1)^{j-1}}{\bar{c}_j} \frac{(-1)^{j+1}}{1} = 1, \quad \text{for: } j \neq 1, N,\end{aligned}$$

using $\bar{c}_j = 1$ for $j \neq 1, N$ in the last equation. For $j = 1$ or N , the other fraction of sines in equation (3.10) also becomes problematic. L'Hôpital's rule has to be applied to that fraction separately, which yields:

$$\begin{aligned}\lim_{k \rightarrow j} \psi_j(\xi_k) &= \lim_{k \rightarrow j} \frac{(-1)^{j-1}}{2\bar{c}_j(N-1)} \frac{\frac{\pi}{N-1} \cos \frac{(k-1)\pi}{N-1}}{\frac{\pi}{2(N-1)} \cos \frac{(k+j-2)\pi}{2(N-1)}} \frac{\pi \cos(k-1)\pi}{\frac{\pi}{2(N-1)} \cos \frac{(k-j)\pi}{2(N-1)}} = \frac{(-1)^{j-1}}{\bar{c}_j} \frac{1}{\frac{1}{2}} \frac{(-1)^{j+1}}{1} = 1, \\ &\quad \text{for: } j = 1, N,\end{aligned}$$

using $\bar{c}_j = 2$ for $j = 1, N$. This completes the demonstration that $\psi_j(\xi_k) = \delta_{jk}$.

Next to the high polynomial approximation associated to the use of T_{N-1} or U_{N-1} when solving differential equations [2, 3], the use of CGL collocation points is notorious for its interpolation properties. According to Burden & Faires [10], the equipment of these nodes provides '*an optimal placing of interpolating points to minimize the error in Lagrange interpolation*', see section 8.3.

Here, two-dimensional functions are to be represented. This is done by extending equation (3.9):

$$f_{N_\eta \times N_\xi}(\xi, \eta) = \sum_{i=1}^{N_\xi} \sum_{j=1}^{N_\eta} f_{ji} \psi_{ji}(\xi, \eta), \quad \text{where } f_{ji} = f_{\text{exact}}(\xi_i, \eta_j). \quad (3.13)$$

It is logical to consider f_{ji} and ψ_{ji} as the components of a matrix f of sample values and a matrix ψ of functions of ξ and η , respectively. Thus, $f \in \mathbb{C}^{N_\eta \times N_\xi}$ and $\psi \in \mathbb{R}^{N_\eta \times N_\xi}$.² Here, N_ξ and N_η are the numbers of collocation points in the ξ - and η -direction, respectively. From this point onwards, the CGL collocation points will be denoted by ξ_i and η_j in the corresponding direction. The grid formed by the node is a *tensor-product grid*.

At this moment, it is important to elaborate on the orientation of these matrices. In this treatment, data for constant ξ -locations (constant i) is stored in the columns and for constant η -locations (constant j) in the rows (therefore the awkward subscripting in equation (3.13)). This is chosen as such because η usually is taken as the numerical vertical coordinate direction; by using this convention vertical information remains vertical in the matrices.

²The conventional notation as in Golub & Van Loan [11] is used.

The components of ψ can be expressed as follows:

$$\begin{aligned}\psi_{ji}(\xi, \eta) &= \lambda_i(\xi) \mu_j(\eta) \\ \lambda_i &= \frac{(-1)^{i+1}}{\bar{c}_i(N_\xi - 1)} \frac{\sqrt{1-\xi^2}}{\xi - \xi_i} U_{N-1}(\xi) \\ \mu_j &= \frac{(-1)^{j+1}}{\bar{c}_j(N_\eta - 1)} \frac{\sqrt{1-\eta^2}}{\eta - \eta_j} U_{N-1}(\eta)\end{aligned}\quad \text{where } \begin{cases} \bar{c}_i = 2 & \text{for } i = 1 \vee i = N_\xi \\ \bar{c}_i = 1 & \text{for } 2 \leq i \leq N_\xi - 1 \\ \bar{c}_j = 2 & \text{for } j = 1 \vee j = N_\eta \\ \bar{c}_j = 1 & \text{for } 2 \leq j \leq N_\eta - 1 \end{cases}, \quad (3.14)$$

3

see Piot [5] or Robitaillié-Montané [6]. Several components of ψ are shown in figure 3.1 for $(i, j) = (2, 3), (3, 1)$ and $(4, 4)$.

When solving the ultimate partial derivative eigenvalue problem, it is practical to use a different storage of the components f_{ji} . One wants to solve for the two-dimensional eigenfunctions through linking them to the eigenvectors of the discrete system. Therefore, the components of the matrix f must be organized in a single vector. This is done simply by stacking all columns of f . This yields:

$$f = \begin{array}{c} f = \\ \begin{array}{ccc} & \xrightarrow{N_\xi \text{ elements}} & \\ \begin{matrix} \xi=1 & & \dots & \dots & \xi=-1 \\ f_{11} & f_{12} & \cdots & \cdots & f_{1N_\xi} \\ f_{21} & f_{22} & & & \vdots \\ \vdots & & \xleftarrow{\xi} \uparrow \eta & & \vdots \\ f_{N_\eta 1} & \cdots & \cdots & \cdots & f_{N_\eta N_\xi} \end{matrix} & \xrightarrow{\text{Stack Columns}} & \begin{matrix} \eta=1 & f_{11} \\ \vdots & \vdots \\ \eta=-1 & f_{N_\eta 1} \\ \eta=1 & f_{12} \\ \vdots & \vdots \\ \eta=-1 & f_{N_\eta 2} \\ \vdots & \vdots \\ \eta=1 & f_{1N_\xi} \\ \vdots & \vdots \\ \eta=-1 & f_{N_\eta N_\xi} \end{matrix} \\ \downarrow \begin{matrix} \eta=1 \\ \uparrow N_\eta \text{ elements} \end{matrix} & & \xi = \cos \frac{\pi}{N_\xi - 1} \\ \end{array} \end{array} \quad (3.15)$$

Note the small distinction between the component $f_{N_\eta N_\xi}$ and the represented function $f_{N_\eta \times N_\xi}$, which is first introduced in equation (3.13). The new column-vector is $N_\eta N_\xi$ elements high and is from here on referred to as the stacked (column-)vector. Note that the collocation points run in the direction of decreasing coordinates as implicitly stated in equation (3.6). This convention is precisely the same as that of Batterson [2]. As he emphasizes, it is very important to recall this structure when applying boundary conditions.

Consider the seemingly trivial case of equating two functions $\xi \eta f(\xi, \eta)$ and $g(\xi, \eta)$, discretely. First the varying coefficient $\xi \eta$ must be discretised, this is done similarly as handled before. Through using a nodal basis, it is logical to satisfy the equation at the CGL collocation points. Using the stacked notation as in equation (3.15), this can be

done rather efficiently:

$$\begin{aligned} (\xi\eta)_{N_\eta \times N_\xi} f_{N_\eta \times N_\xi} &= g_{N_\eta \times N_\xi} \\ \sum_{i=1}^{N_\xi} \sum_{j=1}^{N_\eta} \xi \eta f_{ji} \psi_{ji}(\xi, \eta) &= \sum_{i=1}^{N_\xi} \sum_{j=1}^{N_\eta} g_{ji} \psi_{ji}(\xi, \eta) \quad \text{at the CGL points} \end{aligned} \quad (3.16)$$

$$\begin{aligned} \xi_i \eta_j f_{ji} \psi_{ji}(\xi_i, \eta_j) &= g_{ji} \psi_{ji}(\xi_i, \eta_j), & \text{for } i = 1, \dots, N_\xi \wedge j = 1, \dots, N_\eta \\ \xi_i \eta_j f_{ji} &= g_{ji}, & \text{for } i = 1, \dots, N_\xi \wedge j = 1, \dots, N_\eta. \end{aligned} \quad (3.17)$$

It is important to see that, due to the fact that $\psi_{ji}(\xi_k, \eta_l) = 0$ when $(\xi_k, \eta_l) \neq (\xi_i, \eta_j)$, equation (3.16) can be evaluated non-trivially at each collocation point pair (ξ_i, η_j) . There are $N_\xi N_\eta$ distinct collocation point pairs, therefore this yields $N_\xi N_\eta$ distinct equations (3.17). These equations can be written in a matrix form:

$$\left[\begin{array}{c|ccccc} & & & \overset{N_\xi N_\eta}{\overbrace{\dots}} & & \\ \downarrow \begin{matrix} N_\xi N_\eta \\ \text{elements} \end{matrix} & \begin{matrix} (\xi\eta)_{11} \\ \ddots \\ (\xi\eta)_{N_\eta 1} \\ \ddots \\ (\xi\eta)_{1N_\xi} \\ 0 \end{matrix} & & 0 & \begin{matrix} f_{11} \\ \vdots \\ f_{N_\eta 1} \\ \vdots \\ f_{1N_\xi} \\ \vdots \\ f_{N_\eta N_\xi} \end{matrix} & = \begin{matrix} g_{11} \\ \vdots \\ g_{N_\eta 1} \\ \vdots \\ g_{1N_\xi} \\ \vdots \\ g_{N_\eta N_\xi} \end{matrix} \end{array} \right]. \quad (3.18)$$

Note that, for example, $(\xi\eta)_{N_\eta N_\xi} = \xi_{N_\xi} \eta_{N_\eta} = 1$, $(\xi\eta)_{1N_\xi} = \xi_{N_\xi} \eta_1 = -1$, $(\xi\eta)_{N_\eta 1} = \xi_1 \eta_{N_\eta} = -1$ and $(\xi\eta)_{11} = \xi_1 \eta_1 = 1$, by considering equation (3.6).

Due to the fact that $\psi_{ji}(\xi_k, \eta_l) = 0$ whenever $(\xi_k, \eta_l) \neq (\xi_i, \eta_j)$, the matrix in equation (3.18) is diagonal. So when a variable in an equation has a coefficient that involves no derivative, this coefficient will be represented by a diagonal matrix. Matters become trickier when derivatives *are* involved, this will be handled next.

3.1.3. SPECTRAL DERIVATIVES

Partial derivatives of a function can be calculated by taking the corresponding derivative of equation (3.13), equipped with equations (3.14):

$$\frac{\partial f_{N_\eta \times N_\xi}(\xi, \eta)}{\partial \xi} = \sum_{i=1}^{N_\xi} \sum_{j=1}^{N_\eta} f_{ji} \frac{d \lambda_i(\xi)}{d \xi} \mu_j(\eta), \quad \frac{\partial f_{N_\eta \times N_\xi}(\xi, \eta)}{\partial \eta} = \sum_{i=1}^{N_\xi} \sum_{j=1}^{N_\eta} f_{ji} \lambda_i(\xi) \frac{d \mu_j(\eta)}{d \eta}.$$

Figure 3.1 shows that $\frac{d \lambda_i}{d \xi}(\xi_k) \neq 0$ for $k \neq i$ (recall that $\lambda_i(\xi_i) = 1$). Therefore, when writing out the equation $\frac{\partial f(\xi, \eta)}{\partial \xi} = g(\xi, \eta)$ in a similar way as equation (3.18), the matrix that multiplies the vector of discrete values of f is not diagonal. The elements of that so-called *pseudo-spectral differentiation matrix*, $\mathbf{D}_{\xi, ji}$ in this case, can readily be calculated

beforehand. For the one-dimensional case, these are equal to [2, 3, 5–7]:

$${}_1\mathbf{D}_\xi = \begin{cases} {}_1\mathbf{D}_{\xi,11} & = \frac{2(N_\xi-1)^2+1}{6} \\ {}_1\mathbf{D}_{\xi,N_\xi N_\xi} & = -\frac{2(N_\xi-1)^2+1}{6} \\ {}_1\mathbf{D}_{\xi,ii} & = \frac{-\xi_i}{2(1-\xi_i^2)} \quad \text{for } i = 2, \dots, N_\xi - 1 \\ {}_1\mathbf{D}_{\xi,ji} & = \frac{\bar{c}_i}{\bar{c}_j} \frac{(-1)^{i+j}}{\xi_i - \xi_j} \quad \text{for } i \neq j, \quad i, j = 2, \dots, N_\xi - 1 \end{cases}, \quad (3.19)$$

3

where \bar{c}_i and \bar{c}_j are defined as in equation (3.14). The elements of the differentiation matrix with respect to the other direction, ${}_1\mathbf{D}_{\eta,ji}$, can be calculated similarly. The elements of the second order differentiation matrices, ${}_1\mathbf{D}_{\xi\xi,ji}$ and ${}_1\mathbf{D}_{\eta\eta,ji}$, can be obtained by squaring the first order matrices. This is not advisable for the numerical equivalents, the coefficients of the aforementioned differentiation matrices can be efficiently calculated using the method elaborated on by Weideman and Reddy [12].

Usually, the considered physical domain does not correspond to the perfect square defined by the domain $(\xi, \eta) \in [-1, 1] \times [-1, 1]$, from now on referred to as the *computational domain*. Therefore, most of the time the physical domain is projected onto the computational one, involving a transformation (or: mapping) $\xi = \xi(x)$, or inversely: $x = x(\xi)$. Here x is the (in this case non-dimensional) physical coordinate in the direction of ξ . In section 3.1.4, the specific transformation used in the current treatment will be handled. With respect to the discretisation, this transformation yields only a change in the pseudo-spectral differentiation matrices, which can be illustrated using the chain rule for the exact case:

$$\frac{\partial f_{\text{exact}}(\xi(x), \eta)}{\partial x} = \frac{d\xi(x)}{dx} \frac{\partial f_{\text{exact}}(\xi, \eta)}{\partial \xi} \quad (3.20)$$

Here $\frac{d\xi(x)}{dx}$ is known from the applied transformation; it is the factor that scales the derivatives. In the discrete case precisely the same applies. To get the physical differentiation matrix, the computational one must be multiplied with the appropriate factor:

$${}_1\mathbf{D}_x = {}_1\mathbf{T}_x^\xi {}_1\mathbf{D}_\xi$$

Note that the discrete analogue of the factor $\frac{d\xi(x)}{dx}$ is a diagonal matrix ${}_1\mathbf{T}_x^\xi \in \mathbb{R}^{N_\xi \times N_\xi}$, which consists of the values of $\frac{d\xi(x)}{dx}$ at the collocation points $x_i = x(\xi_i)$, see equation (3.6). The transformation of the η coordinate is performed analogously. Note that for second order derivatives, the derivative of equation (3.20) must be taken once again. As a consequence of the product differentiation rule, it is possible that a combination of lower order derivatives is required to evaluate the higher order ones.

In the following, the treatment will make use of the computational derivatives only. The physical counterparts will be obtained by substituting ${}_1\mathbf{T}_x^\xi {}_1\mathbf{D}_\xi$ for ${}_1\mathbf{D}_\xi$. The same holds for the η -derivative; substituting ${}_1\mathbf{T}_y^\eta {}_1\mathbf{D}_\eta$ for ${}_1\mathbf{D}_\eta$ yields the physical equivalent. This will be proved when appropriate.

Hitherto, the differentiation matrices are derived only for a one-dimensional case. This can be illustrated in the following way. Note that ${}_1\mathbf{D}_\xi \in \mathbb{R}^{N_\xi \times N_\xi}$. Consider one row of the matrix form of the two-dimensional $f \in \mathbb{C}^{N_\eta \times N_\xi}$, to the left in equation (3.15).

I.e. the values of f for constant η . One can post-multiply this row-vector with ${}_1\mathbf{D}_\xi$ to yield the ξ -derivative of $f_{N_\eta \times N_\xi}$ at constant η . Similarly, one can take some column of f and pre-multiply it with ${}_1\mathbf{D}_\eta \in \mathbb{R}^{N_\eta \times N_\eta}$ to yield the η -derivative of $f_{N_\eta \times N_\xi}$ at constant ξ . This means that the partial derivatives of $f_{N_\eta \times N_\xi}$ can be represented by appropriately multiplying f in matrix form:

$$\frac{\partial f_{N_\eta \times N_\xi}(\xi, \eta)}{\partial \xi} = \sum_{i=1}^{N_\xi} \sum_{j=1}^{N_\eta} \left[\sum_{k=1}^{N_\xi} f_{jk} {}_1\mathbf{D}_{\xi,ki} \right] \lambda_i(\xi) \mu_j(\eta), \quad (3.21)$$

$$\frac{\partial f_{N_\eta \times N_\xi}(\xi, \eta)}{\partial \eta} = \sum_{i=1}^{N_\xi} \sum_{j=1}^{N_\eta} \left[\sum_{k=1}^{N_\eta} {}_1\mathbf{D}_{\eta,jk} f_{ki} \right] \lambda_i(\xi) \mu_j(\eta) \quad (3.22)$$

Equations (3.21) and (3.22) are really handy to acquire the partial derivatives of the fields. The problem is that one wants to express the derivatives using not the matrix form of f , but the *stacked column-vector form* as presented to the right in equation (3.15). Later on it will be illustrated why. The two-dimensional pseudo-spectral differentiation matrices will be in $\mathbb{R}^{N_\xi N_\eta \times N_\xi N_\eta}$, just like the matrix in equation (3.18).

This kind of matrix can be efficiently generated by involving the so-called *Kronecker product*.³ This product is denoted by $\mathbf{A} \otimes \mathbf{B} = \mathbf{C}$, where $\mathbf{A} \in \mathbb{C}^{m \times n}, \mathbf{B} \in \mathbb{C}^{p \times q}$ and $\mathbf{C} \in \mathbb{C}^{mp \times nq}$. Following Batterson [2], the product manifests itself by:

$$\mathbf{A} \otimes \mathbf{B} = \begin{array}{c} \xrightarrow{\text{elements}} \\ \uparrow \begin{matrix} mp \\ \vdots \\ A_{m1}\mathbf{B} \end{matrix} \end{array} \left[\begin{array}{ccc} \mathbf{A}_{11}\mathbf{B} & \cdots & \mathbf{A}_{1n}\mathbf{B} \\ \vdots & \ddots & \vdots \\ \mathbf{A}_{m1}\mathbf{B} & \cdots & \mathbf{A}_{mn}\mathbf{B} \end{array} \right] \quad (3.23)$$

Thus each element of \mathbf{A} is multiplied by all elements of \mathbf{B} . The Kronecker product satisfies the mixed-product property: $(\mathbf{D} \otimes \mathbf{E})(\mathbf{F} \otimes \mathbf{G}) = \mathbf{D}\mathbf{F} \otimes \mathbf{E}\mathbf{G}$, when the conventional matrix products \mathbf{DF} and \mathbf{EG} exist, see Tracy & Singh [13].

Consider the upperleft $N_\eta \times N_\eta$ part of the matrix in equation (3.18). Note that this part multiplies the column-vector at constant $\xi = 1$. Consider replacing the $N_\eta \times N_\eta$ part of the matrix with the one-dimensional pseudo-spectral differentiation matrix ${}_1\mathbf{D}_\eta$. Now, multiplication would yield the discrete η -derivative of $f_{N_\eta \times N_\xi}$ at $\xi = 1$ in $[g_{11} \cdots g_{N_\eta 1}]^T$, just as arrived upon above. Performing the same for the next $N_\eta \times N_\eta$ block along the diagonal, one will acquire the η -derivative of $f_{N_\eta \times N_\xi}$ at $\xi = \cos \frac{\pi}{N_\xi - 1}$ in $[g_{12} \cdots g_{N_\eta 2}]^T$. By induction, the complete η -derivative at all ξ -locations will be stored in the stacked vector g when continuing this process. The resulting matrix with square $N_\eta \times N_\eta$ blocks precisely equals the Kronecker product $\mathbf{I}_{N_\xi} \otimes {}_1\mathbf{D}_\eta$. Thus, the equation for the two-dimensional pseudo-spectral differentiation matrix in the η -direction yields:

$$\mathbf{D}_\eta = \mathbf{I}_{N_\xi} \otimes {}_1\mathbf{D}_\eta \quad (3.24)$$

It can be imagined that this matrix consists of $N_\eta \times N_\eta$ diamonds around the diagonal. In a similar way, gathering all elements in f at constant η , will yield the following expression

³This product is also referred to as the tensor product.

for the two-dimensional differentiation matrix in the ξ -direction:

$$\mathbf{D}_\xi = {}_1\mathbf{D}_\xi \otimes \mathbf{I}_{N_\eta} \quad (3.25)$$

This matrix covers the main diagonal and the diagonals in the off-diagonal $N_\eta \times N_\eta$ blocks with respect to the former matrix. Batterson [2] and Trefethen [7] illustrate the structure of the above matrices more clearly at page 99 and 69, respectively.

In a similar way as the derivative matrices, the two-dimensional transformation matrix $\mathbf{T}_x^\xi = {}_1\mathbf{T}_x^\xi \otimes \mathbf{I}_{N_\eta}$. Through the mixed-product identity, it follows that:

3

$$\begin{aligned} \mathbf{D}_x &= \mathbf{T}_x^\xi \mathbf{D}_\xi = ({}_1\mathbf{T}_x^\xi \otimes \mathbf{I}_{N_\eta})({}_1\mathbf{D}_\xi \otimes \mathbf{I}_{N_\eta}) \\ &= {}_1\mathbf{T}_x^\xi {}_1\mathbf{D}_\xi \otimes \mathbf{I}_{N_\eta}^2 \\ &= {}_1\mathbf{T}_x^\xi {}_1\mathbf{D}_\xi \otimes \mathbf{I}_{N_\eta} \end{aligned} \quad (3.26)$$

This identity proves the above statement that substituting ${}_1\mathbf{T}_x^\xi {}_1\mathbf{D}_\xi$ for ${}_1\mathbf{D}_\xi$ yields the corresponding physical result. Analogous results hold for the other derivatives.

Using the above identities, the second order and cross differentiation matrices can be derived:

$$\begin{aligned} \mathbf{D}_{\xi\xi} &= ({}_1\mathbf{D}_\xi)^2 \otimes \mathbf{I}_{N_\eta}, \quad \mathbf{D}_{\eta\eta} = \mathbf{I}_{N_\xi} \otimes ({}_1\mathbf{D}_\eta)^2, \quad \mathbf{D}_{\xi\eta} = ({}_1\mathbf{D}_\xi \otimes \mathbf{I}_{N_\eta})(\mathbf{I}_{N_\xi} \otimes {}_1\mathbf{D}_\eta) \\ &\qquad\qquad\qquad = {}_1\mathbf{D}_\xi \mathbf{I}_{N_\xi} \otimes \mathbf{I}_{N_\eta} {}_1\mathbf{D}_\eta \\ &\qquad\qquad\qquad = {}_1\mathbf{D}_\xi \otimes {}_1\mathbf{D}_\eta \end{aligned} \quad (3.27)$$

Note that the definitions of the pseudo-spectral differentiation matrices are dependent on the way that the stacked vector in equation (3.15) is obtained. One could also have linked all the rows head to tail and transpose the result, for example. In that case all Kronecker products in equations (3.24) to (3.27), should be reversed to obtain the correct results. One could compare Batterson [2] and Trefethen [7] to see the two cases independently, as noted before the current convention corresponds to that of Batterson.

3.1.4. MAPPINGS

Throughout this work, two mappings are used to transform the computational into the physical domain. This is required because resolution is usually required only in a very restricted part of the considered domain. In the case of boundary layers, for example, a high resolution near the wall is required, while the grid can be sparse in the freestream. The first mapping that is discussed, proposed by Malik [14], allows densely resolving a boundary.

For isolated shear layers, on the other hand, one requires high resolution in the interior of the domain. The second mapping is newly developed to allow densely resolving a region in the interior of the domain, which is particularly required for the BiGlobal analyses.

It should be emphasized that, in both cases, the CGL collocation nodes are mapped from the computational to the physical domain. This means that the node distributions will maintain a cosine distribution near the boundaries in the physical domain. Accordingly, the spectral discretisation order and polynomial interpolation properties are maintained, see Canuto *et al.* [3].

MALIK'S MAPPING

Now that the main discretisation machinery is handled, the specific mapping used in the current treatment can be focused on. It was proposed by Malik [14] and Pinna [8] continued to make use of it.

The transformation is given for the wall-normal y -direction as follows:

$$y = \frac{y_i y_{\max} (1 + \eta)}{y_{\max} - \eta (y_{\max} - 2y_i)} \quad (3.28)$$

This transformation maps $\eta \in [-1, 1]$ into $y \in [0, y_{\max}]$. Here, y_{\max} is the maximal y -coordinate of the considered physical domain. Half the number of collocation nodes lies in $[0, y_i]$, while the other half lies in $[y_i, y_{\max}]$. This can be verified by substituting the values $\eta = -1, 0$ and 1 into the transformation (3.28). Malik himself used a slightly different version of the transformation, considering η to be in $[0, 1]$. It must be noted that when y_i is set equal to $\frac{y_{\max}}{2}$, the linear transformation $y = \frac{y_{\max}}{2}(1 + \eta)$ is received. This linear form is used by Batterson [2], for example.

As reported by Grosch & Orszag [15], one can use an algebraic⁴ transformation to map the upper grid points to infinity. In that way, they report that eigenmodes can be determined very accurately. The algebraic mapping they propose can be derived from equation (3.28) as well. By letting $y_{\max} \rightarrow \infty$, one obtains:

$$y = y_i \frac{1 + \eta}{1 - \eta}, \quad (3.29)$$

which corresponds to the mapping proposed by Grosch & Orszag [15].

The main advantage of the current transformation is that it maps half the collocations points into the boundary layer. The general intention is to sufficiently resolve the modes in the neighbourhood of the boundary. This is done by appropriately setting the parameter y_i . For $y_{\max} = \infty$, the mapping converts the differentiation matrices so that the derivatives of the approximated function are zero at infinity; i.e. it enforces a boundary condition. Being able to specify $y_{\max} < \infty$ yields a computational advantage and more freedom in specifying boundary conditions.

One can optimize the combination (y_i, y_{\max}) so that a relatively small amount of collocation points is required for a very accurate solution; the linear transformation and transformation (3.29) can be seen as extremes at two ends of the overarching parameter space. In the current treatment, the parameter y_i is fixed to the values found in the literature, which tends to resolve the boundary layer well. Typical values of y_i , using the Blasius length scale l are 3 to 10. Accordingly, the parameter y_{\max} can be made relatively large, without using a large number of collocation points to fill the uninteresting part of the domain that tends toward infinity. By experience, typical values for y_{\max} of $\mathcal{O}(200)$ yield results that are converged up to algorithm precision. Figure 3.2 illustrates the distribution of the collocation points for the combination $(y_i, y_{\max}) = (10, 100)$.

From equation (3.28), the vertical equivalent of the derivative $\frac{dy}{dx}$ in equation (3.20) can be determined, so the transformation can be incorporated in the pseudo-spectral

⁴They also consider an exponential transformation. However, the algebraic one is pointed out to give more accurate results.

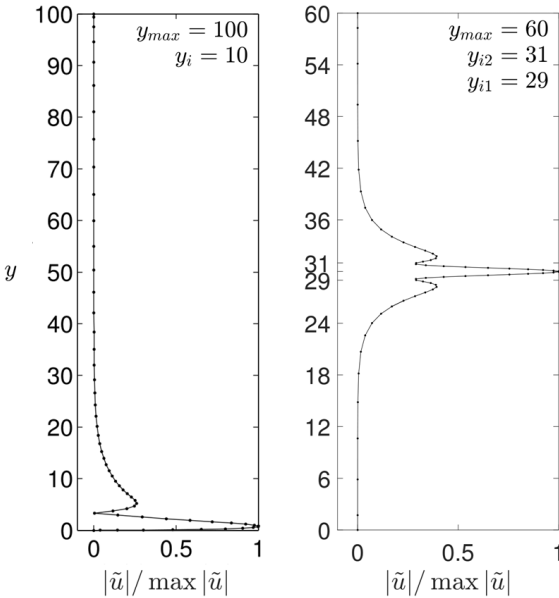


Figure 3.2: The collocation points are equally divided amongst the regions separated by y_i (left) and y_{i1} and y_{i2} (right). Shown profiles are TS (left) and KH (right) eigenfunctions obtained with incompressible LST for $N_\eta = 60$.

derivative matrices. Lastly, it must be noted that the horizontal direction is equipped with the transformation as well. However, the horizontal equivalent of y_i , the parameter x_i , is set equal to $\frac{x_{\max}}{2}$ always, because in the current treatment there is no need to map collocation points a certain way in this eigenfunction direction.

BiQUADRATIC MAPPING

As mentioned, Malik's mapping is intended to resolve boundaries. Many BiGlobal applications, however, require resolution in the interior of the domain. When applying Malik's mapping, y_i in fact controls the point of least node density if placed close to the center of the domain.

For this reason, Malik's bilinear mapping was generalized to the following BiQuadratic form:

$$y = y_{\max} \frac{a\eta^2 + b\eta + c}{d\eta^2 + e\eta + f}, \quad \text{where:} \quad (3.30)$$

$$\begin{aligned} a &= y_{i2} - 3y_{i1} & b &= \frac{3}{2}(y_{i2} - y_{i1}) & c &= (y_{i2} + 3y_{i1})/2 \\ d &= 2(2y_{i2} - 2y_{i1} - y_{\max}) & e &= 0 & f &= 2y_{\max} - y_{i2} + y_{i1} \end{aligned}$$

This mapping is set as to distribute one third of the collocation nodes over the domains $[0, y_{i1}]$, $[y_{i1}, y_{i2}]$ and $[y_{i2}, y_{\max}]$. This can be checked by showing that the points $\eta = -1$, $-1/2$, $1/2$ and 1 are mapped to $y = 0$, y_{i1} , y_{i2} and y_{\max} , respectively. Furthermore, one must specify y_{i1} and y_{i2} such that $0 < y_{i1} < y_{i2} < y_{\max}$, $y_{i2} < 9y_{i1}$ and $9y_{i2} < y_{i1} + 8y_{\max}$ to ensure a regular monotonic behaviour without discontinuities. Specifically, without the

latter two conditions, the resulting node distributions can overshoot either the boundary $y = 0$ or $y = y_{\max}$, meaning regions outside the domain would be covered (twice). Furthermore, e was set to zero, as this term otherwise led to singularities (vertical asymptotes) in the mapping. Figure 3.2 illustrates the distribution of the collocation points for the combination $(y_{i1}, y_{i2}, y_{\max}) - 30 = (-1, 1, 30)$.

It was attempted to generalize the mapping even further, allowing specifying three intermediate points y_{i1} , y_{i2} and y_{i3} ; a bicubic mapping. It was found, however, that the combination of parameters for which this mapping would be well-behaved (i.e. have no singularities and multi-valued parts) was very limited and, in fact, seemed to form a fractal set. That is, to set proper input parameters would require knowing which parameter combination lies within this particular fractal structure. Due to this property, the bicubic mapping was abandoned as a practical tool.

The aforementioned mappings can be altered generalized in a particular way that here will only be described in words. Different amounts of nodes can be specified to be mapped into the regions separated by the y_i 's. The coefficients of the bilinear and biquadratic expressions in equations (3.28) and (3.30) are derived by linking the coordinates in the computational η -domain and the physical y -domain. Specifically, for the Malik mapping, the points $\eta = -1, 0$ and 1 correspond to $y = 0$, y_i and y_{\max} . These η -coordinates divide the computational domain exactly in half. For the biquadratic mapping, $\eta = -1, -1/2, 1/2$ and 1 separate the computational domain in three equal parts. This can be seen by noting that the spacing in θ in equation (3.2), i.e. the angle generating the collocation point locations, is uniform. By shifting these η -locations to $-1, -\sqrt{2}/2, \sqrt{2}/2$ and 1 , one separates the domain into three regions containing $1/4$, $1/2$ and $1/4$ times the total number of nodes.

3.1.5. AMPLITUDE-COEFFICIENT MATRICES (ACM's)

At this stage one is interested in the implementation of the previously handled tools leading to the complete discrete system. This is done by zooming in at the structure of the eigenvalue problem with an appropriate pace.

(GENERALIZED) EIGENVALUE PROBLEM LEVEL

The stability equations considered in this treatment all form a partial differential eigenvalue problem. This means that the equations can be written in the following top eigenvalue problem level form of a generalized non-linear eigenvalue problem:

$$\mathbf{A}\boldsymbol{\Xi} = \lambda \mathbf{B}\boldsymbol{\Xi} + \lambda^2 \mathbf{C}\boldsymbol{\Xi} \quad \text{where } \begin{cases} \lambda \equiv \alpha & \text{for spatial analysis} \\ \lambda \equiv \omega & \text{for temporal analysis} \end{cases} \quad (3.31)$$

Here, λ is a general eigenvalue defined to be equal to ω when considering temporal analysis and equal to α in spatial analysis, \mathbf{A} is the left hand side coefficient matrix, \mathbf{B} is the right hand side coefficient matrix associated with a single eigenvalue λ and \mathbf{C} is the right hand side coefficient matrix being the coefficient of the eigenvalue squared. Note that for temporal analysis this matrix is identically zero, because in that case the eigenvalue appears only linearly in the equation. $\boldsymbol{\Xi}$ is the eigenvector of the system.

The eigenvector consists of four or five physical variables (in discrete form) in the incompressible or compressible case, respectively. For the incompressible case, the con-

ventional set is $\{\tilde{u}, \tilde{v}, \tilde{w}, \tilde{p}\}$. In the compressible case, the combination $\{\tilde{u}, \tilde{v}, \tilde{w}, \tilde{T}, \tilde{p}\}$ is presumed.

The discrete amplitudes all have the stacked column-vector form having $N_\xi N_\eta$ elements each, as introduced in equation (3.15). In turn, these vectors are stacked on each other forming Ξ , to yield:

$$\Xi_{\text{incomp}} = \begin{bmatrix} \tilde{u} \\ \tilde{v} \\ \tilde{w} \\ \tilde{p} \end{bmatrix} \in \mathbb{R}^{4N_\xi N_\eta} \quad \Xi_{\text{comp}} = \begin{bmatrix} \tilde{u} \\ \tilde{v} \\ \tilde{w} \\ \tilde{T} \\ \tilde{p} \end{bmatrix} \in \mathbb{R}^{5N_\xi N_\eta}. \quad (3.32)$$

3

The eigenvector of a matrix can be represented in this way only, this is the reason why the rather technical stacked column-vector form of the physical matrices and Kronecker product pseudo-spectral differentiation matrices (3.24) and (3.25) had to be introduced in the previous sections.

EQUATION-VARIABLE LEVEL

The next layer is called the equation-variable level. It focuses on the amplitudes and equations in the system; the distinction between (non-) derivative contributions is no longer made. The matrices **A**, **B** and **C** are now divided into the sub-matrices that multiply the individual variables of Ξ for the continuity, 1-, 2-, 3-momentum and energy equations, separately. This means that the earlier presented machinery of sections 3.1.2 and 3.1.3 is applicable to precisely these sub-matrices.

The resulting decomposition is presented in equation (3.33), being equivalent to the representations reported by Robinet [16] and Theofilis & Colonius [17]:

$$\begin{bmatrix} \mathcal{L}_1^{\tilde{u}} & \mathcal{L}_1^{\tilde{v}} & \mathcal{L}_1^{\tilde{w}} & \mathcal{L}_1^{\tilde{T}} & \mathcal{L}_1^{\tilde{p}} \\ \mathcal{L}_2^{\tilde{u}} & \mathcal{L}_2^{\tilde{v}} & \mathcal{L}_2^{\tilde{w}} & \mathcal{L}_2^{\tilde{T}} & \mathcal{L}_2^{\tilde{p}} \\ \mathcal{L}_3^{\tilde{u}} & \mathcal{L}_3^{\tilde{v}} & \mathcal{L}_3^{\tilde{w}} & \mathcal{L}_3^{\tilde{T}} & \mathcal{L}_3^{\tilde{p}} \\ \mathcal{L}_c^{\tilde{u}} & \mathcal{L}_c^{\tilde{v}} & \mathcal{L}_c^{\tilde{w}} & \mathcal{L}_c^{\tilde{T}} & \mathcal{L}_c^{\tilde{p}} \\ \mathcal{L}_e^{\tilde{u}} & \mathcal{L}_e^{\tilde{v}} & \mathcal{L}_e^{\tilde{w}} & \mathcal{L}_e^{\tilde{T}} & \mathcal{L}_e^{\tilde{p}} \end{bmatrix} \begin{bmatrix} \tilde{u} \\ \tilde{v} \\ \tilde{w} \\ \tilde{T} \\ \tilde{p} \end{bmatrix} = \lambda \begin{bmatrix} \mathcal{R}_1^{\tilde{u}} & \mathcal{R}_1^{\tilde{v}} & \mathcal{R}_1^{\tilde{w}} & \mathcal{R}_1^{\tilde{T}} & \mathcal{R}_1^{\tilde{p}} \\ \mathcal{R}_2^{\tilde{u}} & \mathcal{R}_2^{\tilde{v}} & \mathcal{R}_2^{\tilde{w}} & \mathcal{R}_2^{\tilde{T}} & \mathcal{R}_2^{\tilde{p}} \\ \mathcal{R}_3^{\tilde{u}} & \mathcal{R}_3^{\tilde{v}} & \mathcal{R}_3^{\tilde{w}} & \mathcal{R}_3^{\tilde{T}} & \mathcal{R}_3^{\tilde{p}} \\ \mathcal{R}_c^{\tilde{u}} & \mathcal{R}_c^{\tilde{v}} & \mathcal{R}_c^{\tilde{w}} & \mathcal{R}_c^{\tilde{T}} & \mathcal{R}_c^{\tilde{p}} \\ \mathcal{R}_e^{\tilde{u}} & \mathcal{R}_e^{\tilde{v}} & \mathcal{R}_e^{\tilde{w}} & \mathcal{R}_e^{\tilde{T}} & \mathcal{R}_e^{\tilde{p}} \end{bmatrix} \begin{bmatrix} \tilde{u} \\ \tilde{v} \\ \tilde{w} \\ \tilde{T} \\ \tilde{p} \end{bmatrix} \quad (3.33)$$

$$+ \lambda^2 \begin{bmatrix} 2\mathcal{R}_1^{\tilde{u}} & 0 & 0 & 0 & 0 \\ 0 & 2\mathcal{R}_2^{\tilde{v}} & 0 & 0 & 0 \\ 0 & 0 & 2\mathcal{R}_3^{\tilde{w}} & 0 & 0 \\ 0 & 0 & 0 & 0 & 0 \\ 2\mathcal{R}_e^{\tilde{u}} & 2\mathcal{R}_e^{\tilde{v}} & 2\mathcal{R}_e^{\tilde{w}} & 2\mathcal{R}_e^{\tilde{T}} & 2\mathcal{R}_e^{\tilde{p}} \end{bmatrix} \begin{bmatrix} \tilde{u} \\ \tilde{v} \\ \tilde{w} \\ \tilde{T} \\ \tilde{p} \end{bmatrix}$$

The subscripts denote the equation and the superscripts the amplitude. Note that ${}_2\mathcal{R}_c^{\tilde{u}} = {}_2\mathcal{R}_c^{\tilde{v}} = {}_2\mathcal{R}_c^{\tilde{w}} = {}_2\mathcal{R}_c^{\tilde{T}} = {}_2\mathcal{R}_c^{\tilde{p}} = 0$, due to the fact that no second order derivatives are present in the continuity equation. The λ^2 related sub-matrices are present only due to second order homogeneous direction derivatives. The remaining zeros are handled in a moment. The blocks of equation (3.33) are from now on referred to as the *amplitude coefficients*. They correspond to the discrete versions of the coefficients of the amplitudes

in the stability equations and thus, as mentioned before, correspond to the matrix in equation (3.18). Each coefficient in equation (3.33) is therefore a matrix in $\mathbb{C}^{N_\xi N_\eta \times N_\xi N_\eta}$. This means that the matrices **A**, **B** and **C** are in $\mathbb{C}^{5N_\xi N_\eta \times 5N_\xi N_\eta}$.

However, when the incompressible case is considered, the energy equation decouples from the system and the temperature amplitude becomes superfluous to obtain the velocity field. Thus, for incompressible flow, one can set, or rather remove, the following coefficients:

3

$$\text{Incompressible flow : } \left\{ \begin{array}{l} \mathcal{L}_e^{\bar{u}} = \mathcal{L}_e^{\bar{v}} = \mathcal{L}_e^{\bar{w}} = \mathcal{L}_e^{\bar{p}} = \mathcal{L}_e^{\bar{T}} = 0 \\ \mathcal{L}_c^{\bar{T}} = \mathcal{L}_1^{\bar{T}} = \mathcal{L}_2^{\bar{T}} = \mathcal{L}_3^{\bar{T}} = 0 \\ \mathcal{R}_e^{\bar{u}} = \mathcal{R}_e^{\bar{v}} = \mathcal{R}_e^{\bar{w}} = \mathcal{R}_e^{\bar{p}} = \mathcal{R}_e^{\bar{T}} = 0 \\ \mathcal{R}_c^{\bar{T}} = \mathcal{R}_1^{\bar{T}} = \mathcal{R}_2^{\bar{T}} = \mathcal{R}_3^{\bar{T}} = 0 \\ {}_2\mathcal{R}_e^{\bar{u}} = {}_2\mathcal{R}_e^{\bar{v}} = {}_2\mathcal{R}_e^{\bar{w}} = {}_2\mathcal{R}_e^{\bar{p}} = {}_2\mathcal{R}_e^{\bar{T}} = 0 \\ {}_2\mathcal{R}_c^{\bar{T}} = {}_2\mathcal{R}_1^{\bar{T}} = {}_2\mathcal{R}_2^{\bar{T}} = {}_2\mathcal{R}_3^{\bar{T}} = 0 \end{array} \right. \quad (3.34)$$

This means that only 4×4 amplitude coefficients are present in **A**, **B** and **C**. Therefore, in the incompressible case these matrices are in the slightly more modest $\mathbb{C}^{4N_\xi N_\eta \times 4N_\xi N_\eta}$.

3.1.6. QUADRATIC EIGENVALUE PROBLEMS

In this treatment mainly the temporal problem will be considered, i.e. the eigenvalue problem with: $\lambda = \omega$ and **C** = **0**:

$$\mathbf{A}\Xi = \lambda \mathbf{B}\Xi \quad (3.35)$$

This means that the *linear* generalized eigenvalue problem $\mathbf{A}\Xi = \omega \mathbf{B}\Xi$ has to be solved, which can be done with standard tools in MATLAB. However, some of the parts of the treatment will be built on the spatial theory; some spatial simulations will be performed. This kind of problem involves the *quadratic* generalized eigenvalue problem, which has the general form illustrated in equation (3.31).

This problem can be reduced to a linear eigenvalue problem, so that it can be solved with standard means again. This is done by augmenting the trivial equation set $\lambda\Xi = \lambda\Xi$ to the system:

$$\begin{aligned} -\lambda \mathbf{B}\Xi + \mathbf{A}\Xi &= \lambda^2 \mathbf{C}\Xi \\ \lambda\Xi &= \lambda\Xi \end{aligned}$$

By orienting the system in this way, one can identify terms that multiply Ξ alone and terms that multiply $\lambda\Xi$. By doing this in a smart way, the system can be factored to yield the following system:

$$\underbrace{\begin{bmatrix} -\mathbf{B} & \mathbf{A} \\ \mathbf{I} & \mathbf{0} \end{bmatrix}}_{\equiv \tilde{\mathbf{A}}} \begin{bmatrix} \lambda\Xi \\ \Xi \end{bmatrix} = \lambda \underbrace{\begin{bmatrix} \mathbf{C} & \mathbf{0} \\ \mathbf{0} & \mathbf{I} \end{bmatrix}}_{\equiv \tilde{\mathbf{B}}} \begin{bmatrix} \lambda\Xi \\ \Xi \end{bmatrix} \quad (3.36)$$

Here, **I** and **0** are the identity and zero matrix that have the same dimensions as **A**, **B** and **C**. By introducing the new eigenvector $\tilde{\Xi} \equiv [\lambda\Xi, \Xi]^T$, the problem can be written as follows:

$$\tilde{\mathbf{A}}\tilde{\Xi} = \lambda \tilde{\mathbf{B}}\tilde{\Xi} \quad (3.37)$$

This system is linear in λ , note that the non-linearity of the system is hidden in the eigenvector. This technique is also referred to as the companion matrix technique, see Dambasoglu & Biringen [18]. This system can be solved with the standard tools again. By generalising this technique, any polynomial order eigenvalue problem can be analysed. The only catch is that the size of the system scales up with the largest power of the eigenvalue in the problem.

3.1.7. BOUNDARY CONDITIONS

3

Now the system of stability equations is automatically implemented by constructing the ACM's, the next step is to consider the boundary conditions. These conditions complete the eigenvalue problem.

For the tool to be as general as possible, many different kinds of boundary conditions are implemented. One can set Dirichlet, Neumann, Robin (all homogeneous) and periodic boundary conditions for any variable at any boundary. Furthermore, one can specify compatibility conditions for the pressure and density (via the momentum and Poisson equations), at any boundary.

Boundary conditions replace the function of the stability equations at the boundaries. They rule over the boundaries, whereas the stability equations rule over the interior of the considered domain. In this way, the boundary conditions can be interpreted quite effectively as, rather trivial, equations. These equations are quite similarly implemented as the stability equations, by specifying the coefficients of the amplitudes at the correct locations within the ACM's **A**, **B** and **C**.

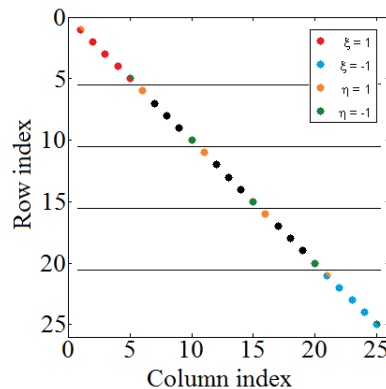


Figure 3.3: Indication of the rows and columns corresponding to the boundaries of the domain.

Recall equations (3.15) and (3.18). They illustrate in which way each row in the coefficient matrix corresponds to an equation evaluated at a specific location within the domain. To exemplify which rows in the amplitude coefficients correspond to the boundary, the element of the diagonal of the matrix in equation (3.18) are coloured appropriately in figure 3.3 for a 5×5 grid. In this figure, the black dots indicate the rows corresponding to the interior locations in the domain, whereas the coloured dots correspond to the indicated boundaries. Doubly coloured dots correspond to corners.

These rows are to be overwritten with the coefficients of the boundary or compatibility conditions. Note that figure 3.3 corresponds to one variable only; only one amplitude coefficient is considered. In the full ACM's, multiple of these blocks are augmented as shown in equation (3.33). As a convention, the first row of blocks is used to equip the boundary condition on \tilde{u} , the second with that on \tilde{v} , etc.

DIRICHLET CONDITIONS

Dirichlet boundary conditions involve the specification of the value of an amplitude at the boundary. In the homogeneous case considered here, this can be illustrated as follows. Take, for example, the velocity amplitude \tilde{u} . The Dirichlet boundary condition at $\xi = -1$ could be written as:⁵

$$\begin{aligned} & \tilde{u}_{\text{exact}}(\xi = -1, \eta) = 0 \\ \text{Discretise} \Rightarrow & \tilde{u}_{N_\eta \times N_\xi}(\xi = -1, \eta) = \sum_{i=1}^{N_\xi} \sum_{j=1}^{N_\eta} \tilde{u}_{ji} \psi_{ji}(\xi = -1, \eta) = 0 \\ & \sum_{j=1}^{N_\eta} \tilde{u}_{jN_\xi} \underbrace{\psi_{jN_\xi}(\xi = -1, \eta)}_{=1 \text{ for } \eta = \eta_j} = 0 \\ & \underbrace{1}_{\substack{\text{coefficient for} \\ \text{Dirichlet condition}}} \cdot \underbrace{\tilde{u}_{jN_\xi}}_{\substack{\text{elements in } \Xi}} = 0 \quad \text{for } j = 1, \dots, N_\eta \end{aligned} \quad (3.38)$$

It is clear that the coefficients in the amplitude coefficients have to be set equal to 1 to yield the Dirichlet boundary condition. In figure 3.3, the rows corresponding to the elements \tilde{u}_{jN_ξ} are indicated by the light blue dots. In this specific case, the blue dots show the locations corresponding to the coefficients, the ones. From equation (3.38), it follows that all other elements in the rows must be zero, also those corresponding to other variables. With the previously mentioned convention, this implies that the corresponding rows in the off-diagonal amplitude coefficient blocks are zero when this condition is applied. The condition does not involve the eigenvalues, so only zeros will be introduced in the **B** and **C** matrices.

The Dirichlet conditions are simply specifying zero amplitudes at the boundaries, so these values do not have any influence on the remainder of problem. For that reason, the row and column corresponding to the substituted 1 can be and are entirely omitted; they are removed from the ACM's, thereby reducing their size slightly. This procedure could be applied to the other conditions as well, but requires the row-reduction of the conditions. For the Dirichlet conditions, removing the corresponding rows and columns is equivalent to row-reducing the ACM's.

NEUMANN CONDITIONS

The Neumann boundary condition involves the specification of the normal derivative of an amplitude with respect to the boundary. This is again illustrated using an example.

⁵Here the same conventions are used as introduced in section 3.1.2.

The Neumann boundary condition at $\xi = -1$ is written as:

$$\begin{aligned}
 & \left. \frac{\partial \tilde{u}}{\partial \xi} \right|_{\text{exact}} (\xi = -1, \eta) = 0 \\
 \Rightarrow \quad & \frac{\partial \tilde{u}_{N_\eta \times N_\xi}}{\partial \xi} (\xi = -1, \eta) = \sum_{i=1}^{N_\xi} \sum_{j=1}^{N_\eta} \left[\sum_{k=1}^{N_\xi} \tilde{u}_{jk} {}_1\mathbf{D}_{\xi,ki} \right] \psi_{ji} (\xi = -1, \eta) = 0 \\
 & \sum_{j=1}^{N_\eta} \left[\sum_{k=1}^{N_\xi} \tilde{u}_{jk} {}_1\mathbf{D}_{\xi,kN_\xi} \right] \underbrace{\psi_{jN_\xi} (\xi = -1, \eta)}_{= 1 \text{ for } \eta = \eta_j} = 0 \\
 & \sum_{k=1}^{N_\xi} \underbrace{{}_1\mathbf{D}_{\xi,kN_\xi}}_{\substack{\text{coefficient for} \\ \text{Neumann condition}}} \cdot \underbrace{\tilde{u}_{jk}}_{\substack{\text{elements in } \Xi}} = 0 \quad \text{for } j = 1, \dots, N_\eta \tag{3.39}
 \end{aligned}$$

3

In equation (3.39), it can be seen that the \tilde{u}_{jk} are summed over the index in the ξ -direction. This means that for a fixed η -position (j index) in the grid, all values in the ξ -direction are equipped with the coefficients ${}_1\mathbf{D}_{\xi,kN_\xi}$, for $k \in 1, \dots, N_\xi$. Note that the pseudo-spectral differentiation matrix ${}_1\mathbf{D}_\xi$ is used in its one dimensional form as introduced in equation (3.19), in this way the notation is argued to be most convenient. This will be continued for the remainder of this section.

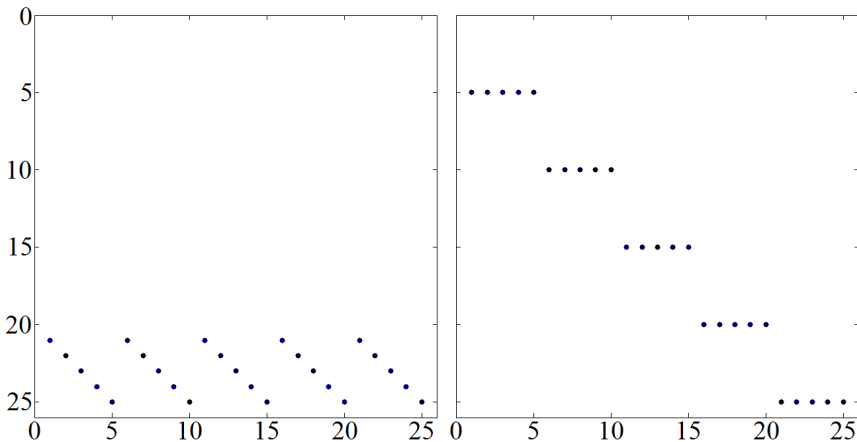


Figure 3.4: Indication of the Neumann boundary condition at $\xi = -1$ (left) and $\eta = -1$ (right).
Vertical axis: row index, horizontal axis: column index.

In figure 3.4, it is shown what form a (diagonal)⁶ amplitude coefficient attains when a Neumann boundary condition is applied to the boundaries $\xi = -1$ (to the left) and $\eta = -1$ (to the right). Again, the 5×5 grid is considered. Of course, the coefficients for the $\eta = -1$ boundary are those of the η -derivative, ${}_1\mathbf{D}_{\eta,N_\eta k}$, see equation (3.22).

⁶The off-diagonal amplitude coefficients are all zero again due to the fact that no other variables are involved.

In both left and right subfigures of figure 3.4, row 25 is occupied in both cases. This row corresponds to the corner $(\xi, \eta) = (-1, -1)$. Therefore, in general this means that at the corners, only *one* boundary condition can be applied. The no-slip boundary conditions are given preference always. It is argued that these conditions are most critical with respect to physical significance.

PERIODIC CONDITIONS

In the case of periodic boundary conditions, one equates the values and first normal derivatives of the amplitudes at contrary boundaries. Again, this is best illustrated with an example. The values across the $\xi = \pm 1$ boundaries are equated as follows:

$$\tilde{u}_{\text{exact}}(\xi = -1, \eta) = \tilde{u}_{\text{exact}}(\xi = 1, \eta)$$

In discrete form, this equation reads:

$$\begin{aligned} \tilde{u}_{N_\eta \times N_\xi}(\xi = -1, \eta) &= \tilde{u}_{N_\eta \times N_\xi}(\xi = 1, \eta) \\ \sum_{i=1}^{N_\xi} \sum_{j=1}^{N_\eta} \tilde{u}_{ji} \psi_{ji}(\xi = -1, \eta) &= \sum_{i=1}^{N_\xi} \sum_{j=1}^{N_\eta} \tilde{u}_{ji} \psi_{ji}(\xi = 1, \eta) \\ \sum_{j=1}^{N_\eta} \tilde{u}_{jN_\xi} \underbrace{\psi_{jN_\xi}(\xi = -1, \eta)}_{= 1 \text{ for } \eta = \eta_j} &= \sum_{j=1}^{N_\eta} \tilde{u}_{j1} \underbrace{\psi_{j1}(\xi = 1, \eta)}_{= 1 \text{ for } \eta = \eta_j} \\ \tilde{u}_{jN_\xi} - \tilde{u}_{j1} &= 0 \quad \text{for } j = 1, \dots, N_\eta \end{aligned} \quad (3.40)$$

Now the values are equated, the normal derivatives have to be equated as well. This is illustrated for the case across the $\xi = \pm 1$ boundaries as follows:

$$\frac{\partial \tilde{u}}{\partial \xi} \Big|_{\text{exact}} (\xi = -1, \eta) = \frac{\partial \tilde{u}}{\partial \xi} \Big|_{\text{exact}} (\xi = 1, \eta)$$

In discrete form, this equation reads:

$$\begin{aligned} \sum_{i=1}^{N_\xi} \sum_{j=1}^{N_\eta} \left[\sum_{k=1}^{N_\xi} \tilde{u}_{jk1} \mathbf{D}_{\xi,ki} \right] \psi_{ji}(\xi = -1, \eta) &= \sum_{i=1}^{N_\xi} \sum_{j=1}^{N_\eta} \left[\sum_{k=1}^{N_\xi} \tilde{u}_{jk1} \mathbf{D}_{\xi,ki} \right] \psi_{ji}(\xi = 1, \eta) \\ \sum_{j=1}^{N_\eta} \left[\sum_{k=1}^{N_\xi} \tilde{u}_{jk1} \mathbf{D}_{\xi,kN_\xi} \right] \underbrace{\psi_{jN_\xi}(\xi = -1, \eta)}_{= 1 \text{ for } \eta = \eta_j} &= \sum_{j=1}^{N_\eta} \left[\sum_{k=1}^{N_\xi} \tilde{u}_{jk1} \mathbf{D}_{\xi,k1} \right] \underbrace{\psi_{j1}(\xi = 1, \eta)}_{= 1 \text{ for } \eta = \eta_j} \\ \sum_{k=1}^{N_\xi} {}_1 \mathbf{D}_{\xi,kN_\xi} \tilde{u}_{jk} - \sum_{k=1}^{N_\xi} {}_1 \mathbf{D}_{\xi,k1} \tilde{u}_{jk} &= 0 \quad \text{for } j = 1, \dots, N_\eta \\ \sum_{k=1}^{N_\xi} \left({}_1 \mathbf{D}_{\xi,kN_\xi} - {}_1 \mathbf{D}_{\xi,k1} \right) \tilde{u}_{jk} &= 0 \quad \text{for } j = 1, \dots, N_\eta \end{aligned} \quad (3.41)$$

In equation (3.41), the form of the periodicity in the derivatives results in a similar form of the amplitude coefficient as the Neumann condition in equation (3.39). Together, the

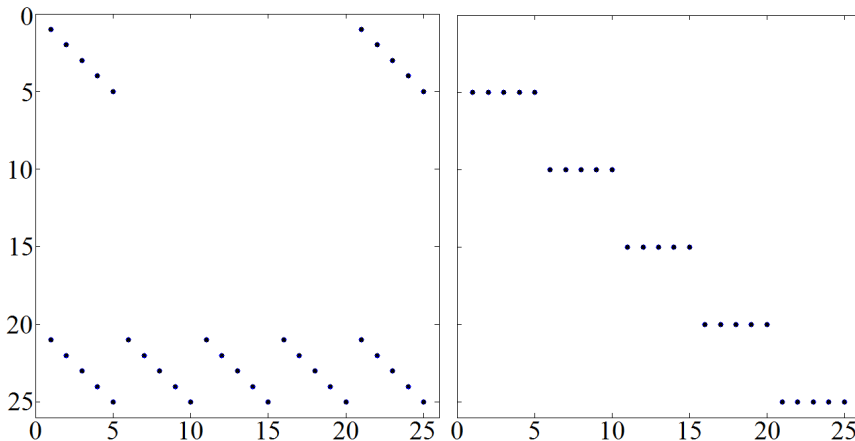


Figure 3.5: Indication of the periodic boundary condition across $\xi = \pm 1$ (left) and $\eta = \pm 1$ (right).
Vertical axis: row index, horizontal axis: column index.

relation of the values and derivatives yields the arrangements as presented in figure 3.5. The subfigure to the right shows the case across the $\eta = \pm 1$ boundaries.

Due to the fact that the periodicity conditions involve 2 equations, a choice has to be made in which rows to put them. Because the conditions are mutual, this choice does not have any influence on the result. In this treatment, it is chosen to relate the values at the rows corresponding to the $\xi = 1$ or $\eta = 1$ boundaries and the derivatives at the rows corresponding to the $\xi = -1$ or $\eta = -1$ boundaries. This is reflected in figure 3.5.

COMPATIBILITY CONDITIONS

In section 2.6, the theoretical background and the derivation procedure of the compatibility and Poisson equations is elaborated on. Here the procedure for the implementation of the compatibility conditions is described. It is important to recall that the momentum compatibility conditions are derived from the momentum equations by evaluating the latter at the boundaries. In doing so, Dirichlet conditions on the velocities, and potentially temperature, have to be incorporated in these equations. The resulting equations can be implemented quite similarly as the stability equations themselves. The same applies to the Poisson equation.

Note that from the first generation of the ACM's, the momentum equations are implemented in the interior as well as on the boundary of the domain. The application of homogeneous Dirichlet conditions at the boundaries automatically zeros the amplitudes \tilde{u} , \tilde{v} and \tilde{w} and their tangential derivatives along the boundary. This means that when the Dirichlet conditions have been applied to yield the no-slip boundary condition and, in doing so, the momentum equations on the boundary have not been replaced, the latter are automatically converted into the compatibility equation form. Thus, the compatibility equations would not have to be derived and inserted into the system separately. Just applying the Dirichlet conditions implies the formation of the compatibility conditions within the system directly.

Despite of this, the compatibility conditions are derived and implemented individually anyway. This is done because of the earlier mentioned convention on the location of the implementation of the boundary conditions. This convention causes the momentum equations at the boundaries to be overwritten; the velocity boundary conditions are implemented in the amplitude coefficients related to the momentum equations. In the compressible (p, T) -formulation, the Dirichlet or Neumann boundary condition on the temperature is implemented alongside the continuity equation and the compatibility condition on the pressure alongside the energy equation. Effectively, this means in this case that the compatibility conditions are removed alongside the momentum equations and substituted back into the system alongside the energy equation. In the incompressible case, they are substituted alongside the continuity equation.

3.1.8. BOUNDARY CONDITION IMPLEMENTATION

In section 3.1.7, the discretised versions of the conditions are all handled. Here, the implementation is shortly elaborated on so to reveal the method used. The conditions are implemented by generating the appropriate coefficient blocks corresponding to the equations derived in section 3.1.7. Recall the convention of the locations of the boundary conditions in the ACM's: the conditions on the velocities are implemented alongside the corresponding momentum equations and the remaining ones alongside the continuity and, if applicable, energy equations.

In figure 3.6, the non-zero elements of the matrix \mathbf{A} from equation (3.31) are shown for a spanwise Cartesian compressible case using the (p, T) -formulation for a 5×5 discretisation. To the left in figure 3.6, the clean version is shown. This is the result from the implementation of the stability equations. To the right in figure 3.6, the final form of the matrix is shown incorporating Neumann conditions on all variables at all boundaries; the red dots show all the associated coefficients. Note that they correspond to the dots shown in figures 3.4 and 3.4, although the conditions in the corners are overwritten by the ones applied to the $\eta = c^{\text{st}}$ boundaries. The Neumann conditions are applied to most clearly indicate the rows that are influenced by the boundary conditions.

To the right in figure 3.6, it is shown which combination of rows corresponds to the boundary condition on which variable. For the order of the equations, the convention illustrated in equation (3.33) is used. From top to bottom first the 1-, 2- and 3-momentum equations are encountered followed by the continuity and energy equations. This causes the nearly symmetrical structure of the matrix.

Next is the implementation of the compatibility or Poisson equations. These equations are implemented quite similarly as the stability equations. This is done after they have been derived as illustrated in subsection 3.1.7 by the automatic derivation tool. Note that this implies that these equations have been first implemented separately for the *complete* domain. Thereafter, precisely those equations evaluated at the appropriate boundary locations are substituted at the boundary locations in the ACM's.

The equivalent of figure 3.6, after compatibility conditions are applied to the pressure at all boundaries, is illustrated in figure 3.7. To the left, the structure of the z - and y -compatibility equations is shown (recall that the system was spanwise), the z -equation is the uppermost one. Note the structural identity when comparing them with the z - and y -momentum equations in figure 3.6. The red elements denote the $z = c^{\text{st}}$ boundary

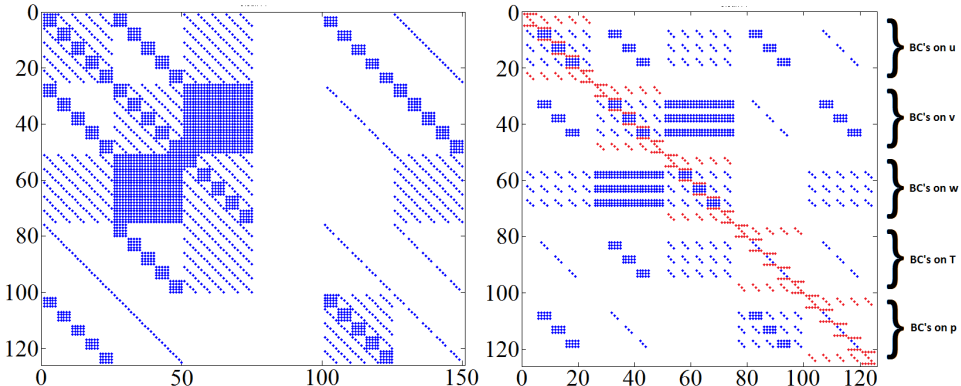


Figure 3.6: (left) Clean matrix \mathbf{A} from equation (3.31) corresponding to a compressible framework using the (p, T) -formulation, no boundary conditions have been applied. (right) Final matrix, incorporating Neumann conditions on all variables at all boundaries (for clarity). Red dots indicate related coefficients. Vertical axis: row index, horizontal axis: column index.

locations in the z -compatibility equation and the $y = c^{\text{st}}$ boundary locations in the y -compatibility equation.

The arrows indicate how (parts of) these equations are substituted in the ACM \mathbf{A} . When the eigenvalue is present in one of these equations, similar substitutions are performed for the \mathbf{B} matrix. The no-slip related y -compatibility condition overwrites the condition in the z -direction at the corners. This is related to the fact that the y -direction is usually taken as the wall-normal direction. After this is done, only the rows and columns corresponding to the (homogeneous) Dirichlet conditions have to be removed.

After this operation is completed, the eigeninformation can be extracted from the system. When homogeneous boundary conditions are present in the physical problem, the eigenvector will be smaller than $4N_\xi N_\eta \times 1$ or $5N_\xi N_\eta \times 1$, for the incompressible or compressible case, respectively. The last part of the code therefore involves the re-substitution of the Dirichlet conditions in the eigenvector. The complete discretised eigenfunctions can thus be extracted from the resulting vector and are ready for post-processing.

Note that the eigenvector contains the nodal values of the eigenfunctions, f_{ji} in equation (3.13). The most complete representation of the functions involves the evaluation of equation (3.13) using the characteristic Lagrange polynomials to obtain $f_{N_\eta \times N_\xi}$.

3.2. EIGENSOLVERS

Given the discretised system, the next step is to extract the eigeninformation. The primary solver used to solve small problems is the standard function `eig` in MATLAB, which performs the QZ algorithm to retrieve the complete spectrum. The accuracy characteristics of this function are handled in section 3.2.1.

Resolving the complete spectrum is usually not required, while doing so results in

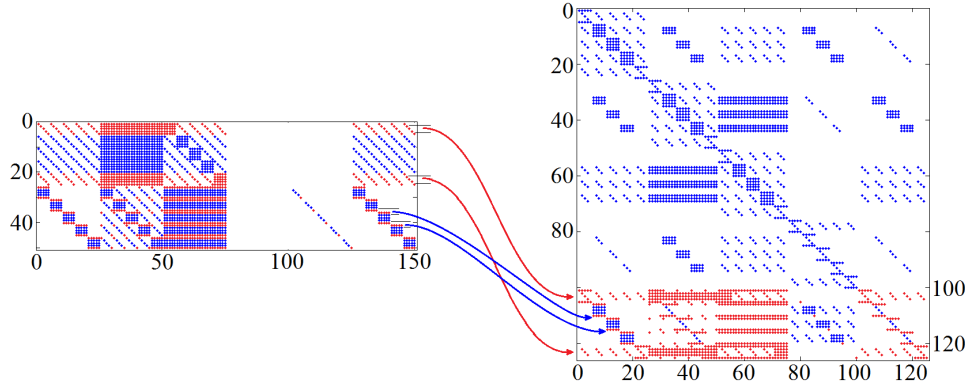


Figure 3.7: Final matrix \mathbf{A} completely analogous to figure 3.6, except that compatibility conditions are applied to the pressure at all boundaries. Red dots indicate related coefficients. Vertical axis: row index, horizontal axis: column index.

stringent requirements on Random Access Memory (RAM), in particular for the BiGlobal problem. The Arnoldi algorithm is an appropriate substitute for the QZ algorithm, in this case, because it allows retrieving only the physically interesting part of the spectrum. The former algorithm can be executed through MATLAB's `eigs`. The essential features of this algorithm are handled in section 3.2.2.

The purpose of this section is to identify error estimates for the numerical algorithms. These error estimates apply to a given discretised system. Note that the discretisation error may be large for a system representing insufficient resolution, while the eigensolver error can be very small. For every application, both the eigensolver and discretisation error should be checked independently for that reason.

3.2.1. QZ ALGORITHM

Due to the fact that the ACM \mathbf{A} is generally complex non-Hermitian and \mathbf{B} complex and singular, MATLAB's `eig` applies the *QZ algorithm* (see section 7.7 of Golub & Van Loan [11]) to obtain the spectrum and the corresponding invariant subspace. The latter, in this case, represents the discretised eigenfunctions. To this end, the function calls LAPACK routines [19], which have a common accuracy statement; they return the solution to a problem that lies close to the to-be-solved problem. The results are hence accurate up to the following criterion:

$$\epsilon_{\text{crit}} = \max(\epsilon \|\mathbf{A}\|_F, \epsilon \|\mathbf{B}\|_F) \quad (3.42)$$

Here, $\|\cdot\|_F$ denotes the Frobenius norm and ϵ is the machine precision [11, 19]. In MATLAB, the latter number conventionally equals $2.2204 \cdot 10^{-16}$. This criterion, referred to as the eigensolver precision, is the absolute lower bound of the error in the numerical results. The accuracy of the eigenvectors is also dictated by this threshold.

As an example case, the errors in the real and imaginary part of an eigenvalue are tracked while increasing the resolution. Figure 3.8 shows this trend versus N_η , for an incompressible and a supersonic TS mode, see Groot [1] for more details.

With the exception of oscillations, the eigenvalues converge exponentially with respect to N_η . At a certain N_η , the real and imaginary parts of the errors both pass the threshold $\varepsilon_{\text{crit}}$. The solution is then as accurate as possible. Note that the supersonic simulations require a larger N_η to converge with respect to the incompressible case. Compressible simulations are notorious for this requirement and this behaviour was expected accordingly.

3

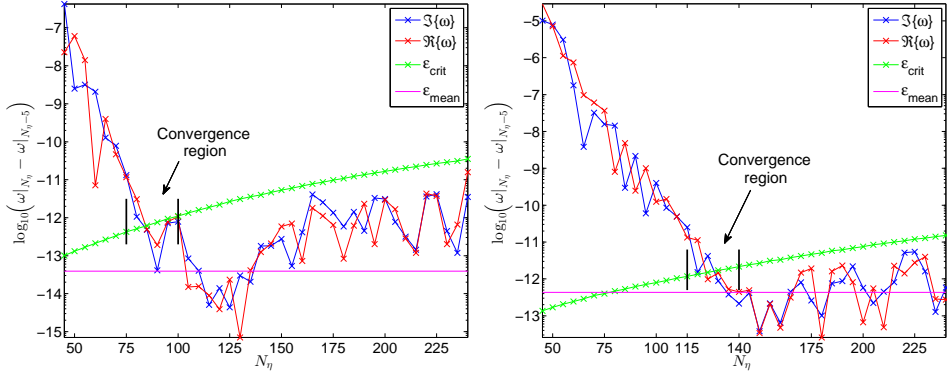


Figure 3.8: LST eigenvalue convergence curves for incompressible (left) and supersonic (right) cases, see Groot [1].

Note that for both cases presented in figure 3.8, the eigenvalues tend to converge a little further after they have passed the algorithm precision. Thereafter, the influence of the errors induced by the solver become apparent. Note that the threshold indicated by $\varepsilon_{\text{crit}}$ increases when further increasing the resolution, so increasing the resolution indefinitely will slowly deteriorate the solutions' accuracy.

3.2.2. ARNOLDI ALGORITHM

Usually, only a small part of the spectrum is of interest. Resolving the whole spectrum, while being very computationally expensive, should therefore be avoided. The Arnoldi algorithm can be tailored to resolve only the required part of the spectrum. In particular, the number of requested eigenmodes N_ω and shift (or eigenvalue search center) ω_g can be specified. This reduces the required duration and memory considerably. The details of the used eigenvalue search center will be discussed per application case. It should be mentioned here that practice indicates that placing the search center at the origin of the spectral variable can yield a significant reduction of the maximum required RAM to complete the extraction of the eigeninformation.

Whereas the QZ algorithm is a direct algorithm, the Arnoldi algorithm is iterative. It is based on the construction of the Krylov subspace, which takes ‘full advantage of the intricate structure of the sequence of vectors naturally produced by the power method,’ see chapter 4 of Lehoucq *et al.* [20] (the ARPACK users’ guide) for an elaboration.

For practice purposes, it should be mentioned that `eigs` supports sparse input matrices, while `eig` does not. In particular, it is suggested convert the ACM’s to sparse-type

matrices before executing `eigs`, e.g. by making sure one executes (either directly or indirectly):

$$\text{eigs}(\text{sparse}(A), \text{sparse}(B)) \quad (3.43)$$

instead of feeding matrices with the regular format to `eigs`. This yields a boost to both execution speed and the required memory.

The individual modes returned by the algorithm can be expected to be accurate up to the following criterion [20]:

$$\epsilon_{\text{crit}}^{\text{Arnoldi}} = \epsilon |\omega| \quad (3.44)$$

where ϵ again denotes the machine precision and ω is the eigenvalue returned by the algorithm. In the current treatment, $|\omega|$ will nearly always be smaller than unity, which means that the lower bound on the error is machine precision.

REFERENCES

- [1] K. J. Groot, *Derivation of and Simulations with BiGlobal Stability Equations*, M.Sc. thesis, Delft University of Technology, The Netherlands (2013).
- [2] J. Batterson, *The BiGlobal Instability of the BiDirectional Vortex*, Ph.D. thesis, University of Tennessee (2011).
- [3] C. Canuto, M. Hussaini, A. Quarteroni, and T. Zang, *Spectral Methods - Fundamentals in Single Domains* (Springer Verlag, Berlin, 2006).
- [4] C. Canuto, M. Hussaini, A. Quarteroni, and T. Zang, *Spectral Methods - Evolution to Complex Geometries and Applications to Fluid Dynamics* (Springer Verlag, Berlin, 2007).
- [5] E. Piot, *Simulation Numérique Directe et Analyse de Stabilité de Couches Limites Laminaires en Présence de Micro-Rugosités*, Ph.D. thesis, l'Institut Supérieur de l'Aéronautique et de l'Éspace (2008).
- [6] C. Robitaillé-Montané, *Une Approche Non Locale pour l'Étude des Instabilités Linéaires*, Ph.D. thesis, l'Institut Supérieur de l'Aéronautique et de l'Éspace, Toulouse, France (2005).
- [7] L. Trefethen, *Spectral Methods in MATLAB* (Society for Industrial and Applied Mathematics, 2001).
- [8] F. Pinna, *Numerical study of stability of flows from low to high Mach number*, Ph.D. thesis, Università di Roma - "La Sapienza", Von Kármán Institute, Rhode-Saint-Genèse (2012).
- [9] R. Hamming, *Numerical Methods for Scientists and Engineers* (Dover Publication, Inc., 1973).
- [10] R. Burden and J. Faires, *Numerical Analysis* (Brooks/Cole, Cengage Learning, 2010).
- [11] G. H. Golub and C. F. Van Loan, *Matrix Computations* (Johns Hopkins University Press, 1996).

- 3
- [12] J. Weideman and S. Reddy, *A matlab differentiation matrix suite*, ACM Trans. Math. Softw. **26**, 465 (2000).
 - [13] D. Tracy and R. Singh, *A new matrix product and its applications in partitioned matrix differentiation*, Statistica Neerlandica **26**, 143 (1972).
 - [14] M. R. Malik, *Numerical methods for hypersonic boundary layer stability*, Journal of Computational Physics **86**, 376 (1990).
 - [15] C. E. Grosch and S. A. Orszag, *Numerical solution of problems in unbounded regions: coordinate transforms*, Journal of Computational Physics **25**, 273 (1977).
 - [16] J. C. Robinet, *Bifurcations in shock-wave/laminar-boundary-layer interaction: global instability approach*, Journal of Fluid Mechanics **579**, 85 (2007).
 - [17] V. Theofilis and T. Colonius, *Three-dimensional instabilities of compressible flow over open cavities: Direct solution of the BiGlobal eigenvalue problem*, in *34th AIAA Fluid Dynamics Conference & Exhibit* (American Institute of Aeronautics and Astronautics, Portland, Oregon, 2004).
 - [18] G. Danabasoglu and S. Biringen, *A Chebyshev matrix method for the spatial modes of the Orr-Sommerfeld equation*, International Journal for Numerical Methods in Fluids **11**, 1033 (1990).
 - [19] E. Anderson, Z. Bai, C. Bischof, L. S. Blackford, J. Demmel, J. J. Dongarra, J. Du Croz, S. Hammarling, A. Greenbaum, A. McKenney, and D. Sorensen, *LAPACK Users' guide (third ed.)* (Society for Industrial and Applied Mathematics, Philadelphia, 1999).
 - [20] R. B. Lehoucq, D. C. Sorensen, and C. Yang, *ARPACK users guide: Solution of large scale eigenvalue problems by Implicitly Restarted Arnoldi Methods.* (1997).

4

MEASURED BASE FLOWS: GENERIC SHEAR PROFILES

In the application cases considered in following chapters, the base flows consist of two-dimensional shear layers embedded in a boundary layer. Despite being embedded, the relevant part of the shear layers is located relatively far from the wall. As will be shown in this chapter, this allows treating these shear layers as if they are free. Moreover, being located far from the wall, these shear layers can be measured adequately with PIV techniques. The Kelvin-Helmholtz mechanism is frequently observed to be the driving instability mechanism, subject to the details of the two-dimensional base flow field.

The well-known Kelvin-Helmholtz mechanism provides a synthetic testing platform allowing to test the influence of the characteristic features of shear flows on stability calculations. As an important goal of this chapter, the model problem allows identifying the inherent effects associated to the use of measured base flows.

Furthermore, the basic physical characteristics of the Kelvin-Helmholtz mechanism are identified. Its basic nature allows demonstrating how the physical mechanism represented by an eigenmode can be traced back to the terms of the stability equations.

4.1. INTRODUCTORY REMARKS

Although it is not a solution of the Navier-Stokes equations, the hyperbolic tangent velocity profile is a classical model of free shear layers. Its inherent perturbations dynamics, of linear and non-linear nature, has been thoroughly studied by many authors, see [1]. Despite being a simplification, it is a good approximation of realistic shear flows, such as jets [2].

A flow situation is considered where x , y and z indicate the streamwise, wall-normal and spanwise coordinates and \bar{U} , \bar{V} and \bar{W} respectively denote the corresponding velocity components of the laminar base flow. In figure 4.1 (a), a y -profile of \bar{U} in the center-plane of the micro-ramp wake is shown, see chapter 5 for more details. A steep jump in the streamwise velocity is featured, which amounts to $\sim 95\%$ of the edge velocity, \bar{U}_e , for

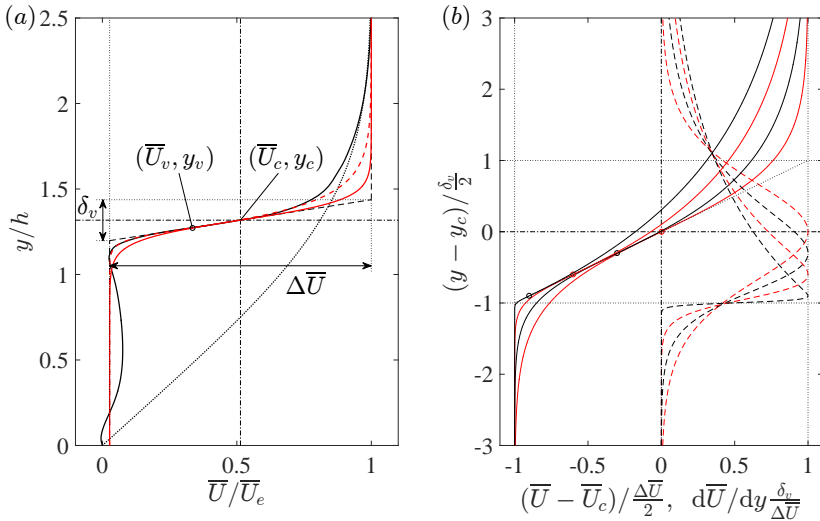


Figure 4.1: (a) Parameter definitions δ_v , $\Delta\bar{U}$, y_c , \bar{U}_c , y_v and \bar{U}_v , based on the center-plane profile at $x/h = 2.5$ (black solid), undisturbed boundary layer profile (black dotted). Fitted gтанh- (red solid) and gтанh- (red dashed) profiles. (b) Generalized tanh- (gтанh-) profiles (solid) and derivatives (dashed) for $(y_v - y_c)/(\delta_v/2) = 0, -0.3, -0.6$ and -0.9 (resp. red, black, red, black), inflection points: where $d\bar{U}/dy$ attains a maximum (○).

this streamwise station. The velocity deficit, $\Delta\bar{U}$, is defined as:

$$\Delta\bar{U} = \bar{U}_e - \bar{U}_{\min}, \quad (4.1)$$

where \bar{U}_{\min} is the first minimum of \bar{U} encountered when entering the boundary layer from above.

As will be detailed later, the shear of the flow, represented by the slope $d\bar{U}/dy$ of the profile, is what causes perturbations to be produced and can therefore be considered the most important parameter for the stability problem. The derivative $d\bar{U}/dy$ represents the primary shear of material particles and will therefore be referred to as the shear from here onwards. To embed the relevance of the shear in the reference scales, the vorticity thickness is considered as the length scale:

$$\delta_v = \Delta\bar{U} / \left. \frac{d\bar{U}}{dy} \right|_{\max}, \quad (4.2)$$

that encodes the maximum shear, $d\bar{U}/dy|_{\max}$. For brevity, $d\bar{U}/dy|_{\max}$ will also be referred to as the shear strength. The latter is attained in the inflection point of the profile, at $y = y_v$, indicated with the circle in figure 4.1 (a). The velocity at the center of the shear layer, \bar{U}_c , equals $\bar{U}_{\min} + \Delta\bar{U}/2$ and the center coordinate, y_c , is defined to be the corresponding coordinate on the tangent line crossing the inflection point.

Using these definitions, the hyperbolic tangent profile is fitted by setting:

$$\bar{U}_{\text{tanh}} = \bar{U}_c + \frac{\Delta\bar{U}}{2} \tanh \left(\left(y - y_c \right) / \frac{\delta_v}{2} \right), \quad (4.3)$$

which is also shown in figure 4.1 (a). The inflection point of this profile is fixed at its center of symmetry, while it can deviate from the center in general realistic cases.

For this reason, use is made of the following generalized hyperbolic tangent profiles:

$$\overline{U}_{\text{gtanh}} = \overline{U}_c + \frac{\Delta \overline{U}}{2} \left(1 - 2 \left[1 + m \exp \left\{ (1+m) \frac{y - y_v}{\frac{\delta_v}{2} - (y_v - y_c)} \right\} \right]^{-\frac{1}{m}} \right), \quad (4.4)$$

where m solves $(1+m)^{1/m} = 2/\left(1 - \frac{y_v - y_c}{\delta_v/2}\right)$ and $|y_v - y_c| < \delta_v/2$. These profiles have their inflection point at $y = y_v$. The profile reduces to the hyperbolic tangent profile for $m = 1$. Instead of m , the most intuitive parameter is $(y_v - y_c)/(\delta_v/2)$, describing the deviation of the inflection point, y_v , from the mid-point of the profile, y_c . For brevity, the former profiles and conventional hyperbolic tangent profile are referred to as the gtanh- and tanh-profiles, respectively.

In this treatment only negative $y_v - y_c$ are considered. Note that the gtanh-profiles are not symmetric for $y_v - y_c$ of opposite sign. The cases with positive $y_v - y_c$ have to be treated with care. For $(y_v - y_c)/(\delta_v/2) > 1 - \frac{2}{e} \approx 0.2642$, $m < 0$, which renders the profiles divergent as $|y| \rightarrow \infty$.¹ Here, negative values for $(y_v - y_c)/(\delta_v/2)$ are considered only.

The gtanh-profiles are a simplified version of the profiles introduced by Michalke [2, 3], who defined spatially compressed equivalents having the same momentum thickness for all $|y_v - y_c|$. This rendered the shear strength to be variable. Instead, all profiles in equation (4.4) have $d\overline{U}/dy|_{\max} = \Delta \overline{U}/\delta_v$, so that δ_v is independent of $|y_v - y_c|$ and, again, encodes the maximum shear magnitude. This is exemplified with the shear profiles in figure 4.1 (b).

The representation of the realistic profile is shown in figure 4.1 (a), displaying a significant improvement of approximation over the tanh-profile. The remaining difference in the freestream is due to the fact that the realistic shear layer develops inside a boundary layer.

4.2. STABILITY PROBLEM FORMULATION

The linear perturbations to the aforementioned profiles is the subject of the remainder of this chapter. To exemplify the impact of solving the stability problem in different ways, the stability equations are briefly restated here.

It is assumed there is no flow in the y - and z -directions, $\overline{V} = \overline{W} = 0$ for all y . The dependency of the \overline{U} -profiles on a single spatial dimension and the search for eigenfunctions that decay outside the shear layer justifies the use of the following discrete Fourier ansatz for the perturbations:

$$q'(x, y, z, t) = \tilde{q}(y) e^{i(\alpha x + \beta z - \omega t)} + c.c., \quad (4.5)$$

see equation (2.14) and the associated discussion. The variable q' represents a perturbation of a base flow variable \overline{Q} , α and β are the streamwise and spanwise wavenumbers, respectively, and ω is the angular frequency. Lastly, *c.c.* indicates the complex conjugate. The complex perturbation amplitudes are governed by the linearized Navier-Stokes

¹Note that $m \rightarrow -1$ corresponds to $(y_v - y_c)/(\delta_v/2) \rightarrow 1$ and $m \rightarrow \infty$ to $(y_v - y_c)/(\delta_v/2) \rightarrow -1$.

equations, incorporating the Fourier, or Linear Stability Theory (LST), ansatz [4]:

$$-\mathrm{i}\omega\tilde{u} + \mathrm{i}\alpha\bar{U}\tilde{u} + \frac{\mathrm{d}\bar{U}}{\mathrm{d}y}\tilde{v} = -\mathrm{i}\alpha\tilde{p} + \frac{1}{Re}\left(\frac{\mathrm{d}^2}{\mathrm{d}y^2} - \alpha^2 - \beta^2\right)\tilde{u} \quad (4.6a)$$

$$-\mathrm{i}\omega\tilde{v} + \mathrm{i}\alpha\bar{U}\tilde{v} = -\frac{\mathrm{d}\tilde{p}}{\mathrm{d}y} + \frac{1}{Re}\left(\frac{\mathrm{d}^2}{\mathrm{d}y^2} - \alpha^2 - \beta^2\right)\tilde{v} \quad (4.6b)$$

$$-\mathrm{i}\omega\tilde{w} + \mathrm{i}\alpha\bar{U}\tilde{w} = -\mathrm{i}\beta\tilde{p} + \frac{1}{Re}\left(\frac{\mathrm{d}^2}{\mathrm{d}y^2} - \alpha^2 - \beta^2\right)\tilde{w} \quad (4.6c)$$

$$\mathrm{i}\alpha\tilde{u} + \frac{\mathrm{d}\tilde{v}}{\mathrm{d}y} + \mathrm{i}\beta\tilde{w} = 0, \quad (4.6d)$$

where \tilde{u} , \tilde{v} and \tilde{w} are the perturbation amplitudes of the streamwise, wall-normal and spanwise velocity components and \tilde{p} the pressure amplitude. This system can be derived from system (2.20) by setting $\bar{V} = \bar{W} = 0$. Re is the Reynolds number based on appropriate scales. It is conventional to use the scales $\delta_v/2$ and $\Delta\bar{U}/2$ in the current context, yielding:

$$Re_{\delta_v} = \frac{\Delta\bar{U}\delta_v}{4\nu}, \quad (4.7)$$

where ν is the kinematic viscosity.

By eliminating the \tilde{u} , \tilde{w} and \tilde{p} amplitudes from equation (4.6a), the Orr-Sommerfeld equation is retrieved that governs the \tilde{v} component:

$$\left[\left(\bar{U} - c_{ph}\right)\left(\frac{\mathrm{d}^2}{\mathrm{d}y^2} - \alpha^2 - \beta^2\right) - \frac{\mathrm{d}^2\bar{U}}{\mathrm{d}y^2} + \frac{\mathrm{i}}{\alpha Re}\left(\frac{\mathrm{d}^2}{\mathrm{d}y^2} - \alpha^2 - \beta^2\right)^2\right]\tilde{v} = 0, \quad (4.8)$$

where $c_{ph} = \omega/\alpha$ is the complex phase speed. This equation, when seen as an operator acting on \tilde{v} , is obtained from the operator (2.27) by setting $\bar{W} = 0$ and dividing by α . Without the $1/Re$ terms, equation (4.8) reduces to the Rayleigh equation. See §2.3.4 for the full derivation of equation (4.8).

Equations (4.6) and (4.8) describe exactly the same perturbation dynamics. An essential difference between the system (4.6) and equation (4.8), however, is that equation (4.6a) contains $\mathrm{d}\bar{U}/\mathrm{d}y$, while equation (4.8) accommodates $\mathrm{d}^2\bar{U}/\mathrm{d}y^2$ instead. Although it is more computationally expensive to solve the system, it only requires the first order derivative of the base flow to be properly represented. The significance hereof becomes apparent when reconsidering figure 4.1 (b). Although the shear profile $\mathrm{d}\bar{U}/\mathrm{d}y$ is bounded above by $\Delta\bar{U}/\delta_v$, it forms a discontinuity as $y_v - y_c \rightarrow -\delta_v/2$, causing $\mathrm{d}^2\bar{U}/\mathrm{d}y^2 \rightarrow \infty$.

The no-slip boundary conditions apply to the velocity components in system (4.6) and equation (4.8) on solid interfaces:

$$\tilde{u} = \tilde{v} = \tilde{w} = 0 \quad \text{and} \quad \tilde{v} = \frac{\mathrm{d}\tilde{v}}{\mathrm{d}y} = 0, \quad (4.9)$$

respectively. In the inviscid case, these conditions reduce to $\tilde{v} = 0$, where momentum compatibility implies that:

$$\tilde{u} = \frac{\alpha}{\omega - \alpha\bar{U}}\tilde{p}, \quad \tilde{w} = \frac{\beta}{\omega - \alpha\bar{U}}\tilde{p}, \quad (4.10)$$

evaluated at the wall.

For the pressure, the one-dimensional equivalent of equation (2.64) is used, which reduces to a Helmholtz equation:

$$\left(\frac{d^2}{dy^2} - \alpha^2 - \beta^2 \right) \tilde{p} = 0, \quad (4.11)$$

where it has been used that $d\bar{V}/dy = 0$, in-line with the parallel flow assumption. Free shear layers have an infinite support, there are no walls, or boundaries for that matter. The problem is approached numerically, however, which requires the restriction of the domain to $y/(\delta_v/2) \in [L^-, L^+]$, where $\pm L^\pm \gg 1$. The aforementioned conditions are applied at the introduced boundaries at $y = \delta_v L^\pm / 2$. They are justified as the solutions of interest are required to decay exponentially as $|y| \rightarrow \infty$; the use of large enough L^\pm renders the solutions independent of the boundary conditions. In addition, the effect of a wall is recovered when letting $L^- \rightarrow 0$.

Both equations (4.6) and (4.8), including the boundary conditions, form an eigenvalue problem. Here the main interest goes out to the temporal formulation, where ω is solved for given α and β , which can be written in the standard eigenvalue problem form: $\mathbf{A}\tilde{\mathbf{q}} = \omega\mathbf{B}\tilde{\mathbf{q}}$, where $\tilde{\mathbf{q}}$ is a vector that consists of all solution variables and \mathbf{A} and \mathbf{B} are matrices containing the coefficients and differentiation operators.

4

4.2.1. EXTRACTING THE UNDERLYING MECHANISMS

The Reynolds-Orr equation is used to evaluate the active terms in system (4.6), see [4], and to interpret the underlying physical mechanisms of the solutions, see [5]. It is obtained by taking the dot product of the system (taking the complex conjugate of the continuity equation) with the variable vector $[\tilde{u}^* \tilde{v}^* \tilde{w}^* \tilde{p}]^T$ and integrating in y . Integrating the continuity equation and viscous terms by parts and solving for ω yields (see §2.5.1 for more details):

$$\omega = A_1 + R_1 - D_1 + P_1, \quad (4.12)$$

where $\tilde{\mathbf{q}} = [\tilde{u} \ \tilde{v} \ \tilde{w}]^T$ and, in this case, $\|\tilde{\mathbf{q}}\|^2 = \int \tilde{\mathbf{q}}^* \cdot \tilde{\mathbf{q}} dy$. From left to right, the right hand side terms represent advection, A_1 , Reynolds stress work, R_1 , viscous dissipation, D_1 , and pressure work, P_1 (zero when $\alpha_i = \beta_i = 0$). The latter 2 terms represent the following combinations:

$$\begin{aligned} A_1 &= \alpha \int \bar{U} \tilde{\mathbf{q}}^* \cdot \tilde{\mathbf{q}} \frac{dy}{\|\tilde{\mathbf{q}}\|^2} \\ R_1 &= -i \int \tilde{u}^* \tilde{v} \frac{d\bar{U}}{dy} \frac{dy}{\|\tilde{\mathbf{q}}\|^2} \\ D_1 &= \frac{i}{Re} \left(\alpha^2 + \beta^2 + \int \left(\left| \frac{d\tilde{u}}{dy} \right|^2 + \left| \frac{d\tilde{v}}{dy} \right|^2 + \left| \frac{d\tilde{w}}{dy} \right|^2 \right) \frac{dy}{\|\tilde{\mathbf{q}}\|^2} \right) \\ P_1 &= (\alpha - \alpha^*) \int \tilde{u}^* \tilde{p} \frac{dy}{\|\tilde{\mathbf{q}}\|^2} + (\beta - \beta^*) \int \tilde{w}^* \tilde{p} \frac{dy}{\|\tilde{\mathbf{q}}\|^2}. \end{aligned}$$

The use of the boundary conditions causes the related terms to evaluate to zero.

Usually R_1 and D_1 contribute dominantly to ω_i , note that $D_1 \in i\mathbb{R}$, while the advection term $\alpha \int \bar{U} \tilde{\mathbf{q}}^* \cdot \tilde{\mathbf{q}} dy / \|\tilde{\mathbf{q}}\|^2$ dominates the ω_r -budget if α is large. In fact, for $\alpha \in \mathbb{R}$, this term is purely real. If α is large enough, the following approximate relationship for the phase speed holds:

$$c_{ph} = \frac{\omega_r}{\alpha} \approx \int \bar{U} \tilde{\mathbf{q}}^* \cdot \tilde{\mathbf{q}} \frac{dy}{\|\tilde{\mathbf{q}}\|^2} \quad (+ \text{ contributions of } R_1 \text{ and } P_1). \quad (4.13)$$

Given the considered velocity profiles are monotonic, the phase speed is a good indication of where, along the velocity profile, the solution is dominant.

Following the recipe described in §2.5.2, the shape of the eigenfunctions is decomposed by multiplying equations (4.6a) to (4.6c) with \tilde{u}^* , \tilde{v}^* and \tilde{w}^* , dividing the result by $D/Dt = -i\omega + i\alpha \bar{U}$ and taking the real part:

$$\begin{bmatrix} |\tilde{u}|^2 \\ |\tilde{v}|^2 \\ |\tilde{w}|^2 \end{bmatrix} = \operatorname{Re} \left\{ \frac{1}{\omega - \alpha \bar{U}} \begin{bmatrix} \alpha \tilde{u}^* \tilde{p} & -i \tilde{u}^* \tilde{v} \frac{d\bar{U}}{dy} - \frac{i}{Re} \left((\alpha^2 + \beta^2) |\tilde{u}|^2 + \left| \frac{d\tilde{u}}{dy} \right|^2 - \frac{d}{dy} \left(\tilde{u}^* \frac{d\tilde{u}}{dy} \right) \right) \\ -i \tilde{v}^* \frac{d\tilde{p}}{dy} & - \frac{i}{Re} \left((\alpha^2 + \beta^2) |\tilde{v}|^2 + \left| \frac{d\tilde{v}}{dy} \right|^2 - \frac{d}{dy} \left(\tilde{v}^* \frac{d\tilde{v}}{dy} \right) \right) \\ \beta \tilde{w}^* \tilde{p} & - \frac{i}{Re} \left((\alpha^2 + \beta^2) |\tilde{w}|^2 + \left| \frac{d\tilde{w}}{dy} \right|^2 - \frac{d}{dy} \left(\tilde{w}^* \frac{d\tilde{w}}{dy} \right) \right) \end{bmatrix} \right\}. \quad (4.14)$$

Similarly, equations are derived for the real and imaginary parts of $\tilde{u}^* \tilde{v}$ by multiplying the x - and y -momentum equations (4.6a) and (4.6a) with \tilde{v}^* and \tilde{u}^* , respectively:

$$\begin{aligned} 2 \operatorname{Re} \left\{ \tilde{u}^* \tilde{v} \right\} &= \tilde{u}^* \tilde{v} \pm \tilde{v}^* \tilde{u} = \\ \frac{1}{\omega - \alpha \bar{U}} \left(\pm \alpha \tilde{v}^* \tilde{p} - i \tilde{u}^* \frac{d\tilde{p}}{dy} \mp i |\tilde{v}|^2 \frac{d\bar{U}}{dy} + \frac{i}{Re} \left(\tilde{u}^* \frac{d^2 \tilde{v}}{dy^2} \pm \tilde{v}^* \frac{d^2 \tilde{u}}{dy^2} - (\alpha^2 + \beta^2) (\tilde{u}^* \tilde{v} \pm \tilde{v}^* \tilde{u}) \right) \right) \end{aligned} \quad (4.15)$$

Note in regard to both equations (4.14) and (4.15), that $\omega \neq \alpha \bar{U}$ for $\alpha \in \mathbb{R}$ and $\omega \in \mathbb{C} \setminus \mathbb{R}$.

Just like equation (4.12), equations (4.14) and (4.15) consist of 3 types of terms. The combination of terms involving \tilde{p} and the Reynolds number are respectively referred to as the pressure and viscous terms. The remaining Reynolds stress term always involves the shear $d\bar{U}/dy$. It is interesting to note that $\tilde{u}^* \tilde{v}$ appears in the Reynolds stress term in the budget for $|\tilde{u}|^2$, whereas $|\tilde{v}|^2$ stars in the budget for $\tilde{u}^* \tilde{v}$. Note that the $|\tilde{v}|^2$ -budget is composed out of a pressure term only; it is linked with $|\tilde{u}|^2$ through continuity.

The pressure in incompressible flows acts purely as a mechanical variable, it does not affect the thermodynamical state of a fluid [6]. A standard transport equation therefore does not exist, a relation for the pressure is therefore discarded from consideration.

4.3. DISCRETIZATION SPECIFICS & VERIFICATION

The Chebyshev spectral collocation method in combination with the BiQuadratic mapping, outlined in §3.1.4, are used to discretize the stability problem in the y -coordinate. The BiQuadratic mapping is required to resolve the eigenfunction structure in the interior of the domain. Placing one-third of the collocation nodes in-between y_{i1} and y_{i2} .

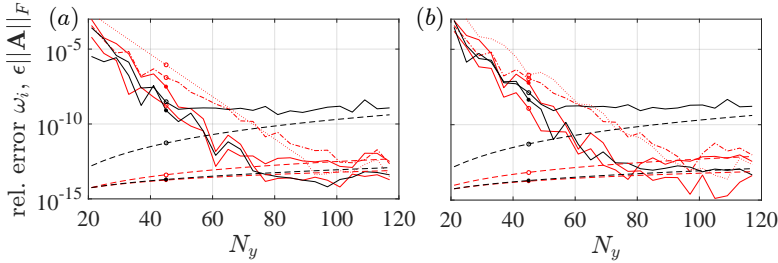


Figure 4.2: Convergence relative error in ω_i versus N_y (with respect to $N_y = 121$ case), for the tanh- (a) and gtanh-profile (b), $y_v - y_c = -0.5\delta_v/2$, $\alpha\delta_v/2 = 0.5$. Solutions to equation (4.8) (\circ) and system (4.6) (\bullet), with $Re_{\delta_v} = \infty$ (red solid) and 50 (black solid) and $y_{i2} - y_{i1} = \delta_v$. Solutions to equation (4.8) with $Re_{\delta_v} = \infty$, setting $(y_{i2} - y_{i1})/\delta_v = 0.5$ (dash-dotted) and 1.5 (dotted). Upper bound error eigensolver, $\epsilon\|A\|_F$ (dashed).

4

If not specified differently, the truncation boundaries and y_{i1} and y_{i2} are each placed at equal distances from the inflection point, $|L^+ - y_v| = |L^- - y_v|$ and $|y_{i2} - y_v| = |y_{i1} - y_v|$. Accordingly, a grid with an odd number of nodes has its central node suspended exactly at the inflection point. If not stated otherwise, $y_{\max} = L^+ - L^- = 300\delta_v/2$ is chosen in this section. The most unstable solutions of interest decay as $\exp(-y\sqrt{\alpha^2 + \beta^2})$, see [4], and at least have $(\delta_v/2)\sqrt{\alpha^2 + \beta^2} \approx 0.2$. Therefore, they attain magnitudes of $\exp(-150 \times 0.2) = 9.4 \times 10^{-14}$ at the boundaries. These solutions are expected to incorporate changes of the same order of magnitude by the truncation boundary conditions. For larger wavelengths, the effect is expected to be larger.

For the one dimensional problems treated in this section, it was possible to approach the discretized eigenvalue problem with the direct QZ algorithm [7]. As discussed in chapter 3, an upper bound on the eigensolver error is $\epsilon\|A\|_F$, where ϵ is the machine precision (2.2×10^{-16}) and $\|A\|_F$ represents the Frobenius norm of the discretized left hand side matrix A .

4.3.1. CONVERGENCE AND VERIFICATION WITH LITERATURE

The spectral accuracy of the numerical approach is verified by checking the convergence of ω_i as N_y is increased. Specifically, the tanh- and gtanh-profile, with $(y_v - y_c)/(\delta_v/2) = -0.5$, are considered. The latter case is chosen because it establishes a significant deviation from the tanh-profile and is referred to as the gtanh-profile. The profile and required derivatives are evaluated algebraically on the collocation node locations. Equations (4.6) and (4.8) are solved separately, with $Re_{\delta_v} = \infty$ (solving the inviscid equations) and 50, the latter being a case where viscosity has a significant impact (see [2, figure 6]) and setting $\alpha\delta_v/2 = 0.5$ and $\beta = 0$ (close to most unstable planar wave).

The results are shown in figure 4.2, verifying exponential convergence with respect to N_y for all cases as $N_y \leq 50$. For $N_y > 50$, the solution of the Orr-Sommerfeld equation saturates at the level 2×10^{-9} . The Frobenius norm of the A -matrices is shown for the different approaches, indicating a larger expected error when solving the Rayleigh and Orr-Sommerfeld equations. The occurrence of the fourth order derivative in the latter equation is the cause of the large norm in that case. The Rayleigh equation yields matrices with a larger norm as opposed to the remaining cases due to the $d^2\bar{U}/dy^2$ term. The

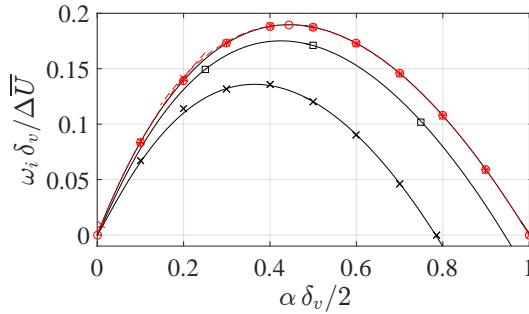


Figure 4.3: Growth rates, $\omega_i = \alpha c_{ph,i}$, for the tanh-profile based on the present results, $N = 81$, $Re_{\delta_y} = 20, 100$ and ∞ , (black solid lines), equations (3.19) and (4.9) of Tatsumi *et al.* [8] (red dashed) and the numerical results of Betchov and Szewczyk [9] for $Re_{\delta_v} = 20$ (black \times) and ∞ (red \times), Michalke [10] (\circ), Metcalfe *et al.* [11] (\square) and Boguslawski [12] (+).

4

Reference	Re_{δ_v}	$\omega_i \delta_v / \Delta \bar{U}$
present result	∞	0.18751095039
Boguslawski [12]		0.1875
Michalke [10]		0.18752
Tatsumi <i>et al.</i> [8]		0.1873
Betchov and Szewczyk [9]		0.1875
present result	100	0.17091128273
Metcalfe <i>et al.</i> [11]		0.171
present result	20	0.12033986465
Betchov and Szewczyk [9]		0.120

Table 4.1: Comparison of ω_i -values for $\alpha \delta_v / 2 = 0.5$, present results based on solving equation (4.6), $N = 81$. Equation (4.9) of Tatsumi *et al.* [8] is evaluated.

use of different separation lengths of y_{i1} and y_{i2} indicates that the solutions are resolved best when setting $y_{i2} - y_{i1} = \delta_v$. This will be used in the remainder of this chapter, if not stated otherwise.

Many authors considered the numerical evaluation of the temporal stability of the tanh-profile. In figure 4.3, the comparison with the current results, based on solving equation (4.6), illustrates a near identical correspondence. This is digitally confirmed with the values displayed in table 4.1, illustrating matches with, at most, all reported decimals. No more digits are presented in the literature due to the assumption that $\bar{V} = 0$, which, with respect to physical flows, yields a model error of $1/Re$.

4.4. SPECTRUM AND EIGENFUNCTIONS

The previously presented characteristics correspond to the most unstable mode in the spectrum only. An overview of the complete spectrum is shown in figure 4.4. Both spectra for the tanh- and gtanh-profiles are computed for $\alpha \delta_v / 2 = 0.41$. When rounding, this

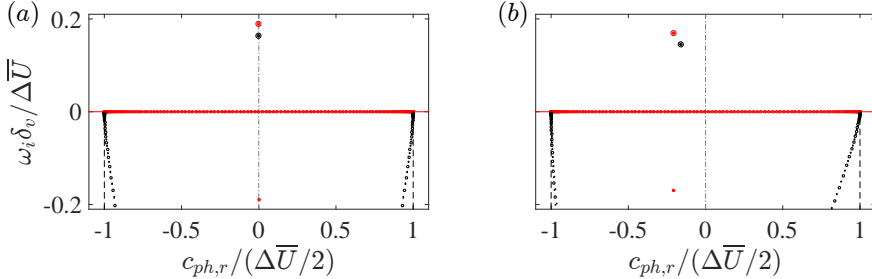


Figure 4.4: ω -Spectra for the tanh- (a) and gtanh- (b), $y_v - y_c = -0.5\delta_v/2$ profiles with $\alpha\delta_v/2 = 0.41$. Solutions to equation (4.8) (\circ) and system (4.6) (\bullet) with $Re_{\delta_v} = 50$ (black) and ∞ (red symbols), $N = 201$ and $y_{i2} - y_{i1} = \delta_v$. Most unstable modes (big circles). Exact limits of the continuous spectrum (dashed lines, $\omega = \pm\alpha\Delta\bar{U}/2 - i(\alpha^2 + k^2)/Re_{\delta_v}$ with $k \in \mathbb{R}$).

corresponds to the most unstable wavenumber for both cases when including viscosity.

The profiles have two different asymptotic states, as $y \rightarrow \pm\infty$. Hence, the spectra corresponding to the viscous perturbations display two branches of modes, that approach a continuum as $|L^+|$ and $|L^-| \rightarrow \infty$. As the domain length increases, the branches approach the indicated vertical lines, oriented around $\omega_r = \pm\alpha\Delta\bar{U}/2$. The interpretation of the phase speed $c_{ph} = \pm\alpha\Delta\bar{U}/2$ with equation (4.13) demonstrates that the corresponding perturbations are supported in the freestream portions on either side of the shear layer. For the gtanh-profile, \bar{U} approaches the asymptotic limit faster as $y \rightarrow -\infty$ than for $y \rightarrow \infty$. For that reason, the branch with $\omega_r/\alpha \rightarrow +\Delta\bar{U}/2$ lies farther from the asymptotic limit than the branch with $\omega_r/\alpha \rightarrow -\Delta\bar{U}/2$. The equivalent of the continuous branches in the spectra corresponding to inviscid perturbations are a collection of modes that densely covers the real ω -axis for $c_{ph,r}/(\Delta\bar{U}/2) \in [-1, 1]$.

The unstable eigenvalues in figure 4.4 are indicated with open circles. The eigenvalues in figure 4.4 (a) have $c_{ph,r} = 0$. Due to the symmetry of the tanh-profile around $y = y_c$, the eigenfunctions are symmetric as well. Therefore $\omega_r = 0$ for all Re_{δ_v} and $\alpha \in \mathbb{R}$, see [13], considering the problem in the moving reference system shown in figure 4.1 (b), having $(\bar{U}, y) = (\bar{U}_c, y_c)$ as the origin. In figure 4.4 (b), the eigenvalues have $c_{ph,r} < 0$, indicating the corresponding eigenfunctions are asymmetric in this case. Furthermore, $c_{ph,r} < 0$ illustrates that the eigenfunctions are oriented in the negative speed region, for $y < y_c$. This is directly confirmed in figure 4.5, which shows the corresponding eigenfunctions $|\tilde{u}|$ and $|\tilde{v}|$. For the case $\beta = 0$, $|\tilde{w}|$ is identically zero. It is demonstrated that the eigenfunctions are concentrated around the maximum in the shear profile $d\bar{U}/dy$. Both $|\tilde{u}|$ and $|\tilde{v}|$ show multiple maxima. For the case $y_v - y_c = -0.5\delta_v/2$, the maxima move toward the inflection point. For $y \rightarrow \pm\infty$, $|\tilde{u}|$ approaches $|\tilde{v}|$. Note that the relative overall magnitude of $|\tilde{v}|$ is larger for finite Reynolds numbers.

For the value $\alpha\delta_v/2 = 0.41$ considered in figure 4.5, the maximum of $|\tilde{u}|$ is larger than that of $|\tilde{v}|$ in both considered cases. In figure 4.6, it is shown that for large α , $|\tilde{v}|$ becomes more dominant. This behaviour is a direct consequence of the continuity equation. Also the outer maxima in $|\tilde{u}|$, attained for $|y - y_c| > \delta_v/2$, become more dominant than that close to $y = y_v$. Again, it is found in particular that this behaviour is amplified at finite Reynolds numbers.

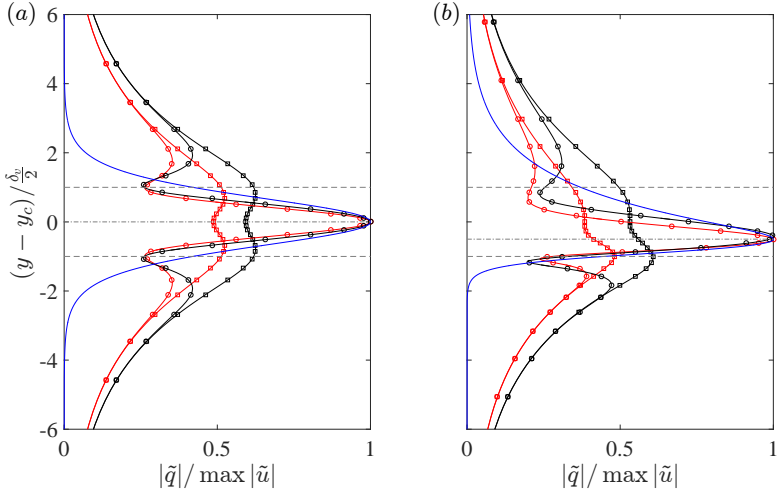


Figure 4.5: Modulus of eigenfunctions, $|u|$ (○) and $|v|$ (□), corresponding to the unstable modes in figure 4.4 for the tanh- (a) and gtanh- (b, $y_v - y_c = -0.5\delta_v/2$) profile with $\alpha\delta_v/2 = 0.41$ and $Re_{\delta_v} = 50$ (black) and ∞ (red symbols), $N = 201$ and $y_{i2} - y_{i1} = \delta_v$. Symbols indicate every fifth collocation node. Shear profile (blue line), $y = y_v$ (dash-dotted line).

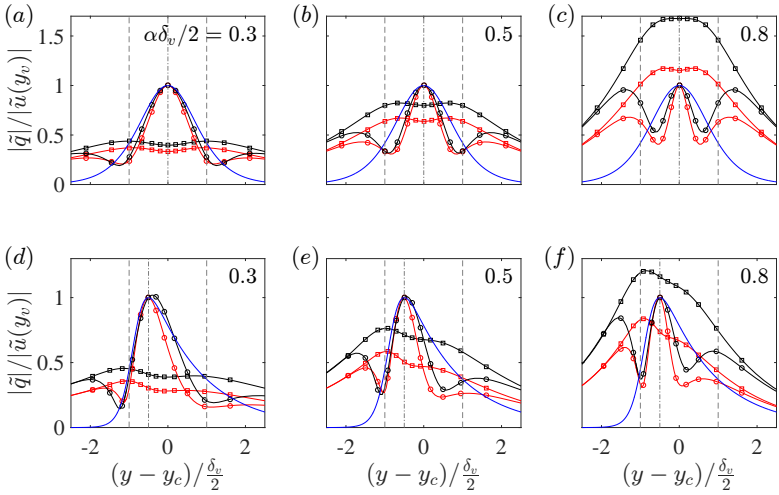


Figure 4.6: Variation of the eigenfunctions $|u|$ (○) and $|v|$ (□) for 3 α -values (as indicated) for the tanh- (a – c) and gtanh- (d – f, $y_v - y_c = -0.5\delta_v/2$) profiles and $Re_{\delta_v} = 50$ (black) and ∞ (red symbols), $N = 121$ and $y_{i2} - y_{i1} = \delta_v$. Symbols indicate every fifth collocation node. Shear profile (blue line), $y = y_v$ (dash-dotted line).

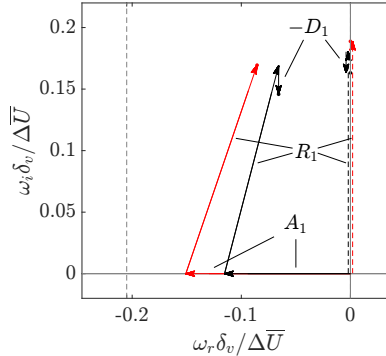


Figure 4.7: Decomposition of the eigenvalue (dots) into the contributions (arrows) of the advection A_1 , Reynolds stress R_1 and the dissipation $-D_1$ terms in equation (4.12) for the tanh- (solid) and gtanh- (dashed, $y_v - y_c = -0.5\delta_v/2$) profiles with $\alpha\delta_v/2 = 0.41$, $Re_{\delta_v} = 50$ (black) and ∞ (red), $N = 121$ and $y_{i2} - y_{i1} = \delta_v$. The frequency corresponding to the base flow velocity at the inflection point (dashed line, $\omega_r = \alpha\delta_v(\bar{U}_v - \bar{U}_c)/\Delta\bar{U}$).

4

4.5. EXPOSING THE PHYSICAL MECHANISM OF THE EIGENMODE

As mentioned before, the stability characteristics of shear layers are very well-known; just as the responsible mechanisms. It is not straightforward, however, to extract this information from just the eigenvalue and eigenfunctions alone. This problem is used to illustrate how this can be done. Inviscid and viscous analysis of both profiles are considered in this regard, setting $\alpha\delta_v/2 = 0.41$.

4.5.1. DECOMPOSITION OF THE EIGENVALUE

The eigenvalue ω is decomposed into the terms of equation (4.12) by numerically evaluating the right hand side terms. This establishes a basic residual check when checking the sum of the terms with ω . When using the same differentiation matrices used to solve the problem, this yields at most $O(10^{-13})$ errors in the absolute values of ω_r and ω_i for $N_y = 121$, which is consistent with the error indicated in figure 4.3. The individual terms' values are visualised in figure 4.7. Due to the consideration of the temporal stability problem, $\alpha - \alpha^* = \beta - \beta^* = P_1 = 0$.

For the tanh-profile, the advection term evaluates to zero due to the perfect anti-symmetry of the integrand in y . The prominently active term is the Reynolds stress R_1 , which is purely imaginary in this case. The term D_1 is purely imaginary, by definition, and thus only shifts the eigenvalue downward with respect to the inviscid case. Interestingly, it is observed that the imaginary part of R_1 has also slightly reduced in the viscous analysis. This demonstrates that the effect of viscosity does not establish itself through the D_1 -term only. It also affects the Reynolds stress term through redistributing the perturbation energy.

For the gtanh-profile, the asymmetry of the eigenfunctions causes a finite contribution of the advection term. At the inflection point, the profile attains the value $\bar{U}_v - \bar{U}_c = -0.5\Delta\bar{U}/2$. Assuming Taylor's hypothesis for the inflection point speed, the combination of this speed with the α -value $0.41/(\delta_v/2)$ yields the frequency $\omega_r \delta_v / \Delta \bar{U} = 0.41(-0.5) = -0.205$. The advection term corresponding to both viscous and inviscid analyses pushes

4

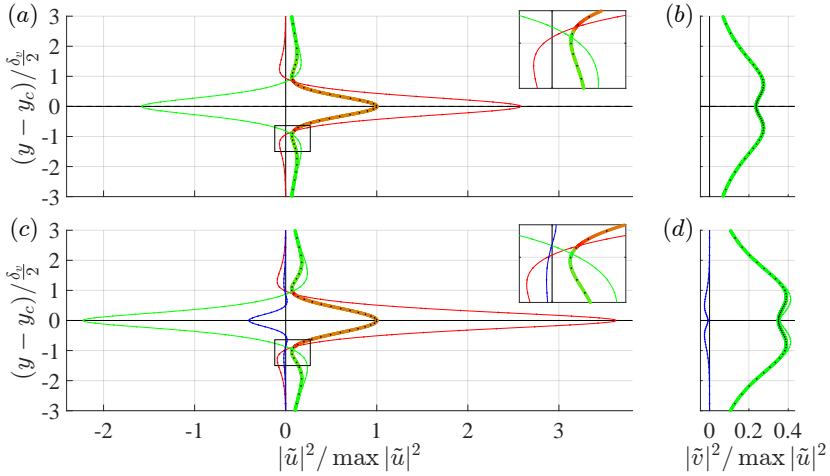


Figure 4.8: Perturbation energy (thick coloured line) in the components \tilde{u} (a,c) and \tilde{v} (b,d) for $\alpha\delta_v/2 = 0.41$, $Re_{\delta_v} = \infty$ (a,b) and 50 (c,d) and the contributions of the Reynolds stress (red), pressure (green) and viscous (blue) terms for the tanh-profile. Insets show zooms on the indicated boxes.

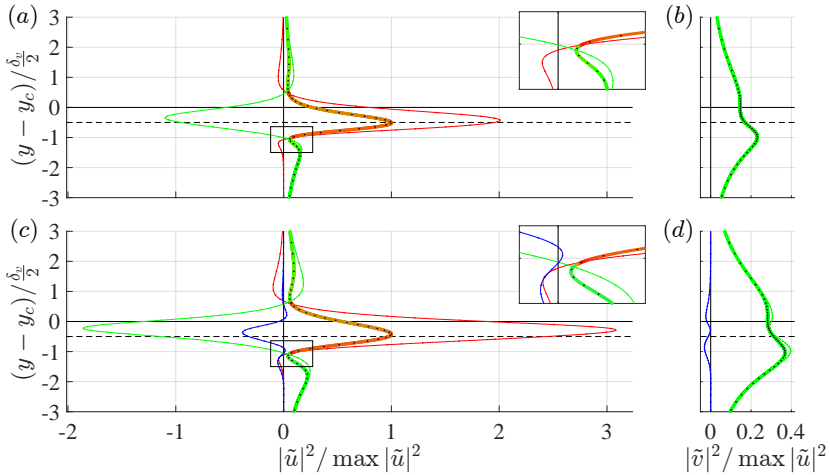


Figure 4.9: Perturbation energy (thick coloured line) in the components \tilde{u} (a,c) and \tilde{v} (b,d) for $\alpha\delta_v/2 = 0.41$, $Re_{\delta_v} = \infty$ (a,b) and 50 (c,d) and the contributions of the Reynolds stress (red), pressure (green) and viscous (blue) terms for the gtanh-profile ($y_v - y_c = -0.5\delta_v/2$). Insets show zooms on the indicated boxes. The line $y = y_v$ is indicated (dashed).

the frequency towards this value. Recall the interpretation of this term with equation (4.13). While the eigenfunctions attain their maximal values near the inflection point, their centroid (i.e. ‘center of mass’) lags behind and is positioned closer to the center of the shear layer, y_c . The diffusive effect of viscosity is to enhance this lag, yielding a smaller off-center shift by the advection term. Next to the expected contribution of R_1 to the ω_i -budget, surprisingly, R_1 also counter-acts the advection term. Furthermore, D_1 adds the expected stabilising contribution. Lastly, note that the introduction of viscosity has a practically indistinguishable effect on the imaginary value of R_1 in this case.

4.5.2. DECOMPOSITION OF THE EIGENFUNCTIONS

Using equations (4.14) and (4.15), the shape of the eigenfunctions can be traced back to the terms in the equations. Figures 4.8 and 4.9 show these decompositions for the tanh- and gtanh-profiles, respectively. Per subfigure, the functions are shown separately for the inviscid and viscous analyses. The thin lines represent the contributions of the pressure, Reynolds stress and viscous terms, that sum up to the square magnitude of the eigenfunctions, indicated with the thick lines. The thick lines are coloured according to the active term(s) at that location.

For $|\tilde{u}|^2$, the domain can be divided into the regions where either the Reynolds stress or the pressure term is the main productive actor; the line representing $|\tilde{u}|^2$ takes red and green colors in these respective regions. The insets indicate that the border between these regions lies very close to $y = y_c \pm \delta_v/2$ for the tanh-profile. The red region could be regarded as the (productive) core of the shear layer. For the gtanh-profile, this region turns out to be slightly smaller. Note that the pressure term acts destructively inside the core of the shear layer. This means that not all energy produced by the Reynolds stress term ends up in the \tilde{u} -component of the perturbation energy. A larger portion of the energy produced by the Reynolds stress term is stored in the pressure perturbation.

In turn, figures 4.8 (b,d) and 4.9 (b,d) show how the pressure term is completely responsible for the generation of the energy in the \tilde{v} perturbation component. This is a clear manifestation of a pressure-strain effect. The Reynolds stress directly produces the \tilde{u} -component only; the pressure enforces flow continuity by producing the \tilde{v} -component. In the case where $\beta \neq 0$, the \tilde{w} -component would be generated through a similar process.

The inset in figure 4.9 (d) demonstrates that the contribution of the Reynolds stress term is not necessarily contained in the region $(y - y_c)/(\delta_v/2) \in [-1, 1]$. On the other hand, the pressure term is clearly responsible for the local secondary maxima in $|\tilde{u}|$ outside this region. Note that the pressure term for $|\tilde{u}|^2$ in equation (4.14) is proportional to α . Accordingly, the increase in magnitude of these exterior maxima and the decrease of the central maximum for larger α -values, as observed in figure 4.6, is expected.

When viscosity is introduced, some of the perturbation energy is directly dissipated. As shown by the thin blue curves, this occurs predominantly in the core of the shear layer for the considered α -values, where the perturbation energy is produced by the Reynolds stress term. Accordingly, a larger contribution of the Reynolds stress term is required to yield an energy output that is comparable to the inviscid case. All profiles are scaled with $\max|\tilde{u}|^2$, therefore the contribution of the Reynolds stress term (and reaction of the pressure term) is relatively larger. Note that viscosity also redistributes a part of the

perturbation energy. This cannot be isolated as one term in the equation; it can be established only by comparing the viscous terms with the inviscid equivalents. For the symmetric tanh-profile, this is very difficult to spot without direct quantification. The effect is visible when comparing figures 4.9 (a) and (c) for the gtanh-profile. Note that the maximum of the \tilde{u} eigenfunction moves away from $y = y_v$ and towards $y = y_c$. Also the Reynolds stress and pressure terms move in this direction. This is another demonstration that the effect of viscosity cannot be simply captured in a term in the equations; other terms change due to its action as well.

4.5.3. DECOMPOSITION OF $\tilde{u}^* \tilde{v}$

It is demonstrated what role the equations' terms play in generating the eigenfunction shapes. The Reynolds stress term drives the perturbation through the overlap of the base flow shear with the combination $\tilde{u}^* \tilde{v}$, which motivates investigating this function in more depth. Figures 4.10 and 4.11 represent this function for the tanh- and gtanh-profiles, respectively. Again, the functions are shown separately for the inviscid and viscous analyses. In this case, the profiles are normalized with respect to $\|\tilde{q}\|^2$, so that integration over the profiles (weighted with $d\bar{U}/dy$) yields the value that appears in the ω -budget (see figure 4.7).²

The Reynolds stress term in the equation for ω reads: $-i\tilde{u}^* \tilde{v} d\bar{U}/dy$. For this function to yield a productive contribution, the real part of $\tilde{u}^* \tilde{v}$ must be negative. This is directly confirmed in figures 4.10 and 4.11. As mentioned before, the main productive term for the real part of $\tilde{u}^* \tilde{v}$ is, again, a Reynolds-stress-like term: $-i|\tilde{v}|^2 d\bar{U}/dy$.³ This term seems to be the last piece of a chain that describes the complete mechanism underlying the unstable modes:

$$|\tilde{u}|^2 \xleftarrow{\frac{d\bar{U}}{dy}} \tilde{u}^* \tilde{v} \xleftarrow{|\tilde{v}|^2} \tilde{v} \xleftarrow{\frac{d\bar{U}}{dy}} |\tilde{u}|^2 \xleftarrow{\tilde{p}^* \frac{d\tilde{v}}{dy} = -i\alpha \tilde{p}^* \tilde{u}} |\tilde{u}|^2, \quad (4.16)$$

or, in words: $\tilde{u}^* \tilde{v}$ produces $|\tilde{u}|^2$, $|\tilde{v}|^2$ produces $\tilde{u}^* \tilde{v}$ and \tilde{u} produces \tilde{v} through the pressure/flow continuity.

The pressure and viscous terms clearly have a counteracting role for the real part of $\tilde{u}^* \tilde{v}$. In the viscous analysis, the Reynolds stress and pressure terms are significantly larger than in the inviscid case, similar as the situation for $|\tilde{u}|^2$. The viscous term acts to yield a slightly smaller overall integral value with respect to the inviscid case. For the gtanh-profile, the viscous term causes the real part of $\tilde{u}^* \tilde{v}$ to take positive values as shown in the inset of figure 4.11 (c).

The imaginary part of $\tilde{u}^* \tilde{v}$ contributes primary to ω_r . For the tanh-profile, this is a perfectly odd function, see figures 4.10 (b) and (d), and therefore the integral value evaluates to zero. For the gtanh-profile, this symmetry is broken. Figures 4.11 (b) and (d) show the case for that profile, the imaginary part of $\tilde{u}^* \tilde{v}$ is altered to be predominantly positive in the region where $d\bar{U}/dy$ is large. The shear profile is also shown in the figures to indicate the weighted region. The primary reason for this is the local dominance of the term $-i|\tilde{v}|^2 d\bar{U}/dy$. Accordingly, the overall contribution to the ω_r -budget is positive.

²Note that care has to be taken in directly interpreting these functions in relation to the eigenfunction \tilde{u} , because of the complex weighting function in equation (4.14).

³The factor $1/(\omega - \alpha \bar{U})$ that multiplies this term in equation (4.15) is dropped here for readability.

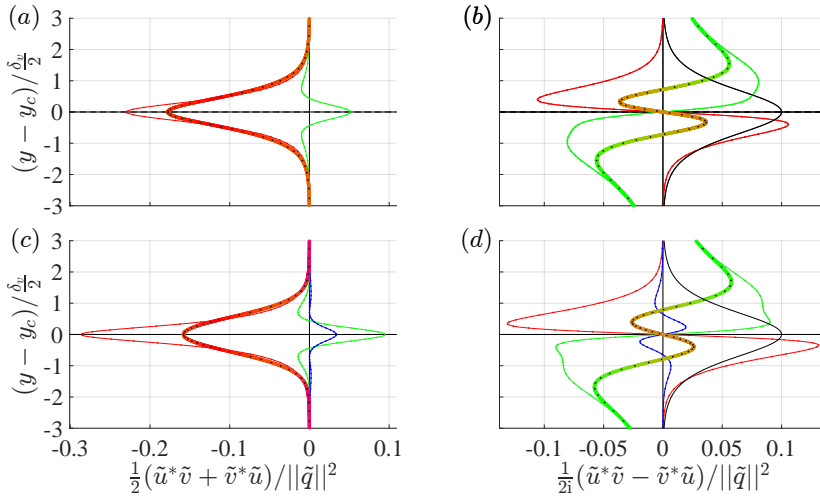


Figure 4.10: Correlations $(\tilde{u}^*\tilde{v} + \tilde{v}^*\tilde{u})/2$ (a,c) and $(\tilde{u}^*\tilde{v} - \tilde{v}^*\tilde{u})/2i$ (b,d) (thick line) for $\alpha\delta_v/2 = 0.41$, $Re_{\delta_v} = \infty$ (a,b) and 50 (c,d) and the contributions of the Reynolds stress (red), pressure (green) and viscous (blue) terms for the tanh-profile. (b,d) Shear profile (black, $0.1d\bar{U}/dy$).

4

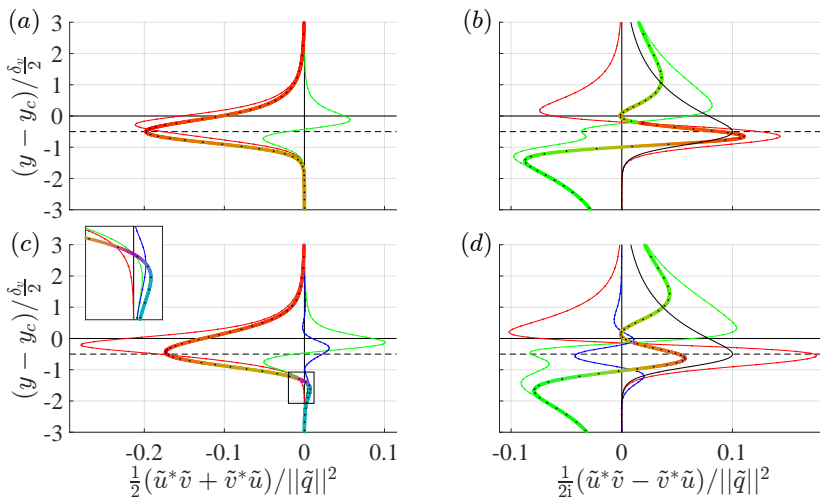


Figure 4.11: Correlations $(\tilde{u}^*\tilde{v} + \tilde{v}^*\tilde{u})/2$ (a,c) and $(\tilde{u}^*\tilde{v} - \tilde{v}^*\tilde{u})/2i$ (b,d) (thick line) for $\alpha\delta_v/2 = 0.41$, $Re_{\delta_v} = \infty$ (a,b) and 50 (c,d) and the contributions of the Reynolds stress (red), pressure (green) and viscous (blue) terms for the gianh-profile ($y_v - y_c = -0.5\delta_v/2$). The line $y = y_v$ is indicated (dashed). (b,d) Shear profile (black, $0.1d\bar{U}/dy$).

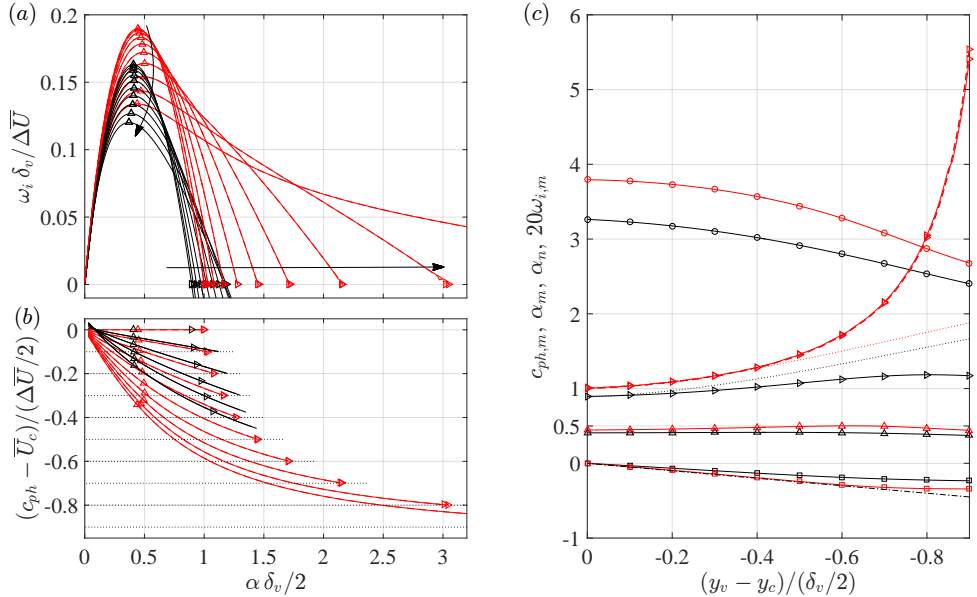


Figure 4.12: Temporal growth rate (a) and phase speed (b) versus α with $(y_v - y_c)/(\delta_v/2) = 0, -0.1, \dots, -0.9$ (arrows: increasing $|y_v - y_c|$) with $Re_{\delta_v} = 50$ (black) and ∞ (red). In (b), $(\bar{U}_v - \bar{U}_c)/(\delta_v/2)$ (dotted), only the first 6 viscous cases are shown. (c) The largest neutral wavenumber, $\alpha_n \delta_v$ (\triangleright), and the phase speed, $(c_{ph,m} - \bar{U}_c)/(\Delta \bar{U}/2)$ (\square), wavenumber, $\alpha_m \delta_v$ (\triangle), and growth rate, $\omega_{i,m} \delta_v / \Delta \bar{U}$ (\circ , scaling factor: 20) of the most unstable wave. Momentum thickness θ rescaled to $\alpha_n \delta_v$ for $(y_v - y_c)/(\delta_v/2) = 0$ (dotted), $\frac{1}{2}(\bar{U}_v - \bar{U}_c)/(\Delta \bar{U}/2)$ (dash-dotted). The inviscid solutions are computed through solving both equations (4.6) (solid) and (4.8) (dashed).

4.6. PHYSICAL PARAMETRIC EFFECTS

By briefly reviewing the stability properties of the hyperbolic tangent profiles, further insight can be gained into the underlying physics of the perturbations. To this end, the parabolic shape of the function $\omega_i = \omega_i(\alpha)$, as shown in figure 4.3, is condensed into several parameters. The subscript m is used for the most temporally unstable wave: $\omega_{i,m}$ is the maximum temporal growth rate; α_m , the real wavenumber corresponding to $\omega_{i,m}$; and the most unstable phase speed is defined as: $c_{ph,m} = \omega_{r,m} / \alpha_m$ (note that the real part is implied). Lastly, the subscript n refers to neutral perturbations at the largest wavenumber. That is, α_n is the largest α for which $\omega_i = 0$.

The focus lies on the effect of the inflection point location, as handled by Michalke [3], influence of the spanwise wavenumber and the proximity of a wall.

4.6.1. EFFECT OF THE INFLECTION POINT LOCATION

By evaluating the temporal stability spectra of the gtanh-profiles for different values of $(y_v - y_c)/(\delta_v/2)$, the effect of the inflection point location is determined. Michalke [2] illustrates the maximal spatial growth rate increases indefinitely when $(y_v - y_c)/(\delta_v/2) \rightarrow -1$, while scaling the results with the momentum thickness. Scaling the results with $\delta_v/2$, figures 4.12 (a,c) indicate the asymmetric gtanh-profiles yield smaller maximum growth rates with respect to the symmetric tanh-profile case. Scaling with $\delta_v/2$ fixes the max-

imum shear, so it illustrates the efficiency with which the shear layer drives perturbations. The symmetric tanh-profile is the most efficient perturbation energy amplifier. For the representative and extreme cases of $(y_v - y_c)/(\delta_v/2) = -0.5$ and -0.9 , the maximum growth in the inviscid case has respectively reduced to 90.7% and 70.6% of the value corresponding to the symmetric profile. In the viscous case, a respective reduction to 89.4% and 73.6% is found. For the representative value $(y_v - y_c)/(\delta_v/2) = -0.5$, the stability properties are only moderately affected by the location of the inflection point. For all values of $(y_v - y_c)/(\delta_v/2)$, the wavenumber of the most unstable wave is nearly invariant with $(y_v - y_c)/(\delta_v/2)$, as shown in figure 4.12 (c), the largest variation with respect to the symmetric profile is 13.7% larger for the inviscid case and 7.9% smaller in the viscous case. In the inviscid case, $\alpha_m \delta_v/2$ does not exceed 0.5014.

As discussed before, the symmetrical tanh-profile yields $\omega_r = 0$ for all Re_{δ_v} and α . This corresponds to the wave moving with the same speed as the reference system. This special situation is irrevocably distorted for non-zero $|y_v - y_c|$, rendering ω_r to become a complicated function of α and Re_{δ_v} .

For inviscid perturbations, the function $\omega_r = \omega_r(\alpha)$ is still tractable, because it is found to be intimately linked to the location of the perturbations relative to the points y_v and y_c . Figure 4.12 (b) illustrates that the phase speed approaches $(\bar{U}_v - \bar{U}_c)/(\Delta \bar{U}/2)$, as indicated with the dotted lines, for $\alpha \rightarrow \alpha_n$. Through the interpretation with equation (4.13), it is deduced that small streamwise perturbation structures (large α) find their comfort close to the inflection point (the location of the perturbations' centroid approaches y_v). While α surpasses α_n , which signifies the perturbations become stable, the perturbations' centroid moves past the inflection point. This suggests the two characteristics, the inviscid perturbations' location and their growth rate, are intimately linked. This link extends to the phase speed of the most unstable wavenumbers, which are found to closely approach $\frac{1}{2}(\bar{U}_v - \bar{U}_c)/(\Delta \bar{U}/2)$ for $|y_v - y_c| < 0.6\delta_v/2$ (up to 97%) as shown with the dash-dotted line in figure 4.12 (c). This implies that the most unstable waves prefer to orient themselves (i.e. their centroid) halfway in-between the inflection point y_v and the midpoint y_c . When including the effects of viscosity, the characteristics deviate slightly from this trend. For $\alpha = \alpha_n$ and α_m , diffusion acts to place the perturbations' centroid closer towards y_c .

As $\alpha \rightarrow 0$, the Reynolds stress term dominates in the ω_r -budget, so inferring the location of the perturbation through equation (4.13) then becomes impossible. Nevertheless, the phase speed of large structures (small α) again tends toward 0. This makes sense, as large structures are advected approximately with the average flow speed of the shear layer. In the viscous case, the phase speed displays a small overshoot with respect to zero. That is, despite $y_v - y_c < 0$, $c_{ph} > 0$ for small enough α .

Although the maximum growth rate decreases as $(y_v - y_c)/(\delta_v/2)$ decreases below 0, the range of unstable wavenumbers increases. The range increases indefinitely in the inviscid analysis, while a maximum is attained in the viscous case. Up to $(y_v - y_c)/(\delta_v/2) = -0.4$, the diverging trend of the largest inviscid neutral wavenumber is closely captured by the momentum thickness, defined as:

$$\frac{\theta}{\delta_v/2} = \frac{1}{2} \int_{-\infty}^{\infty} \left(1 + \frac{\bar{U} - \bar{U}_c}{\Delta \bar{U}/2} \right) \left(1 - \frac{\bar{U} - \bar{U}_c}{\Delta \bar{U}/2} \right) dy = \frac{2m}{1+m} \left(1 - \frac{y_v - y_c}{\delta_v/2} \right) \int_0^1 \frac{1-z}{1-z^m} dz, \quad (4.17)$$

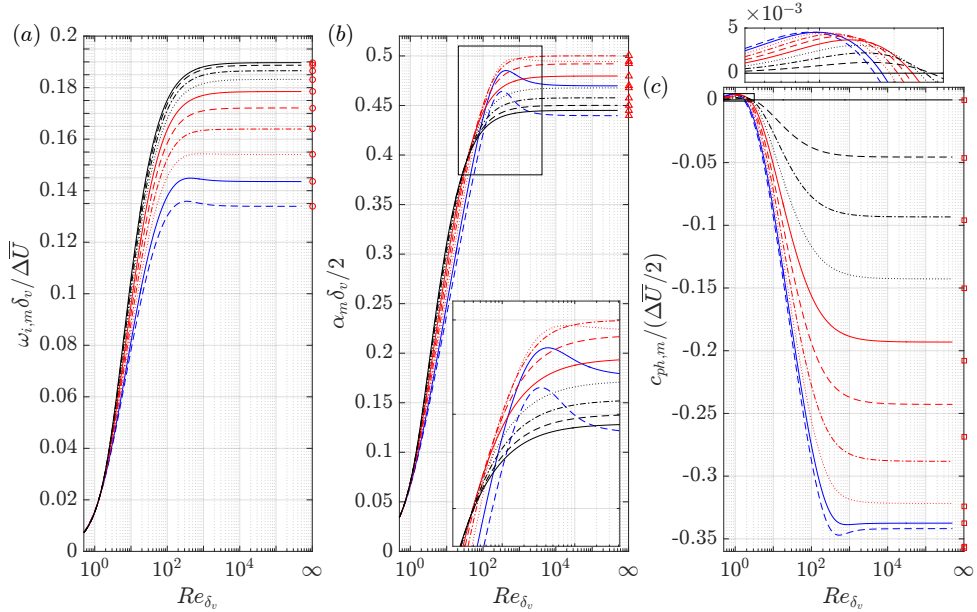


Figure 4.13: Effect of the Reynolds number on the properties, $\omega_{i,m}$ (a), α_m (b) and $c_{ph,m}$ (c), of the most unstable wave for $(y_v - y_c)/(\delta_v/2) = 0, -0.1, \dots, -0.9$ (order: black, red and blue and per color: solid, dashed, dash-dotted, dotted). Insets show zooms on the indicated boxes.

see [2], i.e. $\theta = \delta_v/2$ for $y_v = y_c$, $m = 1$. In figure 4.12 (c), θ is shown but rescaled such that it is equal to α_n for $y_v = y_c$. The matching trend suggests why Michalke used the momentum thickness as the reference length scale. Although the scaling diverges for large $|y_v - y_c|$, it provides a reasonable estimate of the largest neutral α for the cases of interest.

The inviscid solutions with large α required a large N and small $y_{i2} - y_{i1}$ to be resolved properly. To that end, $N = 201$ and $(y_{i2} - y_{i1})/(\delta_v/2) = 0.4$ were used to generate the results presented in figure 4.12. Despite these efforts, for α approaching α_n , the inviscid solutions show an unforgiving sensitivity. Both inviscid solutions to equations (4.6) and (4.8) are presented, only the largest unstable α -values are affected.

4.6.2. EFFECT OF THE REYNOLDS NUMBER

The eigenmodes corresponding to shear layers represent the Kelvin-Helmholtz mechanism. The considered shear layer profiles have an inflection point and therefore have an unstable eigenmode in the limit of inviscid flow, this follows from the Rayleigh-Fjørtoft inflection point criterion [4]. This implies that the effect of viscosity for large Reynolds numbers yields a small correction to the eigenmode characteristics. For small Reynolds numbers, the effect of viscosity is to stabilise the perturbations, as expected of a diffusive mechanism. For $Re_{\delta_v} \rightarrow \infty$, the growth rates are expected to approach the values corresponding to the inviscid case. This is illustrated in figure 4.13 (a).

As $Re_{\delta_v} \rightarrow 0$, one would expect to encounter the critical Reynolds number. For shear

layers this number does not exist, however. The growth rate asymptotically approaches zero as $Re_{\delta_v} \rightarrow 0$, as illustrated with figure 4.13 (a). Drazin and Reid [14, p. 239] present asymptotic expressions for the neutral curve corresponding to the tanh-profile, expressing α_n versus Re_{δ_v} , in particular:

$$\alpha_n \frac{\delta_v}{2} = 1 - \frac{2\pi}{Re_{\delta_v}} \quad \text{for: } Re_{\delta_v} \rightarrow \infty; \quad (4.18a)$$

$$\alpha_n \frac{\delta_v}{2} = \frac{Re_{\delta_v}}{4\sqrt{3}} \left(1 + \frac{7\pi^2}{432} Re_{\delta_v}^2 \right) \quad \text{for: } Re_{\delta_v} \rightarrow 0. \quad (4.18b)$$

It is shown that these expressions become good approximations for $Re_{\delta_v} > 50$ and $Re_{\delta_v} < 1$, respectively. For $Re_{\delta_v} = 5$, the negative contribution of the viscous terms to the eigenfunction in figure 4.9 (c) overtakes the negative contribution corresponding to the pressure terms. This indicates that diffusion prominently dictates the eigenfunction shape for $Re_{\delta_v} < 5$. This switch of mechanisms underlines the different assumptions leading up to the equations (4.18a) (energy transfer to pressure term dominates) and (4.18b) (transfer to viscous terms dominates).

Equation (4.18b) illustrates that an unstable range of streamwise wavenumbers exists for all Re_{δ_v} . Moreover, the largest unstable $\alpha \rightarrow 0$ as $Re_{\delta_v} \rightarrow 0$. Therefore, also the most unstable streamwise wavenumber α_m decreases as $Re_{\delta_v} \rightarrow 0$, this is shown in figure 4.13 (b). For that reason, it is physically acceptable that no critical Reynolds number exists for this case,⁴ because viscosity has a decreasing hold on perturbations with an increasing wavelength.

The gtanh-profiles show the same behaviour. For $(y_v - y_c)/(\delta_v/2) \leq -0.7$, the growth rates are observed to increase slightly for decreasing Re_{δ_v} ; consider the range $Re_{\delta_v} \approx 320$ to 400. For $y_v - y_c = -0.9\delta_v/2$, this increase was found to be 1.5% with respect to the asymptotic value as $Re_{\delta_v} \rightarrow \infty$. Although this is a minor effect, this demonstrates the possibility for viscosity to take a destabilising role. This is found to coincide with an increase in α_m , shown in figure 4.13 (b).

The phase speed of the most unstable perturbations is shown in figure 4.13 (c). Interestingly, the inviscid values display an increasing mismatch with the value for large Re_{δ_v} . As $Re_{\delta_v} \rightarrow 0$, the phase speed approaches zero, which implies that the eigenfunctions are diffused to such an extent that their centroid approaches the center of the profile y_c . As shown in the inset, the centroid even overshoots y_c for $Re_{\delta_v} < 3$ for the considered values of $(y_v - y_c)/(\delta_v/2)$.

4.6.3. ROLE OF A NON-ZERO SPANWISE WAVENUMBER

Up to this point, only planar waves were considered. That is, waves that travel in the streamwise direction. A spanwise propagation of the phase is represented by non-zero spanwise wavenumbers, β .

There is another interpretation of the spanwise wavenumber that is relevant to the application cases. The shear layers considered in later chapters are two-dimensional. Hence the perturbations are not two-dimensional; they are not constant in the spanwise

⁴Fixing $\beta \neq 0$, a critical Reynolds number does exist, because the effective wavenumber of unstable perturbations, $\sqrt{\alpha^2 + \beta^2}$, approaches β as $Re_{\delta_v} \rightarrow 0$. All finite wavelengths are stabilised by viscosity as $Re_{\delta_v} \rightarrow 0$.

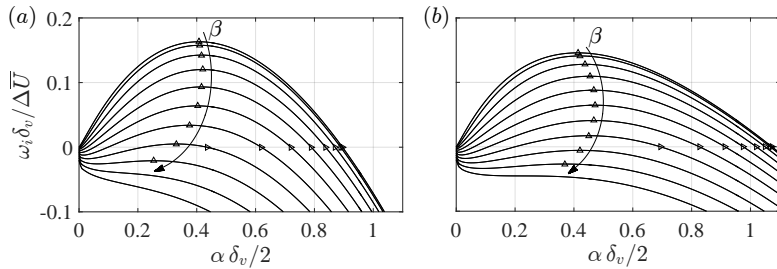


Figure 4.14: Temporal spectra for varying $\beta\delta_v/2$ ($= 0, 0.1, \dots, 1$) for the tanh- (a) and gtanh- (b, $y_v - y_c = -0.5\delta_v/2$) profiles, with $Re_{\delta_v} = 50$. Most unstable (Δ) and largest neutral wavenumber (\triangleright).

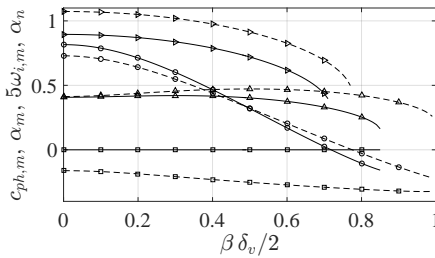


Figure 4.15: Temporal stability characteristics with varying β for the tanh- (solid) and gtanh- (dashed, $y_v - y_c = -0.5\delta_v/2$) profiles, with $Re_{\delta_v} = 50$. The largest neutral wavenumber, $\alpha_n\delta_v/2$ (\triangleright), and the phase speed, $(c_{ph,m} - \bar{U}_c)/(\Delta\bar{U}/2)$ (\square), wavenumber, $\alpha_m\delta_v/2$ (\triangle), and growth rate, $\omega_{i,m}\delta_v/\Delta\bar{U}$ (\circ , scaling factor: 5), of the most unstable wave.

direction. In the context of the analysis with system (4.6), this can also be modelled with a non-zero spanwise wavenumber. The stabilising effect of viscosity on the more complex perturbation structure can be quantified. The spanwise shear can also enhance the instability, but this lies outside the scope of the one-dimensional approach.

Considering a range of β -values of interest, the temporal spectrum displays a strong stabilising effect, see figure 4.14. Non-zero β -values cause an overall larger wavenumber of the perturbation structure, to which viscosity applies a square-proportionally stronger damping. For the inviscid case, no new simulations were performed, because the governing equations for the phase speed, c_{ph} , with $\beta = 0$ are invariant under the transformation $\alpha \mapsto \sqrt{\alpha^2 + \beta^2}$ to the equations with non-zero β , see §IV.18 of Betchov and Criminaile [15]. This implies that exactly the same graphs would be found when plotting all previous results versus $\sqrt{\alpha^2 + \beta^2}$ instead of α and rescaling $\omega/\alpha \mapsto \omega/\sqrt{\alpha^2 + \beta^2}$.

The variation of the stability characteristics with β is summarised for the viscous case in figure 4.15. Although figure 4.12 (c) shows the gtanh-profile generally displays a smaller maximal temporal growth rate with respect to the symmetric tanh-profile, this is no longer the case for non-zero β . For $\beta\delta_v/2 > 0.5$, the gtanh-profile yields a larger maximal growth rate. In turn, for $\beta\delta_v/2 > 0.8$, both profiles are completely stable.

Furthermore, α_n steadily decreases as β increases. Note that α_n is undefined for $\omega_{i,m} < 0$. As β is increased, the most unstable wavenumber α_m first increases slightly and then decreases. For these two profiles and Reynolds number, the value does not ex-

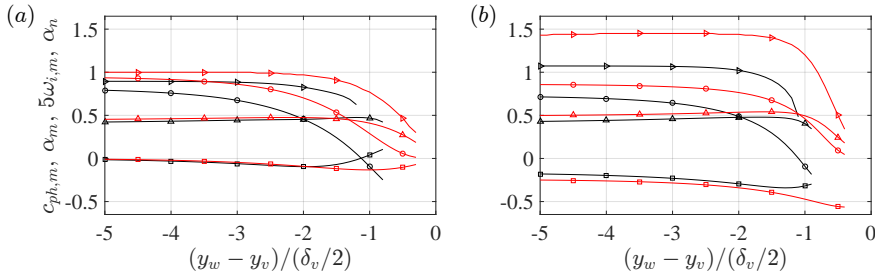


Figure 4.16: Temporal stability characteristics with varying wall distance δ_w for the tanh- (a) and gtaanh- (b) profiles, with $Re_{\delta_v} = 50$ (black) and ∞ (red). The largest neutral wavenumber, $\alpha_n\delta_v/2$ (\triangleright), and the phase speed, $(c_{ph,m} - \bar{U}_c)/(\Delta\bar{U}/2)$ (\square), wavenumber, $\alpha_m\delta_v/2$ (\triangle), and growth rate, $\omega_{i,m}\delta_v/\Delta\bar{U}$ (\circ , scaling factor: 5), of the most unstable wave.

4

ceed $0.5\delta_v/2$. It should be noted that the variables corresponding to $\omega_{i,m}$ consistently refer to the most unstable wave for $\alpha \neq 0$. For large enough β , the temporal growth rate decreases below the growth rate of the wave with $\alpha = 0$ (a standing wave in the streamwise direction), for which it can be derived that $\omega_i = -\beta^2/Re_{\delta_v}$.

4.6.4. EFFECT OF WALL PROXIMITY

Up to now, the boundaries were placed very far from the shear layer. Walls can be located much closer in practice. The influence of wall proximity on the stability characteristics is therefore explored. This is done by increasing the parameter L^- , which represents the proximity of a wall below the shear layer.

While increasing L^- , the shape of the velocity profile is kept fixed. Note that, for small wall proximities, the tanh-profiles may not represent realistic (physical) velocity profiles. Alternative profiles could be considered in the limit where the wall approaches the inflection point. Specifically, Falkner-Skan profiles corresponding to an adverse pressure gradient could be considered. However, the primary goal is to identify for which wall proximity the presence of the wall can no longer be ignored. The use of (possibly unrealistic) tanh-profiles is argued to be justified to this end.

The significant indicator of the location of the wall is the distance with respect to the inflection point in the base flow profile $y_w - y_v$, because $y_w - y_v = 0$ corresponds to a profile without an inflection point, which is stable to inviscid perturbations [4, Rayleigh-Fjørtoft inflection point criterion]. Hence negative values are considered for this parameter only. Note that if $|y_w - y_c| < \delta_v/2$, one has to be careful when interpreting the scales δ_v and $\Delta\bar{U}$, because the lower part of the shear layer indicated by δ_v is now located inside the wall. Furthermore, \bar{U} does not approach zero as $y \rightarrow y_w$ in this case. The value $\bar{U}(y_w)$ can be interpreted as the speed of the wall with respect to the \bar{U}_c -centered reference frame. Despite these facts, δ_v and $\Delta\bar{U}$ are maintained as scales for the purpose of consistency with the rest of the chapter. The boundary conditions (4.9) and (4.11) (representing the realistic no-slip conditions) still apply for the perturbations.

It was found that densely resolving the shear layer is required for the inviscid analysis in this case, which is ensured by placing y_{i1} at y_v . This annihilates the sensitivity of the results for $\alpha \rightarrow \alpha_n$ as previously indicated in figure 4.12, which would currently signifi-

cantly affect the whole α -range for $y_w - y_v > -2.5\delta_v/2$. A high resolution near the wall is established by using $N_y = 201$ points.

The effect of the wall proximity on ω_i , α_m , $c_{ph,m}$ and α_n is illustrated in figure 4.16. Inviscid and viscous analyses are performed on the two characteristic tanh- and gtanh-profiles, while setting the spanwise wavenumber to zero, $\beta = 0$. As the wall distance $|y_w - y_v|$ increases, the characteristics show a rapid convergence to the asymptotic values. For all cases, the relative changes of $\omega_{i,m}$ and α_m are less than 3% and 4%, respectively, when comparing the values for $y_w - y_v = -5\delta_v/2$ with the asymptotic values as $|y_w - y_v| \rightarrow \infty$.

As the wall approaches the inflection point in the profiles, it exerts a significant stabilising effect. The growth rates corresponding to both profiles are reduced below 10% of the asymptotic values at $y_w - y_v = -1.1\delta_v/2$ and $-0.4\delta_v/2$ for the viscous and inviscid cases, respectively. For these proximities, the potential of the inviscid mechanism is very strongly limited. Note that the inviscid cases remain unstable for $|y_w - y_v| > 0$, i.e. as long as the profile has an inflection point.

The other stability characteristics change only slightly as the wall approaches the inflection point. In particular, the most unstable wavenumber remains approximately constant up to $y_w - y_v = -1.5\delta_v/2$. It decreases for $y_w - y_v > -1.5\delta_v/2$, implying the most unstable wavelength increases significantly. The phase speed $c_{ph,m}$ decreases while $|y_w - y_v|$ is large, which signifies that the centroid of the eigenfunctions tends towards the wall. This trend reverses for very small proximities. In the interpretation of the latter trend, it should be noted that the velocity of the wall, $\bar{U}(y_w)$, becomes significantly larger than $-\Delta\bar{U}/2$, which necessitates the increase of $c_{ph,m}$.

4.7. EFFECTS ASSOCIATED TO USING A MEASURED BASE FLOW

The final objective of this chapter is to assess the methodological effects that come into play when using a measured base flow. In particular, the effects associated to PIV measurements are indicated.

The methodological effects associated to PIV measurements that are important within the context of stability analysis are: limited spatial resolution, spatial smoothing and the presence of physical perturbations in the instantaneous flow.

4.7.1. SPATIAL RESOLUTION

There are 2 main factors that limit the spatial resolution of PIV measurements. The flow velocity is determined by performing a cross-correlation over an interrogation volume, which must contain a sufficient amount of particles to yield a reliable measurement. The lower bound of this volume's dimensions is hence determined by the particle seeding intensity. Furthermore, the sensor size of the camera limits the precision of the position with which individual seeding particles is recorded.

The effect of spatial resolution of the stability results is identified by performing stability analysis on analytical profiles that are evaluated and differentiated on a coarse grid and comparing the results to the previously considered reference solutions. The coarse grids are simple uniform grids of which the resolution is increased, so convergence to the reference solution can be assessed. The profile values on the uniform grid are exact, but the derivatives are determined using finite differences and thereafter the solution is

interpolated on the Chebyshev collocation nodes to solve the stability problem.

It should be emphasized that the exact values of δ_v and $\Delta\bar{U}$ are used to scale the results throughout this (entire) section. This is done to establish the difference with the reference solutions consistently with the reference scales. These scales are generally not available, however.

It is unrealistic to capture the maximum shear location exactly, so, next to the number of nodes, the effect of offsets of the center node is considered. This is done by shifting all grid coordinates by the same fraction of Δy , the node spacing for a given grid resolution. By standard, an odd number of equispaced nodes is used, so that a zero shift corresponds to capturing the maximum shear exactly. To be sure, a case with an even number of equispaced nodes without a shift is used to rule out the influence by the different values of L^\pm .

The shear profiles are highly dependent on the order of the used finite difference scheme. Figures 4.17 (a,c,e) show shear profiles calculated on a very coarse grid. The grid spacing, Δy , is set equal to $\delta_v/2$, such that, without shifting, $1 + (\delta_v/\Delta y) = 1 + 2 = 3$ grid points are contained within the shear layer (denoted by: $(y - y_c)/(\delta_v/2) \in [-1, 1]$, including the boundaries), this is used as the measure of resolution. Increasing the differentiation order from 2 to 6, a large variation in the maximum shear on the uniform grid is observed. Using second order differences, the shear magnitude at the grid point exactly capturing the inflection point attains 76% of the exact value, while the maximum shifted node only attains 68%. Using fourth and sixth order, these numbers are 76% and 78% for no shift, while the node on the exact inflection point location attains 86% and 89%, respectively. Comparing the worst to the best case yields a difference of 21 percent points!

It is unconventional to differentiate PIV data with high order finite differences, see Foucaut and Stanislas [16]. This crude example illustrates, however, that the shear can be highly underestimated if lower order differences are used. Given the importance of resolving the maximum shear in the general application of stability theory to measured flows, it is chosen to use higher order differences. Fourth order finite differences were chosen in this particular section, because the fourth order nature is consistent with the used spline interpolation method. A fourth order convergence rate is expected for this reason.

The stability grid is equipped with a fixed number of nodes, $N_y = 81$, because it is known that this yields a converged solution for this particular stability problem. Using this amount implies all error effects are due to the base flow resolution. The parameters y_{i1} and y_{i2} are adapted to surround the discrete base flow node location corresponding to the maximum shear, i.e. this location is off by $\Delta y/2$ for an even node number. This location is illustrated by the crosses in figure 4.17. Figures 4.17 (b,d,f) exemplify the interpolation of the profiles in figures 4.17 (a,c,e), respectively, onto the Chebyshev grid. Although there was a large variation in the maximum shear when shifting the uniform grid points, a nearly identical maximum shear level is retrieved after performing the spline interpolation for this case. The interpolation (of all fields) is performed after the differentiation, so the uniform grid spacing Δy consistently dictates the differentiation error. Figures 4.17 (b,d,f) demonstrate that this yields profiles that closely approach the profile that exactly resolves the inflection point. The profiles that exactly resolve the

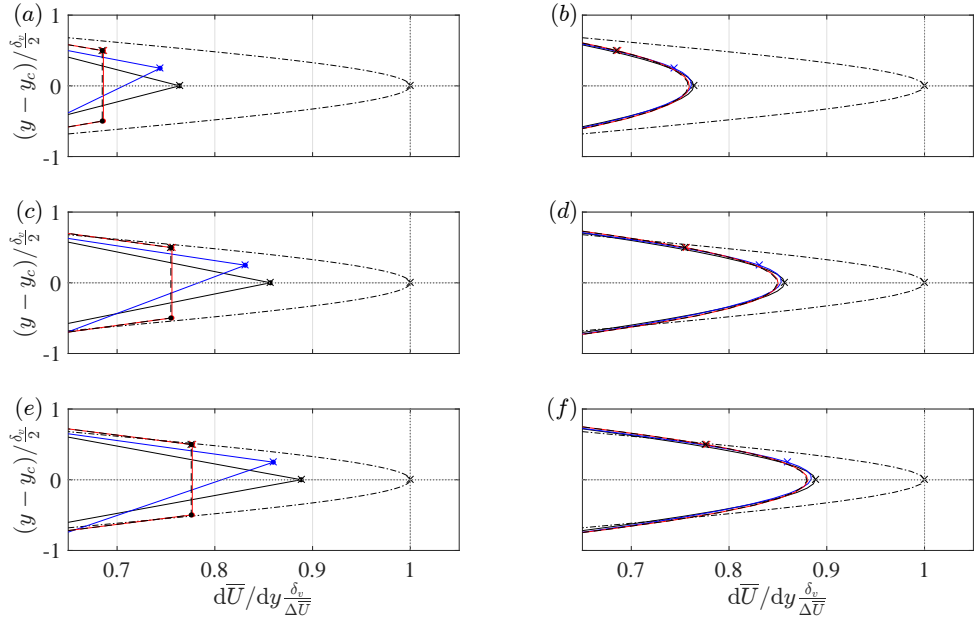


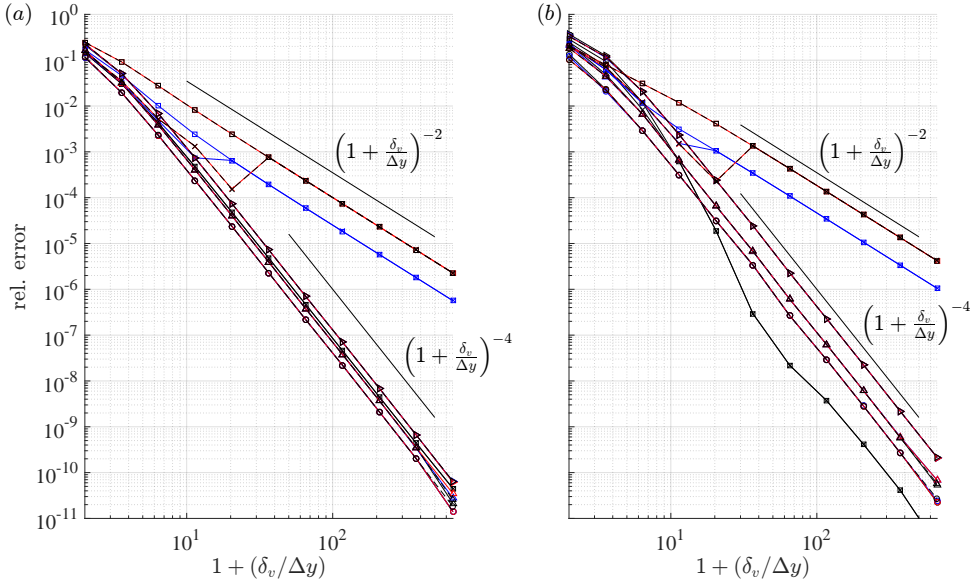
Figure 4.17: Approximations of the shear profile $d\bar{U}/dy$ of the tanh-profile. Exact profile (dash-dotted), calculated profiles using 2nd (a), 4th (c) and 6th (e) order finite differences with the spacing $\Delta y = \delta_v/2$. Profile generated with an odd (solid) and even (dashed) number of nodes, shifting the nodes by 0 (black solid), $\Delta y/4$ (blue) and $\Delta y/2$ (red) with respect to y_c . (b,d,f) Interpolated profiles onto the Chebyshev grid (keeping $N_y = 81$ constant). Shear maxima on the uniform grid (\times).

inflection point are therefore illustrative of the error in the maximum shear value. The difference between the second and fourth order differences is thus approximately 10 percent points, that between the fourth and sixth order schemes is about 3 percent points.

The resulting convergence plots are shown in figure 4.18. The apparent convergence orders are indicated with the straight line segments. The stability results consistently attain fourth order convergence. The error curves corresponding to the stability results for the shifted grids are indistinguishable, even for a very small number of grid points. This illustrates that the convergence of the stability results obtained with the current differentiate-then-interpolate methodology is independent of the specific orientation of the base flow grid. The accuracy of the stability results is not affected by (in)exactly capturing the inflection point.

The results for the tanh- and gtanh-profiles differ primarily in that the relative errors for the latter profile are slightly larger. This is mainly established by α_n , which always resembles the parameter subject to the largest error. This is logical in the sense that the eigenfunctions have a more concentrated character for this larger wavenumber. To ensure relative errors less than 1% for the growth rate only, it is suggested to use at least 5 grid points to resolve the shear layer. At least 8 points are required to yield smaller than 1% relative errors for all parameters.

When measuring the shear exactly at the inflection point for the tanh-profile, the



4

Figure 4.18: Relative error convergence versus the number of grid points having coordinates $(y - y_c)/(\delta_v/2) \in [-1, 1]$ for the tanh- (a) and gтанh- (b, $y_v - y_c = -0.5\delta_v/2$) profiles. Symbols represent: $\alpha_n \delta_v$ ($>$), $\alpha_m \delta_v$ (Δ), $\omega_{i,m} \delta_v / \Delta \bar{U}$ (\circ), the maximum shear on the uniform grid (\square) and on the Chebyshev grid ($+$). The colors represent different shifts with respect to the symmetrical node distribution: 0 (black), $\Delta y/4$ (blue), $\Delta y/2$ (red) with an odd (solid) and even (dashed) number of equispaced nodes.

errors of the stability results closely correspond to the errors in the maximum shear. Figure 4.18 illustrates that the measurement location is quite crucial, however. In all cases where the maximal shear level is measured on the grid points or the Chebyshev collocation nodes, while none lies exactly on the inflection point, a much larger error is extracted. In particular, a second order convergence rate is retrieved. This is expected in the light of the parabolic shape of the shear profile and that the off-center nodes approach the inflection point linearly as Δy decreases.⁵ Nevertheless, the actual error in the stability results consistently displays a fourth order convergence rate. Measuring the error in the shear on the uniform grid points or Chebyshev nodes can thus yield a very pessimistic prognosis of the error in the stability results. When the error in the shear of the gтанh-profile is evaluated exactly at the inflection point, it becomes much smaller than the error in the stability results; it is unknown why this is the case.

4.7.2. SPATIAL SMOOTHING

The velocity vectors delivered by PIV are obtained through the use of an interrogation volume. This means that, instead of a point measurement in space, the vector is a spatial average over the interrogation volume. Therefore, the velocity fields are effectively

⁵The curves jump suddenly to this part displaying second order convergence. This jump corresponds to the uniform grid points becoming more densely spaced than the Chebyshev grid in the shear layer; the latter has 26 nodes inside the shear layer.

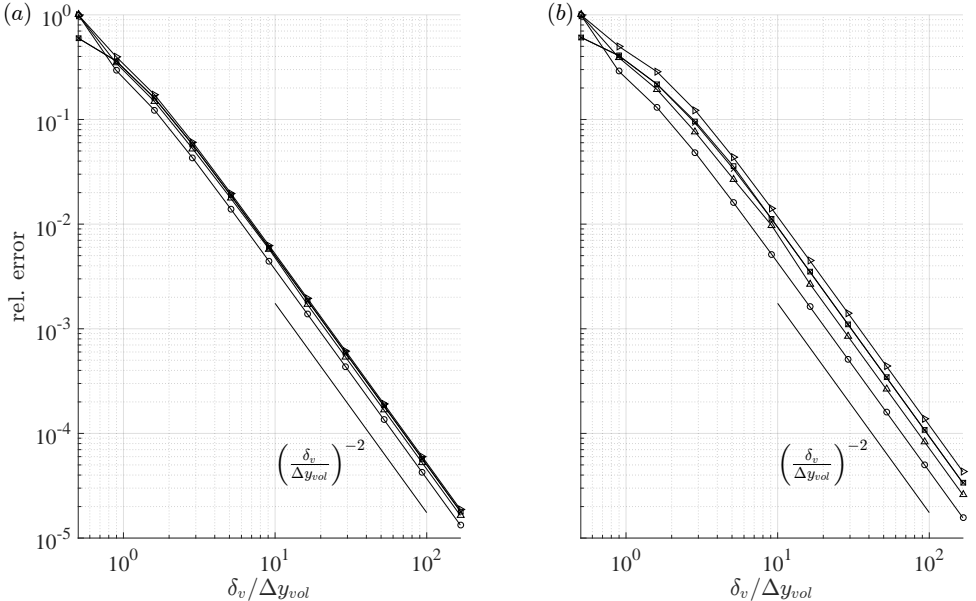


Figure 4.19: Relative error convergence versus the number of interrogation volumes for the tanh- (a) and gtanh- (b, $y_v - y_c = -0.5\delta_v/2$) profiles smoothed using a 5-point spatial average at $Re_{\delta_v} = 50$. Symbols represent: $\alpha_n \delta_v$ (\triangleright), $\alpha_m \delta_v$ (\triangle), $\omega_{i,m} \delta_v / \Delta U$ (\circ), the maximum shear level on the uniform grid (\square) and on the Chebyshev grid (+).

smoothed.

To represent the effect of this smoothing, a simple 5-point spatial average is taken of the exact solution on the uniform grid before the solution is differentiated and interpolated. This is a highly simplified model representation of an interrogation window used for the cross-correlation step in the PIV post-processing, assuming a standard window overlap of 75% is maintained. With respect to base flows measured with PIV, one is interested in the required amount of the model interrogation windows to resolve the shear layer appropriately. These windows have an extent of $\Delta y_{vol} = 4\Delta y$. In turn, $\delta_v / \Delta y_{vol}$ represents the amount of interrogation windows used, put side-to-side, to resolve the shear layer.

The convergence results corresponding to the smoothed profiles are shown in figure 4.19. The convergence rate is significantly obstructed by smoothing; a second order rate is attained. As a consequence, a relatively large number of grid nodes is required to obtain representative results.

It is found that, to ensure relative errors of 1% in the growth rates, the shear layer must be resolved with at least 7 neighbouring interrogation windows. This requirement exceeds what was possible to achieve experimentally, at least for the application cases considered in this thesis. For the most unstable instabilities in the micro-ramp and crossflow vortex cases, the achieved range of these numbers is found to be equal to

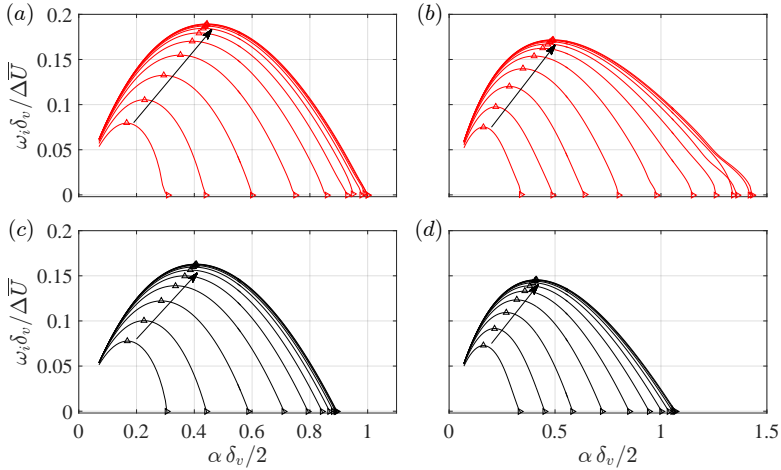


Figure 4.20: Temporal spectra for a varying number of model interrogation window sizes per vorticity thickness $\delta_v/\Delta y_{vol}$ ($= 0.50, 0.71, 1.01, 1.43, 2.03, 2.89, 4.10, 5.82, 8.27, 11.7, 16.7$) for the tanh- (a,c) and gtanh- (b,d), $y_v - y_c = -0.5\delta_v/2$) profiles, with $Re_{\delta_v} = \infty$ (a,b) and 50 (c,d). Most unstable (Δ) and largest neutral wavenumber (\triangleright). Arrows indicate direction of increasing $\delta_v/\Delta y_{vol}$.

1.58 – 2.08 and 1.54 – 1.58, respectively.⁶ This result implies that quantitative information extracted with the current methodology has to be treated carefully. In particular, it demonstrates the requirement of validating the stability results with the experimental measurement data. Covering the other characteristics up to 1% relative errors requires at least 11 neighbouring windows.

MOVEMENT OF SPECTRUM

Due to the relatively large impact of smoothing, its effect on the stability results deserves further investigation. Figure 4.20 shows the spectrum for different small values of $\delta_v/\Delta y_{vol}$. Large changes are observed in all measured properties, but the movement of the spectrum is well-behaved. In particular, all properties, the growth rate, most unstable and largest neutral wavenumber, decrease when applying a stronger smoothing (i.e. decreasing $\delta_v/\Delta y_{vol}$). These trends are shown in figure 4.21. The results are practically indistinguishable from the reference when the shear layer is resolved with more than 8 model interrogation windows. This statement does not apply for the second neutral wavenumber, α_n , corresponding to the inviscid perturbations on the gtanh-profile in figure 4.21 (d). In that case, the deviation from the reference is due to its inherent sensitivity, as discussed previously. The data point at $\delta_v/\Delta y_{vol} = 1.43$ presents a worst-case estimate for the application cases. The most unstable growth rate of inviscid perturbations is subject to a reduction of approximately 19% with respect to the reference value.

⁶For the micro-ramp, the (wall-normal) vorticity thickness ranges from 0.45–0.59 h (see figure 5.10 (a)) and the height of the interrogation volumes equals 0.284 h . For the crossflow vortices, the vorticity thickness equals 0.104–0.107 λ_r , and is rotated 40° with respect to the grid, see table 6.4 and figure 6.34. In the vertical direction, the shear layer appears slightly broader, dividing the previous numbers by cos 40° yields: 0.136–0.140 λ_r . The height of the interrogation volume is 0.088 λ_r .

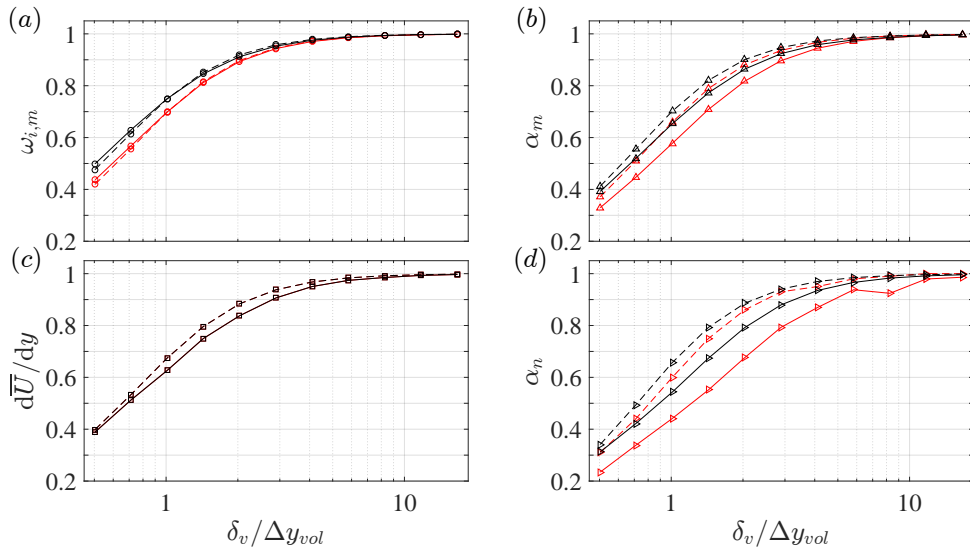


Figure 4.21: Ratios of the stability properties (a: $\omega_{i,m}\delta_v/\Delta\bar{U}$, b: $\alpha_m\delta_v/2$, c: $(d\bar{U}/dy)(\delta_v/\Delta\bar{U})$, d: $\alpha_n\delta_v/2$) over the non-smoothed reference properties for a varying number of model interrogation window sizes per vorticity thickness $\delta_v/\Delta y_{vol}$ ($= 0.50, 0.71, 1.01, 1.43, 2.03, 2.89, 4.10, 5.82, 8.27, 11.7, 16.7$) for the tanh- (dashed lines) and gtanh- (solid lines, $y_v - y_c = -0.5\delta_v/2$) profiles at $Re_{\delta_v} = \infty$ (red) and 50 (black). In (c), the curves corresponding to the inviscid and viscous analyses overlap, because the curves involve the base flow's shear profile only.

The reduction of viscous growth rates is slightly less, approximately 15% with respect to the reference value. The other parameters are reduced more significantly.

The most striking fact observed in figure 4.21 is that the trend in the different variables is very similar. Although there is a difference from variable to variable, these results suggest the data could be successfully corrected for the effect of the smoothing. In particular, the trend in the growth rate, $\omega_{i,m}$, shows an independency with respect to the profile shape (!). These results are found to be independent of the arrangement of the grid, i.e. when shifting the grid by the maximal amount of $\Delta y/2 = \Delta y_{vol}/8$. Figure 4.21 can thus be used to estimate the reduction in, for example, the growth rate and most unstable wavenumber when performing the stability analysis of a smoothed base flow.

INTEGRITY OF THE UNDERLYING PROCESSES

Given the well-behaved nature of the spectrum, the question arises whether particular features of the solutions are preserved. To this end, first the eigenfunctions are considered for several $\delta_v/\Delta y_{vol}$ -values in figures 4.22 and 4.23 for the tanh- and gtanh-profiles, respectively. For the tanh-profile, the smoothing does not change location of the inflection point. Therefore the maximum of the \hat{u} eigenfunction is located at $y = y_c$ consistently. The main effect of the smoothing is to extend the spatial support of the eigenfunctions. Noticing that $\Delta\bar{U}$ is unaffected, the thickness of the shear layer is effectively extended through the reduction of the maximum shear (see equation (4.2)). This extension is visualised with the dash-dotted lines in figures 4.22 and 4.23. Those lines closely

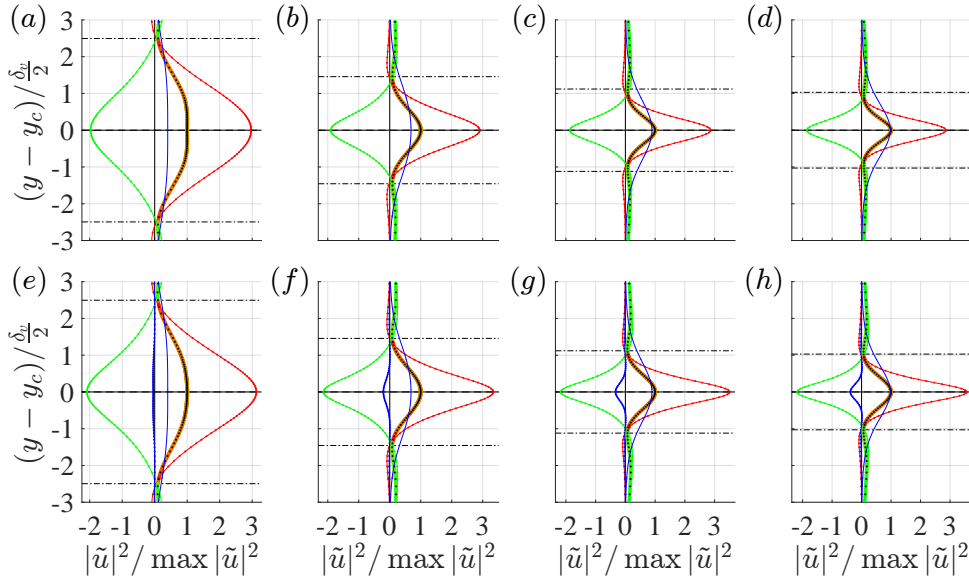


Figure 4.22: Perturbation energy (thick line) in the components \tilde{u} with respect to different interrogation window sizes $\delta_v/\Delta y_{vol}$ ($= 0.50$ (a,e), 1.01 (b,f), 2.03 (c,g), 4.10 (d,h)), $Re_{\delta_v} = \infty$ (a – d) and 50 (e – h) and the contributions of the Reynolds stress (red), pressure (green) and viscous (blue) terms for the tanh-profile. The value $\alpha = \alpha_m$ is used for each individual case as indicated in figure 4.21. Smoothed shear profile (blue). The dash-dotted lines indicate the effective vorticity thickness based on the modified shear strength.

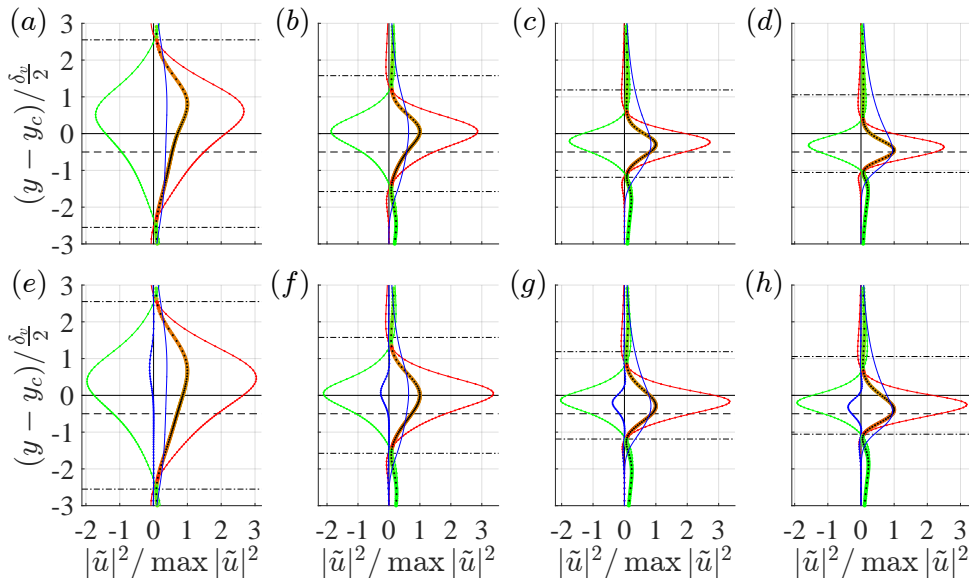


Figure 4.23: Perturbation energy (thick line) in the components \tilde{u} with respect to different interrogation window sizes $\delta_v/\Delta y_{vol}$ ($= 0.50$ (a,e), 1.01 (b,f), 2.03 (c,g), 4.10 (d,h)), $Re_{\delta_v} = \infty$ (a – d) and 50 (e – h) and the contributions of the Reynolds stress (red), pressure (green) and viscous (blue) terms for the granh- $(y_v - y_c = -0.5\delta_v/2)$ profile. The value $\alpha = \alpha_m$ is used for each individual case as indicated in figure 4.21. Smoothed shear profile (blue). The dashed line indicates y_v and the dash-dotted lines indicate the effective vorticity thickness (with respect to y_c).

capture the region where the eigenfunctions are produced by the Reynolds stress terms.

Just as in figures 4.8 and 4.9, the contributions of the different terms to the eigenfunction are shown in figures 4.22 and 4.23. This allows the general observation that, although the *shapes* of these contributions can change, their relative *size* is essentially independent of the smoothing. In this sense, the smoothing does not affect the underlying mechanism of the eigenfunction.

The contribution of the viscous terms changes significantly, but this only has a minor effect on the overall shape of the eigenfunctions, because it is a small contribution (it is completely absent for inviscid perturbations, of course). In particular, the dissipation is activated for large $\delta_v/\Delta y_{vol}$, because the support of the eigenfunction is most limited in that case, which induces the largest gradients.

For the gtanh-profile, the location of the inflection point moves as a function of $\delta_v/\Delta y_{vol}$. The maximum of the \tilde{u} eigenfunction follows this movement. For small enough $\delta_v/\Delta y_{vol}$, therefore, the maximum of \tilde{u} is displaced to the opposite side of $y = y_c$. However, again, the relative size of the contributions is affected only to a minor extent.

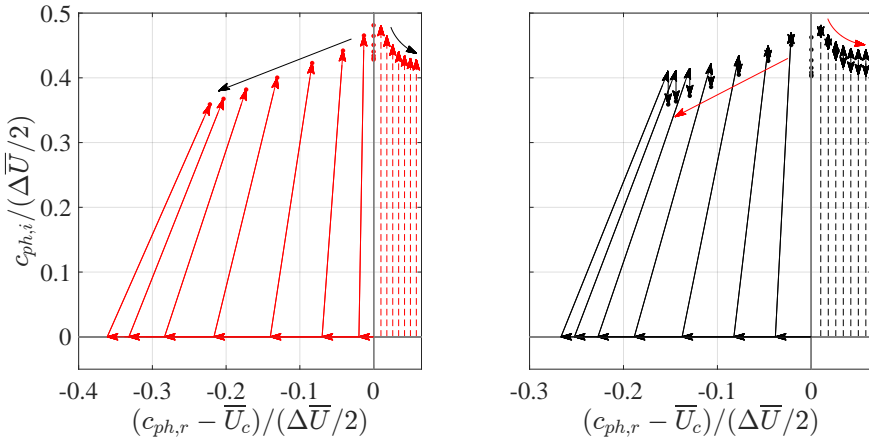
FACTORING THE EFFECTIVE LENGTH SCALE

If the spatial coordinate is rescaled to the effective shear layer, the differences in the eigenfunctions are hard to distinguish, especially for the tanh-profile. This motivates assessing the eigenvalues while factoring out the difference in the inherent length scale. In figure 4.24, the eigenvalues corresponding to different $\delta_v/\Delta y_{vol}$ -values are shown together with their decompositions into the terms of equation (4.12). Instead of presenting the values of ω as in figure 4.7, the complex phase speed, c_{ph} , is shown, which effectively factors the change of the maximum wavenumber α_m . This establishes a fair comparison of the different cases, because it factors the changing inherent length scale for different $\delta_v/\Delta y_{vol}$.

As $\delta_v/\Delta y_{vol}$ increases (the direction indicated with the arrows), $c_{ph,i}$ decreases. This behaviour can be deduced from figures 4.21 (a) and (b), because the line corresponding to α_m lies below that for $\omega_{i,m}$. The variation of $c_{ph,i}$ is much smaller than that for ω_i , which shows that factoring the inherently length scale covers most variation imposed by the smoothing. This is particularly true for the tanh-profile; recording a maximum change of 15% with respect to the reference as opposed to a 58% change of $\omega_{i,m}$ for the considered values of $\delta_v/\Delta y_{vol}$. The change for the gtanh-profile is larger (up to 29%), but still much smaller than that displayed by ω_i . This confirms that the change of the inherent length scale of the shear layer is largely responsible for the change of ω_i .

As mentioned in §4.7.1, all results are scaled with the exact references scales, although they may not be available in practice. The latter results show that scaling with the effective length scale (that would be measured) can significantly mask the stabilised nature of the results. Although care should be taken in interpreting the possibly stabilised results, the described physical processes are indicative of the modes of interest.

The remaining variation of $c_{ph,i}$ is due to redistributions of the contributing terms. When consulting the eigenfunctions, the region over which the Reynolds stress has a productive character and the extent of the shear layer changes. The part of the eigenfunction that is coloured red becomes smaller with respect to the dash-dotted lines as $\delta_v/\Delta y_{vol}$ increases. This is an explanation for the decrease in $c_{ph,i}$ for increasing $\delta_v/\Delta y_{vol}$ (in particular the the decrease of the imaginary contribution of the Reynolds stress terms).



4

Figure 4.24: Change of the terms (arrows) in equation (4.12) making up the most unstable eigenvalues (dots) with respect to different interrogation window sizes $\delta_v/\Delta y_{vol}$ ($= 0.50, 0.71, 1.01, 1.43, 2.03, 2.89, 4.10$) for the tanh- (solid) and gtanh- (dashed, $y_v - y_c = -0.5\delta_v/2$) profiles at $Re_{\delta_v} = \infty$ (a) and 50 (b). See figure 4.7 for a labelling of the terms. The value $\alpha = \alpha_m$ is used for each individual case as indicated in figure 4.21. Arrows (a: black, b: red) indicate the direction of increasing $\delta_v/\Delta y_{vol}$, i.e. the direction of less smoothing.

In the case of the viscous analyses, the contribution of dissipation to $c_{ph,i}$ increases with $\delta_v/\Delta y_{vol}$ as discussed before. It is interesting to note that this increase closely corresponds to an opposing action of the Reynolds stress term that converges more quickly for increasing $\delta_v/\Delta y_{vol}$ than in the inviscid case.

For small $\delta_v/\Delta y_{vol}$, the maximum of the $|\tilde{u}|$ -eigenfunction for the gtanh-profile was found to be located on the opposite side of $y = y_c$. Figure 4.24 illustrates that the phase speed c_{ph} does attain negative values for all considered values of $\delta_v/\Delta y_{vol}$, corresponding to the correct side. As found before, this emphasises that the phase speed is more robust to changes in the location of the inflection point and therefore it is a more reliable parameter for tracking the location of the eigenfunctions. This makes sense from the point of view of equation (4.13), indicating the phase speed is a global, instead of a point-, measurement of the eigenfunction.

4.7.3. RESIDUAL PERTURBATIONS

PIV measures an instantaneous snapshot of the flow field at a given time. By combining many snapshots, one retrieves a time-averaged flow, which may be subject to the presence of perturbations in the instantaneous flow field.

The instantaneous flows of interest can be described as a base flow plus perturbations. In turn, these perturbations consist of a fluctuating and mean part. The mean part is due to the non-linear interaction of finite amplitude perturbations. It is here assumed that the mean flow represents the base flow, i.e. that the perturbations in the instantaneous flow behave as linear waves and are too weak to distort the base flow. That is, the mean part of the residual perturbations is neglected.

Averaging the complementary fluctuating part in time is thus assumed to yield a zero mean. In practice, however, only a finite amount of time samples is available. In that

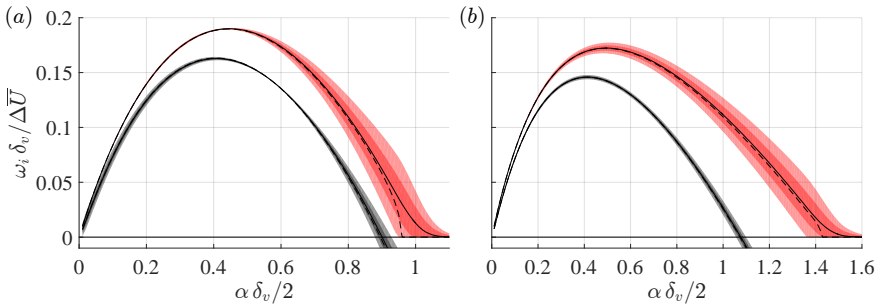


Figure 4.25: Growth rate uncertainty due to fluctuating residual perturbations for $N_{fr} = 25$, each instantaneous field contains perturbations with an r.m.s. amplitude of 20% $\Delta \bar{U}$ and a random phase, for the tanh- (a) and gtanh- (b, $y_u - y_c = -0.5\delta_v/2$) profiles at $Re = \infty$ (red shades), 50 (grey shades). Mean (black solid), one standard deviation σ (inner shaded region), 2σ (outer shaded) for an ensemble of 1000 cases and $N_{fr} = \infty$ (black dashed).

4

case, residual perturbations are expected with respect to the mean flow that would result if infinitely many samples were used. To assess the influence of these perturbations on the stability results, mean flows are constructed by superposing random instances of the most unstable eigenfunctions onto the base flow. This is done N_{fr} times to simulate the use of N_{fr} uncorrelated instantaneous snapshots. Specifically, the eigenfunctions are equipped with a constant amplitude and random phase with an r.m.s. amplitude equal to 20% of $\Delta \bar{U}$ (i.e. the maximum of $|\tilde{u}|$ is set equal to $0.10 \times \sqrt{2}$ with respect to $\Delta \bar{U}/2$). It is unrealistic to assume real perturbations with amplitude of 20% of $\Delta \bar{U}$ still behave linearly and have a zero mean. A relatively large amplitude is chosen to amplify the small errors in the results. To ensure representative statistics corresponding to one value of N_{fr} , 1000 mean flows are generated per N_{fr} . The stability analysis is performed on each flow, performing a sweep over α . Equation (4.8) (o) is used instead of system (4.6), because this is computationally less expensive and the required minimal error, $O(10^{-5})$, is relatively large. This also allowed reducing the resolution; $N_y = 51$ was used.

Surprisingly, for $N_{fr} = 25$, the spectra corresponding to representative cases are only slightly disturbed as shown in figure 4.25. This parameter combination results in an expected residual amplitude of $0.10/\sqrt{25} = 2\%$ relative to $\Delta \bar{U}/2$. The uncertainty increases as α increases. This is expected, because the random cancellation of the perturbation's spatial structure results in an effective perturbation with a relatively large wavenumber in y . For the tanh-profile, it is found that the viscous case is subject to uncertainty for small α . On the other hand, the uncertainty is highly reduced for the viscous perturbations on the gtanh-profile. A possible explanation for the reduced sensitivity of the latter profile is its asymmetric shape in y . The perfect symmetry of the tanh-profile is distorted by the perturbations.

To assess the general behaviour of the uncertainty in the stability results, larger values of N_{fr} are considered. Presenting the worst case scenario, viscous perturbations on the tanh-profile are considered. For each value of N_{fr} , a mean flow is again constructed 1000 times, so to yield trustworthy statistical data. The results are presented in figure 4.26. The symbols indicate the mean error, while the tip of the tails show the standard

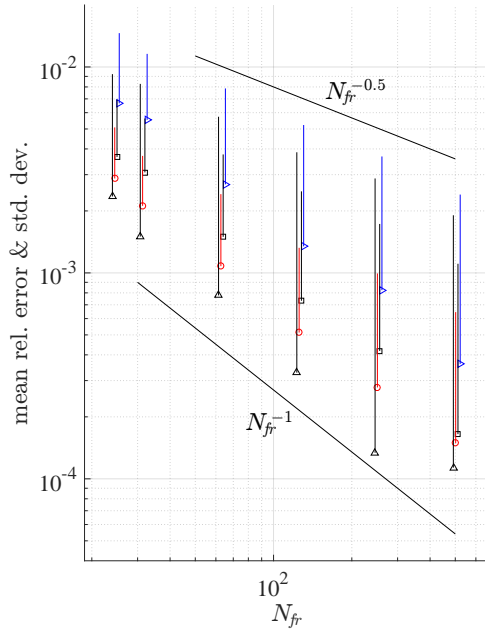


Figure 4.26: Mean error (symbols) and standard deviation (tip of the tail) of the stability properties for 1000 mean flow fields approximating the (most sensitive) tanh-profile, each constructed with N_{fr} instantaneous flow fields ($= 25$ and the powers of 2) at $Re = 50$. Stability properties: $\alpha_n \delta_v$ (\triangleright), $\alpha_m \delta_v$ (\triangle), $\omega_{i,m} \delta_v / \Delta \bar{U}$ (\circ) and the maximum of $d\bar{U}/dy$ (\square). The different properties are located at slightly different N_{fr} -values to allow distinguishing the standard deviation lines.

deviation. The mean values correspond to relative errors less than 1% for all considered values of N_{fr} , while approximately $N_{fr} = 50$ is required to lower the standard deviation below 1%. Also the standard deviation of the growth rate is smaller than 1% for all considered values of N_{fr} .

A convergence rate of $1/\sqrt{N_{fr}}$ is expected, i.e. an algebraic convergence with the rate 0.5. This clearly applies to the standard deviations in this case, a rate of 0.600 is found. For the mean values, instead, a convergence rate of approximately 1 is found. The errors in the maximum shear also resemble this first order rate. It is therefore expected that, while the perturbations yield $1/\sqrt{N_{fr}}$ errors for the values of \bar{U} , the shear is not equally affected. Accordingly, the stability results are also expected to converge faster in the mean. This illustrates that, although $1/\sqrt{N_{fr}}$ is expected, higher convergence rates can be observed.

4.8. CONCLUSION

This chapter reviews the basic stability characteristics of a free shear layer, that are relevant in the context of this thesis.

The analysis is elaborated on in detail to illustrate all practical aspects of the stability methodology. An extensive effort is spent in describing the assessment of the eigenvalue

and -functions from the perspective of the terms in the stability equations. This reveals the mechanisms underlying the eigenmode. For example, it was shown that only the middle part of the streamwise velocity eigenfunction is produced by the Reynolds stress terms, while the outer parts are generated via pressure-strain effects. As known from literature [17–19], it is emphasized that the maximum shear value is the most important base flow quantity. Properly resolving the maximum shear ensures high quality stability results.

Furthermore, several physical effects were identified, notably those due to the shape of the profile (by moving the location of the inflection point as done by [2]), a spanwise wavenumber and the proximity of a wall. All effects were shown to be stabilising when scaling the results with the vorticity thickness, which fixes the maximum shear of the velocity profile.

4

Lastly, the expected methodological effects related to the use of measured base flows are assessed. In particular, the considered errors are those due to spatial resolution of the base flow, the spatial smoothing of the base flow due to PIV processing and the use of a finite number of zero-mean perturbations represented by the most unstable eigenfunction. From the perspective of measured base flows, it is assumed throughout this thesis that the “mean = base flow”-hypothesis holds, i.e. that the mean flow is a good approximation of the base flow. Ordered from most to least important, it is found that:

- *spatial smoothing of the base flow*: establishes a significant stabilising effect for the cases considered in this thesis; it is found that the characteristic parameters follow a well-defined global trend and the main underlying mechanisms are conserved; but the presence of spatial smoothing establishes the requirement of validating the stability results with the instantaneous experimental data, especially in the case of asymmetric shear layers
- *spatial resolution of the base flow*: can be approached by computing the spatial derivatives of the base flow with higher order finite differences and interpolating the base flow onto the grid used for the stability analysis; this yields a better approximation of the shear at the inflection point
- *residual zero-mean perturbations on the base flow*: have a small impact and the related error can converge faster than the expected rate of $1/\sqrt{N_{fr}}$, where N_{fr} denotes the number of instantaneous ‘snapshots’ of the flow field.

To ensure relative errors of less than 1% in the temporal growth rates, it is suggested to resolve the shear layer with at least: 5 uniform grid points and 7 neighbouring interrogation windows (with 75% overlap, this implies using $7 \times 4 + 1 = 29$ grid points for PIV). Using 50 instantaneous snapshots containing zero-mean perturbations with an r.m.s. amplitude of 20% with respect to the streamwise base flow velocity (difference) yields relative errors smaller than 1% for all considered stability characteristics.

REFERENCES

- [1] A. Michalke, *Survey on jet instability theory*, Progress in Aerospace Sciences **21**, 159 (1984).

- [2] A. Michalke, *The instability of free shear layers*, Progress in Aerospace Sciences **12**, 213 (1972).
- [3] A. Michalke, *The influence of the vorticity distribution on the inviscid instability of a free shear layer*, Tech. Rep. (Deutsche forschungs- und versuchsanstalt für Luft- und Raumfahrt EV Berlin, 1970).
- [4] P. J. Schmid and D. S. Henningson, *Stability and Transition in Shear Flows* (Springer Verlag, 2001).
- [5] C. Cossu and L. Brandt, *On Tollmien–Schlichting-like waves in streaky boundary layers*, European Journal of Mechanics-B/Fluids (2004).
- [6] R. L. Panton, *Incompressible flow* (New York: John Wiley and Sons, 1984).
- [7] R. B. Lehoucq, D. C. Sorensen, and C. Yang, *ARPACK users guide: Solution of large scale eigenvalue problems by Implicitly Restarted Arnoldi Methods*. (1997).
- [8] T. Tatsumi, K. Gotoh, and K. Ayukawa, *The stability of a free boundary layer at large Reynolds numbers*, Journal of the Physical Society of Japan **19**, 1966 (1964).
- [9] R. Betchov and A. Szewczyk, *Stability of a shear layer between parallel streams*, The Physics of Fluids **6**, 1391 (1963).
- [10] A. Michalke, *On the inviscid instability of the hyperbolic-tangent velocity profile*, Journal of Fluid Mechanics **19**, 543 (1964).
- [11] R. W. Metcalfe, S. A. Orszag, M. E. Brachet, S. Menon, and J. J. Riley, *Secondary instability of a temporally growing mixing layer*, Journal of Fluid Mechanics **184**, 207 (1987).
- [12] A. Boguslawski, *Inviscid instability of the hyperbolic-tangent velocity profile—spectral “tau” solution*, Task Quarterly **5**, 155 (2001).
- [13] T. Tatsumi and K. Gotoh, *Stability of free boundary layers between two streams*, J. Fluid Mech. **7**, 433 (1960).
- [14] P. G. Drazin and W. H. Reid, *Hydrodynamic Stability* (Cambridge University Press, 2004).
- [15] R. Betchov and J. Criminale, W. O., *Stability of parallel flows* (Academic Press, 1967).
- [16] J. M. Foucaut and M. Stanislas, *Some considerations on the accuracy and frequency response of some derivative filters applied to particle image velocimetry vector fields*, Measurement Science and Technology **13**, 1058 (2002).
- [17] D. Arnal, *Boundary layer transition: Predictions based on linear theory*, in *Special course on Progress in Transition Modelling*, R-793 (AGARD, 1994).
- [18] H. L. Reed, W. S. Saric, and D. Arnal, *Linear stability theory applied to boundary layers*, Annual Review of Fluid Mechanics **28**, 389 (1996).
- [19] V. Theofanis, *Advances in global linear instability analysis of nonparallel and three-dimensional flows*, Progress in Aerospace Sciences **39**, 249 (2003).

5

MEASURED BASE FLOWS: MICRO-RAMP WAKE

The first application case testing the applicability of stability theory on measured base flows involves the flow around a micro-ramp vortex generator. Hairpin shaped Kelvin-Helmholtz waves are observed in tomographic PIV experiments on the micro-ramp's wake. In this study, these waves are reproduced by applying BiGlobal stability theory to base flows conceived with the measurement data. The stability results converge with the number of instantaneous snapshots used for the base flow. The most unstable wavelength lies in the experimentally observed range and the flow structure closely resembles that shown in the snapshots.

5.1. INTRODUCTORY REMARKS

In supersonic flight, jet propulsion has to be approached in a different way as opposed to subsonic flight. Shock waves are formed as the supersonic incident flow rams into the vehicle, that cause a loss of total pressure, which is required for the engine to perform efficiently. The inlet of supersonic jet engines, like those of the Blackbird, are equipped with shock cones, see figure 5.1, inducing an oblique shock wave minimising these losses. The part of the flow entering the engine encounters a sequence of shocks, the first induced by the cowl lip, see the first zoom in figure 5.1. It is imperative to optimise the behaviour of the shock system for the efficient operation of the engine.

An important role is played by the interaction of the shock wave with solid interfaces, that results in the reflection of the shock. The solid interface is enclosed by a boundary layer, so a Shock-Wave/Boundary-Layer Interaction (SWBLI) results, see the second zoom in figure 5.1. This has a significant impact on the evolution of the boundary layer. The static pressure increases as the flow passes through the incident shock. For the subsonic part of the boundary layer, this means that fluid particles are pushed in the upstream direction. For a strong enough pressure jump, this force causes the flow

The paper accompanying this chapter is published as an AIAA conference paper [1].

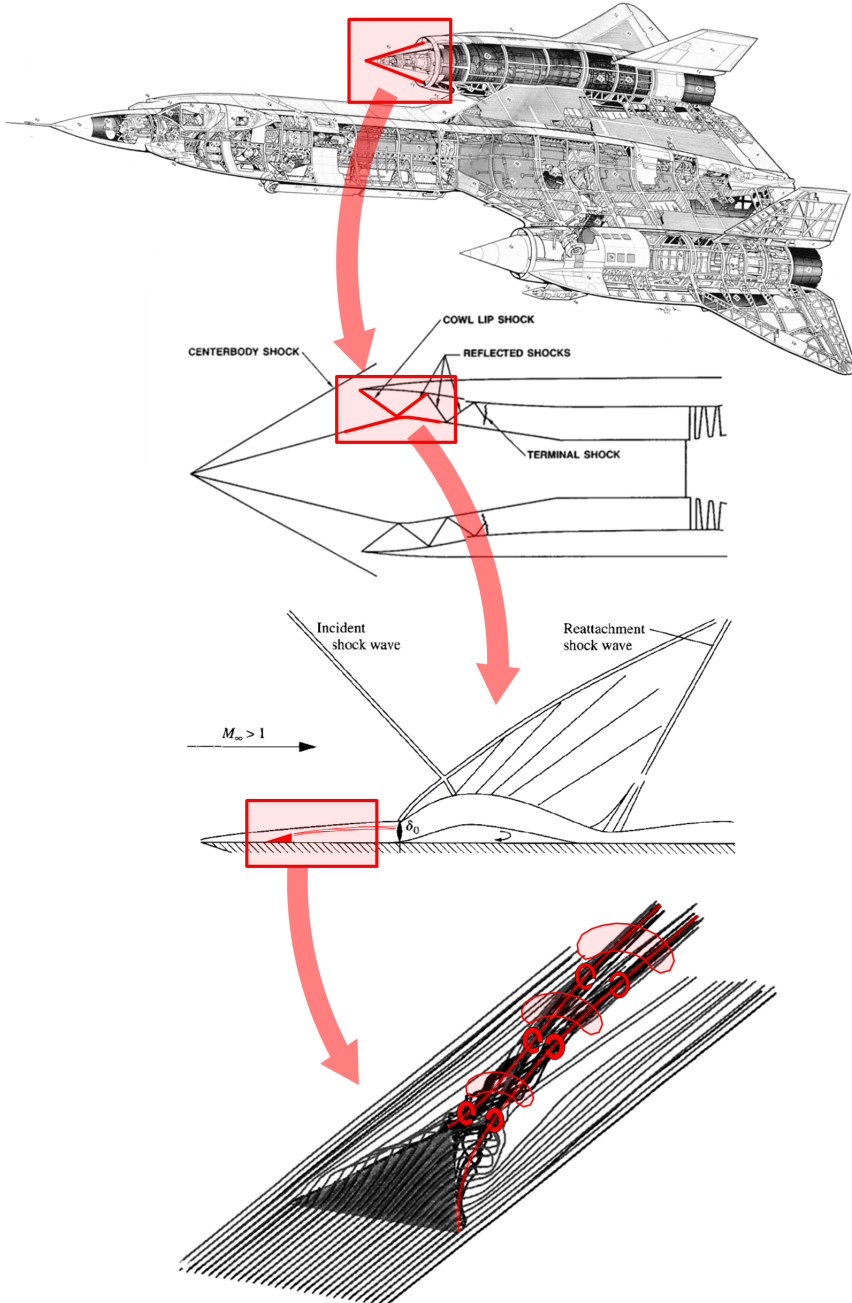


Figure 5.1: Sequences of zooms from the perspective of the inlet cone of the Lockheed YF-12A aircraft [2], a forerunner of the SR-71 Blackbird. First zoom on the shock system inside the cowl, second on the Shock-Wave/Boundary-Layer Interaction (SWBLI, [3]) and third on the flow around a micro-ramp roughness element, figure adapted version of Ghosh *et al.* [4]. The micro-ramp is used to alleviate the flow separation region in the SWBLI, which, in turn, reduces the pressure loss through the shock system, see [5].

to separate. A large scale separation can precipitate unsteady dynamics of the reflected shock system. Babinsky and Harvey [6, cf. page 123] feature a scenario where the separation can result in a catastrophic engine unstart. This prompted research into controlling the SWBLI.

The main technique deployed is a bleed system [7, 8]. By extracting low-momentum fluid from the flow, a fuller boundary layer results that is more resistant against separation. The optimisation study of Anderson *et al.* [9] identified, however, that using an array of micro-ramp roughness elements yields superior performance over boundary bleed. Babinsky *et al.* [5] add that this roughness geometry is structurally robust and therefore attractive for manufacturers in a practical sense.

The geometry of the micro-ramp vortex generator is highlighted in the last zoom in figure 5.1. The flow features two counter-rotating vortices that induce an upwash along the spanwise symmetry plane. This displaces low-momentum fluid to a higher position in the boundary layer in this symmetry plane. At the lateral sides of the vortex pair, high-momentum fluid is entrained deeper into the boundary layer, which causes the fuller boundary layer profile that increases the resistance against separation.

The upwash in the center-plane enhances the flow shear in an arc-shape above the vortex pair. This region is also indicated in figure 5.1. As previously explained, the enhanced shear produces perturbations. Sun *et al.* [10] and Ye *et al.* [11] show that, in particular, Kelvin-Helmholtz (KH) type perturbations are generated that have a hairpin shape, see figure 5.2. Ye *et al.* [11, 12] studied the flow at incompressible speeds, allowing a detailed look into the transition process of the wake. In [12], it was determined that the hairpins protrude into the ultimate turbulent wedge and therefore are expected to play an important role in the transition mechanism. It is shown that the vortex structures named leg-buffers are generated, see figure 5.2, representing a mechanism through which the wake extends in the spanwise direction.

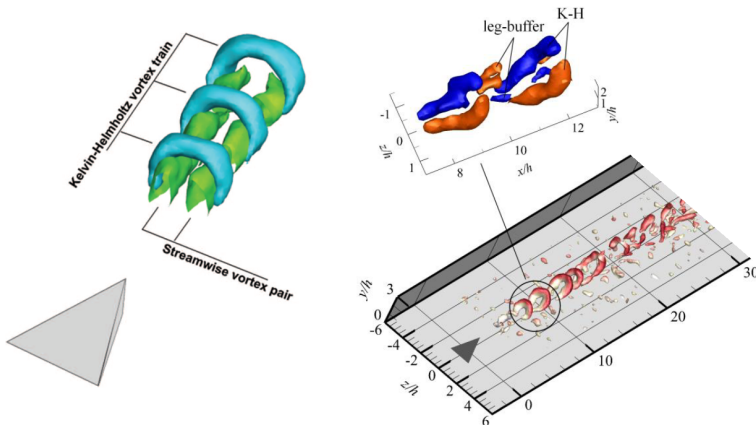


Figure 5.2: (left) Isocontours of the streamwise (green) and magnitude of the spanwise and wall-normal (blue) vorticity component in supersonic flow conditions ($M = 2$) [10]. (right) λ_2 isocontours colour coded by the streamwise velocity (view including ramp) and streamwise vorticity isocontours indicating parts related to the KH eigenmode and leg-buffer parts (inset) [13].

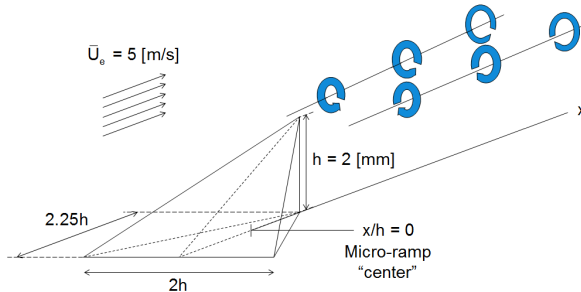


Figure 5.3: Isometric schematic of the micro-ramp geometry and the base flow.

5

In this particular flow case, the perturbation field is found to have a highly monochromatic behaviour, despite its large amplitude, which suggests that the mean flow field is minimally affected by non-linear perturbation dynamics and accurately represents the base flow for a large enough amount of samples, while, at the same time, the perturbation can be measured with high experimental accuracy.

Furthermore, KH-modes, being inviscid instabilities, do not require a highly accurate second order base flow derivative.

These considerations form the justification for the main objective of the present study, which is to investigate whether the hairpins can indeed be reproduced using linear stability theory relying on base flows that have been obtained by experiments.

The approach is to investigate the influence of the different “resolutions” of the experimental base flow on the stability results. The objective is considered fulfilled if the stability characteristics are converged with respect to the base flow parameters on the one hand. On the other hand, experimental validation is relied upon, for which the most unstable wavelength is taken as the main parameter. In the PIV measurement, this was found to be $3.5h \pm 0.5h$ in the streamwise range $x/h \in [8, 11]$. The latter is from now on referred to as the range of interest. Upstream of this region, the structures are too small to be captured by the measurement. The convergence of the spectral information with the base flow characteristics is considered and the most unstable modes are compared with the instantaneous flow structures observed in the experiment to yield the validation of the approach. Furthermore, the spectral results are decomposed in the important physical effect by applying Rayleigh and Orr-Sommerfeld (i.e. local in x and z) analysis to the wall-normal symmetry plane profiles.

5.2. BASE FLOW DESCRIPTION

A schematic of the geometry of the micro-ramp and the laminar base flow is shown in figure 5.3. The micro-ramp is 2 mm high and symmetric about the streamwise-wall-normal center plane, its center is placed 290 mm from the elliptical leading edge of the supporting flat plate. The freestream velocity $\bar{U}_e = 5 \text{ m/s}$, in this case. The associated Reynolds numbers are $Re_h = 685$ and $Re_{hh} = 460$.

Both experimental and computational efforts were undertaken to resolve the base

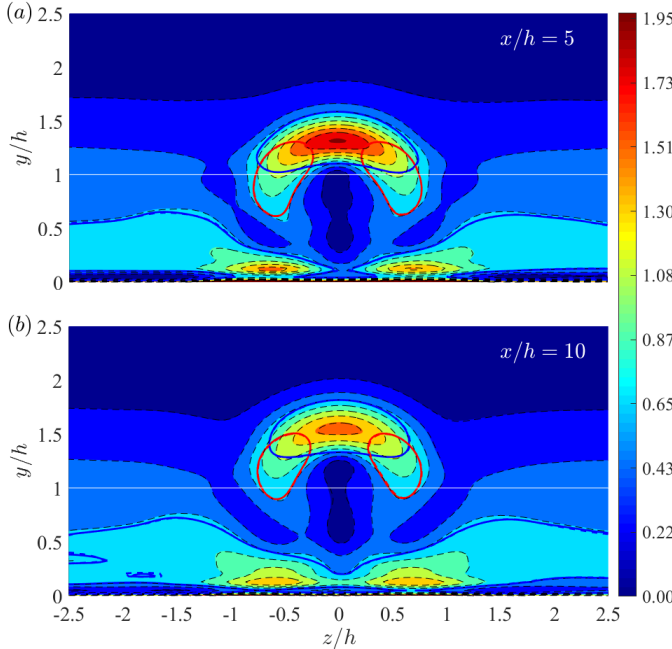


Figure 5.4: In-plane \bar{U} -shear magnitude at (a) $x = 5h$ and (b) $10h$ for the 300 (dashed) and 400 (colored contours) snapshot base flows. Red and blue contours respectively indicate where the z - and y -shear levels attain one-third of the maximum shear.

flow. The experimental base flows are conceived by constructing the mean¹ of multiple instantaneous tomo-PIV snapshots, which were obtained with a sampling frequency of 1.5Hz. Generally, 100 and 200 instantaneous snapshots are used, but up to 400 snapshots were used for one case to demonstrate the convergence of the stability results for the current study. The typical root-mean-squared fluctuation in the experimental cases is equal to $0.10\bar{U}_e$. So, specifically, using an ensemble size of $N_f = 100, 200, 300$ and 400 snapshots for the construction correspond to an estimated mean residual perturbation magnitude of $0.10/\sqrt{N_f} = 1.0 \cdot 10^{-2}, 7.1 \cdot 10^{-3}, 5.8 \cdot 10^{-3}$ and $5.0 \cdot 10^{-3}$ with respect to \bar{U}_e . The used cross-correlation volume size in (x, y, z) is $0.58h \times 0.29h \times 0.58h$. A 75% window overlap was used. Mean flow datasets are created using 300 and 400 instantaneous snapshots.

The experimental three-dimensional base velocity field is confined to the domain $(z, y) \in [-5.43h, 5.43h] \times [0, 3h]$, so vertically up to $3h$, while $\delta_{99} \approx 2.4h$ at the farthest considered location in the range of interest. The eigenmodes require a high domain to sufficiently decay before encountering the upper boundary, therefore, the freestream is extrapolated with the Blasius solution using a cosine weight in an overlap region. This region spans from $y = 2.4h$ to $2.7h$, based on negligible shear and guarantees profile monotonicity in y . It was verified that different combinations of the sizes and positions of this region caused absolute differences in the eigenvalues of maximally $O(10^{-5})$.

¹The experimental base flows should here be referred to as mean flows, but they are not for text uniformity.

In figure 5.4, the magnitude of the in-plane \bar{U} -shear is shown for the different cases. The fields corresponding to 300 and 400 snapshots very closely overlap. Close to the wall, the in-plane shear is not smooth. This is the result of switching from a center to forward finite differencing scheme (both fourth order). It was verified that a different treatment affects the presented stability results insignificantly (absolute growth rate differences of $O(10^{-4})$).

5.3. RESULTS

5.3.1. BASELINE CASE

Following the standard approach for modal spanwise BiGlobal (also: BiLocal) linear stability analysis [14, 15], the changes of the steady base flow in the streamwise (x) direction are neglected, which allows representing the instantaneous flow components q , governed by Navier-Stokes linearized about the base flow \bar{Q} , with the following ansatz:

$$u(x, y, z, t) = \bar{U}(y, z) + \tilde{u}(y, z)e^{i(\alpha x - \omega t)} + c.c., \quad c = \frac{\omega}{\alpha} \in \mathbb{C}, \quad \lambda = \frac{2\pi}{\alpha} \in \mathbb{R}, \quad (5.1)$$

5

where the streamwise perturbation velocity amplitude \tilde{u} , as well as the other perturbation amplitude components, is infinitesimal with respect to the base flow components. Of course, the velocity perturbation components in the wall-normal (y) and spanwise (z) direction and pressure are accounted for as well. The temporal stability set-up is considered, implying that the unknown angular frequency ω and wavespeed c are generally complex, while the specified streamwise wavenumber α and -length λ are real. It is assumed that transient phenomena are negligible and that the asymptotic response is dominated by the most unstable/least stable eigenvalue, i.e. maximal ω_i with respect to λ . The latter is to be compared to the instability developing in the experimental instantaneous signal. The corresponding λ is referred to as the most unstable wavelength.

The problem is discretized using a Chebyshev spectral collocation method, using mappings to densely resolve the perturbation amplitudes dominant in the shear layers. Wall conditions, as discussed by Groot *et al.* [16] are applied on the solid boundary. Dirichlet conditions are used for all amplitudes on the top boundary as it is located high enough and as it resolves the additive-constant non-uniqueness problem with the pressure. At the far-field boundaries for large $|z|$, the velocity amplitudes are set equal to zero, while homogeneous Neumann conditions are used for the pressure.² Using $N_z \times N_y = 60 \times 60$ nodes in the cases where the whole z -domain is considered yields convergence of the absolute value of the eigenvalue with errors of $O(10^{-4})$.

Employing the Arnoldi algorithm, 100 of the most unstable modes in the physically interesting ω -spectrum are resolved, given a fixed λ . In each such spectrum the two most unstable modes, for all considered values of λ , are found to be a symmetric (varicose) and anti-symmetric (sinuous) Kelvin-Helmholtz mode, as represented by the $|\tilde{u}|$ -contours show in figure 5.5. The \tilde{u} component is the largest in both cases. Note that the varicose mode clearly shows an arc shape consisting of an upper part and leg parts,

²Using compatibility conditions for the pressure (implying wall conditions) yielded virtually indistinguishable results, also in the cases where the pressure amplitude attained a small, but significant, magnitude near the boundaries.

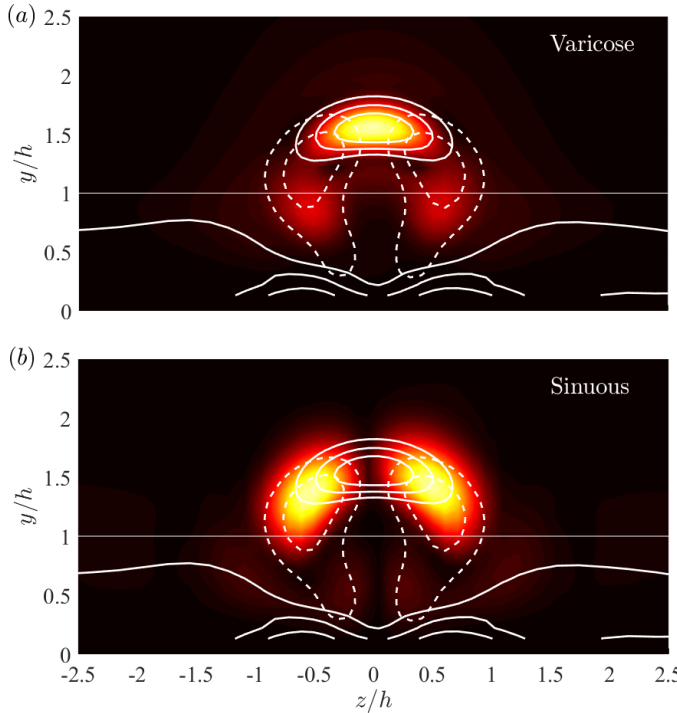


Figure 5.5: $|\tilde{u}|$ -contours of the most unstable (a, $\lambda/h = 3.9$) varicose and (b, 7.8) sinuous modes corresponding to the 400 snapshot base flow at $x = 10h$. Solid and dashed white lines respectively indicate the y - (40%, 60%, 80% of overall in-plane maximum) and z - (20%, 40% of overall in-plane maximum) base flow shear.

which closely resembles the results of Choudhari *et al.* [17]. The base flow shear components are also shown, which indicate that the varicose and sinuous mode are highly, though not solely, related by the y - and z -shear, respectively. The different modes can therefore be related logically to what is referred to as the “ y -” and “ z -mode” seen more often in stability analyses of roughness induced base flows [14, 18]. Note, however, that the spanwise shear contributes to generate the leg parts of the arc-shaped varicose mode, for example. The close overlap of the most dominant amplitude with the \bar{U} -shear hints that the instability might be determined mainly by the \bar{U} component and only to a lesser extent by the in-plane components \bar{V} and \bar{W} , whose magnitude and associated in-plane shear are relatively small.

Q -criterion isosurfaces of these modes superposed on the base flow are shown in figure 5.6. Note that the perturbation must be added to the base flow with a specific amplitude for the Q -criterion to permit a meaningful interpretation in comparison to an instantaneous flow realization. This amplitude was set equal to that observed in the experiments: $|\tilde{u}|/\bar{U}_e = 0.2$, which is actually very large and not respecting the assumption of small perturbation levels that underlies the linear stability theory. Again, it is assumed that this large an amplitude is allowable, because the perturbation signal this close to the micro-ramp is still monochromatic and hence it is likely not to have interacted non-

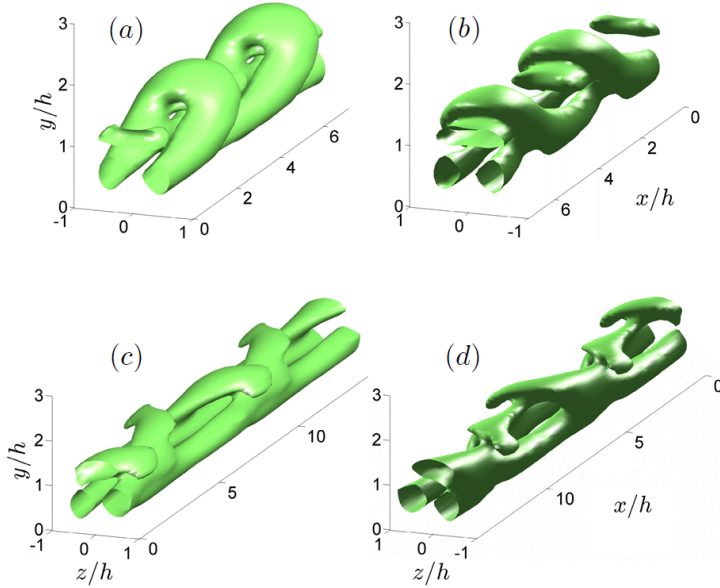


Figure 5.6: Front (b,d) and rear (a,c) views of the Q -criterion of the most unstable varicose (a,b) and sinuous (c,d) modes on the 400 snapshot PIV base flow at $x = 5h$, constantly extrapolated for two wavelengths in the x -direction. The isosurface is 5% of the maximum Q -level setting the maximum $|\tilde{u}|/\bar{U}_e = 0.2$.

5

linearly to yield a non-zero base flow correction. The varicose mode clearly displays the hairpin shape also observed in the instantaneous experimental images, which acts as a justification for the latter assumption. The sinuous mode is found to attain its maximal temporal growth rate, which is about 65% that of the varicose mode, at twice the wavelength of the varicose one. Note that two subsequent vortices are separated by the same distance as those corresponding to the varicose mode.

As the varicose mode is more unstable and hence more prominently observed in the experiments, this mode is focussed upon. Interpreting the varicose vortical structure as a duckling, one clearly observes it to have a “beak”. As the perturbation’s amplitude is increased beyond the current value, this beak turns into another hairpin. This is an artefact associated to the quadratic nature of the Q -criterion as a quantity as opposed to the perturbation variables being linear, as illustrated by the relation $(1 + \alpha \cos(\alpha x))^2 = 3/2 + 2\alpha \cos(\alpha x) + \alpha^2/2 \cos(2\alpha x)$, where the term quadratic in α should drop. In all Q -criterion plots shown in this treatment, where α is far from infinitesimal, this term is not discarded and results in the extra non-physical structure: the beak. This is deemed allowable, as the beak is localized and small ($0.2/4 = 5\%$) as opposed to the main/fundamental structure.

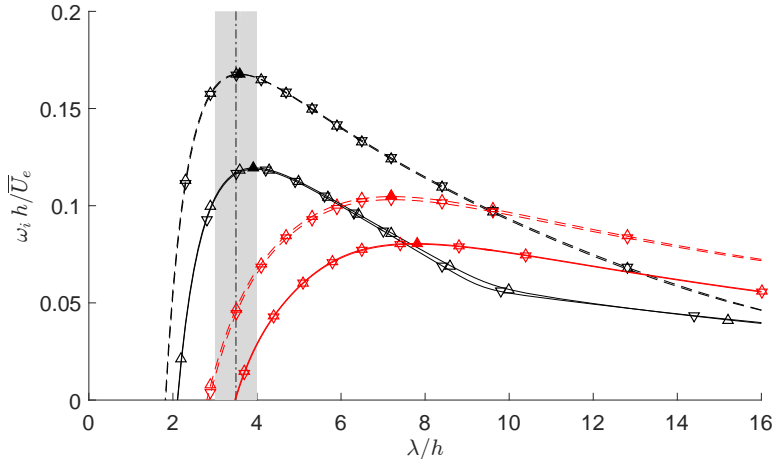


Figure 5.7: (λ, ω_i) -branches corresponding to the station $x = 5h$ (dashed) and $x = 10h$ (solid), for the mean flow with 300 (∇) and 400 (Δ) snapshots. The grey region indicates the experimentally observed wavelength range, $3.5h \pm 0.5h$.

5

5.4. VARICOSE MODE: SPECTRAL BEHAVIOUR

Two downstream planes, at $5h$ and $10h$ behind the ramp, are considered for detailed analysis, to demonstrate convergence with the base flow parameters and discover which physical features are most important. These stations are chosen to lie at and upstream of the start of the region of interest. I.e. upstream of where the KH-structures are observed in the experiment, so to minimize their presence and impact on the base flow determination, but close enough to match reasonably with the experimentally observed instability behaviour. Note that not observing the structures in the experiment does not necessarily correspond to its absence. In the current case, they are too small in magnitude to be captured in the measurement. The spatial details are filtered too much by the cross-correlation, which is advantageous in decreasing the residual perturbation level. If the structures are observed, more snapshots must be used to attain a base flow of the same quality in terms of residual perturbation level. It is therefore logical that the results are converged better at $x = 5h$ as opposed to at $10h$ for the same number of snapshots.

The (λ, ω_i) -branches are shown in figure 5.7, for the different base flows at the stations $x = 5h$ and $10h$. All most unstable wavelengths lie in the experimentally observed range, reaching a good agreement. The difference between the 300 and 400 snapshot cases themselves is of $O(10^{-4})$, which indicates that the results are converged with respect to the number of instantaneous snapshots.

Nevertheless, the differences between these cases remain similar with respect to the $x = 5h$ station. The 300 and 400 snapshot cases do yield significant convergence; in those cases the pinching branch lies deep in the stable half-plane. The most unstable wavelength again lies in the experimentally observed range; it has increased only very slightly with respect to the $x = 5h$ station. The relative decrease in the growth rate is associated to the streamwise decrease of the total in-plane shear.

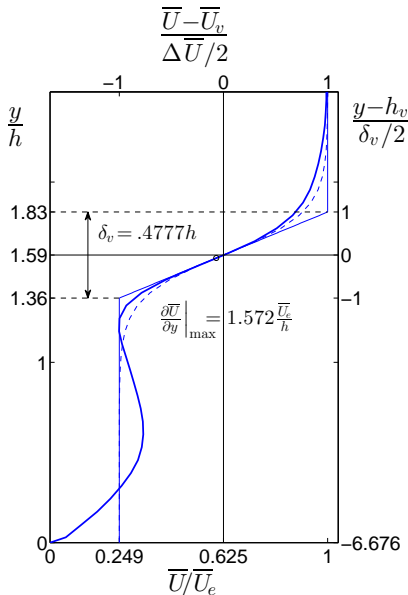


Figure 5.8: Center plane \bar{U} -profile from the 400 snapshot case at $x = 10h$, with the definition of the vorticity thickness δ_v and related linear and hyperbolic tangent profiles.

The negligible difference between the 300 and 400 snapshot cases at both stations, the match of the most unstable wavelength with the experimentally observed range for the latter cases and the expected behaviour of the branches corresponding to all other cases at $x = 5h$ leads to the preliminary conclusion that the stability analysis on the experimental base flow, given the proper treatment, is valid and reliable under these conditions. Before proceeding, it is investigated which physical features are most important for the positions of the branches in the $\lambda\omega_i$ -plane.

Regarding the perturbation's close overlap with the in-plane \bar{U} -shear, simplified one-dimensional stability analysis using Rayleigh and Orr-Sommerfeld approaches were performed to see to what extent the spectral characteristics can be attributed solely to the \bar{U} -profile at $(x, z) = (10h, 0)$. The base flow profile is taken from the 400 snapshot case and is shown in figure 5.8, which also depicts the δ_v -scaling introduced in §4.1. All resulting branches are displayed in figure 5.9, the results for $x = 5h$ are equivalent. The complexity of the different forms of the stability analysis is increased gradually as proceeding downward through the legend, taking into account all possibly relevant physical features cumulatively. To begin with, the profile was idealized as a linear and hyperbolic tangent profile, as illustrated in figure 5.8, based on the vorticity thickness δ_v and maximal shear of the top shear layer. An analytical expression can be derived for the inviscid branches corresponding to the linear profile, with and without incorporating the wall, and these yielded a very optimistic result in terms of the most unstable wavelength. As corroborated by the results in §4.6.4, the distance of the wall ($-3.338\delta_v$) is largest enough to have a negligible impact on the results. The maximal growth rate, however, is more than twice

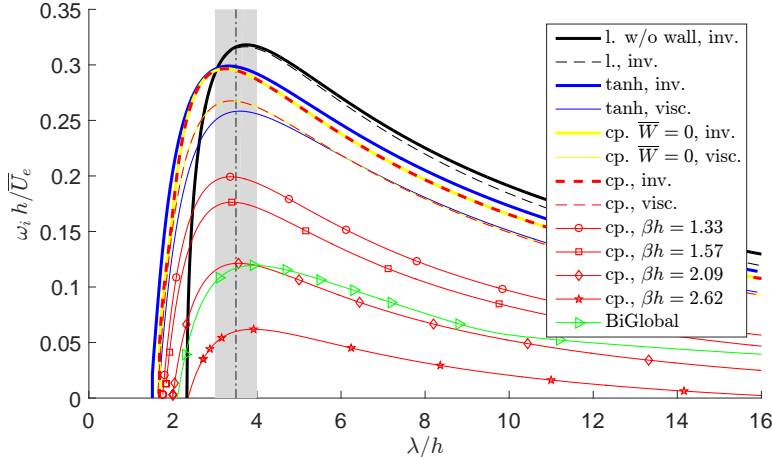


Figure 5.9: (λ, ω_i) -branches obtained from Rayleigh (inv.) and Orr-Sommerfeld (visc.) analysis on the linear (l.) and tanh fits to the center plane profile and the center plane profile itself (cp.), compared to the BiGlobal result, based on the 400 snapshot case at $x = 10h$.

5

as large. The more realistic hyperbolic tangent profile, accounting for the wall, yielded a slight decrease in both the most unstable wavelength and growth rate; the latter being logical regarding the larger momentum thickness associated to that profile. The profile being smooth renders it suitable for viscous analysis with the Orr-Sommerfeld equation, which yields a significant decrease in the maximal growth rate and, once more, a surprisingly good match regarding the wavelength. The effect of viscosity might be unexpected, but the Reynolds number based on the vorticity thickness:

$$Re_{\delta_v} = \frac{\Delta \bar{U} \delta_v}{4\nu} = \frac{0.75 \bar{U}_e \cdot 0.48h}{4\nu} = 0.090 Re_h = 61.4 \quad \text{at } x = 10h, \quad (5.2)$$

is $o(10^2)$; small enough for viscosity to play a significant role [19]. Using the actual/real as opposed to hyperbolic tangent profile yields only a small change in the curves, although more, relatively stable, modes are present in the spectrum due to the multiple inflection points. Subsequently incorporating the effect of the local cross flow component \bar{W} yields nearly identical branches, which is logical due to the nearly symmetrical flow.

The only parameter that remains is the spanwise wavenumber β , which can be directly linked to the perturbation's confinement to the shear layer's finite z -extent. Any such confinement is stabilizing, see §4.6.3 for more details. In that regard, 4 spanwise wavelengths were constructed based in different ways on the BiGlobal eigensolutions' shape. From largest to smallest wavelength, first the perturbation as shown in figure 5.5 (a) is interpreted as a circular arc, spanning $[-\pi/4, 5\pi/4]$ radians and having the approximate radius of $0.5h$, leading to the wavelength $\lambda_z \approx 2 \cdot \frac{6\pi}{4} \cdot 0.5h = 4.71h$. Second, the wavelength was taken to overlap the region where the perturbation is reasonably finite rectilinearly in z , yielding $\lambda_z \approx 2 \cdot 2.0h = 4.0h$. Finally, the wavelength was based on the outer extent of the leg and top parts, leading to $\lambda_z \approx 2 \cdot 1.5h = 3.0h$ and $2 \cdot 1.2h = 2.4h$, respec-

tively. The corresponding wavenumbers respectively are: $1.33h^{-1}$, $1.57h^{-1}$, $2.09h^{-1}$ and $2.62h^{-1}$. Though these definitions are arbitrary to some extent, they do give a good insight into what physical size is chosen in the spanwise direction. The resulting branches are also shown in figure 5.9, which clearly indicate that the wavelength matched to the extent of the legs yields a branch very close to the BiGlobal one. This result seems conclusive, but when performing a BiGlobal simulation with the \bar{U} -component only, a branch closer to the $\beta h = 2.62$ result is found. So, the remaining destabilization is caused by the in-plane velocity components. Finally, note that the sinuous mode can be argued to be more stable than the varicose mode on physical grounds associated to Squire's theorem as well, because its spanwise wavenumber is about twice as large.

5.5. VARICOSE MODE: STREAMWISE DEVELOPMENT

Next, the streamwise development of the varicose mode is considered. The most relevant quantity for this purpose is the total growth that perturbations undergo, which is naturally expressed in the form of N -curves; the gain's logarithm:

5

$$N = - \int_{1.25h}^x \alpha_i(x) dx, \quad (5.3)$$

where the integration is performed keeping ω_r fixed and $-\alpha_i$ is the spatial growth rate per station and frequency. The latter is obtained by applying Gaster's transformation [20] to the temporal growth rates, assuming the temporal growth rates are small enough, see §2.4.5 for more details. The flow is unstable for all stations close to the ramp in the experimental datasets and, theoretically, the profile just behind the ramp's tip is inflectionally unstable already. Therefore the N -curves are set equal to zero at the micro-ramp tip, at $x = 1.25h$.

Instead of resolving the BiGlobal spectra for the entire λ -range as in figure 5.7, a confined λ sweep is performed at every half h unit in x . Only 16 λ -values are resolved about a guess per station, so to reduce computational cost. The guess is obtained from the inviscid linear profile expression [21]:

$$(2\omega_{\delta_v})^2 = (2\alpha_{\delta_v} - 1)^2 - (e^{-2\alpha_{\delta_v}})^2 \quad (5.4)$$

given in the δ_v -scaling. δ_v is obtained from the experimental base flow data as indicated in figure 5.8. Expanding equation (5.4) for $\omega_{\delta_v,i}$, yields $\omega_{\delta_v,i} = \alpha_{\delta_v} \sqrt{1 - 8\alpha_{\delta_v}/3 + O(\alpha_{\delta_v}^2)}$, which implies that $\omega_{\delta_v,i}$ approaches $2\pi/\lambda_{\delta_v}$ from below for large λ_{δ_v} . This limit is exact for the unbounded linear profile, but reflected in all branches in figures 5.7 and 5.9 with a proportionality factor less than unity. This property is used to fit a third order polynomial to the calculated ω_i/α samples for each x -station. This yields a nearly identical fit whenever the most unstable wavelength is indeed captured, which was the case for the current domain of interest. The slopes of the first 5 stations are used to extrapolate the obtained curves to zero upstream.

Subsequently, the envelope of the resulting curves is determined and the latter are shown in figure 5.10 (b). However, the difference between the N -envelopes and N -curves is found to be nearly negligible; for the small 400 snapshot case, for example,

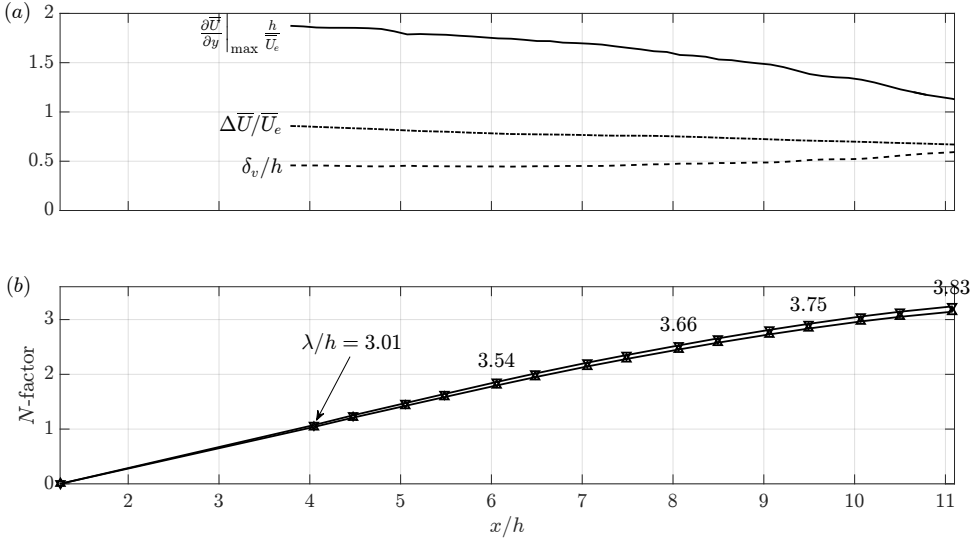


Figure 5.10: (a) Characteristics (maximum shear, velocity difference and vorticity thickness, see figure 4.1 for an elaborate definition) of the center plane velocity profiles for the 400 snapshot case. Horizontal lines indicate the thickness of the top shear layer. (bottom right) N -envelopes for the different experimental base flows, the wavelengths for which the envelope is attained are indicated for the small 400 snapshot case at several x -stations.

the frequency deviates only 2% from 374 [Hz] over the resolved range. This is entirely in-line with the fact that the perturbation field is mono-chromatic. The same applies to the wavelength in the range of interest as shown in figure 5.10 (b). Regarding the negligible frequency change, the latter increase is mainly related to the higher positioning of the perturbation in the boundary layer, accordingly it is convected faster.

The 400 snapshot case has a maximum difference of 0.1 with the 300 snapshot case, which is an acceptable degree of agreement regarding the interpretation of the envelopes. The curves display the onset of linear saturation of the amplitude for $x > 8h$. This is caused by the decrease of the maximal shear $\partial \bar{U} / \partial y \Big|_{\max}$ illustrated in figure 5.10 (a). This is the result of the wake slowly filling up in the downstream direction. It is not yet clear, however, to what extent these features are induced by the residual perturbations. It might not be a coincidence that the saturation sets in right at the range of interest, where the perturbations become experimentally observable.

Note that the overall N -values are fairly benign, despite the relatively strong inviscid instability. This is related on the one hand to the significant stabilization by the spanwise confinement as elaborated on in the previous section and, on the other, to the small streamwise extent considered; the most downstream location displayed in figure 5.10 is only 2.2 cm, 11 h , downstream of the micro-ramp. Moreover, these low levels are expected. Conventional critical N -factors associated to roughness induced transition in quiet environments, bringing linear perturbations to the location of the onset of transition, are 9 and in the current case transition is not observed in the domain of interest [17].

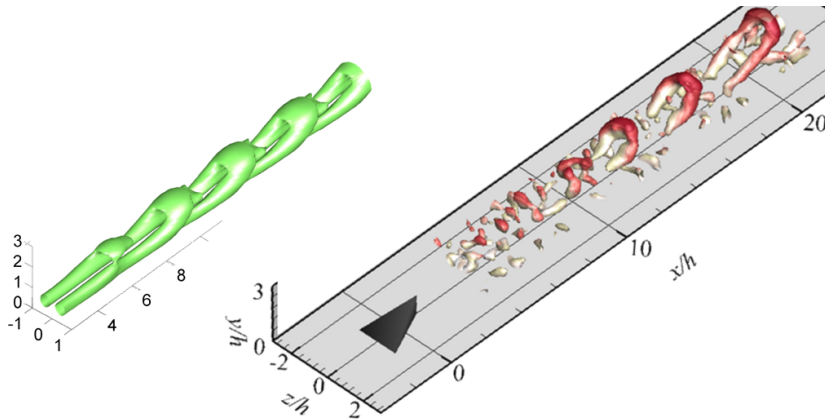


Figure 5.11: Experimentally observed hairpins (right) together with the Q -criterion (5% of the maximum Q -level) of the most unstable varicose mode (left) setting the maximum $|\tilde{u}|/\bar{U}_e = 0.2$. All dimensions are in units of h .

5

At this point, the streamwise development of the flow structure can be examined. This is done by scaling the amplitude with the N -curve so that it attains the experimentally observed amplitude $\max|\tilde{u}|/\bar{U}_e = 20\%$ in the range of interest. The eigenfunction at $x = 10h$ is extrapolated for all x -positions. This approach is justified because of the small changes of the eigenfunction and wavelength while running through the envelope of N -curves for the range of interest. The most unstable wavelength increases significantly beyond $x = 14h$, which is also observed in the instantaneous experimental image, but this is currently discarded. The resulting Q -criterion isosurface is compared to an instantaneous snapshot in figure 5.11.

The overall agreement with the experimental image is quite good in the range of interest, but there are several features that differ. For these amplitudes, the eigenmodes display legs that are still attached from vortex to vortex and the aforementioned artificial “beak,” while this is not the case in the experimental image. Furthermore, the top parts of the eigenmodes are longer in streamwise extent. A reason could be the difference in the actual Q -criterion level plotted in the experiment. Lastly, the vortices in the experiment appear in a more upright position. Despite these discrepancies, the agreement is argued to be good enough to deem the analysis to be validated up to the current results.

Appropriate next steps involve the comparison of more N -envelopes over a larger x -extent and corresponding to other experimental base flow cases, but also with experimental perturbation energy levels in x , so to see how well the gains match and to identify the perturbation’s linearity for this and possibly an even longer streamwise range. N -envelopes corresponding to the other experimental base flows can shed light on the persistence of the linear perturbation saturation. From the point of view of other stability methods, a non-linear BiGlobal-PSE analysis is deemed most appropriate to shed light on the effect of including the evolution history in the streamwise direction and non-linear perturbation dynamics. Lastly, a spatial BiGlobal analysis can be performed to verify the validity of the application of Gaster’s transformation.

5.6. CONCLUSION

The stability of micro-ramp wakes is analysed using the spanwise BiGlobal approach, to find the hairpin shaped Kelvin-Helmholtz (KH) waves observed in tomographic Particle Image Velocimetry (PIV) measurements. The study focused on the case specific validation of applying BiGlobal stability analysis to a measured mean flow constructed with a particular number of instantaneous measurement snapshots, based on the assumption that the perturbation field is monochromatic and hence does not cause a significant base flow correction. The main verification parameter was taken to be the streamwise wavelength of the KH-vortices observed in the PIV measurements, determined to be 3.5 ± 0.5 micro-ramp heights in the x -range $8h$ to $15h$.

The attention is restricted to the most unstable, varicose mode, that closely resembles the experimentally observed hairpin shape. The results for the 300 and 400 snapshot cases were found to be fully converged at $x = 5h$ and $10h$ and the corresponding most unstable wavelengths lie in the experimentally observed range. Local Rayleigh and Orr-Sommerfeld analyses on the center \bar{U} -profile, point out that the most important physical parameters are, in order of decreasing importance, the spanwise confinement to the shear layer, the non-parallel base flow components, viscosity, the profile shape and the wall. The order of magnitude of the growth rates is verified with computational base flows.

N -curves corresponding to the 300 and 400 snapshot cases are converged for all stations in the datasets; the Q -criteria of different cases are visually indistinguishable. Noticeable differences with the experimental structure include the streamwise extent, the linkage of subsequent hairpins, the inclination angle and an artificial “beak.” Despite these features, regarding the convergence of the spectral information at both in detail considered stations, the match of the most unstable wavelength with the experimentally observed range and the close resemblance of the vortical structures with the experiment leads to the preliminary conclusion that the stability analysis on the experimental base flow, given the proper treatment, is valid in this case.

REFERENCES

- [1] K. J. Groot, Q. Ye, B. W. van Oudheusden, Y. Zhang, and F. Pinna, *BiGlobal stability analysis of a micro-ramp wake using piv base flows*, AIAA Paper (2016).
- [2] K. Wang, *Lockheed SR-71 Blackbird*, <http://wangtour.blogspot.nl/> (2017), online; accessed 12-September-2017.
- [3] J. C. Robinet, *Bifurcations in shock-wave/laminar-boundary-layer interaction: global instability approach*, Journal of Fluid Mechanics **579**, 85 (2007).
- [4] S. Ghosh, J.-I. Choi, and J. R. Edwards, *RANS and hybrid LES/RANS simulations of the effects of micro vortex generators using immersed boundary methods*, AIAA Paper, 3728-2008 (2008).
- [5] H. Babinsky, Y. Li, and C. W. Pitt Ford, *Microramp control of supersonic oblique shock-wave/boundary-layer interactions*, AIAA Journal **47**, 668 (2009).

- 5**
- [6] H. Babinsky and J. K. Harvey, *Shock wave-boundary-layer interactions*, Vol. 32 (Cambridge University Press, 2011).
 - [7] J. Syberg and J. L. Koncsek, *Bleed system design technology for supersonic inlets*, Journal of Aircraft **10**, 407 (1973).
 - [8] M. K. Fukuda, W. G. Hingst, and E. Reshotko, *Control of shock wave-boundary layer interactions by bleed in supersonic mixed compression inlets*, Tech. Rep. NASA-CR-2595, FTAS/TR-75-100 (Case Western Reserve Univ., 1975).
 - [9] B. H. Anderson, J. Tinapple, and L. Surber, *Optimal control of shock wave turbulent boundary layer interactions using micro-array actuation*, AIAA Paper, 3197-2006 , 1 (2006).
 - [10] Z. Sun, F. F. J. Schrijer, F. Scarano, and B. W. van Oudheusden, *The three-dimensional flow organization past a micro-ramp in a supersonic boundary layer*, Physics of Fluids **24**, 1 (2012).
 - [11] Q. Ye, F. F. J. Schrijer, and F. Scarano, *Boundary layer transition mechanisms behind a micro-ramp*, Journal of Fluid Mechanics **793**, 132 (2016).
 - [12] Q. Ye, F. F. J. Schrijer, and F. Scarano, *On Reynolds number dependence of micro-ramp-induced transition*, Journal of Fluid Mechanics **837**, 597 (2018).
 - [13] Q. Ye, *Mechanisms of Boundary layer Transition Induced by Isolated Roughness*, Ph.D. thesis, Delft University of Technology, Delft, The Netherlands (2017).
 - [14] E. Piot, *Simulation Numérique Directe et Analyse de Stabilité de Couches Limites Laminaires en Présence de Micro-Rugosités*, Ph.D. thesis, l'Institut Supérieur de l'Aéronautique et de l'Éspace (2008).
 - [15] Y. Shin, U. Rist, and Krämer, *Stability of the laminar boundary-layer flow behind a roughness element*, Experiments in Fluids **56** (2015).
 - [16] K. J. Groot, F. Pinna, and B. W. van Oudheusden, *On closing the streamwise BiGlobal stability problem: the effect of boundary conditions*, in *8th IUTAM-ABCM Symposium on Laminar-Turbulent Transition* (Elsevier, Rio de Janeiro, 2014).
 - [17] M. M. Choudhari, F. Li, M. Wu, C.-L. Chang, J. Edwards, M. Kegerise, and R. King, *Laminar-turbulent transition behind discrete roughness elements in a high-speed boundary layer*, in *48th AIAA Aerospace Sciences Meeting Including the New Horizons Forum and Aerospace Exposition* (2010).
 - [18] M. Malik, W. Liao, F. Li, and M. Choudhari, *Discrete-roughness-element-enhanced swept-wing natural laminar flow at high Reynolds numbers*, AIAA Journal **53**, 1 (2015).
 - [19] A. Michalke, *Survey on jet instability theory*, Progress in Aerospace Sciences **21**, 159 (1984).

- [20] M. Gaster, *A note on the relation between temporally-increasing and spatially-increasing disturbances in hydrodynamic stability*, Journal of Fluid Mechanics **14**, 222 (1962).
- [21] P. G. Drazin and W. H. Reid, *Hydrodynamic Stability* (Cambridge University Press, 2004).

6

MEASURED BASE FLOWS: CROSSFLOW VORTICES

A second case of consideration for the application of BiGlobal stability theory on experimentally measured base flows, is the analysis of the secondary stability of swept-wing boundary layers. These base flows are three-dimensional laminar boundary layers subject to spanwise distortion due to the presence of primary stationary crossflow vortices. A three-dimensional flow description is accessed through the use of tomographic Particle Image Velocimetry (tomo-PIV). The stability analysis solves for the secondary high-frequency modes of type I and II, ultimately responsible for turbulent breakdown. Several pertinent parameters arising in the proposed methodology are investigated, including the mean flow ensemble size and the measurement domain extent. Extensive use is made of the decomposition of the eigensolutions into the terms of the Reynolds-Orr equation, allowing insight into the production and/or destruction of perturbations from various base flow features. Stability results demonstrate satisfactory convergence with respect to the mean flow ensemble size and are independent of the handling of the exterior of the measurement domain. The Reynolds-Orr analysis reveals a close relationship between the type I and type II instability modes with spanwise and wall-normal gradients of the base flow, respectively. The structural role of the in-plane velocity components on the perturbation growth, topology and sensitivity is identified. Using the developed framework, further insight is gained into the linear growth mechanisms and later stages of transition via the primary and secondary crossflow instabilities. Furthermore, the proposed methodology enables the extension and enhancement of the experimental measurability of the pertinent instability eigenmodes. The present work is the first demonstration of the use of a measured base flow for stability analysis applied to the swept-wing boundary layer, directly avoiding the modelling of the primary vortices receptivity processes.

The paper accompanying this chapter is published in the Journal of Fluid Mechanics [1].

6.1. INTRODUCTORY REMARKS

The need for understanding laminar-turbulent transition in the case of commercial airliners was explained in the introduction. However, commercial airliners have swept wings. The first candidate surface for the industrial implementation of laminar flow technology is the vertical tail. Figure 6.1 illustrates the typical boundary layer flow encountered on such a surface. The laminar-turbulent transition scenario establishes itself in a particular way and deserves a dedicated description. To aid the description, four coordinate systems are introduced: the global incoming-flow-attached (X, Z), global leading-edge-attached (x, z), local inviscid-streamline-attached (x_s, z_s) and local crossflow-vortex-attached (x_w, z_w) systems. Please see figure 6.3 for more detail.

Starting at the leading edge, the inviscid flow is parallel to z , as the flow stagnates on the leading edge. For small taper ratios, the flow can be assumed to be invariant in the z -direction, which means that the pressure gradient acts in the x -direction. The airfoils are typically designed to support a favourable pressure gradient over a large portion of the chord. While following the flow in the x -direction, the inviscid flow (pointing in the direction indicated by x_s) curves towards x , while subject to the favourable pressure gradient. The low-momentum part of the boundary layer experiences an immediate impact by the push of the pressure gradient. The inviscid flow and pressure gradient are not aligned (x_s and x are non-parallel), so a crossflow results inside the boundary layer.

The crossflow velocity profile has a zero edge value, because it is directed in the z_s -direction, see the second zoom in figure 6.1. This causes the velocity profiles to be inflec-

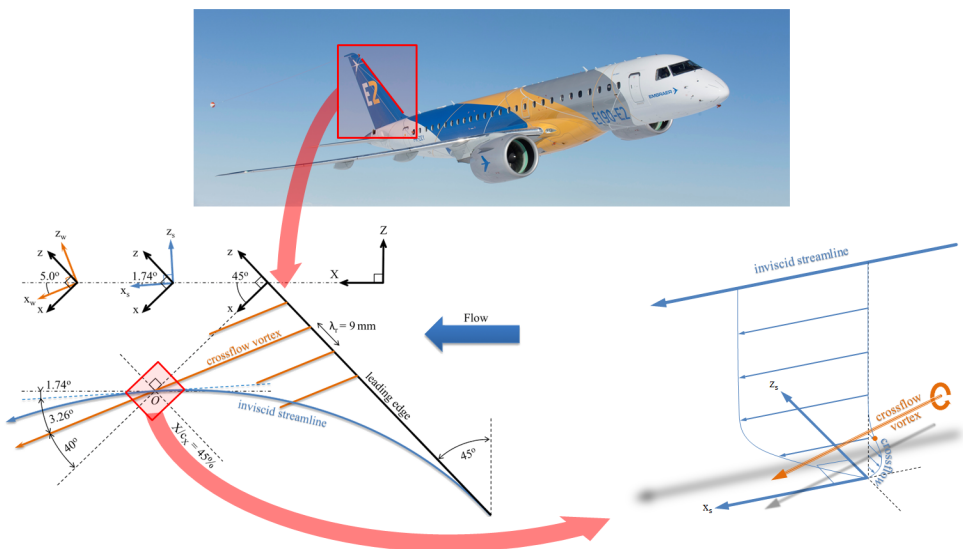


Figure 6.1: Application example: vertical tail of the Embraer E190-E2 [2] (specific numbers based on the work of Serpieri & Kotsonis [3]). The global incoming-flow-attached (X, Z), global leading-edge-attached (x, z), local inviscid-streamline-attached (x_s, z_s) and local crossflow-vortex-attached (x_w, z_w) coordinate systems. Wing and flow are assumed invariant in z : pressure gradient in x -direction.

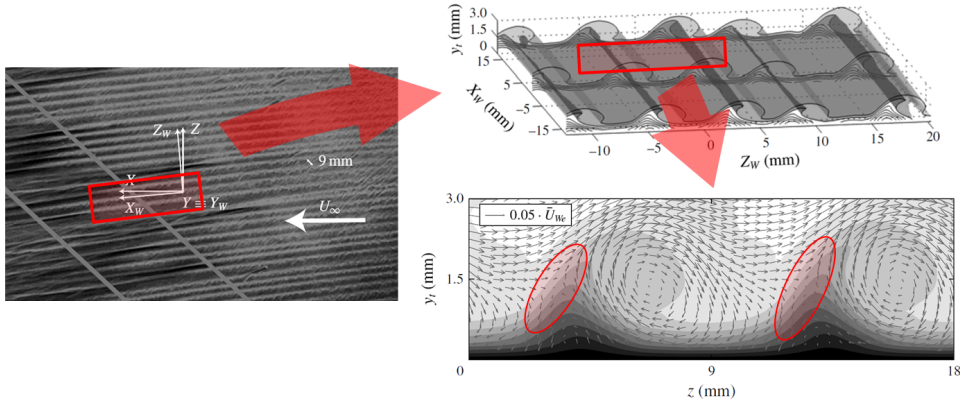


Figure 6.2: Crossflow vortices in detail, excerpts from Serpieri & Kotsonis [3]. Fluorescent oil visualisation (left), isosurfaces of the $X_W \equiv x_w$ -velocity component (top right) and x_w -velocity contour and in-plane flow quiver plot along at a constant x_w -station, highlighting the shear layers around the saddle of the in-plane flow (bottom right). Subfigures on the right are based on a tomo-PIV measurement.

tional, which is the precursor for a strong inviscid instability. In particular, it induces the (primary) crossflow instability, which establishes itself as a spanwise array of stationary co-rotating streamwise vortices. Figure 6.2 shows a compilation of figures by Serpieri and Kotsonis [3] of these vortices. First, a the top view of the vortices visualised with naftaline oil is shown, clearly indicating the vortex array. By deploying the tomo-PIV technique, a volumetric representation of five vortices is presented, here shown as the first zoom. Interestingly, despite the primary vortices are a strong inviscid mechanism, they do not cause breakdown to turbulence. In fact, the vortices saturate non-linearly.

Despite the small amplitude of the primary vortices, they result in a mean flow distortion giving rise to high-frequency secondary instabilities, which ultimately breakdown to turbulence, see Bonfigli and Kloker [4], Reed, Saric, and Arnal [5], Saric, Reed, and White [6] and White and Saric [7]. Detailed information on the secondary instabilities, specifically their amplification and spatial topology, is instrumental in understanding, and ultimately predicting, where laminar-turbulent transition will occur in this case. The resulting perturbations are again produced in the shear layer created by the vortex-induced upwash, see the second zoom in figure 6.2. The strongest part of the shear layer is indicated.

Malik, Li, and Chang [8] and Malik *et al.* [9] explored the e^N -method's applicability to the secondary instability, by accounting for the mean flow distortion induced by the primary instability and validating their results against the experiments of Kohama, Saric, and Hoos [10]. Related experiments on the forcing and receptivity of secondary cross-flow instabilities are reported on by Kawakami, Kohama, and Okutsu [11], Bippes and Lerche [12] and Bippes [13].

Malik, Li, and Chang [14] identified 3 classes of instabilities in the distorted base flow. Here, the classification by Koch *et al.* [15] is followed. The type I mode is generated by the spanwise shear layer in the upwash region of the primary vortex and is usually dominant. Second, the type II mode is mainly generated by wall-normal shear and lives on the top

of the primary vortex. In the nomenclature of Malik *et al.* [14], these modes are also referred to as the z - and y -modes, respectively. Third, Koch *et al.* define the type III mode, which is the travelling primary crossflow instability subject to the distorted base flow. The type I and II modes are proper secondary instabilities to the stationary primary crossflow vortex and are observed at frequencies typically one order of magnitude higher than type III [7, 15, 16].

A handle to the stability features of secondary perturbations can be obtained by applying spanwise BiGlobal stability analysis on the distorted base flow. This accounts for the respective flow inhomogeneities in a chosen plane, i.e. the flow itself and all z_w - and y -shear components, see Theofilis [17]. For conciseness, the base flow distorted by the primary instability will be referred to as the base flow. Investigations of this type for crossflow instabilities have been applied by Fischer, Hein, and Dallmann [18], Malik *et al.* [8, 9], Janke and Balakumar [19] and Bonfigli and Kloker [4]. This method is computationally relatively cheap, but cannot account for non-linear perturbation dynamics or receptivity. An alternative approach is direct numerical simulation (DNS), i.e. solving the three-dimensional linear or fully non-linear perturbation dynamics directly in the form of an initial value problem. This approach is computationally expensive and care has to be taken specifying inhomogeneous initial and in-/outflow boundary conditions [16].

The sensitivity of stability results to the base flow is notorious, see Arnal [20], Reed *et al.* [5] and Theofilis [17]. However, the literature indicates that this does not impede the success of the stability approach in predicting the behaviour of the perturbation field. This applies even in the case of some turbulent flows, see [21] for example, in which case the Reynolds stresses are significantly more dominant than in the present. This applies to secondary crossflow instability analysis in two ways: with respect to boundary layer receptivity and the representation of the base flow. The former is fixed by, e.g., micron-sized surface roughness near the leading edge and freestream turbulence. The secondary instability modes, in turn, depend strongly on the state of the primary vortices. In previous investigations, the latter are computed by performing non-linear parabolized stability equation (NPSE) simulations or DNS, see Malik *et al.* [9], Bonfigli and Kloker [4]. However, these techniques require careful receptivity calibration for the initial conditions. An important example is provided by Fischer *et al.* [18], who successfully model the base flow combining the linear primary instability eigenfunctions with measured amplitude information. That work illustrates that a good model representation of the base flow can suffice for obtaining secondary stability information. Bonfigli and Kloker [4] found that accurately representing the small in-plane (wall-normal and crossflow) velocity components is crucial in this regard; reporting significant growth rate reductions. Kloker and coworkers exploited this by controlling the developed crossflow vortices with suction and plasma actuators [22–26]. However, only a conceptual account of how these components affect the secondary stability modes is given by Bonfigli and Kloker [4].

6.1.1. PRESENT STUDY

Previous work identifies that the modelling of the base flow requires special care. In the present work, the complication of modelling the primary instability is directly circum-

vented by measuring the distorted base flow. The time averaged flow is accessed using tomographic Particle Image Velocimetry (tomo-PIV), fully resolving the three-dimensional boundary layer flow and the mean flow distortion effect due to the primary vortex. The used experimental results are published independently, see Serpieri and Kotsonis [3]. The combination of this experimental and stability approach has also been applied to the flow in the aft of micro-ramp vortex generator, see Groot *et al.* [27].

Avoiding modelling the receptivity of the primary crossflow vortices this way comes at a cost concerning the sensitivity of the stability results to the parameters of the experimental mean flow. The base flow in this work is represented by forming the mean of instantaneous vector fields under the hypothesis that the difference between the base and mean flow becomes negligible as the ensemble size is increased; i.e. the “mean = base flow”-hypothesis. Fischer and Dallmann [28] argue this is a valid assumption in the linear amplification region of the instability of interest, given the mean flow distortion is properly accounted for. The experimentally observed amplitude of the secondary perturbations is large: 10% of the freestream velocity. Therefore, next to quantifying the negligibility of effects associated to other parameters, the sensitivity to the ensemble size, denoted by N_{fr} , is a main subject of investigation amongst the results of this study.

Modelling the primary vortices can be argued to be relatively trivial in cases where they indeed appear as a nearly periodic sequence in the spanwise direction, but this becomes challenging in practical cases where the CF vortices appear non-periodically or even merge. Numerical approaches in this regard are artificial or highly simplified, see Bonfigli and Kloker [4] and Choudhari, Li, and Paredes [29]. The current study opens the possibility to analyse cases that are relevant to the realistic confinements of wind tunnel experiments. In this regard, the sensitivity argument can be used inversely. The current approach, per definition, incorporates all features that are inherent to the experiment; features that might be overlooked by modelling the primary vortices numerically or require opportune calibration with experimental datasets. Furthermore, the secondary eigenmode information is of inherent interest for this particular case. Identifying the instantaneous flow with the eigenmode allows clarifying its underlying stability and growth physics expressed in the terms of the Reynolds-Orr equation, see Malik *et al.* [9] and Schmid and Henningson [30]. In this regard, the main focus will lie on the contributions of the in-plane flow to the Reynolds-Orr terms. Furthermore, the expected dependencies on the Reynolds number and the primary vortex amplitude are checked. Lastly, the approach can be used to extend and enhance experimental measurability as resolving the instantaneous flow field is considerably more challenging than the mean flow in an experimental framework. Thus, within the limits of the assumptions that the instantaneous field is mainly composed of the linear mode superposed on a steady flow, the current approach can be used to identify and describe the pertinent mode to degrees of accuracy beyond what is currently possible in the experimental framework alone.

The article is arranged as follows. First the distorted base flow is characterised in §6.2, followed by the formulation and numerics of the stability problem in §6.3. The latter section also considers the Reynolds-Orr equation emphasizing the (de)stabilizing effect of the (in-plane) advection terms. The results are presented in §6.4, starting off with the analysis of a reference case using all $N_{fr} = 500$ instantaneous frames in §6.4.1, followed by the N_{fr} -convergence study in §6.4.2 and the effect of the wall-normal domain extrap-

olation in §6.4.4. The applicability of the Gaster-transformation is briefly confirmed in §6.4.5, allowing the use of temporal solutions for the experimental validation in §6.4.6. Thereafter the effects of the primary vortex strength and the Reynolds number are considered in §6.4.7 and §6.4.9, respectively. The article is concluded in §6.5.

6.2. EXPERIMENTAL BASE FLOW

In this study, the mean velocity field obtained with three-dimensional tomo-PIV measurements is used as base flow for the secondary stability analysis. A detailed description of the experimental set-up is given by Serpieri and Kotsonis [3]. The experiment was performed in the TU Delft Low Turbulence Tunnel (LTT) facility. The model is a 45° swept wing featuring an airfoil that is an adaptation of the NACA66018 shape, called 66018M3J, with a small leading edge radius to avoid attachment line instability. The geometric angle of attack of the wing was set to 3°, in order to enhance development of the crossflow instability at the pressure side, i.e. the measurement side. At this angle of attack, the pressure minimum is attained at $X/c_X = 63\%$, where X is parallel to the tunnel walls and c_X the chord in the X -direction ($c_X = 1.27\text{ m}$). The full C_p -distribution is given by Serpieri and Kotsonis [3]. The wind tunnel inflow velocity is $\bar{Q}_\infty = 25.6\text{ m/s}$, yielding a chord Reynolds number of 2.17×10^6 and Mach number $M = 0.075$. The freestream turbulence intensity was found to be $Tu/\bar{Q}_\infty = 0.07\%$ at $\bar{Q}_\infty = 24\text{ m/s}$.

6

The tomo-PIV measurement is performed centred at the 45% chord location in the midspan of the wing. This streamwise position is where the crossflow vortices saturate, signifying the onset of secondary instability. The slight downstream location $X/c_X = 45.6\%$ is therefore considered for the stability analysis, 8mm downstream the origin. At that location, the vortices and inviscid streamline have an angle of 5.0° and 1.74° (counter-clockwise positive), respectively, with \bar{Q}_∞ .

Due to the complexity of the flow topology, several coordinate systems are defined, as illustrated in figure 6.3. The tunnel-attached system, (X, Y, Z) , has X parallel to \bar{Q}_∞ , Z in the spanwise direction perpendicular to the tunnel walls and Y normal to the ZX -plane. The crossflow-vortex-attached system, (x_w, y, z_w) , is aligned with the primary crossflow vortices, i.e. x_w is parallel to the vortices, y wall-normal with respect to the airfoil and z_w spanwise, perpendicular to the $x_w y$ -plane. Unless otherwise specified, this will be the main coordinate system used to display the results. The related streamwise and spanwise velocity components are indicated with the subscript w . The inviscid-streamline-attached system, (x_s, y, z_s) , is aligned with the inviscid flow direction; the related streamwise and spanwise (true crossflow) velocity components have the subscript s , i.e. the inviscid edge crossflow velocity $\bar{W}_{s,e}$ is zero, per definition. The wing-attached system, (x, y, z) , is obtained by rotating the (X, Y, Z) -system 45° about the Y -axis. x is orthogonal to the leading edge, z parallel to the leading edge and y orthogonal to the zx -plane. The origin of the (x_w, y, z_w) -system is placed at the 45% chord, spanwise centre position. The primary instability is conditioned by installing an array of cylindrical discrete roughness elements (DRE, Reibert *et al.* [31]; Saric, Carrillo, and Reibert [32]) at $X/c_X = 2.5\%$ parallel to the leading edge, with a spanwise spacing of 9mm along z , this being the naturally occurring wavelength at the transition location. The elements' diameter and height are $2.8\text{ mm} \times 10\mu\text{m}$. The projection of the roughness spacing on the z_w -direction

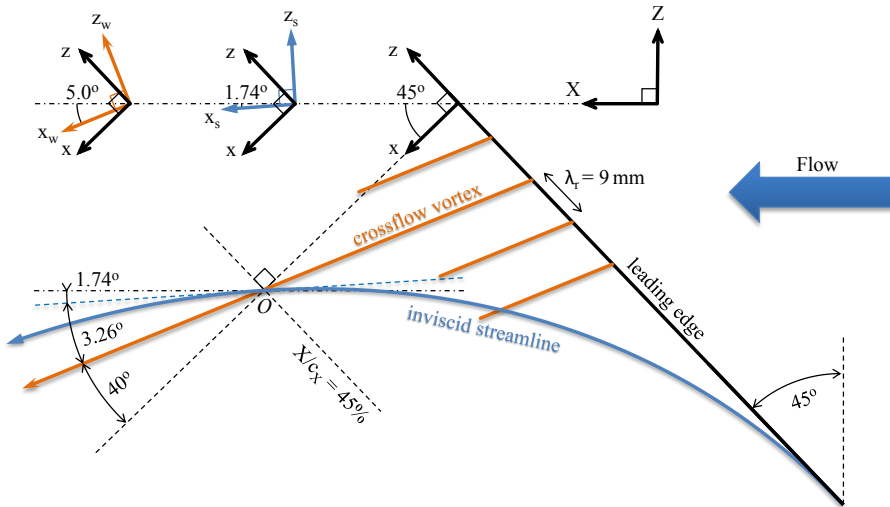


Figure 6.3: Definition of (left to right) crossflow-vortex-attached (x_w, z_w), inviscid-streamline-attached (x_s, z_s), wing-attached (x, z) and tunnel-attached (X, Z) coordinate systems. The origin of the (x_w, z_w) system is at $X/c_X = 45\%$. The individual coordinate system insets present the angles at the 45.6% chord location.

6

is $9 \cos 40^\circ = 6.89$ mm. This length is denoted by λ_r and used as the primary length scale for the entirety of this work. The inviscid edge velocity in the direction of the primary vortex at $X/c_X = 45.6\%$, $\bar{U}_{w,e}$, is 28.0 m/s. This is used as the velocity scale throughout this work and is denoted with \bar{U}_e .

6.2.1. TOMOGRAPHIC PIV

The tomo-PIV setup consisted of four cameras, that were mounted in an arc configuration, located approximately one meter away from the model. The laser light enters the wind tunnel along the Z -direction. The final field of view was $35 \times 35 \times 3$ mm 3 and centred at $X/c_X = 45\%$. Volume reconstruction and correlation were performed in a coordinate system aligned with the primary crossflow vortices, i.e. in the x_w -direction. The final interrogation volume size is $2.6 \times 0.67 \times 0.67$ mm 3 in (x_w, y, z_w) , providing sufficient spatial resolution for both primary and secondary instability features. Given that PIV relies upon correlating the movement of particles in this finite interrogation volume, a spatial smoothing effect cannot be avoided, see Schrijer and Scarano [33]. A 75% overlap of adjacent interrogation volumes was used. The final vector field was interpolated on a grid with a 0.15 mm spacing in all directions, only implying interpolation in x_w .

The tomo-PIV measurement resolves all velocity components. Two-component hot-wire measurements covering the crossflow velocity have been reported by Deyhle and Bippes [34], but Bonfigli and Kloker [4] emphasize the sensitivity of the stability results to the wall-normal velocity component specifically. This sensitivity is confirmed by preliminary stability analyses, despite these components' small magnitude, precluding their structural character. This is the first occasion where this data is available from experiments, rendering the two-dimensional stability approach feasible.

Uncertainties in the mean flow are heuristically linked to the maximum r.m.s. fluctuation and the number of instantaneous snapshots used for the mean flow, see Raffel *et al.* [35]; Sciacchitano, Wieneke, and Scarano [36]. The maximum r.m.s. fluctuation has a magnitude of $0.1\bar{U}_e$ in the shear layer accommodating the type I mode. In §6.4.6 the correspondence between the r.m.s. fluctuations and the type I eigenmode itself will be identified. In total, 500 uncorrelated snapshots were obtained at a sampling frequency of 0.5 Hz. The number of instantaneous frames in the ensemble will be denoted by N_{fr} . When less than 500, the individual snapshots are randomly selected from the total pool. The uncertainty of the mean field is estimated to be $0.1\bar{U}_e/\sqrt{N_f} = 4.5 \times 10^{-3}\bar{U}_e$ for the $N_{fr} = 500$ case. As will be demonstrated, this is a high uncertainty with respect to the sensitivity of the stability analysis. Previous studies, see Groot *et al.* [27], demonstrated sufficient convergence of the stability results with a similar ensemble size as used here. A formal study on the convergence with N_{fr} is considered in §6.4.2.

Finally, Proper Orthogonal Decomposition (POD) analysis is applied to identify the most energetic spatially correlated three-dimensional flow structures, using the snapshot technique introduced by Sirovich [37]. A detailed description of the POD results is given by Serpieri and Kotsonis [3]. For the present study, access to the three-dimensional POD modes is indispensable as it enables topological validation of the applied stability analysis; as presented in §6.4.6.

6

6.2.2. PRE-PROCESSING FOR STABILITY ANALYSIS

Due to the aforementioned sensitivity of the stability results on variations of the base flow, a pre-processing strategy is followed in regard to the mean flow fields. This processing is mainly related to the limited field of view and measurement uncertainty associated to measuring in close proximity to the wall, inherent to tomo-PIV.

Although the stability eigenmodes of interest decay exponentially in the wall-normal direction, see Schmid and Henningson [30], the truncation boundary in this direction must be placed high enough to preclude artificial effects, see Grosch and Orszag [38], Sandstede and Scheel [39]. To this end, the \bar{U}_w and \bar{W}_w base flow velocity components are extrapolated using the Blasius solution in the inviscid streamline direction, i.e. $\bar{W}_{w,e} = \bar{U}_{w,e} \tan 3.26^\circ = 1.59 \text{ m/s}$. An approximation with a Falkner-Skan-Cooke profile would be better, but the field of view extends to such heights, about 2 undisturbed boundary layer thicknesses as shown in figure 6.4, that this approach is deemed sufficient. As expected, the Blasius solution and the PIV dataset do not match exactly at the top of the field of view. Therefore, a cosine weight overlap layer is introduced to make the resulting base flow continuous at the interface. The height up to which the PIV data is unaffected is denoted by δ_p and the height of the overlap region by δ_o , see figure 6.4. \bar{V} is extrapolated in a similar way, approaching zero in the freestream.

A second aspect requiring attention is the PIV fidelity in the near-wall region. Near-wall PIV measurements are subject to a number of decremental factors such as laser-light reflections, low particle density and the strong shear, see Scarano [40]. Effectively, these features result in a deviation of the velocity profile from the no-slip condition. The type III mode is dominant in this region and therefore expected to depend on the near-wall details of the flow. The PIV uncertainty in the near-wall region is judged to render the use of the base flow for the extraction of the type III mode more challenging. While such

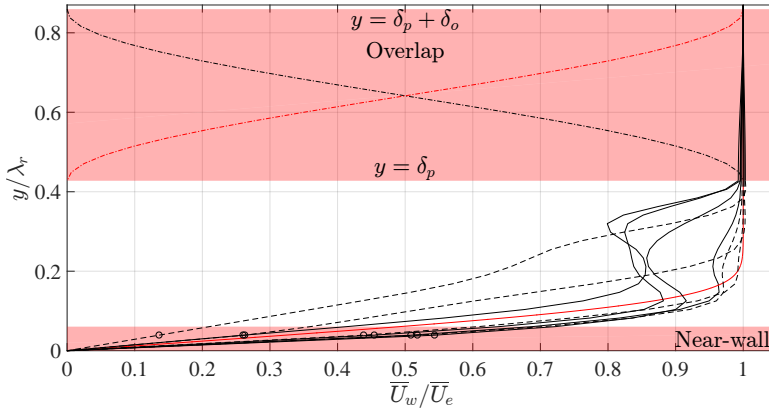


Figure 6.4: Overlap and near-wall region, illustrating cosine weights (dash-dotted) for the rotated Blasius (red solid) and base flow profiles (black solid leeward, dashed windward with respect to \bar{W}_w). Interpolated points in the near-wall region (circles).

6

objective lies out of the scope of the current work, technical improvements on the tomo-PIV technique could enable the resolution of near-wall modes in future explorations. For the present study, the proper secondary modes of type I and II will be considered.

The near-wall region is approached in 2 steps. First, the profiles are connected to the wall by linear extrapolation; artificially imposing the no-slip condition. As a second step, the data at the y -coordinate closest to the wall is overwritten with an interpolation. As such, the no-slip condition is connected smoothly to the data on the second non-zero y -coordinate, $y/\lambda_r = 0.061$, designating the near-wall region, see figure 6.4. The modes of type I and II are found to be affected negligibly by this kind of base flow changes outside their spatial region of dominance, see §6.4.4.

A third and final aspect is the fact that the in-plane flow is not divergence free, i.e. $\partial \bar{V} / \partial y + \partial \bar{W}_w / \partial z_w \neq 0$. As was and will be indicated in §§2.3.5 and 6.3, this is an implicit assumption in the stability approach and can have an impact on the precise growth rate values. [4] discuss a treatment, where the $\partial \bar{V} / \partial y$ - and $\partial \bar{W}_w / \partial z_w$ -fields are integrated to obtain the \bar{W} and \bar{V} fields, respectively. Given the fields in the near-wall region are fitted with the aforementioned approach, integrating the $\partial \bar{V} / \partial y$ - and $\partial \bar{W}_w / \partial z_w$ -fields, which are experimentally measured data that are already differentiated, is expected to yield unreliable results. A better approach to enforce the divergence-free condition on the measured in-plane flow data is to perform solenoidal interpolation, see [41]. Several approaches on the treatment of PIV data to yield a closer match with the equations governing fluid flow have been proposed, for example see [42, 43], however, the main aim of this study is to identify whether stability results can be extracted from PIV mean flows in the first place. As shown by [4], the induced change in the growth rates by considering either the \bar{V} - or \bar{W}_w -fixed approach is noticeable, in particular for the type I instability, but it does not oppose extracting the growth's order of magnitude. It will be shown in §6.4.3 that the expected induced differences lie within the established bounds of uncertainty.

6.2.3. DISTORTED BASE FLOW AND SHEAR FIELDS

A brief analysis of the pertinent features of the PIV mean flow is described in this section, so to distill expectations for the stability results based on available literature. The resulting velocity fields, confined to the measurement domain, are shown in figure 6.5, which is equivalent to figure 18 by Serpieri and Kotsonis [3], but differs in streamwise location and orientation. Two measured stationary primary crossflow vortices are given in the spanwise direction. The two vortices have slightly different strengths, which is possibly a result of minute discrepancies between the individual DREs responsible for the conditioning of these vortices in the receptivity region near the leading edge. While this is an unavoidable effect of experimental conditions, it presents a convenient and realistic opportunity in demonstrating the effect of the base flow, i.e. the amplitude of the primary crossflow vortex, on the secondary instability characteristics. Here, the two vortices are analysed separately, limiting the spanwise domain length to $1\lambda_r = 6.89$ mm as indicated in figure 6.5.

A measure for the primary disturbance amplitude based on the measured mean velocity profiles was introduced by Fischer and Dallmann [28]:

$$\frac{1}{2} \max_y \left(\max_{z_w} \bar{U}_s(z_w, y) - \min_{z_w} \bar{U}_s(z_w, y) \right), \quad (6.1)$$

where the subscript s denotes the inviscid-streamline-attached coordinate system. Using the separate spanwise domains for the two vortices, this yields 28.7% and 27.3% for the strong and weak vortex, respectively, with respect to \bar{U}_e . Scaling with the edge velocity based on \bar{U}_s yields effectively the same numbers to the given precision, thus this distinction is omitted in the remainder. Based on their modelling assumptions and the aforementioned measure, Fischer *et al.* [18] observe high-frequency secondary instabilities for disturbance amplitudes beyond 11% \bar{U}_e . Wassermann and Kloker [16] (cf. page 75) report that the onset of the secondary instability to the maximal in-plane deceleration imposed by the mean flow distortion is equal to 30% \bar{U}_e , based on their DNS. The Reynolds number in both references is about half that considered here, but these values can still act as a sanity check for the current purposes. In the current experiment, the perturbations on the weaker vortex are much weaker than on the strong vortex, so also the instability is expected to be weaker in terms of a lower growth rate.

The magnitude of the components in the $z_w y$ -plane is condensed in a similar way:

$$\begin{aligned} & \frac{1}{2} \max_y \left(\max_{z_w} \bar{V}(z_w, y) - \min_{z_w} \bar{V}(z_w, y) \right) \\ & \frac{1}{2} \max_{z_w} \left(\max_y \bar{W}_w(z_w, y) - \min_y \bar{W}_w(z_w, y) \right) \end{aligned} \quad (6.2)$$

The z_w -component is considered instead of the z_s -component, because the former appears in the stability problem. Note that this measure on \bar{W}_w cannot be directly associated to the amplitude of the primary perturbation as it includes part of the undisturbed laminar boundary layer. One obtains 1.48% and 1.51% for \bar{V} for the strong and weak vortices, respectively, with respect to \bar{U}_e . This component is evidently quite insensitive to variations in the spanwise direction. For \bar{W}_w , values of 4.78% and 4.22% for the strong and weak vortex are observed, respectively. The \bar{U}_s changes more than \bar{W}_w , 1.4 percent

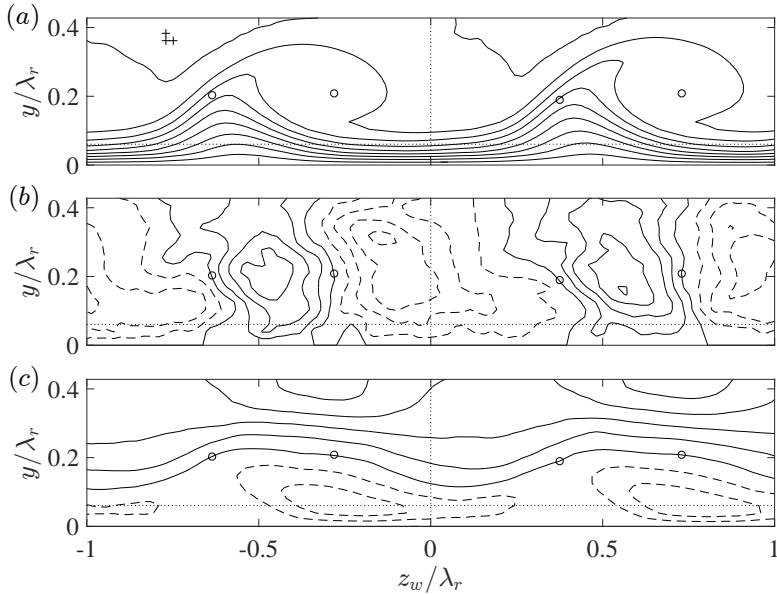


Figure 6.5: (a) \bar{U}_w/\bar{U}_e (10 levels, from 0 to 1), (b) \bar{V}/\bar{U}_e (11 levels from -0.02 to 0.02) and (c) \bar{W}_w/\bar{U}_e (11 levels from -0.05 to 0.05) at constant x_w ($x = 45.6\%$ chord at $z_w/\lambda_r = 0$), negative contours are dashed. (pluses) Spatial resolution of experimental data ($\Delta y = \Delta z_w = 0.022\lambda_r$), (circles) (\bar{V}, \bar{W}_w) -field centre and saddle point locations ($(z_w, y)/\lambda_r = (0.364; 0.202) - (1, 0)$, $(0.719; 0.209) - (1, 0)$, $(0.374; 0.190)$ and $(0.731; 0.209)$), (vertical dotted line) domain separation for strong (right) and weak (left) vortex ($z_w/\lambda_r = 0$), (horizontal dotted line) near-wall region ($y/\lambda_r \leq 0.061$).

points as opposed to 0.6 points. In terms of absolute size, this implies that the in-plane velocity components change negligibly as opposed to the streamwise velocity component. In this regard, following figure 20 of Bonfigli and Kloker [4], it is expected that the type I instability is slightly more pronounced than type II on the weaker vortex.

The total in-plane \bar{U}_w -shear magnitude of the strong vortex corresponding to the $N_{fr} = 500$ mean tomo-PIV flow field is shown in figure 6.6 (a). This is displayed on the mapped Chebyshev grid that is ultimately used to perform the stability analysis; this grid will be introduced in §6.3.3. The height of the measurement domain and the near-wall region are illustrated in figure 6.6 (a,b). Sixth order finite differences are used to determine the derivative fields consistently, i.e. using central differences in the interior and forward/backward differences at the boundaries. Differentiating PIV data with high order finite differences is generally discouraged as they could cause random errors, see Foucaut and Stanislas [44]. The high order was chosen to reduce the truncation error corresponding to the finite spatial resolution of the tomo-PIV. Using lower order finite differences for the derivatives fields affected the results negligibly, see §6.4.2.

As discussed earlier, conditions on the required base flow accuracy are case-dependent and hence difficult to set in general. It is commonly suggested that the base flow should satisfy the Navier-Stokes equations to extreme accuracy, see Theofilis [17] and Reed *et al.* [5]. The work of Ehrenstein and Gallaire [45] and Alizard and Robinet [46] reflect this

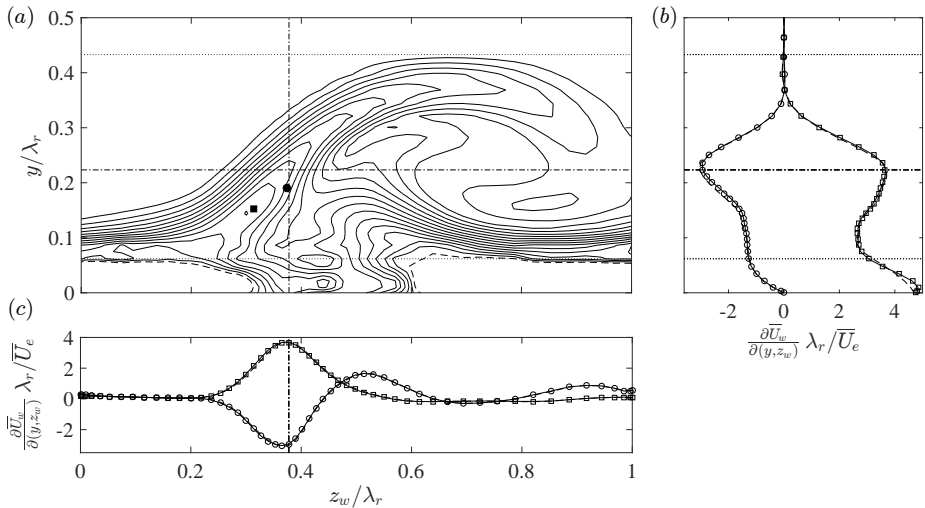


Figure 6.6: (a) In-plane \bar{U}_w -shear magnitude of the strong vortex for $N_{fr} = 500$ (levels from 0 to 7 with steps of 0.5 in \bar{U}_e/λ_r -units, level 7 \bar{U}_e/λ_r is dashed). Position of (\bar{V}, \bar{W}_w) -field saddle point (solid circle), $\partial \bar{U}_w / \partial z_w$ -minimum (solid square) and type I $|\bar{u}_w|$ -maximum (dash-dotted lines). (b) y - and (c) z_w -profiles of $\partial \bar{U}_w / \partial z_w$ (circles) and $\partial \bar{U}_w / \partial y$ (squares) for $N_{fr} = 500$ (symbols), 400 (solid line) and 300 (dashed line) along the dash-dotted lines in (a). Near-wall region ($y/\lambda_r \leq 0.061$) and upper limit PIV domain ($y/\lambda_r = 0.433$) (dotted lines).

6

requirement through their use of Navier-Stokes over Blasius solutions for the flat-plate boundary layer flow. Arnal [20] shows that the maximum shear values must be represented accurately in the case of inviscid inflectional instabilities. To identify how well this criterion is satisfied in the current case, the position of a baseline type I eigenfunction maximum is identified in figure 6.6 (a) by the dash-dotted lines $z_w/\lambda_w = 0.378$ and $y/\lambda_r = 0.223$. Figures 6.6 (b,c) display both derivative profiles $\partial \bar{U}_w / \partial y$ and $\partial \bar{U}_w / \partial z_w$ along these lines, respectively. The $\partial \bar{U}_w / \partial z_w$ component clearly displays a minimum; representing an inviscid unstable inflection point. Next to the profiles for $N_{fr} = 500$, those corresponding to $N_{fr} = 400$ and 300 (single random samplings) are shown. The derivative profiles are found to be nearly identical. At the inflection point location, the differences in the shear magnitudes do not exceed 1.1%. In the near-wall region, the largest deviation is found to be 2.3%.

The total in-plane shear of the weaker vortex shown to the left in figure 6.5 is compared to that associated to the stronger vortex in figure 6.7. Firstly, note that the contours below $y/\lambda_r = 0.15$ near the spanwise domain boundaries are very close for the different vortices. The main difference is that the contours corresponding to the weaker vortex protrude less into the freestream about the type I shear layer. In figure 6.7 (c), this effect manifests itself as a shift of the shear profiles in the negative z_w -direction and in figure 6.7 (b) as a lower value for $\partial \bar{U}_w / \partial z_w$. The profiles shown in both figures 6.6 (b,c) and 6.7 (b,c) suggest the maximum of the type I eigenfunction ($(z_w, y)/\lambda_r = (0.378; 0.223)$ and $(0.367; 0.223)$, respectively) lies close to the overall minimum of the $\partial \bar{U}_w / \partial z_w$ shear component. The symbols in figures 6.6 (a) and 6.7 (a) illustrate this point ($(z_w, y)/\lambda_r = (0.314; 0.162)$ and $(0.300; 0.153)$, respectively), in fact, lies quite far. In both cases, it con-

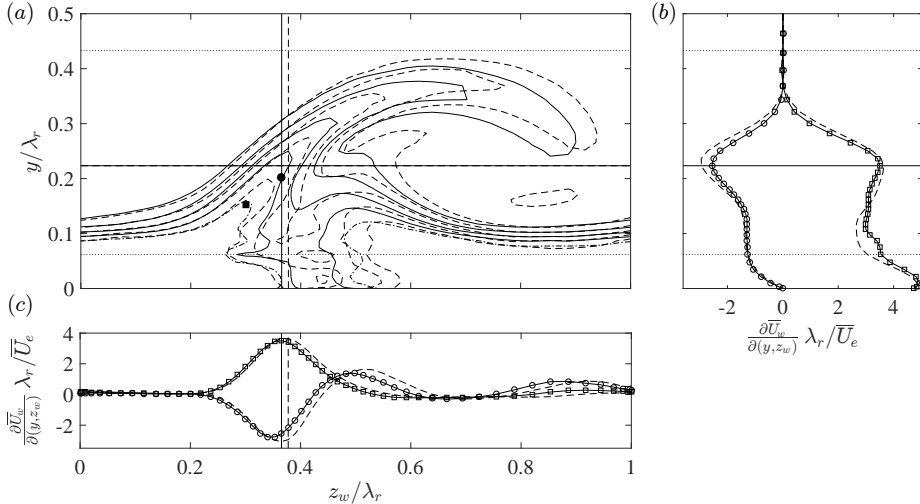


Figure 6.7: (a) In-plane \bar{U}_w -shear magnitude of the weak vortex (solid contours) for $N_{fr} = 500$ (levels from 0 to 5 with steps of 1 in \bar{U}_e/λ_r -units, level 5 \bar{U}_e/λ_r is dash-dotted). Position of (\bar{V}, \bar{W}_w) -field saddle point (solid circle), $\partial \bar{U}_w / \partial z_w$ -minimum (solid square) and type I $|\bar{u}_w|$ -maximum (solid lines). (b) y - and (c) z_w -profiles of $\partial \bar{U}_w / \partial z_w$ (circles) and $\partial \bar{U}_w / \partial y$ (squares) along the straight solid lines in (a). Strong vortex equivalents of the shear profiles and eigenfunction maximum position are given by dashed lines.

sistently lies slightly above the saddle point in the in-plane velocity field imposed by \bar{V} and \bar{W}_w .

In conclusion, both vortices are expected to be unstable to secondary instabilities based on the results of Fischer *et al.* [18]. The weaker vortex, as opposed to the stronger, is expected to yield a smaller growth rate, which is mainly caused by changes in the streamwise velocity component. The in-plane velocity components vary marginally with respect to the streamwise component, resulting in a relatively larger magnitude on the weak vortex, which pronounces the type I as opposed to the type II instability [4]. Moreover, the in-plane location of the maximum amplitude of the type I mode seems to be fixed in close proximity of the saddle point of the in-plane flow. The derivative fields display small discrepancies with changing N_{fr} , being a first requirement for the stability analysis [20].

6.3. SPANWISE BiGLOBAL STABILITY ANALYSIS

6.3.1. FORMULATION

The stability approach accounts for all flow inhomogeneities in a two-dimensional plane. The flow is assumed to be invariant in the third direction. Based on their topological features, the best choice for the invariant direction in the case of the primary crossflow vortices is orthogonal to the wave vector of the primary vortices: the x_w -direction. Implicitly, the curvature of the vortices is neglected, which is *a-posteriori* justified by the small wavelengths of the secondary modes, see Malik *et al.* [9], Theofilis [17] and Bonfigli and Kloker [4] for more details.

Care should be taken in defining boundary conditions on the introduced domain boundaries. The domain is confined to either one of the two vortices shown in figure 6.5, depending on the investigated case. For a semi-infinite swept wing at canonical conditions, the flow is periodic in the leading edge parallel z -coordinate. This suggests considering the zy -plane for the stability analysis and justifies applying periodic boundary conditions. The x_w -direction is non-orthogonal to the zy -plane, which can be accounted for by projecting the velocity vectors on the zy -plane onto the $z_w y$ -plane. Bonfigli and Kloker [4] go into high detail describing a similar approach, illustrating the requirement for a correction concerning flow continuity.

In the present work, the choice is made not to adhere to the most periodic spanwise direction. The $z_w y$ -planes were extracted directly from the tomo-PIV data, since the PIV cross-correlation is performed in this direction and hence yields the most consistent representation of the velocity field. This is equivalent to the *Adapted-vortex-oriented* DNS case of Bonfigli and Kloker [4] (cf. §6.1), crucial for verifying the stability results. The data is directly extracted at $x_w = 8.02\text{ mm}$ with respect to the origin indicated in figure 6.3, which corresponds to 45.6% chord at $z_w = 0$. The introduced departure from periodicity is negligible: the edge velocity changes less than $10^{-3}\bar{U}_e$ across the domain, as a consequence of the small ($6.89 \sin 40^\circ = 4.4\text{ mm}$) chordwise extent of the domain. Note that the base flow quantities, including the shear, change discontinuously across the boundaries, but no new shear elevation is introduced by the aforementioned procedure. The effect of this approach is assessed in §6.4.8.

Regarding the wall-normal direction, no-slip and pressure compatibility conditions are applied at $y = 0$ and homogeneous Dirichlet conditions are used for all amplitudes on the top boundary as it is located high enough (at $4\lambda_r$) and as it resolves the additive-constant non-uniqueness problem with the pressure.

The aforementioned considerations are combined in the spanwise BiGlobal ansatz for the perturbation as follows:

$$q' = \tilde{q}(z_w, y) e^{i(\alpha x_w - \omega t)} + c.c., \quad (6.3)$$

where α is the wavenumber in the x_w -direction, ω the angular frequency, q' and \tilde{q} are the perturbation and amplitude variables and *c.c.* denotes the complex conjugate. Substituting this ansatz into the linearized Navier-Stokes equations yields the system of spanwise BiGlobal stability equations, see system (2.15). With respect to this particular case, the stream- and spanwise coordinates and the velocity components corresponding to the base flow and perturbation should be equipped with the subscript w , consistent with x_w and z_w introduced in this chapter.

The in-plane base flow velocity components \bar{V} and \bar{W}_w appear amongst the coefficients in the equations and have a role as advection and reaction terms. The \bar{V} -terms are no longer absent, as in the one-dimensional Orr-Sommerfeld analyses due to the parallel flow assumption, see equation (4.8) or the equivalent system (4.6). In two-dimensional approaches, this assumption is lifted, because of flow continuity in the plane. Therefore all velocity components are required as part of the measurement data to complete the general eigenmode description.

Together with the aforementioned boundary conditions, the system (2.15) is solved for $\omega \in \mathbb{C}$ (given $\alpha \in \mathbb{R}$) or $\alpha \in \mathbb{C}$ (given $\omega \in \mathbb{R}$); representing the temporal or spatial frame-

work, respectively. In the considered experimental framework, the secondary perturbations of interest are convective; i.e. they grow as they travel in the downstream direction, while having constant amplitude at a fixed point in space, see Wassermann and Kloker [16]. This corresponds to the spatial stability framework. As explained in §3.1.6, the spatial stability problem is computationally more expensive to solve than the temporal problem. Previous work indicates that the Gaster-transformation (see §2.4.5) can be successfully applied to link the spatial and temporal solutions, see Malik *et al.* [8, 9] and Koch *et al.* [15]. The majority of the eigensolutions presented here are hence based on the temporal approach, applying the Gaster-transformation when in need of the spatial characteristics. The validity of the Gaster-transformation is verified in §6.4.5, where the spatial problem is solved, i.e. $\alpha \in \mathbb{C}$ is unknown and $\omega \in \mathbb{R}$ is given.

In what follows, the main interest goes out to the most unstable eigensolutions and the solution that can be compared to the POD mode obtained from the tomo-PIV data. In the latter case, the quantity directly measured from POD is the wavelength of the type I mode, which equals 4.6 mm. Hence solutions are sought for which $2\pi/\alpha_r = 4.6$ mm.

6.3.2. REYNOLDS-ORR EQUATION

To cast the eigenmodes in a more physically interpretable form, the eigenvalues are decomposed into the values attributed to specific terms in the governing system of equations; the Reynolds-Orr equation as presented in §2.5, which for this case takes the following form:

$$\begin{aligned} \omega = & \iint \left(\alpha \bar{U}_w \tilde{\mathbf{q}}^* \cdot \tilde{\mathbf{q}} - i \bar{V} \tilde{\mathbf{q}}^* \cdot \frac{\partial \tilde{\mathbf{q}}}{\partial y} - i \bar{W}_w \tilde{\mathbf{q}}^* \cdot \frac{\partial \tilde{\mathbf{q}}}{\partial z_w} \right) \frac{dy dz_w}{\|\tilde{\mathbf{q}}\|^2} \\ & + (\alpha - \alpha^*) \iint \tilde{u}_w^* \tilde{p} \frac{dy dz_w}{\|\tilde{\mathbf{q}}\|^2} - D + R \end{aligned} \quad (6.4)$$

where $\tilde{\mathbf{q}} = [\tilde{u}_w \ \tilde{v} \ \tilde{w}_w]^T$ and $\|\tilde{\mathbf{q}}\|^2 = \iint \tilde{\mathbf{q}}^* \cdot \tilde{\mathbf{q}} dy dz_w$. From left to right, the terms represent advection, pressure work (zero when $\alpha_i = 0$), viscous dissipation D and Reynolds stress work R . The latter two terms represent the combinations of terms:

$$\begin{aligned} D = & \frac{i}{Re} \left(\alpha^2 + \iint \left(\left| \frac{\partial \tilde{u}_w}{\partial y} \right|^2 + \left| \frac{\partial \tilde{u}_w}{\partial z_w} \right|^2 + \left| \frac{\partial \tilde{v}}{\partial y} \right|^2 + \left| \frac{\partial \tilde{v}}{\partial z_w} \right|^2 + \left| \frac{\partial \tilde{w}_w}{\partial y} \right|^2 + \left| \frac{\partial \tilde{w}_w}{\partial z_w} \right|^2 \right) \frac{dy dz_w}{\|\tilde{\mathbf{q}}\|^2} \right) \\ R = & -i \iint \left(\tilde{u}_w^* \tilde{v} \frac{\partial \bar{U}_w}{\partial y} + \tilde{u}_w^* \tilde{w}_w \frac{\partial \bar{U}_w}{\partial z_w} + |\tilde{v}|^2 \frac{\partial \bar{V}}{\partial y} + \tilde{v}^* \tilde{w}_w \frac{\partial \bar{V}}{\partial z_w} \right. \\ & \quad \left. + \tilde{w}_w^* \tilde{v} \frac{\partial \bar{W}_w}{\partial y} + |\tilde{w}_w|^2 \frac{\partial \bar{W}_w}{\partial z_w} \right) \frac{dy dz_w}{\|\tilde{\mathbf{q}}\|^2} \end{aligned}$$

Note that due to the particular periodic and no-slip boundary conditions on the amplitude functions considered in this case, no boundary terms appear. The different terms of equation (6.4) represent the complex contribution to ω associated to specific physical mechanisms pertinent to the base flow.

The following shorthand symbols are introduced for ease of reference:

$$\left. \begin{aligned} R^y &= \iint -i \tilde{u}_w^* \tilde{v} \frac{\partial \bar{U}_w}{\partial y} \frac{dy dz_w}{\|\tilde{\mathbf{q}}\|^2}; & A^{\bar{U}_w} &= \iint \alpha \bar{U}_w \tilde{\mathbf{q}}^* \cdot \tilde{\mathbf{q}} \frac{dy dz_w}{\|\tilde{\mathbf{q}}\|^2} \\ R^{z_w} &= \iint -i \tilde{u}_w^* \tilde{w} \frac{\partial \bar{U}_w}{\partial z_w} \frac{dy dz_w}{\|\tilde{\mathbf{q}}\|^2}; & A^{\bar{V}} &= \iint -i \bar{V} \tilde{\mathbf{q}}^* \cdot \frac{\partial \tilde{\mathbf{q}}}{\partial y} \frac{dy dz_w}{\|\tilde{\mathbf{q}}\|^2} \\ R_{\bar{W}_w}^y &= \iint -i \tilde{w}_w^* \tilde{v} \frac{\partial \bar{W}_w}{\partial y} \frac{dy dz_w}{\|\tilde{\mathbf{q}}\|^2}; & A^{\bar{W}_w} &= \iint -i \bar{W}_w \tilde{\mathbf{q}}^* \cdot \frac{\partial \tilde{\mathbf{q}}}{\partial z_w} \frac{dy dz_w}{\|\tilde{\mathbf{q}}\|^2} \end{aligned} \right\} \quad (6.5)$$

Whenever a reference is made to the integrands of the above terms, the inclusion of the scaling factor $\|\tilde{\mathbf{q}}\|^2$ is implied.

The individual terms in the ω_r - and ω_i -budgets encode the underlying physical mechanisms of every eigenmode; defining their very nature. This work focuses on the consistency of those terms for each eigenmode, for example that the terms show the same magnitude independent of the ensemble size N_{fr} . In particular those terms involving the (difficult to measure) \bar{V} and \bar{W}_w deserve emphasis, due to the sensitivity of the stability outcomes to those terms, as discussed by Bonfigli and Kloker [4].

Using the appropriate symbol conventions, equation (2.54), representing the contribution of the advection terms in the ω_i -budget, can be written as:

$$\text{Im} \left\{ A^{\bar{U}_w} + A^{\bar{V}} + A^{\bar{W}_w} \right\} = \begin{bmatrix} \bar{U}_w \\ \bar{V} \\ \bar{W}_w \end{bmatrix} \cdot \text{Re} \left\{ - \begin{bmatrix} \tilde{\mathbf{q}}^* \cdot -\alpha_i \tilde{\mathbf{q}} \\ \tilde{\mathbf{q}}^* \cdot \partial \tilde{\mathbf{q}} / \partial y \\ \tilde{\mathbf{q}}^* \cdot \partial \tilde{\mathbf{q}} / \partial z_w \end{bmatrix} \right\}. \quad (6.6)$$

This quantity is (non-)zero whenever the perturbation amplitude gradient is (non-)orthogonal to the in-plane flow. Bonfigli and Kloker [4] argue that a velocity component normal to the shear layer moves the perturbations away from the productive region and hence has a stabilizing effect. However, the former criterion illustrates the opposite and is therefore an object of dedicated analysis in the remainder of this chapter. Whenever the velocity vector is aligned with the direction in which the perturbation decays, this results in a locally destabilizing effect. I.e. a region of high perturbation energy is moved so as to replace a lower energy region. On the other hand, if the perturbation grows in the advection direction, that is stabilizing. Generally, advection is destabilizing if it is effective in transferring energy to the exterior of the vortex core.

6.3.3. DISCRETIZATION SPECIFICS

The problem is discretized using Chebyshev spectral collocation in combination with the BiQuadratic mapping, as outlined in chapter 3, for both y - and z_w -directions in specific areas. It should be noted that an alternative to this discretization involves Floquet theory; solving the Fourier transformed problem in the spanwise direction, see Herbert [47], Janke and Balakumar [19] and Koch *et al.* [15]. Theofilis [17] notes that a large number of Fourier coefficients has to be resolved and hence the method is not necessarily cheaper than solving the partial differential problem directly. As opposed to the commonly used Floquet approach, the Chebyshev collocation approach allows specifying arbitrary, i.e. non-periodic, flow fields. Although periodic boundary conditions are applied

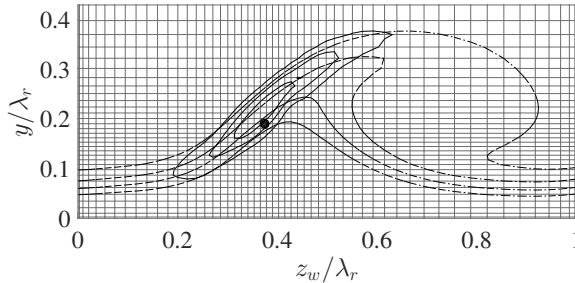


Figure 6.8: Zoom on mapped Chebyshev grid (55×55 nodes). $|\bar{u}_w| / \max|\bar{u}_w|$ of type I (solid contours at 25%, 50% and 75%). \bar{U}_w/\bar{U}_e levels 0.6, 0.7, 0.8 and 0.9 (dash-dotted). Position of (\bar{V}, \bar{W}_w) -field saddle point (solid circle).

at the boundaries in the spanwise direction, periodizing the base flow fields is avoided in the present study, to circumvent introducing artificial shear layers. This is *a-posteriori* justified, as will be shown in §6.4.8.

When considering a domain with a single vortex, the mapping is equipped with specific parameters aimed at densely resolving the region where the type I eigenfunction is located, about the saddle point of the in-plane flow. Using $N_z \times N_y = 55 \times 55$ nodes and setting $(z_{i1}, z_{i2}, z_{max}) = (0.30; 0.55; 1.0)\lambda_r$ and $(y_{i1}, y_{i2}, y_{max}) = (0.18; 0.60; 4.0)\lambda_r$ yields type I eigenvalue errors of $O(10^{-5})$ in absolute sense. An example of the spatial distribution of mode I on the grid is shown in figure 6.8. Grid convergence was verified by increasing the resolution using these mapping parameters and checking against more conventional grids, applying no or the standard bilinear mapping by Malik [48].

In the case of the domain with both vortices, i.e. $z_w/\lambda_r \in [-1, 1]$, the mapping was programmed to distribute the collocation nodes as uniformly as possible, corresponding to $(z_{i1}, z_{i2}, z_{max}) = (-1/3, 1/3, 1)\lambda_r$. The discretization in the y -direction is left unchanged.

Using the BiQuadratic mapping markedly reduces the computational expenses, in terms of RAM and evaluation time. The achieved reduction in the necessary amount of nodes rendered both temporal and spatial problems small enough to be solved on a small workstation in mass.

6.3.4. SHIFT-INVERT STRATEGY

A final step towards improving solving efficiency is setting the centre of the resolved spectrum; i.e. adjusting the parameters for the shift & invert transformation in the Arnoldi algorithm, see [17]. This is done considering specific heuristics: the maxima of the eigenfunctions of interest are all positioned high in the boundary layer, away from the near-wall region indicated in figure 6.4. Conversely, the modes that lie inside the near-wall region are expected to be subject to errors associated to measurement noise. Modes that lie in the near-wall region have low phase speeds corresponding to the low \bar{U}_w values, by inspection smaller than $0.4\bar{U}_e$. Hence, the region with $\omega_r < 0.4\alpha_r$, especially the stable region, is avoided. Figure 6.9 illustrates examples of temporal spectra for $\alpha\lambda_r = 1.0$ and 8.2. The limit $\omega_r = 0.4\alpha_r$ is indicated by the dash-dotted line.

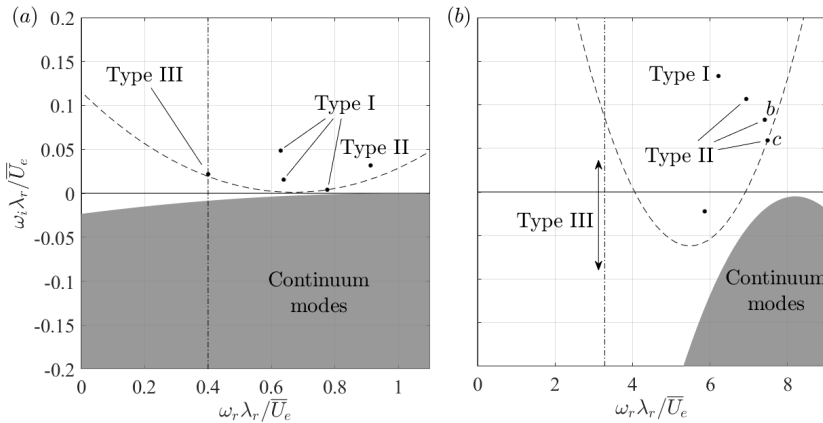


Figure 6.9: Resolved spectra using $\omega_g = (0.669 + 2.02i)\alpha/\bar{U}_e$, corresponding to $\alpha\lambda_r = 1.0$ (a) and 8.2 (b). Continuous spectrum (solid surface). Modes dominant in the near-wall region (left of dash-dotted). ω_g -centred circle enclosing resolved eigenvalues (dashed).

Additionally, the modes of interest are discrete and do not belong to the continuous spectrum. The continuous spectrum contains modes that live in the freestream and have phase velocity equal to 1, accounting for \bar{W}_w . They complete the spectrum, but are very expensive to compute in terms of computational time. Due to $\bar{W}_{w,e}$ being non-zero, the upper bound of the spectrum in the ω -plane is the parabola shown in figure 6.9, with its vertex at $\alpha(1 - i\alpha/Re)$. The shift $\omega_g = (0.669 + 2.02i)\alpha/\bar{U}_e$ is oriented such as to equally avoid both (stable) near-wall and continuous spectrum regions, but capture all interesting discrete modes. See [49] for a similar approach.

As only the modes of interest are captured and the type I mode is usually most unstable, it suffices to reduce the number of resolved modes to 5, which significantly reduces the required time to obtain individual spectra. Note that the imaginary shift value is large, which increases the required computational time; a shift closer to the modes is helpful at the cost of having to resolve continuum modes. This approach is fruitful only for the temporal problem, because another continuous branch is encountered for large negative α_i in the spatial problem. Changing the shift or the number of modes yields eigenvalue changes of $O(10^{-12})$.

The most typical arrangement of the spectrum is shown in figure 6.9 (b). The unstable modes are, from most to least unstable: the type I mode, the type II (fundamental) mode and the second and third harmonic of the latter, by inspection of the eigenfunctions shown in figure 6.10 (b) and (c). These structures correspond closely to those reported by Koch *et al.* [15, cf. figure 16]. The Arnoldi algorithm does not return the type III mode for this number of requested solutions in this particular case. For $\alpha\lambda_r = 1$, the type III mode is contained within the mode horizon, the dashed line in figure 6.9 (a). The location of the type III mode and the near-wall limit corresponds closely to its phase speed reported by [4]. The type III eigenfunction is shown in figure 6.10 (a) and, interestingly, corresponds very closely to the type II/III hybrid shape shown in figure 35 by [4]. The mode horizon approaches the continuous spectrum very closely in this case, indicating

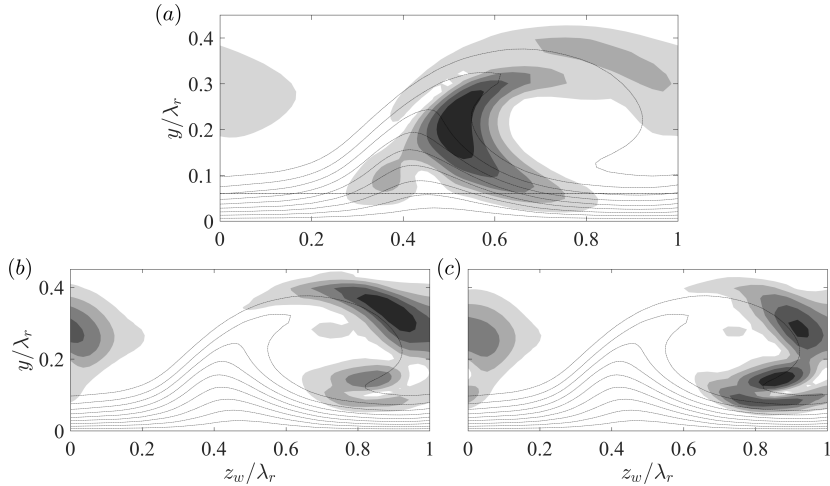


Figure 6.10: $|\tilde{u}_w|/\max|\tilde{u}_w|$ for the type III mode (*a*, in figure 6.9 (*a*)) and the “harmonics” of type II (*b*, *c*, resp. II b , II c in figure 6.9 (*b*) modes, levels span $[1/6, 5/6]$ with $\Delta = 1/6$. Near-wall region (dash-dotted line). $\overline{U}_w/\overline{U}_e$ levels 0.1, 0.2, ..., 0.9 (dotted).

6

the challenge with tracking the type III mode with the optimised set-up. Analysis of the type III mode falls beyond the scope of the present study and will not be considered in the following discussion.

6.4. RESULTS

6.4.1. BASE SPECTRUM

To give a general overview of the spectrum, the base flow plane conceived with 500 instantaneous snapshots is considered as a reference baseline case. The branches of eigenvalues corresponding to the type I and II modes are shown in figure 6.11. The temporal BiGlobal problem is solved for the α -range $[0.5, 18]/\lambda_r$ with a spacing of $0.1/\lambda_r$. In the figure, the branches are shown for the α -range over which the branches are unstable.

Several grid resolutions are used to compute the spectra with the focused grid for the type I mode, going up to $N_z \times N_y = 90 \times 90$ nodes. The mode branches are found to be converged already for $N_z \times N_y = 55 \times 55$ nodes, with eigenvalue errors of $O(10^{-5})$ in absolute sense for the type I instability. Despite the lower grid density in the region of dominance of the type II mode, the spectral discretization captures this mode properly as well. The most unstable type II eigenvalue experiences a $O(10^{-4})$ absolute error, which is deemed sufficiently small for the purposes of this analysis. The remainder of the 5 eigensolutions returned by the Arnoldi algorithm are harmonics of both type I and II modes, due to their more complicated shape these modes display more significant errors.

The type I mode attains the maximum temporal growth rate and is therefore locally most unstable. The type II mode is found to be locally more unstable for $\omega_r > 7.77\overline{U}_e/\lambda_r = 5.0\text{kHz}$. The spectral information associated to the locally most unstable

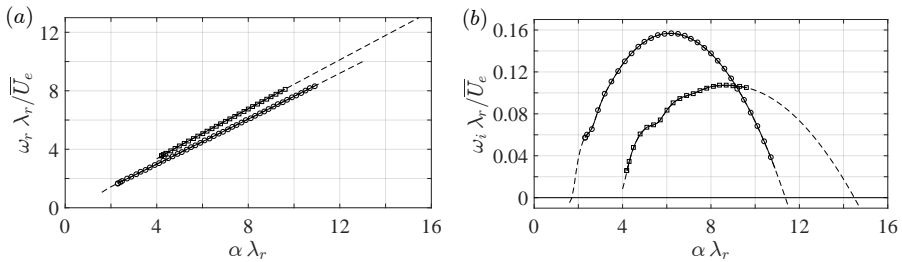


Figure 6.11: Type I (circles) and II (squares) temporal frequency (a) and growth rate (b) versus the wavenumber using the $N_z \times N_y = 55 \times 55$ (dashed) and 90×90 (solid) grid nodes.

Table 6.1: Parameters of the (most temporally unstable and POD wavelength) modes in the base spectrum for the strong vortex.

Type	$\alpha \lambda_r$	$\omega \lambda_r / \bar{U}_e$	f (kHz)	c_{ph} / \bar{U}_e	c_g / \bar{U}_e
(most unstable)	I	6.2	$4.6737 + i 0.1568$	3.0194	0.7538
(most unstable)	II	8.6	$7.272 + i 0.107$	4.698	0.846
(POD wavelength)	I	9.4	$7.1496 + i 0.0970$	4.6190	0.7606

6

type I and II modes are given in table 6.1. It is important to note that these indications do not directly imply these modes are the largest perturbation at this station. To investigate that, the local results, in terms of the spatial amplification rate, have to be integrated in space, i.e. N -factors should be considered.

The $|\tilde{u}|$ -eigenfunctions corresponding to the most unstable type I and II modes are shown in figure 6.12. The spatial distributions of the modes are superimposed over the isocontours of the streamwise velocity of the base flow. Previous investigations from both numerical and experimental perspectives, see Bonfigli and Kloker [4], White and Saric [7], Malik *et al.* [8], indicate the type I mode is positioned on the outer upwashing side of the primary vortex, close to the in-plane saddle point, while the type II mode rides on top of the vortex. As evident, these characteristics are well captured by the BiGlobal analysis. Two spatial mode distributions are to be distinguished in each subfigure and correspond to different grid resolutions. The difference is small, further confirming that the 55×55 grid yields converged eigensolutions.

Using the Reynolds-Orr equation (6.4), the most unstable type I and II eigenmodes can be decomposed into the most dominant contributions shown in figure 6.13, ordered from absolute largest to smallest top to bottom. The remainder is composed out of terms that are individually smaller than the dominant terms in absolute value. The eigenvalues themselves are indicated with dashed lines. Two bars are given for each term, again corresponding to different grid resolutions. The differences in the contributions are consistent with the errors in the eigenvalues.

The ω_i -budget for both mode types is most dominantly dictated by the \bar{U}_w -shear and viscous dissipation. As per the definitions proposed by Malik *et al.* [14], the type I and II (or, z - and y -)modes are produced by the $\partial \bar{U}_w / \partial z_w$ and $\partial \bar{U}_w / \partial y$ shear components, respectively. This is found in the current case as well, as shown in figures 6.13 (b,d). The

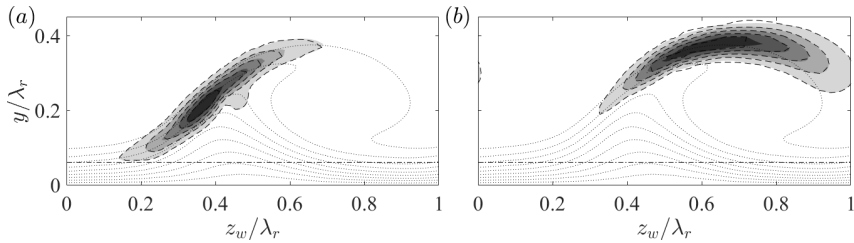


Figure 6.12: $|\tilde{u}_w|/\max|\tilde{u}_w|$ for type I (a) and II (b) (levels span $[1/6, 5/6]$ with $\Delta = 1/6$). 90×90 (filled contours) and 55×55 (dashed) grid resolution. Near-wall region (dash-dotted line). \bar{U}_w/\bar{U}_e levels $0.1, 0.2, \dots, 0.9$ (dotted).

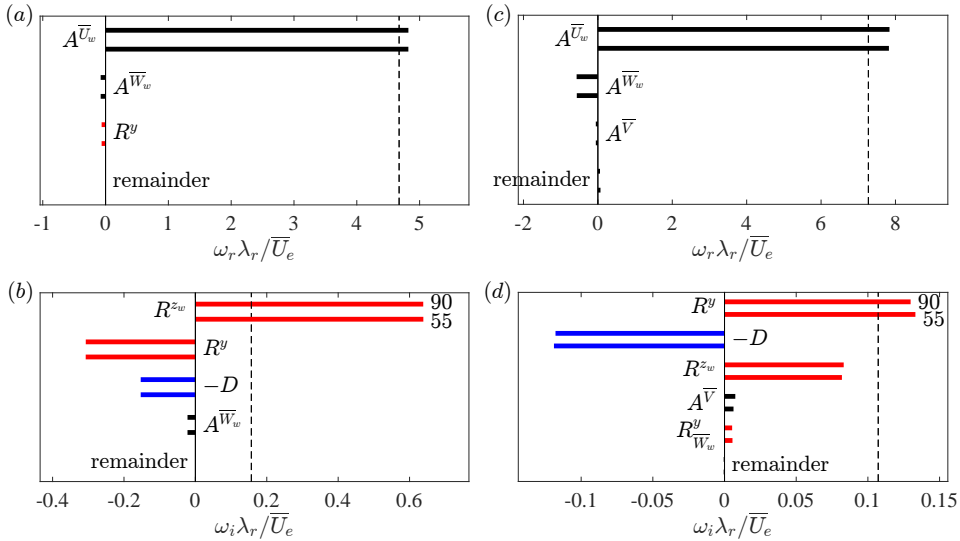


Figure 6.13: (a,c) ω_r - and (b,d) ω_i -budgets (bars) of type I (a,b) and II (c,d), ω eigenvalue (dashed line). Reynolds stress, viscous dissipation and advection terms are coloured red, blue and black, respectively, see equation (6.5) for symbol definitions. Bar pairs: 90×90 (top) and 55×55 (bottom) grid resolution.

other shear components are usually unimportant and can have a net destructive nature, as is the case for the type I mode here. Figure 6.13 (d) illustrates this is not the case for the type II mode; in that case the $\partial\bar{U}_w/\partial z_w$ shear also has a significant net productive role. Modes for which both production terms have comparable contributions are referred to as y/z -modes, see Li *et al.* [50].

Having pinpointed the Reynolds stress terms as most prominent in the ω_i -budget, further insight into their spatial topology is sought. Figure 6.14 shows the integrands of R^y and R^{z_w} for both modes in the plane. After integration over the plane, these functions yield the contributions shown in figures 6.13 (b,d). These terms have their origin in the x_w -momentum equation (2.15a) and hence directly produce the \tilde{u}_w (energy) component. The integrands therefore indicate which part of the \tilde{u}_w eigenfunction they produce. For the type I mode, the integrands clearly reflect the integral values. Interestingly, the downward protrusion located about $(z_w, y)/\lambda_r = (0.45; 0.22)$ is produced by the

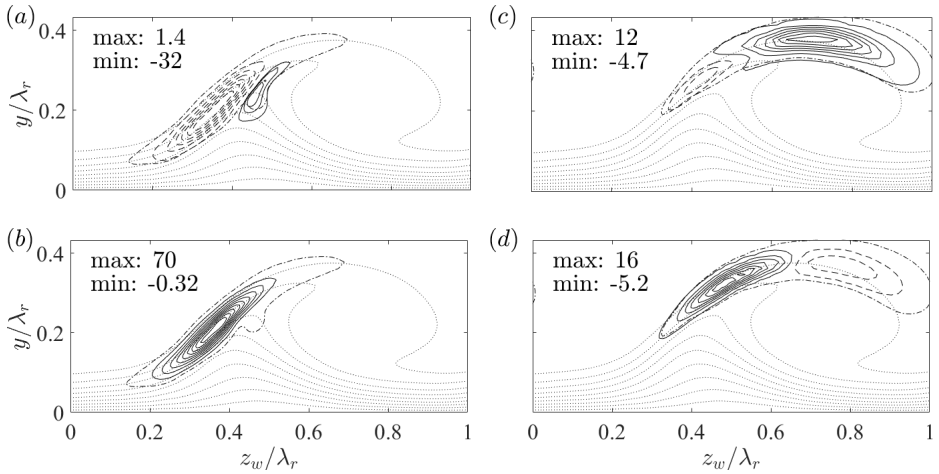


Figure 6.14: Imaginary part of the (a,c) R^y - and (b,d) R^{zw} -integrands for type I (a,b) and II (c,d) (9 levels span (b) [6.71, 63.0], (c) [-3.00, 10.4] and (d) [-3.07, 14.1], negative contours are dashed). Levels in (a) span [-27.5, -3.41], with $\Delta = 4.83$, and [0.350, 1.05], $\Delta = 0.350$. All values are given in \bar{U}_e/λ_r^3 -units. Eigenfunction contour $|\tilde{u}_w|/\max|\tilde{u}_w|=1/6$ (dash-dotted). \bar{U}_w/\bar{U}_e levels 0.1, 0.2, ..., 0.9 (dotted).

6

R^y -term; as illustrated with the additional contours in figure 6.14 (a). The integrands for the type II mode are surprising, because the integrand of R^{zw} attains the largest value, while the $z_w y$ -integral value is smaller. The shape of the positive R^y - and R^{zw} -integrand contours is comparable to that by Malik *et al.* [9] (cf. figure 10).

As mentioned, the participation of the advection terms $A^{\bar{V}}$ and $A^{\bar{W}_w}$ is not restricted to the real dispersion dynamics; as pointed out in figures 6.13 (b,d), they are the next terms in line enhancing or reducing the growth rates of the modes, confirming the inclusion of the \bar{V} - and \bar{W}_w -components in the analysis is essential. With respect to ω_i , $A^{\bar{V}}$ and $A^{\bar{W}_w}$ respectively exert 2.4% and -14.1% contributions for the type I and 7.0% and 2.8% contributions for the type II mode. Figures 6.13 (b,d) show some of these values are larger than the Reynolds stress terms associated to these velocity components.

The origin of the growth induced by the in-plane advection is traced by visualizing the integrands of the related terms in the Reynolds-Orr equation. The previous numbers illustrate $A^{\bar{V}}$ and $A^{\bar{W}_w}$ individually yield a predominant decrease and increase in the type II and type I growth rates, respectively. Figures 6.15 (a,b,d,e) show the integrands associated to $A^{\bar{V}}$ and $A^{\bar{W}_w}$ for both modes. The sign of the sum of these terms is illustrated in figures 6.15 (c,f), indicating the (de)stabilizing regions. The latter figures clearly reflect the criterion based on the term (6.6); whenever the in-plane flow is directed away from elevated perturbation levels, the contribution is destabilizing (black arrows). Conversely, whenever the in-plane velocity is aligned with the perturbation level gradient, the contribution is stabilizing. Contours of the sum of the amplitudes $|\tilde{u}_w| + |\tilde{v}| + |\tilde{w}_w|$ are shown, because equation (6.6) features the gradient of the velocity amplitudes, not the (square root of the) perturbation energy. In the case of the type I mode, the in-plane flow has the tendency to focus the perturbation energy along a spanwise line and therefore has the

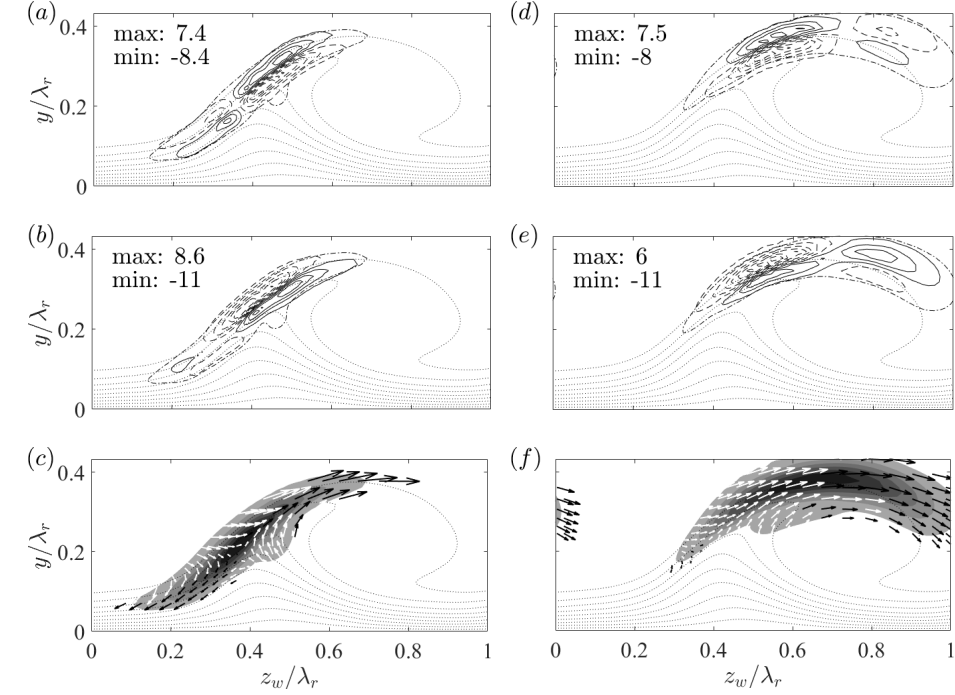


Figure 6.15: (a,b,d,e) Imaginary part of (a,d) $A\bar{V}$ and (b,e) $A\bar{W}_w$ -integrands for type I (a,b) and II (d,e) (9 levels ranging (a) $[-6.84, 5.78]$, (b) $[-8.74, 6.68]$, (d) $[-6.43, 5.93]$ and (e) $[-8.99, 4.32]$ in \bar{U}_e/λ_r^3 -units, negative contours are dashed). Eigenfunction contour $|\tilde{u}_w|/\max|\tilde{u}_w| = 1/6$ (dash-dotted). (c,f) (\bar{V}, \bar{W}_w) -vectors showing where $\text{Im}\{\bar{A}^V + \bar{A}^{\bar{W}_w}\} < 0$ (white arrows) and > 0 (black arrows) for type I (c) and II (f). Amplitude sum $|\tilde{u}_w| + |\tilde{v}| + |\tilde{w}_w|$ (6 filled contours from 0 to maximum). \bar{U}_w/\bar{U}_e levels 0.1, 0.2, ..., 0.9 (dotted).

major effect of increasing the spanwise extent of the eigenfunction. On the other hand, the eigenfunction's maximum is located close to the in-plane flow saddle. This location is thus affected to a minor extent only. For the type II mode, the main effect is advection in the z_w -direction. Therefore it is expected that the location of the eigenfunction's maximum is sensitive to small changes in the productive Reynolds stress.

A large stabilizing pocket is visible in figure 6.15 (b), for which $\bar{W}_w > 0$ and $\tilde{\mathbf{q}}^* \partial \tilde{\mathbf{q}} / \partial z_w > 0$, above the in-plane flow saddle. That region largely contributes to the net \bar{W}_w -advection towards the shear layer's core causing the negative integral value for the type I mode. The magnitude of $A\bar{V}$ in the energy budget for the type II mode is about 3 times smaller than $A\bar{W}_w$ for type I. This is reflected by more evenly matched levels in figure 6.15 (d). The positive contribution in figure 6.13 (d) indicates a net \bar{V} -advection away from the core of the shear layer. The largest contours in figure 6.15 (d) indicate this is largely associated to an imbalance of vertical in- and outward advection on the left hand side of the vortex core. The contours in figures 6.15 (a,e) display a symmetric shape with respect to the absolute eigenfunction contour itself relative to the other cases, explaining negligible integral values. All contours in figure 6.15 are contained within the region of dominance

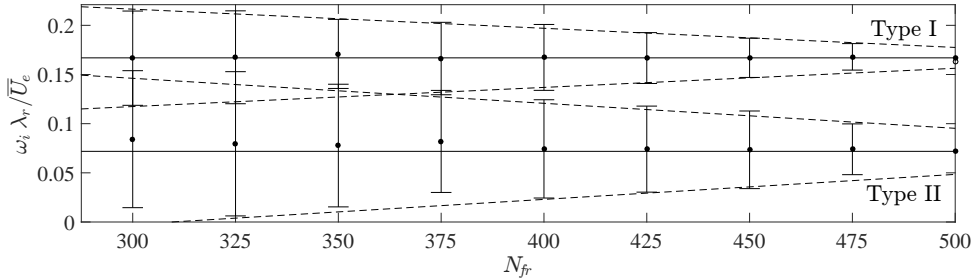


Figure 6.16: Growth rate uncertainty versus ensemble size N_{fr} for both instability modes. Mean (dots) and 2σ (bars) based on 100 random combinations for fixed N_{fr} . The dots at $N_{fr} = 500$ and horizontal lines are the calculated eigenvalue itself. Linear fit to the 2σ -bars (dashed lines).

Table 6.2: Uncertainty and errors in type I and II mode parameters with ensemble size and domain extrapolation parameters. $\dagger z_w$ is based on $N_{fr} = 475$, avoiding extrapolation.

Type I	$\Delta\mu, N_{fr} = 450, 500^\dagger$	2σ at $N_{fr} = 500^\dagger$	error by δ_p	error by δ_o
$\omega_i \lambda_r / \bar{U}_e$	3.92×10^{-5} (0.02%)	1.06×10^{-2} (6.35%)	5.54×10^{-6}	1.22×10^{-5}
$\omega_r \lambda_r / \bar{U}_e$	1.29×10^{-4} (0.003%)	1.45×10^{-3} (0.31%)	2.42×10^{-6}	2.86×10^{-6}
z_w / λ_r	2.68×10^{-4} (0.07%)	5.48×10^{-3} (1.44%)		
Type II	$\Delta\mu, N_{fr} = 450, 500^\dagger$	2σ at $N_{fr} = 500^\dagger$	error by δ_p	error by δ_o
$\omega_i \lambda_r / \bar{U}_e$	1.57×10^{-3} (2.18%)	2.34×10^{-2} (32.6%)	2.32×10^{-4}	6.90×10^{-4}
$\omega_r \lambda_r / \bar{U}_e$	1.61×10^{-4} (0.002%)	1.65×10^{-2} (0.23%)	3.72×10^{-4}	7.24×10^{-4}
z_w / λ_r	1.53×10^{-3} (0.22%)	1.68×10^{-2} (2.44%)		

of the Reynolds stress terms and hence do not generate additional eigenfunction features. Nonetheless, it is noteworthy that the contours in figures 6.15 (*a,b,d,e*) reach the outer limits of the eigenfunction, especially the top right of the type I mode at which the Reynolds stress terms are an order of magnitude smaller.

For both modes, $A^{\bar{U}_w}$ yields the largest contribution to ω_r . The action of the in-plane velocity components is to retard the secondary vortices' advection in the x_w -direction. In total, $A^{\bar{U}_w}$ is cancelled to 3.1% and 7.1% by other terms for the type I and II modes, respectively. The large retardation in the case of the type II mode, considering that the other terms cancel out, is solely caused by \bar{W}_w . This is interpreted to be the consequence of the fact that the eigenmodes travel in the opposite direction of \bar{W}_w . No singular such term can be pointed out for the type I mode. An example of a Reynolds stress term participating in the ω_r -budget is R^y , that slightly reduces the type I mode frequency.

6.4.2. EFFECT OF ENSEMBLE SIZE

The measured mean flow is subject to an uncertainty of $0.1\bar{U}_e/\sqrt{500} = 4.5 \times 10^{-3}\bar{U}_e$, based on the maximum r.m.s. amplitude of $0.1\bar{U}_e$ obtained from the 500 instantaneous PIV snapshots (see §6.4.6). The reported uncertainty stems from both systematic errors (such as tomo-PIV correlation errors), as well as from physical fluctuations of the in-

stantaneous flow. For instance, Serpieri and Kotsonis [3] (cf. §6.3.1) show the r.m.s. field is dominated by a low frequency spanwise shake of the whole primary crossflow vortex, obtained as the most energetic POD mode. While these are acceptable uncertainty levels for flow diagnostics, their effect on the stability analysis should be carefully identified. In this section an effort is provided towards quantifying the effect of the ensemble average on the eigensolutions.

The uncertainty is quantified by deploying a Monte-Carlo approach to the stability analysis. More specifically, stability analysis is performed on mean flows produced by varying the ensemble size, N_{fr} , ranging from 300 to 475, with steps of 25. 100 different random combinations are made per N_{fr} from the total pool of 500 snapshots, resulting in 800 cases in total plus the single case possible for $N_{fr} = 500$; used as baseline case. Stability simulations were performed on the 45.6% chord plane using the 55×55 grid. For both modes, the respective most unstable wavenumber in table 6.1 was used as input.

The results are shown in terms of the mean and 2 standard deviations ($\pm 2\sigma$) of the growth rate in relation to the ensemble size in figure 6.16. While the solution undergoes large fluctuations for small ensemble sizes, which is expected, a clear convergence trend is established for both the mean value and fluctuations. The difference between the estimated mean growth rate for $N_{fr} = 450$ and the single case growth rate for $N_{fr} = 500$ is given in table 6.2 as $\Delta\mu$, illustrating convergence of the mean to errors at most one order of magnitude larger than the grid truncation errors. The percentages in the table are the relative errors with respect to the value for the $N_{fr} = 500$ case.

The growth rate fluctuations within the 100 random cases are relatively large as shown by the standard deviation bars. Nevertheless, they also show an evident linear converging trend, illustrating that the mean value is approached in the limit of large N_{fr} . The linear trend is extrapolated to obtain a measure at $N_{fr} = 500$, also reported in table 6.2. It was shown in §4.7.3 that the convergence rate does not necessarily have to scale like $1/\sqrt{N_{fr}}$. The demonstrated trend allows discarding the fluctuations, under the condition that a minimum threshold N_{fr} can be defined beyond which the integrity of the solution structure can be demonstrated.

The terms in the Reynolds-Orr equation are shown as a function of the ensemble size in figure 6.17. Fluctuations appear, as expected, but the mean term values per N_{fr} are well-defined and indicate a consistent balance for all N_{fr} . Note that some contribution values, including the standard deviations with respect to the mean value, are enlarged by a factor 10 for clarity. For the type II mode the mean value of the Reynolds stress terms R^y and R^{zw} changes considerably, albeit only for $N_{fr} \leq 375$ and the same relative size is retained with respect to the other terms.

Prior to physical underpinning of the energy term fluctuations, it is necessary to confirm whether these are influenced by the numerical treatment and discretization of the problem. To this goal, preliminary simulations were performed by altering several parameters. These included increasing the grid resolution from $N_z \times N_y = 55 \times 55$ to 90×90 and changing the mean flow differentiation method from a 6th to 4th order finite difference scheme. Both changes yielded negligible differences in the stability results, corroborating to a physical mechanism as source of the energy term fluctuations.

Based on the previous, the fluctuations are concluded to be caused by the physical response of the instability modes to base flow changes. Figures 6.17 (b,d) indicate that

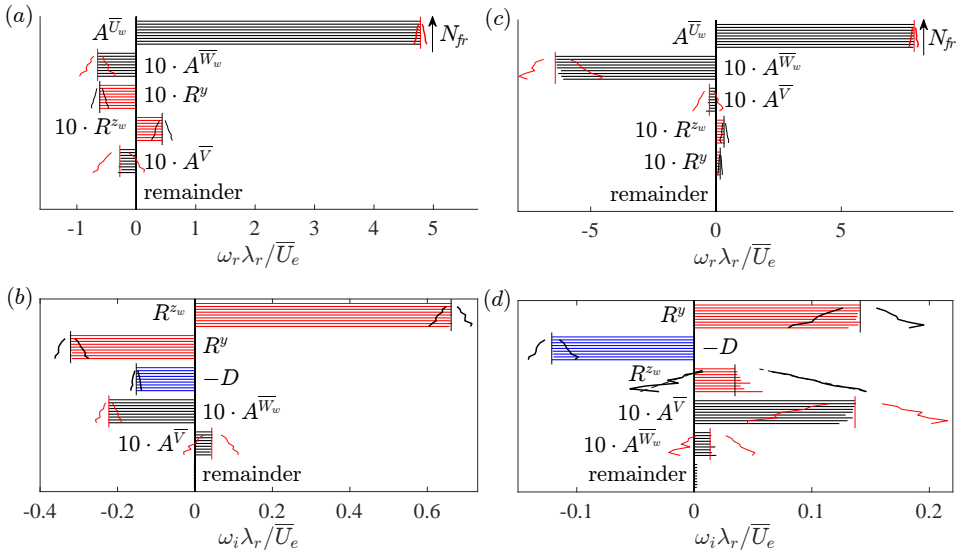


Figure 6.17: (a,c) ω_r - and (b,d) ω_i -budgets of type I (a,b) and II (c,d), mean value (bars) and 2σ (slanted lines) per N_{fr} , ranging from 300 (bottom bar) to 500 (top bar) every 25 samples. Vertical lines indicate the single eigensolution for $N_{fr} = 500$ as a reference. Small terms (mean and 2σ) are magnified with a factor 10, the slanted lines then indicate 20σ .

6

growth rate fluctuations are mainly induced by the fluctuations in the Reynolds stresses R^y and R^{zw} and viscous dissipation D . Correlation analysis is used to quantify the link, using all 800 simulation results (all random combinations for all N_{fr}). The correlation coefficient between the combination of the Reynolds stress and dissipation terms ($R^y + R^{zw} - D$) on one hand and the growth rate ω_i on the other are found to be 0.988 and 0.995 for the type I and II modes, respectively. The dissipation evidently adapts itself to the Reynolds stress terms, which is supported by correlation coefficients larger than 0.958 when omitting the dissipation terms (correlating $R^y + R^{zw}$ to ω_i).

For the type I mode, the fluctuations in the Reynolds-Orr terms are relatively small and never change the energy balance structurally. Additionally, the advection terms for this mode, although small in the mean, display weak fluctuations. The fluctuations are small enough that the relative size of the terms in the energy balance is fixed qualitatively; they do not break its structure. This is not the case for the type II mode. Especially the R^{zw} -term experiences fluctuations large enough to drive the term to negative values ($R^{zw} < 0$) on the one hand and larger values than the dominating Reynolds stress term ($R^{zw} > R^y$) on the other for different random ensembles for fixed N_{fr} . Nevertheless, all fluctuations show a linear convergence trend with N_{fr} , similar to the eigenvalue in figure 6.16. $A^{\bar{V}}$ displays relatively small fluctuations for type II.

The shear values at the (z_w, y) -location of the eigenfunction maximum were extracted (see §6.4.9) and inspected based on the correlation between different energy terms. For both modes, R^{zw} is highly correlated to the $\partial \bar{U}_w / \partial z_w$ values (type I: -0.954, type II: -0.978), as expected. The R^y -term is also most correlated to the $\partial \bar{U}_w / \partial z_w$ values for

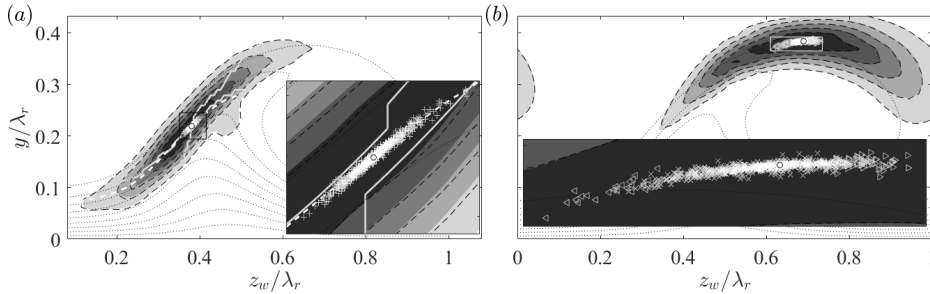


Figure 6.18: $|\tilde{u}_w|/\max|\tilde{u}_w|$ for type I (a) and II (b) (levels span $[1/6, 5/6]$ with $\Delta = 1/6$) for $N_{fr} = 500$ (filled contours) and 450 (dashed lines). Centre of gravity of $\tilde{q}^* \cdot \tilde{q}$ for every case (symbols), the case $N_{fr} = 500$ (black circle), in (b): y is determined along the z_w centre of gravity location, $R^{zw} > R^y$ (\triangleleft) and $R^{zw} < 0$ (\triangleright). \bar{U}_w/\bar{U}_e levels $0.1, 0.2, \dots, 0.9$ (dotted); in (a), $\bar{U}_w/\bar{U}_e = 0.744$ (white dashed) and $\text{Im}\{\bar{A}^V + \bar{A}^W\} = 0$ (gray solid). Insets: zooms on rectangles.

mode II, yielding the coefficient 0.763 with respect to -0.617 for the $\partial\bar{U}_w/\partial y$ value. This indicates the dominant role of the $\partial\bar{U}_w/\partial z_w$ component in the fluctuations of the type II mode.

The type I eigenfunctions corresponding to $N_{fr} = 500$ and 450 (single random sample from the pool of 100 cases) are compared in figure 6.18 (a), confirming the eigenfunction is converged. Furthermore, the centre of gravity of the perturbation velocity contours in the plane is given for all N_{fr} . All points are clustered densely about the indicated $\bar{U}_w = 0.744\bar{U}_e$ contour, slightly lower than the predicted phase speed. Compared to figure 6.14 (b), the points are located close to the maximum of the R^{zw} -integrand. Furthermore, when comparing to figure 6.15 (c), all points turn out to lie in the narrow band where the advection terms are destabilizing. This is indicated by the boundary between the white and black arrows in figure 6.18 (a). The oscillations in this mode appear to be constrained so that the maximum of the eigenfunction remains confined to this narrow band.

The type II eigenfunctions are shown in figure 6.18 (b), corresponding to the $N_{fr} = 500$ and 450 cases. Similar to type I, these eigenfunctions display negligible differences. However, the centre of gravity shows a larger spread. The larger spread reconciles well with the topology of the in-plane advection terms in figure 6.15 (f). Indeed, there is no focus point towards which the maximum of the eigenfunction gravitates, in contrast to the case for the type I mode. Nonetheless, the eigenfunction always displays the characteristic shape shown in figure 6.12; i.e. over-arching the entire crossflow vortex. In many cases within the random Monte-Carlo pool, however, the eigenfunction distinctively leans to the left or right. Selecting two such eigenfunctions with their maximum located at the left- and rightmost position, the R^{zw} -term was found to have a very high and low (negative) value, respectively. Testing the correlation between the z_w -location of the centre of gravity with the R^{zw} -term yields the coefficient -0.994, indicating a direct link between their respective fluctuations. The interpretation follows directly from figure 6.14 (d). Whenever the eigenfunction leans to the left, the destabilizing region of the R^{zw} -integrand increases and vice versa. The shift can be sufficiently large that R^{zw}

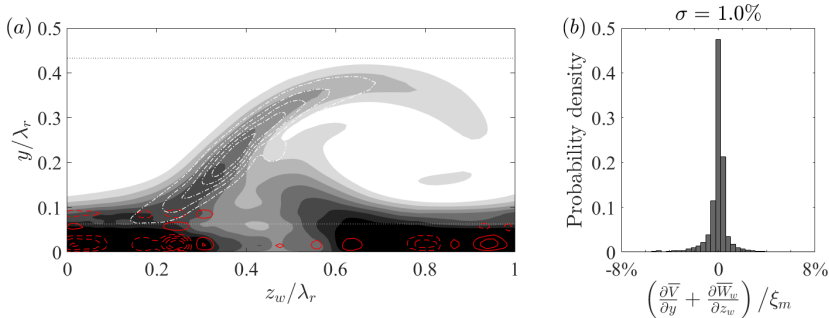


Figure 6.19: (a) In-plane flow divergence (red, levels from $\pm 2\%$ to $\pm 8\%$ with steps of 2% of the maximum in-plane \bar{U}_w -shear: $\xi_m = 16 \bar{U}_e / \lambda_r$, negative levels are dashed). In-plane \bar{U}_w -shear magnitude of the strong vortex for $N_{fr} = 500$ (8 filled contours from 0 to 7 in \bar{U}_e / λ_r -units). $|\tilde{u}_w| / \max |\tilde{u}_w|$ of most unstable type I mode from figure 6.12 (a) (dash-dotted contours). Near-wall region ($y/\lambda_r \leq 0.061$) and upper limit PIV domain ($y/\lambda_r = 0.433$) (dotted lines). (b) Occurrence histogram of divergence values, bar width: 0.4%.

becomes negative (right shift) or exceeds the R^y -term (left shift). In the Monte Carlo framework, out of the 800 solutions these extreme right and left shifts occur 64 and 27 times, respectively. These special occurrences are indicated with the triangles in figure 6.18. The last occurrences of the right and left shift are observed for $N_{fr} = 425$ (once) and 450 (trice), respectively.

The z_w -position of the maximum of the eigenfunction gives a direct handle on the convergence of the mode, which is more conclusive than figure 6.17 (d) can show. The fluctuation amplitudes based on 2 standard deviations and difference in the mean values for $N_{fr} = 475$ and 450 are reported in table 6.2. For $N_{fr} > 400$ the amplitude becomes smaller than the local grid spacing, $1.2 \times 10^{-2} \lambda_r$ and $2.9 \times 10^{-2} \lambda_r$ for mode I and II, respectively. Again displaying approximate linear convergence, at $N_{fr} = 475$ the amplitudes attain the values $5.48 \times 10^{-3} \lambda_r$ and $1.68 \times 10^{-2} \lambda_r$ for mode I and II, respectively.

6.4.3. DIVERGENCE OF THE IN-PLANE FLOW

As mentioned in §§2.3.5 and 6.2.2, the stability approach requires the in-plane velocity field to be solenoidal. However, this cannot be expected from experimentally measured data. It is known from previous work, see [4], that the stability results depend on how this issue is approached. However, the order of magnitude of the growth rates is usually preserved. Properly adjusting the fields is out of the current scope. Nevertheless, for completeness, the in-plane divergence is characterised and the effect on the growth rate of the type I mode is estimated in this section.

The maximum divergence levels are attained at the locations in the near-wall region as shown in figure 6.19 (a), where the in-plane \bar{U}_w -shear is maximal. The type I eigenfunction displays an overlap for $|\tilde{u}_w| / \max |\tilde{u}_w| < 1/3$. Outside the near-wall region, the overall magnitude drops significantly. Figure 6.19 (b) illustrates the overall statistical distribution of the divergence in the PIV domain. The standard deviation is 1% of the maximum in-plane shear in the \bar{U}_w -field.

Basic tests were performed to assess the effect of the terms related to the in-plane divergence for the type I mode, with $\alpha \lambda_r = 6.2$. Artificial manipulations of the $\partial \bar{V} / \partial y$ and

$\partial\bar{W}_w/\partial z_w$ fields were performed, independently of the other fields, to gauge the change in the eigenvalues. By setting $\partial\bar{V}/\partial y = \partial\bar{W}_w/\partial z_w = 0$ and replacing the $\partial\bar{V}/\partial y$ field by $-\partial\bar{W}_w/\partial z_w$, the growth rate changed by -0.0142 and 0.0018 units of \bar{U}_e/λ_r , respectively. The former change lies within the error bound indicated by the 2σ uncertainty specified in table 6.2 for $N_{fr} = 500$. The latter destabilising change is qualitatively consistent with the comparison of the w_v - and v_v - w_v -fixed approaches by Bonfigli and Kloker [4, cf. figure 15 (a)].

6.4.4. EFFECT OF WALL-NORMAL EXTRAPOLATION

Another question related to the use of the measured mean flow is what impact the freestream PIV data extrapolation method has on the results. Specifically, the effect of the overlap region's parameters is to be quantified. To this end, tests were performed applying significant variations in its position, through δ_p , and size, with δ_o , see figure 6.4. The largest value for δ_p is the height of the PIV domain, $\delta_{mp} = 0.433\lambda_r$. By setting $\delta_p < \delta_{mp}$, the upper part of the PIV data is artificially altered, which is to be avoided. By increasing δ_o , the shear caused by the discontinuity is reduced. Increasing both parameters δ_p and δ_o should therefore yield converging eigenvalues.

To test this, a (δ_p, δ_o) -test matrix was set up, setting $\delta_p/\delta_{mp} = 0.9, 0.95$ and 1 and $\delta_o/\delta_{mp} = 0.2, 0.6$ and 1 , see figure 6.20. For $\delta_p = 0.90\delta_{mp}$ the type II mode is covered significantly and $\delta_o = 0.2\delta_{mp}$ is comparable to the vorticity thickness of the shear layer, which is expected to influence the results significantly.

The eigenvalue problem was solved, fixing $\alpha\lambda_r = 8.2$ and using the 55×55 grid resolution on the $N_{fr} = 500$ mean flow. Figure 6.21 shows the resulting eigenvalues. Both modes converge as δ_p and δ_o are increased. As expected, the type II mode is affected more than type I, but the absolute eigenvalue errors are smaller than the discretization error. This is attributed to the small eigenfunction magnitudes in the overlap region. It is concluded that, when taking $\delta_p = \delta_o = 0.433\lambda_r$, the base flow extrapolation influences the results negligibly. Table 6.2 reports the errors for $(\delta_p, \delta_o)/\delta_{mp} = (0.95, 1.0)$ and $(1.00, 0.6)$. These results justify using the Blasius profile for the extrapolation.

6.4.5. APPLICABILITY OF THE GASTER-TRANSFORMATION

The secondary vortices are known to be a convective instability [4]. They grow in space subject to an imposed frequency, which corresponds to the case where $\alpha \in \mathbb{C}$ is unknown and $\omega \in \mathbb{R}$ is given; i.e. the spatial problem. Up to now, only the solutions of the temporal problem have been handled. Equation (3.36) illustrates the spatial stability problem is twice as expensive, because α appears quadratically in the equations. Solving this problem can be circumvented by applying the Gaster-transformation, see Gaster [51] or §2.4.5, based on the fact that spatial and temporal growth are equivalent for convective perturbations. To this end, the simple formula:

$$\alpha_i|_{\omega_i=0} = c_g^{-1}\omega_i|_{\alpha_i=0} + O(\omega_i|_{\alpha_i=0}^2) \quad (6.7)$$

can be used, where c_g is the group speed shown in figure 6.22 (a) for both mode types and compared to the phase speeds. The Gaster-transformation is valid for small ω_i -values only, see Gaster [51]. The inviscid instabilities considered here have relatively large ω_i , which renders its application questionable. Nevertheless, it is well-established

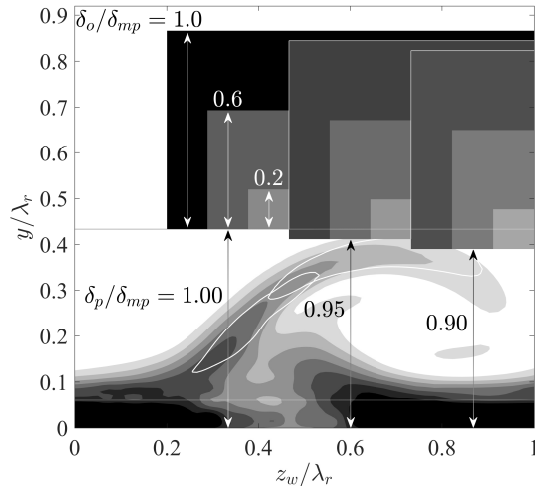


Figure 6.20: Overlap region definition and variations. In-plane \bar{U}_w -shear magnitude of the strong vortex for $N_{fr} = 500$ (40 filled contours from 0 to 7 in \bar{U}_e/λ_r -units). $|\bar{u}_w|/\max|\bar{u}_w| = 0.5$ for most unstable type I and II modes (white contours). Near-wall region ($y/\lambda_r \leq 0.061$) and upper limit PIV domain ($y/\lambda_r = 0.433$) (dotted lines).

6

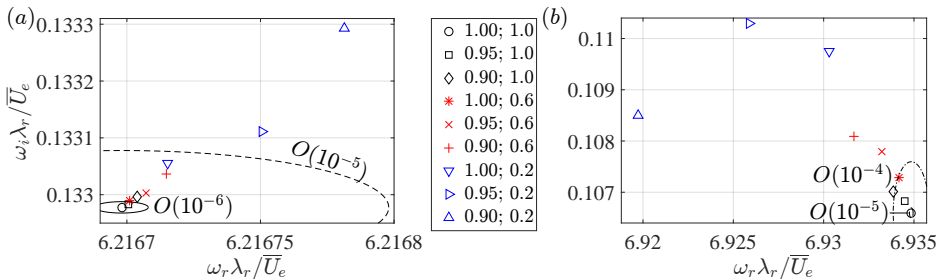


Figure 6.21: Type I (a) and II (b) eigenvalue ($\alpha\lambda_r = 8.2$) for different domain extrapolation parameters (legend indicates δ_p ; δ_o in units of δ_{mp}). 10^{-6} (solid), 10^{-5} (dashed) and 10^{-4} (dash-dotted) neighbourhoods of the eigenvalue with $\delta_p = \delta_o = \delta_{mp}$.

in the literature that the transformation yields near exact results, see Malik *et al.* [9] and Koch *et al.* [15]. Here, this check is reproduced to rule out different sensitivities of the spatial and temporal stability problems to measurement noise in the modified base flow. Furthermore, the difference is regarded from the point of view of the eigenfunctions and the Reynolds-Orr decompositions of the eigenvalues.

The comparison between the spatial amplification rates, obtained by solving equation (3.36), and the Gaster-transformed temporal growth rates, obtained by solving equation (3.36) and applying equation (6.7), are shown in figure 6.22 (b), using the 55×55 grid on the $N_{fr} = 500$ mean flow at 45.6% chord. The eigenvalue error at the most unstable frequencies is $O(10^{-4})$; which is in-line with the grid resolution accuracy. Thus, next to the agreement with the literature, the spatial and temporal problems do not display a relative sensitivity to the used measured flow field.

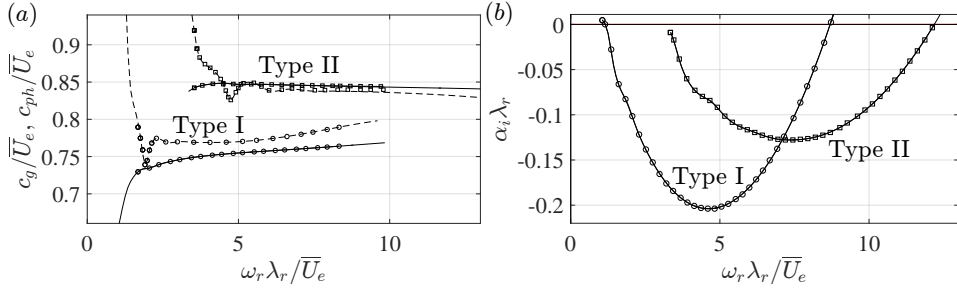


Figure 6.22: (a) Group (dashed lines) and phase (solid lines) speeds for both modes. 55×55 (lines) and 90×90 (symbols) grid resolution. (b) Gaster-transformed temporal amplification rates, $-\omega_i/c_g$, (solid, solving equation (3.35), $\alpha \in \mathbb{R}$) and spatial growth rates, α_i , (symbols, solving equation (3.36), $\omega \in \mathbb{R}$).

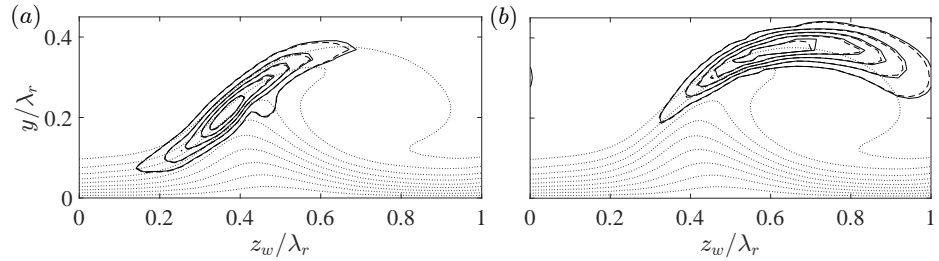


Figure 6.23: Temporal (solid lines, $\alpha \in \mathbb{R}$) and spatial (dashed lines, $\omega \in \mathbb{R}$) eigenfunctions ($|\tilde{u}_w| / \max |\tilde{u}_w|$ levels span $[1/6, 5/6]$ with $\Delta = 1/6$) for type I (a, $\omega_r \lambda_r / \bar{U}_e = 4.5967$) and II (b, $\omega_r \lambda_r / \bar{U}_e = 7.354$). \bar{U}_w / \bar{U}_e levels 0.1, 0.2, ..., 0.9 (dotted).

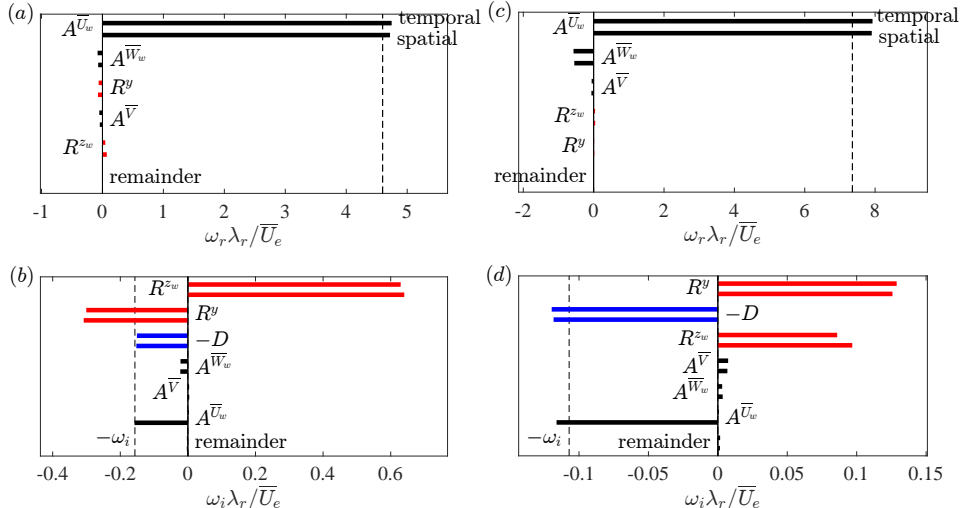


Figure 6.24: (a,c) ω_r - and (b,d) ω_i -budgets (bars) of type I (a,b) and II (c,d), complex conjugate eigenvalue (dashed line). Bar pairs: temporal (top) and spatial (bottom) problem.

Although the eigenvalues are virtually identical, this does not warrant similarity of the eigenfunctions or ω -budgets. Both features are compared in figures 6.23 and 6.24 for the most temporally unstable type I and II modes. It is to be noted that the most amplified modes (maximal α_i) have a slightly lower frequency than the most unstable modes (maximal ω_i). The spatial and temporal eigenfunctions match closely, the only difference is the slightly larger extent of the temporal eigenfunction. Additionally, the phase distribution, accounting for the direction reversal, is found to be identical.

The ω -budgets are the same qualitatively, but individual terms show noticeable changes. A new contribution is that of $\alpha \bar{U}_w$ to ω_i , rendering it identically zero in the spatial problem. It is moreover revealed that the contribution due to the $2\alpha_i \tilde{u}^* \tilde{p}$ -term is negligible; the double integral over $\tilde{u}^* \tilde{p}$ evaluates to (numerical) zero. For this particular case, the changes in the individual contributions for the type I mode cancel, to yield $-\omega_i \approx \alpha_i \iint \bar{U}_w \tilde{\mathbf{q}}^* \cdot \tilde{\mathbf{q}} dy dz_w / \|\tilde{\mathbf{q}}\|^2$. This is not the case in general, shown by the type II case. There, the variation in the individual contributions adds up to the difference between the $-\omega_i$, indicated by the dashed line, and $\alpha \bar{U}_w$ -terms. For the type I mode, this difference turns out to be small. It is noteworthy that the dominant advection terms in the ω_i -budget change negligibly, which, based on the interpretation from equation (6.6), is expected regarding the small change in the eigenfunction.

6.4.6. COMPARISON WITH EXPERIMENTS

6

A detailed account is given on the spatial structure of the type I mode by [3], through means of spectral and POD analysis. In particular, the POD analysis presented by [3] undeniably confirms the presence of the type I mode. This allows a detailed comparison with the retrieved eigenmode in terms of flow structure and spatial growth. Despite the limited temporal resolution of the tomo-PIV technique, the power of the POD method is to extract prominent wavelengths from the experimental data. Based on this, the eigenmode with the same spatial wavelength as the POD mode representing the type I secondary instability reported by [3] is considered. The wavelength is $\lambda = 4.6\text{mm}$, which corresponds to $\alpha \lambda_r = 2\pi \times 9 \cos 40^\circ / 4.6 \approx 9.4$. Note that this corresponds to a larger wavenumber than the locally most unstable mode reported in table 6.1. This is expected; the mode with the largest amplitude at a given location is usually situated closer to the neutral curve at a larger wavenumber.

First, a quantitative comparison with the experimentally measured in-plane amplitude distributions is discussed. Figure 6.25 shows the absolute amplitude of the x_w -velocity component of the type I eigenmode versus both the hot-wire and tomo-PIV measurement results presented by [3]. On the one hand, the eigenmode is compared against the bandpass filtered r.m.s. field associated to the type I mode frequency obtained from hot-wire measurements, see their figure 20 (top center). The considered band corresponds to slightly higher frequencies, 5-6kHz, when compared to the frequency associated to the POD mode pair, 4.6kHz, see table 6.1. On the other hand, it is compared with the magnitude of the total r.m.s. and the POD pair associated to the type I mode obtained with the tomo-PIV measurements, see their figure 28.

The hot-wire was oriented in the Z -direction, measuring the effective velocity in the (X, y) -plane. The y -velocity component is small, as indicated by the base flow and the eigenfunction, and x_w and X deviate only by 5° , so the measured velocity is represen-

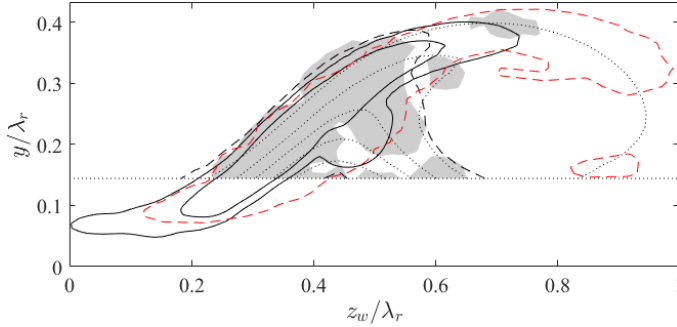


Figure 6.25: Velocity fluctuation fields associated to the eigenmode (solid, $|\tilde{u}_w|$, levels: 6.67% and 20%), the tomo-PIV total r.m.s. (dashed, x_w -component at $x_w = 15.76$ mm, level: 33.3%) and the temporal r.m.s. of the POD mode couple (filled, $\sqrt{\Phi_9^2 + \Phi_{10}^2}$ at $x_w = 15.76$ mm in [3], level: 20%) and the hot-wire bandpass filtered fluctuation field (red dashed, effective velocity in the (X, y) -plane at $x_w = 0$ mm, band 2 in [3], level: 20%). All percentages are relative to the in-plane maximum. Near-wall region for the tomo-PIV and \bar{U}_w/\bar{U}_e levels 0.5, 0.6, ..., 0.9 at $x_w = 15.76$ mm (dotted lines).

tative of the x_w -velocity component. Furthermore, the hot-wire was traversed in the z -direction, the data corresponding to the 45% chord station is here projected onto the z_w -coordinate.

POD of the tomo-PIV measurement data gives two phases per advecting mode (shifted by $\pi/2$), representing all velocity components in the entire measurement volume. [3] reported this pair as Φ_9 and Φ_{10} ; the 9th and 10th POD modes. The Euclidean sum of these modes, weighted with the variance of their respective time coefficients, yields an amplitude distribution with the least phase modulation. The total r.m.s. distribution corresponding to the tomo-PIV measurements is also considered for reference. The attention is focussed on the x_w -velocity component, the symbol Φ will therefore be used to indicate the spatial structure of that component only. The tomo-PIV data is extracted at the location where the POD mode attains its maximum amplitude, at $x_w = 15.76$ mm. The maximum value of the total r.m.s. x_w -velocity component is equal to $0.10\bar{U}_e$; the number used in the uncertainty arguments treated before.

The shape of the $|\tilde{u}_w|$ amplitudes shows a qualitative agreement and can also be compared to the results of [7] and [52]. The bandpass filtered r.m.s. field is found to have an overall similar spatial structure, but it displays a larger longitudinal extent at the leeward side of the primary vortex (towards $z_w/\lambda_r = 1$). The POD mode Φ_9 has a significantly lower magnitude than Φ_{10} for $z_w > 0.5\lambda_r$, consistent with the lower amplitude of the corresponding total r.m.s. distribution. This corroborates the segmented shape of the Euclidean sum of the POD modes. The total r.m.s. distribution shows perturbations are supported in a broader spanwise range under the primary vortex when considering all frequency content.

Effectively, figure 6.25 demonstrates the merits of the stability analysis technique as a tool for experimental data reduction. The method is able to isolate the pertinent monochromatic eigenmodes based on the mean measurement data. Especially in the case of advanced flow diagnostic techniques such as tomo-PIV, it is very challenging to distinguish between the physical r.m.s. field of different modes as well as measure-

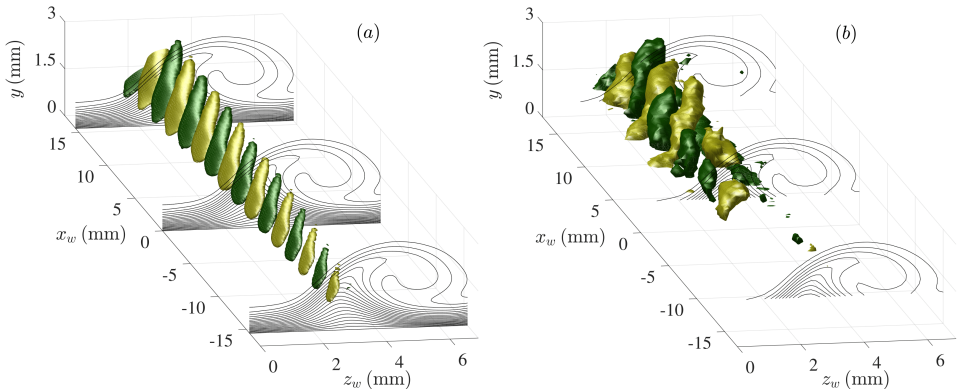


Figure 6.26: x_w -velocity isosurfaces of (a) the type I eigenmode at $\omega/2\pi = 4.6 \text{ kHz}$ ($\alpha_r = 9.4/\lambda_r$), having maximal amplitude 1 at $x = -17.6 \text{ mm}$, plotting the $\pm 84\%$ levels, and (b) the tomo-PIV POD mode (Φ_{10} in [3]), plotting the $\pm 0.086\bar{U}_e$ levels, the near-wall region is cut. \bar{U}_w/\bar{U}_e levels 0, 0.05, ..., 1 (contours).

ment noise. The (most unstable) eigenmodes give an indication of the most dominant frequencies and the expected spatial topology. The proposed methodology *extends* the information on the perturbation field and, furthermore, it enables *enhancing* the measurability of desired features by focusing the experimental set-up accordingly.

The shape of the eigenfunctions is found to be wavelength-independent. However, the relative magnitudes of the $|\tilde{v}|$ and $|\tilde{w}_w|$ components change significantly for different wavelengths. The relative magnitudes of the velocity components of the eigenmode with the wavelength extracted from POD are in close agreement with the total r.m.s. values. The ratios of the in-plane maxima of $|\tilde{v}|$ and $|\tilde{w}_w|$ for the eigenmode are: 23% and 50%, relative to the maximum of $|\tilde{u}_w|$. The same quantities for the total r.m.s. are: 21% and 44%, respectively. These maxima for the eigenmode are located at $(z_w, y)/\lambda_r = (0.38; 0.23)$ for $|\tilde{u}_w|$ and $(0.39; 0.25)$ for $|\tilde{v}|$, the total r.m.s. has both maxima at $(0.36, 0.21)$. The wavelength from POD is used to facilitate this specific comparison. When determined for the most unstable wavenumber reported in table 6.1, for example, the relative maxima of $|\tilde{v}|$ and $|\tilde{w}_w|$ are 14% and 33%, respectively, which are lower than the values corresponding to the POD wavelength. This suggests that the mode's wavelength can be estimated by identifying the eigenmode that has approximately the same amplitude ratios as observed in the total r.m.s. data; POD is not required for that.

A three-dimensional representation of the eigenmode and POD mode associated to the type I instability is shown in figure 6.26 (a) and 6.26 (b), respectively, illustrating their spatial structure. The most unstable eigenmode is extrapolated in space, incorporating the exponential growth in space calculated using the Gaster-transformation: $-\omega_i \lambda_r / c_g = -0.09702/0.7805 = -0.1243$. These structures are compared to the 10th POD mode, Φ_{10} , of [3]. Upstream of $x_w = -4 \text{ mm}$ the isosurfaces are absent in the POD mode. This is a consequence of the limited dynamic range of this particular tomo-PIV experiment and of the very low perturbation amplitude.

Overall, a qualitative match of the topology is established between the modes, the largest difference being the structures' length. [3] documented the orientation of the

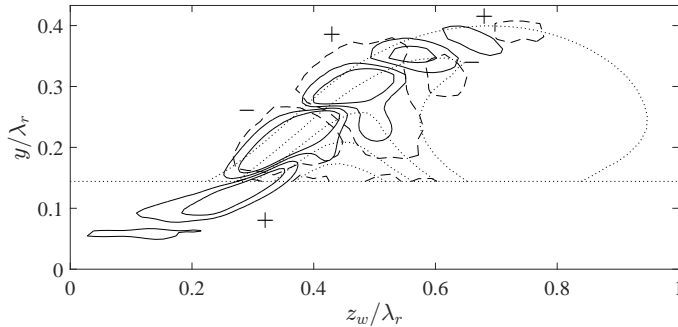


Figure 6.27: Eigenmode $\text{Re}\{\tilde{u}_w\}/\max|\tilde{u}_w|$ (solid) (levels: $\pm 6.67\%$ and $\pm 20\%$) and POD mode x_w -velocity component (Φ_{10} in [3]) at $x_w = 15.76 \text{ mm}$ (dashed) (levels: $\pm 20\%$ of in-plane maximum), level signs are indicated. Near-wall region and \bar{U}_w/\bar{U}_e levels $0.5, 0.6, \dots, 0.9$ at $x_w = 15.76 \text{ mm}$ (dotted lines).

secondary instability structures in terms of their azimuthal angle and inclination: -18.2° and 21° , respectively, with respect to the stationary vortices. The eigenmode displays a comparable azimuthal angle, -17.8° , but a smaller inclination: 12° . The latter angle agrees with the value reported by [19] and [16]; who also report an inclination angle of 12° . A similar difference in the inclination is observed in the application to the instabilities in the wake of a micro-ramp [27]; the structures as observed in the tomo-PIV experiment also display a larger inclination in that case.

The instantaneous flow structures are compared to a higher degree of detail in the $z_w y$ -plane in figure 6.27. The POD mode is extracted at $x_w = 15.76 \text{ mm}$, maximizing its absolute amplitude. Both modes show the same arrangement of positive and negative perturbation velocity pockets, even in locations where the velocity maxima are small, despite a slight misalignment. The orientation of the contours is the same and can be compared to phase-locked hot-wire measurement observations presented by [11] and [52] and the computations of [19]. Two contour levels are shown for the eigenmode, of which the largest corresponds to the POD mode contour level. The lowest level shows that the structure corresponding to the POD mode is broader than the eigenmode in the direction perpendicular to the shear layer, as was already apparent in figure 6.26. But both modes have the same qualitative shape; both show a contour in the centre that has a large downwards protrusion. This illustrates the stability analysis effectively describes the perturbation flow topology. The broader structures observed in the measurement could be explained by the limited capability of the tomo-PIV experiment in capturing complicated flow structures in the presence of strong shear. From the perspective of the (de)stabilizing action of the in-plane advection terms in equation (6.6), the broader structure would be more stabilized as this corresponds to a larger white region in figure 6.15 (c).

Having identified the correspondence between the structures of the eigenmode and POD mode, the exponential growth can be analysed. It should be highly stressed here that there is no reason to expect that the eigenmode and POD mode should display the same growth rate. The POD mode is a data-driven, energy-maximizing coherent structure having a broad spectral content, that is, to a degree, corrupted with systematic and

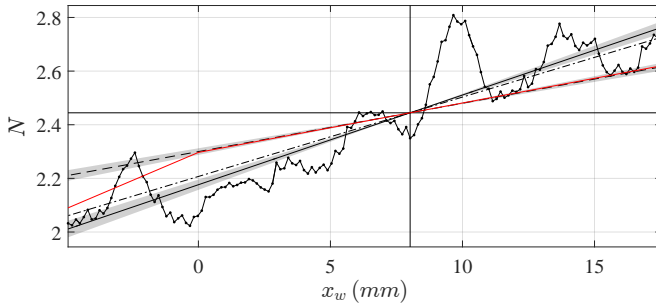


Figure 6.28: N -factors based on the: POD mode couple r.m.s. (dotted line), linear fit to POD r.m.s. (solid line), bandpass filtered hot-wire anemometry velocity fluctuation fields reproduced from figure 21 (b) of [3, band 2] (red), eigenmode: most unstable (dashed, $\alpha \lambda_r = 6.2$) and POD wavelength (dash-dotted, 9.4). Uncertainty in linear fit slope and growth rate based on 2σ in table 6.2 (shaded).

random measurement noise. As stated by [3], other POD modes showed similar structures to that in figure 6.26 and this corroborates with the broad frequency band in the hot-wire spectrum for type I mode fluctuations. An eigenmode, on the other hand, is purely monochromatic and represents a rigorous solution of the governing equations, making it an entirely different entity. Growth rates are moreover notoriously hard to match, as pointed out with the executed sensitivity study and by verification studies in the computational literature, see [4]. For this reason, the scope of this comparison serves more as a qualitative comparison for the methodology, rather than a strict validation.

The r.m.s. field of the coupled POD modes is integrated in both wall-normal and spanwise directions, towards producing a relative amplitude. The N -factor is defined as the natural logarithm of the resulting quantity:

$$N(x_w) = \ln \left(\iint |\Phi(x_w, y, z_w)| dy dz_w \right),$$

where Φ corresponds to the x_w -velocity component of the POD mode couple. The integral can be evaluated in the x_w -range $[-4, 17]$ in millimetres, where the dynamical range of the experiment was sufficient to resolve the mode couple. [3] reported N -curves in their figure 21 (b), based on the bandpass filtered r.m.s. data corresponding to the type I frequency range, measured using hot-wire anemometry. That figure illustrates that the former streamwise range does not include the upstream neutral point. For that reason, the currently extracted N -curve is shifted to the value ($N = 2.44$) extracted from their results at the location currently investigated. The resulting N -curve is shown in figure 6.28. The oscillation in the dotted curve, with a wavelength comparable to the individual POD mode of 4.6mm, reflects the underlying phase undulation of the spatial velocity maxima. A clear growth trend is obtained nonetheless. A linear fit is used to obtain a quantitative means of comparison for the eigenmode growth. The fitted slope corresponds to $-\alpha_i \lambda_r = 0.230 \pm 0.008$. This value is significantly larger compared to the growth rate of the eigenmode with the same wavelength, for which $-\alpha_i \lambda_r = 0.1243$. This is reflected in the mismatch of the slopes of the N -curves in figure 6.28. The grey area about the N -curve for the eigenmode indicates the uncertainty ($\pm 2\sigma = \pm 0.0106$ units) given in table

6.2. Including the worst error estimate, the growth rate does not match that extracted from the POD mode. The N -curve corresponding to the most unstable eigenmode is also included, for which $-\alpha_i \lambda_r = 0.2041$. This value only slightly underestimates the value corresponding to the POD mode.

The N -curve corresponding to the bandpass filtered fluctuation field associated to the type I mode (band 2) shown in figure 21 (b) by [3], corresponding to hot-wire measurements of the same vortices, is repeated here. This curve reflects the growth rate $-\alpha_i \lambda_r = 0.1270$, including the projection onto the x_w -direction (uncorrected value: 0.1272), which does match the considered eigenmode's growth to within the uncertainty. The latter match should, however, be interpreted with caution. The experimental curve corresponds to the r.m.s. amplitude averaged over 3 neighbouring vortices, amongst which are both the currently investigated ones, and the curve has a sample spacing of 0.025% chord, corresponding to 29 mm in the x_w -coordinate. In summary, qualitative agreement between the stability analysis and experimental measurements further demonstrates the applicability of the proposed methodology towards enhancing and extending the experimental measurability.

6.4.7. EFFECT OF PRIMARY VORTEX STRENGTH

As mentioned in §6.2.3, two neighbouring vortices are measured, where the left-hand-side vortex is slightly weaker (27.3% \bar{U}_e) than the right-hand-side vortex (28.7% \bar{U}_e) considered up to now. Next to the reduced strength, the perturbations have been experimentally identified to be much weaker by using the POD technique in the vicinity of the weak vortex, suggesting that the lower primary amplitude results in a reduced growth of the secondary instability modes.

The mild difference in amplitude between the primary crossflow vortices provides an ideal case in demonstrating the ability of the BiGlobal stability approach to identify pertinent stability features based on the measured mean flow alone. The analysis performed so far on the baseline stronger vortex is here repeated for the weaker vortex using the domain $-1 \leq z_w / \lambda_r \leq 0$ indicated in figure 6.5 and a mean field constructed with 500 instantaneous snapshots. For ease of comparison purposes, the domain is translated in the z_w -direction, so the z_w -coordinate again spans $[0, \lambda_r]$. In figure 6.29, the type I and II mode branches are shown and compared with those corresponding to the stronger vortex. The branches are given for two grid resolutions. The most unstable type I and II modes are again found to be subject to $O(10^{-5})$ and $O(10^{-4})$ eigenvalue errors, respectively.

Despite the mild differences in the base flow, the stability characteristics of the weaker vortex are drastically changed towards a more stable state. The type I mode is stable for all wavenumbers and type II is marginally unstable, indicating the weak vortex amplitude of 27.3% \bar{U}_e based on equation (6.1) is close to the neutral secondary instability limit for both currently considered modes. This further corroborates the low perturbation amplitude observed in the experimental flow field. The most unstable modes' characteristics for both vortices are compared in table 6.3.

Due to the apparent extreme sensitivity of stability on the base flow strength, a sanity check is performed by comparing the order of magnitude of the growth rates to the work of Koch *et al.* [15] and Bonfigli and Kloker [4]. The current Reynolds number,

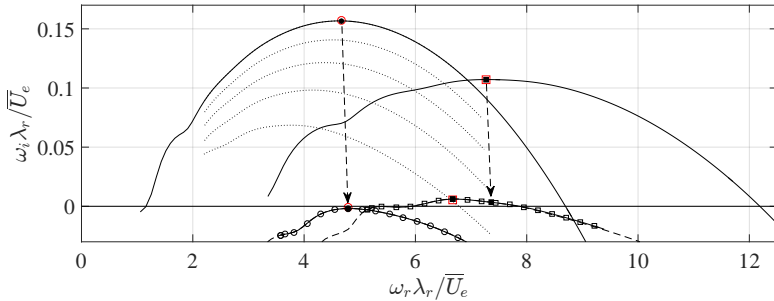


Figure 6.29: Type I (circles) and II (squares) temporal stability branches for the weak vortex using $N_z \times N_y = 55 \times 55$ (dashed) and 90×90 (solid) grid nodes. Strong vortex branches (solid without open symbols). Arrows link type I and II modes with $\alpha\lambda_r = 6.2$ and 8.6 (filled symbols), respectively, on the different vortices. All most unstable eigenvalue symbols are filled. Eigenvalues corresponding to domain containing both strong and weak primary vortices using $N_z \times N_y = 140 \times 70$ (red symbols). Branches corresponding to the interpolated base flows with $\chi = 0.2, 0.4, 0.6$ and 0.8 (dotted lines, bottom to top).

$Re = \bar{U}_e \lambda_r / \nu = 1.32 \times 10^4$, while the latter authors' simulations correspond to 1.34×10^4 and 0.87×10^4 , respectively. Assuming a comparable integral effect of the pressure gradient, the current results are comparable with those of Koch *et al.* [15], while relatively larger shear levels and therefore growth rates are expected in the case of Bonfigli and Kloker [4]. By converting the maximal growth rates in these reference into \bar{U}_e / λ_r units, one respectively retrieves the values 0.49 and 1.5,¹ which, compared to the currently found maximal value of 0.16, are significantly larger. Similarly, the maximal growth rate of the primary instability reported by Koch *et al.* [15] is 0.12. This is taken as an indication that the currently considered strong vortex lingers close to neutral conditions. This is a reasonable explanation for the apparent large decrease of the growth rate of the strong, as opposed to the weak vortex. The near-neutral conditions are also reasonable in the perspective of the small difference in the vortex amplitudes.

The estimate of the primary amplitude leading to neutral secondary modes by Fischer *et al.* [18] of 11% \bar{U}_e is rather low compared to the value found here. The order of magnitude is comparable with the results of Wassermann and Kloker [16], reporting 30%

¹In their nomenclature, for Koch *et al.* [15, cf. figure 18]: $(\sigma_r L_{ref}^* / Q_{ref}^*) \times (\lambda_{zc}^* / L_{ref}^*) \times (Q_{ref}^* / Q_e^*) = 0.029 \times 12 / 0.7092 \times 1 = 0.49$ and for Bonfigli and Kloker [4, cf. figure 13]: $(\text{Im}(\omega) L_{ref}^* / u_\infty^*) \times (\lambda_{0,z}^* / L_{ref}^*) \times (u_\infty^* / u_{b,e}^*) = 10 \times 12 / 100 \times 14 / 11 = 1.5$.

Table 6.3: Parameters of the most temporally unstable modes in the base spectrum corresponding to the weak (w, left) and strong (s, right) vortex in figure 6.5.

Type	$\alpha\lambda_r$	$\omega\lambda_r / \bar{U}_e$	f (kHz)	c_{ph} / \bar{U}_e
I (w)	6.2	4.7956 - i 0.0019	3.0984	0.7735
I (s)	6.2	4.6737 + i 0.1568	3.0194	0.7538
II (w)	7.8	6.675 + i 0.006	4.312	0.856
II (s)	8.6	7.272 + i 0.107	4.698	0.846

\bar{U}_e based on the maximum deceleration imposed by the mean flow distortion. Instances of the type I eigenmode being more stable than type II for all wavenumbers are uncommon, e.g. see [15]. As elaborated on in §6.2.3, the in-plane velocity components show a small increase relative to the primary perturbation amplitude based on \bar{U}_s . Based on figure 20 of Bonfigli and Kloker [4], this effect should render the type II mode more stable than type I.

For the stronger vortex, the most unstable wavenumbers for the type I and II modes are $\alpha\lambda_r = 6.2$ and 8.6, respectively. The dashed arrows in figure 6.29 link the modes corresponding to these wavenumbers for both vortices. Bonfigli and Kloker [4] show (cf. figure 36 (b)) the frequencies for fixed wavenumbers are proportional to the primary vortex strength, i.e. a decrease of about 1.4% is expected. Instead, the frequency at a fixed wavenumber increases 2.6% for type I and 1.2% for type II. By inspection of the terms in the ω_r -budget, the increase of the frequency for a fixed wavenumber cannot be associated to an individual term; it is the integral effect of small changes in all terms. For the type I mode, $\alpha\lambda_r = 6.2$ is again most unstable. For the type II mode, the most unstable wavenumber is smaller for the weaker vortex. This behaviour for the type I mode agrees with the results of Koch *et al.* [15], who report a type I branch (cf. figure 18) that has an invariant most unstable frequency at different streamwise locations, although that type I branch is not the most unstable type I harmonic over the considered streamwise range.

To further assess the reliability of the decrease in the growth rate from the strong to the weak vortex, intermediate temporal stability branches are computed based on the flow obtained by artificially interpolating the two vortices considered here. The strength parameter χ is introduced, defining the interpolated solution as follows:

$$\bar{Q}_\chi(z_w, y) = \chi \bar{Q}_{[0,1]}(z_w, y) + (1 - \chi) \bar{Q}_{[-1,0]}(z_w - \lambda_r, y) \quad (6.8)$$

where \bar{Q} denotes any mean flow variable, \bar{Q}_χ is the interpolated flow variable and $\bar{Q}_{[0,1]}$ and $\bar{Q}_{[-1,0]}$ denote the strong and weak vortices, respectively. A similar approach is deployed by Piot [53] to investigate the effect of a bump on a boundary layer flow. The values $\chi = 0.2, 0.4, 0.6$ and 0.8 are considered and the attention is restricted to the type I mode. The results are shown as the dotted lines in figure 6.30. Evidently, transitioning from the strong to the weak vortex corresponds to a consistent and monotonic decrease of the branch in the ω -plane, further confirming that the decreased growth rate is not a random artefact of the measured flow representation.

A comparison of the most unstable eigenfunctions on the different vortices is shown in figure 6.30. Both eigenfunctions display a broader support about the vortex. This behaviour is qualitatively comparable to the findings of Koch *et al.* [15]. Furthermore, the maxima of the functions have a higher position relative to the distorted base flow contours, which is reflected by slightly higher phase speeds, see table 6.3. In turn, this is directly linked to the slight increase of the frequencies at constant wavenumber discussed before. The difference in the orientation of the highest level contour of the type II mode is important to note. For the stronger vortex, this is located to the left of the primary vortex core and tilted to the left, whereas for the weaker vortex it is located and tilted to the right.

The previous analysis clarifies that while the spatial topology of the type I and type II modes is rather insensitive to mild changes in the base flow, their respective growth rate

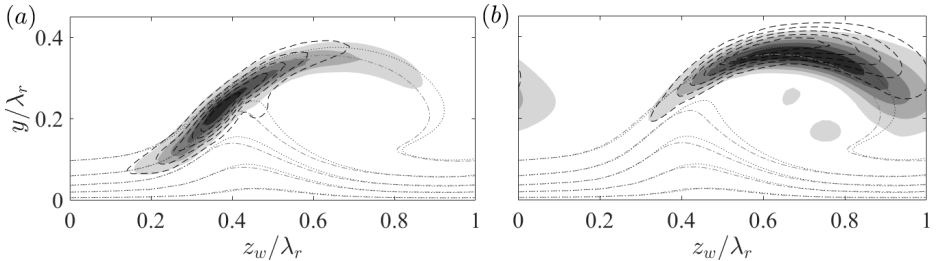


Figure 6.30: $|\bar{u}|/\max|\bar{u}|$ for type I (a) and II (b) (levels span [1/6, 5/6] with $\Delta = 1/6$) for the weak (filled) and strong (dashed) vortex. \bar{U}_w/\bar{U}_e levels 0.1, 0.3, ..., 0.9 for the weak (dash-dotted) and strong (dotted) vortex.

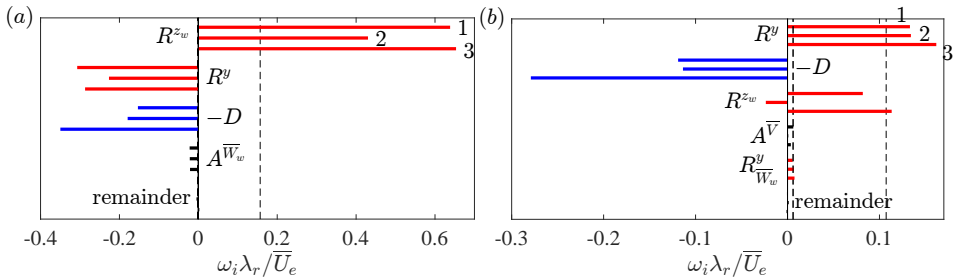


Figure 6.31: ω_i -budgets (bars) of type I (a) and II (b), ω eigenvalues (dashed lines). Bar triplets: strong vortex, nominal Re (top, '1'); weak vortex, nominal Re (middle, '2'); strong vortex, lower Reynolds number (bottom, '3'): $10^{-0.54}Re$ (a) and $10^{-0.55}Re$ (b).

is strongly affected. To identify the physical mechanism that renders the eigenmodes more stable for the weaker vortex, the energy balances corresponding to the most unstable modes is displayed in figure 6.31 (top and middle bars per term). For the type I mode, the vortex strength difference leads to a decrease of both R^y and R^{z_w} in the ω_i -budget. Note that the size of A^{W_w} persists. The topology of the production terms related to the Reynolds stress and advection terms is represented in figure 6.32. The highest level contours are nearly identical to those observed in figures 6.14 and 6.15, which explains the similarity of the ω_i -budgets. The shape displayed by the lower contour levels is quite different, however, and explains the differences in the eigenfunction shape. As the $\partial\bar{U}_w/\partial z_w$ shear component is smaller for the weaker vortex, other productive contributions come into play in the region located above the primary vortex. Figures 6.32 (a,c,d) show productive contributions by the integrands of R^y , A^V and A^{W_w} , respectively. The downwards protrusion of the eigenfunction about the point $(z_w, y)/\lambda_r = (0.45; 0.22)$ in figure 6.12 (a), associated to the marginally positive R^y contribution in figure 6.14 (a), is absent in figure 6.30 (a). In figure 6.32 (a), the equivalent R^y -integrand contours have a smaller magnitude and extend less in the direction orthogonal to the shear layer. The local maximum of the R^y -integrand in the neighbourhood of the protrusion has dropped from 1.41 to 0.92 \bar{U}_e/λ_r^3 for the strong and weak vortices, respectively.

For the type II mode, unexpectedly, the main Reynolds stress production term, R^y ,

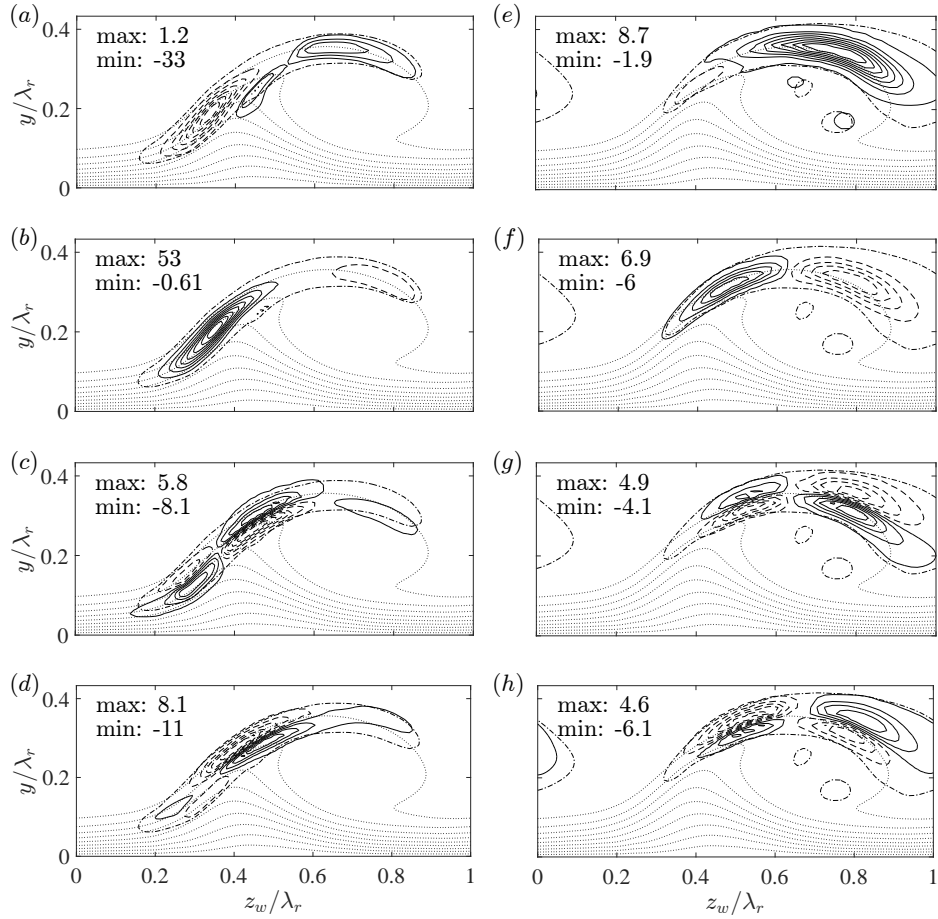


Figure 6.32: Imaginary part of the (a,e) R^y -, (b,f) R^{zw} -, (c,g) $A^{\bar{V}}$ - and (d,h) $A^{\bar{W}_w}$ -integrands for type I (a–d) and II (e–h) on the weaker vortex (9 levels span (b) $[-0.300, 47.2]$, (c) $[-0.873, 7.62]$, (d) $[-4.69, 5.59]$, (e) $[-6.74, 4.42]$, (f) $[-8.76, 6.21]$, (g) $[-3.20, 4.00]$, (h) $[-5.01, 3.56]$, negative contours are dashed). Levels in (a) span $[-27.8, -3.63]$ with $\Delta = 4.84$, and $[0.300, 0.900]$, $\Delta = 0.300$. All values are given in \bar{U}_e/λ_r^3 -units. Eigenfunction contour $|\tilde{u}_w|/\max|\tilde{u}_w| = 1/6$ (dash-dotted). \bar{U}_w/\bar{U}_e levels 0.1, 0.2, ..., 0.9 (dotted) for the weak vortex.

exerts a virtually identical contribution in the ω_i -budget shown in figure 6.31. In fact, the production term R^{z_w} is largely responsible for the stabilization relative to the stronger vortex. This illustrates that, although the type II instability is mainly generated by the Reynolds stress associated to the $\partial \bar{U}_w / \partial y$ shear component, in this case the other component is the main translator of the vortex strength. The apparent link between the spanwise location of the eigenfunction's maximum and the Reynolds stress R^{z_w} , first encountered in §6.4.2, reappears here; as the maximum of the eigenfunction moves in the positive z_w -direction, this production term decreases. The relation to the topology of the production term can be deduced by comparing figure 6.32 (f) with 6.14 (d). The negative contours have approximately the same magnitude, but the positive productive contours change quite considerably, the maximum reducing from 16.2 to $6.9 \bar{U}_e / \lambda_r^3$ for the strong and weak vortices, respectively. Lastly, although it has a small overall magnitude, $A^{\bar{V}}$ reduces significantly in the ω_i -budget; it is comparable to the decrease in D . Comparing figures 6.32 (g) and 6.15 (d), the levels corresponding to the weaker vortex are smaller and are more balanced in the z_w -direction than those corresponding to the stronger vortex.

6.4.8. EFFECT OF PERIODIC BOUNDARY CONDITIONS

As mentioned in §6.3, the measured flow fields of the single strong and weak vortices have not been periodized. The coefficients are left discontinuous across the boundary, so that no artificial shear layer is introduced. To assess the impact of this approach on the solutions, the problem was set up for the domain containing both vortices, as shown in figure 6.5, herein denoted as the double-vortex-domain. The problem was evaluated at the most unstable wavenumbers presented in table 6.3. Given the domain is twice as large, the resolution had to be increased accordingly. The currently available resources maximally allowed $N_z \times N_y = 140 \times 70$, which, for this domain, represents a resolution in between the cases 55×55 and 90×90 on the single-vortex-domains.

The resulting eigenvalues match up to $O(10^{-4})$ absolute errors with those presented in table 6.3, and effectively collapse in figure 6.29. The corresponding eigenfunctions are shown in figure 6.33. Note that each eigenfunction on the different vortices corresponds to a different eigenvalue in the spectrum of the double-vortex-domain problem. They are compared to the eigenfunctions retrieved with the single-vortex-domains, adjusted to appropriately illustrate their support on the double-vortex-domain, using the periodic boundary conditions. All eigenfunctions match perfectly, even the smaller amplitude contours of the type II mode on the weak (left) vortex. Moreover, despite the fact that this eigenfunction significantly protrudes the $z_w / \lambda_r = 0$ boundary, it does not experience distortion due to the minor discontinuity in the coefficients for the single-vortex-domain. This illustrates that, in this case, using discontinuous coefficients across the boundary is justified.

These results are very similar to those presented by Choudhari *et al.* [29] and Bonfigli and Kloker [4, cf. §6.2]. The current results corroborate the notion that the type I and II eigenmodes on different vortices do not participate in the same resonance; they correspond to different modes in the collective spectrum. In this sense, they are proper discrete modes. In addition, in this case, the single-vortex-domain problems are representative of the dynamics in the double-vortex-domain. So, it is deduced that, given the

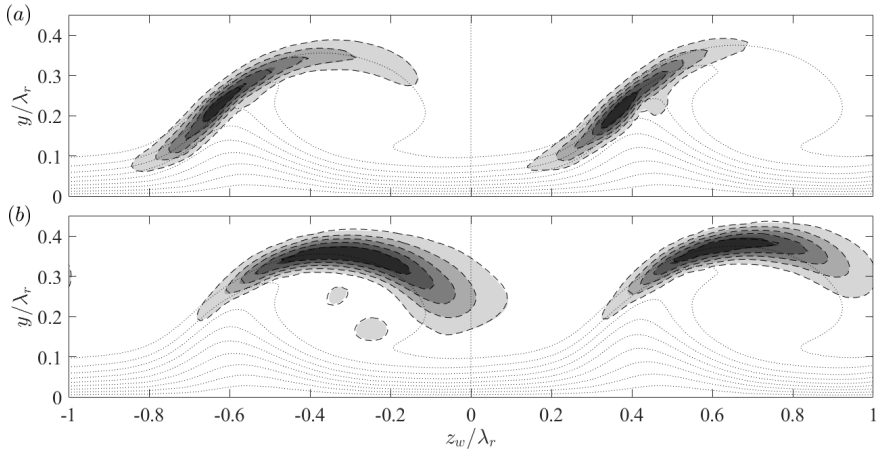


Figure 6.33: $|\tilde{u}_w| / \max|\tilde{u}_w|$ for type I (a) and II (b) (levels span $[1/6 5/6]$ with $\Delta = 1/6$) of respective modes for both vortices, computed on the single (filled) and double (dashed) domain. To emphasize: the eigenfunctions on the different vortices correspond to different eigenvalues; each has a support limited to one vortex. \bar{U}_w/\bar{U}_e levels 0.1, 0.2, ..., 0.9 (dotted). Domain separation for strong (right) and weak (left) vortex (vertical dotted line, $z_w/\lambda_r = 0$).

primary vortices are reasonably separated in space, it is not necessary to consider the more expensive double-vortex-domain problem. Neighbouring primary vortices do not contribute crucial information, in that case.

6

6.4.9. REYNOLDS NUMBER DEPENDENCE

Following the analysis of Bonfigli and Kloker [4], the type I and II modes are Kelvin-Helmholtz instabilities and hence display an independency of the Reynolds number when large enough; this is as opposed to viscous Tollmien-Schlichting instabilities that are stable in the Rayleigh limit, see §4.6.2, Schlichting *et al.* [54] and Drazin and Reid [55]. Similar to the approach by Bonfigli and Kloker [4], the stability problem for the strong vortex is solved, varying just the Reynolds number and fixing all other parameters. While this results in a non-physical flow, the insights regarding the dependency of the solution to Reynolds number variations are instructive. The evolution of modes I and II through the Reynolds number sweep is tracked while fixing the nominally most unstable wavenumber ($\alpha\lambda_r = 6.2$ and 8.6 , respectively). Due to the growth of corresponding eigenfunctions towards more slender shapes with increasing Reynolds numbers, the 90×90 grid is used in order to ensure capturing all amplitude details accurately.

It is well-known that viscosity has a significant impact on the stability of free shear layers when the parameter

$$\alpha \frac{\delta_v}{2} Re_{\delta_v} \equiv \alpha \frac{\delta_v}{2} \frac{\Delta \bar{U}_w \delta_v}{4\nu} = \alpha \frac{\delta_v}{2} \frac{\Delta \bar{U}_w/2}{\bar{U}_e} \frac{\delta_v/2}{\lambda_r} Re, \quad (6.9)$$

is of $o(10^2)$ (small- o notation), where δ_v and $\Delta \bar{U}_w$ are the vorticity thickness and velocity difference relevant for the particular instability, see Michalke [56] and Tatsumi, Gotoh, and Ayukawa [57]. In the present case, these parameters have been determined by

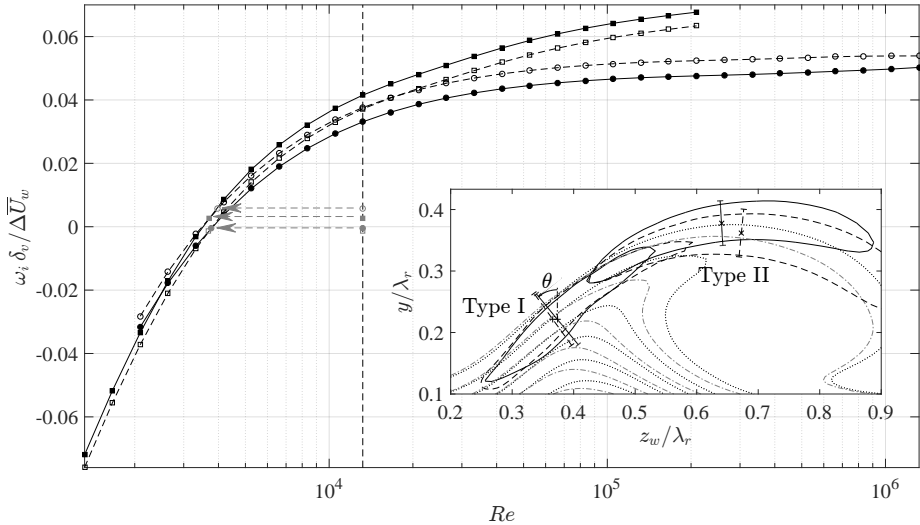


Figure 6.34: Type I ($\alpha\lambda_r = 6.2$, circles) and II (8.6, squares) growth rate in δ_v -scaling versus Re for the strong vortex. Eigenvalues: computed (filled), excluding $A^{\bar{V}}$ and $A^{\bar{W}_w}$ (open symbols), weak vortex (grey symbols). Nominal Re (vertical dashed), interpolation of weak vortex onto strong vortex data (arrows). Inset: $|\bar{u}_w|/\max|\bar{u}_w| = 0.5$ for both modes at nominal Re and \bar{U}_w/\bar{U}_e levels 0.4, 0.5, ..., 0.9 for the strong (solid resp. dotted) and weak (dashed resp. dash-dotted) vortex. $|\bar{u}|$ -maximum location (crosses) and δ_v in the θ -direction (bars).

6

quantifying the in-plane shear components $\partial \bar{U}_w / \partial z_w$ and $\partial \bar{U}_w / \partial y$ at the location where the $|\bar{u}|$ -amplitude is maximal. Along the direction indicated by the shear components, denoted by θ , the closest minimum or, if no minimum exists, the closest "favourable" inflection point of \bar{U}_w is determined under the layer of interest. The difference between the freestream velocity and \bar{U}_w at this point is $\Delta \bar{U}_w$. The vorticity thickness is subsequently determined with the formula:

$$\delta_v \equiv \frac{\Delta \bar{U}_w}{\sqrt{\left(\frac{\partial \bar{U}_w}{\partial z_w}\right)^2 + \left(\frac{\partial \bar{U}_w}{\partial y}\right)^2}}, \quad (6.10)$$

which is consistent with the definition in §4.1, treating the shear layers as being long in the direction orthogonal to the in-plane gradient. For all modes of interest, the inset in figure 6.34 illustrates the location at which the shear components are extracted together with the vorticity thickness δ_v and orientation θ . All relevant parameters are reported in table 6.4, including the parameter $\alpha\delta_v Re_{\delta_v}/2$, the extraction location, the in-plane \bar{U}_w -shear components and the angle θ of their vector sum with respect to the y -axis. Using these scales, which are customised to each mode, insight in how "efficient" the type I and II modes are mutually can be gained.

The resulting growth rates, in the δ_v -scaling, are presented with full black symbols in figure 6.34. It is evident that the growth rates saturate with increasing Reynolds number. Viscosity has a significant effect in the nominal case. This is as expected when considering the values of $\alpha\delta_v Re_{\delta_v}/2$, which are all of $o(10^2)$. The parameter values for the type

Table 6.4: Vorticity thickness parameters for the nominal most unstable modes, s ~ strong, w ~ weak primary vortex. Shear component values are in units of \bar{U}_e/λ_r .

Type	δ_v/λ_r	$\Delta\bar{U}_w/\bar{U}_e$	$\alpha\delta_v/2Re_{\delta_v}$	z_w/λ_r	y/λ_r	$\partial\bar{U}_w/\partial z_w$	$\partial\bar{U}_w/\partial y$	θ
I (s)	0.107	0.506	59.0	0.373	0.221	-3.02	3.65	40°
I (w)	0.104	0.451	50.3	0.366	0.221	-2.53	3.50	36°
II (s)	0.073	0.188	14.1	0.640	0.378	-0.16	2.58	3.5°
II (w)	0.078	0.164	13.4	0.673	0.362	0.22	2.19	-5.6°

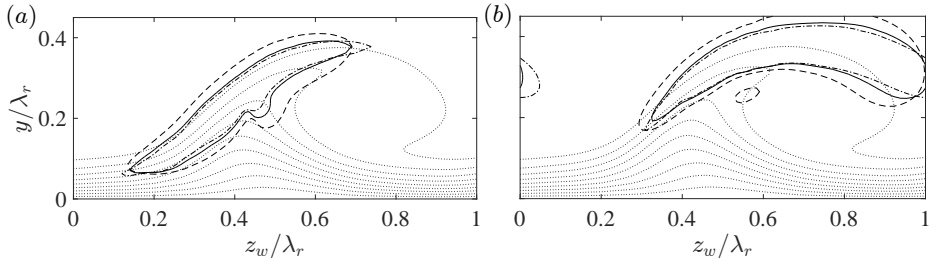


Figure 6.35: $|\tilde{u}_w|/\max|\tilde{u}_w| = 1/6$ for Reynolds number: $10^{-0.8}Re$ (dashed), nominal (solid) and $10^{0.8}Re$ (dash dotted) for type I (a) and II (b). \bar{U}_w/\bar{U}_e levels 0.1, 0.2, ..., 0.9 (dotted).

II mode are smaller than those for type I, which in figure 6.34 is reflected by the slower saturation of the type II growth rate with the Reynolds number.

It is striking that the type II mode is the most unstable of the two, in the custom per-mode scaling. In this sense, the type II mode is the more efficient mechanism. This suggests that the Reynolds stress production terms do not contribute to the growth rate as in the case of a one-dimensional shear layer. For the strong vortex, both shear components act constructively for the type II mode, while the $\partial\bar{U}_w/\partial y$ component acts destructively for the type I mode. However, next to these Reynolds stresses, there are effects associated to the in-plane velocity components; i.e. the equivalents of non-parallel flow effects. The largest contributions in the ω_i -balance are found to vary mildly with the Reynolds number as shown in figure 6.31 (compare top and bottom bars per term), with the exception of the viscous dissipation, of course. Only the Reynolds stress production terms in the type II budget show an increase, but have the same character. The non-parallel contributions, specifically, retain the same character; \bar{V} -advection destabilizes the type II mode and the \bar{W}_w -term stabilizes the type I. For low enough Reynolds numbers ($< 10^{-0.3}Re$) the \bar{V} -advection and $\partial\bar{W}_w/\partial y$ Reynolds stress term exchange dominance as the destabilizing non-parallel term in the budget for the type II mode. Figure 6.31 (b) shows that this is equivalent to the case of the type II mode on the weak vortex. Furthermore, figure 6.34 suggests the eigensolutions corresponding to the weak vortex have common features with those on the strong vortex at a lower Reynolds number.

Based on the previous observations, further links are sought between growth, base flow strength and Reynolds number. The horizontal arrows in figure 6.34 indicate the interpolation of the weak vortex growth rates onto the curve with varying Reynolds num-

ber of the strong vortex. This interpolation yields nearly matching Reynolds numbers for both modes types, $10^{-0.54} Re = 3770$ for type I and $10^{-0.55} Re = 3700$ for type II. The mild variation in the energy budgets with the Reynolds number mentioned before implies that the increased viscous dissipation term is directly equivalent to the net reduction of the Reynolds stress terms for the weaker vortex case. Figure 6.31 visualises this; the energy budgets are given for these specific Reynolds numbers. For the type II instability, the change in the viscous dissipation closely matches the change in the R^{z_w} -term.

Despite these equivalences, the eigenfunctions for the 2 cases are different. As mentioned before, the main dependency of the eigenfunctions on the Reynolds number is their respective width orthogonal to the shear layer. The eigenfunctions corresponding to the strong vortex are shown in figure 6.35 for various Reynolds numbers. For an increasing Reynolds number, the eigenfunction focuses about the region where the Reynolds stresses are active. This allows associating the increase in width with viscous diffusion. In addition, the length along the shear layer changes slightly, but it remains significantly lower than the length displayed by the eigenfunctions for the weak vortex in figure 6.30. The distinction is attributed to the fact that the dissipation acts on all velocity components, while both dominant Reynolds stress terms produce or destroy the \tilde{u}_w component directly. In the weak vortex case the latter is reduced causing a redistribution of the energy balance at local points in the $z_w y$ -plane. The decreased Reynolds number instead has a global impact on all terms, which does not cause a significant redistribution within the plane.

Using the energy decomposition, the solely parallel effects can be separated from the total contributions in the eigenvalue information. This is done by subtracting all contributions involving the \bar{V} - and \bar{W}_w -components from the computed eigenvalue, i.e. all associated advection and Reynolds stress terms, including those in the remainder. The results are the empty symbols shown in figure 6.34. It is revealed that, in close proximity to the nominal Reynolds number for the strong vortex case, the modes are equally matched. In terms of the growth rate, this demonstrates that both mode types are the offspring of the same parallel instability mechanism. This is a non-trivial result regarding the productive and destructive character of the Reynolds stress terms. Nevertheless, the cumulative effect is the same in this particular range.

The previous analysis demonstrates that the eigensolutions incorporating all non-parallel effects, including non-trivial redistribution, generation and destruction effects imposed by the \bar{V} - and \bar{W}_w -components, can be recast into a self-similar parallel form that only depends on the details associated to the main shear layers, viz. δ_v and $\Delta \bar{U}_w$. Capturing those details sets the main physical basis of the perturbation and the non-parallel velocity components are extra effects. Note that the reverse approach, i.e. performing the stability analysis on the \bar{U}_w -field only, does not necessarily yield the same result due to the redistribution imposed by the in-plane velocity components.

From the relationship governing the inviscid stability of the piecewise linear shear layer, see Drazin and Reid [55]:

$$(2\omega\delta_v/\Delta \bar{U}_w)^2 = (1 - 2\alpha\delta_v)^2 - (e^{-2\alpha\delta_v})^2, \quad (6.11)$$

the maximal temporal growth rate $\omega_i = 0.2012\Delta \bar{U}_w/\delta_v$ is found, which is significantly larger than the limiting values shown in figure 6.34. Although it is not in the scope of

the current chapter, next to the destructive nature of the Reynolds stress terms, other effects like the two-dimensionality imposed by the shear layer's finite spanwise extent and wall proximity have to be carefully factored before the results can be expected to be comparable to the one-dimensional shear layer characteristics, see §5.4. As shown in §§4.6.3 and 4.6.4, both effects are stabilizing and not accounted for in the simple scaling. Drazin and Reid [55] also show this for the wall proximity. Measured orthogonally with respect to the shear layers, their centres are located more than $2\delta_v$ from the wall, which indicates no significant effect. The modes have a wavelength in the $z_w y$ -plane parallel to the shear layer, which has a stabilizing effect through viscous dissipation, but is not accounted for in the one-dimensional case. In the case of the strong vortex, the most unstable modes have approximately equal such wavelengths ($\approx 0.3\lambda_r$) for the larger part of the domain and therefore has an equal impact for both modes.

6.5. CONCLUSION

A combined experimental and numerical approach to the analysis of the secondary stability of realistic swept-wing boundary layers is presented, as a continuation of the work of Serpieri and Kotsonis [3]. The studied boundary layer develops on the pressure side of a 45° swept wing at an angle of attack ($Re_{cx} = 2.17 \times 10^6$, $M = 0.075$).

Bonfigli and Kloker [4] point out that the a complete description of the distorted base flow field is essential when performing the secondary stability analysis, especially regarding the wall-normal and spanwise (in-plane) velocity components. However, how the latter components affect the secondary stability is described only in a conceptual manner. Serpieri and Kotsonis [3] used tomographic particle image velocimetry (tomo-PIV) that provides such a complete description of the base flow and fluctuations, allowing applying two-dimensional linear stability theory on the measured mean flow.

Two neighbouring primary vortices, of different strength, extracted at the same streamwise location, are considered in the global stability analysis. The two eigenmodes of type I and II [15], referred to as the z - and y -modes by Malik *et al.* [9], are extracted primarily. The type III mode is obtained as well, but it is expected *a-priori* to be affected by the uncertainty of the current PIV measurement near the wall. The attention is therefore focussed on type I and II.

The energy decompositions of the type I and II modes are investigated in detail, divulging the contribution of the in-plane velocity components. For the type I mode, the effect is stabilizing and mainly caused by the spanwise velocity component. This imposes a net perturbation energy advection towards the vortex core, decreasing the growth rate by 14.1%. For mode II, the growth rate is increased by 7% by advection caused by the wall-normal velocity, that yields a net advection away from the vortex core. Another important difference between the modes regarding advection is that the type I perturbation energy is driven or "squeezed" onto a line, while no such line exists for the type II mode. This renders the position of the type I mode with respect to the primary crossflow vortex more robust than that of the type II mode.

The measured mean flow is subject to an uncertainty, which is highly related to the most energetic POD mode that manifests itself as a spanwise shift of the entire primary vortex structure. A Monte-Carlo approach is deployed to investigate the convergence of the results with the number of instantaneous snapshots, N_{fr} , used for the mean flow.

The mean growth rate and energy decomposition values converge for increasing N_{fr} . The growth rate fluctuations are large, but display a linear convergence trend. Therefore they can be neglected beyond the N_{fr} value where the fluctuations are so small they do not change the solution structure any more. For the type I mode this is straightforward as the arrangement of the energy decomposition is fixed for every considered N_{fr} . For the type II mode, the Reynolds stress production term associated to the spanwise shear component experiences large fluctuations about its mean value. These fluctuations correlate strongly to the movement of the type II eigenfunction in the spanwise direction, which, in turn, is deduced to be the logical result of the most energetic POD mode. The link between the movement and the Reynolds stress production term is physically supported by the topology of the latter. Additionally, the relative sensitivity of the different modes is explained by the different topologies of the in-plane advection terms for the different modes; being more robust for the type I mode.

Using a measured base flow implies the in-plane flow is not divergence-free and the fields have to be extrapolated in the wall-normal direction. A crude estimation points out the non-zero divergence yields smaller growth rate changes compared to the observed uncertainty due to the mean ensemble size. The effect of extrapolation is negligible up to the discretization error when using parameters representative of the non-intrusive limit.

The applicability of the Gaster-transformation when applied the measured base flow is verified. Despite slight changes in the Reynolds-Orr terms, the spatial and temporal eigenfunctions were found to change negligibly.

The flow structure of the type I eigenmode is compared against that of the POD mode, a main difference being the inclination of the vortex structures. The eigenmode growth is found to be underestimated when compared to a measure based on the POD mode. A cause for this could be the latter's low phase resolution, when considering only 2 POD modes. This illustrates the approach is capable of extracting the order of magnitude of the growth rates.

Analysing the weak primary vortex, both modes are found to be (marginally) stable. This is in-line with the experimental observations, but poses a remarkable difference with respect to the strong vortex. Comparing the growth rates reported in the literature illustrates that both vortices linger close to the neutral limit, explaining the (only apparently) large growth rate difference. The robustness of the growth rate is checked by analysing artificially interpolated base flow solutions. For the type I mode, the Reynolds stress terms related to the wall-normal shear layer and the advection terms now have a more pronounced effect and increase the spanwise extent of the eigenfunction, also encountered by Koch *et al.* [15]. Interestingly, the stabilization of the type II mode is mainly caused by a strong decrease in the Reynolds stress production term associated to the spanwise shear layer; while the wall-normal shear layer's contribution remains identical. Furthermore, the eigenfunction displays a significant rightward lean, which can be directly compared to the behaviour observed in the uncertainty quantification. This manifestation demonstrates that behaviour is indeed physical.

Solving the problem with a domain containing both vortices, virtually identical results are retrieved. This indicates that, for the vortices considered, the periodic boundary conditions influence the results negligibly.

The modes' Kelvin-Helmholtz nature of the type I and II modes [4] is confirmed by

analysing the strong vortex and artificially changing the Reynolds number. This mainly results in eigenfunction width changes as a consequence of viscous diffusion. The growth rate results displayed in personalized vorticity thickness scaling shows that the type II mode is the more efficient mechanism over type I with respect to the active shear strength. Omitting the terms related to in-plane advection eliminates the difference. This illustrates the impact of the in-plane flow directly and demonstrates that the stability solutions can be cast into a parallel basis form to which the in-plane velocity components pose a deviation. The elimination of the efficiency difference is not universal; despite the correction for the in-plane velocity components the characteristics diverge when considering a larger Reynolds number range and the weak vortex case.

These outcomes indicate, at least for this application, that resolving the shear layers allows extracting stability data. Having to scrutinize the delicate primary vortices' receptivity in a computational approach is thereby circumvented. With the current approach, these essential features are incorporated in the base flow and, by consequence, in the stability analysis. To model this computationally can be very challenging and requires experimental calibration nonetheless.

More physical understanding results in terms of the solutions' robustness to realistic perturbations of the problem. Therefore, by bringing the stability approach closer to the experiment, making their ever-present relationship more mutual, a better representation and physical understanding can result. This information can be fed back into the design of further experimental campaigns.

The conclusions of this article are expected to be applicable in a broader range of flow topologies and the methodology can extend experimental measurability at other fronts. For example, the perturbation pressure field can be extracted from a PIV base flow.

REFERENCES

- [1] K. J. Groot, J. Serpieri, F. Pinna, and M. Kotsonis, *Secondary crossflow instability through global analysis of measured base flows*, Journal of Fluid Mechanics **846**, 605 (2018).
- [2] EMBRAER Commercial Aviation, *Media & downloads*, <https://www.embraercommercialaviation.com/media-downloads/> (2017), online; accessed 12-September-2017.
- [3] J. Serpieri and M. Kotsonis, *Three-dimensional organisation of primary and secondary crossflow instability*, J. Fluid Mech. **799**, 200 (2016).
- [4] G. Bonfigli and M. Kloker, *Secondary instability of crossflow vortices: validation of the stability theory by direct numerical simulation*, Journal of Fluid Mechanics **583**, 229 (2007).
- [5] H. L. Reed, W. S. Saric, and D. Arnal, *Linear stability theory applied to boundary layers*, Annual Review of Fluid Mechanics **28**, 389 (1996).
- [6] W. S. Saric, H. L. Reed, and E. B. White, *Stability and transition of three-dimensional boundary layers*, Annual Review of Fluid Mechanics **35**, 413 (2003).

- [7] E. B. White and W. S. Saric, *Secondary instability of crossflow vortices*, Journal of Fluid Mechanics **525**, 275 (2005).
- [8] M. R. Malik, F. Li, and C.-L. Chang, *Crossflow disturbances in three-dimensional boundary layers: nonlinear development, wave interaction and secondary instability*, Journal of Fluid Mechanics **268**, 1 (1994).
- [9] M. R. Malik, F. Li, M. M. Choudhari, and C.-L. Chang, *Secondary instability of crossflow vortices and swept-wing boundary-layer transition*, Journal of Fluid Mechanics **399**, 85 (1999).
- [10] Y. Kohama, W. Saric, and J. Hoos, *A high frequency, secondary instability of crossflow vortices that leads to transition*, in *Proc. R. Aeronaut. Soc. Conf. on Boundary-Layer Transition and Control, Cambridge, UK* (1991).
- [11] M. Kawakami, Y. Kohama, and M. Okutsu, *Stability characteristics of stationary crossflow vortices in three-dimensional boundary layer*, in *37th Aerospace Sciences Meeting & Exhibit, Reno* (AIAA, 1998).
- [12] H. Bippes and T. Lerche, *Transition prediction in three-dimensional boundary-layer flows unstable to crossflow instability*, AIAA Paper, 1906-1997 (1997).
- [13] H. Bippes, *Basic experiments on transition in three-dimensional boundary layers dominated by crossflow instability*, Progress in aerospace sciences **35**, 363 (1999).
- [14] M. R. Malik, F. Li, and C.-L. Chang, *Nonlinear crossflow disturbances and secondary instabilities in swept-wing boundary layers*, in *IUTAM Symposium on Nonlinear Instability and Transition in Three-Dimensional Boundary Layers: Proceedings of the IUTAM Symposium held in Manchester, U.K., 17–20 July 1995* (Springer Netherlands, Dordrecht, 1996) pp. 257–266.
- [15] W. Koch, F. P. Bertolotti, A. Stolte, and S. Hein, *Nonlinear equilibrium solutions in a three-dimensional boundary layer and their secondary instability*, Journal of fluid mechanics **406**, 131 (2000).
- [16] P. Wassermann and M. Kloker, *Mechanisms and passive control of crossflow-vortex-induced transition in a three-dimensional boundary layer*, Journal of Fluid Mechanics **456**, 49 (2002).
- [17] V. Theoflis, *Advances in global linear instability analysis of nonparallel and three-dimensional flows*, Progress in Aerospace Sciences **39**, 249 (2003).
- [18] T. Fischer, S. Hein, and U. Dallmann, *A theoretical approach for describing secondary instability features in three-dimensional boundary-layer flows*, in *31st Aerospace Sciences Meeting* (1993) p. 80.
- [19] E. Janke and P. Balakumar, *On the secondary instability of three-dimensional boundary layers*, Theoretical and Computational Fluid Dynamics **14**, 167 (2000).

- [20] D. Arnal, *Boundary layer transition: Predictions based on linear theory*, in *Special course on Progress in Transition Modelling*, R-793 (AGARD, 1994).
- [21] P. Jordan and T. Colonius, *Wave packets and turbulent jet noise*, Annual review of fluid mechanics **45**, 173 (2013).
- [22] M. Kloker, *Advanced laminar flow control on a swept wing-useful crossflow vortices and suction*, in *38th Fluid dynamics conference and exhibit* (2008) p. 3835.
- [23] R. Messing and M. J. Kloker, *Investigation of suction for laminar flow control of three-dimensional boundary layers*, Journal of Fluid Mechanics **658**, 117 (2010).
- [24] T. Friederich and M. J. Kloker, *Control of the secondary cross-flow instability using localized suction*, Journal of Fluid Mechanics **706**, 470 (2012).
- [25] P. C. Dörr and M. J. Kloker, *Stabilisation of a three-dimensional boundary layer by base-flow manipulation using plasma actuators*, Journal of Physics D: Applied Physics **48**, 285205 (2015).
- [26] P. C. Dörr and M. J. Kloker, *Transition control in a three-dimensional boundary layer by direct attenuation of nonlinear crossflow vortices using plasma actuators*, International Journal of Heat and Fluid Flow **61**, 449 (2016).
- [27] K. J. Groot, Q. Ye, B. W. van Oudheusden, Y. Zhang, and F. Pinna, *BiGlobal stability analysis of a micro-ramp wake using piv base flows*, AIAA Paper (2016).
- [28] T. M. Fischer and U. Dallmann, *Primary and secondary stability analysis of a three-dimensional boundary-layer flow*, Physics of Fluids A: Fluid Dynamics (1989-1993) **3**, 2378 (1991).
- [29] M. M. Choudhari, F. Li, and P. Paredes, *Influence of stationary crossflow modulation on secondary instability*, in *46th AIAA Fluid Dynamics Conference* (2016).
- [30] P. J. Schmid and D. S. Henningson, *Stability and Transition in Shear Flows* (Springer Verlag, 2001).
- [31] M. Reibert, W. S. Saric, R. B. J. Carrillo, and K. Chapman, *Experiments in nonlinear saturation of stationary crossflow vortices in a swept-wing boundary layer*, in *34th Aerospace Sciences Meeting and Exhibit* (1996) p. 184.
- [32] W. S. Saric, R. B. J. Carrillo, and M. Reibert, *Leading-edge roughness as a transition control mechanism*, in *36th AIAA Aerospace Sciences Meeting and Exhibit* (1998) p. 781.
- [33] F. F. J. Schrijer and F. Scarano, *Effect of predictor-corrector filtering on the stability and spatial resolution of iterative PIV interrogation*, Experiments in fluids **45**, 927 (2008).
- [34] H. Deyhle and H. Bippes, *Disturbance growth in an unstable three-dimensional boundary layer and its dependence on environmental conditions*, Journal of Fluid Mechanics **316**, 73 (1996).

- [35] M. Raffel, C. E. Willert, S. Wereley, and J. Kompenhans, *Particle image velocimetry: a practical guide* (Springer Science & Business Media, 2007).
- [36] A. Sciacchitano, B. Wieneke, and F. Scarano, *Piv uncertainty quantification by image matching*, Measurement Science and Technology **24**, 045302 (2013).
- [37] L. Sirovich, *Turbulence and the dynamics of coherent structures part i: coherent structures*, Quarterly of applied mathematics **45**, 561 (1987).
- [38] C. E. Grosch and S. A. Orszag, *Numerical solution of problems in unbounded regions: coordinate transforms*, Journal of Computational Physics **25**, 273 (1977).
- [39] B. Sandstede and A. Scheel, *Absolute and convective instabilities of waves on unbounded and large bounded domains*, Physica D: Nonlinear Phenomena **145**, 233 (2000).
- [40] F. Scarano, *Iterative image deformation methods in piv*, Measurement science and technology **13**, R1 (2001).
- [41] P. Vedula and R. J. Adrian, *Optimal solenoidal interpolation of turbulent vector fields: application to ptv and super-resolution piv*, Experiments in fluids **39**, 213 (2005).
- [42] S. Gesemann, F. Huhn, D. Schanz, and A. Schröder, *From noisy particle tracks to velocity, acceleration and pressure fields using b-splines and penalties*, in *18th international symposium on applications of laser and imaging techniques to fluid mechanics, Lisbon, Portugal* (2016) pp. 4–7.
- [43] J. F. G. Schneiders and F. Scarano, *Dense velocity reconstruction from tomographic ptv with material derivatives*, Experiments in Fluids **57**, 139 (2016).
- [44] J. M. Foucaut and M. Stanislas, *Some considerations on the accuracy and frequency response of some derivative filters applied to particle image velocimetry vector fields*, Measurement Science and Technology **13**, 1058 (2002).
- [45] U. Ehrenstein and F. Gallaire, *On two-dimensional temporal modes in spatially evolving open flows: the flat-plate boundary layer*, Journal of Fluid Mechanics **536**, 209 (2005).
- [46] F. Alizard and J. C. Robinet, *Spatially convective global modes in a boundary layer*, Physics of Fluids **19**, 114–105 (2007).
- [47] T. Herbert, *Secondary instability of boundary layers*, Annual Review of Fluid Mechanics **20**, 487 (1988).
- [48] M. R. Malik, *Numerical methods for hypersonic boundary layer stability*, Journal of Computational Physics **86**, 376 (1990).
- [49] P. Wheeler and D. Barkley, *Computation of spiral spectra*, SIAM Journal on Applied Dynamical Systems **5**, 157 (2006).

- [50] F. Li, M. M. Choudhari, L. Duan, and C.-L. Chang, *Nonlinear development and secondary instability of traveling crossflow vortices*, Physics of Fluids **26**, 064104 (2014).
- [51] M. Gaster, *A note on the relation between temporally-increasing and spatially-increasing disturbances in hydrodynamic stability*, Journal of Fluid Mechanics **14**, 222 (1962).
- [52] J. Serpieri and M. Kotsonis, *Spatio-temporal characteristics of secondary instabilities in swept wing boundary layers*, AIAA Paper (2016).
- [53] E. Piot, *Simulation Numérique Directe et Analyse de Stabilité de Couches Limites Laminaires en Présence de Micro-Rugosités*, Ph.D. thesis, l'Institut Supérieur de l'Aéronautique et de l'Éspace (2008).
- [54] H. Schlichting, E. Krause, H. Oertel, K. Gersten, and C. Mayes, *Boundary-Layer Theory* (Springer, 2003).
- [55] P. G. Drazin and W. H. Reid, *Hydrodynamic Stability* (Cambridge University Press, 2004).
- [56] A. Michalke, *The instability of free shear layers*, Progress in Aerospace Sciences **12**, 213 (1972).
- [57] T. Tatsumi, K. Gotoh, and K. Ayukawa, *The stability of a free boundary layer at large Reynolds numbers*, Journal of the Physical Society of Japan **19**, 1966 (1964).

7

LOCAL APPROACH: BRIGGS'S CRITERION FOR ABSOLUTE INSTABILITY

a decaying function can be represented as a super-position of many growing exponentials, as the usual theory of Laplace transforms.

Richard J. Briggs [1, 1964, p. 9]

This chapter presents a review of Briggs's criterion for absolute stability. A thorough understanding of the theory underlying Briggs's criterion is required to bridge the gap between the stability theory chapter 2 and chapter 8, which treats the streamwise BiGlobal problem. In short, the absolute stability of a system identifies whether perturbations propagate in both positive and negative directions of a spatial dimension, while growing in time. The systems studied in this thesis are dissipative. In these systems, examining the existence of an absolute instability is equivalent to inquiring whether or not unstable *stationary* wave packets are supported in a given reference frame. This follows because, while such a wave packet grows in amplitude, diffusion impels the propagation of the wave packet in both spatial directions.

Note that this inquiry concerns a wave packet: a perturbation that has a *finite support* in a spatial direction, i.e. its amplitude becomes arbitrarily small far enough from the core of the support. In particular, moving away from the core of the support, these perturbations have fronts at a finite position that point in the positive and negative direction. For an absolute instability, both fronts move in the direction they face; toward positive and negative infinity. Inquiring the same question for a perturbation with an *infinite* support (like a mono-chromatic sinusoid) is meaningless, because its fronts are located at positive and negative infinity; it *exists* at every finite position already. As deduced in §2.4.3, a perturbation with a finite support can be represented only by treating

its Fourier transform as a continuous function. While the previous chapters predominantly considered discrete eigensolutions to the stability equations, this chapter will instead be concerned with the collective behaviour of continuum solutions.

In this light, the objective is to extract the most unstable dynamics from the integral:

$$q'(\mathbf{x}, \mathbf{x}^\perp, t) = \int_{-\infty+i\gamma}^{\infty+i\gamma} \int \cdots \int_{\mathbb{R}^d} \tilde{q}(\mathbf{x}; \mathbf{k}, \omega) e^{i(\mathbf{k} \cdot \mathbf{x}^\perp - \omega t)} \frac{d\mathbf{k} d\omega}{(2\pi)^{d+1}}, \quad (7.1)$$

while treating $\tilde{q}(\mathbf{x}; \mathbf{k}, \omega)$ as a continuous function in ω and one component of \mathbf{k} .

The steps leading to Briggs's criterion are based on the original treatment, by Briggs [1, chapter 2]. Briggs's treatment starts off with complicated expressions that have to be understood deeply in order to correctly interpret continuous spectra. Therefore, this chapter builds upon the complex integration theory extensively presented in appendix A, that treats all machinery required to handle cases where the Fourier transform of the solution is discrete and bridges the gap to interpreting many of the expressions that, for Briggs, were known from the, for him, ‘usual theory of Laplace transforms’ (see the quote on the previous page). For further information, see references [2–8].

This chapter is arranged as follows. First, the desired integral expression is derived in §7.1, resulting in a reduced form of integral (7.1) over a dispersion function. The particular interest is in cases where non-parallel advection component, denoted by \bar{V}_e , is included. Before investigating the implications of this advection term, the analysis is performed for the case where $\bar{V}_e = 0$, executing the integrals over the component of the wavenumber vector, k , and the frequency ω variables in §§7.2 and 7.3, respectively. Here, the complex integration tools derived in appendix A are deployed. This leads to Briggs's criterion for an absolute instability. Thereafter, the parts of the derivation requiring an adaptation for the case where $\bar{V}_e \neq 0$ are presented in §7.4 and the associated implications are elaborated on. Before the chapter is concluded in §7.6, the shape of the integrands of the ω -integrals is discussed in more detail in §7.5.

7.1. THE FOURIER INVERSION INTEGRALS

The first objective is to derive the expression that describes the solution to the model problem. To this end, first the Green's function and dispersion relation are formulated based on the characteristics of the continuum solutions of interest.

7.1.1. GREEN'S FUNCTION FORMULATION

Continuum solutions of a system depend only on the spatial asymptotic states of the system. This is rigorously supported by the Weyl essential spectrum theorem, see Kapitula and Promislow [7, theorem 2.2.6], which dictates that the continuous spectrum of an operator depends solely on the asymptotically constant part of the operator coefficients. The spatially asymptotic state of flow problems on unbounded domains is the freestream. So, the solutions that are currently of interest are found by evaluating the governing equations in the freestream.

The freestream is associated with the limit $y \rightarrow \infty$, so this is the spatial dimension to which the continuum solutions are naturally associated. In this perspective, it is natural to inquire the perturbation response due to an impulsive force in y and time. To focus

the current treatment on the essentials, perturbations are considered that have a continuous Fourier transform in time and just the y -component of the wavenumber vector and the solution is assumed to have a discrete Fourier transform in the x - and z -directions. The theory can be readily extended to cover the continuity of the Fourier transform of the solution in more wavenumbers.

These requirements can be cast into the following equation governing the Green's function:

$$D \left(-i \frac{\partial}{\partial x}, -i \frac{\partial}{\partial y}, -i \frac{\partial}{\partial z}, i \frac{\partial}{\partial t} \right) G(x-x', y-y', z-z', t-t') = e^{i\alpha_c(x-x')} \delta(y-y') e^{i\beta_c(z-z')} \delta(t-t') \quad (7.2)$$

where $D(-i\partial/\partial x, -i\partial/\partial y, -i\partial/\partial z, i\partial/\partial t)$ is the constant coefficient differential operator representing the governing equations and (x', y', z') and t' denote a reference location and time. The right hand side represents forcing the solution impulsively at $y = y'$ and $t = t'$ and monochromatically with the *real* wavenumbers α_c and β_c in x and z , respectively.

To put the Fourier ansatz in the perspective of the nomenclature introduced in chapter 2, the coefficients have no spatial dependency, i.e. $\mathbf{x} = []$ (empty). Hence, all spatial dimensions are covered in $\mathbf{x}^\perp = [x, y, z]^T$, such that $d = 3$ and $\mathbf{k} = [\alpha, k, \beta]^T$ in equation (7.1), converting the latter into:

$$G(x-x', y-y', z-z', t-t') = \int_{-\infty+i\gamma}^{\infty+i\gamma} \int_{-\infty}^{\infty} \int_{-\infty}^{\infty} \int_{-\infty}^{\infty} \tilde{G}(\alpha, k, \beta, \omega) e^{i(\alpha(x-x')+k(y-y')+\beta(z-z')-\omega(t-t'))} \frac{d\alpha dk d\beta d\omega}{(2\pi)^4}, \quad (7.3)$$

where γ denotes the shift of the ω -contour from the real axis. As explained in §A.1.5, the correct placement of the ω -contour ensures that the solution is causal in time. In particular, the integration contour must lie above all regions where the integrand is non-holomorphic, see §A.1.1.

From this point onwards, the x' , y' , z' and t' reference points are translated to the origin; $x' = 0$, $y' = 0$, $z' = 0$ and $t' = 0$. This is allowed, because the operator D in equation (7.2) has constant coefficients.

Transforming equation (7.2) yields (see §A.2.3 for more details):

$$\tilde{\mathcal{D}}(\alpha, k, \beta, \omega) \tilde{G}(\alpha, k, \beta, \omega) = 2\pi\delta(\alpha - \alpha_c) 2\pi\delta(\beta - \beta_c). \quad (7.4)$$

where $\tilde{\mathcal{D}}(\alpha, k, \beta, \omega)$ is a polynomial dispersion function. Due to the constancy of the coefficients, Fourier transforming the equations does not yield related convolution products.

To arrive at equation (7.4), it should be mentioned that use is made of the implicit boundary conditions. In particular, $G(x, y, z, t)$ and its partial derivatives in y and t must decay at least exponentially as $|y|$ and $|t| \rightarrow \infty$. For more details, see the introduction of appendix A. No equivalent condition is imposed on the x - and z -directions, because the forcing functions also have an infinite support.

Due to the polynomial nature of $\tilde{\mathcal{D}}(\alpha, k, \beta, \omega)$, equation (7.4) can be restated as:

$$\tilde{G}(\alpha, k, \beta, \omega) = \frac{2\pi\delta(\alpha - \alpha_c) 2\pi\delta(\beta - \beta_c)}{\tilde{\mathcal{D}}(\alpha, k, \beta, \omega)}, \quad (7.5)$$

which can be used to rewrite integral (7.3), as:

$$\begin{aligned} G(x, y, z, t) &= \int_{-\infty+i\gamma}^{\infty+i\gamma} \int_{-\infty}^{\infty} \int_{-\infty}^{\infty} \int_{-\infty}^{\infty} \frac{\delta(\alpha - \alpha_c) \delta(\beta - \beta_c)}{\tilde{\mathcal{D}}(\alpha, k, \beta, \omega)} e^{i(\alpha x + ky + \beta z - \omega t)} d\alpha d\beta \frac{dk d\omega}{(2\pi)^2} \\ &= e^{i(\alpha_c x + \beta_c z)} \int_{-\infty+i\gamma}^{\infty+i\gamma} \int_{-\infty}^{\infty} \frac{e^{i(ky - \omega t)}}{\tilde{\mathcal{D}}(\alpha_c, k, \beta_c, \omega)} \frac{dk d\omega}{(2\pi)^2}. \end{aligned} \quad (7.6)$$

The exponential part containing α_c and β_c corresponds to the discrete mode ansatz discussed in §A.2.3. It should be re-iterated that it shall be assumed throughout this chapter that α_c and β_c are real parameters. From here onwards, the parameters α_c and β_c are dropped from the arguments and the subscript c is omitted from α and β for notational convenience. The remaining integrals in equation (7.6) then become:

$$\int_{-\infty+i\gamma}^{\infty+i\gamma} \int_{-\infty}^{\infty} \frac{e^{i(ky - \omega t)}}{\tilde{\mathcal{D}}(k, \omega)} \frac{dk d\omega}{(2\pi)^2}. \quad (7.7)$$

The analysis is restricted to these remaining integrals. First, $\tilde{\mathcal{D}}(k, \omega)$ has to be determined.

7.1.2. THE DISPERSION RELATION

The function $\tilde{\mathcal{D}}(k, \omega)$ results from evaluating the governing differential operator in the freestream and Fourier transforming the resulting expression. In this case, the advection-diffusion operator is considered. The derivation is best illustrated by applying the recipe to the advection-diffusion operator $\tilde{\mathcal{D}}_{\bar{V}}$ from equation (2.21), because it is already Fourier transformed in time and all spatial variables, except y :

$$\tilde{\mathcal{D}}_{\bar{V}} \left(-i \frac{d}{dy}; \omega \right) = -i\omega + i\alpha \bar{U} + \bar{V} \frac{d}{dy} + i\beta \bar{W} - \nu \left(\frac{d^2}{dy^2} - \alpha^2 - \beta^2 \right). \quad (7.8)$$

With respect to boundary layer profiles, the velocity profiles approach their asymptotically constant values in the freestream (as $y \rightarrow \infty$): \bar{U}_e , \bar{V}_e and \bar{W}_e . Accordingly, $\tilde{\mathcal{D}}$ simplifies to:

$$\lim_{y \rightarrow \infty} \tilde{\mathcal{D}} \left(-i \frac{d}{dy}; \omega \right) = \tilde{\mathcal{D}}_{\bar{V}_e} \left(-i \frac{d}{dy}; \omega \right) = -i\omega + i\alpha \bar{U}_e + \bar{V}_e \frac{d}{dy} + i\beta \bar{W}_e - \nu \left(\frac{d^2}{dy^2} - \alpha^2 - \beta^2 \right). \quad (7.9)$$

Fourier transforming this operator in the y -coordinate yields:

$$\tilde{\mathcal{D}}_{\bar{V}_e}(k, \omega) = -i\omega + i\alpha \bar{U}_e + ik \bar{V}_e + i\beta \bar{W}_e + \nu(\alpha^2 + k^2 + \beta^2). \quad (7.10)$$

The variables α and β are merely fixed parameters in the analysis that follows. To reduce the size of the expressions, it is convenient to set β equal to zero.

The zeros of $\tilde{\mathcal{D}}_{\bar{V}_e}(k, \omega)$ play a major role in the remainder of this and the following chapter. Due to the fact that $\tilde{\mathcal{D}}(k, \omega)$ appears in the denominator of the integrand of the integrals (7.7), the zeros of $\tilde{\mathcal{D}}(k, \omega)$ are also referred to as the poles in the integrand (related to $\tilde{\mathcal{D}}(k, \omega)$).

Yet from another point of view, the differential equation:

$$\tilde{\mathcal{D}}_{\bar{V}_e} \left(-i \frac{d}{dy}; \omega \right) \phi(y; \omega) = 0, \quad (7.11)$$

(including boundary conditions) could be seen as an eigenvalue problem for ω . The set of ω -values satisfying this equation are then referred to as the spectrum of the operator $\tilde{\mathcal{D}}_{\bar{V}_e}(-id/dy; \omega)$. The zeros of $\tilde{\mathcal{D}}_{\bar{V}_e}(k, \omega)$ thus correspond to the spectrum of $\tilde{\mathcal{D}}(-id/dy; \omega)$ in the case where $\phi(y; \omega)$ turns out to have the form of the complex exponential function in y , i.e. e^{iky} with any $k \in \mathbb{C}$. Of course, a similar terminology applies to the variable k for the operator $\tilde{\mathcal{D}}(id/dt; k)$.

By setting $\tilde{\mathcal{D}}_{\bar{V}_e}(k, \omega) = 0$ and solving for ω and k yields:

$$\omega = \Omega_{\bar{V}_e}(k) = \alpha \bar{U}_e + k \bar{V}_e - iv(\alpha^2 + k^2); \quad (7.12a)$$

$$k = \kappa_{\bar{V}_e}^{\pm}(\omega) = -i \frac{\bar{V}_e}{2v} \pm i \sqrt{v^{-1} \left(-i\omega + i\alpha \bar{U}_e + v \left(\alpha^2 + \left(\frac{\bar{V}_e}{2v} \right)^2 \right) \right)}. \quad (7.12b)$$

From §7.2 onward, first, the focus will be on the case $\bar{V}_e = 0$. The parameter \bar{V}_e denotes the non-parallel advection and so its effect on the theory is treated separately in §7.4. Therefore, let $\tilde{\mathcal{D}}_0(k, \omega)$ denote the dispersion function for $\bar{V}_e = 0$ and let:

$$\omega = \Omega_0(k) = \alpha \bar{U}_e - iv(\alpha^2 + k^2); \quad (7.13a)$$

$$k = \kappa_0^{\pm}(\omega) = \pm i \sqrt{v^{-1} \left(-i\omega + i\alpha \bar{U}_e + v\alpha^2 \right)}, \quad (7.13b)$$

7

denote the relationships between k and ω corresponding to the zeros of $\tilde{\mathcal{D}}_0(k, \omega)$. Whenever characteristics are used that are specific to either equations (7.12) or (7.13), this will be indicated through the use of the subscripts \bar{V}_e or 0 on $\tilde{\mathcal{D}}$, κ or Ω .

7.1.3. ABSOLUTE STABILITY: ZERO GROUP SPEED

The main goal of this chapter is identifying the absolute stability characteristics of a system. As stated in the introductory remarks, this automatically leads to the inquiry of the dynamics of stationary wave packets. As pointed out in §2.4.3, wave packets travel at the *group speed*, $c_g = d\omega/dk$ in the y -direction. So, the interest is in solutions for which $c_g = 0$. In terms of the introduced nomenclature, this criterion in general becomes:

$$\frac{d\Omega}{dk}(k_s) = 0, \quad (7.14)$$

where the subscript s will denote the evaluation at the zero group speed solution, e.g. it is located at $(k, \omega) = (k_s, \omega_s) = (k_s, \Omega(k_s))$. Interpreting $\Omega(k)$ as a two-dimensional parametric function of $k \in \mathbb{C}$:

$$\frac{d\Omega}{dk}(k) = \frac{d\Omega_r}{dk}(k) + i \frac{d\Omega_i}{dk}(k) = 0, \quad (7.15)$$

a zero group speed solution implies that the path described by $\Omega(k)$ in the ω -plane must halt in both the ω_r - and ω_i -direction. Note that, for the cases of $\Omega = \Omega_0$ and $\Omega_{\bar{V}_e}$ (resp. equations (7.12a) and (7.13a)), the variation of $d\Omega/dk$ with k is linear:

$$\frac{d\Omega_0}{dk}(k) = -2ivk; \quad \frac{d\Omega_{\bar{V}_e}}{dk}(k) = \bar{V}_e - 2ivk. \quad (7.16)$$

Therefore the derivatives $d\Omega_r/dk$ and $d\Omega_i/dk$ simultaneously switch sign at $k = k_s$.¹ The described path therefore leads up to a point, where it halts, and then it returns in the direction where it came from. This results in a parametric curve having the shape of a cusp. The zero group speed solution can therefore be identified in the ω -plane by searching for cusps by evaluating $\Omega(k)$ for a range of k -values along a line in the complex k -plane. The endpoint of the cusp, ω_s , is referred to as a branch point.

Equation (7.14) naturally describes the location of the zero group speed in terms of the zero of the dispersion function in the ω -plane. Some analysis has to be done to extract information about the location in the k -plane. To this end, the variation of $\tilde{\mathcal{D}}$ around the branch point is assessed. Expanding $\tilde{\mathcal{D}}$ around a generic point $(k, \omega) = (k_p, \Omega(k_p))$, one arrives at:

$$\begin{aligned} \tilde{\mathcal{D}}(k, \Omega(k)) = & \left. \tilde{\mathcal{D}} \right|_p + \left. \frac{\partial \tilde{\mathcal{D}}}{\partial k} \right|_p (k - k_p) + \left. \frac{\partial \tilde{\mathcal{D}}}{\partial \omega} \right|_p (\Omega(k) - \omega_p) \\ & + \frac{1}{2} \left. \frac{\partial^2 \tilde{\mathcal{D}}}{\partial k^2} \right|_p (k - k_p)^2 + \left. \frac{\partial^2 \tilde{\mathcal{D}}}{\partial \omega \partial k} \right|_p (k - k_p)(\Omega(k) - \omega_p) + \frac{1}{2} \left. \frac{\partial^2 \tilde{\mathcal{D}}}{\partial \omega^2} \right|_p (\Omega(k) - \omega_p)^2 \\ & + O((k - k_p)^{j_3} (\Omega(k) - \omega_p)^{3-j_3}) \end{aligned} \quad (7.17)$$

7

where the repetition of the exponent j_n denotes the summation over the term letting the exponent vary over the integers 0 to n .

Note that $\tilde{\mathcal{D}}(k, \Omega(k)) = 0$ for all $k \in \mathbb{C}$, per definition of Ω . Now, consider variations of $\tilde{\mathcal{D}}$ with k , while varying $\omega = \Omega(k)$ accordingly. This means that variation of $\tilde{\mathcal{D}}$ with k is considered, while the ω variable traces the locus of the zeros of $\tilde{\mathcal{D}}$ in the ω -plane. The value of $\tilde{\mathcal{D}}$ therefore does not depart from zero and $d\tilde{\mathcal{D}}/dk = 0$, even though the argument is varied. This variation of $\tilde{\mathcal{D}}$ is reconstructed by differentiating equation (7.17) with respect to k , yielding:²

$$\begin{aligned} \frac{d\tilde{\mathcal{D}}}{dk}(k, \Omega(k)) = & \left. \frac{\partial \tilde{\mathcal{D}}}{\partial k} \right|_p + \left. \frac{\partial \tilde{\mathcal{D}}}{\partial \omega} \right|_p \frac{d\Omega}{dk}(k) \\ & + \left. \frac{\partial^2 \tilde{\mathcal{D}}}{\partial k^2} \right|_p (k - k_p) + \left. \frac{\partial^2 \tilde{\mathcal{D}}}{\partial \omega \partial k} \right|_p \left((k - k_p) \frac{d\Omega}{dk}(k) + (\Omega(k) - \omega_p) \right) + \left. \frac{\partial^2 \tilde{\mathcal{D}}}{\partial \omega^2} \right|_p (\Omega(k) - \omega_p) \frac{d\Omega}{dk} \\ & + O((k - k_p)^{j_2} (\Omega(k) - \omega_p)^{2-j_2}). \end{aligned} \quad (7.18)$$

¹Note that this would not necessarily be the case if the variation were quadratic.

²By having substituted $\Omega(k)$ for ω in the second argument of $\tilde{\mathcal{D}}$ before differentiating with respect to k , effectively, the total derivative $d\tilde{\mathcal{D}}/dk$, instead of $\partial \tilde{\mathcal{D}}/\partial k$, is performed.

Setting $d\tilde{\mathcal{D}}/dk(k, \Omega(k))$ equal to zero on the left hand side and letting $(k, \omega) \rightarrow (k_p, \omega_p)$, one finds:

$$0 = \frac{\partial \tilde{\mathcal{D}}}{\partial k} \Big|_p + \frac{\partial \tilde{\mathcal{D}}}{\partial \omega} \Big|_p \frac{d\Omega}{dk} \Big|_p \quad \text{or:} \quad \frac{\partial \tilde{\mathcal{D}}}{\partial k} \Big|_p = - \frac{\partial \tilde{\mathcal{D}}}{\partial \omega} \Big|_p \frac{d\Omega}{dk} \Big|_p. \quad (7.19)$$

In the cases of $\tilde{\mathcal{D}} = \tilde{\mathcal{D}}_0$ and $\tilde{\mathcal{D}}_{\bar{V}_e}$, note that $\partial \tilde{\mathcal{D}}_0 / \partial \omega|_p = \partial \tilde{\mathcal{D}}_{\bar{V}_e} / \partial \omega|_p = -i$; i.e. this partial derivative is constant and non-zero. Equations (7.19) therefore act as a direct relationship between the group speed $d\Omega/dk|_p$ and $\partial \tilde{\mathcal{D}} / \partial k|_p$. It should be emphasized that this relationship holds generically for the points $(k, \omega) \rightarrow (k_p, \Omega(k_p))$.

If $(k_s, \omega_s) = (k_s, \Omega(k_s))$ is substituted for $(k_p, \Omega(k_p))$, the fact that $d\Omega/dk$ equals zero implies that $\partial \tilde{\mathcal{D}} / \partial k|_s = 0$. Furthermore, note that $\tilde{\mathcal{D}}(k_s, \omega_s) = 0$. So, solutions with a zero group speed always correspond directly to double roots of the dispersion relation:

$$\frac{d\Omega}{dk} \Big|_s = 0 \quad \Rightarrow \quad \tilde{\mathcal{D}}|_s = \frac{\partial \tilde{\mathcal{D}}}{\partial k} \Big|_s = 0. \quad (7.20)$$

The converse statement is also true; a double k -root of the dispersion relation corresponds to a zero-group-speed solution:

$$\frac{d\Omega}{dk} \Big|_s = 0 \quad \Leftarrow \quad \tilde{\mathcal{D}}|_s = \frac{\partial \tilde{\mathcal{D}}}{\partial k} \Big|_s = 0. \quad (7.21)$$

This is the fundamental feature of this solution type in the k -plane. Furthermore, it can be deduced that $d\Omega/dk|_p \neq 0 \Rightarrow \partial \tilde{\mathcal{D}} / \partial k|_p \neq 0$, i.e. a non-zero group speed (a point along the Ω -branch that is not a cusp) implies that the corresponding zero of $\tilde{\mathcal{D}}(k, \omega)$ is simple (it has a multiplicity equal to 1 in the k -plane, so $\tilde{\mathcal{D}}|_p = 0$, while $\partial \tilde{\mathcal{D}} / \partial k|_p \neq 0$).

7.1.4. INTEGRATION ORDER

Integral (7.7) is split up in the k - and ω -integrals and corresponding integrands, indicated as follows:

$$\overbrace{\int_{-\infty+i\gamma}^{\infty+i\gamma} e^{-i\omega t} \underbrace{\int_{-\infty}^{\infty} \frac{e^{iky}}{\tilde{\mathcal{D}}(k, \omega)} \frac{dk}{2\pi} \frac{d\omega}{2\pi}}^{k\text{-integral}}}_{\omega\text{-integral}}. \quad (7.22)$$

For convenience, the integration contours corresponding to the k - and ω -integrals are referred to as the k - and ω -contours. The k -integral is performed first in §7.2 and the ω -integral second in §7.3.

7.2. THE k -INTEGRAL

To start out, the double integral can be treated as a nested `for`-loop in programming. First, an ω -value is fixed on the ω -contour and, given this ω -value, the k -integral is evaluated. Once this is done, one proceeds to the next ω -value along the ω -contour and the

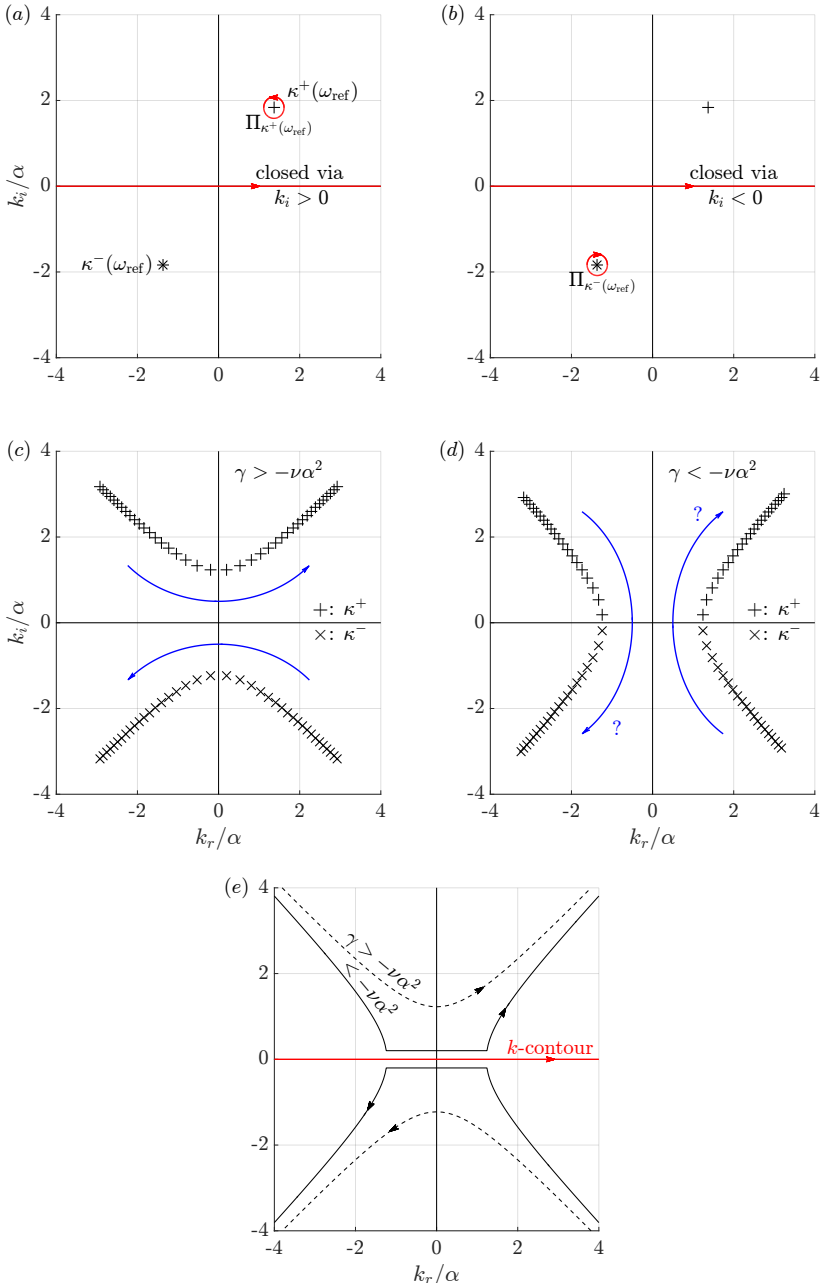


Figure 7.1: (a,b) Location of $\kappa^\pm(\omega_{\text{ref}})$ in the k -plane (for the same ω_{ref}), the straight red line indicates the k -contour. In (a), the integration contour $\Pi_{\kappa^+(\omega_{\text{ref}})}$ is shown, which results from closing the integration contour in the upper half-plane, which describes the solution behaviour for $y > 0$. In (b), the equivalent contour is shown for $y < 0$. (c-e) Typical locations of $\kappa^+(\omega_r + i\gamma)$ (+) and $\kappa^-(\omega_r + i\gamma)$ (x) for discrete choices (c,d) and a continuous range (e) of ω_r and the indicated values of $\omega_i = \gamma$. The blue (c,d) and black (e) arrows indicate the direction of increasing ω_r . In (e), the k -contour is re-introduced, which requires restricting the κ^+ - and κ^- -branches to their respective sides of the k -plane.

process is repeated. Considering $\omega = \omega_{\text{ref}}$ on the ω -contour, the k -integrand consists of the exponential function divided by the dispersion function divided by the dispersion function $\tilde{\mathcal{D}}(k, \omega_{\text{ref}})$.

To be able to proceed, it must first be shown that Jordan's lemma applies (see §A.1.4), which requires showing that $1/|\tilde{\mathcal{D}}(k, \omega_{\text{ref}})| \rightarrow 0$ as $|k| \rightarrow \infty$. For fixed and finite ω_{ref} , the zeros of $\tilde{\mathcal{D}}(k, \omega_{\text{ref}})$ are fixed at a finite location in the k -plane. In demonstrating that $1/|\tilde{\mathcal{D}}(k, \omega_{\text{ref}})| \rightarrow 0$ as $|k| \rightarrow \infty$, $|k|$ can therefore be chosen to be much larger than the $|k|$ -values associated to the zeros of $\tilde{\mathcal{D}}(k, \omega_{\text{ref}})$.³ The attention can accordingly be restricted to $\tilde{\mathcal{D}}(k, \omega_{\text{ref}}) \neq 0$. Using the reverse triangle inequality, for $\tilde{\mathcal{D}} = \tilde{\mathcal{D}}_0$ specifically, yields (see Kwok [9], equation (1.3.3b) and example 1.3.1]):

$$\frac{1}{|\tilde{\mathcal{D}}_0(k, \omega_{\text{ref}})|} = \frac{1}{|-i\omega_{\text{ref}} + i\alpha\bar{U}_e + \nu(\alpha^2 + k^2)|} \leq \frac{1}{\nu|k|^2 - \underbrace{|-i\omega_{\text{ref}} + i\alpha\bar{U}_e + \nu\alpha^2|}_{\text{fixed, finite}}} \rightarrow 0,$$

as $|k| \rightarrow \infty$. So, Jordan's lemma applies.

This allows the use of the major result illustrated in appendix A, which is that the k -integral can be expressed algebraically based on the locations of the zeros of $\tilde{\mathcal{D}}(k, \omega_{\text{ref}})$ in the k -plane. In fact, $\kappa_0^\pm(\omega_{\text{ref}})$, introduced in equation (7.13b), indicate these zeros per definition for $\tilde{\mathcal{D}}_0(k, \omega_{\text{ref}})$. It is important to recognise that this implies that *the zeros of $\tilde{\mathcal{D}}$ in the k -plane are, in general, determined by the ω -contour; $\kappa^+(\omega)$ and $\kappa^-(\omega)$ map the ω -contour onto the zeros of $\tilde{\mathcal{D}}(k, \omega)$ in the k -plane*.

In figure 7.1 (a,b), the zeros $\kappa^\pm(\omega_{\text{ref}})$ are given for $\omega_{\text{ref}} \in \mathbb{C}$. Per definition of the superscripts, $\kappa^+(\omega_{\text{ref}})$ and $\kappa^-(\omega_{\text{ref}})$ lie in the upper and lower half-plane, respectively. As elaborated in §§A.1.3 and A.1.4, the k -integral evaluates to the contour integrals around the zeros $\kappa^\pm(\omega_{\text{ref}})$ for $y \geq 0$, separately. The resulting integrals can be evaluated using equation (A.47):

$$\int_{-\infty}^{\infty} \frac{e^{iky}}{\tilde{\mathcal{D}}(k, \omega_{\text{ref}})} \frac{dk}{2\pi} = \oint_{\Pi_{\kappa^+(\omega_{\text{ref}})}} \frac{e^{iky}}{\tilde{\mathcal{D}}(k, \omega_{\text{ref}})} \frac{dk}{2\pi} = +i \frac{e^{i\kappa^+(\omega_{\text{ref}})y}}{\frac{\partial \tilde{\mathcal{D}}}{\partial k}(\kappa^+(\omega_{\text{ref}}), \omega_{\text{ref}})} \quad \text{for: } y > 0; \quad (7.23a)$$

$$\int_{-\infty}^{\infty} \frac{e^{iky}}{\tilde{\mathcal{D}}(k, \omega_{\text{ref}})} \frac{dk}{2\pi} = \oint_{\Pi_{\kappa^-(\omega_{\text{ref}})}} \frac{e^{iky}}{\tilde{\mathcal{D}}(k, \omega_{\text{ref}})} \frac{dk}{2\pi} = -i \frac{e^{i\kappa^-(\omega_{\text{ref}})y}}{\frac{\partial \tilde{\mathcal{D}}}{\partial k}(\kappa^-(\omega_{\text{ref}}), \omega_{\text{ref}})} \quad \text{for: } y < 0, \quad (7.23b)$$

where $\Pi_{\kappa^\pm(\omega_{\text{ref}})}$ denote the integration contours around the zeros $\kappa^\pm(\omega_{\text{ref}})$, respectively, as shown in figure 7.1 (a,b).

Equations (7.23) present the expression for the k -integral for just one choice of ω_{ref} . In the context of integral (7.22), the k -integral must be evaluated for all ω -values along the integration contour associated to the ω -integral. This must be done with care concerning the value of γ . In figure 7.1 (c), some typical $\kappa^\pm(\omega_r + i\gamma)$ -values are shown for $\gamma > -\nu\alpha^2$. In this case, the evaluation of equation (7.23) can be performed unambiguously, because the $\kappa^+(\omega_r + i\gamma)$ and $\kappa^-(\omega_r + i\gamma)$ clearly remain at their respective sides of the real k -axis, allowing for the application of equations (7.23).

In figure 7.1 (d), a typical situation is illustrated for $\gamma < -\nu\alpha^2$. As ω_r is increased in that case, this figure suggests that the values of $\kappa^\pm(\omega_r + i\gamma)$ cross the real k -axis. However,

³The ω -integral limits $\pm\infty + iy$ merely imply that ω approaches these limits, which means that $|k|$ can always be made large enough accordingly.

as indicated by the symbols used in figure 7.1 (d), the value of κ^+ , indicated by the solid line in the upper half-plane, jumps discontinuously to its mirror image in the imaginary k -axis as ω_r surpasses a threshold value (note that $\kappa_i^+ \geq 0$ and $\kappa_i^- \leq 0$ per definition). Note that for $\kappa_i^+ = 0$, the pole lies on the k -contour; this is the situation discussed in §A.3.1. In figure 7.1 (e), the k -contour is shown: the κ^+ -branch is connected to itself by introducing a branch segment that traces along the k -contour. Equation (7.23a) is applicable in this situation as before. Similar arguments can be used to obtain the κ^- -contribution.

As pointed out before, the ω -contour is intimately linked to the zeros of $\tilde{\mathcal{D}}$ in the k -plane. So, connecting the κ^+ -branch to itself in the k -plane has a particular impact on the ω -contour. It turns out the shape of the corresponding ω -contour in question is useful for the ultimate evaluation of the ω -integral.⁴ The impact could be shown with the inverse mapping: $\Omega(k)$, but this approach is avoided to prevent a confusing discussion, as will be elaborated in §7.4.1. Instead, as a first step, a version of the ω -contour is considered for which κ^\pm do not approach the real k -axis. Second, this contour is deformed with the aim of identifying which ω -contour corresponds to the target shape of the κ^\pm -branches shown in figure 7.1 (e).

As mentioned, for $\gamma > -v\alpha^2$, $\kappa_{0,i}^+ > 0$ and $\kappa_{0,i}^- < 0$. This can be demonstrated using equation (7.13b) and by considering the discriminant of $\tilde{\mathcal{D}}_0(k, \omega)$:

$$\text{Discr}_k(\tilde{\mathcal{D}}_0) = -4v \left(-i\omega + i\alpha \bar{U}_e + v\alpha^2 \right) = -4v \left(\omega_i + v\alpha^2 + i(-\omega_r + \alpha \bar{U}_e) \right). \quad (7.24)$$

The conditions for $\kappa^\pm \in \mathbb{R}$ (which is to be avoided), correspond to the imaginary part of $\text{Discr}_k(\tilde{\mathcal{D}}_0)$ being zero, resulting in:

7

$$\omega_r = \alpha \bar{U}_e \quad (7.25a)$$

(recall that $\alpha \in \mathbb{R}$) and the real part of $\text{Discr}_k(\tilde{\mathcal{D}}_0)$ must be larger than zero, which implies:

$$\omega_i < -v\alpha^2. \quad (7.25b)$$

This confirms that setting $\gamma > -v\alpha^2$ prevents $\kappa^\pm \in \mathbb{R}$. The line described by equations (7.25), i.e. the line that starts at $\omega = \alpha \bar{U}_e - iv\alpha^2$ and shoots off straight down to $-i\infty$, is for now labelled with Ω_A for ‘avoid in the ω -plane’.

The dashed contour in figure 7.2 (a) illustrates a particular ω -contour with $\gamma \gg -v\alpha^2$. The corresponding κ^\pm -branches are shown as the dashed black lines in figure 7.2 (b). In what follows, the integration contours will be depicted with red lines, while the corresponding zero-branches (in the complex plane corresponding to the complementary variable) will be shown in black, with the same line style. The dashed black lines in figure 7.2 (b) do not intersect with the k -contour, indicated by the solid red line, as required.

By letting $\gamma \rightarrow -v\alpha^2$, as exemplified with the red solid line in figure 7.2 (a), the corresponding κ^\pm -branches approach the k -contour. The same combination of lines is repeated as the dashed lines in figures 7.2 (c) and (d). Lowering the ω -contour even more,

⁴In §7.5, it will be shown that the ω -integrand is non-holomorphic when κ^+ or κ^- intersects the k -contour. The intended arrangement of the κ^\pm -branches, for which equations (7.23) are still applicable, is retrieved by deforming the ω -contour while avoiding regions of the ω -plane where the ω -integrand is non-holomorphic. This is equivalent to the approach applied in §A.1.3, where the non-holomorphic regions were discrete points, while here this region is a continuous line (described by equations (7.25)).

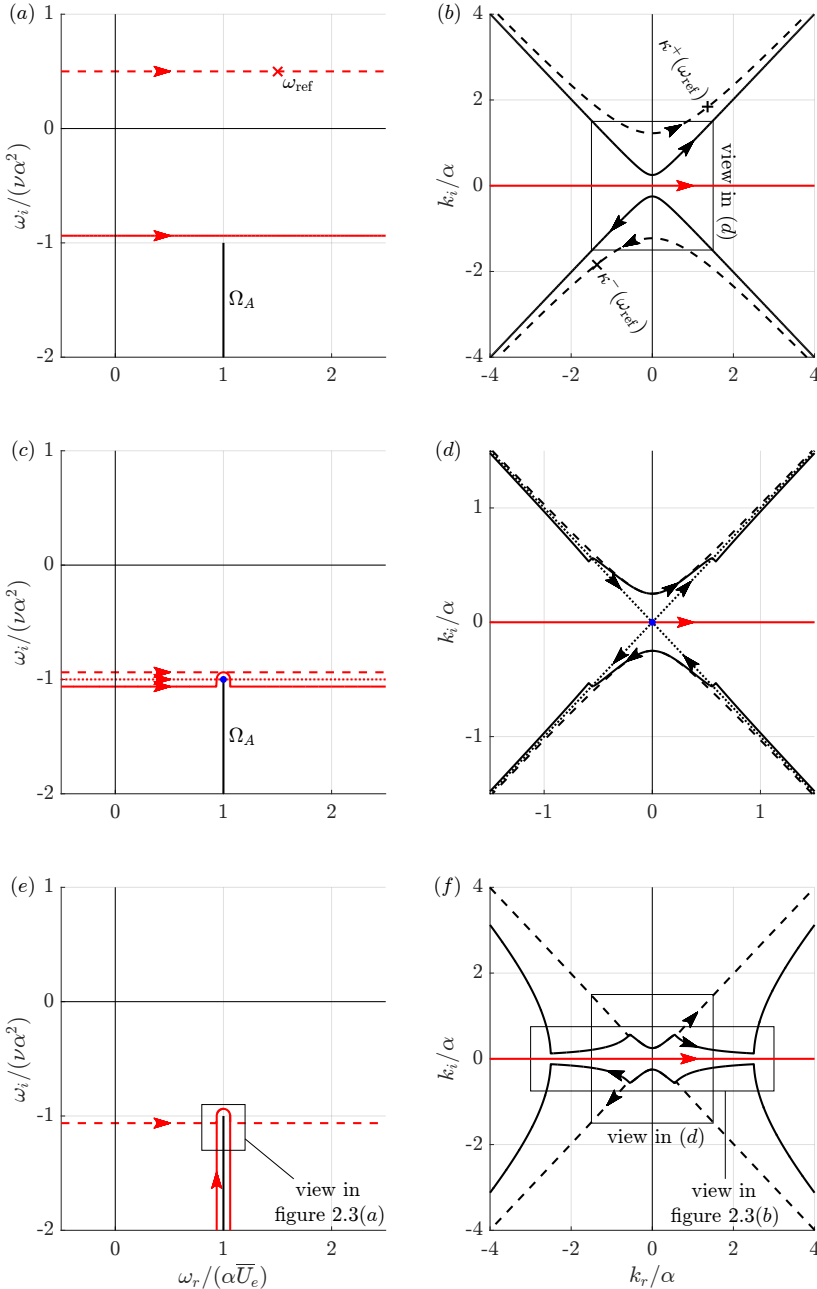


Figure 7.2: Movement of the κ -branches (b,d,f) as the ω -integration contour (a,c,e) is lowered, $\gamma \rightarrow -\infty$. Integration contours are coloured red and branches black. The contours/branches after the movement are solid, while the previous versions are dashed. The line Ω_A is shown as the black line in (a,c,e). The \times 's denote (a) ω_{ref} and (b) $\kappa^-(\omega_{\text{ref}})$, the + indicates $\kappa^+(\omega_{\text{ref}})$. In (c,d), the dotted lines correspond to the straight ω -contour passing through the point $\omega = a\bar{U}_e - i\nu\alpha^2$.

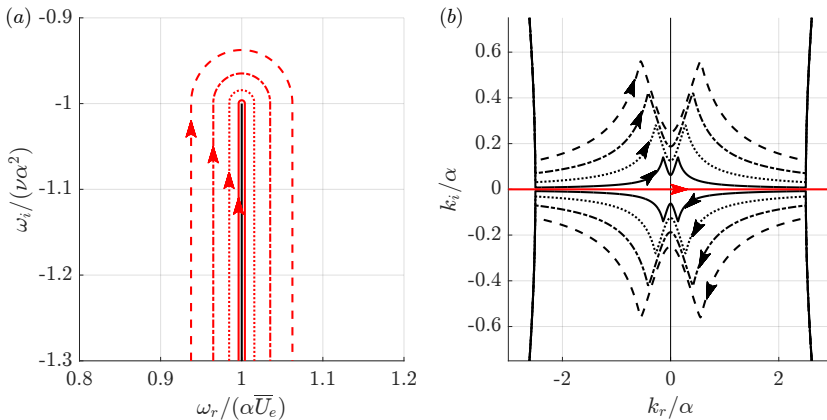


Figure 7.3: Illustration of how the κ^\pm -branches approach the k -contour while letting the branch cut in the ω -plane approach Ω_A . The parameter γ is fixed at $-7.25\nu\alpha^2$; note that this fixes the k_r -value at which the κ^\pm -branches depart from the proximity of the k -contour ($|k_r| = 2.5\bar{U}_e/\nu$ for this γ). The distance of the branch cut from Ω_A is reduced quadratically (for the dashed, dash-dotted, dotted and solid lines $\epsilon_\omega = (16, 9, 4, 1) \cdot \nu\alpha^2/16^2$, respectively), such that the κ^\pm -branches approach the k -contour at a linear rate.

the κ^\pm -branches ‘pinch’ the k -contour at $k = 0 + i0$, see the dotted lines in the latter panels. This illustrates that the endpoint of Ω_A must indeed be avoided. In general, intersecting the whole k -contour is avoided by deforming the ω -contour around Ω_A . A way to do this is to deform the segment of the straight ω -contour that has a distance smaller than ϵ_ω from Ω_A . This can be deformed into the border of the ϵ_ω -neighbourhood of Ω_A , i.e. the equidistant line to Ω_A with distance ϵ_ω ; also referred to as a *branch cut*. Outside the ϵ_ω -proximity of Ω_A , the height of the ω -contour is maintained at $\omega_i = \gamma$.

The appropriateness of the resulting contour is illustrated with the solid lines in figures 7.2 (c) and (d). Even though $\gamma < -\nu\alpha^2$, the corresponding κ^\pm -branches in figure 7.2 (d) have not intersected the k -contour. Note that, this way, the ω -contour can be deformed further down into the complex ω -plane, such that $\gamma \ll -\nu\alpha^2$; as long as a branch-cut is introduced.

In figure 7.2 (e), the ω -contour is pushed further downwards, to $\gamma = -7.25\nu\alpha^2$ (such that the horizontal parts are no longer visible in the figure). The corresponding κ^\pm -branches in figure 7.2 (f) approach, but will never intersect, the k -contour, because Ω_A is avoided per construction of the branch cut. As the distance of the branch cut to Ω_A approaches zero (at the rate ϵ_ω), the κ^\pm -branches approach the k -contour (as $\sqrt{\epsilon_\omega}$), as illustrated in figure 7.3. In the limit, the solid lines that were presented back in figure 7.1 (e) are approached, which was the target. So, connecting the κ^+ -branch to itself in figure 7.1 (e) corresponded to augmenting a branch cut to the ω -contour, preventing the crossing of Ω_A .

This opens the path to the ω -integral, for which an expression is obtained by inserting equations (7.23) into the integral (7.22):

$$\int_{-\infty+i\gamma}^{\infty+i\gamma} \int_{-\infty}^{\infty} \frac{e^{i(ky-\omega t)}}{\tilde{\mathcal{D}}(k, \omega)} \frac{dk d\omega}{(2\pi)^2} = \begin{cases} \int_{\Xi} \frac{e^{i(\kappa^+(\omega)y-\omega t)}}{-i\frac{\partial \tilde{\mathcal{D}}}{\partial k}(\kappa^+(\omega), \omega)} \frac{d\omega}{2\pi} & \text{for: } y > 0; \\ \int_{\Xi} \frac{e^{i(\kappa^-(\omega)y-\omega t)}}{+i\frac{\partial \tilde{\mathcal{D}}}{\partial k}(\kappa^-(\omega), \omega)} \frac{d\omega}{2\pi} & \text{for: } y < 0. \end{cases} \quad (7.26a)$$

$$\int_{-\infty+i\gamma}^{\infty+i\gamma} \int_{-\infty}^{\infty} \frac{e^{i(ky-\omega t)}}{\tilde{\mathcal{D}}(k, \omega)} \frac{dk d\omega}{(2\pi)^2} = \begin{cases} \int_{\Xi} \frac{e^{i(\kappa^+(\omega)y-\omega t)}}{-i\frac{\partial \tilde{\mathcal{D}}}{\partial k}(\kappa^+(\omega), \omega)} \frac{d\omega}{2\pi} & \text{for: } y > 0; \\ \int_{\Xi} \frac{e^{i(\kappa^-(\omega)y-\omega t)}}{+i\frac{\partial \tilde{\mathcal{D}}}{\partial k}(\kappa^-(\omega), \omega)} \frac{d\omega}{2\pi} & \text{for: } y < 0. \end{cases} \quad (7.26b)$$

The integration contour $\Xi = \Gamma \cup \Pi$ consists of two parts. The part Γ is the straight punctured line segment $\Gamma = [-\infty + i\gamma, \infty + i\gamma]$, where $\gamma \rightarrow -\infty$ and the puncture is located at the location where the uninterrupted line segment would intersect with Ω_A . The part Π is the branch cut around Ω_A . Furthermore, note that the pre-multiplying factors $\pm i$ in (7.23) have here been absorbed into the denominator of the integrands.

The set-up of the ω -integral is now complete, so the treatment can proceed in evaluating it.

7.3. THE ω -INTEGRAL

As illustrated in figures 7.3, as the branch cut is pulled tight around Ω_A ; one is forced to integrate around the pinch point $\omega = \alpha \bar{U}_e - i\bar{V}_e$. In figures 7.2 (c) and (d), this point was shown to correspond to $k = \kappa^+ = \kappa^- = 0$ for $\tilde{\mathcal{D}}_0$; the κ_{\pm} -branches pinch the k -contour from opposite sides. Clearly, $\tilde{\mathcal{D}}(k, \omega)$ has a double k -zero at that point. Although the κ^{\pm} -branches are set up to both graze the k -contour, the double zero is unique, due to the second order nature of $\tilde{\mathcal{D}}(k, \omega)$ in k .

Using this information, Briggs [1] derives a general expression for the denominator $\partial \tilde{\mathcal{D}} / \partial k(\kappa^{\pm}(\omega), \omega)$ in the integrals (7.26). To arrive at this expression, Briggs assumes that:

$$\left. \frac{\partial^2 \tilde{\mathcal{D}}}{\partial \omega^2} \right|_s, \left. \frac{\partial^2 \tilde{\mathcal{D}}}{\partial \omega \partial k} \right|_s, \left. \frac{\partial^3 \tilde{\mathcal{D}}}{\partial k^3} \right|_s \text{ and other higher order derivatives are zero.} \quad (7.27a)$$

For $\tilde{\mathcal{D}}_{\bar{V}_e}(k, \omega)$ and $\tilde{\mathcal{D}}_0(k, \omega)$ this is justified, because these derivatives identically evaluate to zero due to their first and second polynomial order in ω and k , respectively. For higher order problems, these terms can have an impact on the final result. In addition, it will be used that the term $\partial^2 \tilde{\mathcal{D}} / \partial k^2$ is positive for the currently considered dispersion functions:

$$\frac{\partial^2 \tilde{\mathcal{D}}_0}{\partial k^2} = \frac{\partial^2 \tilde{\mathcal{D}}_{\bar{V}_e}}{\partial k^2} = 2\nu > 0. \quad (7.27b)$$

With assumptions (7.27a), the Taylor expansion of $\tilde{\mathcal{D}}$ around the pinch point (k_s, ω_s) terminates:

$$\tilde{\mathcal{D}}(\kappa^{\pm}(\omega), \omega) \xrightarrow{0} \tilde{\mathcal{D}} \Big|_s^0 + \frac{\partial \tilde{\mathcal{D}}}{\partial k} \Big|_s^0 (\kappa^{\pm}(\omega) - k_s) + \frac{\partial \tilde{\mathcal{D}}}{\partial \omega} \Big|_s^0 (\omega - \omega_s) + \frac{1}{2} \frac{\partial^2 \tilde{\mathcal{D}}}{\partial k^2} \Big|_s^0 (\kappa^{\pm}(\omega) - k_s)^2, \quad (7.28)$$

allowing to solve for $\kappa^{\pm} - k_s$, which yields:

$$\kappa^{\pm}(\omega) - k_s = \pm i \sqrt{2 \left. \frac{\partial \tilde{\mathcal{D}}}{\partial \omega} \right|_s^0 \left. \frac{\partial^2 \tilde{\mathcal{D}}}{\partial k^2} \right|_s^0^{-1} (\omega - \omega_s)}, \quad (7.29)$$

where the κ^+ and κ^- are linked to the positive and negative branches of the square root on the right hand side.

The evaluation of the term $\partial\tilde{\mathcal{D}}/\partial k$ ($\kappa^\pm(\omega), \omega$) is required in integrals (7.26), so $\tilde{\mathcal{D}}(k, \omega)$ is partially differentiated with respect to k and then evaluated at $k = \kappa^\pm(\omega)$. Incorporating assumptions (7.27a), this yields:

$$\frac{\partial\tilde{\mathcal{D}}}{\partial k}(\kappa^\pm(\omega), \omega) = \left. \frac{\partial\tilde{\mathcal{D}}}{\partial k} \right|_s + \left. \frac{\partial^2\tilde{\mathcal{D}}}{\partial k^2} \right|_s (\kappa^\pm(\omega) - k_s) = \pm i \sqrt{2 \left. \frac{\partial\tilde{\mathcal{D}}}{\partial \omega} \right|_s \left. \frac{\partial^2\tilde{\mathcal{D}}}{\partial k^2} \right|_s (\omega - \omega_s)}, \quad (7.30)$$

where assumption (7.27b) was required to factor $\partial^2\tilde{\mathcal{D}}/\partial k^2|_s$ into the square root. Inserting equation (7.30) into the integrals (7.26) yields:

$$\begin{aligned} \int_{-\infty+i\gamma}^{\infty+i\gamma} \int_{-\infty}^{\infty} \frac{e^{i(ky-\omega t)}}{\tilde{\mathcal{D}}(k, \omega)} \frac{dk d\omega}{(2\pi)^2} &= \int_{\Xi} \frac{e^{i(\kappa^\pm(\omega)y-\omega t)}}{\mp i \left. \frac{\partial\tilde{\mathcal{D}}}{\partial k} \right|_s (\kappa^\pm(\omega), \omega)} \frac{d\omega}{2\pi} \\ &= e^{i(k_s y - \omega_s t)} \int_{\Xi} \frac{e^{i((\kappa^\pm(\omega) - k_s)y - (\omega - \omega_s)t)}}{\sqrt{2 \left. \frac{\partial\tilde{\mathcal{D}}}{\partial \omega} \right|_s \left. \frac{\partial^2\tilde{\mathcal{D}}}{\partial k^2} \right|_s (\omega - \omega_s)}} \frac{d\omega}{2\pi} \quad \text{for } y \geq 0, \end{aligned} \quad (7.31)$$

where the “constant” exponential function $e^{i(k_s y - \omega_s t)}$ is factored from the integrals, similarly as done in the derivation of equation (A.44). Due to the evaluation of $\mp i\partial\tilde{\mathcal{D}}/\partial k$, integrals (7.31) have the same denominator in their integrand.

By letting $t > 0$ and $\gamma \rightarrow -\infty$, it can now be ensured that the contribution of the contour integral over Γ is negligible with respect to that over Π , i.e. that the integration contour of integral (7.31), Ξ , can be reduced to Π . This follows from several facts. First of all, the denominator of the integrand in equation (7.31) is bounded away from zero by taking γ to be smaller (more negative) than $\omega_{s,i}$. By truncating Γ in the real direction, one can estimate the size of this contribution as follows:

$$\left| \int_{\Gamma} \{\cdot\} e^{-i(\omega - \omega_s)t} d\omega \right| = \lim_{\mathcal{R} \rightarrow \infty} e^{(\gamma - \omega_{s,i})t} \left| \int_{-\mathcal{R}+i\gamma}^{\mathcal{R}+i\gamma} \{\cdot\} d\omega \right| \leq \lim_{\mathcal{R} \rightarrow \infty} M \mathcal{R} e^{(\gamma - \omega_{s,i})t}, \quad (7.32)$$

where M is the maximum of the factor indicated by $\{\cdot\}$ for all $\omega \in \Gamma$. That is, the integral of a constant integrand would diverge linearly in \mathcal{R} , also see equation (A.34). Note that $|e^{-i(\omega - \omega_s)t}| \rightarrow e^{(\gamma - \omega_{s,i})t} \rightarrow 0$ exponentially as $\gamma \rightarrow -\infty$. Therefore, by letting γ approach $-\infty$ and \mathcal{R} approach ∞ at the same rate, the integral goes to zero. Hence, the only contribution to the integral over Ξ comes from the branch cut part, Π , only. The limits indicated in the integrals (7.31) are from now on understood to indicate this part only.

Following Briggs [1], the remaining integral can be evaluated asymptotically for $t \rightarrow \infty$, while y is fixed and finite; $t \gg y$. This is useful, because it allows eliminating the factor $e^{i(\kappa^\pm(\omega) - k_s)y}$, determining the spatial character of the solution, from the integrand. This approach is made rigorous in what is referred to as the method of stationary phase. For more details, see Haberman [10, section 14.5] and Miller [11, chapter 5].

The imaginary part of $\kappa^\pm(\omega) - k_s$ can be made arbitrarily small, by choosing a small enough proximity of the branch cut to Ω_A (letting $\epsilon_\omega \downarrow 0$). By setting $t = 0$, this part

represents the Fourier transform of the Dirac δ pulse centered at $y = 0$, as imposed by the Green's function formulation (7.2). As time evolves, the ω -dependency of this term encodes that, for example, viscosity damps different wavenumbers at different rates. Hence, by letting the system evolve for a very long time, the Dirac δ pulse diffuses. In §7.1.3, it was asserted that the group speed of the solution (k_s, ω_s) , about which the expansion is performed, is identically zero, which implies that *the solution must develop fronts that travel to $\pm\infty$ in y* . In the asymptotic evaluation of integral (7.31), it can hence be assumed that the fronts of the perturbation have moved far away from any finite y -location. Accordingly, the solution's spatial distribution becomes asymptotically homogeneous in Fourier space; for $t \rightarrow \infty$, it will consist only of the single most unstable wavenumber k_s . Effectively, $e^{i(\kappa^\pm(\omega) - k_s)y}$ can be set equal to unity in the integrand, thus representing the perfectly homogeneous spatial distribution.

The remaining integral can be solved by performing a special substitution. Define:⁵

$$\left. \begin{array}{l} u = +i\sqrt{a(\omega - \omega_s)}; \\ 2u du = -ad\omega; \\ -i(\omega - \omega_s)t = -\frac{u^2 t}{ia}, \end{array} \right| \quad \begin{array}{l} \text{where: } a = 2 \left. \frac{\partial \tilde{\mathcal{D}}}{\partial \omega} \right|_s \left. \frac{\partial^2 \tilde{\mathcal{D}}}{\partial k^2} \right|_s \\ \text{such that: } ia = i2(-i)(2\nu) = 4\nu > 0 \\ (\text{valid for both } \tilde{\mathcal{D}} = \tilde{\mathcal{D}}_0 \text{ and } \tilde{\mathcal{D}} = \tilde{\mathcal{D}}_{V_e}) \end{array} \quad (7.33)$$

Convergence of the integral is ensured if $t > 0$ (and $ia > 0$, which is demonstrated). The u -integration limits are determined by noticing that the start (-) and end (+) limits prescribed by the branch cut as $\gamma \rightarrow -\infty$ correspond to $\omega - \omega_s = \pm i\epsilon_\omega - iR$, where $\epsilon_\omega \downarrow 0$ and $R \rightarrow \infty$. It can be determined that:

$$u = i\sqrt{a(\pm i\epsilon_\omega - iR)} = i\sqrt{i\epsilon_\omega(\mp i\epsilon_\omega - R)} \rightarrow i(\mp i\infty) = \pm\infty. \quad (7.34)$$

as $\epsilon_\omega \downarrow 0$ and $R \rightarrow \infty$ (note that the imaginary parts of \sqrt{z} and z have the same sign, due to the selection of the positive sign in the definition of u , see Kwok [9, Example 1.2.3]).

Combining everything yields:

$$\int_{\Pi} \frac{e^{-i(\omega - \omega_s)t}}{\sqrt{a(\omega - \omega_s)}} \frac{d\omega}{2\pi} = \int_{-\infty}^{\infty} \frac{e^{-\frac{u^2 t}{ia}}}{-iu} \left(\frac{-u du}{\pi a} \right) = \frac{1}{\pi ia} \int_{-\infty}^{\infty} e^{-\frac{u^2 t}{ia}} du = \frac{1}{\pi ia} \sqrt{\frac{\pi ia}{t}} = \frac{1}{\sqrt{\pi iat}}, \quad (7.35)$$

where the Gaussian integral is evaluated in §2.4.3 (see equations (2.35) to (2.38) with $\sigma = \sqrt{ia/2t}$). Note that the operation $\sqrt{\pi ia}/\pi ia = 1/\sqrt{\pi ia}$ is valid, because $ia > 0$.

Inserting this result into equation (7.31) yields:

$$\int_{-\infty+i\gamma}^{\infty+i\gamma} \int_{-\infty}^{\infty} \frac{e^{i(ky - \omega t)}}{\tilde{\mathcal{D}}(k, \omega)} \frac{dk d\omega}{(2\pi)^2} \rightarrow \frac{e^{i(k_s y - \omega_s t)}}{\sqrt{2\pi it} \left. \frac{\partial \tilde{\mathcal{D}}}{\partial \omega} \right|_s \left. \frac{\partial^2 \tilde{\mathcal{D}}}{\partial k^2} \right|_s}, \quad (7.36)$$

as $t \rightarrow \infty$. This is Briggs's equation (2.22). Note that, as $t \rightarrow \infty$, the square root part $1/\sqrt{t}$ is overshadowed by the exponential part.

⁵Note the correspondence between u and $\left. \frac{\partial^2 \tilde{\mathcal{D}}}{\partial k^2} \right|_s (\kappa^+(\omega) - k_s)$ in equation (7.30). This substitution corresponds directly to the transformation $(\kappa^+(\omega), \omega) \mapsto (k, \Omega(k))$; the integral is, in fact, evaluated over the k -contour *a second time*. Evaluating this k -integral is the natural set-up of the method of stationary phase, see Miller [11].

Equation (7.36) describes the growth characteristics of a stationary wave packet in time, everywhere simultaneously in space; which is, in turn, indicative of the absolute stability characteristics of the system. In particular, the system is absolutely unstable if:

$$\text{Briggs's criterion #1:} \quad \omega_{s,i} > 0, \quad (7.37a)$$

which is referred to as Briggs's criterion for an absolute instability. It must be emphasized that the corresponding k_s must be a pinch point in the k -plane. Double zeros in the k -plane may occur that do not merge through the k -contour. As was shown in §A.3.1, such a double k -zero does not cause a non-holomorphic ω -integrand and therefore does not contribute to the ω -integral. For this reason, the latter is also labelled as one of Briggs's criteria for absolute instability:

$$\text{Briggs's criterion #2:} \quad \begin{aligned} &\text{the double } k\text{-zero must be the result of} \\ &\kappa\text{-branches pinching the } k\text{-contour.} \end{aligned} \quad (7.37b)$$

When referring to Briggs's criterion in this thesis, the criterion indicated by equation (7.37a) is meant. For the current problem of consideration, there are only two κ -branches that are located on the different sides of the k -contour, so this criterion is trivially satisfied.

The term absolute instability can be interpreted to refer to the fact that an asymptotic solution has been constructed that has fronts that propagate away from the solution's point of origin. Once it is excited, the solution will never propagate away from said origin. It is absolute in that sense. As will be demonstrated in §7.4.2, however, there is another mathematically grounded motivation for the label 'absolute.'

In light of the values $(k_s, \omega_s) = (0, \alpha \bar{U}_e - iv\alpha^2)$ corresponding to $\tilde{\mathcal{D}}_0$, it is conclusively demonstrated that $\tilde{\mathcal{D}}_0$ does not govern absolutely unstable solutions. The asymptotic wave packet solution is an infinitely long wave ($k_s = 0$) that oscillates at the frequency $\omega_{s,r} = \alpha \bar{U}_e$ (due to the phase speed in the x -direction imposed by \bar{U}_e and the wavenumber α), while decaying exponentially in time, as $e^{\omega_{s,i} t} = e^{-v\alpha^2 t}$.

Note that equation (7.36) is consistent in the view of the fact that the branch point is the least stable solution of the dispersion relation in the ω -plane that is accounted for. The previous analysis may seem trivial in this perspective; one would have expected the point with the largest ω_i -value to dominate the dynamics. *This argument applies only to branch points, however.* As will be shown in §7.4, allowing the advection term \bar{V}_e to be non-zero, ω -contours may be encountered that do not approach a branch point. Accordingly, the limiting maximum ω_i -value is not necessarily indicative of the absolute stability of the system.

7.4. THE CASE $\bar{V}_e \neq 0$

Lifting the assumption that $\bar{V}_e = 0$ requires retracing the steps executed in §7.2. In particular, the behaviour of the κ^\pm -branches change. Before embarking upon the analysis, it is useful to shed light on a convenient way of finding the region Ω_A in more general cases. It will be very convenient to invoke the use of the Ω -mapping. Therefore, first, its role in the analysis will be clarified in hindsight for the case $\bar{V}_e = 0$.

7.4.1. THE ROLE OF THE Ω -BRANCH

Any reference to the Ω -mapping was explicitly avoided in §7.2 to prevent confusion. The underlying reason is that illustrating its use requires swapping the order of integration (and the definition of the k - and ω -integrand, etc.) defined in §7.1.4. Whereas the k -integral is performed first in equation (7.22), the same result should be encountered when the ω -integral is executed first. This arrangement yields the following (re-)definitions:

$$\overbrace{\int_{-\infty}^{\infty} e^{iky} \underbrace{\int_{-\infty+i\gamma}^{\infty+i\gamma} \frac{e^{-i\omega t}}{\tilde{\mathcal{D}}(k, \omega)} \frac{d\omega}{2\pi} \frac{dk}{2\pi}}_{\omega\text{-integral}}}^{k\text{-integrand}}. \quad (7.38)$$

Having to relabel the parts is the reason for avoiding the swap before. Again, the integration contour corresponding to the ω - and k -integrals are referred to as the ω - and k -contours, respectively.

Logically, the roles of k and ω are now reversed. The total integral can now be approached by fixing a particular k -value on the k -contour, say $k = k_{\text{ref}}$, and executing the ω -integral accordingly. The ω -integrand now consists of the exponential function divided by the dispersion function $\tilde{\mathcal{D}}(k_{\text{ref}}, \omega)$. Jordan's lemma applies, because:

$$\frac{1}{|\tilde{\mathcal{D}}_0(k_{\text{ref}}, \omega)|} \rightarrow \frac{1}{|\omega|} \rightarrow 0,$$

as $|\omega| \rightarrow \infty$, for fixed k_{ref} .

This means that all the machinery from appendix A can be applied again. For a particular $k = k_{\text{ref}}$, the ω -integral can be expressed based on the zeros of $\tilde{\mathcal{D}}_0(k_{\text{ref}}, \omega)$ in the ω -plane. Per definition of Ω_0 , this zero is given by $\Omega_0(k_{\text{ref}}); \tilde{\mathcal{D}}_0(k_{\text{ref}}, \Omega_0(k_{\text{ref}})) = 0$. As was the case for the k -integral in the previous integration order, the latter statement means that *the zeros of $\tilde{\mathcal{D}}$ in the ω -plane are, in general, determined by the k -contour; $\Omega(k)$ maps the k -contour onto the corresponding locus of the zero of $\tilde{\mathcal{D}}(k, \omega)$ in the ω -plane*.

In §7.2, the k -integral was evaluated by integrating over the real k -axis. In figures 7.1, 7.2 and 7.3, the real k -axis was therefore highlighted as the k -contour. Evaluating Ω_0 for $k = k_r \in \mathbb{R}$ yields:

$$\Omega_0(k_r) = \alpha \bar{U}_e - i\nu(\alpha^2 + k_r^2), \quad (7.39)$$

which serves as a parametrization of Ω_A , $\Omega_0(k_r) \in \Omega_A$, which was earlier described with equations (7.25). Note that the deductions required to arrive at equation (7.39) are entirely equivalent to those underlying equations (7.25): letting κ^\pm coincide with the k -contour. The deployment of the Ω -mapping becomes very convenient if the k -contour becomes more complicated.

Note that the κ^\pm -branches, evaluated for a particular ω -contour, could be labelled as κ_A^+ and κ_A^- ; the lines in the k -plane that are to be avoided by the k -contour. The branches κ_A^+ and κ_A^- are the equivalents of Ω_A in the k -plane. Note that using the subscript A is a notational redundancy from now on. To distinguish the loci of the zeros of $\tilde{\mathcal{D}}$ from the

integration contour in the same plane, the former and latter are referred to as a branch and contour, respectively. So, the ω -contour (in the ω -plane) determines the location of the κ^\pm -branches in the k -plane, while the k -contour (in the k -plane) determines the location of the Ω -branch.

Having swapped the integration contours is a short-cut towards showing that Ω and κ^\pm indicate the locations where the ω - and k -integrands are non-holomorphic. These locations are always found at the location indicated by Ω and κ^\pm , irrespective of the chosen order of integration. This follows from analysing the integrands of the second integrals (i.e. the ω -integrand for the arrangement (7.22) and the k -integrand for the arrangement (7.38)). This will be done for the ω -integrand corresponding to equation (7.22) in §7.5, where it will be shown that, why and how it is indeed non-holomorphic when evaluated on the Ω -branch.

In the subsequent analysis, the aforementioned invariance can be utilised to directly identify the regions in the k - and ω -planes where the placement of the integration contours must be avoided.

7.4.2. MANIPULATING THE BRANCHES AND CONTOURS FOR $\bar{V} \neq 0$

The path to considering the case $\bar{V} \neq 0$ is now open. The original order of integration as shown in integral (7.22) will be used again for consistency. The value \bar{V}_e is chosen to be equal to \bar{U}_e to generate the figures. Moreover, the scaling of the figures of the k -plane are adapted; a scaling involving \bar{V}_e is more illustrative in this case.

Going through the same procedure as before, it must first be demonstrated that Jordan's lemma (see §A.1.4) applies. This follows from the fact that:

$$\begin{aligned} \frac{1}{|\tilde{\mathcal{D}}_{\bar{V}_e}(k, \omega)|} &= \frac{1}{\left| -i\omega + i\alpha\bar{U}_e + ik\bar{V}_e + \nu(\alpha^2 + k^2) \right|} \\ &\leq \frac{1}{\nu \left(|k| - \frac{|\bar{V}_e|}{2\nu} - \sqrt{\frac{i\omega - i\alpha\bar{U}_e - \nu\alpha^2}{\nu} - \left(\frac{\bar{V}_e}{2\nu}\right)^2} \right)^2} \rightarrow 0, \end{aligned} \quad (7.40)$$

for $|k| \rightarrow \infty$, where the inequality again follows from the reverse triangle inequality, now applied to the factored dispersion relation. The validity of Jordan's lemma implies that, per $\omega = \omega_{\text{ref}}$ on the ω -contour, the k -integral can be split into the contributions by the residues at the poles at $k = \kappa_{\bar{V}_e}^+(\omega_{\text{ref}})$ and $\kappa_{\bar{V}_e}^-(\omega_{\text{ref}})$ valid for $y > 0$ and < 0 , respectively.

Utilising the invariance referenced in the previous section, the location of the non-holomorphic regions in the k - and ω -plane can be directly identified, given viable choices for the ω - and k -integration contours. As was done in §7.2, the ω -contour is placed far in the upper half of the ω -plane and the k -contour is placed along the real k -axis. Note that:

$$\begin{aligned} \text{Im} \left\{ \kappa_{\bar{V}_e}^\pm(\omega) \right\} &= -\frac{\bar{V}_e}{2\nu} \pm \frac{1}{\sqrt{\nu}} \text{Re} \left\{ \sqrt{\omega_i + \nu \left(\alpha^2 + \left(\frac{\bar{V}_e}{2\nu} \right)^2 \right)} + i(-\omega_r + \alpha\bar{U}_e) \right\} \\ &\rightarrow -\frac{\bar{V}_e}{2\nu} \pm \sqrt{\frac{\omega_i}{\nu}}, \end{aligned} \quad (7.41)$$

as $\omega_i \rightarrow +\infty$, independent of ω_r .⁶ This implies that the κ^\pm -branches lie far away from the current choice of the k -contour; being the real k -axis.

Now, the Ω - and κ^\pm -branches can be evaluated. To that end, first expand $\Omega_{\bar{V}_e}(k)$ for general $k \in \mathbb{C}$:

$$\Omega_{\bar{V}_e}(k) = \alpha \bar{U}_e + k_r \left(\bar{V}_e + 2v k_i \right) + i \left(k_i \left(\bar{V}_e + v k_i \right) - v (\alpha^2 + k_r^2) \right). \quad (7.42)$$

As before, the k -contour is chosen to be equal to the real k -axis, shown as the solid red line in figure 7.4 (b). Hence Ω has to be evaluated for $k \in \mathbb{R}$.

Recall from equation (7.39) that when evaluating $\Omega_0(k)$ for real $k = k_r$, the real part of $\Omega_0(k_r)$ was constant and equal to $\alpha \bar{U}_e$. The real part of $\Omega_{\bar{V}_e}(k_r)$, i.e. setting $k_i = 0$ in equation (7.42), has a term that varies linearly with k_r instead. Together with the quadratic appearance of k_r in its imaginary part, this implies that $\Omega_{\bar{V}_e}(k_r)$ describes a parabola in the ω -plane. In figure 7.4 (a), this parabola is shown as the solid black line. The $\kappa_{\bar{V}_e}^\pm(\omega)$ -branches have the same shape as those for $\bar{V}_e = 0$. This situation is illustrated in figures 7.4 (a) and (b), where the ω -contour and corresponding κ^\pm -branches are shown as the dashed lines.

As done in §7.2, the next step is to lower the ω -contour, its height again being encoded by γ . While γ approaches $-v\alpha^2$, only the κ^+ -branch approaches the k -contour; while the κ^- -branch does not. Even as the ω -contour is made to touch the Ω -branch, see the dotted lines in figure 7.4, only the κ^+ -branch touches the k -contour. Strictly following the approach in §7.2, the attention has to be focussed on avoiding the collision of the κ^+ -branch and the k -contour. This can be done by deforming the ω -contour around the Ω -branch, as demonstrated with the solid ω -contour and κ^+ -branch in figures 7.4 (a) and (b), respectively.

This procedure could be continued indefinitely, letting $\gamma \rightarrow -\infty$. However, in arriving at the expression describing the asymptotic dynamics of the system, equation (7.36), an essential ingredient was the use of the point where the κ^+ - and κ^- -branches pinched the k -contour, so that the corresponding solution had a group speed equal to zero. This situation cannot be established with the arrangement shown in figures 7.4 (a) and (b); the κ^\pm -branches will always be separated by, at least, the extent \bar{V}_e/v in the k_i -direction. Similarly, the absence of a cusp in the Ω -branch indicates that $d\Omega/dk \neq 0$.

Hence, a different approach needs to be considered. Notice that, in a way, the k -contour blocks the κ^+ -branch from reaching the κ^- -branch. In this case, this can be resolved by lowering the k -contour into the lower half-plane. This is illustrated in figure 7.4 (d). As noted in §7.4.1, the Ω -branch must move accordingly, which is shown in figure 7.4 (c). In particular, the parabolic Ω -branch moves further into the lower half-plane and its width is reduced simultaneously. The latter can be deduced from the reduction of the factor $\bar{V}_e + 2v k_i$, that multiplies k_r in the real part of equation (7.42). This allows pushing the straight ω -contour downward further than before.

Clearly, as $k_i = -\bar{V}_e/2v$, the width of the Ω -branch reduces to zero; it then collapses onto a line, see the dotted lines in figure 7.4 (c). A branch point then forms and the κ^\pm -branches can be made to pinch the k -contour, as required. This can be deduced from

⁶Note that, for $a, b \in \mathbb{R}$: $\sqrt{2}\sqrt{a+ib} = \sqrt{a+\sqrt{a^2+b^2}} + i \frac{b}{|b|} \sqrt{-a+\sqrt{a^2+b^2}}$.

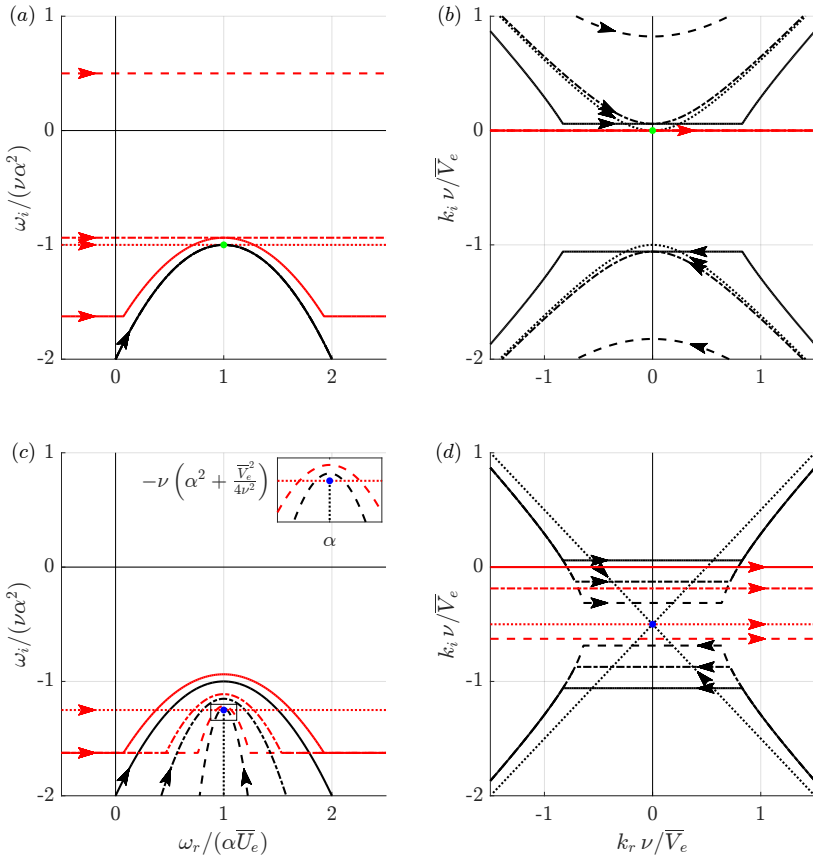


Figure 7.4: Movement of the $\kappa_{\bar{V}_e}$ - and $\Omega_{\bar{V}_e}$ -branches as the ω - and k -integration contours are deformed in the ω - (a,c) and k -planes (b,d). Integration contours are coloured red and branches black; the contours and corresponding branches have the same line style. The inset in (c) shows a zoom on indicated box.

equation (7.12b), by noticing that the only occasion for which $\kappa^+ = \kappa^-$ is at the point $k = 0 - i\bar{V}_e/2\nu$. This is analogous to the situation encountered directly in §7.2, for $\bar{V}_e = 0$. There, the k -contour was coincidentally chosen such that it could be pinched in the initial configuration.

Having found the arrangement of the contours for which the κ^\pm -branches can be made to pinch, the derivation of the characteristics of the asymptotic stationary solution is directly analogous to that discussed in §7.3. Equation (7.36) is, in fact, applicable to all branch points.

An expression can be derived for ω_s by setting $\kappa^+ = \kappa^-$, which is equivalent to setting the argument of the square root in equation (7.12b) to zero, which yields:

$$\omega_s = \alpha \bar{U}_e - i\nu \left(\alpha^2 + \left(\frac{\bar{V}_e}{2\nu} \right)^2 \right). \quad (7.43)$$

In combination with Briggs's criterion (7.37a), this expression for ω_s shows that the inclusion of the advection due to \bar{V}_e does not render an absolute stability. On the contrary, the effect of \bar{V}_e (positive or negative) is to yield a larger temporal decay.

Before proceeding, it is important to note what occurs when the k -contour is displaced further down into the lower half of the k -plane. In that case, the Ω -branch expands into a parabola again. This can be deduced from the fact that the factor $\bar{V}_e + 2\nu k_i$ is now negative, which, in addition, implies that the Ω -branch is now traversed in the negative ω_r -direction, see the dash-dotted line in figure 7.4 (c).

This shows that the k -contour at the constant height $k_i = -\bar{V}_e/2\nu$ is optimal in the sense that it minimises the width of the Ω -branch and its protrusion towards the unstable half-plane.⁷ Whatever adjustment of the k -contour is performed, the region enclosed by the Ω -branch will always encompass this minimal portion. This motivates referring to this manifestation of the Ω -branch as being *absolute*. The point ω_s of the Ω -branch cannot be lowered, because the κ -branches lock the k -contour at the pinch point, as discussed in §A.3.4. Accordingly, ω_s must always be enclosed by the ω -contour and it therefore dictates an inescapable, unavoidable or absolute stability of the system. This is the mathematical incentive for the label "absolute." This particular Ω -branch and the corresponding k -contour are therefore referred to as the absolute Ω -branch and the absolute k -contour from now onward.

Next to ω_s , the asymptotic solution is characterised by the wavenumber k_s , which deserves dedicated attention.

7.4.3. THE PROBLEMATIC SPATIAL CHARACTER AND BOUNDARY CONDITIONS

By having set the square root in equation (7.12b) equal to zero to obtain ω_s , it directly follows from the complement of that equation that:

$$k_s = -i \frac{\bar{V}_e}{2\nu}, \quad (7.44)$$

so the stationary asymptotic solution displays an exponential growth in the positive y -direction, equal to $\bar{V}_e/2\nu$. It cannot be emphasized enough that this growth rate is equal to *the unit Reynolds number associated to the advection in the propagation direction*. If the advection component is \bar{U}_e , instead, this number is very large in practical applications. In those applications, this growth rate can therefore dictate the overall character of the solution. Before continuing, it should be thoroughly isolated why the stationary asymptotic solution must grow exponentially in space, at least from the perspective of the tools derived in this chapter and appendix A.

IMPLICIT BOUNDARY CONDITIONS

First of all, in the formation of the Green's function, see §7.1.1, the solutions were required to satisfy implicit boundary conditions. These conditions required that the solution decays as y approaches both $+\infty$ and $-\infty$. For $\bar{V}_e \neq 0$, this is clearly not the case as $y \rightarrow +\infty$. It may come as a surprise, however, that these conditions are also not satisfied

⁷By letting any point on the k -contour depart from $k_i = -\bar{V}_e/2\nu$ in its imaginary part, the corresponding point on the Ω -branch departs from the value $\omega_r = \alpha \bar{U}_e$ at a linear rate with respect to the parameter $k_i + \bar{V}_e/2\nu$ in a ω_r -direction.

for $\bar{V}_e = 0$. In that case, the situation is arguably even worse, because the asymptotic solution does not decay for both $y \rightarrow \infty$ and $-\infty$. So, what has gone wrong?

This paradox is resolved by recalling that equation (7.36) only indicates the asymptotic behaviour of the solution as $t \rightarrow \infty$, while y remains *finite*. It was inherently assumed that the solution consists of fronts beyond which the solution becomes identically zero. In evaluating the asymptotic expression, it is assumed that these fronts have moved infinitely far away. In this sense, the asymptotic approach does not satisfy the implicit boundary conditions.

For finite times, one has to account for the contributions of the remainder of the Ω -branch, instead of just for the branch point ω_s alone. Back in chapter 2, it was demonstrated with equations (2.35) to (2.38) that, if the (continuous) Fourier coefficients associated to the tail of the branch decay like a Gaussian, the spatial distribution of the solution will decay also like a Gaussian. This is an example of faster-than-exponential, or super-exponential, decay and therefore ensures that the solution ultimately decays as $|y| \rightarrow \infty$ for all finite exponential growth rates $k_{s,i}$ (positive, negative or zero). This argument covers the theory discussed in this chapter.

CONTOUR PLACEMENT

Another strong argument can be given from the perspective of appendix A. It was argued in §A.2.2 that, to satisfy the implicit boundary conditions, the integration contour must always be placed so that it separates the zeros that imply growth from those that imply decay as $y \rightarrow +\infty$. The solution is then separated into a part valid for $y > 0$ and another for $y < 0$. Instead, to obtain the asymptotic solution in this chapter, the integration contour is deformed into the lower half of the k -plane, allowing the κ^+ -branch to imply a growing character as $y \rightarrow \infty$. Note that the asymptotic solution is valid for both positive and negative y , irrespective of the sign of $k_{s,i}$. It should be inquired whether a different k -contour placement or restricting the validity of the solution to the region $y < 0$ for $k_{s,i} < 0$ could be a way to circumvent having to deal with the exponentially growing solution for $y \rightarrow \infty$.

A hypothetical set-up is created to this end, which should eventually point out the problem in trying to place the k -contour elsewhere, while still searching for the asymptotic solution. This is done in two steps. First, a placement has to be found for the contour. In §A.2.2, the region of possible placements of straight contours embodied a finite (open) area of the complex plane, see figure A.5 (e). Due to the continuous nature of the κ^+ -branch in the current situation, one has no choice but to place the k -contour on the real k -axis, because that separates growing from decaying solutions in one y -direction.⁸ Second, to find the asymptotic solution, a zero group speed solution must be created by letting the κ^\pm -branches pinch the k -contour. For $\bar{V}_e \neq 0$, this requires pushing (at least a part of) the κ^+ -branch through the real k -axis.

Analysing the set-up, for a particular $\omega = \omega_{\text{ref}}$ on the ω -contour, both $\kappa^+(\omega_{\text{ref}})$ and $\kappa^-(\omega_{\text{ref}})$ would lie below the k -contour. This arrangement is illustrated in figure 7.5 (a).

⁸Extensive use is made of deforming the contours throughout the analysis. However, note that the original placement of the k -contour is fixed with respect to the ω -contour. While fixing an ω -value on the ω -contour, the k -contour can be freely deformed only with respect to its original location.

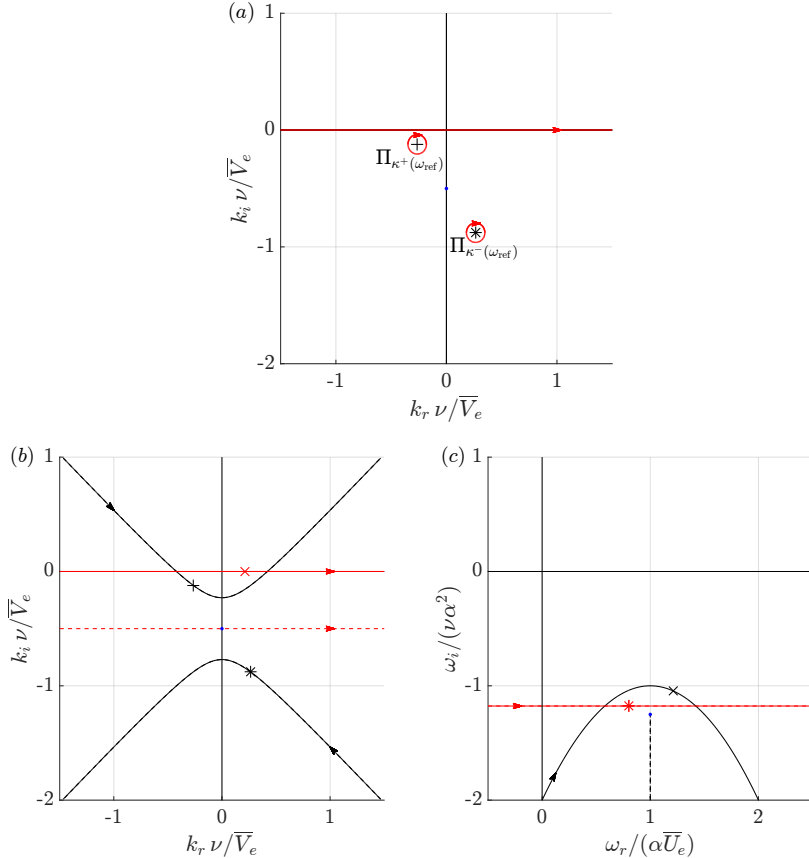


Figure 7.5: Illustration of the case where the two k -zeroes lie below the k -contour, (a) the k -integral can be evaluated, this arrangement is in-line with the set-ups discussed in §A.2.2 for an individual $\omega = \omega_{\text{ref}}$, (b) but the κ^\pm -branches must cross the k -contour for larger $|\omega|$, (c) this implies that the ω -contour must have intersected the Ω -branch. In turn, this implies the Ω -branch lies (partially) above the ω -contour, which is prohibited as it yields a pre-causal response. For this reason, parts of the κ^\pm -branches may protrude into the unstable half-planes.

The k -integral evaluates to:

$$\int_{-\infty}^{\infty} \frac{e^{iky}}{\tilde{\mathcal{D}}(k, \omega_{\text{ref}})} \frac{dk}{2\pi} = -i \frac{e^{ik^+(\omega_{\text{ref}})y}}{\frac{\partial \tilde{\mathcal{D}}}{\partial k}(\kappa^+(\omega_{\text{ref}}), \omega_{\text{ref}})} - i \frac{e^{ik^-(\omega_{\text{ref}})y}}{\frac{\partial \tilde{\mathcal{D}}}{\partial k}(\kappa^-(\omega_{\text{ref}}), \omega_{\text{ref}})}, \quad (7.45)$$

where both $\kappa_i^+(\omega_{\text{ref}}) < 0$ and $\kappa_i^-(\omega_{\text{ref}}) < 0$. So, the region of validity of this solution could be restricted to $y < 0$, because both exponentials decay as $y \rightarrow -\infty$. The solution for $y > 0$ would be identically zero. One could continue this process for the whole κ^+ -branch,⁹ which would result in declaring the entire asymptotic solution to be valid for $y < 0$ only. The problem with this approach can now be revealed.

Figure 7.5 (b) illustrates a continuation of the situation presented in figure 7.5 (a). It turns out that the cases for which the κ^+ -branch lies below the k -contour in the k -plane, the ω -contour must lie in the interior of the Ω -branch in the ω -plane. For a finite protrusion of the κ^+ -branch through the k -contour, this can be deduced through the fact that the intersection points of the k -contour with the κ^+ -branch map directly to the intersection points of the Ω -branch with the ω -contour, see figure 7.5 (c). In turn, this means that when closing the ω -contour in the upper half-plane, it encloses regions where the ω -integrand is non-holomorphic. As demonstrated in A.1.5, this yields a contribution to the solution that is non-zero for $t < 0$. This part of the solution describes a pre-causal response that violates the causality condition. So, ensuring causality is the reason for which the κ -branches may not protrude through the k -contour. This result is highly surprising in the light that the κ -branches would seem to encode the spatial character of the solution only. Note that a similar situation would occur if one would integrate through the branch for the case $\bar{V}_e = 0$; the Ω -branch does not necessarily have to be the parabolic shape as presumed in the worked example.

7

These arguments demonstrate that the growing character of the asymptotic solution is justified, at least from the perspective of the currently discussed tools. To summarise, this follows from, first, having assumed the fronts of the solution's support to have moved beyond all finite y -coordinates in both the positive and negative y -direction as $t \rightarrow \infty$ and, second, from the requirement of a causal solution. Chapter 8 is dedicated to investigating how to handle the exponential growth within a numerical approach.

7.4.4. INCONCLUSIVENESS OF UNSTABLE PARABOLIC BRANCHES

The analysis presented in this chapter has mainly revolved around creating the situation in which the Ω -branch contains a branch point, which led to the smallest, or absolute, Ω -branch. In the majority of literature references involving flow instability theory from a numerical perspective, however, this is not the commonly presented shape, see Alizard and Robinet [12], Ehrenstein and Gallaire [13], Garnaud *et al.* [14], Coenen *et al.* [15], Brynjell-Rahkola *et al.* [16]. Usually, the computed spectra do not contain branch

⁹Also, this would result in pushing the entire κ^+ -branch through the k -contour. This could be taken as a solution for the problem of having to integrate through the contour, because intersections of the k -contour and κ^+ -branch would be completely avoided. A strict reality about integrating through a non-holomorphic region is that it is (in a very unsatisfactory way) *unknown or ambiguous* what contribution should be accounted for. Substituting the acquired quantity obtained while integrating around the region is not allowed, because this is exactly what is attempted to be avoided. In the end, this problem can be entirely avoided, because there is another externally imposed physical criterion whose satisfaction breaks down for this hypothetical set-up.

points. Instead, arc-shape branches are usually encountered in computations, which are equivalent to the parabolic branch manifestations discussed in this chapter. So, it is important to inquire what information can be deduced from these manifestations, especially because these branches attain larger ω_i -values. Of particular interest is whether absolute stability characteristics can still be inferred.

The first thing to recognize is that the parabolic manifestations do not contain a branch point, which is topologically trivially evident. The vertices of the parabolas correspond to the intersection of the k -contour with the imaginary k -axis. This can be demonstrated by considering:

$$\frac{d\Omega_{\bar{V}_e}}{dk}(k_r + ik_i) = \bar{V}_e + 2\nu k_i - 2ivk_r. \quad (7.46)$$

In particular, note that the imaginary part $d\Omega_{\bar{V}_e,i}/dk$ changes sign for $k_r = 0$. Evaluating the group speed for $k_r = 0$ yields:

$$\frac{d\Omega_{\bar{V}_e}}{dk}(ik_i) = \bar{V}_e + 2\nu k_i. \quad (7.47)$$

This is a real value, which implies that this group speed can be interpreted as the propagation speed of the corresponding solution. Recall from equation (7.42) that the parameter $\bar{V}_e + 2\nu k_i$ also represented the width of the parabola. So, for parabolic Ω -branches with a non-zero width, the group speed encoded by the vertex is non-zero.

In terms of executing the asymptotic evaluation of the integral, this implies that possibly both fronts propagate toward $y \rightarrow +\infty$ (or both to $-\infty$); the represented wave packet could be advected away from its point of origin, $y = 0$. Therefore it cannot be guaranteed that the solution around the origin $y = 0$ asymptotically approaches a homogeneous structure (composed out of a single wavenumber) as $t \rightarrow \infty$. It is possible that no non-trivial asymptotic state exists around a fixed finite y -location. This means that the assumption leading up to equation (7.36) breaks down. *The vertex of the parabolas is therefore not directly indicative of the absolute stability of the system.*

By setting $k_r = 0$ in equation (7.42), one can write:

$$\begin{aligned} \Omega_{\bar{V}_e}(ik_i) &= \alpha \bar{U}_e - iv \left(\alpha^2 + \left(\frac{\bar{V}_e}{2\nu} \right)^2 \right) + \frac{i}{4\nu} (\bar{V}_e + 2\nu k_i)^2 \\ &= \omega_s + \frac{i}{4\nu} (\bar{V}_e + 2\nu k_i)^2, \end{aligned} \quad (7.48)$$

showing that the vertices always lie directly above ω_s in the ω -plane. For notational convenience, the largest value of ω_i belonging to a particular Ω -branch is referred to as the maximum of the branch (i.e. specifically the imaginary part is meant).

The fact that ω_i -value corresponding to the branch point is the lower bound of all possible maxima of the Ω -branch is a very general result; i.e. it applies to much more general problems as well. Via the definition of the “absolute resolvent” by Kapitula and Promislow [7, definition 3.2.3], it follows that what is here referred to as the absolute Ω -branch encompasses the minimum portion of the ω -plane. To make this more precise, consider the region of the ω -plane below (or in the interior of) the Ω -branch, which also

includes the Ω -branch itself. This region is denoted by $\overline{\Omega}$ from now on. It can be shown, in fact, that the intersection of all possible $\overline{\Omega}$ regions equals the absolute Ω -branch, see Kapitula and Promislow [7, lemma 3.2.4], and note that $\overline{\Omega}$ is the complement of the absolute resolvent. So, the absolute Ω -branch is the smallest subset of all possible manifestations of $\overline{\Omega}$. From this fact, it follows directly that a random Ω -branch manifestation attains a larger maximum than the absolute Ω -branch does, in general.

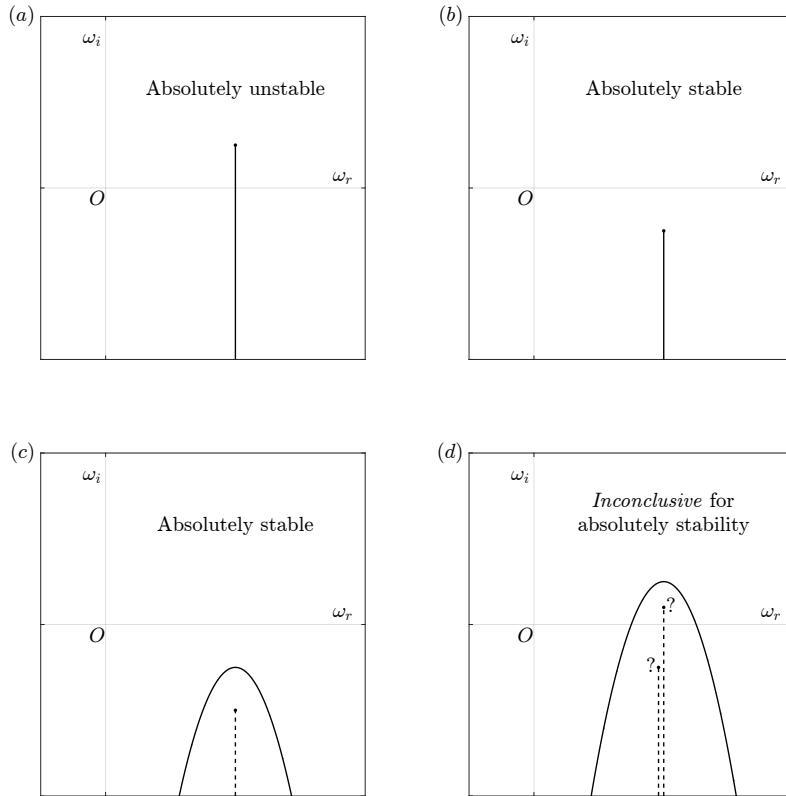
By deforming the integration contours in §§7.2 and 7.4.2, without crossing any of the branches, the integral value (or the resulting solution characteristics) were left unchanged. As discussed in §A.3.4, this property is referred to as analytical continuation. So, although the asymptotic approach cannot be evaluated for such cases, the absolute stability characteristics can still be calculated by performing the ω -integral over any possible manifestation of the Ω -branch that is *not* the absolute Ω -branch. This means that, although the branches can attain (much) larger maxima than $\omega_{s,i}$ in general, the integrals do evaluate to the growth rate $\omega_{s,i}$, as $t \rightarrow \infty$, instead. So, *the particular ω_i -values associated to the maxima of Ω -branches other than the absolute Ω -branch are meaningless in regard to the absolute stability properties of a given system.*

Despite this finding, there are circumstances in which other-than-absolute Ω -branches do yield information about whether a system supports an absolute instability or not. This can be inferred by using the fact that the absolute Ω -branch is the branch that occupies the minimum portion of the ω -plane. In figure 7.6, four Ω -branches are shown. In figures 7.6 (a) and (b), a branch point is identified. In those cases, it can be directly concluded that the system does support (a) or does not support (b) an absolute instability. In figures 7.6 (c) and (d), instead, other-than-absolute Ω -branches are encountered. In figure 7.6 (c), the branch lies entirely in the stable half-plane. The absolute Ω -branch is known to be a subset of the corresponding $\overline{\Omega}$ -region, so, whatever that branch may be, it will have a stable branch point. The branch therefore conclusively determines that the system does not support an absolute instability. In figure 7.6 (d), the Ω -branch lies partially in the unstable half-plane. Now, it cannot be determined whether the branch point is stable or unstable, so no conclusion can be drawn about the absolute stability characteristics of the system.

In summary, the absolute stability characteristics of a system are determined by branch points in the Ω -branch. The integrals over arc-shaped branches yield the same asymptotic response, via analytical continuation, which implies that the growth rates attained by these branches are meaningless with regard to the absolute stability characteristics. The only case in which an arc-shape branch yields conclusive information on the absolute stability characteristics is when it is completely stable; it can then be inferred that the system must be absolutely stable.

7.5. NON-HOLOMORPHIC REGIONS IN THE ω -INTEGRAND

In §7.4.1, a short-cut was presented that illustrated that the Ω -branch, when evaluated for the considered k -contour, indicates the locations in the ω -plane where the ω -integrand, as defined in the integration order in integral (7.22), is non-holomorphic. The goal of this section is to identify the nature of the integrand in the neighbourhood of these non-holomorphic regions. In particular, it will be demonstrated that the integrand does not necessarily attain an infinite magnitude when these regions are approached. The atten-



7

Figure 7.6: Conclusions that can be drawn from the ω -branch. In (a,b) the branch contains a branch point in the: (a) unstable half-plane: an absolute instability is supported, (b) stable half-plane: the system is absolutely stable. In (c,d) the branch does not contain a branch point, but the branch lies (c) in the stable half-plane completely, it can be inferred that the system is absolutely stable, (d) partially in the unstable half-plane, the information is inconclusive on whether an absolute instability is supported; the location of the absolute ω -branch cannot be inferred.

tion is focussed on the ω -integrand in the integration order indicated in integral (7.22). The demonstration for the regions in the k -integrals is identical and therefore follows directly from these results. First, the case where $\bar{V}_e = 0$ is considered.

7.5.1. THE CASE $\bar{V}_e = 0$

In this case, expressions for the ω -integrand are obtained from equation (7.26):

$$+ \frac{i}{2\pi} \frac{e^{i(\kappa^+(\omega)y - \omega t)}}{\partial \tilde{\mathcal{D}} / \partial k(\kappa^+(\omega), \omega)} \quad \text{for: } y > 0; \quad (7.49a)$$

$$- \frac{i}{2\pi} \frac{e^{i(\kappa^-(\omega)y - \omega t)}}{\partial \tilde{\mathcal{D}} / \partial k(\kappa^-(\omega), \omega)} \quad \text{for: } y < 0. \quad (7.49b)$$

Recall that these expressions are the direct result of the k -integral. Their non-holomorphic behaviour, in particular, can therefore be traced back to the way the pole (poles) in the k -plane passes (pass) onto and over the k -contour. All representative cases of interest have been analysed exhaustively in §A.3.

In search of the non-holomorphic behaviour of expressions (7.49), the multiplying constant factors and the exponential function, which is an entire function, have no contribution. The non-holomorphic nature is solely contained in the factors in the denominators: $\partial \tilde{\mathcal{D}} / \partial k(\kappa^\pm(\omega), \omega)$. In the particular case of $\tilde{\mathcal{D}} = \tilde{\mathcal{D}}_0$, this factor can be determined to be:

$$\begin{aligned} \frac{\partial \tilde{\mathcal{D}}_0}{\partial k}(k, \omega) &= 2vk, \\ \text{such that: } \frac{\partial \tilde{\mathcal{D}}_0}{\partial k}(\kappa_0^\pm(\omega), \omega) &= 2v\kappa_0^\pm(\omega) = \pm 2i\sqrt{v(-i\omega + i\alpha\bar{U}_e + v\alpha^2)}, \end{aligned} \quad (7.50)$$

using equation (7.10) with $\beta = \bar{V}_e = \bar{W}_e = 0$. Recalling that $\omega_s = \alpha\bar{U}_e - iv\alpha^2$, the expression of interest becomes:

$$\mathcal{J}_0^+(\omega) = \pm 1 / \left(\frac{\partial \tilde{\mathcal{D}}_0}{\partial k}(\kappa_0^+(\omega), \omega) \right) = 1 / \left(2i\sqrt{-iv(\omega - \omega_s)} \right), \quad (7.51)$$

where the difference in the signs in equations (7.49) is cancelled with that in (7.50), eliminating the distinction between the integrands for the $y \gtrless 0$ regions. So, it is really only this quantity (e.g. not its negative) that has to be considered.

It follows immediately from equation (7.51) that $\mathcal{J}_0^+(\omega)$ is non-holomorphic as ω approaches the branch point, ω_s , because $|\mathcal{J}_0^+(\omega)|$ becomes unbounded in that limit. In this sense, this is what is here referred to as an “infinite singularity.” It has been clearly elaborated that the branch point ω_s directly corresponds to a pinch point in the k -plane. In §A.3.3, it was demonstrated how approaching a pinch point yields an unbounded k -integral. So, this explains the nature of the non-holomorphic behaviour in this case.

This is not the only way, however, in which $\mathcal{J}_0^+(\omega)$ displays non-holomorphic behaviour. The other way is maybe not directly evident from the statement of equation (7.51). It is associated to the fact that the square root is a multi-valued function for a complex argument. This can be effectively shown by representing the complex number

ω in polar representation: $\omega = re^{i\theta}$, where $\tan\theta = \omega_i/\omega_r$ and $r = |\omega|$, consider particularly: $r = 1$. The square root function can then be rewritten as: $\sqrt{\omega} = \sqrt{r}e^{i\theta/2} = e^{i\theta/2}$. Now evaluate the function for $\theta = 0$: $\sqrt{\omega} = e^{i0/2} = 1$. Note that the ω -point corresponding to $\theta = 2\pi$ is identical to that for $\theta = 0$, because $\omega = e^{2\pi i} = e^{0i} = 1$. However, evaluating the function for $\theta = 2\pi$ yields: $\sqrt{\omega} = e^{2\pi i/2} = -1$. Increasing θ to 4π : $\sqrt{\omega} = e^{2i\pi} = 1$ again.

This operation, of increasing θ , can be viewed as having rotated around the point $\omega = 0$ twice. It should be noted that this behaviour results only if one rotates about the origin. In doing so, one has looped through two different sets of values of $\sqrt{\omega}$, while assessing the evaluation for the same set of ω -values. This result generalises into the fact that two values (each others negatives) can be associated to the square root function at every point in the complex plane.

The two-valued nature is usually approached by glueing together two ranges of θ for which the function is single-valued. These ranges are also referred to as Riemann surfaces. The usual choice for this range is $\theta \in [-\pi, \pi]$. This choice is logical from the point of view that the real values of both values associated to $\sqrt{\omega}$ are zero for $\theta = -\pi, \pi, 3\pi$, etc. The radial lines associated with these angles, the negative real line of ω , could be referred to as “glueing lines.”

In the function $\sqrt{-i(\omega - \omega_s)}$, the point corresponding to the origin before has been shifted to the branch point ω_s . To describe rotations on the unit circle around that point, one writes: $\omega = \omega_s + e^{i\theta}$. Evaluating the function yields: $\sqrt{-ie^{i\theta}} = \sqrt{e^{-i\pi/2}e^{i\theta}} = \sqrt{e^{i(\theta-\pi/2)}}$. This means that the glueing lines are subjected to a *positive* rotation of $\pi/2$, so they are now found at $\theta = -\pi/2, 3\pi/2, 7\pi/2$, etc. So, the glueing lines emanate from the branch point shooting straight down to $-i\infty$. This follows, for example, by noting that inserting $\theta = -\pi/2$ results in the evaluation of $\sqrt{e^{i(-\pi/2-\pi/2)}} = \sqrt{e^{i(-\pi)}} = e^{-i\pi/2} = -i$. Inserting $\theta = 3\pi/2$ results in $\sqrt{e^{i(3\pi/2-\pi/2)}} = \sqrt{e^{i\pi}} = e^{i\pi/2} = i$. Both have a real part equal zero (for all considered radii), as per definition of the glueing lines.

Using this information, one can evaluate characteristic values for \mathcal{J}_0^+ :

$$\lim_{\theta \rightarrow -\frac{\pi}{2}} \mathcal{J}_0^+ (\omega_s + re^{i\theta}) = \frac{1}{2i(-i)\sqrt{vr}} = +\frac{1}{2\sqrt{vr}}; \quad (7.52a)$$

$$\lim_{\theta \rightarrow \frac{3\pi}{2}} \mathcal{J}_0^+ (\omega_s + re^{i\theta}) = \frac{1}{2i(+i)\sqrt{vr}} = -\frac{1}{2\sqrt{vr}}. \quad (7.52b)$$

This clearly illustrates that, when considering a single Riemann surface, the function \mathcal{J}_0^+ is discontinuous in its real part when approaching the glueing line. The real part associated to this Riemann surface is visualised in figure 7.7 (a).

Note that the glueing line corresponds directly to Ω_A , or the Ω -branch evaluated for the k -contour being the real k -axis in this case (see integral (7.22)). From the current perspective, having to integrate around the Ω -branch corresponds to avoiding the border across which the Riemann surface of interest is discontinuous. This clearly shows that, whereas the branch point is an infinite singularity, the “tail” of the Ω -branch corresponds, instead, to a jump discontinuity. As shown with equations (7.52), the integrand attains finite values in the limit of approaching the Ω -branch. In fact, the integrand tends to zero as $r \rightarrow \infty$.

One could inquire what happens when one integrates through the Ω -branch from the perspective of the Riemann surfaces. As mentioned before, by making a revolution

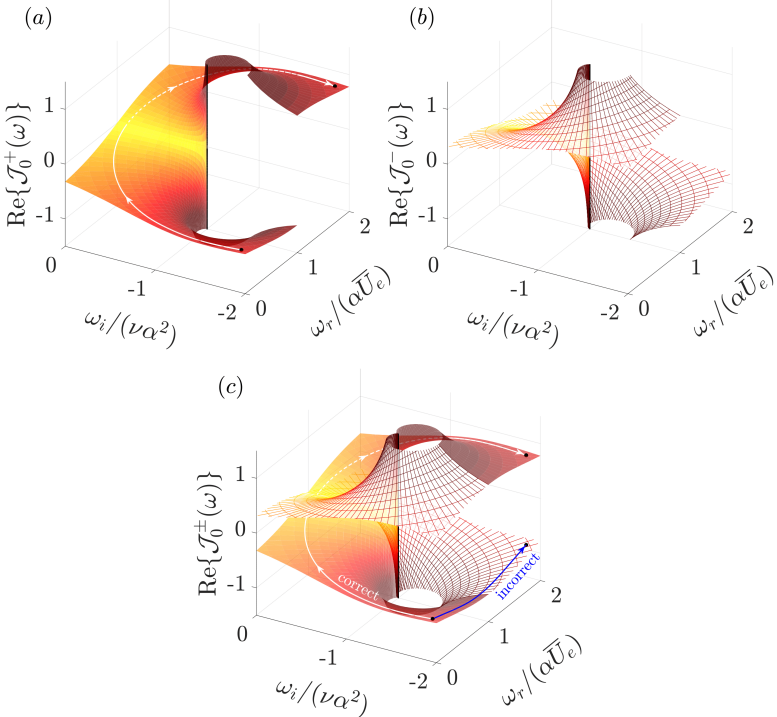


Figure 7.7: Real part of the integrand (a,c) \mathcal{J}_0^+ (continuous, first Riemann surface) and (b,c) \mathcal{J}_0^- (grid, second Riemann surface). In (c), the Riemann surfaces are combined. Click (a,b) twice for the animation of the combination. The branch point $\omega = \alpha\bar{U}_e - i\nu\alpha^2$ is indicated with the thick vertical black line. In (a) and (c), the white arrow indicates the path of a typical integration contour. In (c), the blue arrow illustrates how integrating through the Ω -branch causes the integrand to attain incorrect values.

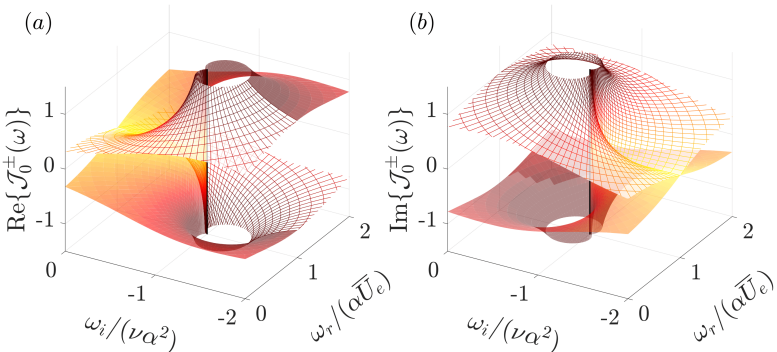


Figure 7.8: Real (a) and imaginary (b) parts of the integrands \mathcal{J}_0^+ (continuous) and \mathcal{J}_0^- (grid). The branch point $\omega = \alpha\bar{U}_e - i\nu\alpha^2$ is indicated with the vertical black line.

around the origin, the natural tendency of the square root function is not to behave discontinuously. Instead, the function loops through the second Riemann surface. The function attains exactly the same values on this surface, but with the opposite sign. Accordingly, one could define the second surface as: $\mathcal{J}_0^-(\omega) = -\mathcal{J}_0^+(\omega)$. By integrating through the discontinuity in \mathcal{J}_0^+ , one transfers into the second Riemann surface $\mathcal{J}_0^-(\omega)$. The real part associated to this surface is shown in figure 7.7 (b). As mentioned before, the integrand consists of the quantity $\mathcal{J}_0^+(\omega)$, not of its negative counter part. By integrating through the Ω -branch, one accidentally flips the sign with respect to the intended quantity. In figure 7.7 (c), it is illustrated how one ends up at the wrong value. To complete the description of the Riemann surface, also the imaginary part must be considered. Both real and imaginary parts are shown in figure 7.8. Note that the imaginary parts are, in fact, continuous and equal to zero when evaluated at the ω -branch.

The jump discontinuity has a counterpart in terms of the behaviour of the k -integral. Recall that figure 7.1 (d) illustrates the movement of the κ^\pm -branches as the ω -contour passes through the Ω -branch. While passing through the branch, the zero corresponding to κ^+ jumps discontinuously from the limiting value $k = -c < 0$ to $k = c > 0$. An equivalent reasoning describing the jump was derived in §A.3.1, which also considered a single zero passing through the integration contour.

This demonstrates how the region where the ω -integrand is non-holomorphic directly corresponds to the k -contour. For this reason, $\Omega(k)$ maps the k -contour into the locus of points where the ω -integrand is non-holomorphic. This proves the used assertion in §7.4.1; the Ω -branch indicates the non-holomorphic regions in the ω -integrand, irrespective of the order of integration.

7.5.2. THE CASE $\bar{V}_e \neq 0$

For this case, it is tempting to directly evaluate the same expressions as used before. One finds the following for the partial derivative of $\tilde{\mathcal{D}}_{\bar{V}_e}(k, \omega)$:

$$\frac{\partial \tilde{\mathcal{D}}_{\bar{V}_e}}{\partial k}(\kappa_{\bar{V}_e}^\pm(\omega), \omega) = i\bar{V}_e + 2v\kappa_{\bar{V}_e}^\pm(\omega) = \pm 2vi\sqrt{-i(\omega - \omega_s)/v}, \quad (7.53)$$

having used:
$$\begin{cases} \kappa^\pm = -i\frac{\bar{V}_e}{2v} \pm i\sqrt{-i(\omega - \omega_s)/v}; \\ \omega_s = \alpha\bar{U}_e - iv\left(\alpha^2 + \left(\frac{\bar{V}_e}{2v}\right)^2\right). \end{cases}$$

This allows finding the expression for the integrand:

$$\mathcal{J}_{\bar{V}_e}^+(\omega) = \pm 1 / \frac{\partial \tilde{\mathcal{D}}_{\bar{V}_e}}{\partial k}(\kappa_{\bar{V}_e}^\pm(\omega), \omega) = 1 / 2i\sqrt{-iv(\omega - \omega_s)}. \quad (7.54)$$

The function $\mathcal{J}_{\bar{V}_e}^+(\omega)$ is identical to $\mathcal{J}_0^+(\omega)$. However, $\mathcal{J}_{\bar{V}_e}^+(\omega)$ encodes the shape of the integrand only if the k -contour is the absolute k -contour; i.e. it should lie at the height $k_i = -\bar{V}_e/2v$. Note that, for the case $\bar{V}_e = 0$, this was implicitly assumed by choosing the k -contour to coincide with the real k -axis.

For other choices of the k -contour, $\mathcal{J}_{\bar{V}_e}^+(\omega)$ is valid only where the κ^+ - and κ^- -branches lie on their respective sides of the k -contour. In the ω -plane, this corresponds to evaluating the integrand for ω -values above the Ω -branch. In the evaluation of the ω -integral, a knowledge of the shape of the integrand below the Ω -branch is not required. As explained in §7.4.3, one should not integrate through the Ω -branch. Still, this knowledge is important from the perspective of the behaviour of the problem when treated numerically.

Here the example is considered where the k -contour is straight and placed at the height $k_i = -\bar{V}_e/v$. It was demonstrated before that straight contours placed at equal heights above and below $k_i = -\bar{V}_e/2v$ yield the same Ω -branch, except that the latter is traversed in the opposite direction. The choice $k_i = -\bar{V}_e/v$ would yield the same Ω -branch as the real k -axis; it is only traversed in the opposite direction.

When evaluating the integrand for ω -values below the Ω -branch, the corresponding points in the k -plane indicated by κ^+ and κ^- lie on the same side of the k -contour, like the situation illustrated with the solid lines in figure 7.5. For the currently considered choice of the k -contour, both branches lie above the k -contour.

Closing the k -contour in the upper and lower half of the k -plane does not result in the same quantity. By closing the integral in the upper half-plane, no zeros will be enclosed. This integral, describing the solution in the region $y < 0$, will therefore evaluate to zero identically. In figures 7.9 (a) and (b), the shape of the real part of the integrand is illustrated for the Riemann sheets, $\mathcal{J}_{\bar{V}_e}^+(\omega)$ and $\mathcal{J}_{\bar{V}_e}^-(\omega) = -\mathcal{J}_{\bar{V}_e}^+(\omega)$, respectively. For ω -values that lie above the Ω -branch, the integrand is dictated by $\mathcal{J}_{\bar{V}_e}^\pm(\omega)$. When passing the Ω -branch, the integrand discontinuously jumps to the value zero. In figure 7.9 (c), the two Riemann sheets are combined together. Finally, the combination of the Riemann sheets of the imaginary part of $\mathcal{J}_{\bar{V}_e}^\pm(\omega)$ is shown in figure 7.9 (d).

7

By closing the contour in the upper half-plane, valid for $y > 0$, now the zeros corresponding to both branches are enclosed. Evaluating the residues at the poles yields:

$$\begin{aligned}\mathcal{J}_{\bar{V}_e}(\omega) &= \int_{-\infty-i\bar{V}_e/v}^{\infty-i\bar{V}_e/v} \frac{e^{iky}}{\tilde{\mathcal{D}}_{\bar{V}_e}(k, \omega)} \frac{dk}{2\pi} = +i \frac{e^{i\kappa_{\bar{V}_e}^+(\omega)y}}{\frac{\partial \tilde{\mathcal{D}}_{\bar{V}_e}}{\partial k} \Big|_{\omega}^{\kappa_{\bar{V}_e}^+(\omega)}} + i \frac{e^{i\kappa_{\bar{V}_e}^-(\omega)y}}{\frac{\partial \tilde{\mathcal{D}}_{\bar{V}_e}}{\partial k} \Big|_{\omega}^{\kappa_{\bar{V}_e}^-(\omega)}} \quad \text{for: } y > 0 \\ &= i \frac{e^{\frac{\bar{V}_e}{2v}y} e^{-y\sqrt{-i(\omega-\omega_s)/v}}}{+2vi\sqrt{-i(\omega-\omega_s)/v}} + i \frac{e^{\frac{\bar{V}_e}{2v}y} e^{y\sqrt{-i(\omega-\omega_s)/v}}}{-2vi\sqrt{-i(\omega-\omega_s)/v}} \\ &= -\frac{\sinh(y\sqrt{-i(\omega-\omega_s)/v})}{v\sqrt{-i(\omega-\omega_s)/v}} e^{\frac{\bar{V}_e}{2v}y},\end{aligned}\tag{7.55}$$

using that $(e^{-z} - e^z)/2 = -\sinh z$. Note that this $\mathcal{J}_{\bar{V}_e}(\omega)$, corresponding to the ω -integrand without the factor $e^{-i\omega t}$, now includes the exponential factors $e^{i\kappa^\pm(\omega)y}$ that were discarded in equations (7.51) and (7.54). Therefore the symbol \mathcal{J} , not \mathcal{J} , is used here. To illustrate the shape of the integrand in this case, valid for $y > 0$, one would have to include the exponential factors in the quantity in the region above the Ω -branch or replace the

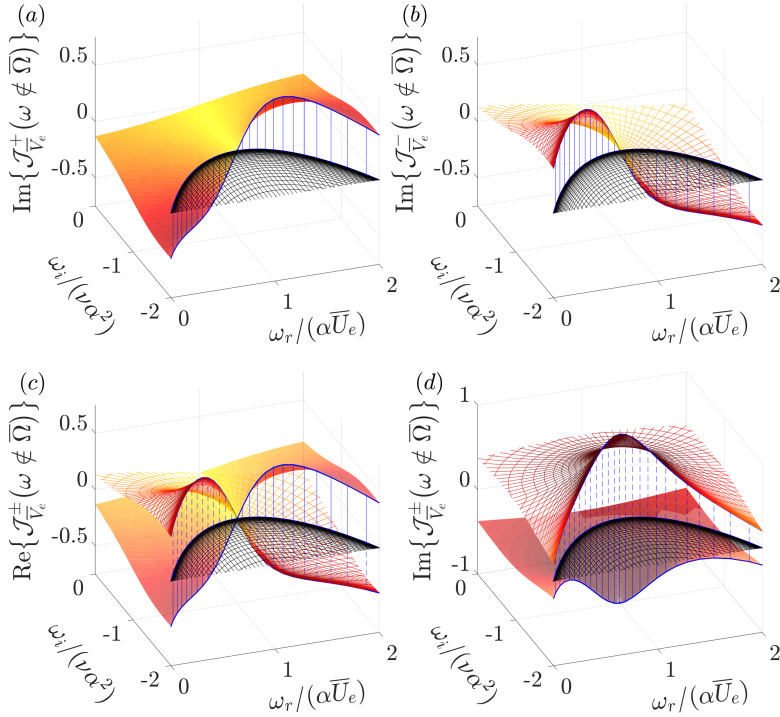


Figure 7.9: Real part of the integrand (a,c) $\mathcal{J}_{\bar{V}_e}^+$ (continuous, first Riemann surface) and (b,c) $\mathcal{J}_{\bar{V}_e}^-$ (grid, second Riemann surface), for $\omega \notin \bar{\Omega}$, where $\bar{\Omega}$ denotes the Ω -branch, which itself is indicated with the thick blue line, and the region below it in the ω -plane. For $\omega \in \bar{\Omega}$, the integrand valid for $y < 0$ evaluates to zero identically. In (d), the combination of the Riemann surfaces corresponding to the imaginary part of the integrand are shown.

7

zero-plateaus in figure 7.9 by the “ $\mathcal{J}(\omega)$ -equivalent” of $\mathcal{I}(\omega)$. Here, the discussion will focus on describing $\mathcal{I}_{\bar{V}_e}(\omega)$ from a mathematical perspective solely.

Contrary to $\mathcal{J}_{\bar{V}_e}^+(\omega)$, $\mathcal{J}_{\bar{V}_e}(\omega)$ is a single-valued function. At $\omega = \omega_s$, an infinite singularity was encountered in $\mathcal{J}_{\bar{V}_e}^+(\omega)$. Note that the inclusion of the exponential factors in $\mathcal{J}^+(\omega)$ would not alter this behaviour. In the case of $\mathcal{J}_{\bar{V}_e}(\omega)$, however, a 0/0 situation is encountered at $\omega = \omega_s$, due to the fact that the exponential factors are combined. In fact, $\mathcal{J}_{\bar{V}_e}(\omega)$ attains a removable singularity as $\omega \rightarrow \omega_s$, because the limit exists:

$$\begin{aligned} \lim_{\omega \rightarrow \omega_s} \mathcal{J}_{\bar{V}_e}(\omega) &= -e^{\frac{\bar{V}_e}{2\nu} y} \lim_{\omega \rightarrow \omega_s} \frac{\sinh(y\sqrt{-i(\omega - \omega_s)/\nu})}{\nu\sqrt{-i(\omega - \omega_s)/\nu}} \\ &= -e^{\frac{\bar{V}_e}{2\nu} y} \lim_{\omega \rightarrow \omega_s} \frac{y}{\nu} \cosh\left(y\sqrt{-i(\omega - \omega_s)/\nu}\right) = -y e^{\frac{\bar{V}_e}{2\nu} y}/\nu, \end{aligned} \quad (7.56)$$

which follows through the application of L'Hôpital's rule. To demonstrate the function's one-valued nature, the limits toward the glueing line of the square root function are eval-

uated:

$$\lim_{\theta \rightarrow -\frac{\pi}{2}} \mathcal{I}_{\bar{V}_e}(\omega_s + re^{i\theta}) e^{-\frac{\bar{V}_e}{2\nu}y} = -\frac{\sinh(y\sqrt{r/\nu}\sqrt{e^{i(-\pi)}})}{\nu\sqrt{r/\nu}\sqrt{e^{i(-\pi)}}} = -\frac{-i\sin(y\sqrt{r/\nu})}{-iv\sqrt{r/\nu}} = -\frac{\sin(y\sqrt{r/\nu})}{v\sqrt{r/\nu}};$$

$$\lim_{\theta \rightarrow \frac{3\pi}{2}} \mathcal{I}_{\bar{V}_e}(\omega_s + re^{i\theta}) e^{-\frac{\bar{V}_e}{2\nu}y} = -\frac{\sinh(y\sqrt{r/\nu}\sqrt{e^{i(+\pi)}})}{\nu\sqrt{r/\nu}\sqrt{e^{i(+\pi)}}} = -\frac{+i\sin(y\sqrt{r/\nu})}{+iv\sqrt{r/\nu}} = -\frac{\sin(y\sqrt{r/\nu})}{v\sqrt{r/\nu}},$$

using the identity $\sinh iz = (e^{iz} - e^{-iz})/2 = i(e^{iz} - e^{-iz})/2i = i\sin z$. These limits are equal at the only point where the square root function could introduce a consistent glueing line. The multi-valued nature of the square roots in the numerator and denominator cancels each other. It is furthermore demonstrated that, as $\omega - \omega_s \rightarrow -i\infty$, $\mathcal{I}_{\bar{V}_e}(\omega)$ oscillates under an algebraically decaying envelope.

Focusing instead on the region of the ω -plane right above the point ω_s yields:

$$\lim_{\theta \rightarrow \frac{\pi}{2}} \mathcal{I}_{\bar{V}_e}(\omega_s + re^{i\theta}) = -\frac{\sinh(y\sqrt{r/\nu})}{v\sqrt{r/\nu}} e^{\frac{\bar{V}_e}{2\nu}y}. \quad (7.57)$$

As $\omega - \omega_s \rightarrow +i\infty$, $\mathcal{I}_{\bar{V}_e}(\omega)$ diverges exponentially. If the integrand attains large enough values, a numerical approach could mistake these values for an infinite singularity; like the branch point. This is discussed in detail by Reddy and Trefethen [17]; who treat the same model problem.

To the former end, it is useful to investigate the typical size of the integrand while approaching the Ω -branch. In particular, it is inquired what magnitudes are attained at the vertex of parabolic Ω -branches. In the previous sections, it was pointed out that the vertices correspond to the point where the k -contour intersects the imaginary axis. The corresponding point in the ω -plane always lies straight above ω_s :

$$\Omega_{\bar{V}_e}(ik_i) = \omega_s + iv \left(\frac{\bar{V}_e}{2\nu} + k_i \right)^2. \quad (7.58)$$

Inserting this expression into $\mathcal{I}(\omega)$ yields:

$$\mathcal{I}_{\bar{V}_e}(\Omega_{\bar{V}_e}(ik_i)) = -\frac{\sinh\left(\left|\frac{\bar{V}_e}{2\nu} + k_i\right|y\right)}{\nu\left|\frac{\bar{V}_e}{2\nu} + k_i\right|} e^{\frac{\bar{V}_e y}{2\nu}} = -\frac{e^{\left(\frac{\bar{V}_e}{2\nu} + \left|\frac{\bar{V}_e}{2\nu} + k_i\right|\right)y} - e^{\left(\frac{\bar{V}_e}{2\nu} - \left|\frac{\bar{V}_e}{2\nu} + k_i\right|\right)y}}{\left|\bar{V}_e + 2\nu k_i\right|}. \quad (7.59)$$

for the considered example, $k_i = -\bar{V}_e/\nu$, which yields:

$$\mathcal{I}_{\bar{V}_e}\left(\Omega_{\bar{V}_e}\left(-i\frac{\bar{V}_e}{\nu}\right)\right) = -\frac{e^{\frac{\bar{V}_e y}{\nu}} - 1}{\bar{V}_e}. \quad (7.60)$$

using that \bar{V}_e and ν are positive. This expression shows that the magnitude of the integrand is dictated by the Reynolds number based on the advection \bar{V}_e . Without going into further detail here, this demonstrates that considering set-ups other than those with

the absolute Ω -branch, can become problematic from the numerical point of view, see Reddy and Trefethen [17] for more details. The computational approach is dealt with directly in chapter 8.

The isolines of $|\mathcal{J}_{\bar{V}_e}^+(\omega)| = c^{\text{st}}$ in the ω -plane are concave downward, though non-parabolic, curves that do not exactly align with the Ω -branch, so the integrand may attain larger magnitudes when approaching the Ω -branch from below at other points than its vertex. Equation (7.59) therefore only yields an estimate of the magnitude of the integrand.

7.6. CONCLUSION

In this chapter, a thorough review is presented of the derivation of Briggs's criterion for an absolute instability. The stability of the stationary wave packet in the (y, t) -plane can be expressed asymptotically as (equation (7.36)):

$$G(y, t) = \int_{-\infty+i\gamma}^{\infty+i\gamma} \int_{-\infty}^{\infty} \frac{e^{i(ky - \omega t)}}{\tilde{\mathcal{D}}(k, \omega)} \frac{dk d\omega}{(2\pi)^2} \rightarrow \frac{e^{i(k_s y - \omega_s t)}}{\sqrt{2\pi i t \left. \frac{\partial \tilde{\mathcal{D}}}{\partial \omega} \right|_s \left. \frac{\partial^2 \tilde{\mathcal{D}}}{\partial k^2} \right|_s}}, \quad (7.61)$$

as $t \rightarrow \infty$, where the subscript s refers to the branch point in the ω -plane and the pinching point in the k -plane, for which the dispersion function $\tilde{\mathcal{D}}(k, \omega)$ and the $\Omega(k)$ -branch (defined by $\tilde{\mathcal{D}}(k, \Omega(k)) = 0$) satisfy:

$$\tilde{\mathcal{D}}(k_s, \omega_s) = \frac{\partial \tilde{\mathcal{D}}}{\partial k}(k_s, \omega_s) = 0 \quad \text{and:} \quad \frac{d\Omega}{dk} = 0, \quad (7.62)$$

where the first part implies that k_s is a double root of $\tilde{\mathcal{D}}(k, \omega)$ in the k -plane and the second part represents that the group speed of the wave packet is equal to zero.

The parameters k_s and ω_s encode the stability characteristics, i.e. growth rates in y and t and the frequency and wavenumber, of a stationary wavepacket. If the branch point is unstable, the system supports an absolute instability; i.e. a solution that propagates in both directions of a spatial coordinate as it grows in time.

If the Ω -branch does not have a cusp, the growth rates attained by the branch are not representative of the absolute instability characteristics. A branch point is attained by the “smallest” possible manifestation of the Ω -branch in the ω -plane. This Ω -branch could be viewed as unavoidable and is therefore labelled as the *absolute* Ω -branch.

When including an advection term, \bar{V}_e , it has a stabilising effect in terms of $\omega_{s,i}$. However, it imposes a spatial growth rate in the advection direction. This growth is required to ensure the solution satisfies the causality condition. The implicit boundary conditions, which require that the solution decays as $|y|$ approaches infinity do not apply to the asymptotic solution. For finite times, the solution is assumed to consist of fronts, beyond which the solution becomes identically zero. As $t \rightarrow \infty$, the combination of the system having a dissipative nature and the group speed being equal to zero implies that these fronts move beyond any finite y -coordinate.

Stability spectra are usually interpreted by looking for the largest growth rate, because they usually dictate the asymptotic behaviour of the solution. In the current case, where the spectrum is continuous, the asymptotic behaviour of solutions is characterised

by a branch point. For $\bar{V}_e \neq 0$, typical Ω -branches may not contain a branch point. In general, the Ω -branches attain larger growth rates than that associated to the branch point, which suggests a more unstable asymptotic behaviour than the branch point. Analytical continuation shows that this suggestion is false when considering absolute stability characteristics. The integral over the more unstable form of the Ω -branch is identical to the integral over the branch containing the branch point; both result in the growth rate $\omega_{s,i}$ as $t \rightarrow \infty$. If an Ω -branch does not contain a branch point, it yields conclusive information on the absolute stability of a system only if the whole branch is stable. Then the system is absolutely stable.

REFERENCES

- [1] R. Briggs, *Electron-stream Interaction with Plasmas*, M.I.T. Press research monographs (M.I.T. Press, 1964).
- [2] P. J. Schmid and D. S. Henningson, *Stability and Transition in Shear Flows* (Springer Verlag, 2001).
- [3] L. Brevoort, *Three-dimensional absolute and convective instabilities, and spatially amplifying waves in parallel shear flows*, Zeitschrift für angewandte Mathematik und Physik ZAMP **42**, 911 (1991).
- [4] P. Huerre and P. A. Monkewitz, *Local and global instabilities in spatially developing flows*, Annual Review of Fluid Mechanics **22**, 473 (1990).
- [5] P. Huerre and P. A. Monkewitz, *Absolute and convective instabilities in open shear layers*, Journal of Fluid Mechanics **159**, 151 (1985).
- [6] J.-M. Chomaz, *Global instabilities in spatially developing flows: non-normality and nonlinearity*, Annu. Rev. Fluid Mech. **37**, 357 (2005).
- [7] T. Kapitula and K. Promislow, *Spectral and dynamical stability of nonlinear waves* (Springer, 2013).
- [8] B. Sandstede and A. Scheel, *Absolute and convective instabilities of waves on unbounded and large bounded domains*, Physica D: Nonlinear Phenomena **145**, 233 (2000).
- [9] Y. K. Kwok, *Applied complex variables for scientists and engineers* (Cambridge University Press, 2010).
- [10] R. Haberman, *Applied Partial Differential Equations: With Fourier Series and Boundary Value Problems* (Pearson Education, Limited, 2012).
- [11] P. D. Miller, *Applied asymptotic analysis*, Vol. 75 (American Mathematical Soc., 2006).
- [12] F. Alizard and J. C. Robinet, *Spatially convective global modes in a boundary layer*, Physics of Fluids **19**, 114-105 (2007).

- [13] U. Ehrenstein and F. Gallaire, *On two-dimensional temporal modes in spatially evolving open flows: the flat-plate boundary layer*, Journal of Fluid Mechanics **536**, 209 (2005).
- [14] X. Garnaud, L. Lesshafft, P. J. Schmid, and P. Huerre, *Modal and transient dynamics of jet flows*, Physics of Fluids **25**, 044103 (2013).
- [15] W. Coenen, L. Lesshafft, X. Garnaud, and A. Sevilla, *Global instability of low-density jets*, Journal of Fluid Mechanics **820**, 187 (2017).
- [16] M. Brynjell-Rahkola, N. Shahriari, P. Schlatter, A. Hanifi, and D. S. Henningson, *Stability and sensitivity of a cross-flow-dominated Falkner–Skan–Cooke boundary layer with discrete surface roughness*, Journal of Fluid Mechanics **826**, 830 (2017).
- [17] S. C. Reddy and L. N. Trefethen, *Pseudospectra of the convection-diffusion operator*, SIAM Journal on Applied Mathematics **54**, 1634 (1994).

8

GLOBAL APPROACH: ABSOLUTE STABILITY FROM GLOBAL SPECTRA

In chapter 7, it was derived how the asymptotic (for the evolution time $t \rightarrow \infty$) solution behaviour of a particular system can be determined by algebraically operating on a model problem. In particular, this led to the criterion for an absolute instability.

In this chapter, the same model problem is considered from the numerical perspective. In particular, it is inquired: how the asymptotic solution characteristics can be determined based on a spectrum that is computed numerically and how an eigenfunction expansion should be performed to determine the solution behaviour for finite times numerically.

8.1. INTRODUCTORY REMARKS

As pointed out at the beginning of chapter 7, the classification of an absolute instability inherently refers to perturbations that are localized in space at a given time, i.e.: wave packets. A convective instability is an absolute instability in a moving reference frame.

The typical perturbation solutions to boundary layer flows corresponding to all ansatzes discussed in §2.3.3, however, have an infinite support in the streamwise direction, i.e. the solutions are not confined in space. In the streamwise BiGlobal approach, for example, the convective nature of Tollmien-Schlichting (TS) waves in the streamwise direction implies that they enter and leave a finite domain through opposite boundaries, see Alizard [1], Groot [2]. The support is the entire domain. All streamwise harmonics are retrieved that comply with the domain length and boundary conditions. In the limit of an infinite domain length, the eigenvalues approach a continuum parametrized by the streamwise wavenumber, see Grosch and Salwen [3], Coenen *et al.* [4]. In that sense, these solutions are continuous, not discrete, modes. Their spatially unconfined nature prohibits the interpretation of individual continuum modes as convective or absolute perturbations. These modes are not proper *eigenmodes* of the system. They are not supported in an isolated spatial region of the considered domain.

As shown in chapter 7, the bridge to extracting the stability characteristics of wavepackets from the continuum modes is applying Briggs's criterion in the global stability framework. Briggs's criterion, inherited from the local approach, relies upon the fact that spatially localized wave packets are built from spatially unconfined continuum modes through the inverse Fourier transform integral. For finite times, this translates naturally into interpreting a sum of modes, instead of each mode individually, as a physically relevant perturbation. While the individual building blocks may not be interpretable, their superposition can yield a wave packet that is.

To apply Briggs's criterion, the spectrum corresponding to a given base flow must be known. Analytical solutions are unavailable in general, so numerical approaches are resorted to, requiring the truncation of the domain, at the freestream in the wall-normal direction and far enough upstream and downstream in the streamwise direction. The resulting discretized spectrum must converge as the domain length approaches infinity. The literature indicates, however, that domain length convergence studies are challenging. For developing boundary layers, specifically, the eigenvalue growth rates in time seem to increase as the domain length is increased, e.g. see figure 1 of Ehrenstein and Gallaire [5] and figure 3 of Alizard and Robinet [6]. A similar trend is observed in a recent global stability study of a Falkner-Skan-Cooke boundary layer with roughness elements by Brynjell-Rahkola *et al.* [7]. In the same vein, Theofilis [8] states: ‘the discretized approximation of the continuous spectrum will always be under-resolved.’

The fact that the spectrum does not seem to converge is a major concern. In an attempt to shed light on the convergence issues encountered when treating the problem numerically, Rodríguez *et al.* [9] perform BiGlobal analysis of a spatially uniform flow. Even though convective instability is precluded on physical grounds in that case, because there is no shear, the aforementioned advection-induced spatial growth is encountered nevertheless. Rodríguez *et al.* [9] hence labelled the spatial growth an artefact of the finite domain length; the box formulation. Nonetheless, a physical localized perturbation structure is built successfully by using the (discretized) continuum modes in a Fourier expansion. The non-local continuum modes cancel far from the center of the wave packet rendering its localized nature. To ensure the downstream exponentially growing mode shape is properly cancelled on larger and larger domains, however, an increasing number of modes is required, making the approach computationally expensive.

8.1.1. PRESENT STUDY

In order to resolve the aforementioned issues, the objectives of this chapter are to:

1. Establish an adequate approach to numerically approximate the spectrum encoding the absolute stability characteristics.
2. Determine how the solution behaviour for finite evolution times can be represented best via an eigenfunction expansion.

A model problem is introduced in §8.2, which is chosen over the full streamwise BiGlobal problem, because it contains the essential physical features and it simplifies the analysis. The exact solutions of the constant coefficient problem in the cases of separated and periodic boundary conditions are derived in §8.3, the physical origin of the

spatial exponential growth associated to the former solutions is identified, the general interpretation in terms of Briggs's criterion is exposed and a solution method regularising this spatial growth is proposed in §8.3.4. The problem with constant and varying coefficients is treated numerically in §8.4, showing the implications for a numerical approach and the effect of inhomogeneity. The performance in representing wavepackets via an eigenfunction expansion is elaborated on in §8.5 and the chapter is concluded in §8.7.

8.2. MODEL PROBLEM

Let x , y and z denote the streamwise, wall-normal and spanwise coordinates and \bar{U} , \bar{V} and \bar{W} the x -, y - and z -components of the base flow velocity, respectively. The base flow velocities are considered functions of y and $\bar{W}(y) \equiv 0$. Moreover, the spatial perturbation structure in the z -direction is omitted (infinite spanwise wavelength). The z -velocity perturbation component is denoted by w' , that represents the linear perturbation to \bar{W} . Under the aforementioned assumptions, w' is governed by the following equation:

$$\mathcal{L}\left(-i\frac{\partial}{\partial x}, -i\frac{\partial}{\partial y}, i\frac{\partial}{\partial t}\right) w' = \left(\frac{\partial}{\partial t} + \bar{U}(y)\frac{\partial}{\partial x} + \bar{V}(y)\frac{\partial}{\partial y} - \nu\left(\frac{\partial^2}{\partial x^2} + \frac{\partial^2}{\partial y^2}\right)\right) w' = 0. \quad (8.1)$$

Here, t is time and ν is the kinematic viscosity. Non-parallel boundary layer profiles are considered for which $\bar{U}(y)$ and $\bar{V}(y)$ approach positive asymptotic (edge) values $\bar{U}_e > 0$ and $\bar{V}_e > 0$, respectively, see figure 8.1.

The following Fourier ansatz can be made for the temporal and spatial structure of the perturbations:

$$w'(x, y, t) = e^{i\alpha x} \int_{-\infty+i\gamma}^{\infty+i\gamma} \tilde{w}(y; \omega) e^{-i\omega t} \frac{d\omega}{2\pi} + c.c., \quad (8.2)$$

where \tilde{w} is the z -velocity perturbation amplitude component, α is the streamwise wavenumber, ω is the angular frequency, γ is the distance of the integration contour from the real ω -axis (see §A.1.5) and *c.c.* denotes the complex conjugate. Note that a discrete ansatz is prescribed in the x -direction, see §§A.2.3 and 7.1.1 for more details. The function \tilde{w} depends on ω , this dependency will be dropped from the notation in the remainder.

Substituting ansatz (8.2) in equation (8.1) yields:

$$\tilde{\mathcal{L}}\left(-i\frac{d}{dy}; \alpha, \omega\right) \tilde{w} = \left(-i\omega + i\alpha \bar{U}(y) + \bar{V}(y) \frac{d}{dy} + \nu\left(\alpha^2 - \frac{d^2}{dy^2}\right)\right) \tilde{w} = 0, \quad (8.3)$$

a non-parallel version of the Squire equation, see Schmid and Henningson [10, p. 57]. This equation corresponds to equation (2.20c) from chapter 2, setting \bar{W} and β equal to zero. For a thorough elaboration on the considerations for choosing equation (8.3), see appendix B.

At $y = 0$, a no-slip (homogeneous Dirichlet) condition is applied, $\tilde{w}(0) = 0$, consistent with the boundary condition for the base flow. Furthermore, it is required that for the domain length $L \rightarrow \infty$, the solutions must decay as $y \rightarrow \infty$, as a minimal integrability requirement. Although this does not follow from physical first principles, solutions that 'blow up' are not physically interpretable.

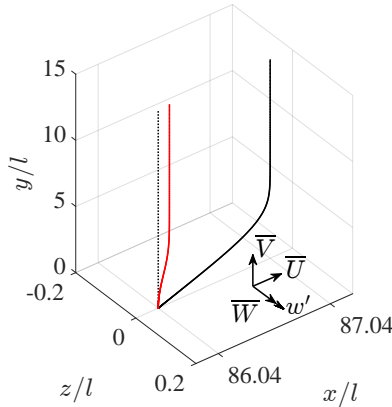


Figure 8.1: Definition of the velocity variables and \bar{U}/\bar{U}_e (black) and $10\bar{V}/\bar{U}_e$ (red), $\bar{W} \equiv 0$, boundary layer velocity profiles, see table 8.1.

Analytical solutions usually cannot be found and numerical approximations have to be constructed. In that case, the domain has to be truncated at a finite length L , which implicitly removes the requirement that solutions should decay for large y . Instead, an artificial boundary condition is introduced, that should yield the required behaviour as $L \rightarrow \infty$.

A condition allowing perturbations to pass through the boundary freely would be ideal from a physical point of view, because it would render the effect of the truncation boundary on the solution negligible. It is argued that the hypothetical use of the differential equation (8.3) itself as a boundary condition yields such behaviour. Given its second differential order, however, this condition does not close the boundary value problem and is therefore not allowed. So, non-ideal means have to be resorted to. Periodic conditions also allow perturbations to freely pass through the boundary, but comes at the cost of having to artificially periodize the problem (here: near $y = 0$), which is equivalent to introducing a fringe layer, see Bertolotti *et al.* [11] for a classical example. It is *a-priori* unknown whether the solution is affected by this locally, in this layer, only. The most common approach in the currently cited literature is to apply Robin type or higher order derivative conditions at the in-/outflow. In general, this does not allow waves to pass through the boundary freely.

The mathematical literature, principally consisting of the work of Sandstede and Scheel [12], describes that two kinds of conditions are distinguished in general: using either separated or periodic boundary conditions. A separated boundary condition is a condition that does not link solution information of opposite boundaries. Most generally, that is, any Dirichlet, Neumann or Robin type condition specifying a relationship for the solution evaluated at one particular boundary. Periodic boundary conditions are different in this regard, because they link solution information at opposite boundaries by equating the respective values and derivatives.

Furthermore, Sandstede and Scheel [12] prove the use of *any* separated (Dirichlet, Neumann or Robin type) condition yields the same spectrum limit as $L \rightarrow \infty$, while peri-

odic conditions yield a different result. The significance hereof will be further addressed in §8.3.3. To exemplify these results, the model problem (8.3) will be studied, using both separated and periodic conditions. In particular, a homogeneous Neumann condition: $d\bar{w}/dy(L) = 0$, is chosen as separated boundary condition, simulating (artificial) standing wave behaviour at $y = L$.

8.3. ALGEBRAIC SPECTRUM ANALYSIS

The problem with constant background velocity profiles can be solved analytically, i.e. when all y -dependency, or y -inhomogeneity, is absent from \bar{U} and \bar{V} . Of special interest are the profiles equal to the asymptotic constant values attained as $y \rightarrow \infty$, $\bar{U} = \bar{U}_e$ and $\bar{V} = \bar{V}_e$, as this corresponds to letting the thickness of the boundary layer approach zero. This presents a similar situation as the one encountered in chapter 7. For general \bar{U} and \bar{V} , this assumption corresponds to considering the asymptotic solutions as $y \rightarrow \infty$, see Grosch and Salwen [3].

For constant profiles, independent of x , y and t , the structure of the problem allows posing a Fourier ansatz in all independent variables for w' :

$$w'(x, y, t) = e^{i(\alpha x + ky - \omega t)} + c.c. \quad (8.4)$$

without having to introduce convolution integrals in the spectral variables.

Substituting ansatz (8.4) into equation (8.1) yields (see Bouthier [13]):

$$-i\omega + i\alpha \bar{U}_e + ik\bar{V}_e + \nu(\alpha^2 + k^2) = 0.$$

Grosch and Salwen [3] considered the equivalent with $\bar{V}_e = 0$. Solving ω for given k , yields:

$$\Omega(k) = \alpha \bar{U}_e + k \bar{V}_e - i\nu(\alpha^2 + k^2), \quad (8.5a)$$

and solving for k , given ω , results in:

$$\kappa_{1,2}(\omega) = -i \frac{\bar{V}_e}{2\nu} \pm i \sqrt{\left(\frac{\bar{V}_e}{2\nu}\right)^2 + \nu^{-1}(-i\omega + i\alpha \bar{U}_e + \nu\alpha^2)}. \quad (8.5b)$$

where Ω and κ describe the homogeneous solutions of the underlying system. These expressions correspond identically to those for $\Omega_{\bar{V}_e}$ and $\kappa_{\bar{V}_e}^\pm$ derived in §7.1.

For arbitrary $k \in \mathbb{C}$, the following holds:

$$\kappa_{1,2}(\Omega(k)) = \begin{cases} +k \\ -k - i\bar{V}_e\nu^{-1} \end{cases}. \quad (8.6)$$

This clearly shows that, when $\Omega(k)$ corresponds to a given $k \in \mathbb{C}$, there is another complex wavenumber, given by $-k - i\bar{V}_e/\nu$, that belongs to a perturbation with the same $\Omega(k)$. This is demonstrated as follows:

$$\begin{aligned} \Omega(k) &= \alpha \bar{U}_e + k \bar{V}_e & -i\nu(\alpha^2 + k^2) \\ &= \alpha \bar{U}_e - k \bar{V}_e - i\bar{V}_e^2 \nu^{-1} - i\nu(\alpha^2 + k^2 + 2ik\bar{V}_e\nu^{-1} - \bar{V}_e^2\nu^{-2}) = \Omega(-k - i\bar{V}_e\nu^{-1}). \end{aligned} \quad (8.7)$$

An individual continuum solution is constructed by combining both homogeneous solution shapes in y corresponding to the same frequency. For $k \in \mathbb{C}$, this is generally expressed as follows:

$$\underbrace{\left(A e^{iky} + B e^{i(-k-i\bar{V}_e/\nu)y} \right)}_{\tilde{w}(y)} e^{i(\alpha x - \Omega(k)t)}, \quad (8.8)$$

where A and B must be determined by the boundary conditions. In particular, the separated and periodic boundary condition cases are treated subsequently from here onward.

8.3.1. SEPARATED BOUNDARY CONDITIONS

The no-slip condition at $y = 0$ requires that $B = -A$. The Neumann condition at $y = L$ results in a condition for k . By replacing B by $-A$ in equation (8.8) and evaluating the Neumann condition, one arrives at:

$$\frac{d\tilde{w}}{dy}(L) = A i k e^{ikL} + (-A)(-i k + \bar{V}_e \nu^{-1}) e^{-i k L + \frac{\bar{V}_e L}{\nu}} = 0.$$

The non-zero combination $A e^{\frac{\bar{V}_e L}{2\nu}}$ can be factored from this expression allowing the following manipulation:

$$\begin{aligned} A e^{\frac{\bar{V}_e L}{2\nu}} \left(i k e^{i(k+i\frac{\bar{V}_e}{2\nu})L} + \left(i k - \frac{\bar{V}_e}{\nu} \right) e^{-i(k+i\frac{\bar{V}_e}{2\nu})L} \right) &= 0 \\ A e^{\frac{\bar{V}_e L}{2\nu}} \left(2 i k \cos a + \frac{\bar{V}_e}{\nu} (-\cos a + i \sin a) \right) &= 0, \quad \text{where: } a = \left(k + i \frac{\bar{V}_e}{2\nu} \right) \\ 2 i A e^{\frac{\bar{V}_e L}{2\nu}} \cos a \left(k + i \frac{\bar{V}_e}{2\nu} + \frac{\bar{V}_e}{2\nu} \tan a \right) &= 0, \end{aligned}$$

where the original expression holds only if:

$$k + i \frac{\bar{V}_e}{2\nu} = -\frac{\bar{V}_e}{2\nu} \tan \left(\left(k + i \frac{\bar{V}_e}{2\nu} \right) L \right). \quad (8.9)$$

The only solutions to equations (8.9) have $k_i = -\bar{V}_e/2\nu$.¹ This demonstrates that no decaying individual solutions exist. The function \tilde{w} must grow as:

$$\tilde{w} \sim e^{-(\kappa_{2,i} - \kappa_{1,i})y/2} = e^{\bar{V}_e y/2\nu}, \quad (8.10)$$

independently of k_r , see Bouthier [13]. The spatial growth rate of \tilde{w} is directly proportional to \bar{V}_e , which illustrates it is a direct consequence of the violation of the parallel

¹ $x + iy$ and $a \tan(x + iy) = -a(\sin 2x + i \sinh 2y)/(\cos^2 x + \sinh^2 y)$ must have equal arguments: $y/x = \sinh 2y / \sin 2x$, but $|\sinh 2y / \sin 2x| \geq |y/x|$, with equality only for either $x = 0$ (one solution: $x = y = 0$) or $y = 0$ (infinite solutions).

flow assumption, $\bar{V} \not\equiv 0$. Clearly, the spatial growth rate is proportional to the *Reynolds number representative of the dominant advection*.

Whereas the imaginary part is fixed, the real part can take many values. The value $k_r = 0$ is one of those values. The other values of k satisfying equation (8.9) can be expressed as:

$$k_n = k_{r,n} - i \frac{\bar{V}_e}{2\nu}, \quad (8.11)$$

where $k_{r,n} \rightarrow (2n+1)\pi/2L$ as $|n| \rightarrow \infty$. Note that $n \in \mathbb{Z}$; next to positive, it can also take negative integer values.

Due to their non-localized nature, the individual solutions or building blocks do not satisfy the boundedness requirement for $y \rightarrow \infty$. Nonetheless, a localized wave packet can still be constructed by superposing the individual solutions as follows:

$$w'(x, y, t) = e^{i\alpha x} \sum_{n=-\infty}^{\infty} A_n \left(e^{ik_{r,n}y} - e^{-ik_{r,n}y} \right) e^{\bar{V}_e y / 2\nu} e^{-i\Omega(k_{r,n} - i\bar{V}_e / 2\nu)t} + c.c., \quad (8.12)$$

where A_n are the equivalents of A in equation (8.8); the Fourier coefficients corresponding to an initial condition. Note that the contribution associated to $k = 0 - i\bar{V}_e / 2\nu$ drops.

The separation of the $k_{r,n}$ -values, denoted by Δk_r , approaches:

$$\Delta k_r = k_{r,n+1} - k_{r,n} \rightarrow \frac{(2(n+1)+1)\pi}{2L} - \frac{(2n+1)\pi}{2L} = \frac{\pi}{L}, \quad (8.13)$$

from above as $|n| \rightarrow \infty$. By inspection of the 3 intersections of the left and right hand side functions of equation (8.9), it follows that $3\pi/2L$ is an upper bound for Δk . By letting $L \rightarrow \infty$, this implies that the separation $\Delta k_r \rightarrow 0$. Therefore the set of k_n -values forms a continuum in the limit $L \rightarrow \infty$.

Accordingly, as $L \rightarrow \infty$, expansion (8.12) may be re-expressed as an integral in the k -plane:

$$w'(x, y, t) = e^{i\alpha x} \int_{-\infty}^{\infty} \tilde{A}\left(k_r - i\bar{V}_e / 2\nu\right) e^{i((k_r - i\bar{V}_e / 2\nu)y - \Omega(k_r - i\bar{V}_e / 2\nu)t)} \frac{dk_r}{2\pi} + c.c., \quad (8.14)$$

where it must be emphasized that the k -integral is performed over the real $k_{(r)}$ -values. Note that Ω is evaluated for the corresponding complex wavenumber $k_r - i\bar{V}_e / 2\nu$. The consistent appearance of the factor $-i\bar{V}_e / 2\nu$ allows re-writing this integral as:

$$w'(x, y, t) = e^{i\alpha x} \int_{-\infty - i\bar{V}_e / 2\nu}^{\infty - i\bar{V}_e / 2\nu} \tilde{A}(k) e^{i(ky - \Omega(k)t)} \frac{dk}{2\pi} + c.c., \quad (8.15)$$

where, now, the k -integration contour is the horizontal line at the height $k_i = -i\bar{V}_e / 2\nu$ in the k -plane. Note that this is directly equivalent to the *final* arrangement of the integration contours in §7.4.2.

8.3.2. PERIODIC BOUNDARY CONDITIONS

The current base flow is non-periodic, thus periodic boundary conditions are inapplicable for the current model as it is. Nevertheless, as pointed out by Sandstede and Scheel

[12], these conditions yield access to an another limit of the continuous spectrum as $L \rightarrow \infty$. The flow profiles have to be artificially adapted; periodicity must be enforced. Here, it is chosen to perform the adaptation in a localized region near the wall, see §8.4.3. In the limit of an infinite extent of this region, the adapted profiles approach the constant profiles, $\bar{U} = \bar{U}_e$ and $\bar{V} = \bar{V}_e$, and the corresponding problem can again be approached analytically. This limit is also treated by Reddy and Trefethen [14, cf. theorem 2].

Imposing periodic boundary conditions on \tilde{w} in equation (8.8) yields:

$$A(1 - e^{ikL}) + B(1 - e^{-ikL + \bar{V}_e L / \nu}) = 0; \quad (8.16)$$

$$ikA(1 - e^{ikL}) + (-ik + \bar{V}_e / \nu)B(1 - e^{-ikL + \bar{V}_e L / \nu}) = 0. \quad (8.17)$$

Solving this system yields two independent solutions that can form a continuum:²

$$\left. \begin{array}{ll} B = 0, & k = \frac{2\pi}{L}n \\ A = 0, & k = -\frac{2\pi}{L}n - i\frac{\bar{V}_e}{\nu} \end{array} \right\} \quad (8.18)$$

with $n \in \mathbb{Z}$. By evaluating the solutions, it turns out that $\kappa_1(\Omega(k_r))$ and $\kappa_2(\Omega(k_r - i\bar{V}_e / \nu))$ both evaluate to real numbers. Therefore, despite k being complex-valued for the solution with $A = 0$, both ($B = 0$ and $A = 0$) solutions display zero spatial growth rates. Again, the individual solutions are not localized. Using the same argument as before, they are not interpretable as physical modes by themselves. One must rely on the Fourier expansion to convert the solutions into localized (wave packet) solutions.

The separation between the solutions approaches zero for $L \rightarrow \infty$. So, after inserting the solutions corresponding to $B = 0$ into equation (8.4), the perturbation w' can again be expressed as an integral in the k -plane:

$$w'(x, y, t) = e^{i\alpha x} \int_{-\infty}^{\infty} \tilde{A}(k_r) e^{i(k_r y - \Omega(k_r)t)} \frac{dk_r}{2\pi} + c.c. \quad (8.19)$$

For the solutions with $A = 0$, one finds:

$$\begin{aligned} w'(x, y, t) &= e^{i\alpha x} \int_{-\infty}^{\infty} \tilde{B}(k_r) e^{i(k_r y - \Omega(-k_r - i\bar{V}_e / 2\nu)t)} \frac{dk_r}{2\pi} + c.c., \\ &= e^{i\alpha x} \int_{-\infty}^{\infty} \tilde{B}(k_r) e^{i(k_r y - \Omega(k_r)t)} \frac{dk_r}{2\pi} + c.c. \end{aligned} \quad (8.20)$$

The last equation follows by using equation (8.7) for $\Omega(-k_r - i\bar{V}_e / 2\nu)$. Integrals (8.19) and (8.20) are equal, which illustrates that the expansions in the $B = 0$ and $A = 0$ solutions are also the same.

It is found that the representative integral for periodic boundary conditions has a k -integration contour that is placed on the real k -axis, in contrast to the placement off the real k -axis encountered in integral (8.15) for the separated boundary conditions. Note that this is directly equivalent to the *initial* arrangement of the integration contours in §7.4.2.

²There is an extra discrete solution, for $k = -i\bar{V}_e / 2\nu$, which requires that $A + B = 0$, much like the Dirichlet condition treated in the previous subsection. This solution is discarded in the subsequent analysis.

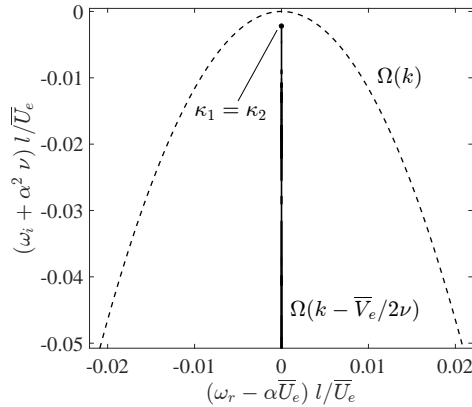


Figure 8.2: Absolute (solid) and essential (dashed) spectrum limits ($k \in \mathbb{R}$) corresponding to the parameters in table 8.1. Branch point (•).

8.3.3. ABSOLUTE AND ESSENTIAL SPECTRUM LIMITS

By imposing different boundary conditions, two specific limits of the spectrum were evaluated in the previous subsections. These limits of the spectrum are here characterized in general.

By inserting the eigensolutions presented in equation (8.11) into equation (8.6), it follows that:

$$\kappa_{1,2}\left(\Omega\left(k_r - i\bar{V}_e/2\nu\right)\right) = \pm k_r - i\bar{V}_e/2\nu, \quad (8.21)$$

i.e. this is a situation in which $\kappa_{1,i} = \kappa_{2,i} = -\bar{V}_e/2\nu$. Sandstede and Scheel [12] and Kapitula and Promislow [15, cf. definition 3.2.3] define the associated spectrum, with $\kappa_{1,i} = \kappa_{2,i}$ in general, as the *absolute spectrum*:

8

$$\begin{aligned} &\text{Absolute spectrum:} \\ &\text{(separated conditions)} \quad \Omega\left(\pm k - i\bar{V}_e/2\nu\right), \quad \text{for } k \in \mathbb{R}. \end{aligned} \quad (8.22)$$

Sandstede and Scheel [12] prove (cf. theorem 5) that, as $L \rightarrow \infty$, the spectrum converges to the absolute spectrum, if separated boundary conditions are considered. The result holds for all separated conditions, so if any Dirichlet, Neumann or Robin condition is imposed at $y = L$, the same spectrum would be found in the limit of $L \rightarrow \infty$.³

The locus of $\Omega(k - i\bar{V}_e/2\nu)$ traced in the ω -plane for $k \in \mathbb{R}$ is shown in figure 8.2 for the parameters given in table 8.1. Shifts are applied to cancel the terms containing α . The corresponding eigenfunctions are here referred to as the absolute eigenfunctions.

The absolute spectrum contains branch points, for which $\kappa_1 = \kappa_2$ (i.e. both real and imaginary parts coincide), see Kapitula and Promislow [15, definition 3.2.5]. As discussed in detail in chapter 7, the branch point in the ω -plane encodes the stability characteristics of a stationary wave packet; it dictates the absolute stability characteristics of a given system. The results of Sandstede and Scheel [12] therefore imply that separated

³E.g. considering the condition $d\tilde{w}/dy = \bar{V}_e \tilde{w}/2\nu$ yields $k_{r,n} = (2n-1)\pi/2L$ in (8.9) (i.e. equals instead of approaches); showing k_r is affected only. Small $|k_r|$ -values are affected most.

boundary conditions must be applied if the absolute/convective nature of perturbations is to be investigated.

Sandstede and Scheel [12] and Kapitula and Promislow [15] (cf. definition 2.2.3) define the spectrum for which $\kappa_{1,i}(\omega) = 0$ and/or $\kappa_{2,i}(\omega) = 0$, as the *essential spectrum*:

$$\begin{aligned} \text{Essential spectrum:} \\ (\text{periodic conditions}) \end{aligned} \quad \Omega(\pm k), \quad \text{for } k \in \mathbb{R}. \quad (8.23)$$

Sandstede and Scheel [12] prove (theorem 4) the spectrum converges to the essential spectrum, as $L \rightarrow \infty$, if periodic boundary conditions are considered.

This spectrum is also illustrated in figure 8.2. In particular, it attains larger ω_i -values than the absolute spectrum. As mentioned in chapter 7, a general property of the absolute spectrum is its minimal extent (upwards protrusion) in the ω -plane, see Kapitula and Promislow [15, lemma 3.2.4], i.e. $\max_{k_r} \Omega_i(k_r + i\phi)$ is minimal with $\phi = -\bar{V}_e/2\nu$.

For the current model problem with $\bar{V}_e \neq 0$, $\kappa_1(\Omega(k)) \neq \kappa_2(\Omega(k))$ for all $k \in \mathbb{R}$. Hence, the essential spectrum does not contain branch points and Briggs's criterion cannot be applied. It therefore *does not yield information* on whether wave packets are absolute or convective.

This can be interpreted by noting that periodic boundary conditions represent perturbations with infinite spatial support in its own sense. There are infinitely many periodic copies of a localized wave packet. A perturbation moving through the outlet re-enters through the inlet, rendering the absolute/convective classifications meaningless. The spectrum (as $L \rightarrow \infty$) indicates this through the absence of branch points. The absolute/convective behaviour of wave-packets can still be represented with these solutions through Fourier expansion, as will be shown in §8.5, but the spectrum does not indicate the behaviour of its amplitude. Note that when $\bar{V}_e = 0$, the absolute and essential spectrum coincide. This case is an exception to the rule, because perturbations then do not re-enter the domain as the action of advection is turned off.

8.3.4. SOLUTION METHOD: WEIGHTED FORMULATION (SYMMETRIZATION)

It is now identified that the absolute spectrum must be found to determine the absolute stability characteristics of the system. In approaching the problem numerically, one must resolve the spatially growing absolute solutions encountered in §8.3.1 by using separated boundary conditions. As will be illustrated in detail in §8.4, their inherent spatial growth makes numerically resolving these solutions very challenging, especially for large L , see Rodríguez *et al.* [9]. In this subsection, an approach is proposed that allows circumventing having to numerically represent the spatial growth in the absolute solutions.

The exponential spatial growth can be factored from the \tilde{w} eigenfunctions by multiplying them with an exponential weighting function $\sigma = \sigma(y)$. For general $\bar{V} = \bar{V}(y)$, this weight function reads:

$$\sigma = e^{-\int_0^y \bar{V}(\tilde{y}) d\tilde{y}/2\nu}, \quad (8.24)$$

where \tilde{y} denotes the (dummy) integration variable equivalent of y . The governing differential equation is retrieved by substituting $\hat{w} = \sigma \tilde{w}$ in equation (8.3), forming what

is referred to as the conjugated operator: $\sigma \tilde{\mathcal{L}}(\sigma^{-1}\sigma \tilde{w}) = \sigma \tilde{\mathcal{L}}(\sigma^{-1} \hat{w}) \equiv \hat{\mathcal{L}}(\hat{w})$ (Kapitula and Promislow [15, pp. 53–54]; Sandstede and Scheel [12]):

$$\begin{aligned}\sigma \tilde{\mathcal{L}}(\sigma^{-1} \hat{w}) &= \sigma \left(-i\omega + i\alpha \bar{U}(y) + \nu \alpha^2 \right) \sigma^{-1} \hat{w} + \sigma \bar{V}(y) \frac{d\sigma^{-1} \hat{w}}{dy} - \sigma \nu \frac{d^2 \sigma^{-1} \hat{w}}{dy^2} = 0 \\ \hat{\mathcal{L}}(\hat{w}) &= \left(-i\omega + i\alpha \bar{U}(y) + \frac{\bar{V}^2(y)}{4\nu} - \frac{1}{2} \frac{d\bar{V}}{dy}(y) + \nu \left(\alpha^2 - \frac{d^2}{dy^2} \right) \right) \hat{w} = 0.\end{aligned}\quad (8.25)$$

The Neumann boundary condition transforms to:

$$\sigma \frac{d\sigma^{-1} \hat{w}}{dy} \Big|_{y=L} = \left(\frac{d\hat{w}}{dy} + \frac{\bar{V}(y)}{2\nu} \hat{w} \right) \Big|_{y=L} = 0. \quad (8.26)$$

Effectively, the advection term $\bar{V}d/dy$ in equation (8.3) is replaced by the reaction term $(\bar{V}^2/2\nu - d\bar{V}/dy)/2$ in equation (8.25). Removing the former term is, in fact, the recipe to deriving the expression for σ . It will be shown shortly that the spectra of the operators \mathcal{L} and $\tilde{\mathcal{L}}$ are identical. The eigensolutions will differ only in that the eigenfunction $\sigma \tilde{w} = \hat{w}$ is obtained instead of \tilde{w} . This result can be demonstrated in general for the absolute spectrum, see Kapitula and Promislow [15, lemma 3.2.4].

The problem for \hat{w} is a regular Sturm-Liouville eigenvalue problem, see Haberman [16]. The eigenfunctions thus form an orthonormal basis: $\langle \hat{w}_i, \hat{w}_j \rangle = \delta_{ij}$, where $\langle \cdot, \cdot \rangle$ is the L^2 -function inner product and δ_{ij} is the Kronecker delta. This approach is equivalent to the “symmetrization method” treated by Reddy and Trefethen [14]. As noted in the same reference, the weighting function σ signifying eigenfunction growth in space is the sole property that renders the \tilde{w} solutions mutually non-orthogonal. The direct relationship of the weighting function to the non-parallel advection \bar{V} in equation (8.24) illustrates how the non-orthogonality of the eigenfunction basis is, in turn, directly related to the velocity component.

Taking a step back, note that equation (8.15) could be viewed as a Fourier ansatz for \tilde{w} ; substituting it for w' into equation (8.1) results in the relationship for $\Omega(k)$ in equation (8.5a). By considering the weighted problem, for \hat{w} , one effectively accounts for an adapted ansatz. This can be extracted from equation (8.14) by recognising that the exponential growth factor in y equals σ^{-1} and replacing $\Omega(k - i\bar{V}_e/2\nu)$ by $\hat{\Omega}(k)$:

$$\begin{aligned}w'(x, y, t) &= e^{i\alpha x} \int_{-\infty}^{\infty} \sigma^{-1} e^{i(ky - \hat{\Omega}(k)t)} \frac{dk}{2\pi} + c.c., \\ &= e^{i\alpha x} \sigma^{-1} \int_{-\infty}^{\infty} e^{i(ky - \hat{\Omega}(k)t)} \frac{dk}{2\pi} + c.c.,\end{aligned}\quad (8.27)$$

By inserting this ansatz into equation (8.1) (evaluated in the freestream), one obtains:

$$\hat{\Omega}(k) = \alpha \bar{U}_e - i \frac{\bar{V}_e}{4\nu} - i\nu(\alpha^2 + k^2), \quad (8.28a)$$

$$\hat{\kappa}_{1,2}(\omega) = \pm i \sqrt{\left(\frac{\bar{V}_e}{2\nu} \right)^2 + \nu^{-1} \left(-i\omega + i\alpha \bar{U}_e + \nu \alpha^2 \right)}, \quad (8.28b)$$

where, the expression for $\hat{\kappa}_{1,2}$ follows by substituting $\hat{\kappa}(\omega)$ for k and ω for $\hat{\Omega}(k)$ into equation (8.28a) and isolating $\hat{\kappa}$.

A substitution reveals that $\hat{\kappa}_{1,2}(\hat{\Omega}(k)) = \pm k$. By having factored the spatial exponential growth analytically, $\hat{\kappa}_1$ and $\hat{\kappa}_2$ have the same (zero) imaginary part and have to be evaluated along the real k -contour. Both homogeneous solutions, and hence the eigenfunctions \tilde{w} , therefore have a constant amplitude in y . Again, they are non-decaying and are thus not integrable, so Fourier expansion must be applied to yield physically interpretable solutions.

It follows from the definition of $\hat{\Omega}$, that:

$$\hat{\Omega}(k) = \Omega \left(k - i \frac{\bar{V}_e}{2\nu} \right), \quad (8.29)$$

i.e. the spectra $\Omega(k - i\bar{V}_e/2\nu)$ and $\hat{\Omega}(k)$ are the same, see Reddy and Trefethen [14]. If the absolute eigenfunctions can be properly represented, solving equation (8.3) numerically would thus result in the same spectrum, in fact the physically interpretable absolute spectrum, as the transformed problem (8.25). This will be illustrated in §8.4.

All properties are here discussed in the perspective of the constant coefficient problem. All mentioned properties in fact generalise to the non-constant coefficient problem, i.e. problems where the coefficients depend on y . As a side note for non-constant coefficient problems, Kapitula and Promislow [15, remark 3.1.17] state that the aforementioned spectrum invariance also applies for the discrete part of the spectrum.

8.4. COMPUTATIONAL SPECTRUM ANALYSIS FOR LARGE L

The main goal of this section is to test the performance of the method presented in the previous section via numerical experiments. This pertains to the first objective mentioned in §8.1.1: to establish an adequate approach to numerically approximate the spectrum encoding the absolute stability characteristics. In particular, it has to be shown that the absolute spectrum is retrieved with the weighted problem formulation as $L \rightarrow \infty$, while the numerical solution breaks down in the case of the original problem formulation. The constant coefficient and non-parallel Blasius boundary layer profile cases are considered in turn as test cases. It was demonstrated that separated boundary conditions have to be imposed to retrieve the absolute spectrum.

The eigenvalue problems are discretized using Chebyshev spectral collocation in y , using the standard cosine node distribution (see Canuto *et al.* [17], Weideman and Reddy [18]). No extra mapping is used, because the cosine grid yields the best performance in representing the continuum modes. The boundary layer profiles are interpolated onto these nodes using spline interpolation. N denotes the number of collocation nodes used in the interior of the domain. The problem is solved with the QZ algorithm (see Golub and Van Loan [19]).

8.4.1. CONSTANT COEFFICIENT PROBLEM

First, the unweighted equation (8.3) is solved for \tilde{w} with the asymptotic coefficients $\bar{U}(y) = \bar{U}_e$ and $\bar{V}(y) = \bar{V}_e$. Table 8.1 indicates the parameters used, representative of edge conditions for the Blasius boundary layer, for which $\bar{V}_e l/\nu = 1.7208/2$, where l is

Table 8.1: Nominal simulation parameters.

\bar{U}_e (m/s)	l (m)	ν (m ² /s)	$x/l = \bar{U}_e l/\nu$	\bar{V}_e/\bar{U}_e	αl
15	8.3792×10^{-5}	1.4608×10^{-5}	86.040	0.01	2π

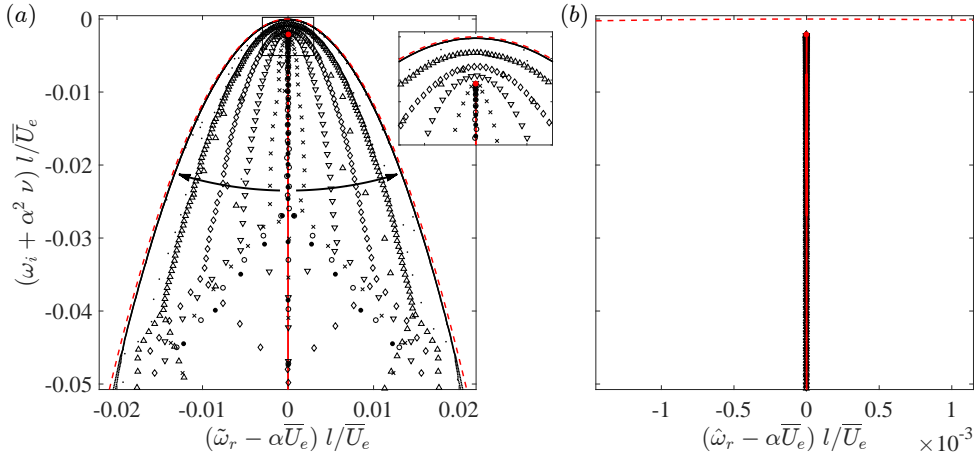


Figure 8.3: Computed (a) $\tilde{\omega}$ - and (b) $\hat{\omega}$ -spectrum for $\bar{U} = \bar{U}_e$, $\bar{V} = \bar{V}_e$ (symbols), branch point (red dot). $L/l = 60$ (\bullet), 72 (\circ), 90 (\times), 120 (∇), 180 (\diamond), 360 (Δ), 3600 (\cdot), $N = L/l$, $\bar{V}_e l/\nu = 1.7208/2$. Algebraic essential spectrum (red dashed) and absolute spectrum (red solid). Arrows indicate the direction of increasing L . Inset shows zoom on box.

the Blasius length scale. Computed eigenvalues corresponding to equations (8.3) and (8.25) are respectively denoted by $\tilde{\omega}$ and $\hat{\omega}$. Figure 8.3 (a) presents the spectrum changes with the domain length, L . If not indicated otherwise, the resolution is varied proportionally with L : $N = L/l$. Typically, $N = 60$ and $L/l = 60$ are used when calculating the discrete spectrum, but mappings refining the near-wall region are then deployed.

For $L/l = 60$ and 72 , the $\tilde{\omega}$ -spectrum closely overlaps the absolute spectrum (the solid red line), as given by $\Omega(k - i\bar{V}_e/2\nu)$ evaluated for real k , see equation (8.5a). The resulting pattern corresponds to that found by Reddy and Trefethen [14], see their figure 6.

For $L/l \geq 90$, the spectrum starts to deviate from the absolute spectrum, forming a parabolic shape. As $L/l = N \rightarrow \infty$, the spectrum approaches the curve $\Omega(k)$ evaluated for real k ; the essential spectrum. The pseudospectrum level, see Trefethen and Embree [20], below the branch point is calculated to be quite severe: $O(10^{-16})$ for $L/l > 72$; the pseudospectrum pushes the spectrum away from the absolute spectrum limit, see Reddy and Trefethen [14]. The latter reference directly links the exponential spatial growth of the eigenfunctions to resolvent estimates (cf. theorem 7), indicating the pseudospectrum levels in the direct neighbourhood of $\Omega(k_r - i\bar{V}_e/2\nu)$ decay exponentially with L . In §7.5.2, the derivation of these estimates is reproduced. Brynjell-Rahkola *et al.* [7] and Lesshafft [21] report similar levels below their computed continuous spectra.

Executing the same sequence of simulations for the weighted problem formulation

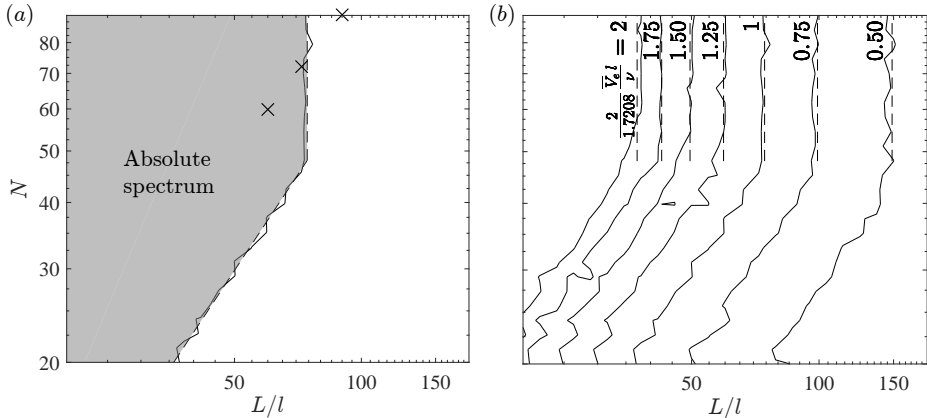


Figure 8.4: Divergence boundary where (if crossed towards the right) the $\tilde{\omega}$ -spectrum diverges from the absolute spectrum. (a) Fixed $\bar{V}_e l/v = 1.7208/2$, cases $L/l = N = 60, 72$ and 90 (\times). (b) Varying $\bar{V}_e l/v$. Fits with equation (8.31) and $c(L/l)^{1.20}$ (dashed lines).

for \hat{w} , equation (8.25), yields the spectra shown in figure 8.3 (b). Despite a zoom in the ω_r -direction (the ω_i -axis is the same as for figure 8.3 (a)), the spectra are indistinguishable from the absolute spectrum, including the case $L/l = N = 3600$. The largest departures are of $O(10^{-13})$ in absolute value.

The spatial growth rate of the computed eigenfunctions match the $-\kappa_{1,i}(\tilde{\omega})$ value up to eigensolver precision for all constant coefficient cases. The exact absolute spectrum corresponds to $\kappa_{1,i}(\tilde{\omega}) = -\bar{V}_e/2\nu$. So, whenever $\kappa_{1,i}(\tilde{\omega})$ departs from the value $-\bar{V}_e/2\nu$ when solving the unweighted problem formulation, the computed spectrum diverges from the absolute spectrum. To isolate under what conditions the $\tilde{\omega}$ -spectrum diverges from the absolute spectrum, the locus of the points $(L/l, N)$ is determined where $\kappa_{1,i}(\tilde{\omega})$ deviates more than one percent from $-\bar{V}_e/2\nu$. This reliably indicates the deviation. In this case, N and L are varied independently. The boundary is indicated for the parameters in table 8.1 in figure 8.4 (a); the grey area indicates the parameter values for which the absolute spectrum is retrieved. A clear twofold trend is observed, the first is linear on the log-log scale and the other constant in L . The testing values corresponding to figure 8.3 are indicated with the crosses. These cases $L/l = 60$ and 72 lie to the left of the boundary. The case $L/l = 90$ lies to the right, indicating the spectrum has departed significantly from the absolute spectrum.

The spectrum always departs from the absolute spectrum beyond a specific domain length L , independent of N , for a given \bar{V}_e . In figure 8.4 (a), this threshold domain length, from now on denoted by L_{th} , is approximately $74l$. For N smaller than 48 , the Nyquist limit controls the departure, resulting in a linear trend on the double log scale, relating $N \approx c(L/l)^{1.20}$ for some constant c . The latter trend is obviously dependent on the numerical scheme deployed. Figure 8.4 (b) indicates that both trends persist for other \bar{V}_e -values, keeping all other parameters fixed. Specifically, the boundary moves to the left and right for larger and smaller values of \bar{V}_e , indicating self-similarity with the pa-

parameter $\bar{V}_e L/v$.

The behaviour for $L > L_{th}$ becomes apparent when considering the eigenfunctions. Figure 8.5 shows both \tilde{w} and $\sigma^{-1}\hat{w}$ on log scale, i.e. the solutions to equation (8.3), but applying the spatial growth σ^{-1} to \hat{w} algebraically, which allows representing values smaller than 10^{-15} . It is immediately clear the considered domain lengths are so large that the exact eigenfunction magnitudes near $y = 0$ are smaller than machine precision. The computed eigenfunctions \tilde{w} grow exponentially in space for large y/l , but with a growth rate smaller than $\bar{V}_e/2v$. Specifically, they link the points $(y, \log_{10}|\tilde{w}(y)|) \approx (30, -12)$ and $(L, 0)$. Accordingly, the spatial growth rate of \tilde{w} is observed to decay as $1/L$. This trend is used for the choice of the domain lengths used in figure 8.3 to illustrate convergence, following the rule $L/l = 360/6, 360/5, \dots, 360/1$. The case $360/0.1$ is a feasible representation of the next term in line. Due to the dependency of $-\kappa_{1,i}(\tilde{\omega})$ on the domain length and the eigensolver precision, the computed spectrum is highly sensitive to perturbations (in the parameters and the discretization details), which is directly conform with the behaviour of the pseudospectrum.

Given the spatial growth rate matches with $-\kappa_{1,i}(\tilde{\omega})$, that still applies despite the aforementioned behaviour, the computed eigensolutions are still solutions to the dispersion relation (8.5a). However, they are evaluated at a spatial growth rate that is reduced with respect to that corresponding to the absolute spectrum. The spectrum is thus observed to depart from the absolute spectrum and approaches the essential spectrum, that inherently corresponds to zero spatial growth rates. It can therefore no longer be used to deduce absolute stability information. But it explains the consistency with LST and PSE results, as shown by Alizard and Robinet [6] and Rodríguez [22]. While accounting for the altered spatial growth rates, the solutions can still be used in a Fourier expansion, but a (much) larger number of modes is required to yield converging expansions, as will be illustrated in §8.5.

While varying \bar{V}_e , the relative magnitude of the eigenfunctions for the corresponding L_{th} values consistently yield:

$$e^{(\bar{V}_e l/2v) \times (L_{th}/l)} = O(10^{14}), \quad (8.30)$$

8

which is comparable to the reciprocal of the precision of the eigensolver $\epsilon||A||_F$, where ϵ is the machine precision and $||A||_F$ the Frobenius norm of the discretized operator matrix (see Anderson *et al.* [23]). Using this observation, an upper bound on the domain length, L_{th} , is synthesized:

$$\frac{L_{th}}{l} = -\frac{\ln \epsilon ||A||_F}{\frac{\bar{V}_e l}{2v}}. \quad (8.31)$$

By fitting the vertical dashed curve for the case $\bar{V}_e l/v = 1.7208/2$ in figure 8.4 (a), the other dashed curves in figure 8.4 (b) follow from equation (8.31).

In conclusion, for $L < L_{th}$, the absolute spectrum is retrieved by solving both equations (8.3) and (8.25). For $L > L_{th}$, the $\tilde{\omega}$ -spectrum deviates from the absolute spectrum and approaches the essential spectrum as $L \rightarrow \infty$, a seemingly conflicting result with theorem 5 of Sandstede and Scheel [12]. The numerically infinitesimal magnitude of the eigenfunctions for small y/l indicates that this is a consequence of the combination of finite precision arithmetic and the spatial growth inherent to the absolute eigenfunctions.

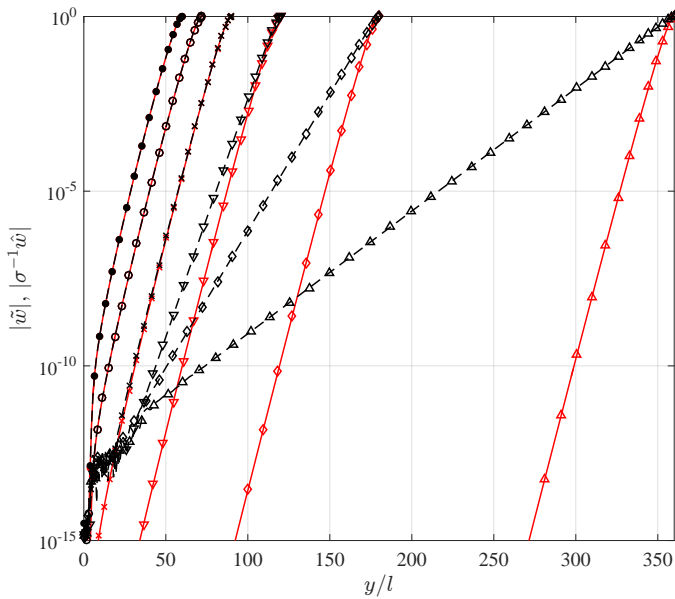


Figure 8.5: Computed zeroth harmonic continuum modes $|\tilde{w}|$ (dashed black), $|\sigma^{-1}\hat{w}|$ (solid red), with $L/l = N = 60$ (\bullet), 72 (\circ), 90 (\times), 120 (∇), 180 (\diamond) and 360 (\triangle), $\bar{V}_e l/\nu = 1.7208/2$.

By factoring the spatial growth, the weighted problem formulation avoids this issue entirely. The $\hat{\omega}$ -spectrum overlaps the exact absolute spectrum to eigensolver precision for all L .

8.4.2. BLASIUS BOUNDARY LAYER PROBLEM

8

The Blasius boundary layer provides a more realistic set of inhomogeneous \bar{U} and \bar{V} profiles. The steady boundary layer equations were solved using second order finite differences in x and Chebyshev spectral collocation in y . To obtain a machine precision accurate solution, 400 nodes are used in the wall-normal direction, mapping the median of the collocation node coordinates to $y = 2.5l$, half the boundary layer thickness. The equations are solved by marching in the x -direction, starting with the Blasius self-similar solution at $x/l \approx 1$ up to $x/l = \bar{U}_e l/\nu$ as given in table 8.1, yielding exactly the same parameters as for the constant coefficient problem. The boundary layer thickness, δ_{99} , equals $4.92l$. The resulting profiles are shown in figure 8.6.

The $\hat{\omega}$ -spectra obtained by solving equation (8.3) for different domain lengths are shown in figure 8.7 (a). Again for small enough L , the spectrum resides closely to the analytical absolute spectrum. Tracing the spectrum downwards with respect to the branch point, the value $\hat{\omega}_r$ decreases continuously, i.e. $\hat{\omega}_r < \alpha \bar{U}_e$. This feature is well-known in the literature, e.g. see Antar and Benek [24], Spalart *et al.* [25], Maslowe and Spiteri [26]. This behaviour is due to $\bar{U}(y) < \bar{U}_e$ as $y \rightarrow 0$. The eigenfunctions have a small support inside the boundary layer as opposed to that in the freestream. The usual observation is that, as $L \rightarrow \infty$, the relative extent in the boundary layer diminishes and the real part

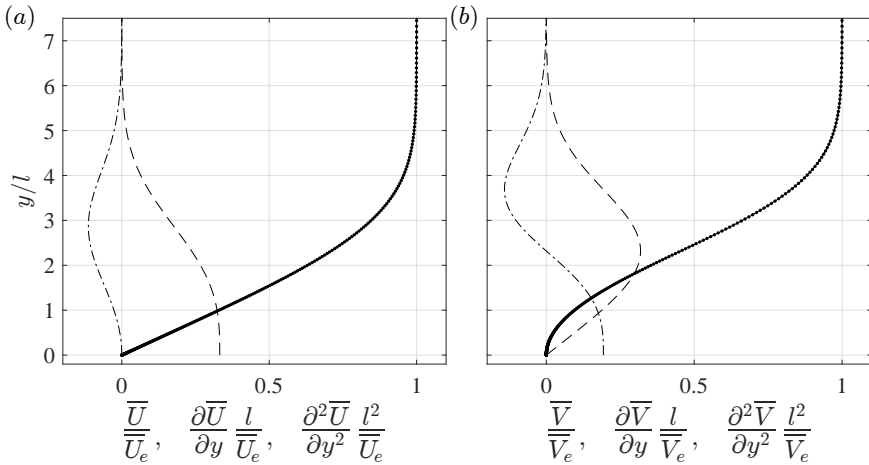


Figure 8.6: Function (dotted, dots indicate nodes), first (dashed) and second (dash-dotted) y -derivative of (a) $\bar{U}(y)$ and (b) $\bar{V}(y)$, see table 8.1 for parameter values.

8

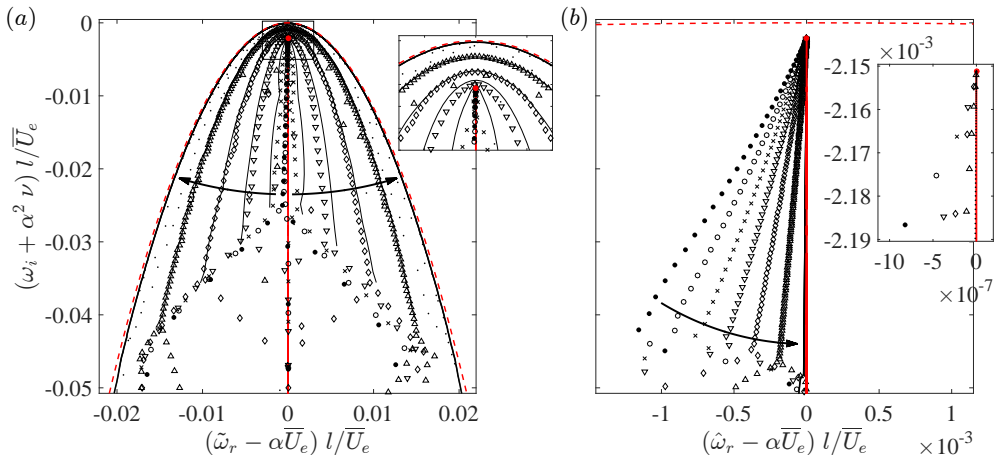


Figure 8.7: Computed (a) $\tilde{\omega}$ - and (b) $\hat{\omega}$ -spectrum for $\bar{U} = \bar{U}(y), \bar{V} = \bar{V}(y)$ (symbols), branch point (red dot). $L/l = 60 (\bullet), 72 (\circ), 90 (\times), 120 (\nabla), 180 (\diamond), 360 (\Delta), 3600 (\cdot)$, $N = L/l, \bar{V}_e l/v = 1.7208/2$. Algebraic essential spectrum (red dashed) and absolute spectrum (red solid). Parabolic spectra excerpts for constant \bar{U}, \bar{V} (solid black lines) from figure 8.3. Arrows indicate the direction of increasing L . In (a), the inset shows zoom on box. In (b), the inset shows a zoom on the values closest to the branch point, the last points belonging to a particular computed spectrum are coloured blue.

of all continuum eigenvalues approach $\alpha\bar{U}_e$ as a consequence. Instead, for larger L , the spectrum again moves away from the absolute spectrum and forms a parabolic shape. It is impossible to let $\omega_r \uparrow \alpha\bar{U}_e$ for the whole branch, at least with the unweighted problem formulation.

The manner in which the spectrum departs from the absolute spectrum in this case as opposed to that observed for the constant coefficient case is investigated. This is done by showing excerpts of the parabolic parts of the corresponding spectra in figure 8.3 (a) as the thin solid lines in figure 8.7 (a). The width of the parabolas corresponding to the constant coefficient case is larger than that corresponding to the varying coefficient cases.

The equivalent $\hat{\omega}$ -spectra obtained by solving equation (8.25) are shown in figure 8.7 (b), again note the different scale for ω_r (the scale is same as that in figure 8.3 (b)). All $\hat{\omega}$ -spectra have the shape of a slanted line up to the Nyquist limit, that converges to the absolute spectrum as $L \rightarrow \infty$, showing $\hat{\omega}_r \rightarrow \alpha\bar{U}_e$ as expected. This is directly in-line with theorem 5 of Sandstede and Scheel [12].

With this finding, it is conclusively demonstrated that the weighted problem formulation is the appropriate approach to numerically approximate the absolute spectrum, set out as the first objective in §8.1.1.

The representative shape of the eigenfunctions is presented by considering the fourth harmonic continuum mode eigenfunctions in figure 8.8. The different panels show the results for different domain lengths, note that the y -coordinate is scaled with L . The solid black lines (visible only for $y/L > 0.8$) show the growing character of \tilde{w} , the proper absolute modes in the stationary reference frame. The \hat{w} solutions, shown as the red lines, display no growth from peak to peak for $y > \delta_{99}$. The function $\sigma\tilde{w}$ can be compared with \hat{w} , see equation (8.24). For sufficiently small L , both are identical, see figure 8.8 (a) and (b). For $L > L_{th}$, the truncated magnitude of the \tilde{w} eigenfunctions for small y/l causes the match to fail, as represented by figure 8.8 (c).

Inside the boundary layer ($y < \delta_{99}$), the solutions $|\hat{w}|$ and $|\sigma\tilde{w}|$ show a significant amplitude reduction (also see Grosch and Salwen [3], Maslowe and Spiteri [26]). This is clearly related to the strong y -dependency of the \bar{U} - and \bar{V} -profiles in this region. Therefore, one could name this the ‘local effect’ of the boundary layer profiles on the continuum solutions. In fact, note that the use of the Dirichlet boundary condition in the problem with constant coefficients represents this behaviour; the amplitudes going to zero. Therefore, this condition could be seen as a representative model for the local perturbation dynamics in the boundary layer.

The fact that the eigenfunctions approach a zero magnitude inside the boundary layer implies that they see a smaller effective domain length. Therefore, when deploying the unweighted problem formulation for the varying coefficient case, the spectrum departs from the analytical absolute spectrum for larger L than for the constant coefficient case. Accordingly, the spectra corresponding to the varying coefficient case lie closer to the absolute spectrum compared to those corresponding to the constant coefficient case. The latter problem has the largest effective domain length, so it represents the worst case scenario.

The inhomogeneity of \bar{U} and \bar{V} introduces δ_{99} as a finite length scale. In turn, that causes the spectrum to have a discrete subset with proper eigenmodes that occupy the

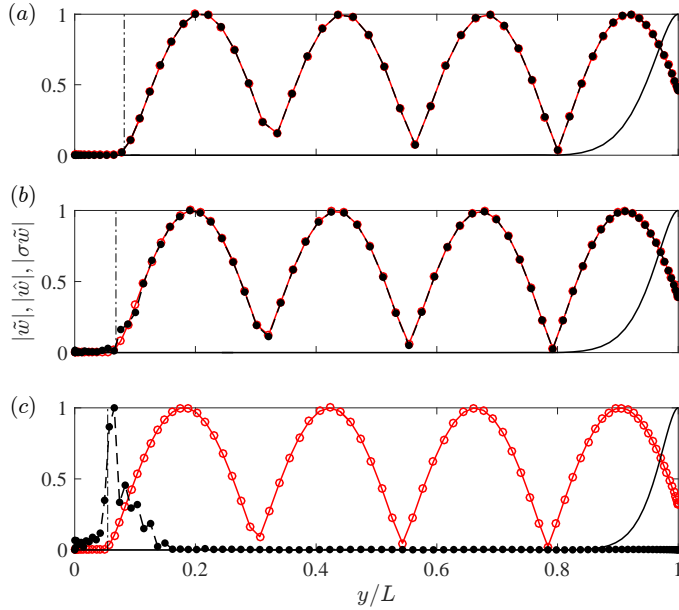


Figure 8.8: Computed continuum modes $|\tilde{w}|$ (solid black) and $|\hat{w}|$ (solid red) and $|\sigma \tilde{w}|$ (dashed black) for comparison, fourth harmonic with $L/l = N = 60$ (a), 72 (b) and 90 (c), $\bar{V}_e l/v = 1.7208/2$, all functions are scaled with respect to their maximum value. Boundary layer thickness $\delta_{99} = 4.921$ (dashed-dotted).

interior of the boundary layer and decay exponentially for $y > \delta_{99}$. The former property implies that $\omega_r < \alpha \bar{U}_e$, in line with the interpretation attached to equation (4.13) in chapter 4; the solutions are advected with speeds associated with the interior of the boundary layer. The latter property renders them integrable and thus they are individually interpretable as physical mode shapes. As $L \rightarrow \infty$, the properties of these modes converge exponentially, see Sandstede and Scheel [12, lemma 4.3]. In particular, $L/l = 90$ was used. The resolution N was increased significantly with respect to the domain length. No mapping is used to yield the best grid for the continuum solution. Therefore, the discrete solutions are underresolved when using $N = L/l = 90$; so $N = 1000$ was used instead. Figure 8.9 (a) illustrates the complete spectrum for both problem formulations (8.3) and (8.25). The eigenvalue errors are shown for the converged eigenvalues with $\omega_r l/\bar{U}_e < 4$, comparing the results from the different formulations. For the higher harmonics with larger ω_r , the error increases (up to $10^{-4} \bar{U}_e/l$), but remains insignificant with respect to the change ($10^{-1} \bar{U}_e/l$) of the continuum modes, as shown in the inset. The discrete $\sigma \tilde{w}$ (in black) and \hat{w} (red) eigenfunctions are shown in figure 8.9 (b). Both formulations produce virtually identical discrete eigensolutions. Note that when \bar{V} would be set to zero, other discrete modes would be found. That base flow feature is fully incorporated through the extra reaction terms in equation (8.25).

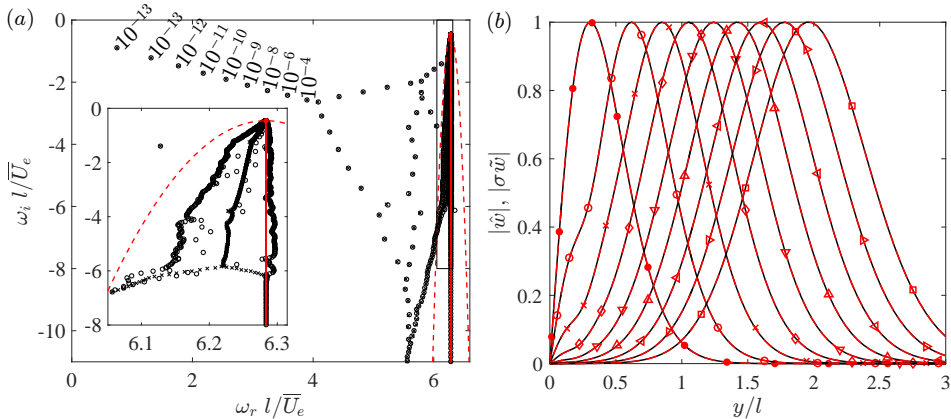


Figure 8.9: (a) Comparison of discrete parts of $(\circ) \tilde{\omega}$ - and $(\times) \hat{\omega}$ -spectrum. $N = 1000$, $L/l = 90$, $\bar{V}_e l/v = 1.7208/2$. Labels indicate $|\tilde{\omega} - \hat{\omega}|$. Inset: zoom on continuous branches. (b) Discrete modes for unweighted (solid black, $|\sigma \tilde{u}|$) and weighted (dashed red, $|\hat{u}|$) problem. Profiles from left to right correspond to labelled modes in (a) from left to right.

8.4.3. ENFORCED PERIODICITY AND VANISHING INHOMOGENEITY

It was shown in §8.3 that imposing periodic boundary conditions results in the essential spectrum as $L \rightarrow \infty$, which corresponds to solutions that have a zero spatial growth rate. This may suggest that periodizing the problem could be an alternative solution to the numerical issues associated to the spatial growth of the absolute solutions. The aim of this subsection is to show that this is, in fact, not the case.

To consider the case of enforced periodic boundary conditions, adapted profiles are to be considered such that those conditions are applicable. The following adaptation is considered specifically:

$$\bar{U}_a = \bar{U} + (\bar{U}_e - \bar{U}) \cos^2 \frac{\pi y}{2\delta_c}, \quad \text{for } y < \delta_c \quad (8.32)$$

and $\bar{U}_a = \bar{U}$, for $y \geq \delta_c$. Hence for $\delta_c = 0$, \bar{U}_a equals the Blasius profile \bar{U} throughout the domain and is discontinuous at $y = 0$. For $\delta_c \rightarrow \infty$, \bar{U}_a approaches \bar{U}_e for all y . \bar{V}_a is defined similarly. The \bar{U}_a profile and y -derivative are shown for several δ_c in figure 8.10. For $\delta_c > 0$, the profile and its derivative are continuous across the top and bottom boundaries, as shown in the inset. Loci of the velocity minimum location and the inflection point above this minimum are shown in figure 8.10 (a), varying δ_c continuously. As $\delta_c \rightarrow \infty$, they respectively approach $y/l = 2.36$ and 4.25 .

Equation (8.3) is solved for several adapted boundary layer profiles, keeping $L/l = 60$ fixed. Due to the high complexity of the eigenfunctions near $y = 0$, $N = 360$ nodes were used throughout, yielding converged results for all considered δ_c . The resulting spectra are shown in figure 8.11.

For $\delta_c = \infty$, the essential spectrum is captured up to the eigensolver precision for any L and N . In figure 8.11, the spectrum is shown as the rightward pointing triangles, which shows a close overlap with the parabola described by $\Omega(k)$ for $k \in \mathbb{R}$ in the ω -

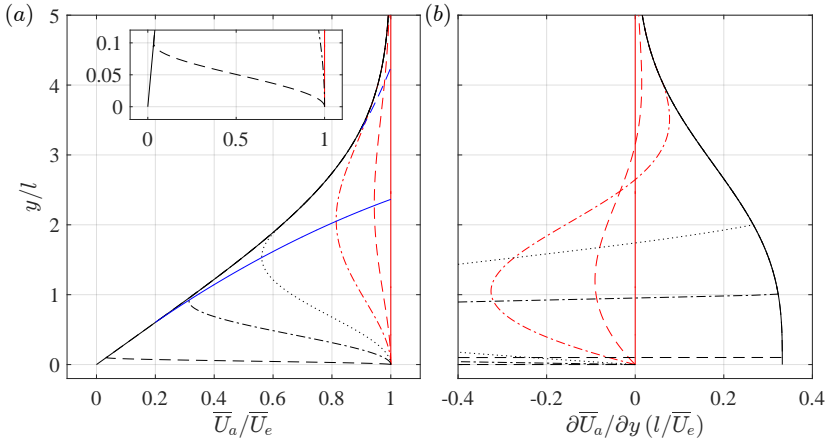


Figure 8.10: Adapted boundary layer profile (a) and first y -derivative (b) with $\delta_c/l = 0$ (black solid), 0.1 (black dashed), 1 (black dash-dotted), 2 (black dotted), 4 (red dash-dotted), 8 (red dashed), ∞ (red solid). Loci of the velocity minimum (blue solid) and upper inflection point (blue dashed) with varying δ_c . Inset: zoom on $\delta_c/l = 0.1$ case.

plane. This limit was encountered before in figures 8.3 (a) and 8.7 (a) in the context of the numerics being unable to represent the small eigenfunction magnitudes. Here, however, this parabolic spectrum is well-defined. The solutions display zero spatial growth as was also derived in §8.3.2.

Due to these features, this spectrum limit can be physically interpreted as the temporal spectrum (per definition corresponding to zero spatial growth). Upwards (downwards) moving waves, $\Omega_r(k)/k > 0$ (< 0), have a higher (lower) frequency for $\bar{V}_e > 0$, with respect to the $\bar{V}_e = 0$ case. The parabolic shape hence represents the Doppler effect.

Alizard and Robinet [6] and Rodríguez [22, p. 78] found similarly shaped continuum branches (and their x -harmonics) in BiGlobal spectra of boundary layer flows, but did not link a physical explanation. Separated boundary conditions were used, so the parabolas most probably appeared due to the reduced spatial growth rate, given $L > L_{th}$. Rodríguez [22] commented that the right hand side part of the parabola represents modes travelling faster than the freestream, based on $\Omega_r(k)/\alpha > \bar{U}_e$. He argued this to be related to the changing length scale in the developing flow problem. Equation (8.5a) shows that an appropriate interpretation is to account for the vertical phase speed by considering $\Omega_r/\sqrt{\alpha^2 + k^2}$, which in absolute value does not exceed $\sqrt{\bar{U}_e^2 + \bar{V}_e^2}$.

By decreasing $\delta_c < \infty$, keeping $L/l = 60$ fixed, flow inhomogeneity is slowly but surely introduced into the problem. In figure 8.11, a complicated displacement of the spectrum is revealed. As δ_c is decreased, first the whole parabola moves to the left. Particular modes depart from the left hand side of the continuum and continue as discrete modes. When decreasing δ_c beyond a given threshold, the continuous spectrum approaches the absolute spectrum. Figure 8.12 (a) shows the $|\tilde{w}|$ distributions for the solution with the smallest (zeroth) wavenumber, which are characteristic for all other solutions. As δ_c decreases from ∞ , the functions develop a well-defined minimum. The location of this

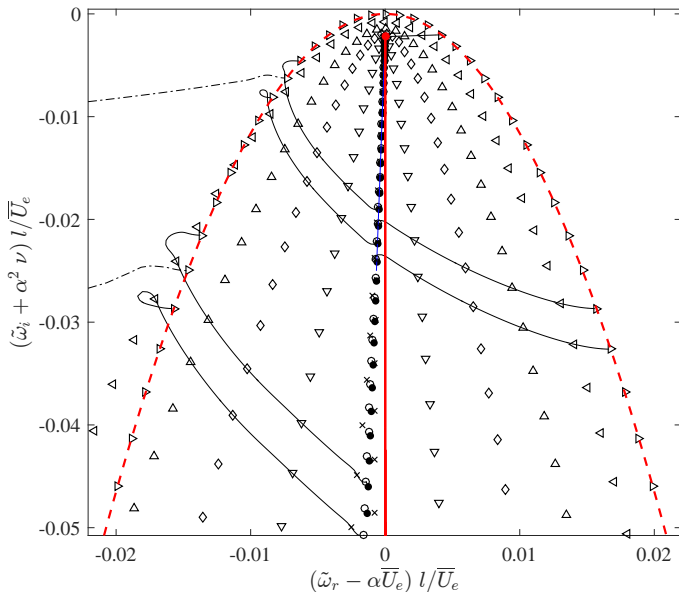


Figure 8.11: Computed $\tilde{\omega}$ -spectrum for the adapted periodic boundary layer profile, with $\delta_c/l = 0, 2, 3, 4.5, 6.8, 10.1, 18.6, \infty$ (resp. $\bullet, \circ, \times, \nabla, \diamond, \triangle, \lhd, \rhd$), $L/l = 60$ and $N = 360$. Loci of the continuum (black solid) and discrete (black dash-dotted) eigenvalue as δ_c is varied in $[0, \infty)$. Algebraic essential spectrum (red dashed), absolute spectrum (red solid) and computed spectrum with separated boundary conditions from figure 8.7 with $N = L/l = 60$ (blue solid).

minimum does not exceed $5.25l$ and approaches $3.37l$ as $\delta_c \rightarrow \infty$. For $y > \delta_{99}$, the solutions display exponential spatial growth for large, finite δ_c . This is complemented by a spatial decay in the region where the profiles are artificially periodized. This is equivalent to the solution behaviour in cases where a sponge or fringe layer is introduced at the outflow.

This illustrates that, next to advection, flow inhomogeneity is a necessary ingredient for eigenfunction growth in space. When either inhomogeneity or outward advection is absent, the amplitudes of the eigenfunctions are constant in y . Together these features yield the spatial growth and the associated numerical issues.

As $\delta_c \rightarrow 0$, the absolute spectrum is approached once again. Figure 8.11 illustrates the limit is equal to the computed absolute spectrum incorporating separated conditions (the slanted solid line). The limiting $|\tilde{w}|$ distributions closely resemble the absolute eigenfunction with the exception of details near the boundaries as shown in figure 8.12 (a); $|\tilde{w}| \sim e^{k_i y}$, with $k_i = -\bar{V}_e/2\nu$.

This shows that, although the perturbation energy is not led out of the system through the boundary conditions and the model does not include Reynolds stress terms that produce or destroy perturbation energy, the solutions still display exponential spatial growth. This is caused by the asymmetry of the flow profile; the fact that the profile is artificially periodized. Using periodic boundary conditions in cases with significant flow inhomogeneity does not remedy this problem; this is not a problem of the bound-

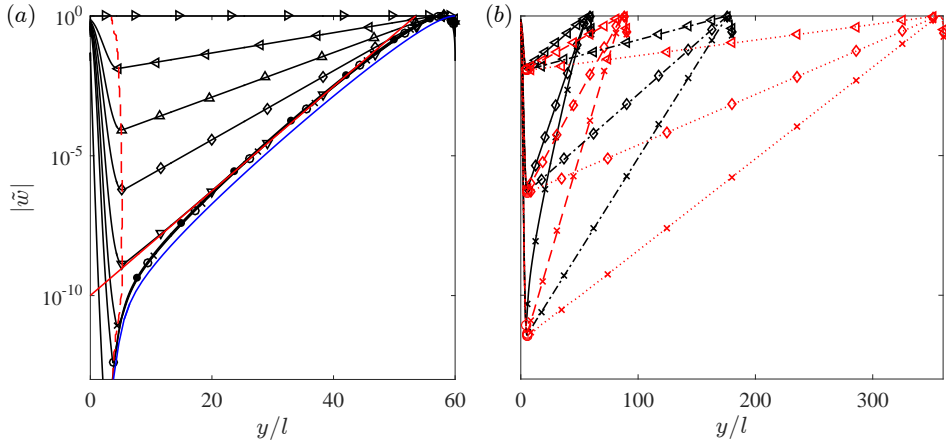


Figure 8.12: (a) Computed zeroth harmonic $|\tilde{w}|$ for the adapted periodic boundary layer profile, with $N/6 = L/l = 60$ and $\delta_c/l = 0, 2, 3, 4.5, 6.8, 10.1, 18.6, \infty$ (resp. $\bullet, \circ, \times, \nabla, \diamond, \Delta, \triangleleft, \triangleright$), path of the eigenfunction minimum for $\delta_c/l \in [0, \infty)$ (red dashed), absolute eigenfunction spatial growth rate: $\exp(\sqrt{\nu_e} y/2\nu)$ (red solid) and eigenfunction corresponding to figure 8.7 (a) with $L/l = 60$ (blue solid). (b) Zeroth harmonic $|\tilde{w}|$ as in (a), but with $N/6 = L/l = 60, 90, 180, 360$ (resp. solid, dashed, dash-dotted, dotted) and $\delta_c/l = 3, 6.8, 18.6$ (resp. $\times, \diamond, \triangleleft, \triangleright$), eigenfunction minima (red circles).

ary conditions. To avoid the detrimental effect of the spatial growth on the numerical solution, it is necessary to consider the weighted problem formulation.

As noted in §8.3.3, Sandstede and Scheel [12] prove that the spectrum corresponding to problems with periodic coefficients and boundary conditions converges to the essential spectrum as $L \rightarrow \infty$. That is, for all cases where $\delta_c > 0$, the spatial growth should vanish in the limit as $L \rightarrow \infty$. When increasing L beyond the threshold value, while fixing δ_c to a small value, the spectrum departs from the absolute spectrum and approaches the essential spectrum in the limit as $L \rightarrow \infty$, similarly as the case presented in figure 8.7 (a). So, the two limiting procedures (L fixed, $\delta_c \rightarrow \infty$) and ($L \rightarrow \infty$, δ_c fixed and small) both yield a spectrum that approaches the essential spectrum. It is paramount to note, however, that the eigenfunctions do not approach the same limit. This is best exemplified by considering the $|\tilde{w}|$ -profile corresponding to the zeroth harmonic, because it has a single, non-zero minimum. In the first limit procedure, $\min |\tilde{w}|$ approaches 1, while it approaches 0 in the second.⁴ The effectiveness of the weighted formulation, instead, applies for all L .

The last limit considered is $L \rightarrow \infty$, while δ_c is fixed and large. This limit is representative of small inhomogeneity in the base flow profiles. Figure 8.12 (b) illustrates the behaviour of the eigenfunctions for increasing L observed in figure 8.5 is found here as well. Note that the minimum of the zeroth harmonic eigenfunction, $\min |\tilde{w}|$, is approximately constant for fixed δ_c . Specifically, far from the boundaries, $|\tilde{w}|$ is proportional to $e^{-k_i y}$, with $k_i \approx \min(\ln |\tilde{w}|)/L$. So, k_i decays as $1/L$. This is an explanation for the decrease of the energy loss due to advection with the domain length reported by Brynjell-

⁴For small enough δ_c , $\min |\tilde{w}|$ approaches the smallest numerically representable value.

Rahkola *et al.* [7, cf. figure 13]. The decay as $1/L$ is analogous to the observed behaviour when using separated conditions and $L > L_{th}$. Similarly, this spatial growth rate dictates the position of the spectrum in the ω -plane, through $\Omega(k_r + ik_i)$. This implies that the spectrum approaches the essential spectrum as $L \rightarrow \infty$. It is concluded that all results are in correspondence with theorems 4 and 5 of Sandstede and Scheel [12].

For base flow profiles with small variations in y , using periodic conditions (and periodizing the profiles) can yield significantly smaller spatial growth rates as opposed to using separated boundary conditions. In the latter case, the spatial growth rate depends on $\min(\ln|\tilde{w}|)$ as illustrated, which approaches 0 as $\delta_c \rightarrow \infty$, i.e. the solutions then display zero spatial growth and are relatively easy to compute. The (worst case, viz. Dirichlet) separated boundary conditions, instead, can force $\min|\tilde{w}|$ to be in the order of the eigensolver precision. This explains why reported minimum magnitudes of the eigenfunctions and pseudospectrum levels in the literature (see Coenen *et al.* [4], Alizard and Robinet [6], Brynjell-Rahkola *et al.* [7], Lesshafft [21]), do not necessarily attain such severely low values.

To quantify the behaviour in the latter limit, the minimum of $|\tilde{w}|$ was tracked while varying L and δ_c , ensuring a sufficient resolution for all cases ($N = 6L/l$). The results are summarized in figure 8.13. As L is increased, the eigenfunction minima approach a limiting value that is a function of δ_c . On the double log scale, this function approaches a constant slope in the limits of both small and large δ_c , this slope approaches zero as $\delta_c \rightarrow \infty$. A function representing exactly these characteristics is the integral of $b(1 - \tanh x)/2$, as follows:

$$\ln|\tilde{w}| \approx -\frac{1}{2} \frac{d\ln|\tilde{w}|}{d\ln\delta_c} \Big|_{\delta_c \ll \delta_c^r} \ln\left(1 + \left(\frac{\delta_c}{\delta_c^r}\right)^{-2}\right) \quad (8.33)$$

where δ_c^r is a reference value and $b = d\ln|\tilde{w}|/d\ln\delta_c|_{\delta_c \ll \delta_c^r}$ is the slope for $\delta_c \rightarrow 0$. The approximate values of these parameters were respectively determined to be $17.1l$ and 14.5 (red line in figure 8.13), based on the case with $L/l = 360$. So, for large δ_c :

$$\ln|\tilde{w}| \rightarrow -2130 \left(\frac{\delta_c}{l}\right)^{-2}, \quad \text{for } \delta_c \gg 17.1l. \quad (8.34)$$

Thus the logarithm of the minimum of the eigenfunction approaches zero inversely proportionally to the second power of the length scale associated with the flow inhomogeneity.

8.5. WAVE PACKET EVOLUTION

The second main objective mentioned in §8.1.1 is to determine how the solution behaviour for finite evolution times can be represented best via an eigenfunction expansion. To that end, the results of the different problem formulations presented in the previous section (i.e. different boundary conditions, profiles and weighted versus unweighted formulation) are used to represent the evolution of a wave packet. Not all spectra may yield the relevant (absolute) temporal growth rates and the continuum eigenfunctions may individually not be physically interpretable. Nevertheless, Fourier expansion, whether Briggs's method is applicable or not, can yield a localized, and therefore

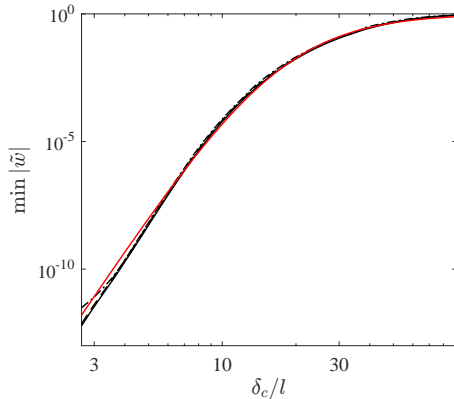


Figure 8.13: Eigenfunction minimum trend with δ_c , with $N/6 = L/l = 60, 90, 180$ and 360 (resp. black dash-dotted, dashed and solid). Equation (8.33) with $d\ln|\tilde{w}|/d\ln\delta_c|_{\delta_c \ll \delta_c^r} = 14.5$ and $\delta_c^r/l = 17.1$ (red).

interpretable, signal. As will be shown, the different formulations yield virtually identical results for small enough domain lengths only. The weighted formulation is necessary to ensure an appropriate expansion basis for arbitrary L . Inspiration is taken from Rodríguez *et al.* [9], who similarly approach a two-dimensional problem.

Four different formulations of the eigenfunction expansion problem are considered. The first and second cases involve the separated boundary conditions (no-slip and Neumann), posed in the original (abbreviated: SG) and weighted (SN) formulation, see equations (8.3) and (8.25), respectively. Next, the two limiting cases involving periodic boundary conditions are solved, one with the unaltered Blasius profile ($\delta_c = 0$, PG) and the other with the freestream (constant) profile ($\delta_c \rightarrow \infty$, PN). The second letter in the abbreviations indicates whether the eigenfunctions grow (G) or are neutral (N) in y . The latter represents zero inhomogeneity. The spectra and eigenfunctions were computed for domain lengths $L/l = 60$ and 90 , for which it was found previously that the absolute eigenfunctions could and could not be resolved, respectively. The resolution $N = 6L$ was chosen, so to ensure the most complicated eigenfunctions (encountered in the PG case) were sufficiently resolved.

The spectra for all cases are illustrated in figure 8.14, shifted in the real direction with ϕ_{case} for clarity purposes. The differences are significant. The eigenfunctions are used to represent a simple wave packet formed by the product of a Gaussian and sine function, representing a longitudinal vortex sheet:

$$w'(y, 0) = e^{-\frac{1}{2}\left(\frac{y-y_w}{\Delta_w}\right)^2} \sin \frac{y-y_w}{\Delta_w} \quad (8.35)$$

where $\Delta_w/l = 1/2$ is the width and y_w is the location of its center. The main value for the latter is set equal to $L - 25l$, which corresponds to a specific position relative to the truncation boundary. That way, the wave packet has the same relative size compared to the weighting function σ per domain length, see figures 8.15 (a) and 8.16 (a).

A general initial condition $w'(0, y, 0)$ can be expanded in terms of the \hat{w} and \tilde{w} solu-

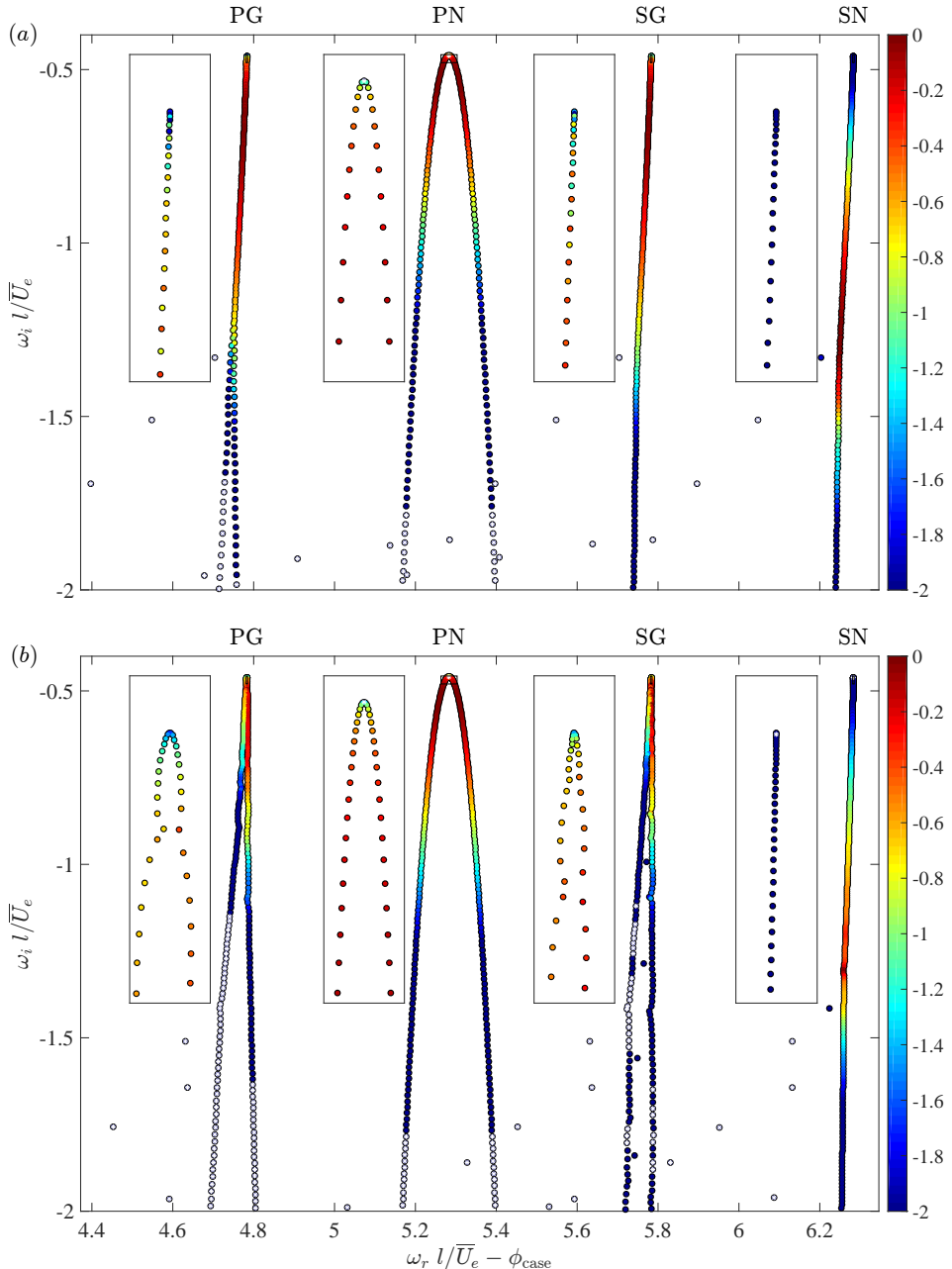


Figure 8.14: Spectrum color-coded with the absolute value expansion coefficients (color: \log_{10} relative to maximum) per continuum eigenvalue for $N/6 = L/l = 60$ (a) and 90 (b) for separated conditions in the weighted (SN) and original (SG) formulation; periodic conditions with $\delta_c = \infty$ (PN) and 0 (PG) (respectively: $\phi_{\text{case}} = 0, -0.5, -1, -1.5$). Small expansion coefficients: $a_i / \max_i a_i < 10^{-4}$ (white *'s). Insets show zooms on eigenvalues with largest ω_i , vertical viewing range is the same for the different boxes.

tions as follows:⁵

$$w'(0, y, 0) = \sum_{i=0}^{\infty} a_i \tilde{w}_i = \sigma^{-1} \sum_{j=0}^{\infty} a_j \hat{w}_j. \quad (8.36)$$

Note that the coefficients in the summation over the functions \tilde{w} and \hat{w} are equal, $a_i = a_j$ for $i = j$. The factorization of σ^{-1} symbolizes algebraically applying the spatial growth after the \hat{w} solutions are solved numerically. The coefficients a_j can be found through the use of the weight σ :⁶

$$a_k = \langle \hat{w}_k, w'(0, y, 0) \rangle_{\sigma} = \langle \tilde{w}_k, w'(0, y, 0) \rangle_{\sigma^2} \quad (8.37)$$

where $\langle f, g \rangle_{\sigma} = \langle f, \sigma g \rangle = \langle \sigma f, g \rangle$, σ being real.

By projecting the wave packet onto the entire eigenfunction basis, the expansion coefficients are obtained. In the SG and PG cases, the coefficients attain large absolute values, due to the eigenfunctions' exponential spatial growth: maximally $O(10^4)$ with respect to the norm of the eigenfunctions. This signals the ill-conditioning of the eigenfunction basis, see Reddy and Trefethen [14]. For the other cases, the maximal absolute magnitudes of the coefficients do not exceed $O(10^{-1})$. The relative size of the coefficients (per case) is indicated along the spectrum branches in figures 8.14. For the SN case, the modes dominantly contributing to the wave packet are located further down the branch as opposed to the others. The wavepacket's predominant wavenumber, $k_r l = l/\Delta_w = 2$, appears around $0.04l/\bar{U}_e$ below the most unstable continuum modes in the ω -plane, correspondent with the distributions in the SG, PG and PN cases. Those modes that have a coefficient with a relative magnitude smaller than 10^{-4} are indicated with a white cross. The majority of the discrete part of the spectrum belongs to this category, because the initial condition is prescribed far from the boundary layer.

Given the coefficients, the exact wave packet initial condition is reconstructed using all eigenfunctions in figures 8.15 (a,c), resulting in a nearly identical overlap of the reconstructed functions with the exact initial condition. This representation is very regular for all cases for $L/l = 60$; although relatively small oscillations do occur near $y = L$ for the SG and PG cases. For $L/l = 90$, the representation of the initial condition in the SG and PG cases displays a divergent "tail" when approaching $y = L$. This is caused by the spatial growth that, for this domain length, cannot be properly cancelled out, even though all computed eigenmodes are used in the expansion. The function σ^{-1} represents the amplitude distribution of the tails. Nevertheless, the relevant structure associated with the initial wave packet is captured, because $L/l = 90$ is small enough so that the tails do not completely destroy the relevant solution structure. Hence the shape could still be normalized with the maximum amplitude of the relevant solution part. For $L/l > 90$ (not shown), the tails completely overwhelm the relevant solution.

⁵The asymptotically least stable wave packet has, in fact, no structure at all, because diffusion damps all non-zero wavenumbers; it has $k_r = 0$. Pinpointing a definite shape for $t < \infty$ is immaterial in light of the asymptotic character.

⁶The bi-orthogonality condition $\langle \tilde{w}_k, \tilde{w}_j \rangle_{\sigma^2} = \langle \sigma^2 \tilde{w}_k, \tilde{w}_j \rangle = \langle \sigma \tilde{w}_k, \sigma \tilde{w}_j \rangle = \delta_{kj}$, implies $\sigma^2 \tilde{w}_k^{(\dagger)}$ is the adjoint eigenfunction corresponding to \tilde{w}_k , where here the dagger denotes complex conjugation. Note: \tilde{w} and $\sigma^2 \tilde{w}$ grow in the opposite y -directions, as stated by Chomaz [27]. The structural sensitivity: $\sigma^2 |\tilde{w}|^2 \approx \min |\tilde{w}|^2$ is thus approximately constant and virtually zero for $L > L_{th}$.

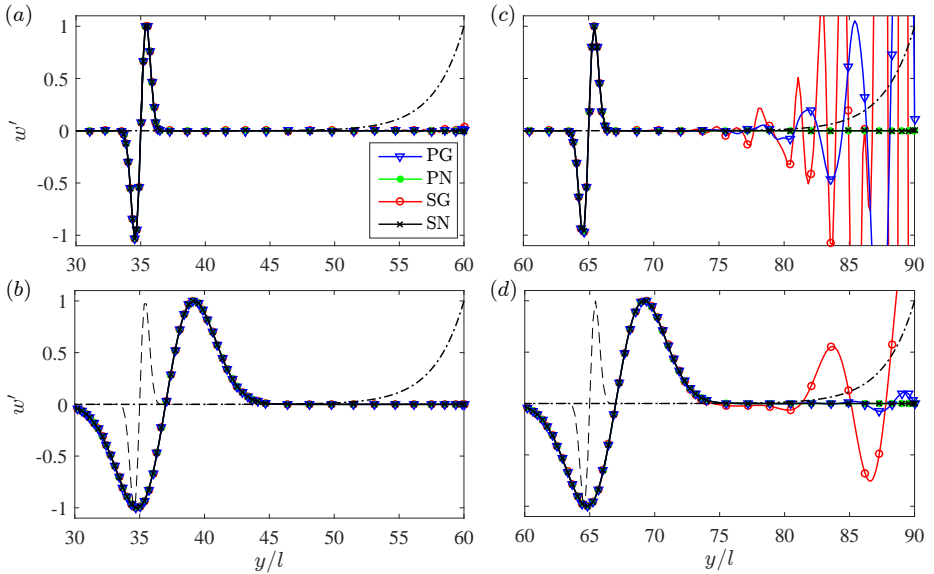


Figure 8.15: Spatial shape scaled with the maximum size of the (relevant) wave packet structure (see the dotted red line in figure 8.17 for its evolution in time) for $N/6 = L/l = 60$ (a,b) and 90 (c,d) at $t = 0$ (a,c) and $t = 200l/\bar{U}_e$ (b,d) and for the different boundary conditions and problem formulations. The initial condition has $y_w = L - 25l$ (dashed), exponential weighting function σ^{-1} (black dash-dotted).

To identify how the wave packets evolve through the truncation boundary, the parameter y_w is set to $L - 6l$, keeping all other parameters the same. The resulting wave packet evolution is shown in figures 8.16. A different outflow behaviour is not circumvented when applying the different methods. The case PN illustrates the unaffected shape (flowing through the boundary freely), while the cases SG and SN reflect the Neumann condition corresponding to the original problem formulation. The function σ^{-1} is observed to be representative of the differences in the solutions, which indicates their localized nature. This also renders it a means of identifying the spatial extent of the expected boundary layer behaviour.

Returning to the cases with $y_w = L - 25l$ from now on, the maximum amplitude of the relevant flow structure is tracked to investigate the decay rate, see figure 8.17. The relevant structure can still be distinguished for all cases, because a small enough L is considered in which the tails do not destroy the complete solution structure. Note that the evolved wavepackets represented by all problem formulations overlap virtually identically. For the SN and PN cases, the absolute error is as low as $O(10^{-11})$ for both domain lengths. The SG and PG cases display a $O(10^{-2})$ and $O(10^{-5})$ error, repectively, for $L/l = 90$. Despite the spatial growth issues apparent in figure 8.15 (c) and (d), the size of the wave packet most closely follows the absolute time asymptotic trend indicated by the result of Briggs's method; varying proportionally to $e^{\omega_i t}/\sqrt{t}$, taking the branch point value for ω_i . Note that the maximum temporal growth rate in the spectrum in the case PN is larger than the maximum rate in all other cases. Nevertheless, the amplitude

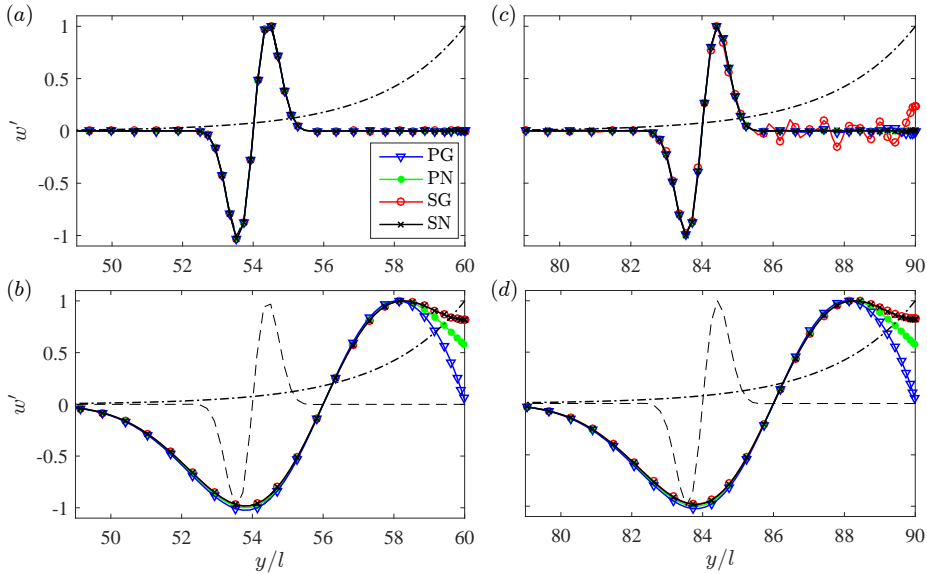


Figure 8.16: Spatial shape scaled with the maximum size of the (relevant) wave packet structure for $N/6 = L/l = 60$ (a,b) and 90 (c,d) at $t = 0$ (a,c) and $t = 200l/\bar{U}_e$ (b,d) and for the different boundary conditions and problem formulations. The initial condition has $y_w = L - 6l$ (dashed), exponential weighting function σ^{-1} (black dash-dotted).

is dictated by the branch point in the absolute spectrum, that attains a lower temporal growth rate. The maximum amplitude of the tails, found at $y = L$, is monitored and illustrated as the dashed lines in figure 8.17. For $L/l = 90$, they are very large for the PG and SG cases. They decay in time, because they flow out of the domain. The tails are non-existent in the PN and SN cases, where modes do not display spatial growth. The manifestation of w' at $t = 200l/\bar{U}_e$ is shown in figures 8.15 (b) and (d). Again, the results corresponding to the different cases overlap very closely, showing at most $O(10^{-7})$ and $O(10^{-5})$ absolute errors for $L/l = 60$ and 90, respectively, measured in the wave packet's center. This shows that large domains can be tackled with the standard formulation, but a much larger number of modes is needed to result in non-divergent Fourier expansions in space.

It is concluded that, only if L is small enough, the spatially exponentially growing eigenfunctions can accurately represent flow structures and their growth or decay in time can be tracked in all cases. The resulting solutions are then independent of the boundary conditions and the solution method, except when the main structure reaches the outflow boundary, as indicated by the weighting function in figure 8.16.

The weighted formulation shows very promising results, without altering the discrete spectrum part, the absolute spectrum is retrieved with high precision. The results in this section show that it moreover yields convergent Fourier expansions for large domain lengths. This completes the second objective of this chapter mentioned in §8.1.1.

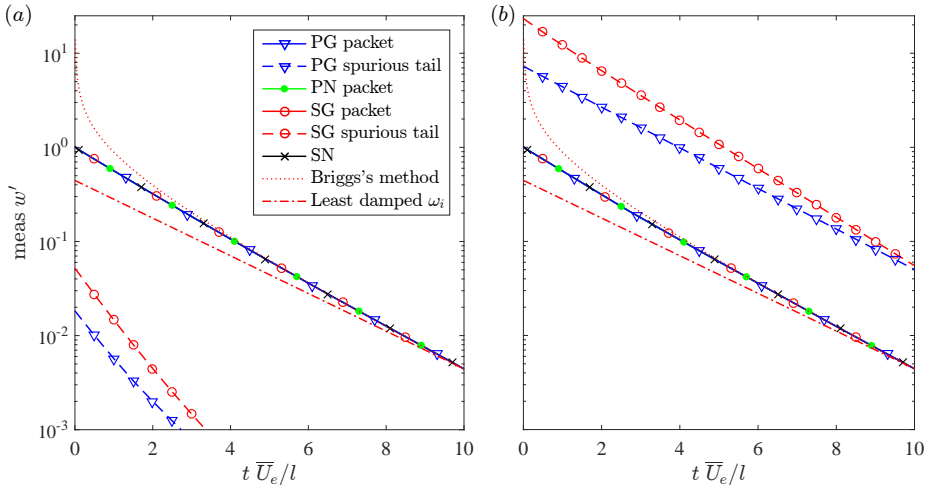


Figure 8.17: Amplitude evolution of the (relevant) wave packet part (solid lines with symbols) and the spurious tail (dashed lines) for $N/6 = L/l = 60$ (a) and 90 (b) corresponding to the different boundary conditions and problem formulations, based on the initial condition having $y_w = L - 25l$. Largest temporal decay growth (smallest decay) rate $e^{\omega_l t}$ corresponding to the PN case (dash-dotted red) and Briggs's method result $e^{\omega_l t}/\sqrt{t}$ (dotted red).

8.6. DISCUSSION OF PHYSICAL INTERPRETATIONS

The growing continuum solutions and the appropriate solution method to handle their growth are the central topic of this chapter. Besides the mathematical implications, there are important physical interpretations to be made regarding both aspects. The physical interpretation associated to the growth in the continuum solutions is detailed in §8.6.1, while the interpretation of the symmetrization approach is treated in §8.6.2.

8

8.6.1. THE SPATIAL GROWTH RATE: A PHYSICAL IMPERATIVE

First of all, it is important to track the physical cause of the spatial growth in the absolute solutions. It was determined in §7.4.3, of chapter 7, that the growth is required for otherwise the solution would violate causality. Another equivalent condition can be derived.

The specific case treated in §8.3.1 is considered, where the separated boundary conditions are the Dirichlet and Neumann condition. The presumption of this specific case is without loss of generality in the perspective that the absolute spectrum is retrieved when applying any separated Dirichlet, Neumann or Robin boundary conditions as $L \rightarrow \infty$; different though equivalent interpretations must exist for the other cases.⁷

RELATIVE GROWTH OF THE HOMOGENEOUS SOLUTIONS

As shown with equation (8.10), the spatial growth rate in the \tilde{w} solutions equals the difference in the imaginary parts of κ_1 and κ_2 in this particular case. This is the conse-

⁷Choosing a different set of conditions in fact only changes the k_r -values, not k_i , corresponding to \tilde{w} . Changes in the k_r -values are irrelevant in the limit $L \rightarrow \infty$, because they will form the same continuum. Theoretically, this allows phase shifting through the entire continuum for a single $L < \infty$.

quence of the fact that the κ_1 and κ_2 solutions have to be combined to form \tilde{w} via equation (8.8). It can be deduced from equation (8.6), that, if $\kappa_1 \in \mathbb{R}$, κ_2 must have a non-zero imaginary part. So, the only way of preventing the \tilde{w} solutions to have a spatial growth is to somehow prevent the κ_2 solution from getting involved in the construction of \tilde{w} . Hypothetically, one would have succeeded in doing this if B in equation (8.8) equals zero. In this case, the no-slip condition renders this scenario impossible however. Its statement is: $B = -A$, which requires that $B \neq 0$; no non-trivial solution would exist otherwise, even for finite L . Physically, this implies that a reflected wave ($A \neq 0$) cannot exist without the incident wave ($B \neq 0$).

As was shown in §8.4, the choice of the Dirichlet condition at $y = 0$ is justified from the context of the inhomogeneity in non-constant $\bar{U}(y)$ for small y corresponding to boundary layers. In fact, the no-slip condition models “local effects” at $y = 0$. The preceding deduction is a particular demonstration that local effects generally require the incorporation of both homogeneous solutions. Both κ_1 and κ_2 must be taken into account and the mismatch in their imaginary part causes the spatial growth in \tilde{w} .

This shows that, to understand the physical mechanism underlying the growth in the \tilde{w} solutions, one must first identify the cause of the relative exponential growth of the κ_2 solution compared to the κ_1 solution. This can be done in a similar way as the Reynolds-Orr analyses (see §2.5.1), by writing $\Omega(\kappa_2)$ as follows:

$$\begin{aligned}\Omega(-k - i\bar{V}_e/v) &= \alpha \bar{U}_e - iv\alpha^2 + (-ik + \bar{V}_e/v)[\bar{V}_e - v(-ik + \bar{V}_e/v)] \\ &= \alpha \bar{U}_e - iv\alpha^2 + \underbrace{(-ik + \bar{V}_e/v)}_{d/dy} \underbrace{[\bar{V}_e]}_{(a)} + \underbrace{ivk}_{(b)} - \underbrace{\bar{V}_e}_{(c)}.\end{aligned}\quad (8.38)$$

The terms inside the square brackets represent the fluxes due to advection ($+\bar{V}_e$) and viscous diffusion ($-v(-ik + \bar{V}_e/v)$) of the solution. The shape of the κ_2 -solution in the y -direction, $e^{ik_2 y} = e^{-iky + \bar{V}_e y/v}$, consists of two factors: a travelling wave part ($-ik$) and a spatial exponential growth part (\bar{V}_e/v). The flux due to advection of the perturbation, (a) in equation (8.38), cancels the flux due to diffusion of the spatial exponential growth part of the perturbation, (c), while the diffusion of the travelling wave part, (b), results in an apparent advection in the *positive* y -direction with the speed \bar{V}_e (note that the positive advection is unexpected in light of the appearance of $-ik$ as the exponent).

So, the propagation of the κ_2 -solution in the positive y -direction is due to the viscous flux, instead of the advective flux. This explains the growth rate: for the viscous flux to cancel the advective flux, the solution must have a strong gradient in the positive y -direction.

In summary, it can be deduced that there are 2 essential effects that together cause the spatial growth of the \tilde{w} solutions:

1. local effects demand both the κ_1 and κ_2 solutions to be combined
2. advection induces $\kappa_{1,i} \neq \kappa_{2,i}$ and $(\kappa_{1,i} - \kappa_{2,i})/2$ is the spatial growth rate

Local effects can be present explicitly, through inhomogeneity of the flow, or implicitly, in the form of boundary conditions (as illustrated for the Dirichlet condition considered here).

GROWTH IN THE EIGEN SOLUTION

The combination of the homogeneous solutions causes \tilde{w} to grow as $e^{\bar{V}_e y/2\nu}$. On a domain with length L , this means that one must be able to represent solutions that grow by the factor $e^{\bar{V}_e L/2\nu}$ as a worst-case scenario. By considering numbers $\bar{U}_e = 10 \text{ m/s}$, $L = 0.1 \text{ m}$ and $\nu = 1.4 \times 10^{-5} \text{ m}^2/\text{s}$, that are reasonable in the context of minimal, but practically relevant, low-speed BiGlobal problem (i.e. \bar{U}_e takes the role of \bar{V}_e), one obtains:

$$e^{\bar{V}_e L/2\nu} = e^{3.57 \times 10^4} = 10^{10^{4.19}} = 10^{100 \times 155}. \quad (8.39)$$

This number is monstrous.⁸ The number of digits required to represent these solutions is equal to the 155th power of a googol (10^{100}). The total number of elementary particles in the observable universe (10^{97} , see Munafó [28]) or the total number of chess games (Shannon's number: 10^{120} , see Shannon [29]), both close to "just" the first power of a googol, pale next to this number. These solutions cannot be attacked with double (2^1) or quad (2^2) precision computers, one would, in fact, require a 2^{51521} -precision computer (having rounded up the final decimal). Approaching these solutions numerically is clearly not feasible.

This velocity ratio, in fact, exceeds the largest possible velocity ratio that could be measured in the universe (at this date).⁹ Clearly, the \tilde{w} solutions represent entities that are impossible to establish physically. This illustrates why the \tilde{w} solutions, by themselves, are not physically interpretable. Their growth is an artefact of the eigenfunction concept subject to advection. The superposition of these solutions, however, eliminates the exponential growth. The spectrum corresponding to these growing eigenfunctions, as a mathematical construct, does answer the questions of interest: the absolute stability characteristics of a system. So, still, inquiring why the eigensolutions display their spatial growth is meaningful from the physical perspective.

The spatial growth can be interpreted kinematically, by considering the action of advection individually; discarding the action of diffusion. Figure 8.18 (a) regards the local kinetic energy associated to an eigenfunction, $|\tilde{w}|^2$,¹⁰ displaying spatial growth around a given location in the interior of the domain, $y = y_i$, at a given time instant. The energy portion that flows past the location $y = y_i$ during an elapsed time $\Delta t = \Delta y / \bar{V}_e > 0$, equals:

$$\int_{y_i - \Delta y}^{y_i} |\tilde{w}|^2 dy, \quad (8.40)$$

which is highlighted in figure 8.18 (a). After Δt , the independent action of advection, without diffusion, is to move the function to $|\tilde{w}(y - \bar{V}_e \Delta t)|^2$, which, due to the spatial growth, lies below $|\tilde{w}(y)|^2$. In fact:

$$|\tilde{w}(y - \bar{V}_e \Delta t)| = |\tilde{w}(y - \Delta y)| = e^{-\bar{V}_e \Delta y / 2\nu} |\tilde{w}(y)| = e^{-\bar{V}_e^2 \Delta t / 2\nu} |\tilde{w}(y)| < |\tilde{w}(y)|. \quad (8.41)$$

⁸For airliner conditions, cruising at $M = 0.8$, $\bar{U}_e = 274 \text{ m/s}$ and $L = 1 \text{ m}$, $e^{\bar{V}_e L/2\nu} = e^{9.80 \times 10^6} = 10^{10^{7.0}}$.

⁹The largest speed is the speed of light, $3.00 \times 10^8 \text{ m/s}$. Quantum mechanics does not produce a lower bound on a velocity, but instead one could consider the currently smallest speed possible to travel one Planck length: $1.67 \times 10^{-35} \text{ m}$, namely by dividing it into twice the Hubble age of the universe: $2 \times 4.35 \times 10^{17} \text{ s}$. This ratio equals: $1.92 \times 10^{-53} \text{ m/s}$. The ratio of the speed of light to this number turns out to be: 1.56×10^{62} , which is approximately $10^{100 \times 154}$ orders of magnitude too short.

¹⁰The factor $1/2$ in $e^{\bar{V}_e y/2\nu}$ signifies the fundamental quantity is the energy $|\tilde{w}|^2$, that grows as $e^{\bar{V}_e y/\nu}$.

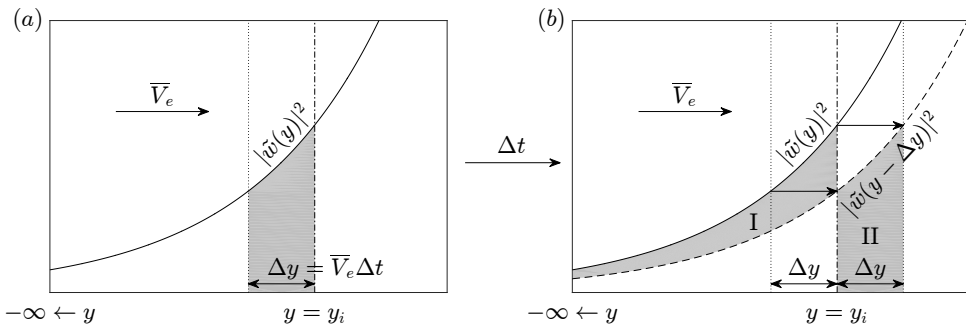


Figure 8.18: Eigenfunction representation of perturbation outflow. (a) Kinetic energy flowing through the interface $y = y_i$ in Δt (filled region). (b) After Δt , the total energy loss (region I), due to advection only, must equal the energy flown out of the domain (region II).

Given that $\tilde{w}(y)$ is exponential, the shape does not change by applying this operation, meaning the shifted $\tilde{w}(y - \bar{V}_e \Delta t)$ is a legitimate manifestation of $\tilde{w}(y)$ as an eigenfunction in time. In fact, this indicates how advection in the spatial amplification direction and a temporal decay are interlinked by kinematics.

Assuming the domain extends infinitely far in the negative y -direction, one can determine the total energy loss over the region with $y < y_i$ (the area of region I in figure 8.18 (b)):

$$\begin{aligned} \int_{-\infty}^{y_i} (|\tilde{w}(y)|^2 - |\tilde{w}(y - \Delta y)|^2) dy &= \int_{-\infty}^{y_i} |\tilde{w}(y)|^2 dy - \int_{-\infty}^{y_i - \Delta y} |\tilde{w}(y)|^2 dy \\ &= \int_{y_i - \Delta y}^{y_i} |\tilde{w}(y)|^2 dy \end{aligned} \quad (8.42)$$

The last step is allowed, because $|\tilde{w}|^2$ decays exponentially as $y \rightarrow -\infty$. The areas of regions I and II in figure 8.18 (b) are equal. So, in this case, the total energy loss (region I) is equal to the amount of energy that has propagated out of the domain $y \in (-\infty, y_i]$ (region II). This must be the case, because advection is by itself an energy conserving process.

For a hypothetical eigenfunction with a constant amplitude in y (considering a finite domain), the total energy loss (the area of region I) would be zero. However, advection would still remove energy through the truncation boundary. Energy therefore must be generated elsewhere. That kind of energy production is impossible in the current version of the model problem (constant coefficients and no-slip condition at $y = 0$). A similar argument applies for the hypothetical case where the eigenfunction decays in the streamwise direction. The spatial growth is thus required to satisfy the conservation of energy.

The combination of advection and boundary conditions requires the total energy in the considered domain to decay at every time instant; a temporal energy decay. Under the action of advection, the eigenfunctions can represent this by growing in space only. For advection terms imposing an inflow, the situation is reversed. The eigenfunction must then decay while entering.

It is important to note this temporal decay is required to represent the outflow through the truncation boundary. Eigenfunctions happen to have to represent this behaviour through spatial growth. Note that this effect could be avoided by letting the domain travel along with the perturbation (or with the base flow velocity), so that all advection imposing in-/outflow is removed from the transformed problem. These observations are reflected upon in the following subsection.

8.6.2. PHYSICAL INTERPRETATION OF SYMMETRIZATION

Next to the interpretation of the spatial growth in the solutions, an interpretation can be attached to the symmetrization method. This interpretation follows from the following observations.

Since there is no linear term in k in equation (8.28a), the real part of the phase and group speeds in the y -direction is zero. The \hat{w} solutions are *standing waves* in the y -direction, that decay in time according to the reaction terms in equation (8.25). This implies that a homogeneous Neumann boundary condition for \hat{w} would adhere exactly to the dynamics in the interior, for all possible $\hat{\Omega}(k)$ with $k \in \mathbb{R}$. This means that an ideal, interior-dynamics-consistent, boundary condition exists in this case.

While wave packets built with \hat{w} solutions are stationary, the multiplication with σ^{-1} reinstates advection. This can be illustrated with a wave packet with a Gaussian shape: $e^{-y^2/\Delta}$, where $\Delta > 0$ represents its width. One forms $\sigma^{-1} \hat{w}$ by weighting this shape by an exponentially growing function $\sigma^{-1} = e^{ay}$, with amplification rate $a > 0$. Using this, one can write:

$$\underbrace{e^{-y^2/\Delta}}_{\text{stationary wave packet that purely broadens as } \Delta \text{ increases}} \sigma^{-1} = e^{-y^2/\Delta} e^{ay} = \underbrace{e^{-(y - \frac{a}{2}\Delta)^2/\Delta}}_{\text{shifted original wave packet}} e^{\Delta a^2/4}. \quad (8.43)$$

So, the original Gaussian is shifted in position by the amount $a\Delta/2$ (while maintaining its shape) and amplified or attenuated by the factor $e^{\Delta a^2/4}$. Note that the latter scaling factor is constant in y ; it applies globally. By increasing the width Δ , the original wave packet only broadens. The action of σ (keeping it fixed) is to move the original Gaussian function in the growth direction. This situation is represented in figure 8.19 (a). So, the exponential weighting function makes a broadening standing wave packet move effectively in the direction in which σ^{-1} grows.

Note that, the original wave packet in this example is representative of \hat{w} and the resulting wave packet of $\tilde{w} = \sigma^{-1} \hat{w}$. The illustrated relative behaviour of \hat{w} and \tilde{w} can also be extracted from the difference in Ω and $\hat{\Omega}$. Their difference evaluates to:

$$\Omega(k) - \hat{\Omega}(k) = \left(k + i \frac{\bar{V}_e}{4\nu} \right) \bar{V}_e, \quad (8.44)$$

where the first term, $k\bar{V}_e$, represents the spatial shift due to advection. The second term, $i\bar{V}_e^2/4\nu$, represents the global scaling factor. In fact, a direct link with (8.43) can be made by setting $\Delta = 4\nu t$ and $a = \bar{V}_e/2\nu$. The term $a\Delta/2 = \bar{V}_e t$ then precisely denotes the expected spatial shift imposed by the advection due to \bar{V}_e , while $\Delta a^2/4 = \bar{V}_e^2 t/4\nu$ represents the global scaling factor.

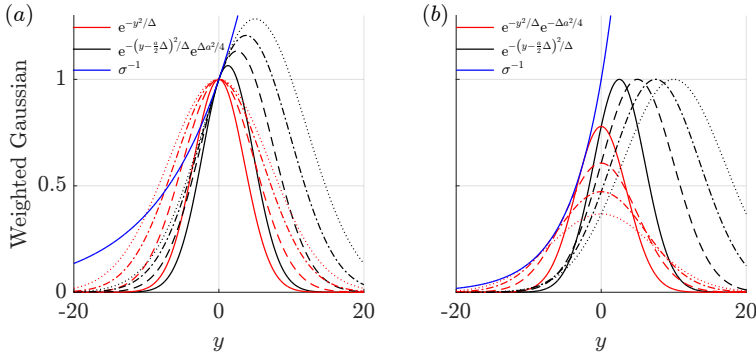


Figure 8.19: (a) Illustration that, by multiplying a “spreading” function (red lines, $\Delta = 25$ (solid), 50 (dashed), 75 (dash-dotted), 100 (dotted)) with an exponentially growing factor (blue line, $a = 0.1$) yields an effective movement of the resulting function (black lines) in the spatial growth direction. The red (blue) areas indicate the part where the exponential weight increases (decreases) with respect to the original function. (b) Illustration that multiplying a stationary “diffusing” function (red lines, same Δ ’s, $a = 0.2$) can result in a movement plus the spread of the resulting function.

These observations can be synthesized in the interpretation that symmetrization in this case corresponds to a (complex) Galilean transformation. By introducing the moving reference frame $(x, \hat{y}, \hat{t}) = (x, y - \bar{V}_e t, t)$, moving in the y -direction with the speed \bar{V}_e with respect to (x, y, t) :

$$e^{i[ky - \Omega(k)t]} = e^{i[k(y - \bar{V}_e t) - (\Omega(k) - k\bar{V}_e)t]} = e^{i[k\hat{y} - (\hat{\Omega}(k) + i\bar{V}_e^2/4v)\hat{t}]}, \quad (8.45)$$

see Briggs [30] for more details. The transformation is nearly equivalent to enforcing the parallel flow assumption, setting $\bar{V}_e \equiv 0$. Note that, instead subtly, only the effect of \bar{V} as an advection term is removed.

As an additional note, by considering a stationary wave packet that decays specifically like $e^{-\Delta a^2/4}$ while it broadens, i.e. it diffuses, one finds:

$$\underbrace{e^{-y^2/\Delta} e^{-\Delta a^2/4}}_{\text{stationary wave packet that diffuses as } \Delta \text{ increases}} \sigma^{-1} = \underbrace{e^{-(y - \frac{a}{2}\Delta)^2/\Delta}}_{\text{wave packet that advects and spreads with equal amplitude}}. \quad (8.46)$$

So, for this special arrangement of the original wave packet, the resulting wave packet will maintain its amplitude while it is advected in the growth direction of σ^{-1} and spreads simultaneously, see figure 8.19 (b).

As mentioned at the end of the previous subsection, note that the spectra $\Omega(k - i\bar{V}_e/2v)$ and $\hat{\Omega}(k)$ for $k \in \mathbb{R}$ are both indicative of the stability properties for the original, stationary, reference frame only. The weighted approach only applies the Galilean transformation “under the hood.” The original problem statement has to be adapted to consider a moving reference frame, the current approach can be adapted accordingly, which allows extracting insight about deploying moving reference frames directly.

Accounting for a reference frame moving with the constant speed c is done by adjusting both the governing equation (8.25) and the corresponding factor σ by substituting $\bar{V} - c$ for \bar{V} . By considering the equivalent of equation (8.25) that would result in the case of constant coefficients, it is straightforward to determine the solutions attain maximal temporal growth (minimal decay) for $c = \bar{V}_e$ in the considered moving reference frame. For the constant coefficient problem it can be moreover directly deduced from the adapted weight factor σ , that the spatial growth in the solution is minimized for $c = \bar{V}_e$.

This illustrates that the use of a moving reference frame is an effective methodology to eliminate the notorious spatial growth in the solutions, which is a (possibly) simple(r) aid in resolving the solutions numerically. For the non-constant coefficient problem, a spatially non-homogeneously moving reference frame can be considered. In fact, this is also what the factor σ^{-1} represents for a non-constant \bar{V} .

8.7. CONCLUSION

In this chapter, we propose a method to properly represent linear localized perturbations with a basis consisting of continuum modes on a finite but large domain, representing the dynamics on the infinite domain. This is a first step towards consistently representing such perturbations in the BiGlobal stability approach.

Two solution methods are presented in the literature, using different truncation boundary conditions. Predominantly, the original problem formulation is considered with separated (e.g. Robin) boundary conditions, see Ehrenstein and Gallaire [5], Alizard and Robinet [6], Rodríguez *et al.* [9], Åkervik *et al.* [31]. Attaining convergence of the spectrum is troublesome, because the modes grow exponentially toward the in- and outflow boundaries. They hence display a sensitive dependency on the choice for the truncation boundary condition. In a second approach, the problem is artificially periodized, which is equivalent to introducing a fringe/sponge layer, for examples see Brynjell-Rahkola *et al.* [7], Bertolotti *et al.* [11]. This only alleviates the spectrum convergence problems and the problem is inherently changed, while it is unknown whether the solutions are affected by this locally in space only.

To overcome the spectrum convergence problems, in the currently proposed method the localized perturbations are built using the modes from the absolute spectrum, obtained by imposing *any* separated boundary condition. These modes grow exponentially in space as a consequence of the combination of advection and flow inhomogeneity. To ensure convergence for all domain lengths L , a weighted problem formulation is used.

Apart from providing the building blocks for the spatial part, the absolute spectrum provides stability properties of the least stable wave packet. If the least stable wave packet is unstable, the problem supports an absolutely unstable perturbation in the reference frame considered.

As a first step, the non-parallel Squire equation is considered as model problem, because it is representative of problems displaying convective properties. Imposing a boundary layer profile as the base flow yields solutions that rapidly decay inside the boundary layer, see Grosch and Salwen [3], Maslowe and Spiteri [26]. This shows that the Dirichlet condition in the constant coefficient problem represents explicit flow inhomogeneity. Flow inhomogeneity can thus be accommodated explicitly, through a non-

constant profile shape, or implicitly, by imposing separated boundary conditions.

Sandstede and Scheel [12, cf. theorems 5 and 4] prove that using separated and periodic boundary conditions yields, respectively, the so called absolute and essential spectrum limits for generic one-dimensional problems as $L \rightarrow \infty$. This proves that *the continuous spectrum does converge* to one of these limits. The absolute spectrum contains branch points and is therefore interpretable in light of Briggs's criterion for absolute instability, i.e. an absolute instability is supported only if the absolute spectrum is unstable, see Schmid and Henningson [10], Briggs [30], Huerre and Monkewitz [32], Brevdo [33]. Spectra other than the absolute spectrum do not, in general, contain branch points, rendering Briggs's criterion inapplicable. This reflects that the classification of absolute or convective perturbations breaks down for periodic problems. If a computed spectrum of a global stability problem does not display a branch point, the absolute or convective nature of the perturbation cannot be directly deduced.

Using the weighted problem formulation, no numerical inaccuracies are encountered and the spectrum always converges to the absolute spectrum as $L \rightarrow \infty$, which is in accordance with theorem 5 of Sandstede and Scheel [12]. The discrete modes in the original and weighted formulation are identical weighted equivalents.

Solving the original, unweighted formulation of a global stability problem corresponding to a domain with a length L that exceeds a threshold value, L_{th} , the spectrum converges to the, according to Sandstede and Scheel [12] incorrect, essential spectrum as $1/L$. The convergence is very slow, it has an algebraic rate. Furthermore, the essential spectrum does not result in the growth rate nor does it indicate the absolute/convective nature of the least stable wave packet, see Briggs [30]. Low pseudospectrum levels indicate the essential spectrum bound convergence in this formulation. For $L > L_{th}$, adapted spatial growth rates are observed, explaining the consistency with LST and PSE (see Alizard and Robinet [6], Rodríguez *et al.* [9]): the global solutions are spatio-temporal solutions evaluated at a slowly decreasing spatial growth rate. Periodized problems with non-zero flow inhomogeneity also approach the essential spectrum as $L \rightarrow \infty$, at the same algebraic rate, in accordance with Sandstede and Scheel [12]. The essential spectrum bound convergence cannot be avoided by imposing different boundary conditions.

A wave packet is Fourier expanded with modes obtained with different problem formulations. For unweighted formulations, the expansions diverge exponentially as $y \rightarrow L$ for $L > L_{th}$. Only if $L < L_{th}$, the change in formulations represents a numerically consistent change of basis. The weighted formulation yields converging expansions as $y \rightarrow L$, even for $L \gg L_{th}$. An outflow boundary layer cannot be circumvented, whose spatial extent is indicated by the weighting factor of the ansatz.

Extending the proposed method to the complete two-dimensional BiGlobal stability problem allows the computation of the absolute spectrum corresponding to a given base flow. This spectrum allows the direct identification of whether absolutely unstable perturbations to the base flow are supported in the given reference frame. For many flow problems this is an open question.

Global pressure effects are excluded in the currently considered model problem, a next step is to test the proposed approach for models that incorporate such effects. It is recommended to involve the complete two-dimensional BiGlobal stability problem in that regard. Further studies involve the use of the weighted problem formulation for

non-linear perturbation problems.

REFERENCES

- [1] F. Alizard, *Etude de stabilité linéaire globale d'écoulement fortement décollé de couche limite de plaque plane*, Ph.D. thesis, L'École Nationale Supérieure d'Arts et Métiers, Paris, France (2007).
- [2] K. J. Groot, *Derivation of and Simulations with BiGlobal Stability Equations*, M.Sc. thesis, Delft University of Technology, The Netherlands (2013).
- [3] C. E. Grosch and H. Salwen, *The continuous spectrum of the Orr-Sommerfeld equation. part 1. the spectrum and the eigenfunctions*, J. Fluid Mech. **87**, 33 (1978).
- [4] W. Coenen, L. Lesshafft, X. Garnaud, and A. Sevilla, *Global instability of low-density jets*, Journal of Fluid Mechanics **820**, 187 (2017).
- [5] U. Ehrenstein and F. Gallaire, *On two-dimensional temporal modes in spatially evolving open flows: the flat-plate boundary layer*, Journal of Fluid Mechanics **536**, 209 (2005).
- [6] F. Alizard and J. C. Robinet, *Spatially convective global modes in a boundary layer*, Physics of Fluids **19**, 114–105 (2007).
- [7] M. Brynjell-Rahkola, N. Shahriari, P. Schlatter, A. Hanifi, and D. S. Henningson, *Stability and sensitivity of a cross-flow-dominated Falkner-Skan-Cooke boundary layer with discrete surface roughness*, Journal of Fluid Mechanics **826**, 830 (2017).
- [8] V. Theofilis, *Advances in global linear instability analysis of nonparallel and three-dimensional flows*, Progress in Aerospace Sciences **39**, 249 (2003).
- [9] D. A. Rodríguez, A. Tumin, and V. Theofilis, *Towards the foundation of a global modes concept*, 6th AIAA Theoretical Fluid Mechanics Confer., 1 (2011).
- [10] P. J. Schmid and D. S. Henningson, *Stability and Transition in Shear Flows* (Springer Verlag, 2001).
- [11] F. P. Bertolotti, T. Herbert, and P. R. Spalart, *Linear and nonlinear stability of the blasius boundary layer*, Journal of Fluid Mechanics **242**, 441 (1992).
- [12] B. Sandstede and A. Scheel, *Absolute and convective instabilities of waves on unbounded and large bounded domains*, Physica D: Nonlinear Phenomena **145**, 233 (2000).
- [13] M. Bouthier, *Sur la stabilité des écoulements non parallèles et le specre continu*, C. R. Acad. Sc. Paris **296** (1983).
- [14] S. C. Reddy and L. N. Trefethen, *Pseudospectra of the convection-diffusion operator*, SIAM Journal on Applied Mathematics **54**, 1634 (1994).

- [15] T. Kapitula and K. Promislow, *Spectral and dynamical stability of nonlinear waves* (Springer, 2013).
- [16] R. Haberman, *Applied Partial Differential Equations: With Fourier Series and Boundary Value Problems* (Pearson Education, Limited, 2012).
- [17] C. Canuto, M. Hussaini, A. Quarteroni, and T. Zang, *Spectral Methods - Fundamentals in Single Domains* (Springer Verlag, Berlin, 2006).
- [18] J. Weideman and S. Reddy, *A matlab differentiation matrix suite*, ACM Trans. Math. Softw. **26**, 465 (2000).
- [19] G. H. Golub and C. F. Van Loan, *Matrix Computations* (Johns Hopkins University Press, 1996).
- [20] L. N. Trefethen and M. Embree, *Spectra and pseudospectra: the behavior of nonnormal matrices and operators* (Princeton University Press, 2005).
- [21] L. Lesshafft, *Artificial eigenmodes in truncated flow domains*, arXiv preprint arXiv:1704.08450 (2017).
- [22] D. A. Rodríguez, *Global Instability of Laminar Separation Bubbles*, Ph.D. thesis, Universidad Politécnica de Madrid (2010).
- [23] E. Anderson, Z. Bai, C. Bischof, L. S. Blackford, J. Demmel, J. J. Dongarra, J. Du Croz, S. Hammarling, A. Greenbaum, A. McKenney, and D. Sorensen, *LAPACK Users' guide (third ed.)* (Society for Industrial and Applied Mathematics, Philadelphia, 1999).
- [24] B. N. Antar and J. A. Benek, *Temporal eigenvalue spectrum of the Orr–Sommerfeld equation for the Blasius boundary layer*, Physics of Fluids **21**, 183 (1978).
- [25] P. R. Spalart, R. D. Moser, and M. M. Rogers, *Spectral methods for the Navier-Stokes equations with one infinite and two periodic directions*, Journal of Computational Physics **96**, 297 (1991).
- [26] S. A. Maslowe and R. J. Spiteri, *The continuous spectrum for a boundary layer in a streamwise pressure gradient*, Physics of Fluids **13**, 1294 (2001).
- [27] J.-M. Chomaz, *Global instabilities in spatially developing flows: non-normality and nonlinearity*, Annu. Rev. Fluid Mech. **37**, 357 (2005).
- [28] R. Munafo, *Notable properties of specific numbers*, <http://mrob.com/pub/math/numbers-19.html> (2018), accessed: 2018-05-10.
- [29] C. E. Shannon, *Programming a computer for playing chess*, in *Computer Chess Compendium*, edited by D. Levy (Springer New York, New York, NY, 1988) pp. 2–13.
- [30] R. Briggs, *Electron-stream Interaction with Plasmas*, M.I.T. Press research monographs (M.I.T. Press, 1964).

- [31] E. Åkervik, U. Ehrenstein, F. Gallaire, and D. S. Henningson, *Global two-dimensional stability measures of the flat plate boundary-layer flow*, European Journal of Mechanics B/Fluids **27**, 501 (2008).
- [32] P. Huerre and P. A. Monkewitz, *Absolute and convective instabilities in open shear layers*, Journal of Fluid Mechanics **159**, 151 (1985).
- [33] L. Brevdo, *Three-dimensional absolute and convective instabilities, and spatially amplifying waves in parallel shear flows*, Zeitschrift für angewandte Mathematik und Physik ZAMP **42**, 911 (1991).

9

CONCLUSION

Flow stability theory is concerned with the description of small perturbations to laminar flows. The BiGlobal stability method applies to flow cases that display dominant dimensionality in two spatial directions. The corresponding perturbations are governed by a system of partial differential equations, that, together with the boundary conditions, form an eigenvalue problem. The eigenvalue represents either the exponential growth rate of the perturbations in time or space. The eigenfunction represents the flow structure of the perturbation.

This thesis focusses on two problematic aspects of this specific stability methodology. The first involves the application of the theory to measured base flows. Specifically, incompressible mean flows representing free shear layers are considered, that are measured through experimental means. The second involves the convergence issues of the eigenvalue spectrum associated to streamwise BiGlobal analyses.

9.1. MEASURED BASE FLOWS

The first central question of this thesis is whether the BiGlobal stability method can be successfully applied to experimentally measured flows. This aspect is approached in two ways. First, it is briefly touched upon in a computational way and, second, it is considered in great detail concerning two linked experimental campaigns executed and published separately.

9.1.1. ANALYTICAL GENERIC SHEAR PROFILES

The computational approach involves the well-established one-dimensional analysis of a hyperbolic tangent profile, which is a model representation of a free shear layer. This case is considered to obtain detailed information on both physical effects and expected effects due to the methodology of using measured base flows.

The considered experimental base flow cases also essentially represent free shear layers, so this model problem allows building a basic understanding of the typical Kelvin-Helmholtz mechanism. This mechanism extracts perturbation energy from the base

flow shear via a Reynolds stress term and redistributes the energy via pressure-strain effects. It is illustrated how this information can be extracted from the solutions by inserting them into the governing equations. Furthermore, the impact of the location of the inflection point relative to the center of the shear layer, viscosity, a non-zero spanwise wavenumber and the presence of a wall on the stability properties were identified. With the exception of extreme cases, all effects are found to have a stabilising influence.

The methodological effects that come into play when using a measured base flow are assessed. In particular, the effects associated to PIV measurements are indicated. It is assumed throughout this thesis that the “mean = base flow”-hypothesis holds, i.e. that the time-averaged flow is a good approximation of the laminar base flow. The assessed effects are: the spatial smoothing, limited spatial resolution and the presence of physical perturbations in the instantaneous flow. Ordered from most to least important, it is found that:

- *spatial smoothing of the base flow*: establishes a significant stabilising effect for the cases considered in this thesis; the main underlying mechanisms are conserved, but the presence of spatial smoothing establishes the requirement of validating the stability results with the instantaneous experimental data, especially in the case of asymmetric shear layers
- *spatial resolution of the base flow*: can be approached by computing the spatial derivatives of the base flow with higher order finite differences and interpolating the base flow onto the grid used for the stability analysis; this yields a better approximation of the shear at the inflection point
- *residual zero-mean perturbations on the base flow*: have a small impact and the related error can converge faster than the expected rate of $1/\sqrt{N_{fr}}$, where N_{fr} denotes the number of instantaneous ‘snapshots’ of the flow field.

An outlook with respect to this model problem is the generalisation to two dimensions. It is suggested to construct velocity fields representative of typical isolated shear layers, such as those considered in the micro-ramp and crossflow vortex cases, to study the additional effects associated to the higher dimensional case. Based on the finding that the underlying mechanisms are robust to changes of details in one-dimensional profiles, it is moreover suggested to prioritise considering general, though representative, velocity profiles over their satisfaction of the Navier-Stokes equations. This favours the creation of a knowledge database that is useful in general. This is needed in addition to the case-specific information presented in the current literature.

9.1.2. MICRO-RAMP WAKE

The wake of the micro-ramp is the first case involving experimental data. The BiGlobal stability method is applied successfully. The expected instability modes, the varicose and sinuous modes, are retrieved.

A challenge is the significant amplitude of the observed perturbations close to the ramp, which could significantly distort the stability results. It is found, however, that the stability results converge with the number of instantaneous snapshots used for the mean flow. The main coherent structure, in terms of POD modes in and the instantaneous

fields of the measurement data, is found to have a hairpin shape and this is retrieved within the varicose mode. The most unstable wavelength matches with the experiment. Limited amplification factors (N -factors) are retrieved, which is expected, because the wake does not transition to turbulence in the considered region of the flow.

It is found that the BiGlobal stability characteristics closely match LST simulations applied exclusively to the centerline profile only. In this case, the spanwise confinement to the shear layer is modelled by imposing a spanwise wavenumber; which imposes a highly stabilising effect to the mode. Accordingly, the following effects could be decomposed in order of decreasing importance. First, the net shear value drives the perturbations essentially, the spanwise wavenumber imposes a strong stabilising effect, viscosity has a significant impact in reducing the instability mechanism and, lastly, the profile shape proximity to the wall is of inferior significance.

An outlook with respect to this case is to compare the results to the stability analysis of a direct numerical simulation (DNS). This allows validating the analysis and identify which specific solution features are conserved in this two-dimensional case. Furthermore, successfully comparing the computational and experimental data on the level of the stability results is unprecedented.

9.1.3. CROSSFLOW VORTICES

The second experimental case involve crossflow vortices in a swept-wing boundary layer. The challenge in this case is the complicated topology of the base flow, which supports 3 instability mechanisms. The spanwise BiGlobal method is also successfully applied in this case. All 3 structurally complicated instability modes, type I, II and III, are recovered from the measured base flow field. The type III instability is located close to the wall. Therefore, in anticipation of being subject to uncertainty of the base flow data near the wall, it is discarded from further analysis.

The type I instability, which is found as a coherent structure (POD mode) in the experimental data, is successfully compared against the spatial structure of the eigenmode with the same wavelength. The spatial growth rate of this mode underestimates the growth extracted from the POD mode, but it matches the growth rate based on hot-wire measurements.

The uncertainty of the stability results is assessed by deploying a Monte-Carlo approach. The mean and the fluctuation of the stability results converges and decreases, respectively, as the number of snapshots is increased. The type I mode, in particular, is determined to be structurally sound in terms of the fluctuations in the Reynolds-Orr terms. The characteristics of the type II mode also converge, but they are found to be more sensitive.

The Kelvin-Helmholtz nature of both type I and II modes is verified by artificially increasing the Reynolds number. Viscosity is found to have a significant influence at nominal conditions.

Via the Reynolds-Orr equation, the shear component primarily responsible for the type I (spanwise) and type II mode (wall-normal) is identified and matches with the literature. These results are extended to assess the effect of the in-plane advection (i.e. the flow orthogonal to the vortical axis). The in-plane flow forms a saddle point in the shear layer housing the type I instability, which imposes a relative structural robustness for

the type I mode, because it locks the location of the maximum perturbation energy at the saddle point.

Although the wall-normal shear is primarily responsible for the production of the type II mode, the spanwise shear controls its nature most sensitively, being strongly correlated to a spanwise movement of the type II eigenfunctions. In particular, it is found that the crossflow vortex strength is communicated primarily through the spanwise shear for both modes I and II, although, again, that is not the strongest production term for mode II. This is found both in the context of the uncertainty quantification and the analysis of a weaker vortex. The absence of the saddle point structure in the in-plane flow for the type II mode corroborates the higher sensitivity of the type II mode as opposed to the type I mode.

From the perspective of the methodology of applying the BiGlobal stability method to measured base flow, this case clearly demonstrates a success and further potential. Although obstacles have to be overcome in establishing the validity of the results on a case to case basis, this process can reveal new insights into the nature of the pertinent instability mechanisms. In this way, the methodology extends the experimental measurability.

An outlook regarding this specific case is performing the analysis of more complicated flows; in cases where computational approaches are very challenging, for example, such as the situation where crossflow vortices merge.

Together, the conclusions for the individual model problems establish the applicability of the BiGlobal stability theory to measured base flows.

9.2. THE STREAMWISE BiGLOBAL PROBLEM

When representing convective instability modes in a streamwise BiGlobal formulation, the modes appear as a continuum in the eigenvalue spectrum. An important question this methodology should be able to resolve is whether absolute instabilities are supported in a given case. Absolutely unstable perturbations propagate both in the upstream and downstream direction, while growing in time.

This information can be extracted only from branch points of the continuous frequency spectrum, i.e. parts that form a cusp shape. That is, if a computed spectrum does not contain a branch point, it does not yield information on the absolute instability characteristics of the system. Moreover, if the continuous spectrum is unstable, but it does not display branch points in the unstable half-plane, the spectrum *does not* indicate an absolute (or global) instability mechanism.

Literature indicates that numerical solutions are sensitive to the size of the domain. The combination of advection and base flow inhomogeneity in the advection direction is identified as a principal contributing feature, because it enforces solutions to grow exponentially in space. This causes numerical problems if the domain is too large. The advection-induced-growth can be identically factored out of the problem by applying the proposed weighted formulation of the problem. Using a representative one-dimensional model problem, the computed spectrum converges to the analytical solution, even for extremely long domain lengths.

The mathematical literature indicates that the absolute spectrum, that per definition

contains branch points, is obtained when applying separated boundary conditions, i.e. *any* Robin type boundary condition that does not link the information of the in- and outflow boundary. If the weighted problem formulation is not used, the spectrum diverges from the absolute spectrum and approaches the essential spectrum. The latter spectrum does not contain branch points in general. Interestingly, the essential spectrum is the correct mathematical limit if periodic boundary conditions are prescribed.

The working principle of the weighted approach is to transform the reference frame into one having a local speed equal to the most dangerous (streamwise) velocity component of the base flow. This renders these waves, that would otherwise be advected by the base flow, stationary. This indicates that transforming to a uniformly moving reference frame at an effective convection speed of the perturbations of interest can already solve the numerical issues due to advection-induced-growth.

These conclusions identify an important cause underlying the convergence problem encountered in the streamwise BiGlobal stability problem and a solution is proposed accordingly.

Although this thesis considers a model problem only, the results are directly generalisable to the full two-dimensional problem, which serves as an important outlook. In a first endeavour, the global absolute stability of the Blasius boundary layer should be demonstrated. Thereafter, unanswered questions can be approached, such as whether laminar separation bubbles or the flow around steps support global absolute stability mechanisms.

A

COMPLEX INTEGRATION THEORY

In this appendix, the essential aspects of complex integration theory are reviewed. In particular, the Fourier inversion of a constant coefficient system,

$$D \left(-i \frac{d}{dx} \right) q'(x) = 0, \quad (\text{A.1})$$

is discussed, where $D(-id/dx)$ is a differential operator acting on the solution $q'(x)$, where $x \in \mathbb{R}$. The attention is restricted to integrals of meromorphic functions, i.e. functions whose singularities in the complex plane are simple poles only. An example of a differential operator that yields such integrals is:

$$D \left(-i \frac{d}{dx} \right) = \left(\frac{d}{dx} - \xi_1 \right) \left(\frac{d}{dx} - \xi_2 \right) \cdots \left(\frac{d}{dx} - \xi_n \right), \quad (\text{A.2})$$

where $\xi_j = a_j + ib_j$ are n complex scalars, with $a_j, b_j \in \mathbb{R}$.

The Green's function for this problem satisfies:

$$D \left(-i \frac{d}{dx} \right) G(x - x') = \delta(x - x'), \quad (\text{A.3})$$

where x' is a reference point in x .

The differential equation has constant coefficients, so the problem can be Fourier-transformed without introducing convolution integrals; the resulting expressions are algebraic. Handling algebraic expressions is significantly simpler than differential ones, so Fourier transforming the problem is an attractive approach to finding solutions to equation (A.3).

The Fourier transform ansatz pair can be stated as follows:

$$\tilde{G}(\xi) = \int_{-\infty}^{\infty} G(x - x') e^{-i\xi(x-x')} dx; \quad (\text{A.4a})$$

$$G(x - x') = \int_{-\infty}^{\infty} \tilde{G}(\xi) e^{i\xi(x-x')} \frac{d\xi}{2\pi}, \quad (\text{A.4b})$$

A

where equations (A.4a) and (A.4b) are referred to as the (forward) Fourier transform and the inverse Fourier transform, respectively, see Kwok [1], equations (6.4.1) and (6.4.6)] or, for more details, Tolstov [2].

In transforming equation (A.3), it is multiplied with $e^{-i\xi(x-x')}$ and integrated over the real line. The integration contour is also referred to as the Bromwich contour, see Kwok [1], McLachlan [3]; its manipulation is a major aspect in this appendix. The terms involving the derivatives of G are integrated by parts until the equation is an algebraic function of $\tilde{G}(\xi)$. In the process of integrating by parts, $G(x-x')$ and its derivatives up to the $(n-1)^{\text{th}}$ order are to be evaluated as $x-x' \rightarrow \pm\infty$. It is imposed that these terms are zero. This can only be ensured if

$$G(x-x'), \frac{dG}{dx}, \dots, \frac{d^{n-1}G}{dx^{n-1}} \rightarrow 0 \text{ exponentially, as: } |x-x'| \rightarrow \infty. \quad (\text{A.5})$$

These are implicit ‘boundary’ conditions. Accordingly, the Fourier transformation of equation (A.3) becomes:

$$\tilde{\mathcal{D}}(\xi)\tilde{G}(\xi) = (\xi - \xi_1)(\xi - \xi_2) \cdots (\xi - \xi_n)\tilde{G}(\xi) = \int_{-\infty}^{\infty} \delta(x-x')e^{-i\xi(x-x')} = e^{-i\xi \cdot (x'-x')} = 1. \quad (\text{A.6})$$

Note that the ξ_j 's are the zeros of:

$$\tilde{\mathcal{D}}(\xi) = (\xi - \xi_1)(\xi - \xi_2) \cdots (\xi - \xi_n). \quad (\text{A.7})$$

Equation (A.6) is an entirely algebraic expression, so it can be rewritten as follows:

$$\tilde{G}(\xi) = \frac{1}{\tilde{\mathcal{D}}(\xi)}. \quad (\text{A.8})$$

With equation (A.8), the inverse Fourier transform (A.4b) becomes:

$$G(x-x') = \int_{-\infty}^{\infty} \frac{e^{i\xi(x-x')}}{\tilde{\mathcal{D}}(\xi)} \frac{d\xi}{2\pi}. \quad (\text{A.9})$$

Due to the x -independency of the coefficients, Green's function can be freely translated in x . The reference station x' is translated to the origin for convenience, i.e. $x' = 0$. It is important to remember that a Green's function corresponds to the isolated response due to an impulsive forcing originating at any chosen x' .¹ Applying the $x' = 0$ translation to equation (A.9) yields:

$$G(x) = \int_{-\infty}^{\infty} \frac{e^{i\xi x}}{\tilde{\mathcal{D}}(\xi)} \frac{d\xi}{2\pi}. \quad (\text{A.10})$$

The goal of this appendix is to develop the required theory to find an expression for the integral (A.10) and understand its behaviour. This is divided over 3 sections:

- First, the line integral is truncated and closed in the complex plane. The resulting contour integral can be decomposed into contributions from the contour integrals around the zeros of $\tilde{\mathcal{D}}$

¹Note that, for more general forcing functions than $\delta(x-x')$ in equation (A.3), the numerator of the right-hand side fraction will contain the Fourier transform of that particular forcing function.

- Second, a general expression is given for each such single contour integral, allowing to piece together the total integral. The link with the discrete mode ansatz (the ansatz commonly used throughout the field of stability analysis) is made; indicating the implied restriction of the dynamics
- Third, situations are analysed in which the zeros of $\tilde{\mathcal{D}}$ intersect (or move onto) the integration contour. Depending on the situation considered, the integral yields different kinds of singular behaviour, the understanding of which explains the required course of action in chapter 7

The main reference, that is highly recommended for engineers, is the book by Kwok [1].

A.1. DECOMPOSING COMPLEX INTEGRALS

To decompose integral (A.10), some tools are required. The most important one is the:

A.1.1. CAUCHY-GOURSAT THEOREM

This theorem states that the integral over a closed contour that encloses a region in the complex plane in which the integrand is *holomorphic* evaluates to zero. The latter term requires some elaboration.

Consider the complex function $f = u + iv$ of the complex variable $z = x + iy$, where $u = u(x, y)$ and $v = v(x, y)$ are the real and imaginary parts of f and x and y are the real and imaginary parts of z . In general, a complex function f depends on x and y . Alternatively, its dependency can be expressed in terms of z and its complex conjugate: $\bar{z} = x - iy$. Note that $x = (z + \bar{z})/2$ and $y = (z - \bar{z})/2i$. This allows expressing the following relations between the partial derivatives of f with respect to z , \bar{z} , x and y :

$$\frac{\partial f(z, \bar{z})}{\partial x} = \frac{\partial f}{\partial z} \frac{\partial z}{\partial x}^1 + \frac{\partial f}{\partial \bar{z}} \frac{\partial \bar{z}}{\partial x}^1 = \frac{\partial f}{\partial z} + \frac{\partial f}{\partial \bar{z}} \Rightarrow \frac{\partial}{\partial x} = \frac{\partial}{\partial z} + \frac{\partial}{\partial \bar{z}} \quad (\text{A.11a})$$

$$\frac{\partial f(z, \bar{z})}{\partial y} = \frac{\partial f}{\partial z} \frac{\partial z}{\partial y}^i + \frac{\partial f}{\partial \bar{z}} \frac{\partial \bar{z}}{\partial y}^{-i} = i \frac{\partial f}{\partial z} - i \frac{\partial f}{\partial \bar{z}} \Rightarrow \frac{\partial}{\partial y} = i \left(\frac{\partial}{\partial z} - \frac{\partial}{\partial \bar{z}} \right) \quad (\text{A.11b})$$

$$\frac{\partial f(x, y)}{\partial z} = \frac{\partial f}{\partial x} \frac{\partial x}{\partial z}^{\frac{1}{2}} + \frac{\partial f}{\partial y} \frac{\partial y}{\partial z}^{\frac{1}{2i}} = \frac{1}{2} \frac{\partial f}{\partial x} - \frac{i}{2} \frac{\partial f}{\partial y} \Rightarrow \frac{\partial}{\partial z} = \frac{1}{2} \left(\frac{\partial}{\partial x} - i \frac{\partial}{\partial y} \right) \quad (\text{A.11c})$$

$$\frac{\partial f(x, y)}{\partial \bar{z}} = \frac{\partial f}{\partial x} \frac{\partial x}{\partial \bar{z}}^{\frac{1}{2}} + \frac{\partial f}{\partial y} \frac{\partial y}{\partial \bar{z}}^{-\frac{1}{2i}} = \frac{1}{2} \frac{\partial f}{\partial x} + \frac{i}{2} \frac{\partial f}{\partial y} \Rightarrow \frac{\partial}{\partial \bar{z}} = \frac{1}{2} \left(\frac{\partial}{\partial x} + i \frac{\partial}{\partial y} \right) \quad (\text{A.11d})$$

The function f is holomorphic in a particular region if it is complex differentiable in every point of this region, see Kwok [1, definition 2.5.1]. If this is the case, the function's partial derivative with respect to \bar{z} , $\partial f / \partial \bar{z}$, is identically zero² in that region, see Kwok [1, §2.4 and equation (2.4.5)]. The converse is not true in general. The satisfaction of $\partial f / \partial \bar{z} = 0$ does not imply the differentiability of f ; it is a necessary condition only.

²This justifies the use of regular d's instead of partial ∂'s to indicate the derivative of a complex function. The statement $df(z)/dz$ then automatically incorporates the assumption that $f(z)$ is complex differentiable.

A

Using equation (A.11d), this relationship can be expressed in terms of u and v :

$$2 \frac{\partial f}{\partial \bar{z}} = \frac{\partial u}{\partial x} + i \frac{\partial v}{\partial x} + i \left(\frac{\partial u}{\partial y} + i \frac{\partial v}{\partial y} \right) = \frac{\partial u}{\partial x} - \frac{\partial v}{\partial y} + i \left(\frac{\partial v}{\partial x} + \frac{\partial u}{\partial y} \right) = 0. \quad (\text{A.12})$$

Imposing the relationship for both the real and imaginary parts (note: u and v are real per definition) of this expression yields the Cauchy-Riemann equations:

$$\frac{\partial u}{\partial x} - \frac{\partial v}{\partial y} = 0; \quad \frac{\partial u}{\partial y} + \frac{\partial v}{\partial x} = 0. \quad (\text{A.13})$$

This information is very useful in the evaluation of contour integrals. A complex contour integral can be written as follows:

$$\oint_{\Gamma} f(z) dz = \oint_{\Gamma} (u + iv)(dx + idy) = \oint_{\Gamma} (u dx - v dy) + i \oint_{\Gamma} (v dx + u dy), \quad (\text{A.14})$$

where Γ is an integration contour that encloses a region in the complex plane. By applying Green's theorem, the contour integrals can be replaced by area integrals over the region enclosed by Γ :

$$\oint_{\Gamma} f(z) dz = \iint_{\Gamma} \left(\frac{\partial u}{\partial y} + \frac{\partial v}{\partial x} \right) dx dy + i \iint_{\Gamma} \left(\frac{\partial u}{\partial x} - \frac{\partial v}{\partial y} \right) dx dy. \quad (\text{A.15})$$

Now, if f is holomorphic in the region enclosed by Γ , the Cauchy-Riemann equations (A.13) apply, so the integrands in (A.15) evaluate to zero everywhere. This causes both surface integrals and also the original contour integral to evaluate to zero.

By applying Green's theorem, continuity of the integrand is assumed. This is Cauchy's version of the proof, see Kwok [1, theorem 4.2.1]. Goursat extended the result to general holomorphic functions, see Kwok [1, theorem 4.2.2]. So, in summary:

$$\textbf{Cauchy-Goursat theorem:} \quad \oint_{\Gamma} f(z) dz = 0, \quad \begin{matrix} \text{if } f \text{ is holomorphic in the} \\ \text{region enclosed by } \Gamma. \end{matrix} \quad (\text{A.16})$$

Functions that are holomorphic on the whole complex plane are referred to as *entire*. Examples of entire functions are the exponential function, so the partial derivative with respect to \bar{z} must evaluate to zero:

$$\frac{\partial e^{iaz}}{\partial \bar{z}} = \left(\frac{\partial}{\partial x} + i \frac{\partial}{\partial y} \right) e^{iaz} (ia + i(-a)) = 0. \quad (\text{A.17})$$

The same holds for all finite order polynomials. So, for any integer p :

$$\begin{aligned} \frac{\partial z^p}{\partial \bar{z}} &= \left(\frac{\partial}{\partial x} + i \frac{\partial}{\partial y} \right) \sum_{k=0}^p \binom{p}{k} x^{p-k} (iy)^k \\ &= \sum_{k=0}^{p-1} \binom{p}{k} (p-k) x^{p-k-1} (iy)^k + i \sum_{k=1}^p \binom{p}{k} x^{p-k} ik (iy)^{k-1} \\ &= \sum_{k=0}^{p-1} \left[\binom{p}{k} (p-k) - \binom{p}{k+1} (k+1) \right] x^{p-k-1} (iy)^k = 0, \end{aligned} \quad (\text{A.18})$$

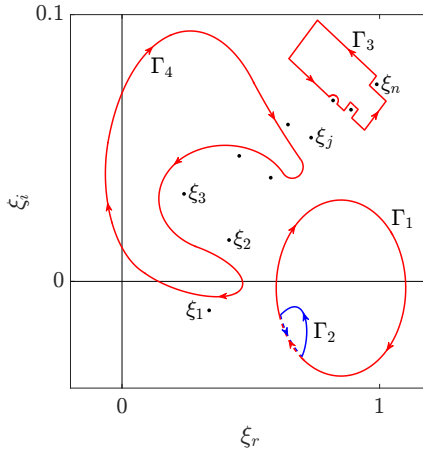


Figure A.1: Locations of the zeros of $\tilde{\mathcal{D}}(\xi)$, ξ_j , in the ξ -plane and examples of integration contours Γ_k , with $k = 1, \dots, 4$, over which the contour integral evaluates to zero.

where the sums are merged by redefining $k \mapsto k + 1$ in the second sum. The evaluation of equation (A.18) to zero follows when using the definition of the binomial coefficients:

$$\binom{p}{k+1} = \frac{p!}{(k+1)!(p-k-1)!} = \frac{p!}{(k+1)k!\frac{(p-k)!}{p-k}} = \frac{p-k}{k+1} \binom{p}{k}. \quad (\text{A.19})$$

The current integrand, $e^{i\xi x}/\tilde{\mathcal{D}}(\xi)$, consists of the exponential function divided by a polynomial. This function is holomorphic everywhere except at the zeros of $\tilde{\mathcal{D}}(\xi)$. By applying the quotient rule, one therefore finds:

$$\frac{\partial}{\partial \xi} \left[\frac{e^{i\xi x}}{\tilde{\mathcal{D}}(\xi)} \right] = \frac{\tilde{\mathcal{D}}(\xi) \frac{\partial e^{i\xi x}}{\partial \xi} - e^{i\xi x} \frac{\partial \tilde{\mathcal{D}}}{\partial \xi}}{\tilde{\mathcal{D}}^2(\xi)} = 0, \quad (\text{A.20})$$

where the derivatives in the numerator evaluate to zero due to the previous findings. This suggests the integrand is holomorphic in the whole plane. However, in applying the quotient rule, it is inherently assumed that the denominator is non-zero. At the zeros of $\tilde{\mathcal{D}}(\xi)$, in fact, the integrand is not differentiable and therefore not holomorphic. From these facts it can be deduced that, when executing a contour integral around any region that does not enclose any zero(s) of $\tilde{\mathcal{D}}(\xi)$, the integral evaluates to zero.

In this appendix, the zeros of $\tilde{\mathcal{D}}(\xi)$ conveniently coincide with the points $\xi = \xi_j$, $j = 1, \dots, n$. In figure A.1, a particular arrangement for $n = 10$ such zeros is given in the ξ -plane. Furthermore, a number of closed integration contours is shown, denoted by Γ_k , with $k = 1, \dots, 4$, none of which encloses one of the zeros. Given the Cauchy-Goursat theorem, the contour integrals

$$\oint_{\Gamma_k} \frac{e^{i\xi x}}{\tilde{\mathcal{D}}(\xi)} \frac{d\xi}{2\pi} = 0, \quad (\text{A.21})$$

A

all evaluate to zero.

As a second tool on the path to decomposing integral (A.10), it is required to show that complex integration contours can be deformed in a particular way. This can be derived by deploying the Cauchy-Goursat theorem.

A.1.2. DEFORMING INTEGRATION CONTOURS

The contours Γ_1 and Γ_2 in figure A.1 consist of a solid ($\Gamma_{1,s}$ and $\Gamma_{2,s}$) and dashed ($\Gamma_{1,d}$ and $\Gamma_{2,d}$) part. In particular, their dashed parts trace out the same line,³ but $\Gamma_{2,d}$ is traced in the opposite direction of $\Gamma_{1,d}$. This implies that:

$$\int_{\Gamma_{1,d}} = - \int_{\Gamma_{2,d}}. \quad (\text{A.22})$$

Furthermore, by applying the Cauchy-Goursat theorem, it can be derived that:

$$\int_{\Gamma_{2,s}} + \int_{\Gamma_{2,d}} = \oint_{\Gamma_2} = 0 \quad \text{or:} \quad \int_{\Gamma_{2,s}} = - \int_{\Gamma_{2,d}}. \quad (\text{A.23})$$

That is, the integral over $\Gamma_{2,s}$ is equal to the integral value obtained by integrating over $\Gamma_{2,d}$, but with the opposite sign. Equivalently, the integral over $\Gamma_{2,s}$ is equal to the integral over $\Gamma_{2,d}$, but traversing $\Gamma_{2,d}$ in the direction opposite to that indicated in figure A.1.

Equations (A.22) and (A.23) can be combined to obtain:

$$\int_{\Gamma_1} = \int_{\Gamma_{1,s}} + \int_{\Gamma_{1,d}} = \int_{\Gamma_{1,s}} - \int_{\Gamma_{2,d}} = \int_{\Gamma_{1,s}} + \int_{\Gamma_{2,s}}. \quad (\text{A.24})$$

So, the integral over the whole Γ_1 contour is equal to the integral over the contour consistent of the solid parts of Γ_1 and Γ_2 . This identity can be interpreted as having *deformed* the Γ_1 contour into the union of $\Gamma_{1,s}$ and $\Gamma_{2,s}$.⁴

Note that the only ingredients that were used in deriving equation (A.24) are that the contour Γ_2 does not enclose zeros and that $\Gamma_{1,d}$ and $\Gamma_{2,d}$ are equal but have an opposite orientation; nothing was assumed about the integral over the Γ_1 contour. Equation (A.24) therefore applies when replacing Γ_1 by *any* integration contour; closed or not and enclosing zeros or not. Any integration contour can be freely deformed into regions in which the integrand is holomorphic without changing the value of the integral. This means, for example, that Γ_1 in figure A.1 can be freely deformed into any of the other shown contours.⁵

³In figure A.1, the contours Γ_1 and Γ_2 are depicted as adjacent lines. This is done to be able to distinguish them as contours that are both closed.

⁴In fact, the statement of equation (A.23) implies that, while fixing the endpoints, an integration path can be deformed freely, as long as no region is crossed where the integrand is non-holomorphic. If the latter is guaranteed, the integral from one point to another is independent of the traversed path. This is equivalent to the fact that a real integral can be expressed as subtracting the primitive function evaluated at the endpoints.

⁵ Γ_1 and Γ_3 have an opposite orientation; they are traversed in the clockwise and counter-clockwise direction, respectively. The integrand is holomorphic inside Γ_1 , so Γ_1 can be deformed into a line segment, i.e. a contour that encloses a region of zero area. Thereafter, it can be expanded, to enclose non-zero area again, but in such a way that its orientation has flipped. This contour can be deformed into its opposite orientation counterpart. So, the integral over Γ_1 , I , is equal to $-I$ and therefore $I = 0$. This cannot be done if a non-holomorphic region is enclosed, because the contour would have to be deformed through that region.

This completes the toolset required to decompose integral (A.10). A logical question that arises is how the Cauchy-Goursat theorem aids in evaluating integral (A.10). Why is there the need for integrating over a contour in the complex plane, while the integration path of interest is defined over the real line? This will become apparent after the integration path of integral (A.10) is truncated and closed in the complex plane, so that the derived tools can be applied.

A.1.3. CLOSING THE INTEGRATION CONTOUR

The integral of interest is evaluated along the real line. The integration path can be described as a finite part of the real line, of which the endpoints approach $\pm\infty + 0i$. That is:

$$\int_{-\infty}^{\infty} = \lim_{R \rightarrow \infty} \int_{\Gamma}, \quad (\text{A.25})$$

where, from now onwards, the symbol Γ will specifically denote the special interval:

$$\Gamma = \{ \xi : |\xi - \xi_{\text{ref}}| \leq R \} \subseteq \mathbb{R}, \quad (\text{A.26})$$

where R is the radius of the interval and $\xi_{\text{ref}} \in \mathbb{R}$ is a reference point on the real line, see figure A.2 (a).

After truncating the integration contour to Γ with a particular finite R , a closed contour integral can be formed by extending Γ into the complex plane; connecting the right-most endpoint $\xi = \xi_{\text{ref}} + R$ to the left-most endpoint $\xi = \xi_{\text{ref}} - R$. In order to apply the Cauchy-Goursat theorem, this has to be done such that no regions are enclosed in which the integrand is non-holomorphic. Here, this is approached by choosing R small enough, at first, so that the new part of the contour, referred to as the return path, R , is semi-circular with the radius R , see figure A.2 (b). First, the contour is closed in the upper half-plane, indicated by giving R a superscript: R^+ . This choice implies that the orientation of the complete contour is positive as it is traversed in the counter-clockwise direction.

The next step to making the integral useful is letting $R \rightarrow \infty$. The semi-circular shape of R^+ is maintained in this process, which renders encountering the zeros of $\tilde{\mathcal{D}}$ inevitable. The contour R^+ is deformed around the zeros by introducing “cuts”, denoted by Π_{ξ_j} for the particular zero ξ_j . Specifically, such a cut consists of a circular part around the zero and two line segments, $\Pi_{\xi_j}^\downarrow$ and $\Pi_{\xi_j}^\uparrow$, that reach from the circular contour around ξ_j to the semi-circular part of R^+ , see figure A.2 (c). As R is increased, more and more zeros will be equipped with a cut, see figure A.2 (d). Given the finite order of equation (A.2), all zeros of $\tilde{\mathcal{D}}(\xi)$ in the upper half-plane will be covered as $R \rightarrow \infty$. For the zeros illustrated in figure A.1, the integral over R^+ can therefore be written as:

$$\int_{R^+} = \int_{P^+} + \sum_{j=2}^{10} \int_{\Pi_{\xi_j}} \quad (\text{A.27})$$

where P^+ denotes the perforated semi-circular remainder of R^+ , excluding the cut parts.

The parts $\Pi_{\xi_j}^\downarrow$ and $\Pi_{\xi_j}^\uparrow$ can be deformed so that they overlap the same line. This gives

A

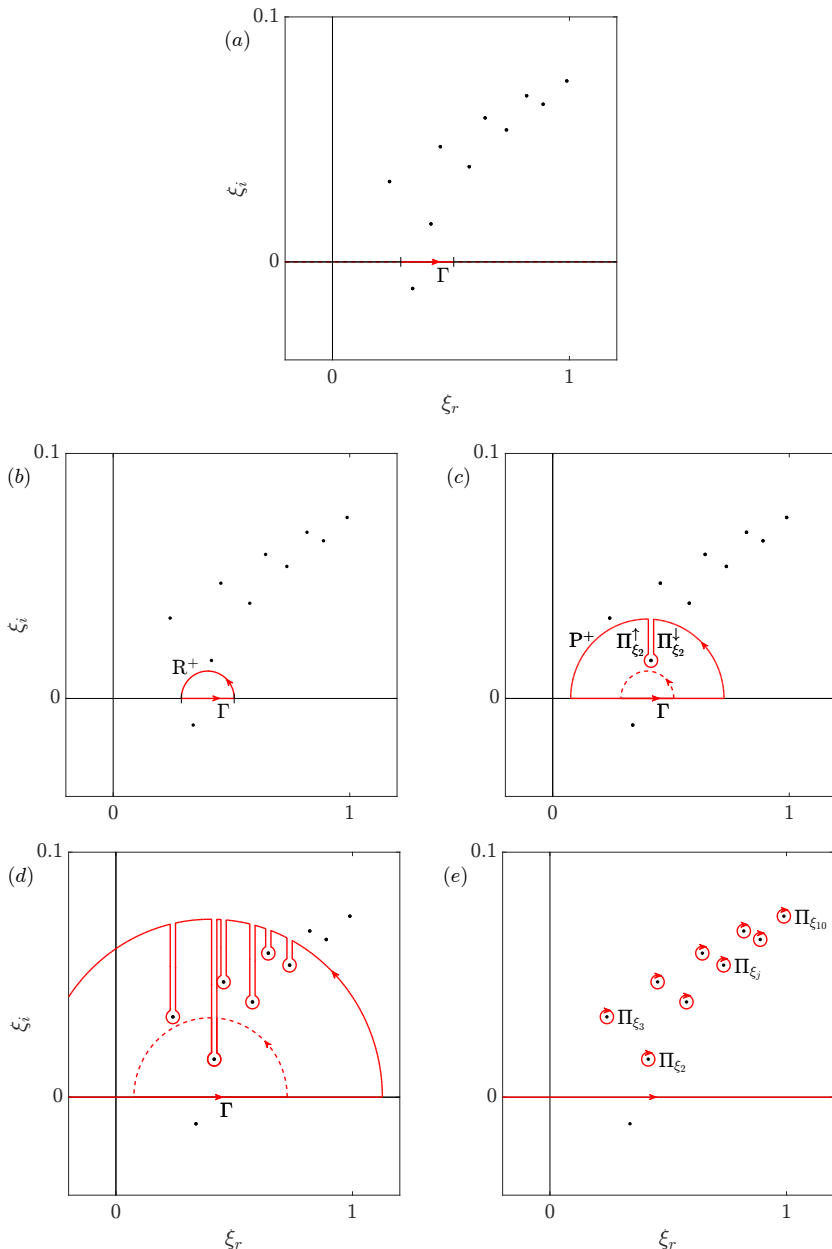


Figure A.2: Illustration of the steps to close the integration contour in the ξ -plane (click (a) twice to activate the animation, music reference: R. Strauss (composer) *et al.* [4]). (a) Truncate the real line to the bounded interval Γ with radius R , (b) connect the endpoints of Γ via the upper half complex plane by introducing the return path R^+ , hence forming a closed contour, (c) extend R , while excluding the zeros of $\tilde{\mathcal{D}}(\xi)$ using the cuts Π (subscript denotes the particular zero), P^+ indicates the (perforated) semi-circular remainder of R^+ and $\Pi^{\uparrow\downarrow}$ indicate the lines connecting P^+ and the circular contour around the zero, (d) let $R \rightarrow \infty$, creating cuts around all zeros, (e) let Π^{\uparrow} and Π^{\downarrow} approach each other to allow their cancellation (so $\Gamma \rightarrow \mathbb{R}$ and the remainder of every Π is the closed contour integral (traversed in the clockwise direction) around the zeros of $\tilde{\mathcal{D}}(\xi)$ in the upper half-plane).

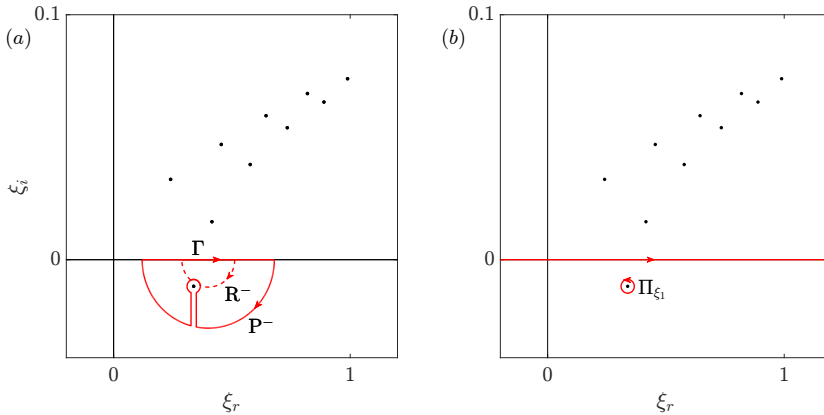


Figure A.3: Closing the integration contour in the lower half-plane. (a) Complete the closure of the contour with the return path R^- , again forming cuts around the zeros of $\tilde{\mathcal{D}}(\xi)$ when extending the radius $\mathcal{R} \rightarrow \infty$, where P^- denotes the (perforated) semi-circular remainder of R^- . (b) Let Π_\downarrow^\dagger and Π_\uparrow^\dagger approach each other to allow their cancellation (so $\Gamma \rightarrow \mathbb{R}$ and the remainder of every Π is the closed contour integral (traversed in the counter-clockwise direction) around the zeros of $\tilde{\mathcal{D}}(\xi)$ in the lower half-plane).

a similar situation as encountered in equation (A.22):

$$\int_{\Pi_{\xi_j}^\downarrow} = - \int_{\Pi_{\xi_j}^\uparrow}; \quad (\text{A.28})$$

the parts cancel due to their opposite orientation. Note that the perforations in P^+ are removed this way.

Accordingly, the entire integration contour can be expressed as:

$$0 = \oint = \int_\Gamma + \int_{P^+} + \sum_{j=2}^{10} \oint_{\Pi_{\xi_j}}, \quad (\text{A.29})$$

where the remainder of the cuts are closed contours around the zeros. Note that the orientation of the latter contours is negative.

Instead of closing Γ in the upper half-plane, it can also be closed in the other direction. This yields a closed contour with a negative (clockwise) orientation. Going through the same process, the final expression for the zeros illustrated in figure A.3 is:

$$0 = \oint = \int_\Gamma + \int_{P^-} + \oint_{\Pi_{\xi_1}}, \quad (\text{A.30})$$

where R^- denotes the return path that traverses the lower half-plane and P^- is the (perforated) semi-circular remainder of R^- , see figure A.3 (a). Only one Π -integral is accounted for due to the single zero in the lower half-plane; note that it has a counter-clockwise (positive) orientation, see figure A.3 (b).

Equations (A.29) and (A.30) establish the first progress in re-expressing the original integral (A.10). That integral is now equated to the P^\pm -integrals and the resulting sum

A

over the Π -integrals as $\mathcal{R} \rightarrow \infty$. For general $\xi_j = a_j + ib_j$, this is written as follows:

$$\text{closing } \Gamma \text{ in upper half-plane: } \int_{-\infty}^{\infty} = \lim_{\mathcal{R} \rightarrow \infty} \int_{\Gamma} = - \lim_{\mathcal{R} \rightarrow \infty} \int_{P^+} + \sum_{b_j > 0} \oint_{\Pi_{\xi_j}}, \quad (\text{A.31a})$$

$$\text{closing } \Gamma \text{ in upper lower-plane: } \int_{-\infty}^{\infty} = \lim_{\mathcal{R} \rightarrow \infty} \int_{\Gamma} = - \lim_{\mathcal{R} \rightarrow \infty} \int_{P^-} + \sum_{b_j < 0} \oint_{\Pi_{\xi_j}}, \quad (\text{A.31b})$$

Note that the orientation of the Π -contours in equations (A.31) has been flipped with respect to equations (A.29) and (A.30). This is done to cancel the negative sign that remains in front of the P^\pm -integrals.

To advance, the P^\pm -integrals are to be determined.

A.1.4. JORDAN'S LEMMA

Jordan's lemma establishes an estimate for the P^\pm -integrals, see Kwok [1, §6.4.2]. Before embarking upon proving it, an observation should be made about the integrand. As $\mathcal{R} \rightarrow \infty$, the integrand has to be evaluated for $\xi_i \rightarrow \pm\infty$ for P^\pm , respectively. Note that:

$$\left| \frac{e^{i\xi x}}{\tilde{\mathcal{D}}(\xi)} \right| = \frac{e^{-\xi_i x}}{|\tilde{\mathcal{D}}(\xi)|} \sim \frac{e^{-\xi_i x}}{|\xi_i|^n} \quad (\text{A.32})$$

for $|\xi_i| \rightarrow \infty$. It is required for the integrand to remain finite. This establishes a restriction on the sign of the physical coordinate x . In particular,

$$\text{the integral over } \begin{cases} P^+ (\xi_i > 0) \text{ can converge only for } x > 0. \\ P^- (\xi_i < 0) \text{ can converge only for } x < 0. \end{cases} \quad (\text{A.33})$$

Otherwise the integral hopelessly diverges at an exponential rate.⁶ This illustrates that closing the contour in the upper (lower) half-plane yields information for the behaviour of $G(x)$ for $x > 0$ (< 0) only. Given this restriction, the path to Jordan's lemma is cleared.

To generalise the statement of Jordan's lemma, it is assumed that the return paths are semi-circular with respect to a point with a possibly non-zero imaginary part, i.e. $\xi_{\text{ref},i} = \gamma$. The contours P^\pm are parametrized by $\xi = \xi_{\text{ref}} + \mathcal{R}e^{\pm i\theta}$, where $\theta \in [0, \pi]$, such that $d\xi = \pm i\mathcal{R}d\theta$.

By substituting the parametrization for P^+ and executing the first estimation gives:

$$\begin{aligned} \left| \int_{P^+} \frac{e^{i\xi x}}{\tilde{\mathcal{D}}(\xi)} d\xi \right| &= \left| \int_0^\pi \frac{e^{i(\xi_{\text{ref}} + \mathcal{R}e^{i\theta})x}}{\tilde{\mathcal{D}}(\xi_{\text{ref}} + \mathcal{R}e^{i\theta})} (i\mathcal{R}) d\theta \right| \leq \frac{\mathcal{R}}{\min_{\xi \in P^+} |\tilde{\mathcal{D}}(\xi)|} \int_0^\pi |e^{i(\xi_{\text{ref}} + \mathcal{R}e^{i\theta})x}| d\theta \\ &= \frac{\mathcal{R}e^{-\gamma x}}{\min_{\xi \in P^+} |\tilde{\mathcal{D}}(\xi)|} \int_0^\pi e^{-\mathcal{R}x \sin \theta} d\theta \end{aligned} \quad (\text{A.34})$$

where the following estimation of the modulus of the integral has been deployed:

$$\left| \int_C f(x)g(x) dx \right| \leq \int_C |f(x)g(x)| dx \leq \max_{x \in C} |f(x)| \int_C |g(x)| dx = \frac{1}{\min_{x \in C} \frac{1}{|f(x)|}} \int_C |g(x)| dx, \quad (\text{A.35})$$

⁶Note that the case $x = 0$ is excluded, which does not have to be the case necessarily.

see Kwok [1, p. 137].

The integrand of the final integral in equation (A.34) is symmetric with respect to $\theta = \pi/2$, so one can write:

$$\frac{\mathcal{R}e^{-\gamma x}}{\min_{\xi \in P^+} |\tilde{\mathcal{D}}(\xi)|} \int_0^\pi e^{-\mathcal{R}x \sin \theta} d\theta = \frac{2\mathcal{R}e^{-\gamma x}}{\min_{\xi \in P^+} |\tilde{\mathcal{D}}(\xi)|} \int_0^{\pi/2} e^{-\mathcal{R}x \sin \theta} d\theta. \quad (\text{A.36})$$

The resulting integral of $e^{a \sin \theta}$ can be significantly simplified by deploying another estimation. In particular, $\sin \theta \geq 2\theta/\pi$ for $0 \leq \theta \leq \pi/2$. So, for negative a , $e^{a \sin \theta} \leq e^{2a\theta/\pi}$. For the argument in equation (A.36), this requires that $x > 0$ for P^+ . For P^- , the equivalent requirement is that $x < 0$. This is perfectly in-line with the requirements (A.33). Accordingly, the estimation can be finalised:

$$\begin{aligned} \frac{2\mathcal{R}e^{-\gamma x}}{\min_{\xi \in P^+} |\tilde{\mathcal{D}}(\xi)|} \int_0^{\pi/2} e^{-\mathcal{R}x \sin \theta} d\theta &\leq \frac{2\mathcal{R}e^{-\gamma x}}{\min_{\xi \in P^+} |\tilde{\mathcal{D}}(\xi)|} \int_0^{\pi/2} e^{-\frac{2\mathcal{R}x}{\pi} \theta} d\theta \\ &= \frac{\pi}{\min_{\xi \in P^+} |\tilde{\mathcal{D}}(\xi)|} \frac{e^{-\gamma x}}{(-x)} \left[e^{-\frac{2\mathcal{R}x}{\pi} \theta} \right]_0^{\pi/2} \\ &= \frac{\pi}{\min_{\xi \in P^+} |\tilde{\mathcal{D}}(\xi)|} \frac{e^{-\gamma x} (1 - e^{-\mathcal{R}x})}{x}. \end{aligned} \quad (\text{A.37})$$

Performing the derivation for P^- yields a directly equivalent expression. To summarize:

$$\left| \int_{P^\pm} \frac{e^{i\xi x}}{\tilde{\mathcal{D}}(\xi)} d\xi \right| \leq \frac{\pi}{\min_{\xi \in P^\pm} |\tilde{\mathcal{D}}(\xi)|} \frac{e^{-\gamma x} (1 - e^{-\mathcal{R}|x|})}{|x|}, \quad \text{for: } x \gtrless 0, \quad (\text{A.38})$$

i.e. P^+ corresponds to $x > 0$ and P^- to $x < 0$.

In the limit of $|\xi| \rightarrow \infty$, the polynomial character of $\tilde{\mathcal{D}}$ implies that:

$$\min_{\xi \in P^\pm} |\tilde{\mathcal{D}}(\xi)| \rightarrow |\xi|^n = |\mathcal{R}|^n, \quad (\text{A.39})$$

so, for fixed x , the right hand side of equation (A.38) decays algebraically as $\mathcal{R} \rightarrow \infty$.

The factor $e^{-\gamma x}$ in equation (A.38) requires caution as $|x| \rightarrow \infty$ if $\gamma \neq 0$. If \mathcal{R} is kept fixed and finite, the right hand side of equation (A.38) decays as $|x| \rightarrow \infty$ only if:

$$\gamma x > 0, \quad (\text{A.40})$$

otherwise the right hand side diverges exponentially as $|x| \rightarrow \infty$ (\mathcal{R} finite, fixed). Based solely on equation (A.38), the Γ -contour could be displaced from the real axis, but it has to lie on the same side as the P -contours. Note, however, that when keeping x fixed, the right hand side always converges to zero as $\mathcal{R} \rightarrow \infty$, even if criterion (A.40) is not satisfied. As $|x|$ increases, \mathcal{R} must grow exponentially relative to $|x|$. This can be ensured implicitly, so requirement (A.40) is not compulsory in the current context.

A

In conclusion, the right hand side of equation (A.38) and therefore the integrals over the P-contours tend to zero in the limit of $\mathcal{R} \rightarrow \infty$. This is referred to as:

$$\text{Jordan's lemma: } \lim_{\mathcal{R} \rightarrow \infty} \left| \int_{P^\pm} \frac{e^{ix}}{\tilde{\mathcal{D}}(\xi)} d\xi \right| = 0, \quad \text{for } x \gtrless 0. \quad (\text{A.41})$$

Accordingly, the P^\pm -integrals evaluate to zero in equations (A.31):

$$\int_{-\infty}^{\infty} = \lim_{\mathcal{R} \rightarrow \infty} \int_{\Gamma} = \sum_{b_j > 0} \oint_{\Pi_{\xi_j}} \quad \text{for: } x > 0 \quad \text{and:} \quad \int_{-\infty}^{\infty} = \sum_{b_j < 0} \oint_{\Pi_{\xi_j}} \quad \text{for: } x < 0. \quad (\text{A.42})$$

In words, equations (A.42) re-express integral (A.10) into the contributions of the (counter-clockwise and clockwise) contour integrals around the zeros in the upper and lower half-planes for positive and negative x , respectively.

The next step in re-expressing and interpreting integral (A.10) is evaluating the contour integrals around the zeros of $\tilde{\mathcal{D}}(\xi)$, which is done in §A.2. To complete the current section with a brief discussion of the physical implications, a small intermezzo is given in the following subsection in relation to the temporal ansatz.

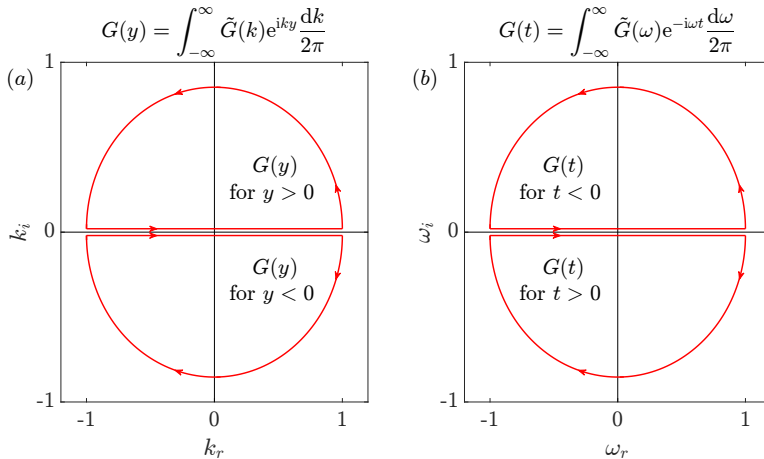


Figure A.4: Indication which integral closure (upper or lower half-plane) corresponds to which part of the domain (positive or negative part) of the Green's function for the typical spatial (having $+iky$ in the exponent) and temporal (having $-i\omega t$ in the exponent) ansatz. Moreover, the contours are shown such that they satisfy criterion (A.40), i.e. the Γ -contour is placed on the real axis or at the same side as the semi-circular part. Note: the contour integrals around the zeros of the dispersion relation have to be performed in the indicated direction to add up to the Γ -integral.

A.1.5. THE TEMPORAL ANSATZ & CAUSALITY

The generic ansatz pair (A.4a) is considered in this appendix. In chapter 2, it was shown that the common statement of the ansatzes involves different signs in the case where ξ is a wavenumber (when x represents a spatial dimension) or a frequency (when x represents a temporal dimension), see equation 2.7 for example. To specialise the findings up

to this point for these special cases, figure A.4 illustrates which integral closure direction corresponds to which part of the physical domain (space or time). Note that, as opposed to ξ , ω has a negative sign in the (inverse) ansatz and therefore the inequality signs in figure A.4 (b) are flipped.

The fact that the different closures of the contour integrals separate the Green's function's behaviour for the positive and negative domain of the physical domain allows discussing the implication of causality if the physical variable is time. The solutions of physical problems are usually responses to either an initial condition or an imposed forcing; they *cause* the response of the system. In turn, they should not have an impact in past events. This translates into the requirement that the response should be zero before the initial condition has occurred or the forcing is turned on. This means that $G(t)$ must be identically zero for $t < 0$. Figure A.4 (b) shows that $G(t)$ for $t < 0$ corresponds to closing the Γ -contour in the upper half of the ω -plane. The resulting integral, in essence, corresponds to the "pre-causal response". The cancellation of this integral is ensured by the Cauchy-Goursat theorem if its contour does not enclose any zeros. Therefore, to ensure causality for systems that have zeros with positive ω_i , the Γ -contour must be placed above the largest such ω_i -value.

This implies that the zeros of a causal dispersion relation $\tilde{\mathcal{D}}(\omega) = 0$ cannot approach $+i\infty$. An upper bound $\omega_{i,m}$ must exist, so that all zeros of $\tilde{\mathcal{D}}(\omega)$ satisfy $\omega_i \leq \omega_{i,m}$, only then Γ can be placed above all zeros. In the mathematical literature, this is referred to as the *well-posedness hypothesis*, see Kapitula and Promislow [5, p. 61] and Sandstede and Scheel [6, hypothesis 1, point 2].

A.2. EVALUATION FOR SIMPLE POLES

The evaluation of the integral (A.10) has been reduced to the contour integrals around the zeros of $\tilde{\mathcal{D}}(\xi)$. An expression will be derived for these integrals in this section.

A.2.1. RESIDUE AT THE POLE

It is assumed that the zeros each have a multiplicity of 1, meaning that $\tilde{\mathcal{D}}(\xi_j) = 0$, but $d\tilde{\mathcal{D}}/d\xi \neq 0$ when evaluated at the zero.⁷ Per definition, such a zero of $\tilde{\mathcal{D}}$ is a *simple pole* of $1/\tilde{\mathcal{D}}$. Due to the requirement of evaluating the integrand only in a close proximity of a particular ξ_j , use can be made of the Taylor expansion of $\tilde{\mathcal{D}}$ about ξ_j :

$$\tilde{\mathcal{D}} = \tilde{\mathcal{D}}|_{\xi_j} + \frac{d\tilde{\mathcal{D}}}{d\xi}\Big|_{\xi_j} (\xi - \xi_j) + \frac{1}{2} \frac{d^2\tilde{\mathcal{D}}}{d\xi^2}\Big|_{\xi_j} (\xi - \xi_j)^2 + O((\xi - \xi_j)^3). \quad (\text{A.43})$$

Now, investigate the integral value when enclosing a simple pole with the positively oriented contour Π_{ξ_j} . Using expansion (A.43) for the integrand $e^{i\xi x}/\tilde{\mathcal{D}}(\xi)$, one can factor the

⁷The approach presented here is generally applicable to modes with a positive integer multiplicity in the sense of a generalized eigenspace, see Kapitula and Promislow [5, definition 2.1.9].

A

constant combination $e^{i\xi_j x} / d\tilde{\mathcal{D}}/d\xi|_{\xi_j}$, allowing the following manipulation:

$$\begin{aligned}
 & \frac{e^{i\xi_j x}}{\left. \frac{d\tilde{\mathcal{D}}}{d\xi} \right|_{\xi_j}} \oint_{\Pi_{\xi_j}} \frac{e^{i(\xi - \xi_j)x}}{\xi - \xi_j + a(\xi - \xi_j)^2 + O((\xi - \xi_j)^3)} \frac{d\xi}{2\pi} \\
 &= \frac{e^{i\xi_j x}}{\left. \frac{d\tilde{\mathcal{D}}}{d\xi} \right|_{\xi_j}} \oint_{\Pi_{\xi_j}} \frac{1}{\xi - \xi_j} [1 + (ix - a)(\xi - \xi_j) + O((\xi - \xi_j)^2)] \frac{d\xi}{2\pi} \\
 &= \frac{e^{i\xi_j x}}{\left. \frac{d\tilde{\mathcal{D}}}{d\xi} \right|_{\xi_j}} \left[\frac{1}{2\pi} \oint_{\Pi_{\xi_j}} \frac{d\xi}{\xi - \xi_j} + \frac{ix - a}{2\pi} \oint_{\Pi_{\xi_j}} d\xi + \oint_{\Pi_{\xi_j}} O(\xi - \xi_j) \frac{d\xi}{2\pi} \right]. \tag{A.44}
 \end{aligned}$$

In the first step, the integrand is Taylor expanded in the variable ξ around ξ_j . It is assumed that the resulting series converges, allowing integrating the series term-by-term.⁸

The first integral is the only one enclosing a singularity, at $\xi = \xi_j$. The integration contour is taken to be the circle with radius r around ξ_j , which corresponds to setting $\xi - \xi_j = re^{i\theta}$. Traversing the contour implies that r is fixed and θ is varied from 0 to 2π , i.e. $d\xi = ire^{i\theta} d\theta$. Accordingly, the integrand of the first term is transformed:

$$\oint_{\Pi_{\xi_j}} \frac{d\xi}{\xi - \xi_j} = \int_0^{2\pi} \frac{ire^{i\theta} d\theta}{re^{i\theta}} = i \int_0^{2\pi} d\theta = 2\pi i. \tag{A.45}$$

Note that the (small) radius of the contour does not have an impact on the final result. Note that this is in-line with the Cauchy-Goursat theorem; the radius of the contour can be varied freely as long as crossing other poles is avoided.

When inspecting the other integrals in equation (A.44), it is found that the integration contour does not enclose singularities. The integrals should therefore evaluate to zero, by virtue of the Cauchy-Goursat theorem. This can be demonstrated with a direct integration:

$$\oint_{\Pi_{\xi_j}} \frac{d\xi}{(\xi - \xi_j)^l} = \int_0^{2\pi} \frac{ire^{i\theta} d\theta}{r^l e^{il\theta}} = ir^{1-l} \int_0^{2\pi} e^{i(1-l)\theta} d\theta = r^{1-l} \left[\frac{e^{2\pi i(1-l)} - 1}{1-l} \right] = 0 \tag{A.46}$$

for all integers $l \neq 1$; even for $l \geq 2$. This confirms that the expansion of the integrand in equation (A.44) converges.

So, if $1/\tilde{\mathcal{D}}$ has a simple pole at ξ_j , it is established that:

$$\oint_{\Pi_{\xi_j}} \frac{e^{i\xi x}}{\tilde{\mathcal{D}}(\xi)} \frac{d\xi}{2\pi} = i \frac{e^{i\xi_j x}}{\left. \frac{d\tilde{\mathcal{D}}}{d\xi} \right|_{\xi_j}}, \quad \text{and: } \oint_{\Pi_{\xi_j}} \frac{e^{i\xi x}}{\tilde{\mathcal{D}}(\xi)} \frac{d\xi}{2\pi} = -i \frac{e^{i\xi_j x}}{\left. \frac{d\tilde{\mathcal{D}}}{d\xi} \right|_{\xi_j}} \tag{A.47}$$

where the value for the negatively oriented contour follows by setting: $d\xi = ire^{i\theta} (-d\theta)$ in equation (A.45). Note that $d\tilde{\mathcal{D}}/d\xi(\xi_j)$ are just complex scalar constants. Equations (A.47)

⁸For higher order poles, higher order partial derivatives $d^m \tilde{\mathcal{D}}/d\xi^m$ are zero, which effectively implies equation (A.44) will single out a different term as a result of the expansion of the exponential function in the numerator.

hold for any isolated simple pole ξ_j . The determined quantity is also referred to as the ‘residue at the pole,’ see Kwok [1, §6.2].

From the mathematical point of view, it is important to realise the approximation introduced by using the Taylor expansion in equation (A.44) is undone by performing the contour integration. Equation (A.47) is an exact result.

The combination of equations (A.42) and (A.47) imply that, for $x > 0$ ($x < 0$), integral (A.10) can be expressed as the sum over the residues at the poles in the upper (lower) half-plane. For the zeros illustrated in figure A.1, integral (A.10) evaluates to:

$$\int_{-\infty}^{\infty} \frac{e^{i\xi x}}{\tilde{\mathcal{D}}(\xi)} \frac{d\xi}{2\pi} = \sum_{b_j > 0} \oint_{\Pi_{\xi_j}} \frac{e^{i\xi x}}{\tilde{\mathcal{D}}(\xi)} \frac{d\xi}{2\pi} = i \sum_{b_j > 0} \frac{e^{i\xi_j x}}{\frac{d\tilde{\mathcal{D}}}{d\xi}(\xi_j)} = i \sum_{j=2}^{10} \frac{e^{i\xi_j x}}{\frac{d\tilde{\mathcal{D}}}{d\xi}(\xi_j)} \quad \text{for: } x > 0, \quad (\text{A.48})$$

$$\int_{-\infty}^{\infty} \frac{e^{i\xi x}}{\tilde{\mathcal{D}}(\xi)} \frac{d\xi}{2\pi} = \sum_{b_j < 0} \oint_{\Pi_{\xi_j}} \frac{e^{i\xi x}}{\tilde{\mathcal{D}}(\xi)} \frac{d\xi}{2\pi} = -i \sum_{b_j < 0} \frac{e^{i\xi_j x}}{\frac{d\tilde{\mathcal{D}}}{d\xi}(\xi_j)} = -i \frac{e^{i\xi_1 x}}{\frac{d\tilde{\mathcal{D}}}{d\xi}(\xi_1)} \quad \text{for: } x < 0. \quad (\text{A.49})$$

Recall that integral (A.10) represents, in fact, the solution, G , of equation (A.3). Apparently, G can be expressed as the aforementioned sum over the residues. This allows interpreting the residues as the pertinent building blocks of G .

Each such building block is an exponential function in x with the growth rate b_j ; proportional to $e^{-b_j x}$. Therefore each decays exponentially as $|x| \rightarrow \infty$ for the part of the domain in which it is defined ($b_j x > 0$ always). So, each building block satisfies the implicit boundary conditions (A.5). This is important, because it implies that, in its domain of validity, each building block is, by itself, an admissible solution of equation (A.3).

A.2.2. POSSIBLE PLACEMENTS OF THE CONTOUR

The latter findings can be used to extract insight into the placement of the original integration contour. Per definition of the inverse Fourier ansatz (A.4b), it corresponds to the real line. From its definition it is unclear, however, why it should be placed there. Just as in §A.1.4, let γ denote the shift of the contour into the imaginary direction.

Figures A.5 (a,b) illustrate a situation in which the contour is shifted to a location in between ξ_5 and ξ_6 . In this case, the integral is closed in the upper and lower part of the complex plane *with respect to this line*, so integral (A.10) would evaluate to:

$$\int_{-\infty+i\gamma}^{\infty+i\gamma} \frac{e^{i\xi x}}{\tilde{\mathcal{D}}(\xi)} \frac{d\xi}{2\pi} = \sum_{b_j > \gamma} \oint_{\Pi_{\xi_j}} \frac{e^{i\xi x}}{\tilde{\mathcal{D}}(\xi)} \frac{d\xi}{2\pi} = i \sum_{j=6}^{10} \frac{e^{i\xi_j x}}{\frac{d\tilde{\mathcal{D}}}{d\xi}(\xi_j)} \quad \text{for: } x > 0, \quad (\text{A.50})$$

$$\int_{-\infty+i\gamma}^{\infty+i\gamma} \frac{e^{i\xi x}}{\tilde{\mathcal{D}}(\xi)} \frac{d\xi}{2\pi} = \sum_{b_j < \gamma} \oint_{\Pi_{\xi_j}} \frac{e^{i\xi x}}{\tilde{\mathcal{D}}(\xi)} \frac{d\xi}{2\pi} = -i \left(\frac{e^{i\xi_1 x}}{\frac{d\tilde{\mathcal{D}}}{d\xi}(\xi_1)} + \sum_{j=2}^5 \frac{e^{i\xi_j x}}{\frac{d\tilde{\mathcal{D}}}{d\xi}(\xi_j)} \right) \quad \text{for: } x < 0, \quad (\text{A.51})$$

where the terms in the red sum are proportional to $e^{-b_j x}$, with $b_j > 0$. While belonging to the region $x < 0$, these terms diverge as $x \rightarrow -\infty$, violating the implicit boundary conditions (A.5).

In a similar vein, if the contour is, instead, chosen to lie below ξ_1 , see figure A.5 (c,d),

A

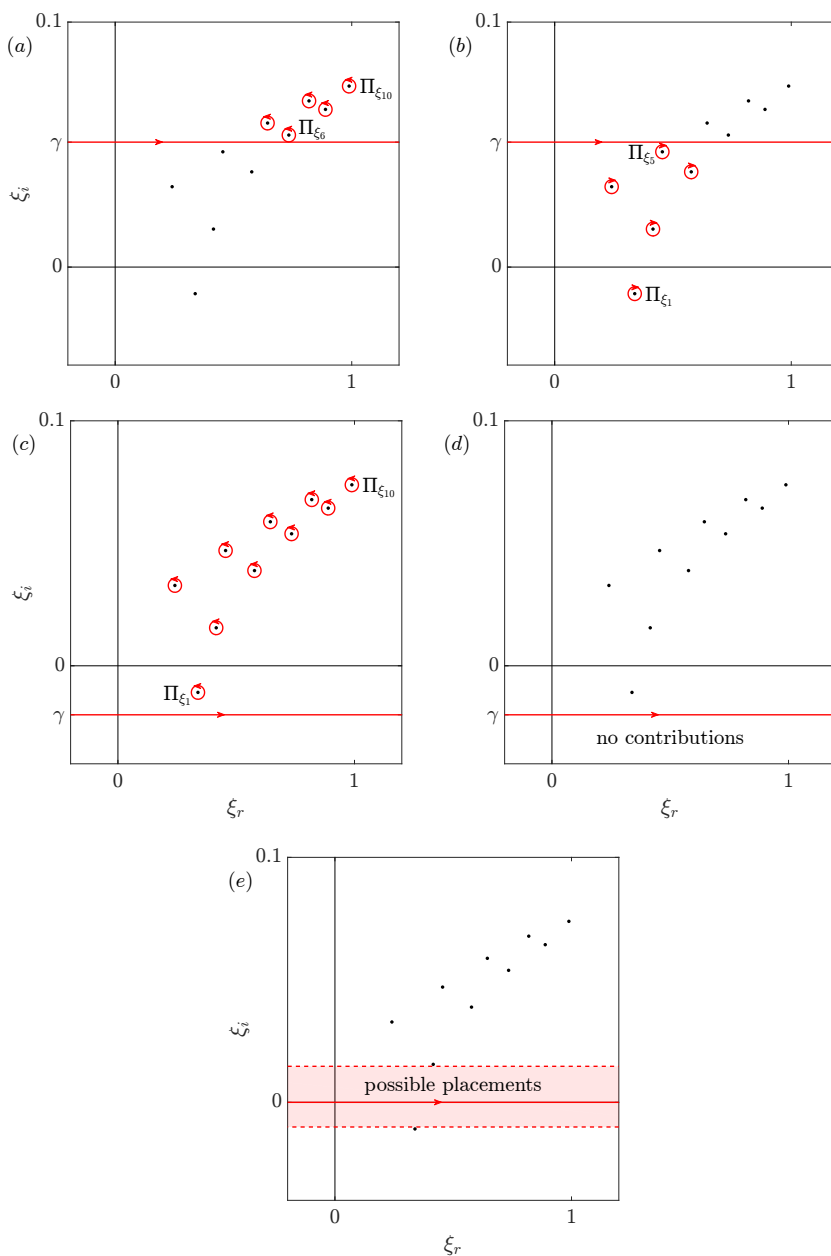


Figure A.5: (a,b,c,d) Selected zeros for $x \geq 0$ for different placements of the original integration contour, upward (a,b) and downward shift (c,d), $x > 0$ (a,c) and < 0 (b,d). (e) Indication of the possible straight placements so that the implicit boundary conditions (A.5) are satisfied.

integral (A.10) would evaluate to:

$$\int_{-\infty+i\gamma}^{\infty+i\gamma} \frac{e^{i\xi x}}{\tilde{\mathcal{D}}(\xi)} \frac{d\xi}{2\pi} = \sum_{b_j > \gamma} \oint_{\Pi_{\xi_j}} \frac{e^{i\xi x}}{\tilde{\mathcal{D}}(\xi)} \frac{d\xi}{2\pi} = i \left(\frac{e^{i\xi_1 x}}{\frac{d\tilde{\mathcal{D}}}{d\xi} \Big|_{\xi_1}} + \sum_{j=2}^{10} \frac{e^{i\xi_j x}}{\frac{d\tilde{\mathcal{D}}}{d\xi}(\xi_j)} \right) \quad \text{for: } x > 0, \quad (\text{A.52})$$

$$\int_{-\infty+i\gamma}^{\infty+i\gamma} \frac{e^{i\xi x}}{\tilde{\mathcal{D}}(\xi)} \frac{d\xi}{2\pi} = \sum_{b_j < \gamma} \oint_{\Pi_{\xi_j}} \frac{e^{i\xi x}}{\tilde{\mathcal{D}}(\xi)} \frac{d\xi}{2\pi} = 0 \quad \text{for: } x < 0, \quad (\text{A.53})$$

where, now, the red term diverges as $x \rightarrow \infty$, again violating the implicit boundary conditions.

In conclusion, to satisfy the implicit boundary conditions, the integration contour must separate the zeros closest to the real ξ -line. The real ξ -line is itself the obvious candidate complying with this criterion, but it is not the only possible location. As demonstrated in §A.1.2 the contours can be deformed freely as long as no zeros of $\tilde{\mathcal{D}}(\xi)$ are crossed. The region indicated in figure A.5 (e) represents all up- and downward shifts of the real ξ -line without crossing any of the zeros, contours in this region therefore automatically satisfy the aforementioned criterion. The contour can, in fact, be deformed without keeping it straight. It can freely meander through the complex plane, as long as it separates the zeros that lie in the upper half-plane from those in the lower half-plane.

In this appendix, the regions in which the integrand becomes non-holomorphic are discrete points, exclusively. As determined just now, the integration contour should separate these points in the upper and lower half-plane to satisfy the implicit boundary conditions. As is explored in the main body of this thesis, this criterion does not generally apply if the region in which the integrand is non-holomorphic forms a continuum. As an example, consider a zero of $\tilde{\mathcal{D}}(\xi)$ with $\xi_j \in \mathbb{R}$, so with $b_j = 0$. This solution remains bounded as $x \rightarrow +\infty$ and $-\infty$. As a building block, it cannot make up G , by itself, because G must decay for $x \rightarrow \pm\infty$ as required by the implicit boundary conditions (A.5). By combining infinitely many of these neutral solutions, however, it can still be ensured that G and its derivatives decay as $x \rightarrow \pm\infty$. The Gaussian integral, see §2.4.3, is a famous example of this. Surprisingly, this argument can even be extended to *growing exponentials in the unbounded spatial direction*. As stated by Briggs: ‘even when some [...] solutions of the dispersion equation [display growth in an unbounded direction], [...] a decaying function can be represented as a super-position of many growing exponentials’.

A.2.3. DISCRETE MODE ANSATZ AND $\tilde{\delta}$ -FUNCTIONS

It is important to note that the results of this section suggest the function $1/\tilde{\mathcal{D}}$ behaves as a *particular type of* delta function $\tilde{\delta}$ centred at $\xi = \xi_j = a_j + ib_j$. This holds in the sense that the integral:

$$\int_{-\infty}^{\infty} 2\pi \tilde{\delta}(\xi - \xi_j) e^{i\xi x} \frac{d\xi}{2\pi} = e^{i\xi_j x} \text{sign}(b_j) \quad (\text{A.54})$$

is reminiscent of the integral:

$$\int_{-\infty+ib_j}^{\infty+ib_j} 2\pi \delta(\xi - \xi_j) e^{i\xi x} \frac{d\xi}{2\pi} = e^{i\xi_j x}. \quad (\text{A.55})$$

A

The function δ in the latter expression has the properties of the usual Dirac delta function; that equality holds, because the integration contour goes *through* the point ξ_j . In equation (A.54), this is not the case, because $b_j \neq 0$ in general. The function $\tilde{\delta}$ satisfying equation (A.54) is, in fact, defined as follows:

$$\tilde{\delta}(\xi) = \frac{1}{2\pi i\xi}. \quad (\text{A.56})$$

Accordingly, the equality in equation (A.54) follows when the integration contour is closed around the pole at ξ_j . This demonstrates that zeros, ξ_j , with multiplicity 1 of $\tilde{\mathcal{D}}(\xi)$ represent responses due to a perfect monochromatic forcing at the complex wavenumber/frequency ξ_j .

The commonly used form of the solution ansatz, see equation (2.10):

$$q'(x) \sim e^{i\alpha x}, \quad (\text{A.57})$$

is retrieved when substituting $\tilde{G}(\xi) = 2\pi\tilde{\delta}(\xi - \alpha)$ into:

$$q'(x) = \int_{-\infty}^{\infty} \tilde{G}(\xi) e^{i\xi x} \frac{d\xi}{2\pi}. \quad (\text{A.58})$$

Note that by assuming this ansatz, *the discrete nature of the solution is imposed*.

A.3. SINGULARITIES: POLES MOVING ONTO THE CONTOUR

In chapter 7, the analysis presented here is extended by integrating a subsequent time, where the zeros ξ_j are functions of the second integration variable. As illustrated with the Cauchy-Goursat theorem, the contributions to complex integrals are due to regions where the integrand is non-holomorphic. So, as the next step, it is required to know in which situations the expressions (A.47) yield non-holomorphic behaviour. As opposed to the search for regions where the *integrand* is non-holomorphic, as done in §A.1.1, here the situations are studied where the *integral* is non-holomorphic.

The non-holomorphic behaviour of the integral is directly related to the movement of the poles ξ_j onto the integration contour. The contour deformation tools can then no longer be applied, because, while one or more poles lie on the contour, it is unclear in which direction the contour can be closed. This ambiguity is, in fact, the core of the problem. Direct integration must hence be resorted to in order to extract information.

The function $e^{i\xi x}/\tilde{\mathcal{D}}(\xi)$ cannot be directly integrated. However, the singular behaviour of the integral is solely associated to the fact that $\tilde{\mathcal{D}} = 0$ on the integration contour. Representative information can be extracted by accounting for that factor by itself. The exponential function is therefore dropped from the integrand to simplify the analysis.

The following integrals represent three ways in which the poles can move onto the integration contour:

$$\underbrace{\int_{-\mathcal{R}}^{\mathcal{R}} \frac{d\xi}{\xi - ie}}, \quad \underbrace{\int_{-\mathcal{R}}^{\mathcal{R}} \frac{d\xi}{(\xi - ie)^2}}, \quad \underbrace{\int_{-\mathcal{R}}^{\mathcal{R}} \frac{d\xi}{(\xi - ie)(\xi + ie)}}$$

I II III

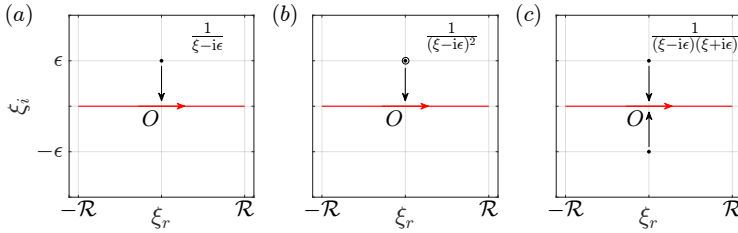


Figure A.6: Illustration of the movement of (a, integral I) a single and (b, integral II) a double ξ -pole moving onto the ξ -contour from the upper half-plane. (c, integral III) Movement of two ξ -poles onto the ξ -contour from either sides; ‘pinching’ the contour.

where the contour is placed over the real ξ -axis. Each will be treated in a separate subsection. In all cases, the intention is to let $\mathcal{R} \rightarrow \infty$. Next to the assumption $\mathcal{R} > 0$, it is assumed that $\epsilon \geq 0$ and finite, i.e. ϵ may be zero. The particular interest goes out to assessing the cases $\epsilon = 0$ corresponding to the poles in the ξ -plane moving onto the ξ -contour. The corresponding arrangements of the poles, the contours in the ξ -plane and the way the poles move onto the contour is shown in figure A.6.

A.3.1. SINGLE POLE

To evaluate integral I, use is made of the following primitive function:

$$\int \frac{d\xi}{\xi - ie} = \log(\xi - ie) + C = \frac{1}{2} \ln(\xi^2 + \epsilon^2) - i \arctan \frac{\epsilon}{\xi} + C, \quad \text{where: } \xi, \epsilon \in \mathbb{R}, \quad (\text{A.59})$$

where \ln and \log respectively denote the real and complex natural logarithm and C is an arbitrary constant. The arctan-term shows that care has to be taken around $\xi = 0$. Integral I should therefore be treated as an improper integral. To this end, $\epsilon_1 > 0$, $\epsilon_2 > 0$ are defined. Note that: $\arctan(-x) = -\arctan x$, $\arctan x \rightarrow 0$ as $x \rightarrow 0$ and $\arctan x \rightarrow \pi/2$ as $x \rightarrow \infty$.

Evaluating integral I yields:

$$\begin{aligned} \int_{-\mathcal{R}}^{\mathcal{R}} \frac{d\xi}{\xi - ie} &= \lim_{\epsilon_1, \epsilon_2 \downarrow 0} \left[\int_{-\mathcal{R}}^{-\epsilon_1} \frac{d\xi}{\xi - ie} + \int_{\epsilon_2}^{\mathcal{R}} \frac{d\xi}{\xi - ie} \right] \\ &= \lim_{\epsilon_1, \epsilon_2 \downarrow 0} \left[\frac{1}{2} \ln(\epsilon_1^2 + \epsilon^2) + i \arctan \frac{\epsilon}{\epsilon_1} - \frac{1}{2} \ln(\mathcal{R}^2 + \epsilon^2) - i \arctan \frac{\epsilon}{\mathcal{R}} \right. \\ &\quad \left. + \frac{1}{2} \ln(\mathcal{R}^2 + \epsilon^2) - i \arctan \frac{\epsilon}{\mathcal{R}} - \frac{1}{2} \ln(\epsilon_2^2 + \epsilon^2) + i \arctan \frac{\epsilon}{\epsilon_2} \right] \\ &= \lim_{\epsilon_1, \epsilon_2 \downarrow 0} \left[\frac{1}{2} \ln \frac{\epsilon_1^2 + \epsilon^2}{\epsilon_2^2 + \epsilon^2} + i \arctan \frac{\epsilon}{\epsilon_1} + i \arctan \frac{\epsilon}{\epsilon_2} \right] - 2i \arctan \frac{\epsilon}{\mathcal{R}} \\ &\rightarrow \lim_{\epsilon_1, \epsilon_2 \downarrow 0} \left[\frac{1}{2} \ln \frac{\epsilon_1^2 + \epsilon^2}{\epsilon_2^2 + \epsilon^2} + i \arctan \frac{\epsilon}{\epsilon_1} + i \arctan \frac{\epsilon}{\epsilon_2} \right], \end{aligned} \quad (\text{A.60})$$

as $\mathcal{R} \rightarrow \infty$. From this point onwards, the value of ϵ comes into play. First, assume $\epsilon > 0$,

A

then:

$$\lim_{\mathcal{R} \rightarrow \infty} \int_{-\mathcal{R}}^{\mathcal{R}} \frac{d\xi}{\xi - i\epsilon} = \lim_{\epsilon_1, \epsilon_2 \downarrow 0} \left[\frac{1}{2} \ln \frac{\epsilon_1^2 + \epsilon^2}{\epsilon_2^2 + \epsilon^2} + i \arctan \frac{\epsilon}{\epsilon_1} + i \arctan \frac{\epsilon}{\epsilon_2} \right] = \ln \frac{\epsilon}{\epsilon} + i \frac{\pi}{2} + i \frac{\pi}{2} = i\pi. \quad (\text{A.61})$$

So, for $\epsilon > 0$, the integral evaluates unequivocally to $i\pi$. This calculation can be compared to equation (A.45) in the sense that the current integral from $-\infty$ to ∞ over the real axis corresponds to the integration over a semicircle under the pole in the clockwise direction.

Now, instead, set $\epsilon = 0$, i.e. let $\epsilon \rightarrow 0$ before ϵ_1 and ϵ_2 do. In that case:

$$\lim_{\mathcal{R} \rightarrow \infty} \int_{-\mathcal{R}}^{\mathcal{R}} \frac{d\xi}{\xi} = \lim_{\epsilon_1, \epsilon_2 \downarrow 0} \lim_{\epsilon \downarrow 0} \left[\frac{1}{2} \ln \frac{\epsilon_1^2 + \epsilon^2}{\epsilon_2^2 + \epsilon^2} + i \arctan \frac{\epsilon}{\epsilon_1} + i \arctan \frac{\epsilon}{\epsilon_2} \right] = \lim_{\epsilon_1, \epsilon_2 \downarrow 0} \ln \frac{\epsilon_1}{\epsilon_2}. \quad (\text{A.62})$$

This shows that the integral value depends on the rate at which ϵ_1 and ϵ_2 approach zero relative to each other. Setting $\epsilon_1 = a\epsilon_2$, where a is any positive real number and signifies the relative rate, the integral evaluates to $\ln a$, which is non-unique (it can assume all real values). It is therefore determined that the integral *does not exist* for $\epsilon = 0$.

Note that the case $\epsilon = 0$ corresponds to the integration contour going through the pole of the integrand. This type of integral is an improper integral per definition. There are well-defined improper integrals, but others are infinite (divergent integrals) or do not exist. In the latter case, the Cauchy principal value of the integral is a consistent way of associating values to these integrals still, see Kwok [1, p. 288] for an equivalent explanation. The Cauchy principal value is obtained by restricting $\epsilon_1 = \epsilon_2 = \epsilon^*$, i.e. ϵ_1 and ϵ_2 are forced to approach zero at exactly the same rate. This assumption is indicated with the letter P .

The previous integral, for example, evaluates to:

$$\lim_{\mathcal{R} \rightarrow \infty} P \int_{-\mathcal{R}}^{\mathcal{R}} \frac{d\xi}{\xi} = 0. \quad (\text{A.63})$$

Note that when $\epsilon > 0$, the Cauchy principal value of the integral equals the value of the integral.

The Cauchy principal value of integral I can be interpreted in terms of complex contour integration the following way. The case $\epsilon = 0$ corresponds to the pole lying on top of the integration contour. Closing the contour via both the lower and upper half-planes will not *enclose* the pole and, if no pole is enclosed, the Cauchy-Goursat theorem states the contour integral should evaluate to zero.

Note that the latter result implies that the integral value jumps discontinuously when distinguishing the cases $\epsilon = 0$ (integral equal to 0) versus $\epsilon \rightarrow 0$ (integral equal to $i\pi$). In fact, when ϵ attains negative values, the integral value jumps again; to $-i\pi$. This follows from equation (A.61), because $\arctan x \rightarrow -\pi/2$ as $x \rightarrow -\infty$. This is also consistent with contour integration. The return path now has to be defined in the lower half-plane, so the integration contour now passes around the pole in the clockwise direction.

Despite these results' consistency, the ultimate conclusion is that the integral displays singular behaviour for $\epsilon = 0$. Other than the infinite singularity associated to poles, the current singularity can be viewed as one of non-uniqueness or a jump discontinuity.

A.3.2. DOUBLE POLE

Integral II is considered with $\epsilon > 0$, first. In that case, the primitive function is continuous and bounded around $\xi = 0$. The integral can therefore be directly integrated:

$$\int_{-\mathcal{R}}^{\mathcal{R}} \frac{d\xi}{(\xi - i\epsilon)^2} = \left[-\frac{1}{\xi - i\epsilon} \right]_{-\mathcal{R}}^{\mathcal{R}} = -\frac{1}{\mathcal{R} - i\epsilon} - \frac{1}{\mathcal{R} + i\epsilon} = -\frac{2\mathcal{R}}{\mathcal{R}^2 + \epsilon^2} \rightarrow 0, \quad (\text{A.64})$$

as $\mathcal{R} \rightarrow \infty$. This illustrates that when two poles have merged at one side of the integration contour, they have a zero contribution.⁹ This is in fact a demonstration of equation (A.46) for $l = 2$.

The case $\epsilon = 0$ corresponds to the integral:

$$\begin{aligned} \int_{-\mathcal{R}}^{\mathcal{R}} \frac{d\xi}{\xi^2} &= \lim_{\epsilon^* \downarrow 0} \left[\int_{-\mathcal{R}}^{-\epsilon^*} \frac{d\xi}{\xi^2} + \int_{\epsilon^*}^{\mathcal{R}} \frac{d\xi}{\xi^2} \right] \\ &= \lim_{\epsilon^* \downarrow 0} \left[-\frac{1}{\xi} \Big|_{-\mathcal{R}}^{-\epsilon^*} - \frac{1}{\xi} \Big|_{\epsilon^*}^{\mathcal{R}} \right] = \lim_{\epsilon^* \downarrow 0} \left[\frac{2}{\epsilon^*} \right] - \frac{2}{\mathcal{R}} = \infty. \end{aligned} \quad (\text{A.65})$$

So, integrating through a double pole yields an infinite integral. Note that, in light of equation (A.64), the integral value instantaneously explodes from the value zero to infinity as the double pole moves onto the integration contour.

A.3.3. SINGLE POLES FROM OPPOSITE SIDES

Integral III can be expanded in terms of integral I, as shown in what follows. Integral I is known to be well-behaved for $\epsilon > 0$, so integral III is directly probed for the Cauchy principal value to cover the case $\epsilon = 0$:

$$\begin{aligned} P \int_{-\mathcal{R}}^{\mathcal{R}} \frac{d\xi}{(\xi - i\epsilon)(\xi + i\epsilon)} &= -\frac{i}{2\epsilon} P \int_{-\mathcal{R}}^{\mathcal{R}} \frac{d\xi}{\xi - i\epsilon} + \frac{i}{2\epsilon} P \int_{-\mathcal{R}}^{\mathcal{R}} \frac{d\xi}{\xi + i\epsilon} \\ &= \frac{1}{\epsilon} \left(\lim_{\epsilon^* \downarrow 0} \left[\arctan \frac{\epsilon}{\epsilon^*} \right] - \arctan \frac{\epsilon}{\mathcal{R}} \right) - \frac{1}{\epsilon} \left(-\lim_{\epsilon^* \downarrow 0} \left[\arctan \frac{\epsilon}{\epsilon^*} \right] + \arctan \frac{\epsilon}{\mathcal{R}} \right) \\ &= \frac{\pi}{\epsilon} - \frac{2}{\epsilon} \arctan \frac{\epsilon}{\mathcal{R}} \rightarrow \frac{\pi}{\epsilon}. \end{aligned} \quad (\text{A.66})$$

as $\mathcal{R} \rightarrow \infty$. While integral III is finite for $\epsilon > 0$, it is infinite for $\epsilon = 0$. If two simple poles coalesce onto the integration contour, this renders an infinite integral value. This is consistent with the result for integral II.

In the first step of evaluating integral (A.66), the integral is decomposed into two parts by factoring the denominator. This is an alternative demonstration of the fact that an integral over multiple isolated singularities can be decomposed into multiple integrals over every individual singularity. In each such individual integral, the other singularities in the integrand do, in fact, not exist.

⁹This result should not be confused with the result obtained when evaluating the inverse Fourier transform, where the integrand would equal $e^{i\zeta y}/(i\zeta - \epsilon)^2$. The expansion of the exponential kernel then produces the non-zero contribution.

A

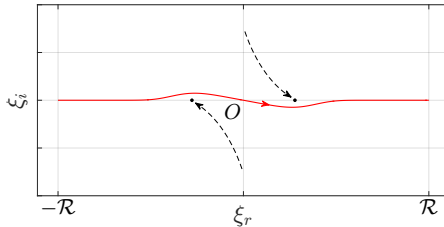


Figure A.7: Movement of two ξ -poles onto the real ξ -axis from either sides, but not pinching the contour. The latter can thus be deformed, causing the integral to be ‘analytically continued.’

A.3.4. ANALYTICAL CONTINUATION AND CONTOUR PINCHING

All aforementioned integrals yield singular behaviour as the poles move onto the integration contour. In particular, the integrals are not complex differentiable and therefore non-holomorphic in the limit. This shows that all will, somehow, come into play when evaluating a subsequent integral. However, the singularity described by integral III is of a fundamentally different nature than those described by integrals I and II.

In fact, the jump in the integral value in the set-ups of integrals I and II can be avoided. In general, the ξ -contour is not constrained to lie on the real axis. As already mentioned in §§A.1.2 and A.1.4, it can be continuously deformed into the complex plane, around the ξ -poles, while these poles move onto the real axis. An example is shown in figure A.7. In this case, the integral value changes smoothly as a pole crosses over the real axis. Changing the ξ -contour to ensure the integral’s continuity is referred to as *analytical continuation*, see Kwok [1], Briggs [7].

Now consider the set-up of integral III from this perspective. In that case, the poles coalesce onto the ξ -contour from different sides. The poles *pinch* the ξ -contour at the point of coalescence, which is therefore referred to as a pinch point. The pinching implies that the ξ -contour cannot be moved out of the way from both poles at the same time. Therefore, the location in the ξ -plane where this occurs is *absolute*. Furthermore, the coalescence of the poles creates a double root, which, in turn, implies that $d\tilde{\mathcal{D}}/d\xi = 0$. This makes this point an interesting candidate for evaluating the expressions (A.47), containing $d\tilde{\mathcal{D}}/d\xi$ in the denominator. As will be shown in chapters 7 and 8, pinch points bare a fundamental importance in characterising solutions that can be built with continuum building blocks of the dispersion relation.

REFERENCES

- [1] Y. K. Kwok, *Applied complex variables for scientists and engineers* (Cambridge University Press, 2010).
- [2] G. P. Tolstov, *Fourier series* (Courier Corporation, 2012).
- [3] N. W. McLachlan, *Complex Variable Theory and Transform Calculus with Technical Applications* (Cambridge University Press, 1953).
- [4] R. Straus (composer), S. Bychkov (conductor), and Philharmonia Orchestra & Royal

- Concertgebouw Orchestra, *Also sprach Zarathustra, Op. 30 (Opening movement)* (Digital Classics, 1990).
- [5] T. Kapitula and K. Promislow, *Spectral and dynamical stability of nonlinear waves* (Springer, 2013).
- [6] B. Sandstede and A. Scheel, *Absolute and convective instabilities of waves on unbounded and large bounded domains*, Physica D: Nonlinear Phenomena **145**, 233 (2000).
- [7] R. Briggs, *Electron-stream Interaction with Plasmas*, M.I.T. Press research monographs (M.I.T. Press, 1964).

B

MODEL PROBLEM IN CHAPTER 8

The model problem considered in chapter 8 involves equation (8.3), which is an ordinary differential equation simulating the advection of the function \tilde{w} in the wall-normal coordinate, the y -direction, while the essential problematic properties of the BiGlobal problem are due to the advection in the x -direction. It is important to emphasize that, in the streamwise BiGlobal problem, the equivalent problematic advection is that by \bar{U} .

The physical perturbations of interest are those on non-parallel boundary layer flows, $\bar{U}(x, y)$, $\bar{V}(x, y)$, that satisfy the steady boundary layer equations, see Schlichting *et al.* [1]. The x -derivatives are assumed to be zero in the considered stability approach, reducing the base flow representation to the profiles $\bar{U}(y)$ and $\bar{V}(y)$ per x -station. Through flow continuity and the no-penetration boundary condition at the wall, this assumption requires that $\bar{V} = 0$. Neglecting the x -derivatives is therefore called the parallel flow assumption, see §2.3.5.

However, \bar{V} simulates the advection of perturbations; the most important term in the current study. Therefore it is retained as a toy problem. It is representative of the inevitable streamwise \bar{U} velocity component in the streamwise BiGlobal analyses. This directly illustrates the link between the complications in the BiGlobal problem and the alleviation of the parallel flow assumption in the LST framework.

The issues in the BiGlobal problem emerge due to advection in the streamwise direction. Here, the problem in the wall-normal direction is chosen instead, because:

- its continuous spectrum has been studied thoroughly, even when the non-parallel flow is included in the formulation, see Grosch and Salwen [2], Bouthier [3], Herndon [4], Balakumar and Malik [5], Schmid and Henningson [6]
- boundary layer profiles have a well-defined asymptotic limit as $y \rightarrow \infty$. The limit flow, a non-parallel uniform flow, does not support convective growth. Any obtained growth is hence related to the non-local nature of the solutions, see Rodríguez *et al.* [7]
- the wall-normal problem can make use of the physically substantiated no-slip

boundary condition, so that no ambiguity exists for this particular boundary condition

In-line with these reasons, further reasons for the consideration of this problem are, that: the solutions are well-established to be absolutely and convectively stable, the referenced theorems by Sandstede and Scheel [8], Kapitula and Promislow [9] are applicable to this problem and, lastly, obtaining numerical solutions is inexpensive. The final two reasons support the consideration of a one- over a two-dimensional problem.

The model problem can be interpreted as a special form of the Ginzburg-Landau model often considered in literature on global instability theory, see Huerre and Monkewitz [10], Chomaz [11]. This form implies the absence of pressure terms. Buell and Huerre [12] report a pressure feedback from the outlet to the inlet is responsible for the generation of transient perturbation growth near the domain inlet. Lesshaft [13] consequently models a pressure feedback in the Ginzburg-Landau model. In this chapter, the effects of the advection and inhomogeneity on the (computation of the) continuous spectrum is focused upon. The role of the pressure is highly important in ultimately understanding the complete streamwise BiGlobal problem, but it is independent of the effects that are here accounted for. As a next incremental step, the model can be extended to include global pressure effects, by considering the (non-parallel Orr-Sommerfeld) problem for \tilde{u} , \tilde{v} and \tilde{p} , Herron [4].¹

REFERENCES

- [1] H. Schlichting, E. Krause, H. Oertel, K. Gersten, and C. Mayes, *Boundary-Layer Theory* (Springer, 2003).
- [2] C. E. Grosch and H. Salwen, *The continuous spectrum of the Orr-Sommerfeld equation. part 1. the spectrum and the eigenfunctions*, J. Fluid Mech. **87**, 33 (1978).
- [3] M. Bouthier, *Sur la stabilité des écoulements non parallèles et le spectre continu*, C. R. Acad. Sc. Paris **296** (1983).
- [4] I. H. Herron, *The Orr-Sommerfeld equation on infinite intervals*, SIAM review **29** (1987).
- [5] P. Balakumar and M. Malik, *Discrete modes and continuous spectra in supersonic boundary layers*, Journal of Fluid Mechanics **239**, 631 (1992).
- [6] P. J. Schmid and D. S. Henningson, *Stability and Transition in Shear Flows* (Springer Verlag, 2001).
- [7] D. A. Rodríguez, A. Tumin, and V. Theofilis, *Towards the foundation of a global modes concept*, 6th AIAA Theoretical Fluid Mechanics Confer., 1 (2011).
- [8] B. Sandstede and A. Scheel, *Absolute and convective instabilities of waves on unbounded and large bounded domains*, Physica D: Nonlinear Phenomena **145**, 233 (2000).

¹It is conjectured that the pressure effect is triggered by the velocity components having large amplitudes at the outflow boundary, which in itself is induced predominantly by advection.

- [9] T. Kapitula and K. Promislow, *Spectral and dynamical stability of nonlinear waves* (Springer, 2013).
- [10] P. Huerre and P. A. Monkewitz, *Local and global instabilities in spatially developing flows*, Annual Review of Fluid Mechanics **22**, 473 (1990).
- [11] J.-M. Chomaz, *Global instabilities in spatially developing flows: non-normality and nonlinearity*, Annu. Rev. Fluid Mech. **37**, 357 (2005).
- [12] J. C. Buell and P. Huerre, *Inflow/outflow boundary conditions and global dynamics of spatial mixing layers*, in *Proc. 2nd Summer Prog., Stanford Univ. Cent. Turbul. Res.* (1988) pp. 19–27.
- [13] L. Lesshafft, *Artificial eigenmodes in truncated flow domains*, arXiv preprint arXiv:1704.08450 (2017).

ACKNOWLEDGEMENTS

In rethinking who contributed to my PhD project, I should start with the section of aerodynamics in its entirety. During my master thesis project, I practically begged my supervisor for a job as a PhD student. Despite no project nor funding were available in the near future, the section hired me based solely on my performance as a master student. For this trust, really a blind leap of faith, I feel ever indebted to the section.

That brings me to my promotor, dr. *Bas W. van Oudheusden*. As my supervisor for my master thesis project, you convinced the aerodynamics section to take the aforementioned leap of faith in hiring me. For my master thesis project, I brought in my research topic from the Von Kármán Institute (VKI) and you allowed and supported me to keep focusing on it for the entirety of my PhD studies. This gave me an immense feeling of freedom and that acted as a very important driving force during my PhD. On my first working day, I asked if I could help out lecturing the Viscous Flows course. In allowing me to do so, you have helped me to further develop my dream of becoming an experienced lecturer and public speaker. Another beloved element associated to these lectures was our detailed preliminary discussions on the theory. These helped me develop my expertise on the Navier-Stokes equations and their infamously complicated behaviour to such an extent that I can confidently teach it to others. I want to sincerely thank you for the opportunities you gave me, your support and your ever-present listening ear.

When starting my PhD research, I soon ran into some of the hardest mathematical challenges I have ever faced. I could not have tackled these challenges without the help and encouragement of my co-promotor, dr. *Henk M. Schuttelaars*. After being an important advisor for my master thesis project, you were not enrolled into any official function for my PhD project up until the very last week before the submission of this thesis. Despite this, you have been the supervisor I visited most over my project's entire duration and you have had the most dominant impact on my work. Some of our meetings lasted more than 8 uninterrupted hours and I always returned in joy of having advanced my understanding of the problems we discussed. Next to being especially grateful for this, I like to thank you for teaching me the mathematician's over the engineer's way and some key ingredients to being 'the true Dutch scientist:' being assertive, bold, determined, persistent and precise. Most of all, I thank you for guiding me more as a friend than as a supervisor.

Co-promotor dr. *Marios Kotsonis*, you entered my PhD project half-way through; I soon realised I should have worked with you from the very beginning. You gave me the opportunity to deploy my capabilities in developing tools for an industrial company and I feel honoured to have fulfilled that role. Your straightforward view on topics that vary from applied experimental aerodynamics to extremely dense mathematical theories has blown my mind. You are a leader with true authority, while emitting a very accessible and relaxed atmosphere. The support you gave has been an important, necessary ingredient for the development of this thesis, I thank you wholeheartedly for your contribution.

Dr. *Fabio Pinna*, you facilitated my success during my master internship and thesis project, which created the possibility for me to do my PhD research in the same field. You allowed me to further develop and make use of the VKI Extensible Stability and Transition Analysis (VESTA) toolkit and provided my collaborative PhD status at the VKI. This has provided a very fruitful environment for both my PhD and future career. Thank you sincerely for this.

Prof. *Arjen Doelman* and dr. *Vivi Rottschäfer* of the Mathematics Institute in Leiden are acknowledged for their welcome attitude towards my participation in their lectures and seminars and inviting me to present my work at their faculty. It has been very refreshing to share my work with Dutch mathematical minds beyond the borders of a technically oriented university. Furthermore, my brief communication with prof. Björn Sandstede at Brown University in Rhode Island via Arjen, was essential to understanding and synthesising the findings presented in chapter 8.

Prof. *J. L. van Ingen*, thank you for the many fruitful discussions and your elaborations. I feel honoured to have witnessed your devotion; it has inspired me in wanting to become a passionate scientist and teacher. I wish you the best of luck in the developments of the technical problems you are working on.

Next, I extend my thanks to the staff of the high speed laboratory and the faculty of aerospace engineering. Specific persons deserve an elaboration. First and foremost is *Colette J. J. Russo*, I wholeheartedly thank you for solving all kinds of problems, ranging from small matters that Google could not solve to complex logistical conundrums. You are always ready to help, to have in-depth social discussions and you can dispense a well-deserved kicking of the posterior if required. For that, I regard you as a friend. Second, I should mention the night security guard, mr. *Smoor*. This deserves an explanation. In my blind persistence in finishing papers and my thesis (or just my entire PhD), I may have occasionally forgotten that the lab officially closes at 22:00. During my third year, this usually meant that, whenever the building was checked, I was gracefully picked up by the university's version of the ME (the Mobile Entertainment squad) and deposited on the pavement in front of the lab. At that time this was done at sporadic intervals. In my fourth year, I think that security silently conceded in that my persistence could not be tamed; maybe the previously applied methodology was simply too expensive despite its sporadic nature. The measurable result was that, amongst others, mr. Smoor was put on the job at a daily rate. To my joy, mr. Smoor exercised an approach based on solidarity, instead of an agitated one. I thank him for the nightly talks and his unrelentingly friendly escort to the exit. Lastly, I like to thank *Nico van Beek* for his support in regard to my computer hardware.

I like to thank all PhD colleagues in Delft, especially *Beppe Caridi*, *Liesbeth Florentie*, *Paul L. van Gent*, *Valeria Gentile*, *Varun Jain*, *Theo Michelis*, *Mustafa Perçin*, *Alberto F. Rius* and *Wouter Terra*. In particular, I thank you all for being unfailingly relentless in persuading me to join in for lunch, despite my equally relentless dismissal thereof. Amongst these people I like to extend an extra acknowledgement to Theo, Alberto and Varun for their friendship and as excellent training partners in lifting heavy beverages. Furthermore, I like to acknowledge *Tomas Sinnige* for the interesting discussions on the occasional train ride to and from Leiden and *Thea M. J. Vuik* as the steadfast welcoming person during the mathematics seminars given at the faculty of mathematics (EWI).

Lastly, I like to thank all colleagues at the VKI, especially *Florian Danvin*, *Iván Padilla*, *Pedro M. Santos* and *Ludovico Zanus*. Pedro, I thank you sincerely for your friendship, all the times that I could stay over at the White House and, of course, sharing your amazing sense of humour.

Much of my work has been executed in collaboration with my PhD colleagues, who therefore deserve a special acknowledgement. Although not all collaborative work is a part of this thesis, I like to thank everyone I collaborated with here. First of all, *Henry J. Tol*, in our technical discussions on the streamwise BiGlobal stability problem early in my PhD, you convinced me that this problem was actually majestically hard and worth dedicating nearly all my time to. Thank you for being one of the few people who understood the difficulty and made very useful suggestions. This strongly encouraged me in my lonely path to dissecting the mathematical beast. Lastly, thank you for sharing your stability data of the cylinder wake, this was an essential ingredient in our joint paper with Jordi. Second, *Qingqing Ye*, thank you for sharing your tomo-PIV data of the micro-ramp wake, constructively participating in interpreting my results and withstanding my perpetual queries on details of the experiment. Our collaboration convinced me of the promise of applying stability theory to measured base flows. Third, *Jacopo Serpieri*, thank you for sharing your tomo-PIV data of the crossflow vortices. I was exhilarated by the complexity of the case and, as you know, not always equally convinced my methodology would actually work. Thank you for your trust and support, that helped me making it a success. As an extension to that, I like to acknowledge your friendship besides being PhD colleagues. I value your opinion about life and, of course, the serious and, every so often, less serious conversations. Lastly, I like to acknowledge my PhD colleague *Fernando Miró Miró* from the VKI. I feel we became equally great collaborators as friends during my short visit at Texas A&M University. Being an exceptionally constructive critic and very knowledgeable in our field, your presence was essential for the smooth and very swift completion of an impressive piece of (team)work, while having a lot of fun at the same time. I expect that returning to Texas will not be the same.

During the last month of my PhD project, I visited the Computational Stability & Transition (CST) lab of Texas A&M University. I want to wholeheartedly thank prof. *Helen L. Reed* for having me over for my visit and her support over the years, starting at our first encounter during the VKI lecture series in 2014. Furthermore, I want to thank Helen, Fernando, *Ethan S. Beyak*, *Travis S. Kocian*, *Alex J. Moyes*, *Ch. (Daniel) Mullen*, and *Andrew Riha* for their dedication and patience in hearing me out on some of the most complicated matters I have ever tried to convey. This gave me a very strong feeling of solidarity. Chapters 7, 8 and appendix A have been written in devotion to that feeling.

I want to thank my master students: *Fleur J. M. Kessels*, *Nishant Kumar*, *Jelle Y. Boersma*, *Jordi Casacuberta* and *Sébastien E. M. Niessen*. I especially thank you all for persevering in the struggle with my over-engaged tutoring technique. I hope I helped guide you in defining your goals (without bending them completely to my own due to my naive, overwhelming, but mostly blind enthusiasm) and to have encouraged you to become passionate about pursuing your goals. I feel that my interaction with you has led to my best research and has inspired me in wanting to become a passionate teacher. It was a pleasure to be your supervisor, I wish you the best of luck in the future. Fleur, you taught me how to lead a student individually; to discover their personal goals and how to help

accomplish them, thank you for the great experience. Nishant, your work introduced me into the extremely dense mathematics underlying the concept of absolute stability, thanks for giving me a head-start. Jelle, thanks for teaching me the minimal proficiency in programming and for withstanding, though carefully encouraging, atrociously bad puns. Jordi, your stubbornness in finding the complete, unequivocal truth will lead you to greatness in your career. Thank you for the numerous constructive discussions and your seemingly tireless interest in my inexhaustible technical drivel. Sébastien, you showed me that I alone could not solve one of the greatest problems in our field of study. Thanks for trusting me and enduring in the wild jungle of complex integration theory.

In the similar vein, I like to thank the VKI internship students *Fabio Naddei* and *Alfonzina Esposito*. My involvement was only brief, but it was a pleasure to collaborate.

Friends and family have had an important contribution to the completion of my PhD.

Gabriel D. Maher, it is, in a way, cruel how some of your best friends can be so close while not knowing about it (our bachelor studies) and so far when you do know about it (our PhD studies). I am really grateful for how our friendship thrived during our master studies, for it strongly contributed to the foundations of who I am today. For example, we were roommates during our internship at the VKI. You were there and supported me during my kick-off in the field of flow stability theory; that I stuck with from the summer of 2012 onwards. As another example, the care for your mother Annelies and brother Sebastiaan is inspiring to me. Visiting you and your family has always been a heart-warming experience. I hope we can keep steadily advancing our progress (“bliven shinen”) at ‘Shining in the Darkness.’ We are of like minds in regard to a social and analytical perspective, but also dedicatedly balanced in terms of humour and empathy. The ease of having deep conversations and your accompanying understanding, makes you are like a brother to me.

Michael Hameleers and *Gijs Beets*, ever since our pre-university education, your friendship has been something I could always rely upon in my life. I am very grateful to have been in touch so often with you, even after going to different universities. You are integral contributors to who I am in life, having developed in me my confidence, stoic nature and, maybe most of all, my humour. While pursuing my academic dream abroad, I am really going to miss our frequent meetings, the unwithstandably wrong, worthless and wrath-inspiring word-witticism, the infamously villainous and ever-unfailingly virtuous film ‘cascade’ charades and, of course, to conquer the harder escape rooms. Michael, I look up to you for what you have accomplished. You are my example for how I want to manage my academic career, but also my relationships and further personal life. Thank you for always having been there for me, in the good times and the bad. Gijs, I highly respect your strong commitment to your passions in life and that you have always been exactly who you are. Seeing how you live your life with Franscina is endearing. Thank you for being such a sincere friend.

V. Thys Metz, we met each other in the competition for a room at the Van Hasseltlaan and we each got admitted to one. Moving into that place signified the start of my student life in Delft. I realise just now that the room facilitating my PhD defence, the end of my studies in Delft, is named after the same person, J. B. Frans van Hasselt. Your presence back then was essential, for you single-handedly made my aerospace bachelor

freshman year an insanely cool and unforgettable experience. You principally inspired me to teach; I can vividly remember that intense ad-hoc session in the library, in which we contemplated the rules of trigonometry. I highly value your endless supply of beautifully practical technical stories. Thank you for your invaluable contributions to making me who I am, pointing me to the vacant room in the Kloksteeg and being a friend who I can always count on during bad times.

Mark van Doorne, our friendship is proof of that becoming good friends does not require a common occupation. After first meeting at the aerospace bachelor freshmen weekend, our then shared paths soon bifurcated, but that did not stand in our companionship's way. The quality of meeting up with you always made up for its infrequency. I value your broad technical knowledge and your talent in finding the true cause of a problem over the one that is spelled out, which always yields the most interesting stories and discussions. To find the true cause of a problem, I feel you view the world from an unbiased supervisory perspective. I think this may be one of the most important virtues to become a prominent scientist. Thanks for teaching me that.

Jan F. G. Schneiders, you are without a doubt one of my best friends I made during my studies. We met at the very first possible study-related occasion; the group introduction for the first-year bachelor project. Although the paths we took have occasionally been very different, I feel our goals were always very strongly alike and that made us gravitate towards each other. We both had an urge to become the very best in—what we thought was—the topic that at least provided most challenge in terms of technical difficulty. In recognising that, people have (quite sporadically) called us ‘the terrible two’. As opposed to a possibly expected competition, for me this situation created the feeling that I always had someone to lean on, even while we can disagree very strongly at times. You have an unfailing talent in keeping group conversations interesting and even more so in getting unforgettable parties started. Thank you for your critical intellectual support and your unwavering friendship.

This brings me to one of the both most intellectually and at the same time most recreationally pleasing companies, the ‘PhD party group’, consistent of the PhD colleagues Jan, *Rogier H. M. Giepman*, *Kyle P. Lynch* and *Wouter C. P. van der Velden*. Some reminiscent events that deserve mention are the numerous drinks and parties in places like Utrecht, Den Bosch, Rotterdam (viz. bingo at Paddy Murphy’s) and The Hague, a holiday in Florida and attending Oktoberfest in Munich. Rogier, I am honoured to have acted as a master of ceremonies for your wedding. Thanks for the many meaningful conversations on technical or personal topics, I highly appreciate the dedicated care and sincerity that you emit. Kyle, thanks for organising that one barbecue in April 2015, for conspiring in the ‘Jerry = Valentijn’-debacle and your steadfast ability to do the Utrecht challenge, i.e. to bridge the gap over which no trains return to Delft or Leiden. Wouter, thanks for sharing your Hyatt room in June 2018, for having great discussions and sharing your view on relationships.

I like to acknowledge the members of Coon & Friends, especially: Gabriel, Jan, *Darun Barazanchy*, *Julius Berens*, *Rijk de Rooij* and *Ruben Sevenois*. They are lasting friends originating from our aerospace master studies, who never shy back from a good conversation or having a fun time together. First, I should thank them for calling the group Coon & Friends regardless of my opinion or approval, as a reference to one of my favourite

TV series. The principal reason for their acknowledgement, however, is having given me a copy of the book of Kapitula & Promislow as an aptly chosen present for my master degree graduation. While the book seemed interesting in a circumstantial way at first only, it turned out to be extremely important for understanding the concept of absolute and essential spectra and the associated theorems, as the many citations in chapters 7 and 8 show. In turn, this was quintessential for advancing our knowledge of the behaviour of spectra in the perspective of the field of flow stability theory. Thanks Friends!

From December 2014 to April 2016, I moved into my room at the Kloksteeg in Delft. I must acknowledge this place and its occupants, *Jos Aalbers, Floor Rosman, Daniël Prins, Ivo Gels, Stephan Jacobs* and, undeniably, *Michelle Warboult*, for one of the most amazingly fun periods during my PhD. Michelle, thank you for bringing sunshine into my life.

Vera M. J. Bakker, thanks for having been my dance partner; dancing was a very necessary distraction from work. I value our conversations ranging from technicalities in aircraft maintenance to discussions on relationships.

Marjolein Mol, thanks for being an excellent sparring partner when it comes down to difficult moral questions, even after not having met for about 9 years. I highly appreciate your friendship and teaching me that being myself is a difficult task in itself, that has been an essential lesson in my path to becoming a scientist.

Mam, pap, Crystel, Jan, Germaine, Gerard & Gees, you gave me the strength to feel capable of tackling the hardest of problems. Your support has been quintessential in completing this document. Mam, you taught me to fight for my passion, to communicate emphatically with others and to listen to my superiors, but listen to my inferiors even more closely. During the tedious concluding months of my PhD, I called you on a daily basis. That kept me sane and helped me push through to the end. Pap, you inspired me to work as hard as I can to accomplish my goals and it is through your warm support and encouragement that I want to succeed. You taught me how to make my own abstraction models and solve problems accordingly. I remember the specific ‘click’; it involved converting various units in secondary school, e.g. m^2 to dm^2 . My joy in further exploiting my abstract intuition has been a defining factor in having performed this work in the first place. Pap & mam, you each taught me important things, abstract problem solving and to fight for and communicate my passion, respectively. It is the combination of these things, your combined effort, that has enabled me to complete this document. I am so proud to honour you through these virtues. Crystel, my dear sister and paronymph. Although I do not show this regularly, my love for you is, as the mathematicians would say, unbounded in magnitude. With you, I can discuss anything without ever feeling judged and you are one of the few people I feel completely and unconditionally at ease and at home with. I highly value your opinion and your view of life. For these reasons, you are the best friend I have. Germaine, you strongly inspire me to play and enjoy music, but maybe most of all: to passionately present (myself) confidently at any time. Gees, your view on life humbles and refreshes me every time we meet. Thank you for your advice in life and being like a second mom to me.

Katelynn L. Alcorn, you make my life as a PhD student conclude with a bang. Thanks for giving me much more than my academic life to look forward to across the pond.

CURRICULUM VITÆ

Koen Jasper Groot was born on July 20th, 1990 in Hoorn, Noord-Holland in the Netherlands. He obtained his Bachelor of Science degree in Aerospace Engineering at Delft University of Technology (TUD) in July 2010 and thereafter continued the Master of Science (MSc) studies at the same faculty, focussing on aerodynamics. During the summer of 2012, he completed an internship at the Von Kármán Institute (VKI) for Fluid Dynamics under dr. Fabio Pinna. This work involved the development of the automatic derivation tool in VESTA, the VKI Extensible Stability and Transition Analysis toolkit and resulted in the technical report entitled ‘Error Free Derivation of Parabolised Stability Equations’. He continued his master thesis project on the same topic at Delft University of Technology under dr. Fabio Pinna and dr. Bas W. van Oudheusden (Aerospace Engineering, TUD). This work entailed developing the BiGlobal stability framework in VESTA, resulting in the MSc thesis entitled ‘Derivation of and Simulations with BiGlobal Stability Equations’. The high quality of the work was awarded the highest possible grade, 10/10, and nominated for the NVvL & KIVI NIRIA best aerospace thesis award. In August 2013, he obtained his MSc degree with Honours, recording a general point average of 9.2/10.

In November 2013, he continued his MSc studies as his PhD research at Delft University of Technology, under the supervision of dr. Henk Schuttelaars (Electrotechnics, Mathematics & Computer Science, TUD), dr. Marios Kotsonis (Aerospace Engineering, TUD) and dr. Bas W. van Oudheusden. He moreover attained the status of collaborative PhD at the VKI under dr. Fabio Pinna. The research concerned the BiGlobal stability framework from two perspectives: its practical application to experimentally measured base flows and the advancement of the understanding of the numerical problems encountered when deploying the method in the streamwise direction; the results are included in this thesis. In January 2017, he won the AIAA SciTech & Aviation best paper award for the paper entitled ‘Secondary Stability Analysis of Crossflow Vortices using BiGlobal Theory on PIV Base Flows’, corresponding to chapter 6 of this thesis. In the summer of 2016, he developed the boundary layer and stability tools for Embraer.

From the first month of employment as a PhD student, he lectured and modernised the course ‘Viscous Flows’, treating the derivation of the Navier-Stokes equations, stability theory and turbulence. From the third year onwards, his enthusiasm in presenting the course culminated in performing half the lectures ($8 \times 2 \times 45$ min.). To emphasize his love for the practice of lecturing, he performed the course the year after the termination of his contract as a PhD student voluntarily.

LIST OF PUBLICATIONS

5. **K.J. Groot**, J. Serpieri, F. Pinna & M. Kotsonis, *Secondary crossflow instability through global analysis of measured base flows*, *Journal of Fluid Mechanics* **846**, 605–653 (2018).
4. **K.J. Groot**, J. Serpieri, M. Kotsonis & F. Pinna, *Secondary Stability Analysis of Crossflow Vortices using BiGlobal Theory on PIV Base Flows*, *AIAA Aerospace Sciences Meeting* **55**, 1880 (2017).
3. **K.J. Groot**, Q. Ye, B.W. van Oudheusden, Y. Zhang & F. Pinna, *BiGlobal Stability Analysis of a Micro-Ramp Wake using PIV Base Flows*, *AIAA Fluid Dynamics Conference* **46**, 4383 (2016).
2. **K.J. Groot**, F. Pinna & B.W. van Oudheusden, *On Closing the Streamwise BiGlobal Stability Problem: The Effect of Boundary Conditions*, *Procedia IUTAM* **14**, 459–468 (2015).
1. F. Pinna & **K.J. Groot**, *Automatic Derivation of Stability Equations in Arbitrary Coordinates and for Different Flow Regimes*, *AIAA Fluid Dynamics Conference* **44**, 2634 (2014).



ISBN: 978-94-6366-115-7